The Dissertation Committee for Taichiro Okazaki Certifies that this is the approved version of the following dissertation:

SEISMIC PERFORMANCE OF LINK-TO-COLUMN CONNECTIONS IN STEEL ECCENTRICALLY BRACED FRAMES

Committee:

Michael D. Engelhardt, Supervisor

Eric B. Becker

Karl H. Frank

Sharon L. Wood

Joseph A. Yura

SEISMIC PERFORMANCE OF LINK-TO-COLUMN CONNECTIONS IN STEEL ECCENTRICALLY BRACED FRAMES

by

Taichiro Okazaki, BE, ME, MA

Dissertation

Presented to the Faculty of the Graduate School of
The University of Texas at Austin
in Partial Fulfillment
of the Requirements
for the Degree of

DOCTOR OF PHILOSOPHY

The University of Texas at Austin
December, 2004

Dedication

To My Family

Acknowledgements

The financial support for this research was provided by the National Science Foundation (Grant No. CMS-0000031) and the American Institute of Steel Construction.

I would like to express my most sincere gratitude to Dr. Michael Engelhardt for his guidance, support, patience, and encouragement during the course of this research. I would like to thank Dr. Eric Becker, Dr. Karl Frank, Dr. Sharon Wood, and Dr. Joseph Yura for serving on my dissertation committee. Special appreciation is addressed to Dr. Masayoshi Nakashima, Dr. Keiichiro Suita, and Dr. Taijiro Nonaka for their encouragement and kindness over many, many years.

I cannot thank enough for the devoted effort made by the staff of the Phil M. Ferguson Structural Engineering Laboratory at the University of Texas at Austin, Mike Bell, Dennis Phillip, and Blake Stasney. Master's students Gabriela Arce and Pedro Galvez, and undergraduate students Joe Fleishman, Ian Delahunty, and Omar Garza contributed significantly to the required manual labor. The careful workmanship of Dwayne Schuessler and Tim Wharton is gratefully appreciated.

I owe the completion of this research to my friends and colleagues who provided confidence in me when I seriously lacked it.

I thank George Lucas for giving me a reason to come to the United States.

This dissertation is dedicated to my parents, Takeshi and Kazuko Okazaki, for their unconditional love and support.

Austin, Texas, December 2004
Taichiro Okazaki

SEISMIC PERFORMANCE OF LINK-TO-COLUMN CONNECTIONS IN STEEL ECCENTRICALLY BRACED FRAMES

Publication No._____________

Taichiro Okazaki, Ph.D.
The University of Texas at Austin, 2004

Supervisor: Michael D. Engelhardt

This dissertation describes a research program on the seismic performance of link-to-column connections in steel eccentrically braced frames (EBFs). Since the 1970's, EBFs have been accepted as a high performing steel building system for seismic regions. Many of the same design, detailing, and construction features that contributed to the widespread damage in welded moment connections in the 1994 Northridge Earthquake are present in link-to-column connections in EBFs. However, little research has previously been conducted on link-to-column connections. The research program combined an experimental investigation involving large-scale cyclic loading tests, and an analytical study including detailed finite element simulations to study link-to-column connections. A total of sixteen large-scale link-column specimens were tested in the experimental study. Four different connection types with varying configuration and welding details were tested. Each of the four connection types was tested with a variety of link lengths to consider a wide range of force and deformation environment at the link-to-column connection. The specimens representing the pre-Northridge practice failed after developing only half of the inelastic link rotation required in the building code provisions. Implementing improvements in welding was beneficial, but this alone was not nearly sufficient to improve the connection performance to the required level. Improved connection details developed for moment connections did not necessarily provide good performance for link-to-column connections. The force and deformation demand at EBF link-to-column connections were found to be significantly more severe than at moment connections. The local stress and strain environment predicted by finite element simulations correlated well with the fracture behavior observed in the test specimens. The finite element simulations also agreed with the experimental observations in that fracture of the link flange near the groove weld connecting to the column flange is a major concern for links of all practical lengths. The findings from this research suggest that until further research is available, EBF arrangements with links attached to columns should be avoided.

Table of Contents

List of Tables xvii

List of Figures.. xviii

CHAPTER 1 Introduction 1

1.1 General...1

1.2 Objectives of Research 4

1.3 Outline of Dissertation...5

CHAPTER 2 Background...7

2.1 Overview..7

2.2 Eccentrically Braced Frames (EBFs)..8

2.2.1 Introduction..8

2.2.2 Overall Behavior..13

2.2.3 Design Procedure 15

2.2.4 Ductile Behavior of Links...17

2.2.5 Link Strength 22

2.2.6 Unequal End Moments and Axial Forces 27

2.2.7 Composite Slabs and Lateral Stability.....................................29

2.2.8 Brace Connection Panel and Brace-to-Link Connection..........30

2.3 Recent Research on EBF Links 32

2.3.1 General..32

2.3.2 Behavior of EBF Links Tested by Arce....................................32

2.3.3 Link Web Fracture 37

2.3.3.1 Stiffener Spacing..38

2.3.3.2 k-area Properties 40

2.3.3.3 Cyclic Loading Protocol 43

2.3.4 Link Performance under the Revised Loading Protocol..........44

2.3.5 Comparison with Earlier Tests...48

2.3.5.1 Inelastic Rotation Capacity 48

2.3.5.2 Link Overstrength 50

2.4 Moment Connections in MRFs 51

2.4.1 Damage during the Northridge Earthquake 51

2.4.2 Welding Quality 54

2.4.2.1 Weld Metal 54

2.4.2.2 Welding and Inspection Practices 55

2.4.2.3 Welding Details 56

2.4.2.4 Effect of Welding Improvements 57

2.4.3 New Connections Developed After the Northridge Earthquake... 58

2.4.3.1 Problems Inherent to the Pre-Northridge Configuration 58

2.4.3.2 Reinforced Connections 59

2.4.3.3 Reduced Beam Section 63

2.4.3.4 Unreinforced Connections 66

2.4.3.5 Free-Flange Connection 68

2.4.3.6 Other Connections 69

2.4.4 Other Key Issues 69

2.4.4.1 Qualifying Tests 69

2.4.4.2 Span-to-Beam Depth 71

2.4.4.3 Panel Zone Strength 71

2.4.4.4 Continuity Plates 73

2.4.4.5 Web Connection 73

2.4.4.6 Composite Floor Slab 73

2.4.4.7 Material 75

2.4.4.8 Beam Section Size 76

2.4.4.9 Deep Columns 76

2.4.4.10 Loading Rate 77

2.5 Japanese Moment connections 78

2.5.1 Japanese Design and Construction 78

2.5.2 Damages Observed After the Kobe Earthquake 80

2.5.3 Improved-Weld-Access-Hole and No-Weld-Access-Hole Connections....81
  2.5.4 Other New Connections....83
  2.5.5 Other Key Issues....84
    2.5.5.1 Dynamic Loading....84
    2.5.5.2 Runoff Tabs....85
  2.5.6 RBS Connection versus No Weld Access Hole Connection....85
2.6 Link-to-Column connections....87
  2.6.1 General....87
  2.6.2 Force and Deformation Demands at EBF link-to-Column Connections....87
  2.6.3 Link-to-Column Connections Prior to the Northridge Earthquake....89
  2.6.4 Post-Northridge Studies....92
  2.6.5 Code Requirements....93
2.7 Discussion....94
  2.7.1 Link Length....94
  2.7.2 Link Section....95
  2.7.3 EBF Arrangement....98
  2.7.4 Welding Details....102
  2.7.5 Connection Details....103
    2.7.5.1 Reduced Beam Section....103
    2.7.5.2 Reinforced Connections....106
    2.7.5.3 Unreinforced Connection....109
    2.7.5.4 Free Flange Connection....109
    2.7.5.5 No Weld Access Hole Connection....110
    2.7.5.6 Bolted Connections....111
    2.7.5.7 Other Connections....112
    2.7.5.8 Connections Selected for Investigation....113
  2.7.6 Loading Protocol....114
  2.7.7 Other Factors....115
    2.7.7.1 Dynamic Loading....115

2.7.7.2 Composite Slabs..115
2.7.7.3 Panel Zone Strength..116
2.7.8 Summary..116

CHAPTER 3 Test Program 118

3.1 Introduction..118
3.2 Test Plan...119
3.2.1 Test Setup..119
3.2.2 Test Specimen..127
3.2.3 Loading Sequence..133
3.2.4 Instrumentation..135
3.2.5 Data Reduction..140
3.2.6 Evaluation Criteria...146
3.3 Materials 147
3.3.1 General..147
3.3.2 Hardness Tests 147
3.3.3 Tension Coupon Tests..150
3.3.4 Weld Metal CVN Tests..153
3.4 Design Details and Fabrication Procedures of Specimens 157
3.4.1 General..157
3.4.2 PN-Specimens..158
3.4.3 MW-Specimens..161
3.4.4 FF-Specimens 164
3.4.5 NA-Specimens 167

CHAPTER 4 Test Results 180

4.1 Introduction..180
4.2 PN-specimens 182
4.2.1 Specimen PNS 183
4.2.2 Specimen PNI 185
4.2.3 Specimen PNM..188
4.2.4 Discussion of PN-specimens...189

4.3 MW-specimens 193
  4.3.1 Specimen MWS 193
  4.3.2 Specimen MWI 195
  4.3.3 Specimen MWM 198
  4.3.4 Discussion of MW-specimens 199
4.4 FF-specimens 201
  4.4.1 Specimen FFS 202
  4.4.2 Specimen FFI 204
  4.4.3 Specimen FFM 206
  4.4.4 Specimen FFS-RLP 208
  4.4.5 Specimen FFSL-RLP 210
  4.4.6 Discussion of FF-specimens 211
4.5 NA-specimens 215
  4.5.1 Specimen NAS 216
  4.5.2 Specimen NAI 218
  4.5.3 Specimen NAM 220
  4.5.4 Specimen NAS-RLP 221
  4.5.5 Specimen NASL-RLP 223
  4.5.6 Discussion of NA-specimens 224
4.6 Discussion of Test Results 228
  4.6.1 Overview 228
  4.6.2 Connection Type 229
  4.6.3 Link Length 233
  4.6.4 Loading Sequence 237
  4.6.5 Failure Modes 239
    4.6.5.1 Dominant Failure Modes 239
    4.6.5.2 Fracture of Link Flange 239
    4.6.5.3 Fracture of Link Web at the Stiffener Welds............241
    4.6.5.4 Failure Modes Unique to FF-Connections................242
  4.6.6 Additional Comments 243
4.7 Summary 244

CHAPTER 5 Further Discussion of Test Results 321

5.1 Introduction...321
5.2 Evaluation of Test Setup..321
5.2.1 Initial Elastic Response...321
5.2.2 Beam End of the Link...323
5.2.3 Rigid-Plastic Mechanisms 325
5.3 Alternative Measures of Performance 329
5.3.1 General..329
5.3.2 Dissipated Energy 329
5.3.3 Skeleton Curve...334
5.3.4 Cumulative Inelastic Rotation...............................342
5.3.5 Discussion 346
5.4 Link Forces 348
5.4.1 Maximum Link Forces...348
5.4.2 Link Overstrength 351
5.4.3 Moment-Shear Interaction 352
5.4.4 Moment Redistribution 359
5.5 Fracture Surface Examination...366
5.5.1 PN-Connections 366
5.5.2 MW-Connections...367
5.5.3 FF-Connections..369
5.5.4 NA-Connections 370
5.5.5 Further Discussions..371
5.5.6 Hardness Measurements near the Fusion Line 379
5.6 Strain Gauge Data 383
5.6.1 Longitudinal Strain History 383
5.6.2 Shear Strain History...385
5.6.3 Longitudinal Strain Distribution in Link Flange 387
5.6.4 Strain Distribution through Thickness of Link Flange 389
5.7 Panel Zone Deformation and Panel Zone Strength............................392

5.7.1 Test Data 392

5.7.2 Discussion 394

5.8 Summary 398

CHAPTER 6 Finite Element Simulation of Link-to-Column Connections..... 403

6.1 Overview 403

6.2 Description of The Finite Element Analyses 404

6.2.1 Finite Element Models 404

6.2.2 Nonlinear Analysis 409

6.2.3 Material Model Verification 412

6.3 Global Model Analysis 415

6.3.1 Global Response 415

6.3.2 Link Deformation 416

6.3.3 Global Model Analysis Results 426

6.4 Submodeling Analysis and Sampling Method 435

6.4.1 Submodeling Analysis 435

6.4.2 Validity of Submodeling Analysis 437

6.4.3 Identification of Critical Locations 437

6.4.4 Stress and Strain near Link Flange Groove Weld 441

6.4.5 Sampling Method 444

6.5 Simulation and Observed Fracture Behavior 449

6.5.1 Effect of Link Length on MW-Models 449

6.5.2 Link Flange-Groove Weld Interface 456

6.5.3 Link Web and Shear Tab Groove Weld in FF-Models 462

6.5.4 Model NAS and Model NASL 465

6.5.5 Correlation with Observed Fracture Behavior 467

6.5.6 Limitations of the Finite Element Simulations 470

6.6 Panel Zone Strength 473

6.6.1 Yielding Mechanism 473

6.6.2 Response of Link-Column Subassemblage 479

6.6.3 Local Stress and Strain Environment 483

6.6.4 Discussion 487
6.7 Summary 488

CHAPTER 7 Summary and Conclusions 491

7.1 Summary 491
7.1.1 Literature Review and Synthesis 491
7.1.2 Experimental Study 491
7.1.3 Finite Element Simulation 492
7.2 Results and Design Implications 493
7.3 Recommendations for Future Research 499

APPENDIX A End Plate Welds 502

A.1 General 502
A.2 Failures Observed by Arce (2002) 503
A.2.1 Specimens 1A, 1B and 1C 503
A.2.2 Specimens 6A and 6B 506
A.2.3 Discussion 507
A.3 End Plate Welds in Other Tests 510
A.4 Welding Procedure Used for End Plate Welds 510

APPENDIX B Tension Coupon Test Summary 515

B.1 General 515
B.2 Certified Mill Test Report 515
B.3 Measured Tension Properties 515

APPENDIX C Certified Mill Test Reports 516

APPENDIX D Charpy V-Notch Test Reports 521

APPENDIX E Welding Procedures 524

E.1 General 524
E.2 Specified Procedures 524
E.3 Welding Records 549
E.3.1 Notes on actual procedures 549
E.3.2 Tack weld location 556

E.3.3 Weld repair 557

APPENDIX F Ultrasonic Testing Inspection Reports................................558

APPENDIX G Strain Gauge Data...577

References..606

Vita 621

List of Tables

Table 3.1: Test matrix 127
Table 3.2: Specimen summary..128
Table 3.3: Cyclic loading protocol..134
Table 3.4: Dimensions of link and column sections 147
Table 3.5: Tension test results..152
Table 3.6: Section properties...153
Table 4.1: Summary of test results..249
Table 4.2: Connection forces 250
Table 4.3: Key observations..251
Table 5.1: Elastic Response 322
Table 5.2: Alternative measures of connection performance..........................330
Table 5.3: Normalized maximum link forces 349
Table 5.4: Normalized maximum moment 350
Table B1: W18x40 Tension Coupon test results 516
Table B2: W12x120 Tension Coupon test results 516
Table E1: Summary of Welding Procedures 525
Table E2: Welding records for link flange CJP groove welds 550
Table E3: Welding records for link web CJP groove welds...........................551
Table G1: Summary of Strain Gauge Hysteresis Data 578

List of Figures

Figure 1.1: Example of recently constructed EBF 2

Figure 1.2: Example of link-to-column connection 2

Figure 2.1: Typical EBF arrangements 8

Figure 2.2: Typical force distribution in an EBF 10

Figure 2.3: Free body diagram of link..11

Figure 2.4: Energy dissipation mechanisms...12

Figure 2.5: Link rotation capacity 20

Figure 2.6: Link overstrength...24

Figure 2.7: Link maximum shear strength 26

Figure 2.8: Test results from Arce (2002) and Ryu *et al.* (2004).......................33

Figure 2.9: Specimen 4B after test (Arce 2002)...35

Figure 2.10: Termination of link stiffener welds in Specimens 4A, 4B, and 4C ..36

Figure 2.11: Fracture initiation in link web of Specimen 4A-RLP (Ryu *et al.* 2004) 37

Figure 2.12: K-area of a wide flange section (2002 AISC Seismic Provisions)...42

Figure 2.13: Effect of loading protocol on link performance...............................46

Figure 2.14: Pre-Northridge detail 52

Figure 2.15: Examples of connection reinforcement 60

Figure 2.16: Examples of reduced beam sections 64

Figure 2.17: Prequalified RBS design (from Engelhardt *et al.* 1998)..................65

Figure 2.18: Free flange connection (from Choi *et al.* 2003)...............................68

Figure 2.19: Through diaphragm connection 79

Figure 2.20: Pre-Northridge connections 91

Figure 2.21: Non-dimensional link length factor 96

Figure 2.22: Isolated link model..98

Figure 2.23: End moment ratios estimated from elastic frame analyses. 100

Figure 2.24: RBS applied to intermediate links of e = $2M_p/V_p$..........................105

Figure 2.25: Example of EBF link-to-column connection reinforced with coverplates. 108

Figure 3.1: Loading system 120

Figure 3.2: Details of the loading system 121

Figure 3.3: Lateral bracing system 122

Figure 3.4: Overall view of the test setup (Before testing Specimen PNI) 122

Figure 3.5: Link force distribution 123

Figure 3.6: Arrangement of loading system with different link lengths 125

Figure 3.7: Example of test specimen. Specimen PNI is shown 129

Figure 3.8: Example of links 130

Figure 3.9: Connection at link end-plate 132

Figure 3.10: Location of displacement and rotation transducers 137

Figure 3.11: Strain gauge location for MWS 139

Figure 3.12: Data reduction to evaluate internal forces 142

Figure 3.13: Data reduction to evaluate deformations 144

Figure 3.14: Hardness test results...148

Figure 3.15: Distribution of hardness in W18x40 section..................................149

Figure 3.16: Tension coupon locations 151

Figure 3.17: Stress-strain curves for W18x40 section..152

Figure 3.18: CVN Coupons sampling scheme 155

Figure 3.19: CVN test results 156

Figure 3.20: PN-connection..170
Figure 3.21: MW-connection 171
Figure 3.22: Connection FFS 172
Figure 3.23: Connections FFI and FFM...173
Figure 3.24: Connections FFS-RLP and FFSL-RLP..................................174
Figure 3.25: NA-connection..175
Figure 3.26: Weld access hole and flange bevel 176
Figure 3.27: Weld wrapping around corners of shear tab 178
Figure 3.28: Backing bars used for NA-connections 179
Figure 4.1: Specimen PNI: Connection before testing..............................253
Figure 4.2: Response of Specimen PNS...254
Figure 4.3: Photographs of Specimen PNS 256
Figure 4.4: Response of Specimen PNI..258
Figure 4.5: Photographs of Specimen PNI 260
Figure 4.6: Response of Specimen PNM 262
Figure 4.7: Photographs of Specimen PNM. 264
Figure 4.8: Specimen MWM: Connection before testing 265
Figure 4.9: Response of Specimen MWS..266
Figure 4.10: Photographs of Specimen MWS 268
Figure 4.11: Response of Specimen MWI 270
Figure 4.12: Photographs from MWI 272
Figure 4.13: Response of Specimen MWM 274
Figure 4.14: Photographs of Specimen MWM..276
Figure 4.15: Specimen FFI before testing 277
Figure 4.16: Specimen FFS-RLP: Connection before testing....................278

Figure 4.17: Response of Specimen FFS 279
Figure 4.18: Photographs of Specimen FFS..281
Figure 4.19: Response of Specimen FFI 283
Figure 4.20: Photographs of Specimen FFI..285
Figure 4.21: Response of Specimen FFM 287
Figure 4.22: Photographs of Specimen FFM 289
Figure 4.23: Response of Specimen FFS-RLP..291
Figure 4.24: Photographs of Specimen FFS-RLP 293
Figure 4.25: Response of Specimen FFSL-RLP 295
Figure 4.26: Photographs of Specimen FFSL-RLP..297
Figure 4.27: NA-Connection before testing 299
Figure 4.28: Response of Specimen NAS 300
Figure 4.29: Photographs of Specimen NAS 302
Figure 4.30: Response of Specimen NAI 304
Figure 4.31: Photographs of Specimen NAI 306
Figure 4.32: Response of Specimen NAM..308
Figure 4.33: Photographs of Specimen NAM 310
Figure 4.34: Response of Specimen NAS-RLP 312
Figure 4.35: Photographs of Specimen NAS-RLP..314
Figure 4.36: Response of Specimen NASL-RLP 316
Figure 4.37: Photographs of Specimen NASL-RLP 318
Figure 4.38: Link Rotation Capacity 320
Figure 5.1: Energy dissipation mechanisms of link-column specimen.............326
Figure 5.2: Inelastic link rotation capacity versus dissipated energy...............331
Figure 5.3: Inelastic link rotation vs. dissipated energy...................................332

Figure 5.4: Dissipated energy..334
Figure 5.5: Skeleton curve constructed for Specimen MWI. 336
Figure 5.6: Positive skeleton curves for specimens with I-links.......................336
Figure 5.7: Inelastic skeleton rotation vs. maximum link shear........................337
Figure 5.8: Inelastic link rotation vs. inelastic skeleton rotation.......................340
Figure 5.9: Inelastic skeleton rotation 340
Figure 5.10: Skeleton energy and Bauschinger energy.......................................341
Figure 5.11: Computation of cumulative inelastic rotation................................343
Figure 5.12: Inelastic link rotation vs. cumulative inelastic link rotation...........343
Figure 5.13: Cumulative inelastic link rotation vs. dissipated energy 344
Figure 5.14: Cumulative inelastic rotation...345
Figure 5.15: Shear force vs. column face moment...354
Figure 5.16: Detailed behavior of Specimen NAS...357
Figure 5.17: Moment redistribution 361
Figure 5.18: Photographs of fracture surfaces of PN-connections.....................373
Figure 5.19: Photographs of fracture surfaces of MW-connections...................375
Figure 5.20: Photographs of fracture surfaces of FF-connections 377
Figure 5.21: Photographs of fracture surfaces of NA-connections.....................378
Figure 5.22: Vickers hardness test results of CJP groove welds.........................380
Figure 5.23: Longitudinal strain history...384
Figure 5.24: Longitudinal strain history in Specimens MWS.............................385
Figure 5.25: Shear strain history in Specimen MWS...386
Figure 5.26: Strain distribution along link longitudinal direction in link flange 388
Figure 5.27: Strain distribution along width of flange 390

Figure 5.28: Panel zone deformation vs. column face moment 396

Figure 5.29: Panel zone deformation vs. link shear 397

Figure 6.1: Global model for Specimen MWI and enlarged view of joint region 405

Figure 6.2: Boundary and loading conditions 407

Figure 6.3: Submodel for Specimen MWI 408

Figure 6.4: Material models 410

Figure 6.5: Command lines for material properties 411

Figure 6.6: Tension coupon model...413

Figure 6.7: Comparison of stress-strain relationships......................................413

Figure 6.8: Simulated loading curve vs. skeleton curves.................................417

Figure 6.9: Comparison of link deformation in Specimen FFS 423

Figure 6.10: Comparison of link deformation in Specimen NAM.....................424

Figure 6.11: Simulated link deformation...427

Figure 6.12: Link deformation in Models FFS and FFS-RLP............................434

Figure 6.13: Link in global model and submodel..436

Figure 6.14: Check of driving boundaries in submodel 438

Figure 6.15: Mises stress distribution in global model and submodel 439

Figure 6.16: Discontinuities in Mises stress..440

Figure 6.17: Comparison between global model and submodel 442

Figure 6.18: Sampling points near link flange groove weld 445

Figure 6.19: Sampling points near link web groove weld..................................446

Figure 6.20: Stress-strain relationship measured at sampling point...................448

Figure 6.21: Effect of link length on the link flange-groove weld interface.......450

Figure 6.22: Stress and strain distribution along thickness of link flange..........453

Figure 6.23: Principal stress distribution near link flange-groove weld interface 453
Figure 6.24: Effect of link length on the link web-groove weld interface 455
Figure 6.25: Link flange-groove weld interface in S-links 457
Figure 6.26: Link flange-groove weld interface in I-links 459
Figure 6.27: Link flange-groove weld interface in M-links 460
Figure 6.28: Link flange-groove weld interface at moment connections............461
Figure 6.29: Link web-groove weld interface in FF-models..............................463
Figure 6.30: Shear tab-groove weld interface in FF-models..............................464
Figure 6.31: Comparison between Model NAS and Model NASL-RLP 466
Figure 6.32: Panel zone strength and link deformation......................................474
Figure 6.33: Contribution of panel zone deformation 478
Figure 6.34: Column face moment vs. panel zone deformation..........................479
Figure 6.35: Effect of weak panel zone on response of link-column assemblage 480
Figure 6.36: Effect of weak panel zone on link flange weld interface...............485
Figure 6.37: Effect of weak panel zone in link web weld interface 486
Figure A1: Fracture in Specimen 1A 504
Figure A2: Fracture in Specimen 1B..505
Figure A3: Fillet weld made for Specimen 1C...506
Figure A4: Fracture in Specimen 6A 508
Figure A5: Specimen 6B after test 508
Figure A6: Typical end plate weld (Specimen PNI) 512
Figure A7: Schematic view of end plate fillet weld..512

Figure E1: Specified welding procedures for continuity plates in PN- (and MW-) Specimens 526
Figure E2: Specified welding procedures for continuity plates in FF- and NA- Specimens 529
Figure E3: Shear tab welds for PN-connection..532
Figure E4: Shear tab welds for MW-connection 533
Figure E5: Shear tab welds for FF-connection 534
Figure E6: Link-to-column connection welds in PN-connection 536
Figure E7: Link-to-column connection welds in MW-connection 540
Figure E8: Link-to-column connection welds in FF-connection......................545
Figure E9: Link-to-column connection welds in NA-connection.....................547
Figure E10: Weld Profile 553
Figure E11: Tack welds for link top flange of Specimen NAS-RLP 556
Figure E12: Discontinuity in link top flange of Specimen FFS-RLP................557
Figure G1: Specimen MWS: Top flange outer face...579
Figure G2: Specimen MWS: Top flange inner face...581
Figure G3: Specimen MWS: Bottom flange inner face 582
Figure G4: Specimen MWS: Bottom flange outer face 583
Figure G5: Specimen MWS: Bending stress near column face 585
Figure G6: Specimen MWS: Web panel shear stress.......................................586
Figure G7: Specimen MWI: Top flange outer face..588
Figure G8: Specimen MWI: Top flange inner face..590
Figure G9: Specimen MWI: Bottom flange inner face 591
Figure G10: Specimen MWI: Bottom flange outer face 592
Figure G11: Specimen MWI: Bending stress near column face 594

Figure G12: Specimen MWI: Web panel shear stress 595
Figure G13: Specimen MWM: Top flange outer face 597
Figure G14: Specimen MWM: Top flange inner face 599
Figure G15: Specimen MWM: Bottom flange inner face 600
Figure G16: Specimen MWM: Bottom flange outer face 601
Figure G17: Specimen MWM: Bending stress near column face.......................603
Figure G18: Specimen MWM: Web panel shear stress 604

CHAPTER 1

Introduction

1.1 GENERAL

As seismic-resistant steel building systems, eccentrically braced frames (EBFs) are a popular alternative to moment resisting frames (MRFs) and concentrically braced frames (CBFs), due to their ability to combine high lateral stiffness and excellent ductility. EBFs are braced frame systems characterized by an eccentricity introduced in the beam that isolates a segment referred to as the *link*. Figure 1.1 shows an example of an EBF, with the link located at the center of the beam, between two braces. As discussed later, the link plays a key role in the seismic performance of EBFs. In some EBF configurations, one end of the link is attached to a column, as shown in Figure 1.2. Since their initial applications to building construction projects in the late 1970's to early 1980's (Libby 1981; Merovich *et al.* 1982) the use of seismic-resistant EBFs has continued to increase.

The widespread damage observed at welded beam-to-column moment connections in steel MRFs following the 1994 Northridge and 1995 Kobe Earthquakes (*e.g.* Bertero *et al.* 1994; *FEMA-355E* 2000; *Reconnaissance* 1997) raised broad concerns about the performance of welded steel frames in strong earthquakes, and motivated extensive research in the US, Japan, and elsewhere. This research effort resulted in recommended changes to design practices in the US (*FEMA-350* 2000) as well as in significant changes to building code provisions (AISC 1997; 2002) for seismic-resistant steel moment connections. However, much less attention has been given to link-to-column connections in EBFs (See Figure 1.2), even though these connections possess many of the same

Figure 1.1 Example of recently constructed EBF

Figure 1.2 Example of link-to-column connection

design, detailing, and construction features identified as having contributed to the poor performance of moment connections. Prior to the Northridge Earthquake, EBF link-to-column connections were designed and constructed in a manner very similar to MRF moment connections. On the other hand, EBF link-to-column connections are expected to experience different, and in some cases, significantly more severe forces and deformations than occur at moment connections in MRFs. Therefore, the improved design, detailing, and construction procedures developed for moment connections since the Northridge Earthquake may not necessarily be applicable to EBF link-to-column connections. For example, the reduced beam section (RBS) connection is now commonly used in MRFs. However, the large moment gradient along the relatively short length of the link makes the RBS difficult if not impossible to implement in links.

Following the Northridge Earthquake, the *AISC Seismic Provisions for Structural Steel Buildings* (1997) changed the previous design requirements for EBF link-to-column connections. Currently, the *AISC Seismic Provisions* require the designer to either use a connection validated by qualification testing, or use a short shear link with suitable reinforcement to preclude inelastic action in the link-to-column connection. However, very limited test data are available for the cyclic loading performance of EBF link-to-column connections, including connections with reinforcement as suggested in the provisions. Although the code provisions in effect discourage using EBFs with link-to-column connections, designers encounter situations where such arrangements are desirable, or sometimes even necessary to accommodate architectural requirements of a building.

This dissertation describes a research program conducted at the Phil M. Ferguson Structural Engineering Laboratory oat the University of Texas at Austin to study the performance of link-to-column connections in seismic-resistant EBFs.

This program combined an experimental investigation involving a total of sixteen large-scale cyclic loading tests, and an analytical study including detailed finite element simulations. To the knowledge of the author, the tests conducted in this program were the first series of experiments specifically aimed at studying the seismic performance of large-scale EBF link-to-column connections constructed using realistic detailing and welding according to the US practices.

1.2 OBJECTIVES OF RESEARCH

The primary objectives of this research were as follows:

1. To evaluate the performance of EBF link-to-column connections designed and constructed according to practices commonly used prior to the 1994 Northridge Earthquake.

2. To investigate the applicability and effectiveness of improving welding practices and design innovations developed for MRF moment connections for use in EBF link-to-column connections.

3. To further the understanding of the force and deformation environment at EBF link-to-column connections.

4. To investigate the possibility of predicting the performance of link-to-column connections based on finite element simulations.

5. To investigate alternative details and configurations for link-to-column connections considering structural performance characteristics as well as economy and constructability.

6. To provide recommended design guidelines, to the extent possible, for steel seismic EBF link-to-column connections.

1.3 OUTLINE OF DISSERTATION

In order to address the objectives listed above, a comprehensive literature review was conducted, followed by a combined experimental and analytical study.

Chapter 2 of this dissertation discusses the background and scope of the research program. A comprehensive literature review of EBFs and MRFs is provided. Emphasis is placed on recent research on EBF links and the extensive efforts in the US and Japan on the development of improved moment connections following the Northridge and Kobe Earthquakes. The review is synthesized and analyzed to provide a detailed scope of the research program.

Chapters 3 to 5 discuss the large-scale tests. A total of sixteen link-column specimens were constructed and tested in the course of the research. A test setup was devised to properly simulate the force and deformation environment of the link-to-column connection. The specimens had various link-to-column connections, from a connection detailed and fabricated according to the pre-Northridge practice, a connection adopting recommended modifications in welding, and two new connection types with specific configurations that reflect recent research developments in moment connections. The link lengths of the specimens were varied to cover a wide range of link length that may be used in the design practice. Additionally, two different loading protocols were used for the testing to evaluate the effect of loading protocols on connection performance.

Chapter 3 describes the test plan. Discussion of the test setup, test procedure, and material test results is followed by the design and fabrication details of the link-column test specimens.

Chapter 4 describes the individual test results as well as the characteristic behavior of the four connection types. The effect of the three primary test parameters, namely the connection type, link length, and loading protocol is discussed. Important design implications of the experimental observations are highlighted.

Chapter 5 provides further analysis and discussion of the test results. The test setup and measured data are analyzed to establish the limitations of the experimental findings. Test data are analyzed in further detail to provide additional insights into connection performance, link overstrength, and panel zone deformation. An evaluation is also provided for fracture surfaces in the connection after testing.

Chapter 6 describes the analytical portion of the research program. Detailed 3-D nonlinear finite element simulations of the tested specimens were performed to supplement the findings from the tests. Correlation between the experimental performance and analytical simulation was studied to investigate the possibility of predicting the connection performance controlled by fracture near the weld interface based on finite element simulations. Additional analyses were conducted to study the effect of column panel zone strength on the performance of EBF link-to-column connections.

Chapter 7 summarizes findings of the research program. Key observations and discussions from the literature review, experimental program, and analytical program are compiled. Finally, design recommendations are developed and suggestions for further research are provided.

CHAPTER 2

Background

2.1 OVERVIEW

This chapter reviews past research on seismic-resistant steel EBFs and other issues related to EBF link-to-column connections. Prior to the 1994 Northridge Earthquake, EBF link-to-column connections were designed, detailed, and constructed in a manner very similar to that of beam-to-column moment connections in special moment frames, with the exception that a welded web connection was used instead of a bolted web connection. Therefore, the extensive research programs conducted following the Northridge Earthquake to improve moment connections were central to the goals of this research program on link-to-column connections. Based on the synthesis of available research, four types of EBF link-to-column connections were selected for detailed investigation. These will be discussed later.

Section 2.2 summarizes significant research that forms the background of EBF design as prescribed in the *AISC Seismic Provisions*. Section 2.3 summarizes research on the performance of links made of A992 steel conducted at the University of Texas at Austin. Section 2.4 discusses the highlights of recent research on moment connections following the Northridge Earthquake. Section 2.5 introduces similar efforts in Japan following the 1995 Hyogoken-Nanbu (Kobe) Earthquake. Section 2.6 discusses past research and the current code provisions on EBF link-to-column connections. Section 2.7 discusses the scope of this research program in the context of the background presented in this chapter.

2.2 ECCENTRICALLY BRACED FRAMES (EBFS)

2.2.1 Introduction

EBFs are braced frame systems in which an eccentricity is introduced in the beam between two adjacent brace-to-beam connections, or between adjacent brace-to-beam connections and beam-to-column connections. The segment of the beam isolated between the braces or between a brace and a column is referred to as the link, or link-beam. Some typical EBF arrangements are illustrated in Figure 2.1, where the link is indicated by its length, e.

In an EBF, the axial force developed in the diagonal brace is transmitted to the column or to another brace through shear and bending in the link. In a well-designed EBF, seismic energy is dissipated primarily by inelastic action in the links. Therefore, the ductile behavior of the link is essential to the ductile performance of EBFs. In order to facilitate large deformation of the link without

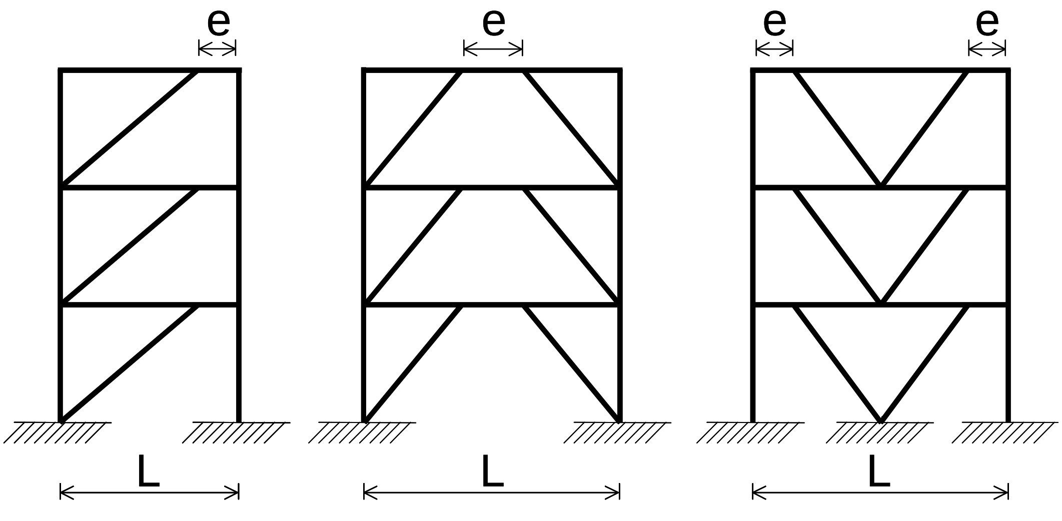

(a) (b) (c)

Figure 2.1 Typical EBF arrangements

loss of strength, the link should be detailed to delay fracture, local buckling, and lateral torsional buckling prior to development of sufficient inelastic rotation. The link also acts as a fuse limiting the forces developed in adjoining members, including the brace, column, and beam segment outside of the link.

EBFs can be considered to be a hybrid framing system, with the stable cyclic behavior and predictable energy dissipation capacity of a moment resisting frame (MRF) and the high lateral stiffness of a concentrically braced frame (CBF). The combined advantages present EBFs as an attractive alternative to MRFs and CBFs. As noted by Hjelmstad and Popov (1983a; 1984), a continuous spectrum of possible EBF arrangements can be recognized between a CBF and an MRF. For example, in arrangements (a) and (b) shown in Figure 2.1, $e = 0$ reduces the EBF to a CBF, while $e = L$ reduces to an MRF. In arrangement (c), a CBF corresponds to $e = 0$, an MRF to $e = L/2$. EBFs can be designed to balance stiffness and ductility, by maintaining the frame stiffness similar to that of CBFs, while selecting a reasonable link length to efficiently dissipate seismic energy. As discussed later, the link length controls the inelastic behavior of the link.

Figure 2.2 illustrates typical force distributions in the link, beam, and brace of an EBF subjected to lateral load. The force in an EBF link is characterized by constant shear, V, along its length, reverse curvature bending, M, and typically a small axial force, N. The force distributions in the figure also indicate that the region at the link ends require special attention. The link-to-column connection is subjected to significant shear and flexure developed in the link. The region of the beam immediately outside of the link, referred to as the brace connection panel, must resist the large axial force developed in the diagonal brace as well as flexure developed at the link end.

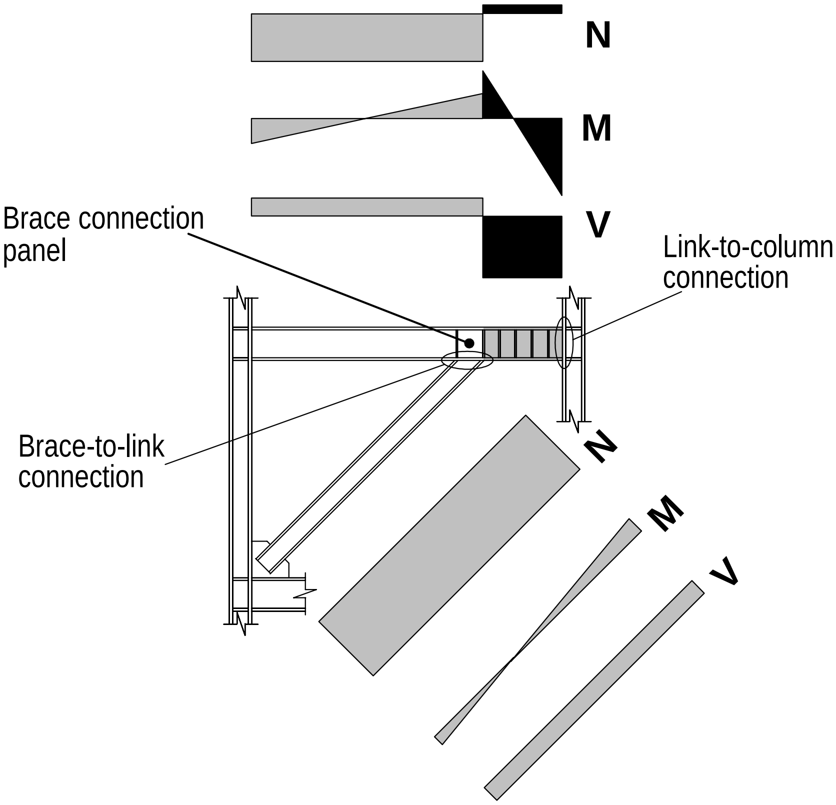

Figure 2.2 Typical force distribution in an EBF

Figure 2.3 further illustrates the forces developed in an isolated link. In this figure, M_B and M_C are the moments at the beam and column ends of the link, and V is the link shear. Axial force in the link is assumed to be negligible. In the case where the end moments are equal in magnitude, such that $M_B = M_C = M$, static equilibrium of the link reduces to: $Ve = 2M$. For an elastic-perfectly plastic link with no interaction between shear and flexure, $e = 2M_p/V_p$ would be the dividing length between links that yield in shear and those that yield in flexure. Here, M_p and V_p are the full plastic moment and shear strength, respectively, defined as follows:

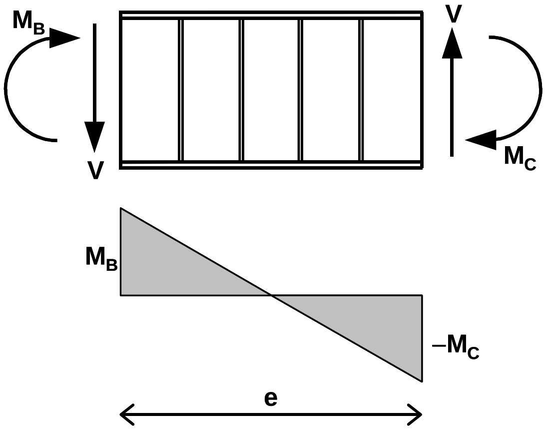

Figure 2.3 Free body diagram of link

$$V_p = 0.60\ F_y\ (d - 2t_f)\ t_w, \tag{2.1a}$$

$$M_p = F_y\ Z_p. \tag{2.1b}$$

In the above equations, F_y is the yield strength of the steel, d is the link depth, t_w is the web thickness, t_f is the flange thickness, and Z_p is the plastic section modulus.

Yielding in shear is more desirable, since it involves uniform participation of the web panels along the entire length of the link. Flexural yielding restricts plastic deformation near the link ends, and consequently, leads to less ductile behavior. Because of strain hardening, shear-flexure interaction occurs over a wide range of link length. Therefore, in order to assure shear yielding behavior, the link must comply with the limitation on length (Kasai and Popov 1986c):

$$e \le 1.6 \frac{M_p}{V_p}. \tag{2.2}$$

The function of EBFs can be examined through their rigid-plastic energy dissipation mechanisms. The diagrams shown in Figure 2.4 assume that plastic

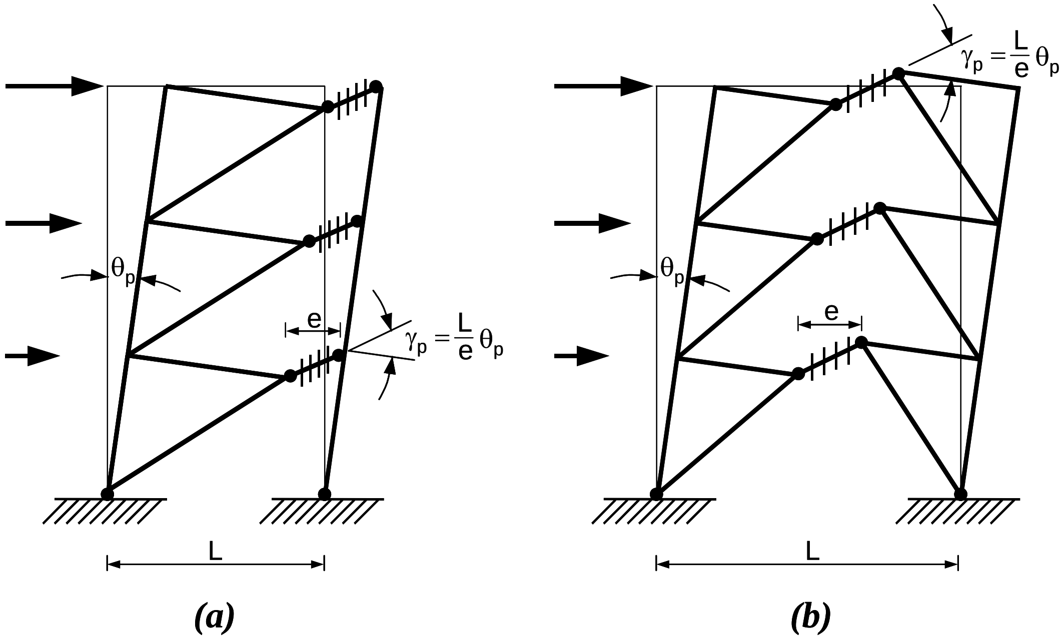

Figure 2.4 Energy dissipation mechanisms

deformation is strictly concentrated in the ductile links and column bases. The figure depicts the energy dissipation mechanisms for arrangements (a) and (b) in Figure 2.1. Based on the geometry of the mechanisms, a relationship between the inelastic frame drift angle, θ_p, and inelastic link rotation, γ_p, is established as follows:

$$\gamma_p = \frac{L}{e}\theta_p . \tag{2.3}$$

Equation (2.3) states that the link rotation demand depends on the configuration of the EBF, specifically on the bay span-to-link length ratio, L/e. The rotation demand is increased in direct proportion to this ratio. For the same inter-story drift angle, a link in an EBF experiences significantly greater rotation demand compared to a plastic hinge in an MRF. Since the link rotation demand increases as link length decreases, the links should not be too short. The link length should be chosen so that the rotation demand can be met by the link rotation capacity. The inelastic rotation capacity of links has been well established, as discussed in Section 2.2.4.

The basis of EBF design was developed from the mid-1970's through the 1980's, largely based on research conducted at the University of California at Berkeley. Extensive experimental and analytical research demonstrated the excellent seismic performance of EBFs, and provided invaluable data essential to establishing a cohesive design procedure and provision. Earlier research is well summarized by Popov and Engelhardt (1988), Engelhardt and Popov (1989b), and Popov *et al.* (1989a), among others. This section provides an updated review of the subject, including recent research conducted at the University of Texas at Austin and at the University of California, San Diego.

2.2.2 Overall Behavior

Roeder and Popov (1977) conducted two-dimensional (2-D) nonlinear dynamic analyses on a set of EBF, CBF, and MRF models to compare their performance under severe earthquake ground motion. The analyses indicated that EBFs perform well compared to the other framing systems due to their combined high stiffness and stable hysteretic behavior. An interesting note was that the EBF and CBF performed significantly better than the MRF when excited by the 1971 Pacoima Dam-record. This record included a large velocity pulse, characteristic of near field ground motion with directivity effects. This comparison indicates that the higher initial stiffness of braced frames might provide an advantage over MRFs against near field pulses. Roeder and Popov (1977; 1978a) further examined EBF behavior and basic connection details issues with cyclic loading tests of reduced-scale three-story single bay EBF specimens. The EBF specimens exhibited large initial stiffness, and maintained stable hysteretic behavior even after one of the five links failed. It was recommended that the design link strength should be evaluated as at least one-and-a-half times the nominal link strength in order to prevent buckling of the diagonal brace, and the accompanying unfavorable response of the frame. Kasai and Popov (1986a) later determined that the EBF arrangement tested by Roeder and Popov that placed a link at both ends of a brace tends to generate inactive links, and consequently recommended placing a link at only one end of each brace.

Results of intensive pseudo-dynamic loading tests of a full-scale six-story EBF-MRF dual structure, conducted in Tsukuba, Japan were reported by Roeder *et al.* (1987) and Foutch (1989). Although the structure exhibited excellent cyclic behavior, it was observed that the energy dissipation and story drift was concentrated in the lower stories. Failure of a brace-to-beam connection in the gusset plate significantly affected the structural response. Underestimation of link strength and the concentration of deformation at the lower stories were believed to be the primary causes of the premature failure of this connection. Whittaker *et al.* (1987; 1989) further examined the same six story dual frame by earthquake simulator tests of a 0.30-scale model. The scaled model exhibited a soft story mechanism in lower stories under large ground motion, confirming the observations by Roeder *et al.* (1987) and Foutch (1989). Forces developed in the composite slab were found to contribute significantly to the forces in the diagonal braces.

Ricles and Popov (1987a; 1994) performed 2-D nonlinear dynamic analyses of a six-story-four bay EBF. The analyses demonstrated that the design procedure described in Section 2.2.3 leads to excellent performance of the frame, where the links accounted for the majority of energy dissipation, and the link inelastic rotation was reasonably well distributed along the frame height.

More recently, Richards and Uang (2003) conducted extensive 2-D nonlinear dynamic analyses of EBFs to investigate the deformation demands on shear yielding links. Three EBFs with shear yielding links (described in Section 2.2.4), two 3 story-frames and one 10 story-frame, were subjected to a large number of recorded and synthesized ground motions for the Los Angeles area, scaled for 10 percent probability of exceedance in 50 years. The cyclic loading protocol for testing link-to-column connections established based on these analyses was used for some of the large-scale tests conducted in this research program (See Section 3.2.3). These analyses also demonstrated that EBFs designed according to the current provisions perform adequately during severe earthquakes.

2.2.3 Design Procedure

In an appropriately designed EBF, inelastic action and damage is restricted primarily to the links. With such a design, the links act as structural fuses, limiting the forces developed in adjacent members. The capacity design procedure (Popov and Engelhardt 1988) is a practical yet simple approach to accomplish such design goals. In this procedure, the links are sized and detailed for code specified forces. Subsequently, all other members are designed for the forces developed in a fully yielded and strain hardened link. Since a link with ductile detailing is capable of developing forces significantly greater than its nominal plastic strength, overstrength must be considered carefully when evaluating the link forces for capacity design of adjoining members.

Kasai and Popov (1986a) derived an approximate relationship between lateral forces acting on the frame and the resulting link shear force. According to this relationship, the link shear force, V_{link}, can be evaluated as follows:

$$V_{\text{link}} = V_{\text{story}} \frac{h}{L} \,. \tag{2.4}$$

In the above equation, V_{story}, h, and L are the story shear force accumulated from the top of the frame to the story level under consideration, floor height, and span length, respectively. If there are multiple links per story, V_{story} must be distributed accordingly. Ricles and Popov (1987b) and Popov *et al.* (1992) demonstrated the advantage of designing EBFs to have uniform values of ratio $\alpha \equiv V_n/V_{\text{link}}$ along the height for design lateral forces. Here, V_n is the nominal shear strength of the link, defined in Section 2.2.5. The *2002 AISC Seismic Provisions* require $V_{\text{link}} < 0.9V_n$ for V_{link} derived from factored earthquake loads, where 0.9 represents the resistance factor. During earthquakes, EBFs proportioned as such are likely to distribute inelastic deformation of links reasonably well throughout their height.

Once the link sections are selected, all other frame members are designed to remain essentially elastic when the full strength of the link is developed. The *AISC Seismic Provisions* provide an estimate of the ultimate shear force and end moments that can be achieved by a link, as discussed in Sections 2.2.5 and 2.2.6.

It is important to note that a shallow intersect angle between the diagonal brace and beam can introduce very large axial force in the beam outside of the link. The axial force combined with the large moment developed at the link end can lead to instability in beam segment outside of the link well before the link can develop its full strength (Kasai and Popov 1986a). Engelhardt and Popov (1989a; 1992) demonstrated that instability in the beam leads to drastic loss of strength of the EBF. Therefore, EBFs should be arranged with a reasonably large angle between the diagonal brace and beam. Otherwise, capacity design may not be possible.

Tests by Roeder and Popov (1977; 1978a) and Whittaker *et al.* (1987; 1989), as well as dynamic analyses by Ricles and Popov (1987a; 1994) indicate that links in different stories typically do not yield simultaneously or uniformly. Therefore, the direct application of capacity design forces can be overly conservative for columns, especially at lower levels of high-rise buildings. For this reason, a reduction in column design force is justified (Engelhardt and Popov 1989b). The *AISC Seismic Provisions* specify a reduced link overstrength factor for column design (See Section 2.2.5).

After arranging the frame and sizing the members, a check must be carried out to assure that the link can accommodate the rotation demand corresponding to the frame drift requirement. The relation between the link rotation and ultimate drift can be approximated using the energy dissipation mechanisms, as shown in Figure 2.4, or simply by equation (2.3). The *AISC Seismic Provisions* defines the link rotation capacity, as discussed in Section 2.2.4

2.2.4 Ductile Behavior of Links

Ductile behavior of a link is ensured by selection of a section that meets the appropriate flange and web slenderness limits, and by appropriate placement of web stiffeners. The *2002 AISC Seismic Provisions* specify the maximum width-thickness ratio allowed for link sections to be identical to those limits for beams in special moment frames. Currently, the limit is $0.30(E_s/F_y)^{1/2}$ for flanges and $3.14(E_s/F_y)^{1/2}$ for webs. The flange slenderness limit is evaluated as 8.51 for A36 steel (E_s = 29,000 ksi and F_y = 36 ksi), and 7.22 for A992 steel (E_s = 29,000 ksi and F_y = 50 ksi). The shift from A36 steel to A992 steel prohibited the use of a number of economical wide flange sections. Finite element simulations by Richards and Uang (2002) provide justification that the width-thickness ratio limit for link flanges of A992 steel can, in fact, be relaxed to the compact section limit given in the *AISC LRFD Manual of Steel Construction* (AISC 1999) of $0.38(E_s/F_y)^{1/2}$, or 9.15.

Roeder and Popov (1978b) established that shear yielding of a beam is an excellent energy dissipation mechanism, in which stable hysteretic behavior is maintained under large cyclic deformation. Three-point loading tests exemplified that long links are less desirable for EBFs since they exhibit inferior cyclic behavior compared to short shear yielding links.

Hjelmstad and Popov (1983a; 1983b) and Malley and Popov (1983; 1984) conducted an extensive experimental investigation of the cyclic behavior of shear yielding links. Isolated links were tested with a variety of link lengths and stiffening details. These tests demonstrated that link stiffeners are critical elements to control and limit inelastic web buckling. Based on these tests and additional later tests, Kasai and Popov (1986a; 1986c) established web-stiffening criteria for shear yielding links. Kasai and Popov (1986b) suggested defining the link length limit as equation (2.2) in order to avoid developing large end moments, and consequently to ensure shear-yielding behavior. All frame tests and dynamic analysis described in Section 2.2.2 used links satisfying equation (2.2).

Engelhardt and Popov (1989a; 1992) investigated the cyclic behavior of long flexural yielding links. Tests indicated that, as the relative significance of flexure over shear increases with increasing link length, the primary mode of instability shifts from inelastic web buckling caused by shear to flange buckling and lateral torsional buckling caused by flexure. Stiffeners placed near both link ends appeared to delay strength degradation caused by flexure induced instability. Since shear buckling in the web is not possible for flexure yielding links, only the end stiffeners were deemed necessary. For links in which both shear and flexure affects their behavior, it was suggested that stiffeners be placed also within the remaining central portion of the link, as for short shear links.

The *AISC Seismic Provisions* define three different link length categories associated with three distinctive ranges of inelastic behavior. Since the inelastic behavior of links of $e \leq 1.6M_p/V_p$ is dominated by shear, these links are generally termed *shear links*. Flexure is dominant for links of $e \geq 2.6M_p/V_p$, which are termed *moment links*. The inelastic behavior of links of $1.6M_p/V_p < e < 2.6M_p/V_p$ is significantly affected by both shear and flexure. Links in this transition length range are termed *intermediate links*. Based on the large number of tests discussed above, the *2002 AISC Seismic Provisions* provide design limits for the inelastic link rotation angle. The limit is defined as 0.08 rad for shear links, and 0.02 rad for moment links. For intermediate links, the rotation limit is evaluated by linear interpolation between 0.02 rad and 0.08 rad according to their length. Engelhardt and Popov (1992a) observed strong influence of shear in links of length close to $2.6M_p/V_p$, prompting a suggestion that the intermediate length range between shear and moment links be taken as $1.6M_p/V_p < e < 3M_p/V_p$. The provisions also provide requirement for link stiffeners according to design link rotation.

Figure 2.5 plots the relation between link rotation capacity, $\gamma_{p\text{-max}}$, and non-dimensional link length, $e/(M_p/V_p)$, obtained from past tests. The link rotation capacity is defined as the maximum inelastic rotation angle at which one full cycle of loading was completed without a drop in link shear resistance to below 80% of the maximum shear achieved during the course of the test. All test data studied by Engelhardt and Popov (1989a) as well as more recent tests are included in this figure. Test results that were clearly influenced by premature fracture of the link end connection or by the presence of axial force were omitted. Monotonic loading tests were also omitted. The values for V_p and M_p were computed based on the following equations:

$$V_p = 0.60\, F_{yw}\, (d_b - 2t_f)\, t_w, \tag{2.5a}$$

$$M_p = F_{yf}\, Z_{pf} + F_{yw}\, (Z_{pw} + Z_{pr}). \tag{2.5b}$$

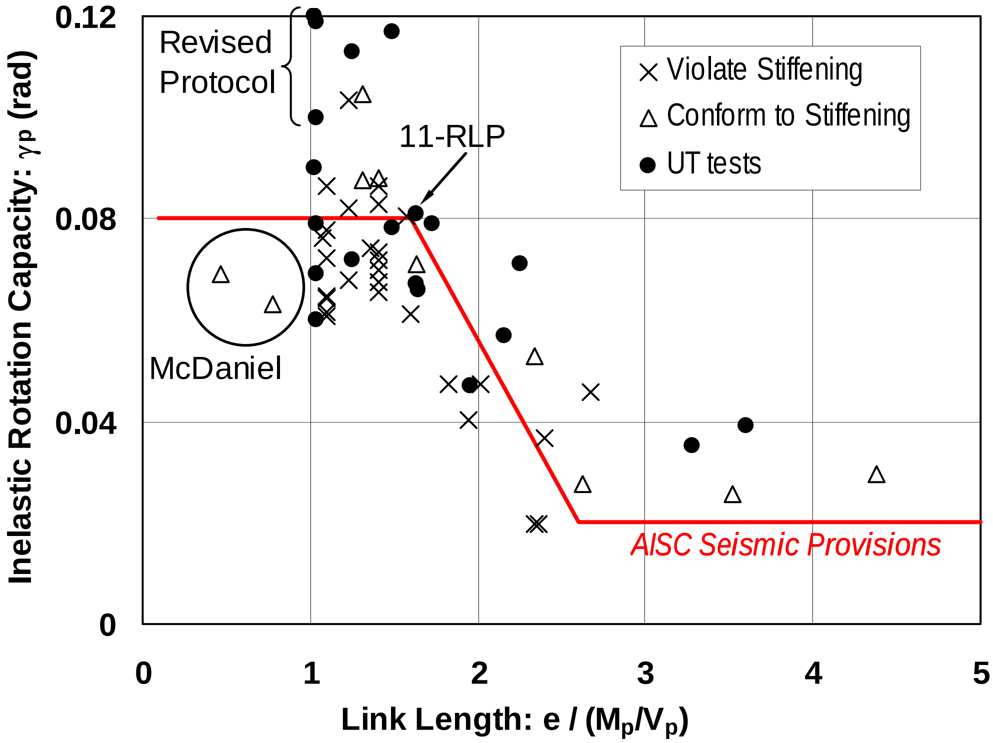

Figure 2.5 Link rotation capacity

In the above equations, F_{yf} and F_{yw} are the yield strength of the flange and web, respectively, measured by tension coupon tests; Z_{pw}, Z_{pf}, and Z_{pr} are the plastic section modulus of the beam flanges only, the web only, and the flange-web fillets only, respectively; d_b is the section depth, t_f is the flange thickness, and t_w is the web thickness. In equation (2.5), the static yield strength was used when both the static and dynamic yield strengths were stated. The measured section dimensions instead of the nominal dimensions were used when the former were available. Figure 2.5 separates the test specimens into three groups: (a) earlier specimens that violated the stiffening criteria specified in the *2002 AISC Seismic Provisions*; (b) earlier specimens that conform to the these criteria; and (c) recent tests conducted at the University of Texas at Austin (UT) by Arce (2002) and Ryu *et al.* (2004). All tests included in (c) conformed to the stiffening criteria specified in the *2002 AISC Seismic Provisions*. It should be stressed that the link specimens included in the figure were constructed of different grades of steel and tested with various cyclic loading sequences. The rotation capacity defined by the *2002 AISC Seismic Provisions* is indicated in the figure by a solid line.

Figure 2.5 suggests that the link length categories divided by link length of $1.6M_p/V_p$ and $2.6M_p/V_p$ are quite adequate. The figure also shows clearly that many link specimens failed to meet the inelastic rotation required in the provisions. Most of these links violated the stiffening criteria. However, a remarkable number of specimens that adhered to the stiffening criteria failed to meet the rotation requirement, including many links tested recently at UT. Richards and Uang (2003) suggested that shear links tested in recent years were likely penalized by overly severe testing requirements defined by the *AISC Seismic Provisions* (2000; 2002). Links tested under more realistic deformation requirements achieved rotations well beyond the capacity defined in the priovisions (Ryu *et al.* 2004). These tests are indicated in Figure 2.5 as “Revised Protocol” and “11-RLP.” A detailed account of this issue is provided in Section 2.3.

Richards and Uang (2002) performed three-dimensional nonlinear finite element simulations of cyclically loaded links. The simulations predicted remarkably accurately the flange and web buckling observed in tests as well as the associated strength degradation. An extensive parametric study suggested that intermediate links of $1.7M_p/V_p < e < 2.1M_p/V_p$ are susceptible to premature strength degradation due to flange and web buckling. It was recommended that reduced stiffener spacing should be used for these links in order to ensure the rotation capacity prescribed in the provisions.

2.2.5 Link Strength

A reasonable estimate of the ultimate shear force and end moments that can develop in a link is vital to the capacity design procedure discussed in Section 2.2.3. An underestimation of link forces can lead to premature failure of a member outside of the link. A link with appropriate stiffener spacing, as mentioned in Section 2.2.4, can achieve very large inelastic deformation, and develop a very large degree of strain hardening. The effect of strain hardening is accounted for in the *AISC Seismic Provisions* by the link overstrength factor. The link overstrength factor is defined as the ratio of maximum link shear, V_{max}, over the nominal shear strength of the link, V_n. The nominal shear strength is evaluated as the smaller of V_p and $2M_p/e$. For links of $e \leq 2M_p/V_p$, $V_n = V_p$, while for links of $e \geq 2M_p/V_p$, $V_n = 2M_p/e$.

The various tests discussed in Sections 2.2.2 and 2.2.4 suggest that a link overstrength factor of 1.5 or greater should be used for shear links. For example, Foutch (1986) suggested that an overstrength factor of 1.8 to 2.0 is required to take into account the forces developed in composite slabs. Recently, Itani *et al.* (1998; 2003) and McDaniel *et al.* (2003) tested large built-up shear links, which were constructed of grade 50 steel and intended for bridge application. These links developed very large link overstrength, close to twice the nominal strength. Richards and Uang (2002) cautioned that significant shear resistance could develop in the relatively thick flanges in built-up sections, similar to thick column flanges in the column panel zone. However, other tests by Arce (2002) and Ryu *et al.* (2004) gave contradictory results, suggesting that the flange-to-web area ratio has little effect on link behavior. At present, the reason why the built-up sections exhibited greater overstrength is unclear.

The correlation between link length and link overstrength was first established by Engelhardt and Popov (1989a). In order to account for the significant shear-moment interaction in intermediate links, an analytical interaction relation between maximum shear and maximum moment was developed. The interaction model was based on 2-D plasticity and the assumptions that the flanges carry no shear stress and that stresses are distributed uniformly in the web. This model does not account for the shear resistance developed in the flanges. The interaction model suggests that shear-moment interaction has a very significant effect on intermediate links, while shear links and moment links are relatively unaffected. Comparison with test results suggested that the analytical interaction model provides a reasonable estimate for the maximum link forces.

Based on past research, the *2002 AISC Seismic Provisions* specify a capacity design procedure based on an assumed link overstrength factor of 1.5. The procedure uses a link shear force of $1.25R_yV_n$ for diagonal braces, $1.25V_n$ for reinforced link-to-column connections, $1.1R_yV_n$ for columns, and $1.1V_n$ for the beam outside of the link. Here, R_y is the ratio of expected yield strength to the minimum specified yield strength, and $R_y = 1.1$ for A992 steel. The reduced overstrength factor for column design reflects the observation that links in different stories typically do not yield simultaneously. The reduced overstrength factor for beam design reflects the observation that limited yielding in the beam outside of the link in the brace connection panel (See Figure 2.2) can benefit the overall performance by reducing the inelastic link rotation demands (Engelhardt and Popov 1989a; 1992). R_y is omitted for the beam design because typically, a continuous member is used for the link and the beam segment outside of the link, and therefore, the variation in material yield strength need not be accounted for. The residual differences between the design forces and $1.5V_n$ account for the use of resistance factors when computing the strength of members outside of the link, the ability to sustain limited yielding in members outside of the link, and the beneficial effects of the floor slabs, among other factors.

Figure 2.6 plots the relation between the link overstrength, V_{max}/V_n, and non-dimensional link length, $e/(M_p/V_p)$. The same database used for Figure 2.5 is used, except that the links with a composite slab tested by Ricles and Popov (1987b; 1989) are excluded. Figure 2.6 suggests that, in the link length range of $e < 2M_p/V_p$, link overstrength tends to increase with decreasing link length. The lower overstrength factor for intermediate links is attributed to shear-moment interaction (Engelhardt and Popov 1989a). In the range of $M_p/V_p < e < 2.7M_p/V_p$, where comparative test data are available, no clear correlation can be drawn

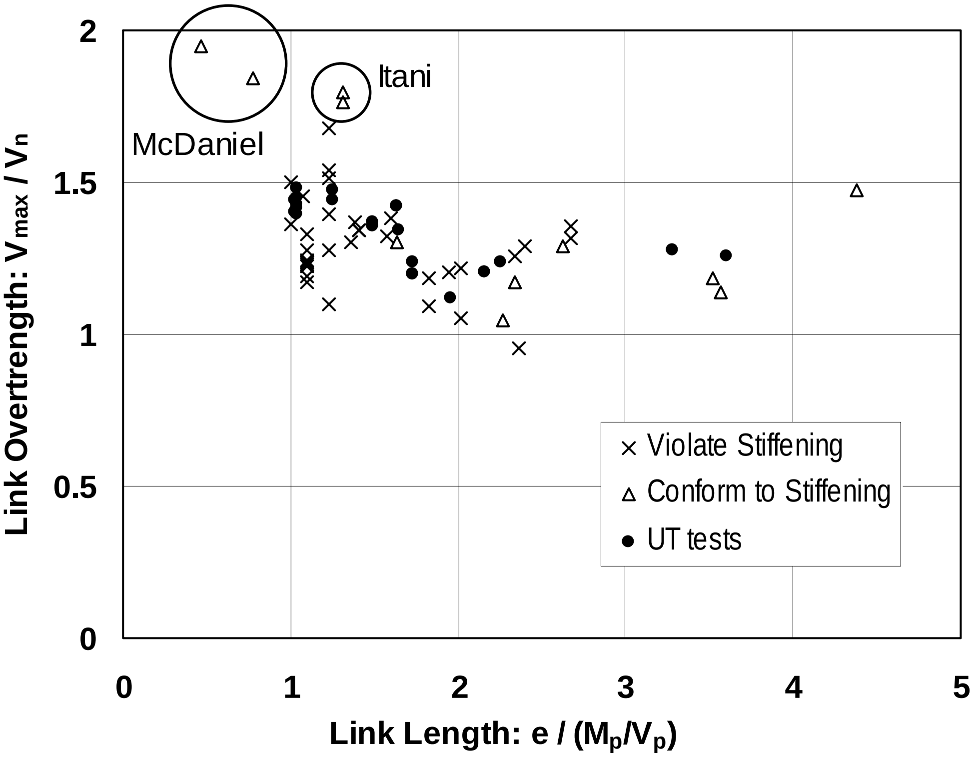

Figure 2.6 Link overstrength

between the link overstrength and stiffening criteria. It is possible that prior to strength degradation induced by flange and/or web buckling, specimens violating the current stiffening criteria had already developed much of their inherent overstrength capacity.

Based on the data plotted in Figure 2.6, it appears that the assumed overstrength factor of 1.5 is reasonable for links constructed of typical rolled wide flange shapes. However, for short links constructed of built-up sections with heavy flanges, such as those tested by Itani *et al.* (1998; 2003) and McDaniel *et al.* (2003) circled in the figure, a higher overstrength factor, on the order of about 1.75 to 2.0, may be appropriate.

Figure 2.7 plots the relation between maximum link shear and link length. The same dataset used for constructing Figure 2.6 is used. The two solid lines represent the overstrength factor evaluated as $1.5V_n$, as implied in the *2002 AISC Seismic Provisions*, and the theoretical link strength proposed by Engelhardt and Popov (1989a). Comparison of the two lines suggests that the theoretical strength incorporating shear-moment interaction provides a better estimation than the overstrength factor defined in the priovisions. The increase in shear strength with decrease in length for links shorter than $2M_p/V_p$ is well accounted for by the theoretical correlation, except for the very high overstrength observed in large built-up sections (Itani *et al.* 1998, 2003; McDaniel *et al.* 2003). The theoretical strength depends on the assumed ratio between ultimate stress and yield stress (a ratio of 1.5 is assumed for both normal stress and shear stress in Figure 2.7), and assumes that no shear force is carried by the flanges. The second assumption can be false for built-up sections with relatively thick flanges and thin webs. Figure 2.7 also shows that the provisions are likely to give conservative overstrength factors for links of near $e = 2M_p/V_p$ as a result of neglecting significant shear-moment interaction in this length range.

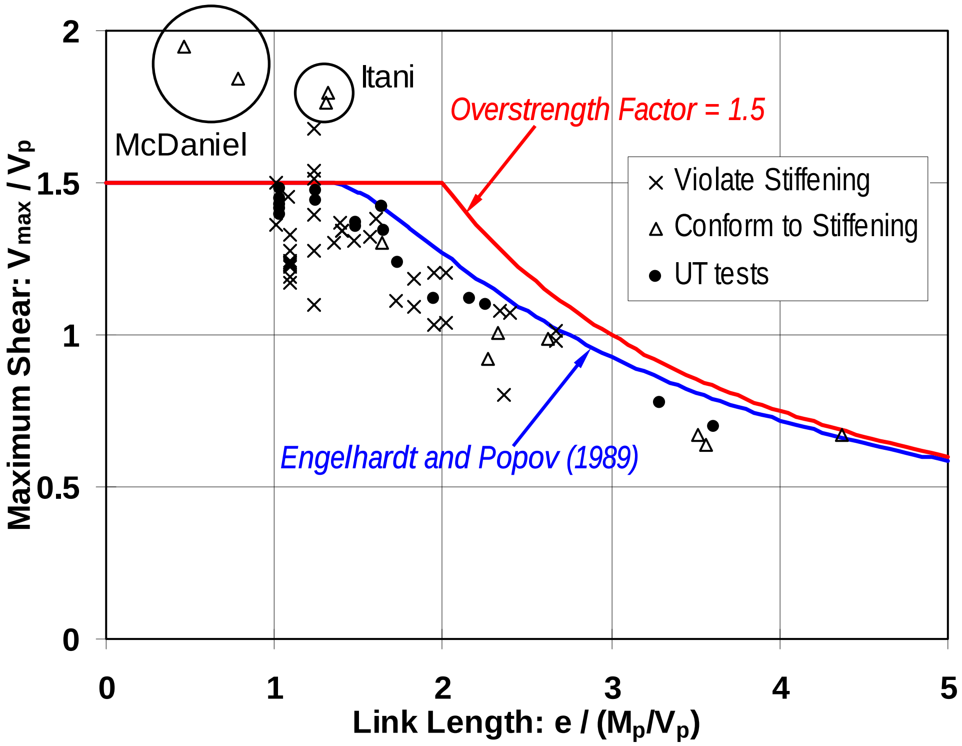

Figure 2.7 Link maximum shear strength

For symmetric EBF arrangements with links located in the center of the bays, as type (b) in Figure 2.1, the link end moments are normally assumed to remain equal in magnitude under any deformation history until failure. Therefore, the design link moment can be deduced from the design link shear force, simply from statics. However, in non-symmetric arrangements, such as types (a) and (c) in Figure 2.1, link moment is distributed according to the end restraints, resulting in unequal end moments. Nonetheless, in many cases, the link end moments tend to redistribute until they fully equalize, after undergoing large inelastic deformation. In other cases, estimate of link end moments require further consideration. This issue is discussed in Section 2.2.6.

2.2.6 Unequal End Moments and Axial Forces

EBF arrangements with links attached to columns, such as types (a) and (c) in Figure 2.1, introduce two additional design concerns. First, the rotational restraint of the link is typically much greater at the column end of the link than at the beam-brace end of the link, giving rise to unequal link end moments as illustrated in Figure 2.2. Secondly, the large force and deformation developed in the link generates a severe environment at the link-to-column connection. This second issue was the prime concern of this research program, and is discussed separately in Section 2.6. The first issue is discussed in the following.

As a link undergoes large inelastic deformation, and shear force increases, unequal end moments tend to equalize. However, there are circumstances where the link can reach its shear or flexural capacity before full equalization is achieved. In such cases, the assumption of moment equalization can lead to underestimation of design link moments. Kasai and Popov (1986a; 1986b) examined the effect of unequal end restraints. Shear link specimens of $e = 1.08M_p/V_p$, $1.36M_p/V_p$, and $1.64M_p/V_p$ were tested in a test setup that imposed greater rotational restraint at one end of the link than at the other. In the link of $e = 1.08M_p/V_p$, the initially unequal end moment remained unequal throughout the loading history until link failure. Full moment equalization was achieved in the links of $e = 1.36M_p/V_p$ and of $e = 1.64M_p/V_p$. In all cases, link moments at both ends were bounded approximately at M_p. The unequal end restraints had little effect on the overall behavior and rotation capacity of the shear links. Ricles and Popov (1987b) observed that links of $e = 1.4M_p/V_p$ with unequal end restraints did not achieve moment equalization.

Engelhardt and Popov (1989a) noted that moment equalization might not be achieved in links (of any length) attached to columns for the direction of loading that generates compression in the beam segment outside of the link (See

Figure 2.2). Large compression in the beam could decrease the flexural stiffness of the beam, even in the absence of instability. The beam with decreased stiffness attracts less moment from the column end to the beam end of the link, and thus prevents moment equalization. It was cautioned that, due to this mechanism, the moment at the column end might be higher than would be expected from assuming complete moment equalization, and thereby place additional demands on the link-to-column connection. Clearly, significant yielding and instability in the beam results in a large loss of stiffness at the beam end of the link, and inhibits moment equalization.

Based on the above, the *AISC Seismic Provisions* recommend considering unequal link end moments for links of $e < 1.3M_p/V_p$ attached to columns, and evaluating the link moment at the column end based on the moment capacity of the link member. The link moment at the beam-brace end follows from static equilibrium, as shown in Figure 2.3. Caution is required in relating the limit length of $1.3M_p/V_p$ stated in the provisions with the tests discussed above. Studies by Kasai and Popov (1986a; 1986b) and Ricles and Popov (1987b; 1989) may in fact suggest increasing this limit length to $1.4M_p/V_p$. It is to be reiterated here that the M_p/V_p values presented in this chapter were evaluated based on the reported dimensions and yield strength, using equation (2.5), and do not necessarily coincide with the corresponding values provided in the original reports (Note that various researchers also used somewhat different definitions for M_p and V_p). Typically, the reevaluated M_p/V_p value is smaller than the value provided in the original report. Consequently, the non-dimensional link length, $e/(M_p/V_p)$, reported herein is longer than in the original report.

Kasai and Popov (1986a; 1986b) also examined the effect of axial forces on link behavior. Links were tested under an extreme condition in which axial force equal to link shear was present throughout the loading history. The maximum axial force amounted to approximately $0.35P_y$, where P_y is the axial yield strength of the link. It was demonstrated that compressive axial force in the link promotes buckling in the compressed flange, while tensile axial force tends to reduce flange buckling. Enhanced flange buckling led to significant reduction in energy dissipation. While both specimens failed prematurely by combined flange and web buckling near the link ends, degradation in rotation capacity was more significant in the longer link of $e = 1.64M_p/V_p$ than in the other link of $e = 1.36M_p/V_p$. Therefore, it was recommended that if significant axial forces in the link cannot be avoided, the link length should be reduced. Also based on these tests, interaction relations between shear force and axial force, and between end moment and axial force were established. The *AISC Seismic Provision* treats axial forces smaller than $0.15P_y$ as negligible.

2.2.7 Composite Slabs and Lateral Stability

Ricles and Popov (1987b; 1989) compared the behavior of shear link-composite slab systems with that of bare steel links. Tests demonstrated that composite action could significantly increase stiffness during small loading cycles. However, after the composite floor experienced significant damage, the shear strength of composite links became comparable to that of bare steel links. The ultimate shear forces developed in the composite links were 1 to 13% greater than those in the corresponding bare links; the ultimate end moments were 1 to 25% greater. The overall hysteretic behavior of composite shear links was very similar to that of bare steel shear links. Damage to the composite slab concentrated in the region immediately above the links. Interestingly, the extent of slab damage was remarkably small considering the large link rotation of up to 0.10 rad. The same tests also demonstrated that composite slabs alone do not provide sufficient lateral support for links. In order to maintain stability of both the link and the diagonal brace, transverse support members are needed at the link ends. Popov *et al.* (1989b) cautioned that these lateral support members framing into the link must not interfere with the large in-plane motion of the link.

Engelhardt and Popov (1989a; 1992) demonstrated that instability outside of the link leads to a drastic reduction of strength and deformation capacity of the EBF. Accompanied with the development of such instability were increasingly large out-of-plane forces at the lateral supports. Again, composite slabs alone cannot be relied on to provide sufficient resistance against these lateral forces. Engelhardt and Popov also noted that in EBFs where braces connect from below to the lower flange of the link, the presence of the composite slab could be quite beneficial for stability control. In such EBFs, the direction of loading that places the beam segment outside of the link in compression (same direction as illustrated in Figure 2.2) also generates bending moment that adds compression to the top flange of the beam, and relaxes the compression in the bottom flange. Since the composite concrete slab connects to the top flange of the beam, which is critical for stability of the beam, the composite concrete slab is expected to provide substantial restraint against lateral torsional buckling of the beam.

2.2.8 Brace Connection Panel and Brace-to-Link Connection

Since the brace connection panel (See Figure 2.2) is subjected to a combination of large axial force transferred from the diagonal brace and large flexure transferred from the link end, special care must be taken to prevent severe damage in this region. Roeder and Popov (1977) noted that a pair of stiffeners is required in the brace connection panel to prevent local yielding and web crippling induced by local stress concentrations.

Engelhardt and Popov (1989a; 1992) and Engelhardt *et al.* (1992) noted that if a continuous section is used for the link and the beam outside of the link, as is typically the case, yielding in the brace connection panel is unavoidable for a wide range of EBF configurations. Nonetheless, tests indicated that limited yielding in the brace connection panel (and in the column panel zone) could reduce the inelastic rotation demands on the link without jeopardizing the overall behavior of the EBF, and therefore, can be beneficial. On the other hand, instability in the brace connection panel can lead to significant reduction in strength and ductility of the EBF. As discussed in Section 2.2.7, the top flange is normally critical for stability in the brace connection panel. Therefore, addition of partial depth stiffeners welded to the top flange and web within the brace connection panel could lessen the strength degradation caused by local buckling in the panel.

Roeder and Popov (1977) stressed that the brace-to-link connection should not extend into the link, so as not to interfere with the large deformation in the link. Roeder *et al.* (1987) and Foutch (1989) observed in a full-scale frame test that failure of a brace-to-link connection could have a significant effect on the behavior of the EBF. After severe buckling developed in the gusset plate at a brace-to-link connection, the diagonal brace was unable to develop large axial forces, which in turn, limited the forces imposed on the link.

Engelhardt and Popov (1989a; 1992) tested EBF specimens with three different brace-to-link connection configurations. The configurations were: (a) a fully welded connection for wide flange braces; (b) a fully welded connection for rectangular tube braces; and (c) a stiffened gusset plate connection for rectangular tube braces. Configuration (c) was designed to prevent buckling in the gusset plate reported by Roeder *et al.* (1987) and Foutch (1989). All connections were designed to develop the strength of the brace under combined axial force and bending. The three brace-to-link configurations, (a), (b), and (c), generally performed well in the tests. It was noted that the ability for the brace to attract and develop large bending moments could significantly reduce the demands on the beam, and benefit EBFs with long links. Engelhardt and Popov suggested that fully welded connections, (a) and (b), might be preferred over the gusset plate connection, (c), for cases where lateral torsional buckling of the beam segment outside of the link is expected. Combined with a composite slab, such braces can be beneficial in supplying the large lateral forces required to control buckling.

2.3 RECENT RESEARCH ON EBF LINKS

2.3.1 General

In recent tests conducted by Arce (2002), a large number of shear links failed prematurely before achieving the inelastic rotation required in the *AISC Seismic Provisions* (2002), due to fracture of the link web. It was suspected that low ductility material present in the k-area of the rolled wide-flange shapes may have contributed to the observed failures. In a subsequent study by Ryu *et al.* (2004), some of the same link specimens tested by Arce were retested using a revised loading protocol. The revised loading protocol is less severe than the protocol used by Arce, and is more reasonable representation of the link rotation demand arising from earthquake ground motion. Although the retested links still failed by web fracture in a manner identical to those observed by Arce, the large rotations achieved by the retested links easily satisfied the rotation requirements of the *AISC Seismic Provisions*. Further details of the research by Arce (2002) and Ryu *et al.* (2004) are provided in the remainder of this section.

2.3.2 Behavior of EBF Links Tested by Arce

Arce (2002) tested a total of sixteen isolated link specimens with four different wide flange sections and a wide variety of link lengths. Both ends of the links were welded to 2-inch steel plates, which in turn, were connected to the loading system by means of A490 bolts. These link specimens were tested alongside the current research program, using the test setup described in Section 3.2.1. The cyclic loading protocol provided in Section S of the *2002 AISC Seismic Provisions* was followed.

Figure 2.8 summarizes the test results, by plotting the inelastic rotation capacity, $\gamma_{p\text{-}max}$, against the normalized link length, $e/(M_p/V_p)$. The inelastic rotation angle required in the *2002 AISC Seismic Provisions* is shown in a solid line. Failure of the link was defined as the point when the specimen failed to maintain shear force corresponding to 80% of the maximum magnitude achieved

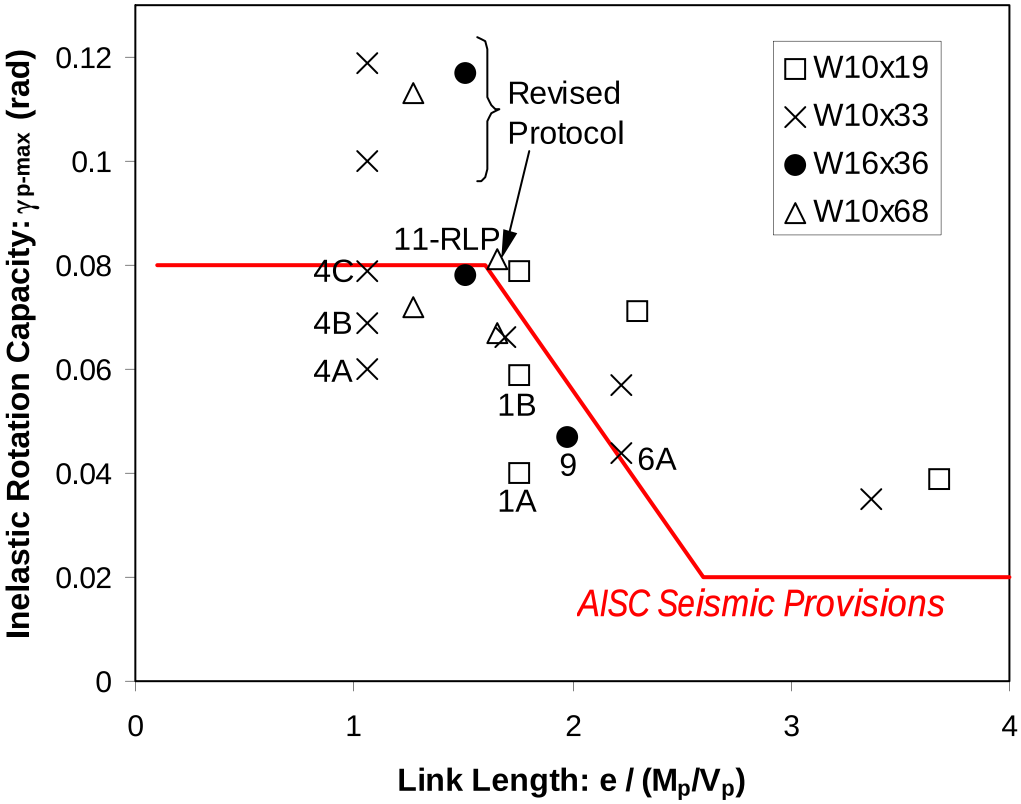

Figure 2.8 Test results from Arce (2002) and Ryu et al. (2004)

during earlier cycles. Figure 2.8 also plots five specimens from Ryu *et al.* (2004), indicated as “Revised Protocol.” These specimens are discussed in Section 2.3.4.

Three specimens, labeled as Specimens 1A, 1B, and 6A in Figure 2.8, failed by fracture of the welds between the link and the end plates (Refer to Appendix A for details). These three specimens are excluded from the following discussion. Excluding Specimens 1A, 1B, and 6A, there remained thirteen valid specimens.

Most importantly, Figure 2.8 indicates that eight of the thirteen valid specimens failed to reach their link rotation requirements. The inelastic rotations achieved by these eight specimens were 0.002 rad to 0.02 rad below, or 1% to 25% below the required level. Of the eight specimens that failed to achieve their link rotation requirements, all but one specimen failed by fracture of the link web. The failure process initiated from a crack that formed at the end of the vertical fillet welds connecting the link stiffeners to the link web. These cracks formed at the top and bottom termination points of the fillet welds, and often propagated in a horizontal direction, parallel to the link flanges. Ultimately, rapid growth of these cracks led to a large reduction in link shear resistance. Figure 2.9 shows an example of a link that failed by web fracture. The seven specimens that experienced such web fractures had link lengths of $e \leq 1.7M_p/V_p$, with two specimens slightly exceeding the shear link length limit of $e = 1.6M_p/V_p$.

McDaniel *et al.* (2003) observed similar web fractures in built-up shear links that also led to premature failure of the link. However, the failure mode controlled by web fracture was not typically reported in earlier link tests (*e.g.* Kasai and Popov 1986a), in which severe web buckling dominated the ultimate state. The recent emergence of this particular failure mode deserves detailed consideration, and is discussed separately in Section 2.3.3.

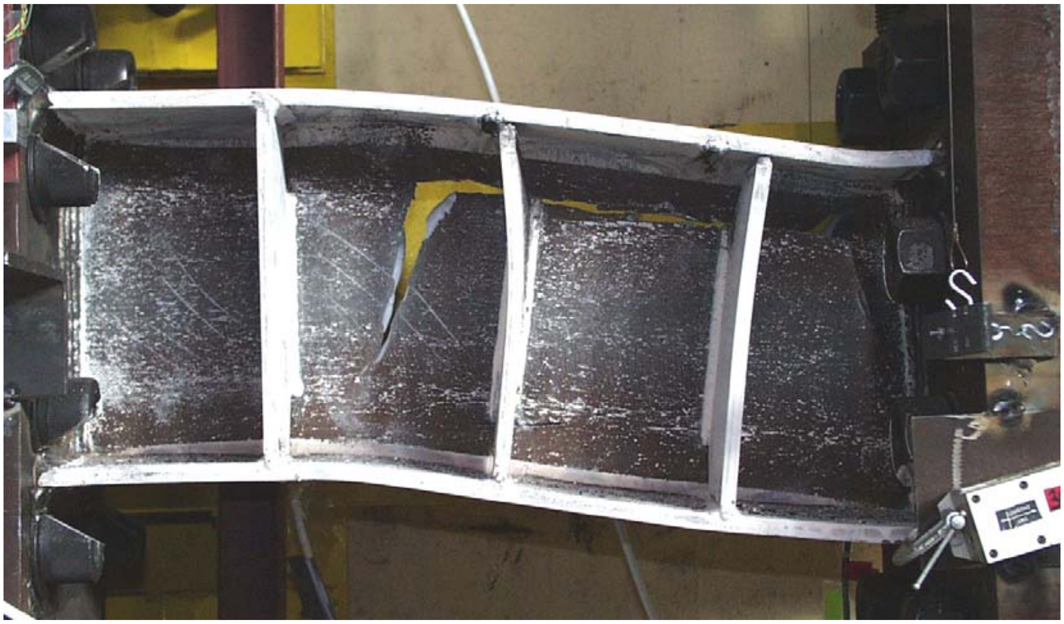

Figure 2.9 Specimen 4B after test (Arce 2002)

In the tests by Arce, an attempt was made to prevent premature web fracture by moving the termination of link stiffener fillet welds farther away from the flange. This approach aimed to reduce the stress concentration at the end of the stiffener, as suggested by McDaniel *et al.* (2003). Another aim was to move the weld terminations away from the k-area of the section, where roller straightened sections are likely to exhibit degraded mechanical properties, as discussed in Section 2.3.3.2. Specimens 4A, 4B, and 4C had identical section (W10x33) and length ($e = 1.0M_p/V_p$), but had different spacing between the k-line and the termination of stiffener weld, as illustrated in Figure 2.10. Figure 2.8 indicates that increasing the distance between terminations of stiffener welds and the flange and k-line, as in Specimen 4A, 4B, 4C, delayed, but did not prevent the premature failure of the link.

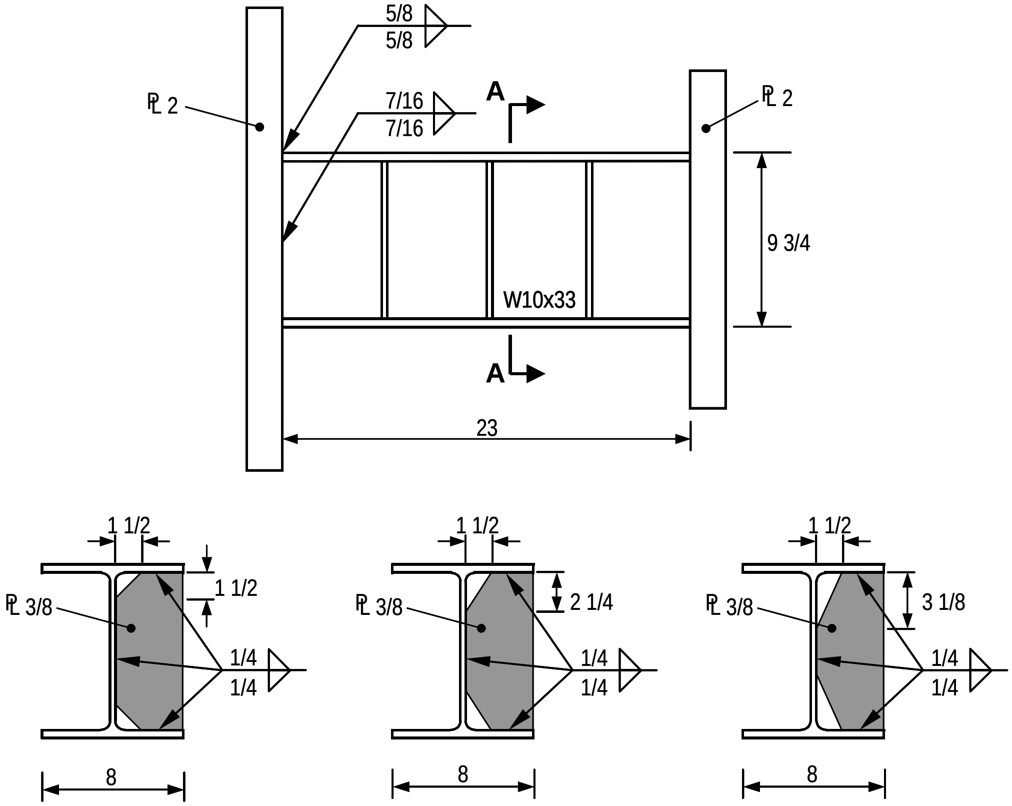

Section A-A
for Specimen 4A (4A-RLP)

Section A-A
for Specimen 4B (4C-RLP)

Section A-A
for Specimen 4C (4C-RLP)

Figure 2.10 Termination of link stiffener welds in Specimens 4A, 4B, and 4C

Arce's Specimen 9 was the only specimen that failed to meet the rotation requirement while not exhibiting web fracture. This specimen had an intermediate link length of $e = 2.0M_p/V_p$, and failed prematurely due to strength degradation associated with severe flange and web buckling near both link ends. Based on finite element analysis, Richards and Uang (2002) suggest that the current stiffening requirement for links of this immediate length range may not be adequate. They propose spacing stiffeners more closely near the ends for these links, since the combined flexure and shear generates a severe condition for local instability in those regions.

The five specimens that successfully achieved their required link rotation did not exhibit web fracture, and ultimately failed due to combinations of severe flange buckling, web buckling, and in some cases, lateral torsional bucking.

2.3.3 Link Web Fracture

Arce (2002) observed typical occurrence of web fractures initiating at the top and bottom end of the stiffeners, at the termination of the fillet welds connecting the stiffeners to the link web. Figure 2.11 shows an example of this fracture at the initiation stage. In this figure, a small fracture is visible in the circled area, at the toe of the bottom termination of the vertical fillet weld. These fractures often propagated in the horizontal direction, running parallel to the

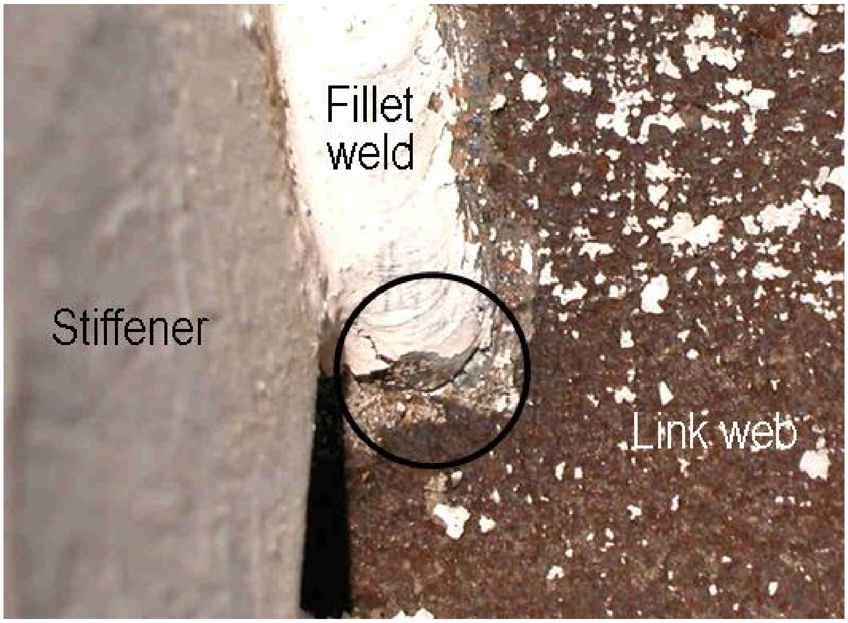

Figure 2.11 Fracture initiation in link web of Specimen 4A-RLP (Ryu et al. 2004)

flanges, and ultimately grew large enough to cause failure of the link. Figure 2.9 shows a specimen that failed in such manner. In the investigation by Arce, all link specimens with links of $e < 1.7M_p/V_p$ failed prematurely due to this type of web fracture. Therefore, a serious concern was raised that shear links might not be capable of developing their required rotation due to the occurrence of web fracture.

Based on a review of past link tests, it appears that this type of web fracture was not reported in previous tests, with the exception of McDaniel *et al.* (2003). Richards and Uang (2002) noted three significant differences between the links tested by Arce (2002) and McDaniel *et al.* (2003) and those in earlier tests, including: (a) web stiffening; (b) link material; and (c) cyclic loading sequence. The influence of the three factors is examined in the following.

2.3.3.1 Stiffener Spacing

As noted by Richards and Uang (2002), the majority of shear link specimens tested earlier in the 80's did not meet the stiffening requirement per the current *AISC Seismic Provisions*. In fact, prior to Arce (2002), only six shear link specimens met the stiffening requirements; two specimens violated the requirements by only a small margin. The former group of specimens includes Specimen A2 with a composite slab tested by Ricles and Popov (1987b), Specimen 5 tested by Kasai and Popov (1987), two built-up link specimens tested by Itani *et al.* (1998; 2003), and two built-up link specimens tested by McDaniel *et al.* (2003). These specimens are indicated in Figure 2.5 by triangles. The latter group of specimens includes Specimens 3 and 7 tested by Kasai and Popov (1987). Out of the combined eight specimens, only three achieved an inelastic link rotation of 0.08 rad or greater: they were Specimen A2 with a composite slab tested by Ricles and Popov (1987b), and the two specimens of built-up sections tested by Itani *et al.* (1998; 2003). As noted by Richards and Uang (2002), these three specimens were tested using a more relaxed loading sequence compared to the specimens tested by Arce (2002).

Kasai and Popov (1986) reported that Specimen 5, with $e = 1.64M_p/V_p$, failed by fracture of the weld connecting the link flange to the steel end plate (similar to the failure discussed in Appendix A). Specimens 3 and 7, with $e = 1.36M_p/V_p$ and $e = 1.08M_p/V_p$, respectively, exhibited significant flange and web buckling near the end, and ultimately failed by "tearing initiated from the perimeter of the stiffener closest to [the link end with greater rotational restraint]." Details of the web fracture were not provided. Ricles and Popov (1987b) reported that no buckling or fracture had occurred in Specimen A2 at the termination of the test. Itani *et al.* (1998; 2003) reported that one specimen failed by fracture at the link end connection, while the other failed after the link web buckled and immediately fractured. Details of the web fracture were not provided. As mentioned earlier, McDaniel *et al.* (2003) reported that both specimens failed due to brittle fracture of the web. The fractures initiated "at the ends of vertical welds of the intermediate stiffeners, near the highly restrained location where the flange-to-web groove weld and the vertical and horizontal stiffener welds of the stiffeners met," similar to the location observed by Arce (2002).

Meanwhile, the majority of tests conducted in the 1980's (*e.g.* Hjelmstad and Popov 1983a) provided the link with sparse stiffening, and therefore, did not meet the requirement in the current *AISC Seismic Provisions*. Shear links with sparse stiffening typically suffered severe web buckling, and thereafter, developed fracture of the web panels at locations of large localized deformations associated with buckling and post-buckling tension fields. Based on the realization that tighter spacing can control web buckling and result in superior link rotation capacity (Kasai and Popov 1986a; 1986c), the current provisions require tighter stiffener spacing than that used in earlier tests. Consequently, the specimens tested by Itani *et al.* (1998; 2003), McDaniel *et al.* (2003), and Arce (2002) typically placed the stiffeners with tighter spacing than the specimens tested in the 1980's.

The above discussion indicates that the tighter stiffening required in the current provisions may alter the failure mode from those reported from the majority of earlier tests. It is possible that preclusion of web buckling shifts the critical failure mode to one controlled by fracture at locations of high constraints due to low cycle fatigue. Nonetheless, the web fracture observed by Arce (2002) was not reported previously, with the exception of McDaniel *et al.* (2003).

2.3.3.2 k-area Properties

The proximity of the fracture in many of Arce's specimens to the k-area of the section raised concerns that degraded material properties in the k-area region may have played a significant role in the fracture process. The k-area issue is a consequence of modern steel shape production practices that includes cold roller straightening.

There has been a large change in steel manufacturing in recent years. The traditional integrated process of steel production is now largely obsolete for structural shapes. Presently, all structural shapes produced domestically, or produced for use in the US are continuously cast from scrap steel melted in electric furnaces (*FEMA-355A* 2000). As a result of this change in manufacturing, the steel today has somewhat different chemical composition, and tends to have increased yield strength. A new specification for structural steel, ASTM A992, has been adopted in order to reflect this change (Barlett *et al.* 2001). A992 steel has more stringent requirements than A36 and A572 Grade 50 in chemical composition and in mechanical properties. Like A572 Grade 50, A992 has a minimum specified yield strength of 50 ksi and a minimum specified tensile strength of 65 ksi. However, A992 limits the maximum yield strength to 65 ksi, and limits the maximum yield-to-tensile strength ratio to 0.85.

Tension coupon tests reported from link test programs exemplify the change in mechanical properties. All links tested in the 80's were constructed of A36 steel. For example, links tested by Hjelmstad and Popov (1983) had measured yield strength values in the flange ranging between 35 ksi and 50 ksi, with yield-to-tensile strength ratios between 0.58 and 0.72. In comparison, all links tested by Arce (2002) were constructed of A992 steel. Arce reported dynamic yield strength in the flange between 49 ksi and 55 ksi, with yield-to-tensile strength ratios between 0.70 and 0.75. Compared to links tested by Hjelmstad and Popov, the yield strength was clearly higher, and the yield-to-tensile strength ratio was slightly higher in the links tested by Arce.

The *AISC Seismic Provisions* (1997; 2002) recognize that roller straightening of wide-flange shapes can cause degradation in mechanical properties at the k-area region, by imposing locally severe strains during the straightening process. As shown in Figure 2.12, the *AISC Seismic Provisions* define the k-area as "the region of the web extending from the k-line, or the point of tangency between the fillet and web, to approximately 1 to 1-1/2 inches beyond the k-line". Miller (1999) investigated rolled shapes produced by alternative processes: quenched self-tempering; roller straightening; and without roller straightening or heat treatment. The material properties in the k-area were studied by hardness tests, Charpy-V notch tests, and tensile coupon tests. The material tests from roller-straightened sections indicated that the k-area region has higher hardness, higher yield and tensile strength, and lower notch-toughness compared to the remainder of the section. The k-area issue appears to be unique to roller-straightened sections, and is not encountered in shapes produced without this

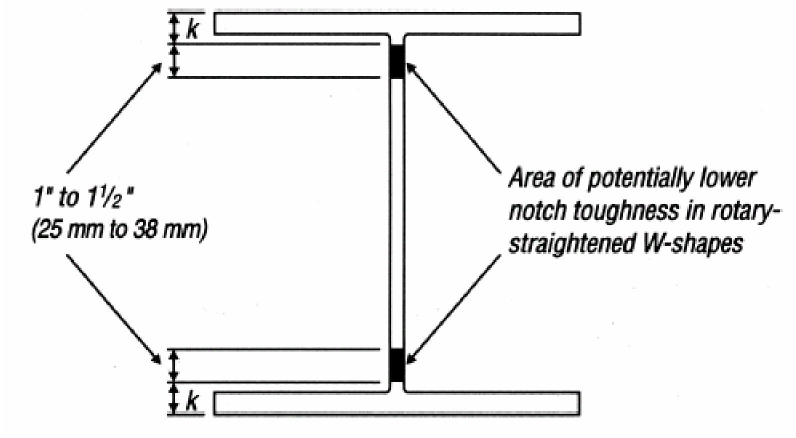

Figure 2.12 K-area of a wide flange section (2002 AISC Seismic Provisions)

particular process.

Incidents of fracture of wide flange members initiating at the k-area during construction (Tide 2000) prompted the AISC (Iwankiw 1997) to issue an advisory including recommended precautionary measures. Most notable was the suggestion to detail welds between continuity plates and columns so that no weld is placed directly in the k-area. The latest research on k-area material properties generally justifies these recommendations (Iwankiw *et al.* 2002). *FEMA-350* (2000) extended the recommendations to all rolled shapes, noting the difficulty in identifying whether or not the delivered steel product had been roller-straightened.

Out of the four wide flange sections tested by Arce (2002), only the W10x19 section successfully achieved the required inelastic rotations for all the link lengths tested (See Figure 2.8). The shortest W10x19 section link of e = $1.73M_p/V_p$ failed due to severe flange and web buckling at the ends, similar to Specimens 3 and 7 reported by Kasai and Popov (1986). Evidently, the W10x19 was the only section that showed no significant degradation in material property in the k-area, according to hardness tests and tensile coupon tests reported by Arce. In the other three sections, the tensile strength and hardness in the k-area was significantly elevated and the strain at fracture significantly reduced compared to the remainder of the web. Currently, Galvez (2004) is conducting a more comprehensive investigation of the effect of k-area properties on the observed web fracture of shear links.

McDaniel *et al.* (2003) reported very similar fractures in built-up links constructed from A709 grade 50 steel plates. Although the k-area issue is not present in built-up sections, these links failed due to fracture initiating in the web where the proximity of the flange-to-web groove welds and stiffener welds created a location of high restraints. McDaniel *et al.* recommended terminating the stiffener welds at a minimum distance of three times the web thickness away from the toe of the flange-to-web groove weld.

No clear evidence has been established linking k-area properties with the web fractures observed in Arce's specimens. However, based on the response of Specimens 4A, 4B, and 4C mentioned in Section 2.3.2, Arce (2002) recommends that stiffener welds should be terminated at a distance of five times the web thickness away from k-line of the link section. This measure is expected to delay, if not prevent, the occurrence of web fractures. Increasing the distance between the stiffener welds to the k-line to more than five times the web thickness is likely impractical for many sections, since little space would be left to place welds between the stiffener and the web.

2.3.3.3 Cyclic Loading Protocol

Richards and Uang (2002) noted the possibility that the loading protocol used by Arce (2002) unfairly penalized shorter links by requiring a significantly larger number of inelastic loading cycles compared to longer links. McDaniel *et al.* (2003) used the same protocol for shear links, and also observed premature failure. This protocol, hereafter referred to as the “AISC protocol”, was first introduced in *Supplement No. 2* (2000) to the *1997 AISC Seismic Provisions* for qualifying cyclic tests of EBF link-to-column connections. Earlier shear link specimens that either did or did not achieve the required inelastic rotation were tested using less severe loading sequences. It was suspected that the larger number of inelastic cycles as required in the provisions could promote low cycle fatigue at locations of high constraint, such as the termination of stiffener welds.

Under this notion, Richards and Uang (2003) developed a revised loading protocol for testing shear links, based on extensive 2-D nonlinear dynamic frame analyses. The analyses suggested that the AISC protocol was, indeed, too severe. Compared to the AISC protocol, the revised protocol requires less number of inelastic cycles to achieve the same rotation level. Moreover, the revised protocol is a more reasonable representation of seismic demands. The two loading protocols are compared in Section 3.2.3. Later, Richards and Uang (2004) extended their previous work and proposed a general loading protocol for testing links of all length categories. This general loading protocol is practically identical to the revised loading protocol intended for shear links only, and possesses characteristics consistent with the loading protocol for testing moment connections provided in the *2002 AISC Seismic Provisions*.

Ryu *et al.* (2004) examined the effect of loading protocols on link performance, as detailed in the following section.

2.3.4 Link Performance under the Revised Loading Protocol

Ryu *et al.* (2004) duplicated and retested five of the shear link specimens tested by Arce (2002). Arce observed all five of these specimens to fail prematurely due to fracture of the link web. Ryu *et al.* constructed the links from the same heats of steel used by Arce. The duplicated links had identical length as the corresponding original, and were provided with identical stiffening details, including stiffener spacing and clear distance between k-line to termination of the stiffener welds. Ryu *et al.* used the same test setup and same testing procedure as Arce, except that the AISC loading protocol used by Arce was replaced with the revised protocol described in Section 2.3.3.3. The five tests by Ryu *et al.* combined with the corresponding five tests by Arce allow comparison of the two loading protocols: the AISC protocol and the revised protocol.

Figure 2.13 illustrates the effect of loading protocol on link response. The figure compares the relation between inelastic rotation and shear force obtained from two identical links: Specimen 4A (Figure 2.13a) was tested under the AISC protocol, while Specimen 4A-RLP (Figure 2.13b) was tested under the revised loading protocol. The revised loading protocol allowed Specimen 4A-RLP to achieve an inelastic rotation capacity of 0.10 rad, a 64% increase compared to Specimen 4A. Both specimens lost their strength drastically at the final stage, due to rapid development of link web fracture. From this comparison, it is clear that the more relaxed testing demand defined by the revised protocol allows the link to develop significantly greater rotation.

The five specimens tested by Ryu *et al.* (2004) are indicated in Figure 2.8 as “Revised Protocol.” The figure shows that all five specimens achieved inelastic rotations greater than the 0.08 rad required for shear links. It is to be noted that the loading sequence was altered for Specimen 11-RLP due to limitation in the stroke of the loading ram. Although this specimen failed during the third repeated cycle (instead of a single repetition) at inelastic rotation amplitude of +0.081/−0.093 rad, it is likely that the specimen was capable of achieving greater rotation. The remaining four specimens tested by Ryu *et al.* achieved increases in inelastic link

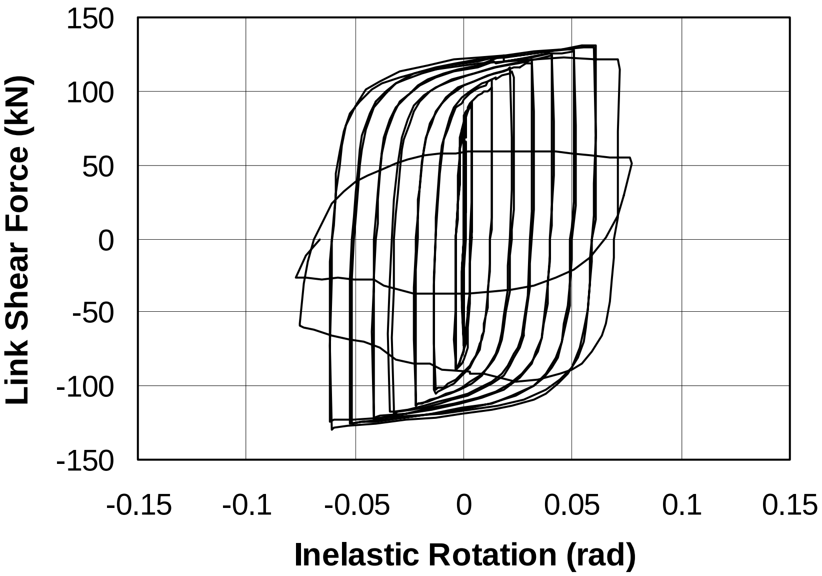

(a) Specimen 4A (Arce 2002)

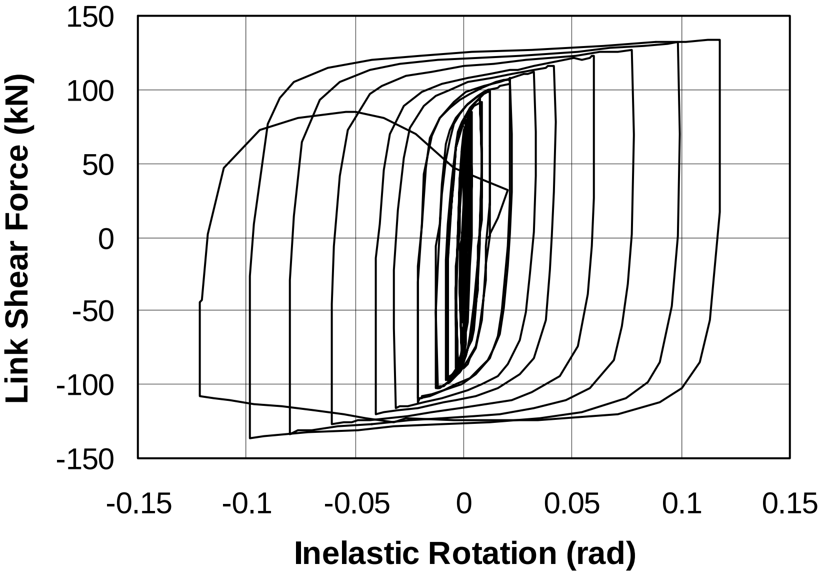

(b) Specimen 4A-RLP (Ryu 2004)

Figure 2.13 Effect of loading protocol on link performance rotation capacity of 50% or more compared to the corresponding specimen tested by Arce (2002).

These tests suggest that the effect of loading sequence on the link rotation capacity is substantial. The same shear links that previously did not meet the rotation requirement under the AISC protocol exceeded the required rotation with a comfortable margin under the revised protocol. The revised protocol was developed based on a more rational basis, and is considered to be more adequate to represent seismic demands than the AISC protocol (Richards and Uang 2003). Therefore, the concern raised by Arce (2002) that shear links may not be capable of achieving the required rotation is now largely resolved.

The large effect of loading sequence on link performance underscores the importance of selecting a loading sequence that reasonably reflects seismic demand. The revised loading protocol was developed explicitly for testing shear links (Richards and Uang 2003). The intermediate links and moment links tested by Arce (2002) have not been retested with the revised protocol. However, Richards and Uang (2004) showed that the AISC protocol is not as penalizing to intermediate links as it is to shear links, and fairly adequate for moment links.

Meanwhile, although the loading sequence had a significant effect on the rotation capacity of shear links, the difference in loading sequence did not change the controlling failure mode. All ten shear link specimens mentioned above, including five specimens from Arce (2002) and five from Ryu *et al.* (2004), failed due to fracture of the web as shown in Figure 2.9. Therefore, it is reasonable to believe that the other two factors discussed in Section 2.3.3, namely the web stiffening and k-area property, may be responsible for the occurrence of web fracture in shear links.

2.3.5 Comparison with Earlier Tests

The tests by Arce (2002) and Ryu *et al.* (2004) provide a comprehensive set of data on links constructed of A992 steel. All specimens in the two programs were tested using the same test setup and identical procedures, except for the loading sequence. The thirteen valid tests by Arce (2002) used the AISC protocol, while the five tests by Ryu *et al.* used the revised protocol. Prior to these tests, very limited information was available on the behavior of links constructed of A992 steel and detailed according to the current *AISC Seismic Provisions*.

2.3.5.1 Inelastic Rotation Capacity

Figure 2.5 compares the inelastic rotation capacity obtained in tests by Arce (2002) and Ryu *et al.* (2004), together indicated as "UT tests," with those from earlier tests. The figure shows that the UT tests tended to develop larger rotations than earlier tests for links of $e > 2M_p/V_p$. One UT specimen with a link of $e = 2.0M_p/V_p$ did not meet its rotation requirement. However, there appears to be no other specimen tested to date with a link length in this immediate range that achieved its required rotation.

The inelastic rotation capacity from the UT tests showed wide scatter in the range of $1.0M_p/V_p < e < 1.7M_p/V_p$. This was primarily due to two reasons. The first reason was the difference in stiffening details. Arce (2002) established that by increasing the distance between the k-line of the link section and the termination of the stiffener weld, occurrence of web fracture could be delayed, and the rotation capacity could be increased. As described in Section 2.3.2, some of the specimens tested earlier (*e.g.* Specimen 4A), with a smaller distance between the k-line and the stiffener weld developed smaller rotation compared to later specimens (*e.g.* Specimen 4C) with a larger distance between the k-line and the stiffener weld. The second reason was the use of two different loading protocols. As described in Section 2.3.4, the more relaxed protocol used by Ryu *et al.* (2004) resulted in significantly greater rotation capacity for identical specimens tested by Arce (2002) with a more severe protocol. Since the relaxed protocol (referred to as the revised protocol in Section 2.3.4) is more reasonable representation of seismic demands on shear links, the link rotation capacity in the range of $1.0M_p/V_p < e < 1.6M_p/V_p$ is more reasonably represented by the test data indicated as "Revised Protocol" in Figure 2.5. Specimen 11-RLP is believed to have developed a greater rotation had it not been for limitations of the test setup. The shear link specimens that developed significantly smaller rotations were penalized by the overly severe loading sequence (referred to as the AISC protocol in Section 2.3.4).

The substantial effect of loading sequence on link performance mentioned above, and discussed in Section 2.3.4, underscores the importance of selecting a loading sequence that reasonably reflects seismic demands. Unlike links of range $1.0M_p/V_p < e < 1.7M_p/V_p$, links of range $e > 1.7M_p/V_p$ were tested only with the AISC protocol. The AISC protocol was not developed on a rational basis, and may not be appropriate for evaluating links of $e > 1.7M_p/V_p$. Since the AISC protocol is increasingly relaxed with link length, the AISC protocol may actually be unconservative for long moment links.

Figure 2.5 indicates that links constructed of A992 steel, represented by tests by Arce (2002) for links of $e > 1.7M_p/V_p$ and tests by Ryu *et al.* (2004) for links of $e < 1.7M_p/V_p$, developed greater rotation than links in earlier tests. However, it should be cautioned that different loading sequences and stiffening criteria were used in earlier tests. Therefore, Figure 2.5 does not allow direct comparison of the effect of material on link performance. Special caution is required in interpreting the performance of moment links and intermediate links, since they were not tested under a rational loading protocol. As discussed above, it is possible that the moment links were tested under an unconservative loading sequence. With the exception of Specimen 9 tested by Arce (2002), UT tests developed link rotations well in excess of the level required in the *2002 AISC Seismic Provisions*. Specimen 9 failed to meet the rotation requirement due to strength degradation associated with severe flange and web buckling. Richards and Uang (2002) suggested reducing the stiffener spacing near the link ends to better control local instability for link of range near $e = 2M_p/V_p$. With modified stiffening, Specimen 9 might achieve greater rotation capacity.

The tests by Arce (2002) and Ryu *et al.* (2004) suggest that, with the exception of the immediate range of $e = 2M_p/V_p$, links constructed of A992 steel and detailed according to the current provisions are capable of developing their required inelastic rotation.

2.3.5.2 Link Overstrength

Figure 2.6 shows that the link overstrength data from Arce (2002) and Ryu *et al.* (2004), together indicated as "UT tests," are in good agreement with earlier tests. As in earlier tests, link overstrength tended to decrease with link length in the range $M_p/V_p < e < 2M_p/V_p$, but remain constant with link length in the range $e > 2M_p/V_p$. Link overstrength was minimal for intermediate links with length near $e = 2M_p/V_p$. However, a notable discrepancy exists between the UT tests and recent tests of built-up sections by Itani *et al.* (1998; 2003) and McDaniel *et al.* (2003), in which link overstrength of close to twice the nominal shear strength was developed. The reason why the built-up sections exhibited greater overstrength is unclear.

As stated in Section 2.2.5, the overstrength factor of 1.5 assumed in the current *AISC Seismic Provisions* may be unconservative for shear links, but are reasonable for intermediate links and moment links. The UT tests found the average overstrength factors for links of range $M_p/V_p < e < 1.7M_p/V_p$ and $e > 2M_p/V_p$ to be 1.41 and 1.26, respectively. A specimen of $e = 2.0M_p/V_p$ (Specimen 9 by Arce (2002)), showed an overstrength factor of 1.12, a considerably smaller value than any other specimen. This specimen failed prematurely, likely due to severe interaction of shear and flexure, and potentially inadequate stiffening as noted by Richards and Uang (2002). By neglecting shear-moment interaction, the current provisions tend to overestimate the link overstrength for links in the length range near $e = 2M_p/V_p$.

Overall, Figure 2.6 indicates that the effect of the change in material from A36 steel, used in the majority of the earlier tests, to A992 steel, used by Arce and Ryu *et al.* and applied widely in recent construction, on link overstrength is minimal. The link overstrength provided in the current provisions is just as suitable for A992 steel as for A36 steel.

2.4 MOMENT CONNECTIONS IN MRFS

2.4.1 Damage during the Northridge Earthquake

The design intent of steel MRFs is to dissipate seismic energy through inelastic action in the region of beam-column joint. Inelastic action may take place through the formation of plastic hinges in the beam, formation of plastic hinges in the clear span portion of columns, formation of plastic shear hinges in the column panel zone, or through a combination of these mechanisms. Since plastic hinging in the clear span portion of columns is less desirable, a strong column-weak beam design is typically adopted.

Prior to the 1994 Northridge earthquake, the welded flange-bolted web detail was predominantly used for beam-to-column connections in MRFs. As illustrated in Figure 2.14, this detail had the beam flanges welded to the column

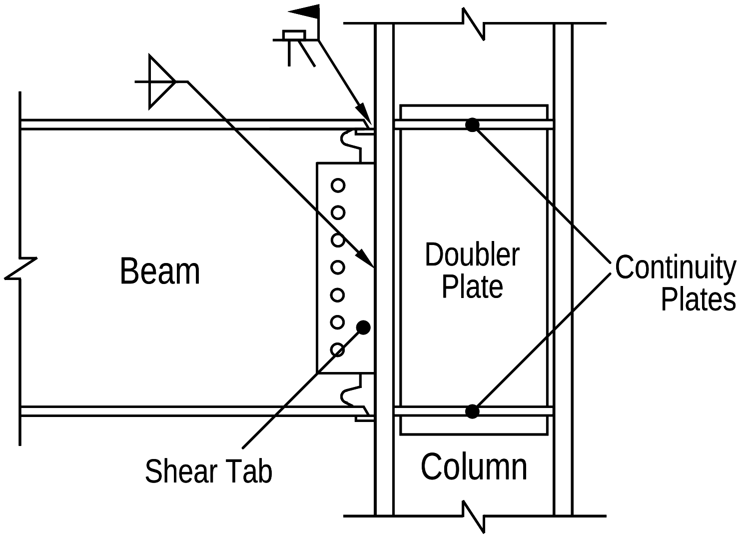

Figure 2.14 Pre-Northridge detail

flange by a complete join penetration (CJP) groove welds. Field welding of the beam flange groove welds was most commonly accomplished using the self shielded flux cored arc welding (SS-FCAW) process with E70T-4 electrodes. These electrodes provide a specified minimum tensile strength of 70 ksi but have no minimum specified notch toughness. The backing bars and weld tabs used to make the groove welds were normally left in place after completion of the weld. The beam web for this connection was bolted to a shear tab, which in turn, was shop welded to the column flange by fillet or groove welds. If required, a doubler plate and/or continuity plates were added to the column panel zone, and fillet welds were sometimes placed between the corners of the shear tab and the beam web. This connection is now commonly referred to as the “pre-Northridge” connection.

The welded flange-bolted web detail was developed based on tests by Popov and Pinkney (1968), Popov and Stephen (1970), Krawinkler *et al.* (1971), Bertero *et al.* (1972), Popov and Bertero (1973), and Tsai and Popov (1988), among others. These tests demonstrated that satisfactory inelastic cyclic behavior was possible with the welded flange-bolted web connections. However, the laboratory data also showed a high incidence of fracture occurring near beam flange groove welds, often prior to the development of significant ductility in the beam-column assemblages.

During the Northridge Earthquake, a large number of MRFs were damaged at the beam-to-column connections. By far the most common type of damage was fracture initiating in the beam bottom flange at the root pass of the CJP groove weld (Kaufmann and Fisher 1995; Kaufmann *et al.* 1997). Lack of evidence of appreciable plastic deformation indicated that many of these connections failed before the development of any yielding in the beams, and therefore performed exceedingly poorly. Further, many of the damaged MRF buildings were located at sites that experienced only moderate ground motion, and many of the damaged buildings were quite new, designed and constructed to the latest building codes. Detailed accounts of the damage can be found, for example, in Bertero *et al.* (1994), Bruneau *et al.* (1998), *FEMA-355E* (2000), and Youssef *et al.* (1995).

The widespread damage discovered after the earthquake combined with tests conducted by Tsai and Popov (1988) and Engelhardt and Husain (1993) provided convincing evidence that the connection shown in Figure 2.14 was not suitable for supplying high levels of cyclic ductility. Tests of pre-Northridge connections conducted immediately after the earthquake (*e.g.* Popov *et al.* 1998a; Hajjar *et al.* 1998; Shuey *et al.* 1996; Uang *et al.* 1998) reproduced all the major types of damage seen in the field, and also exhibited little or no plastic deformation.

Extensive research following the Northridge Earthquake identified a number of factors that contributed to the premature fractures observed after the earthquake. This included factors related to welding, factors related to the connection configuration, as well as others. These factors are discussed in the following, along with various techniques developed to improve the performance of moment connections. Recommendations for a number of methods to achieve improved connection performance based on post-Northridge research are summarized in *FEMA 350 — Recommended seismic design criteria for new steel moment-frame buildings* (2000).

2.4.2 Welding Quality

Engelhardt and Sabol (1997) stressed that welding problems in pre-Northridge connections involved several aspects, ranging from the lack of fracture toughness of the weld metal, poor workmanship and quality control, configuration of the connection that interfered with placement of the weld and inspection, to the practice of leaving backing bars and weld tabs after completion of the weld.

2.4.2.1 Weld Metal

Prior to the Northridge earthquake, nearly all CJP welds between the beam flange and column flange were made using the SS-FCAW process using an E70T-4 or E70T-7 electrode. The popular use of these electrodes was driven primarily by their high deposition rate and economy. However, both electrodes have no specified minimum notch toughness requirement. In fact, it was not until the publication of the 1997 edition of the *AISC Seismic Provisions* that a US building code specified a Charpy V-Notch (CVN) toughness requirement for welds used in seismic force resisting systems.

Kauffman *et al.* (1997) reports fracture analysis of samples taken from beam flange to column connections damaged during the Northridge earthquake. The CVN toughness of the welds, which were likely made from E70T-4 electrodes, ranged between 7 and 15 ft-lbs in room temperature. These values are significantly lower than the level required by *FEMA-350* for beam flange welds in special moment frames. Analyses by Kauffman *et al.* (1997) and Chi *et al.* (2000) indicate that the various brittle fractures could have been prevented if a notch tough weld metal was used for bottom flange welds. Other studies (*e.g.* Kauffman 1997) also confirm the exceedingly low CVN toughness of the E70T-4 weld metal.

Kauffman (1997) constructed beam flange-to-column flange connection specimens using varying SS-FCAW electrodes, and subjected these specimens to monotonic tensile loading with relatively high strain rates, of the order of 0.02 sec^{-1}. These tests confirmed that the CVN toughness requirement of 20 ft-lbs at minus 20˚F is adequate for preventing the brittle fracture of the welds observed in pre-Northridge connections. The *2002 AISC Seismic Provisions* require the filler metal used in seismic load resisting frames to be capable of producing welds that have a minimum CVN toughness of 20 ft-lbs at minus 20˚F and 40 ft-lbs at 70˚F. Johnson *et al.* (2000) established that the SS-FCAW process using an E70T-6 or E70TG-K2 electrode can meet these CVN toughness requirements.

2.4.2.2 Welding and Inspection Practices

Engelhardt and Sabol (1998) noted at least one case in which the welding procedure caused a substantial difference in the performance of a tested moment connection. They stressed that violation of the voltage and current limits in the properly formulated welding procedure can result in a weld metal with exceedingly low fracture toughness. Since the loss of fracture toughness resulting from improper welding procedures cannot be detected by ultrasonic testing of the completed weld, in-process inspection should be carried out during completion of the weld to assure conformance with proper procedures.

In a typical field condition, placement of the CJP weld at the bottom beam flange is interrupted by the beam web. Consequently, near the weld access hole, where the weld must be started or terminated, the bottom flange weld is likely to include defects. On the other hand, the presence of the beam web is an obstacle for ultrasonic testing of the weld at this critical location, since the beam web interferes with the ultrasonic procedure. Therefore, *FEMA-350* recommends removal of the bottom flange backing bar to enable visual inspection of the weld root and removal of detected flaws. It is also recognized (Engelhardt and Sabol 1997) that ultrasonic testing should be performed from both the top and bottom side of the flange to achieve a thorough examination of the weld.

2.4.2.3 Welding Details

Fracture surface analysis of damaged moment connections (Kaufmann *et al.* 1997), analytical studies (Chi *et al.* 2000; El Tawil *et al.* 1998; Popov *et al.* 1998), and large-scale tests (*e.g.* Leon *et al.* 1998; Popov *et al.* 1998b) suggest that the notch effect of the backing bar and high likelihood of weld defects at the root of the weld, combined with the lack of fracture toughness of the weld metal, initiated the widespread fractures at beam bottom flange groove welds discovered after the Northridge earthquake. Chi *et al.* (2000) compared the benefits of (a) removing the backing bar and placing a fillet weld between the root of the weld and the column flange, and (b) placing a fillet weld between the backing bar and column flange. Based on fracture mechanics analysis, Chi *et al.* suggested that both (a) and (b) are effective fracture mitigation measures. Nonetheless, removal of the backing bar can provide a vital benefit to the bottom flange, by enabling detection and correction of defects at the weld root.

The weld metal in the runoff tabs is also likely to include weld defects. Weld tabs are located at the two ends of the weld passes, so that the initiation and termination points could be placed outside of the primary stress path. Nonetheless, if the weld tabs were left in place, the defects contained in the weld tabs may cause fracture.

Based on the observations discussed above, *FEMA-350* suggests adhering to the following measures for beam flange CJP welds: (1) remove the weld tabs from both the top and bottom flanges; (2) provide a reinforcing fillet weld between the backing bar and column flange at the top flange; and (3) remove the bottom backing bar, back gouge the weld root, and then provide a reinforcing fillet weld at the root of the bottom flange groove weld.

2.4.2.4 Effect of Welding Improvements

Stojadinovic *et al.* (2000) tested moment connections with the pre-Northridge configuration, as shown in Figure 2.14, but adopting the recommended welding improvements discussed above, including the use of a notch-tough weld metal, improved welding details, and better practices in welding and inspection. Although a clear improvement over the pre-Northridge connections was noted, the average inelastic rotation developed by the improved connections was roughly half of the 0.03 rad required for special moment frames in the *AISC Seismic Provisions*. Due to the smaller stiffness of the bolted web connection compared to the welded flange connection, the web connection cannot fully participate in transferring the beam moment and shear from the beam to the column. Consequently, beam flange welds can be subjected to excessively high levels of stresses. Stojadinovic *et al.* concluded that improvements in welding alone may not be sufficient to achieve the ductility required for severe seismic application. Similar results were also reported by Ricles *et al.* (2002).

The general notion (*e.g. FEMA-350*) is that weld improvements should be implemented together with modified connection design and detailing to achieve reliable performance of welded moment connections.

2.4.3 New Connections Developed After the Northridge Earthquake

2.4.3.1 Problems Inherent to the Pre-Northridge Configuration

Goel *et al.* (1997), Lee (1998), and Popov *et al.* (1998b) demonstrated by finite element analyses that the configuration of the conventional moment connection draws shear stresses in addition to bending stresses to the beam flange welds, and away from the web connection. A detailed study by Lee (1998) suggests that the stress distribution in the beam is strongly affected by the Poisson effect and warping restraint caused by the column, and by the flange-web interaction of the beam, besides the column panel zone deformation and bending deformation of the column. Noting that these effects can build up to cause much higher stresses in the beam flange welds than considered in the traditional design procedure, Goel *et al.* (1997) and Lee (1998) proposed a truss analogy to model the force flow near the connection, and further utilized this model to develop improved connection configurations.

The shear force in the beam flanges causes secondary bending of the beam flanges. When the flange is subjected to tension, the local bending adds to the tensile stresses at the outer face of the flange and reduces the tensile stresses at the inner face of the flange. At the bottom flange, the elevated tensile stresses act at the weld root, where likely weld defects are located and the backing bar can cause notch effects (Chi *et al.* 2000). At the top flange, on the other hand, the secondary bending decreases the tensile stresses acting at the weld root. Therefore, the pre-Northridge connection was particularly vulnerable to fracture at the bottom flange.

In a welded flange-bolted web connection, the lack of participation of the bolted web connection can further increase the proportion of beam shear force transmitted through the welded flange connections. The presence of weld access holes causes additional stress concentrations near the flange welds.

The deformation restraint at the beam flange near the column face has adverse effects from the fracture mechanics point of view (*e.g.* Miller 1998; Popov *et al.* 1998b). This restraint causes a triaxial stress state, which delays yielding of the material and can therefore promote brittle behavior.

Consequently, the pre-Northridge connection was inherently flawed due to the overall configuration that draws a significant portion of the beam forces to the beam flanges, the likelihood of weld defects located at the root of the flange bottom weld where the highest stress level is expected, additional stress concentrations near the flange weld due to the presence of the weld access hole, and high stress triaxiality near the flange weld. This notion combined with the caution against over-reliance on welding quality led to the suggestion in *FEMA-267 — Interim Guidelines* (1995) that the intent of the connection design should be to force the plastic hinge away from the face of the column, and thereby, maintain the connection essentially elastic at the face of the column. This philosophy generally dictated the direction of US research and development in the following years.

2.4.3.2 Reinforced Connections

The design purpose of reinforced connections is to force the plastic hinge formation away from the column face by stiffening the beam near the column face, and consequently reduce the stress and strain levels at the vulnerable region near the beam flange welds. Reinforcement can be accomplished, for example, by employing cover plates, upstanding ribs, or haunches at the beam near the column face, as shown in Figure 2.15. The widespread damage during the Northridge Earthquake caused a demand not only to repair damaged connections, but also to upgrade existing connections in high seismic areas to avoid future occurrence of similar damage. During that time, the cover plate reinforcement (See Figure 2.15a) received special attention due to the lower cost and smaller space requirements compared to other reinforcing methods. Engelhardt and Sabol

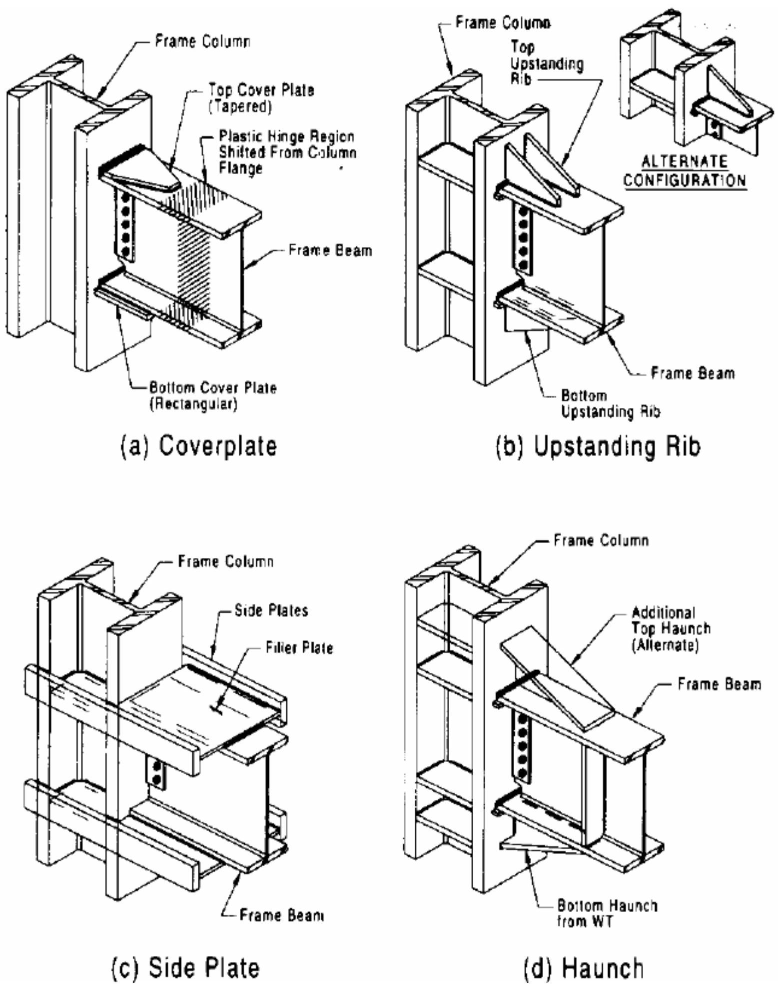

Figure 2.15 Examples of connection reinforcement (from Engelhardt and Sabol 1998)

(1998) observed that excellent cyclic ductility can be achieved by connections reinforced with cover plates. However, Engelhardt and Sabol also emphasized that the use of cover plates does not preclude the need for fracture toughness of the groove welds, and that the cover plates introduce a series of additional concerns. The additional welds required by the cover plates introduce unique welding and inspection issues. The gap between the cover plate and beam flange can potentially act as a fracture initiating notch, particularly when the column is subjected to large tension. The cover plates increase the beam flexural capacity, and thereby increase the required panel zone size to maintain the strong column-weak beam system.

Kim *et al.* (2002a; 2002b) developed a variation of cover plate connection where only the cover plate is welded to the flange, while the beam flange itself is not directly connected to the column flange. This connection, designated as the flange plate connection, was demonstrated by Kim *et al.* (2002a) to perform similarly to cover plate connections.

Limited data is available for connections with upstanding ribs (See Figure 2.15b). Tsai and Popov (1988) tested one such connection and reported that the reinforcement resulted in somewhat greater plastic rotation, even though the weld connecting the ribs to the connection was inadequate. Engelhardt and Sabol (1994) tested two connections with upstanding ribs and observed acceptable performance. Due to the limited amount of test data and the questionable behavior observed in tests, *FEMA-267* did not view the upstanding rib reinforcement favorably.

Engelhardt and Sabol (1994) tested two side plate connections with the configuration shown in Figure 2.15c. Although this specific variation proved to be unsuccessful, with some alteration, the side plate concept may be used to develop a sufficiently ductile connection, as evidenced by the proprietary side plate connection (*FEMA-350*). In Japan, the Council on New Frame System (2003) developed a reinforced connection combining coverplates and side plates.

The haunch reinforcement (See Figure 2.15d) was studied primarily as a method to repair damaged connections and to upgrade existing connections. *Shuey et al.* (1996) observed that better performance can be achieved when haunches are welded to both the top and bottom flanges of the beam, as shown in Figure 2.15d, instead of to only the bottom flange of the beam. However, for repairing and upgrading existing connections, it is preferred not to disturb the existing composite slab, and to place reinforcing elements only beneath the slab. Consequently, the design with only the bottom haunch was mainly investigated in research. A large number of connections have been tested with a triangular haunch, made from a wide flange section, welded to the bottom flange. Shuey *et al.* (1996) and Uang *et al.* (1998) investigated the use of haunches as a means to repair damaged pre-Northridge connections. Civjan *et al.* (2000) and Uang *et al.* (2000) examined the effect of composite slabs on haunch reinforced connections. It was commonly observed that, while the addition of a bottom haunch makes the connection insensitive to the quality of the bottom flange weld, the connection is vulnerable to fracture of the top flange weld unless fracture tough welds are used or reinforcements are placed. The presence of a composite slab was found to significantly delay fracture of the top flange weld and increase the plastic rotation capacity of the connection. Therefore, when a reinforcement element is placed to the top flange welds, or when a composite slab was present, the bottom haunch connections were capable of achieving sufficient performance.

Based on these experimental data, Yu *et al.* (2000) and Gross *et al.* (1999) established a design procedure for the reinforcing haunches. Lee and Uang (2001) and Lee *et al.* (2003) developed an alternative haunch reinforcement which utilizes “straight” haunches which are much easier to install than triangular haunches.

In general, connection reinforcement reduces the effective length of the beam, reduces the span-to-depth ratio, and increases the plastic hinge rotation demand. Although reinforcement is extremely effective in shielding the beam flange welds from large stresses, fabrication of these connections requires placing welds at the plastic hinge region. These welds can introduce new sources of stress concentration and weld defects. Therefore, similar to pre-Northridge connections, the performance of reinforced connections depends on the quality of welding.

Based on these studies, *FEMA-351 — Recommended seismic evaluation and upgrade criteria for existing welded steel moment-frame buildings* (2000) approves the cover plate and haunch reinforcement for upgrading existing moment connections. However, *FEMA-350* includes only the flange plate connection as a prequalified connection for new construction. According to the commentary on *FEMA-350*, the flange plate connection was regarded to be more reliable than the cover plate connection, since the former requires welding of a single thickness plate, while the latter requires welding of both the beam flange and a cover plate. The commentary also states that the cover plate connection and haunch connection are not listed as prequalified because they are more costly and no more reliable than alternative connections, such as the reduced beam section connection.

2.4.3.3 Reduced Beam Section

The basic concept of the reduced beam section (RBS) connection is similar to the reinforced connections. In an RBS connection, the plastic hinge is forced away from the column face by selectively weakening a region of the beam near the column face. By taking into account the moment distribution, the beam flanges can be strategically weakened to distribute inelastic action in an enlarged region, while limiting the moment developed at the beam-to-column connection. Various RBS shapes have been proposed and examined, such as the constant cut (Plumier 1997), linearly tapered cut (Chen *et al.* 1996; 1997; 2001a; 2001b), perforated (Lee *et al.* 2002), and radius cut, each illustrated in Figure 2.16. Among these varieties, the radius cut RBS gained favor in research and in construction practice due to ease in fabrication and due to test results (*e.g.* Chen *et al.* 1996; Engelhardt *et al.* 1998) demonstrating that stress concentrations at abrupt transitions of flange cut can cause fracture, and the smooth transition as in the radius cut leads to better performance. Stable ductile behavior of radius cut RBS connections have been verified by numerous other studies (*e.g.* Suita *et al.* 1999, Jones *et al.* 2002, Gilton and Uang 2002, Chi and Uang 2002).

Although the initially proposed RBS (Chen *et al.* 1996; Plumier 1997) aimed to simply enlarge the plastic zone in a segment away from the column face, researchers (Engelhardt *et al.* 1998; Engelhardt 1999) eventually arrived at a specific RBS design that attempts to limit yielding near the column face. The

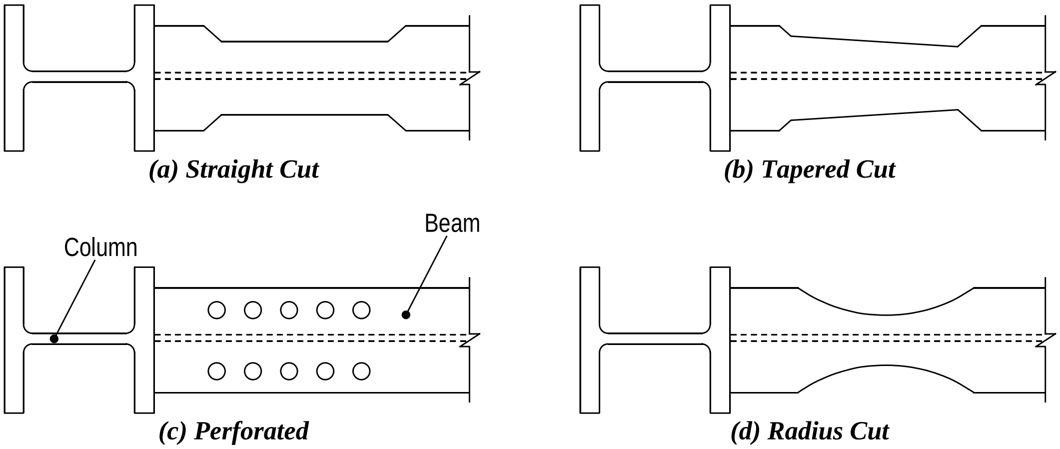

Figure 2.16 Examples of reduced beam sections

objective of this design, illustrated in Figure 2.17 with key dimensions, is to assure that inelastic action is concentrated in the RBS segment, while the moment developed at the face of the column does not exceed the plastic moment of the full beam section. This RBS design is now accepted as a prequalified connection in *FEMA-350*. Since the stresses developed near the flange welds are limited, the prequalified RBS connection is somewhat less sensitive to the quality of welds, unlike the reinforced connections discussed in Section 2.4.3.2. Nonetheless, Engelhardt *et al.* (1998) and Chen *et al.* (2001b) cautioned that the quality and fracture toughness of the beam flange welds is important for the robustness of the RBS connection. Civjan *et al.* (2000) and Jones *et al.* (2002) noted that the excellent performance of RBS can be jeopardized if a bolted beam web connection is used rather than a welded beam web connection.

Due to the removal of flange material, with the flange width reduced by as much as 50%, RBS beams are more prone to web buckling compared to beams without an RBS, and tend to be controlled by instability of the RBS segment. Jones *et al.* (2002) cautioned that severe lateral torsional buckling of the RBS beam can destabilize the entire frame. Uang and Fan (2001) proposed a web

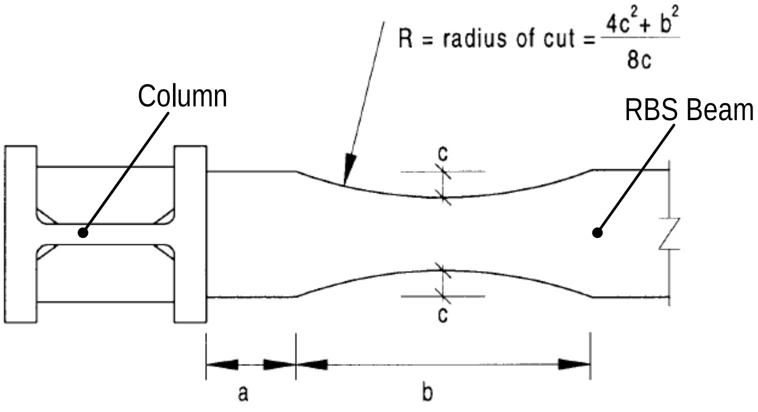

Figure 2.17 Prequalified RBS design (from Engelhardt et al. 1998)

slenderness limit more stringent than that required by the *1997 AISC Seismic Provisions* to be used for RBS beams, to control web buckling and assure sufficient rotation capacity of the beam. Numerical analyses by Nakashima *et al.* (2002) demonstrated that RBS beams can, in fact, be less prone to lateral torsional buckling compared to beams without an RBS, due to the enlarged plastic hinge region and smaller forces. However, the analysis did not include local buckling of the flange and the web. Instability of RBS beams typically initiates by local buckling in the web, followed by local buckling in the flange and lateral torsional buckling (Uang *et al.* 2001; Jones *et al.* 2002).

When applying the RBS concept to repairing or upgrading of existing buildings, it is advantageous to trim only the bottom flange so that the composite slab need not be removed. However, the non-symmetric RBS section and composite action of the slab can cause a shift in the neutral axis and raise the strain demand at the bottom flange. Civjan *et al.* (2000) and Uang *et al.* (2000) tested RBS moment connections with only the bottom flange trimmed. The tests demonstrated that the existing E70T-4 groove weld in the beam top flange is vulnerable to premature fracture. With or without composite slabs, the RBS connections with only the bottom flange trimmed achieved smaller rotation compared to RBS connections with both top and bottom flanges trimmed.

2.4.3.4 Unreinforced Connections

Finite element analyses conducted by Mao *et al.* (2001) suggested that the weld access hole configuration and fixity of the web connection can significantly alter the local stress and strain distribution near the weld access holes and beam flange welds. Based on the analyses, Mao *et al.* proposed an optimum weld access hole configuration that minimizes the propensity for fracture.

Mao *et al.* (2001) analyzed moment connections adopting the proposed weld access holes and various web connections, such as: (a) conventional bolted web connection (See Figure 2.14); (b) beam web directly connected to the column by groove welds; (c) beam web connected to the shear tab with fillet welds; and (d) groove welded web supplemented by fillet welds between the beam web and shear tab. The analysis showed that the web connection can significantly affect connection performance. Web connections with greater fixity as (c) with a heavy shear tab and (d) resulted in greater inelastic rotation capacity compared to other connections. Ricles *et al.* (2002) tested unreinforced connections using an improved access hole geometry and using a beam web connection that combined a groove weld with supplemental fillet welds (option (d) described above). Most of these test specimens achieved inelastic rotations greater than the 0.03 rad required by the *AISC Seismic Provisions*, and this connection type was prequalified in the *FEMA-350* for use in special moment frames. Ricles *et al.* (2002) noted that the quality of the beam web groove welds can be improved if runoff tabs were used when placing the welds. Further large-scale tests by Dexter *et al.* (2004) also demonstrated that the unreinforced welded flange-welded web connection (web connection (d)) can meet the requirement for special moment frames.

A welded flange-bolted web connection specimen tested by Ricles *et al.* (2002) combining improvements in weld access hole configuration combined and the welding improvements proposed by *FEMA-350* could not provide the 0.03 rad of plastic rotation required of special moment frame connections. Therefore, based on the above tests as well as tests by Stojadinovic *et al.* (2000), *FEMA-350* did not prequalify welded flange-bolted web connections for special moment frames.

2.4.3.5 Free-Flange Connection

Choi *et al.* (2000; 2003) proposed the free flange connection as an effective moment connection which reduces the stress level at the vulnerable beam flange welds. As shown in Figure 2.18, the free flange connection uses an extended free flange length (distance between the face of the column and toe of the weld access hole) and a heavy shear tab welded to the beam web, which in combination, controls the relative stiffness of the flange connection and web connection. The free beam flange is flexible in shear, while the beam web is provided with significant additional stiffness and strength by the shear tab. The intent is to direct the beam shear away from the beam flanges, and thereby

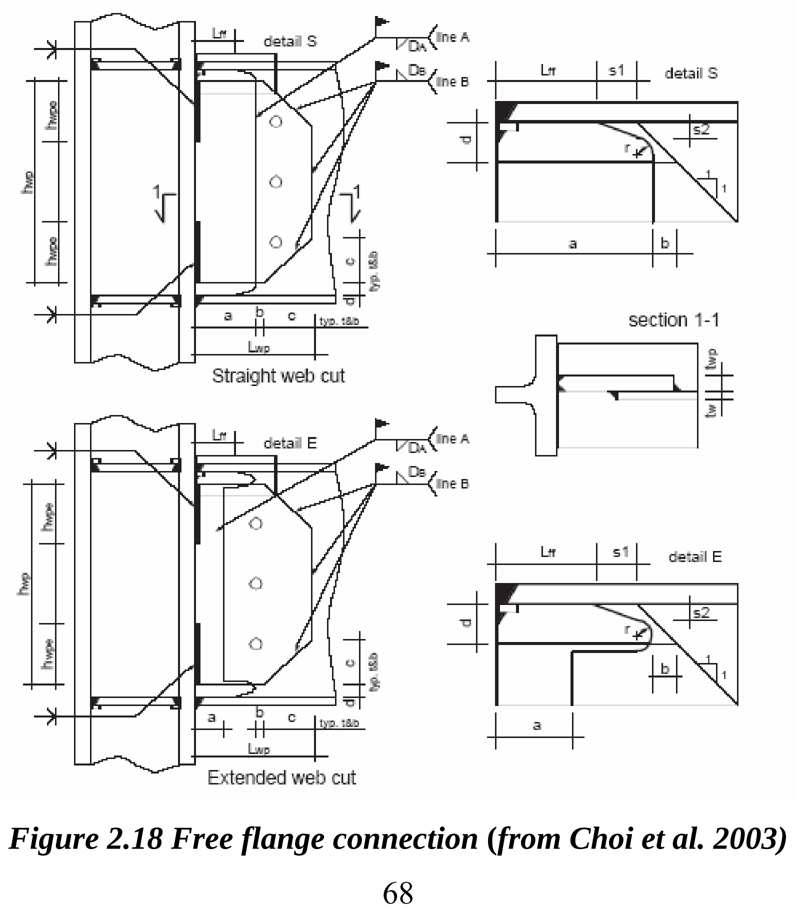

Figure 2.18 Free flange connection (from Choi et al. 2003)

reduce the local bending introduced near the beam flange welds. The beneficial effect of a stiff web connection was also recognized by Ricles *et al.* (2002), as discussed in Section 2.4.3.4. Satisfactory performance of the free flange connection was demonstrated by tests conducted by Choi *et al.* (2000), Gilton *et al.* (2000), and Venti and Engelhardt (2000).

2.4.3.6 Other Connections

Besides the connections discussed above, various other types of welded and bolted connections are also prequalified by *FEMA-350*. Several proprietary connections are also in use, including the slotted web connection and the side plate connections. These proprietary connections are not prequalified in *FEMA-350*, but are described in *FEMA-350* as an alternative that designers may wish to consider.

Christopoulos *et al.* (2002) and Ricles *et al.* (2001) proposed designs of self-centering systems as alternatives to MRFs with welded moment connections. The self-centering properties provided by post-tensioned steel bars or tendons restore the structural system to its original position after an earthquake, and reduce the damage to main structural elements. These systems also avoid reliance on welding quality.

2.4.4 Other Key Issues

2.4.4.1 Qualifying Tests

Prior to the Northridge earthquake, there were no widely agreed upon criteria to determine whether or not a connection performs satisfactorily in a cyclic loading test. There appeared to be a vague agreement that a minimum inelastic rotation of 0.015 rad is required to justify the reduction factor of $R_w = 12$ granted to special moment frames (Bertero *et al.* 1994; Popov *et al.* 1998a).

However, little attention was paid to actually quantifying the deformation demands on steel moment frame connections.

Following the Northridge earthquake, *FEMA-267* suggested that qualifying cyclic loading tests should be required for all moment connections to demonstrate their strength and inelastic rotation capacity. Test specimens were to adequately represent the essential features of those used in the actual design, such as member size, span-to-depth ratio of the beam, material, welding process and details, and connection configuration including doubler plates and continuity plates. The qualifying test procedure has been implemented and further refined in the *AISC Seismic Provisions* since its 1997 edition.

The most important aspects of the qualifying cyclic loading test were the required rotation level and cyclic loading protocol. The *FEMA-267* proposed a required plastic rotation capacity of 0.03 rad as a reasonable upper-bound estimate of moment frame connection deformation demands in actual earthquake, based on a review of analytical research. Large-scale test data available at the time also suggested that connections capable of achieving this rotation level would fail in the members, by local and lateral torsional buckling, rather than in the connection. This required capacity has since been adopted in the *AISC Seismic Provisions*.

Many of the tests conducted after the Northridge earthquake used a testing protocol reported in Clark *et al.* (1997). This protocol was based on extensive dynamic frame analyses of MRFs conducted by Gupta and Krawinkler (1999). This loading protocol has since been adopted by *FEMA-350* as well as by the *AISC Seismic Provisions*. Later, Krawinkler *et al.* (2000) also proposed a near-fault loading protocol to specifically address the significant difference in demand arising from near-fault events.

2.4.4.2 Span-to-Beam Depth

Since the 1970's, there has been a trend of reducing the number of fully rigid connections in the MRFs to achieve better economy (*FEMA-267* 1995; Roeder and Foutch 1996). It became quite typical to provide moment connections only in perimeter frames of the structure, or only in selected bays. Adoption of these designs with only a small number of moment frames led to a significant increase in member sizes in the moment frames to meet code specified drift limits. The use of deep beams and columns to control drift led to beams with smaller span-to-depth ratios. However, a beam with a small span-to-depth ratio produces steeper moment gradients along the beam span, and forces strain hardening to take place in a limited region near the beam ends. Such beams must develop very severe plastic strains at the ends in order to supply plastic hinge rotation.

FEMA-350 specifically addresses the span-to-depth ratio by limiting the use of prequalified connections to MRFs proportioned with span-to-depth ratios greater than a certain limit. For special moment frames, the limit is typically set at 8, where the span is taken as the clear distance between two columns at the ends of the beam.

2.4.4.3 Panel Zone Strength

Krawinkler (1978) and Popov (1987) suggested that shear yielding in the column panel zone is an efficient energy dissipation mechanism for MRFs, while also cautioning that excessive panel zone deformation can cause kinks in the column flanges, and consequently generate large strain demands in the region of the beam flange welds. The high strains imposed by these kinks can lead to premature fracture of the beam flange welds, or in some cases, fracture of the column flanges. Nonetheless, the notion of beneficial panel zone yielding led to a relaxed panel zone strength requirement in the code provisions prior to the

Northridge Earthquake, to permit substantial inelastic deformation in the panel zone and to provide savings by reducing the need for column web doubler plates (Roeder and Foutch 1996).

El-Tawil (2000) showed that the relaxed strength requirement can lead to premature fracture of the beam flange welds. Moreover, the strength of the beam connecting to the joint was frequently underestimated (see Section 2.4.4.7). As a consequence, the panel zones could be subjected to forces and deformations significantly greater than the code provisions intended. Finite element analyses by El-Tawil *et al.* (1999) suggested that, in joints with thick column flanges and deep beams, the narrow rectangular panel zones can deform primarily in flexure. Therefore, the design equation, which assumes simultaneous shear yielding in the panel zone and kink formation at the corners of the panel zone as observed by Krawinkler (1978), may not be appropriate for narrow panel zones.

Many other analytical studies and large-scale tests were conducted to investigate the effect of strength balance between the panel zone and beam. Finite element analyses by Chi *et al.* (2000), and Mao *et al.* (2001) suggests that large inelastic panel zone deformation can promote fracture of the beam flange, and thus, a stronger panel zone that limits inelastic deformation in the panel zone is desirable. Ricles *et al.* (2002) observed in large-scale tests that although panel zone yielding can increase overall beam rotation, large panel zone deformation can cause fracture near the flange welds, and thus, negate any of its benefit to beam rotation. Nonetheless, a number of large-scale tests suggest that the debate on whether panel zone yielding is acceptable or desirable remains open.

The above research led to the notion that better performance can be achieved by limiting inelastic deformation in the column panel zone. The *2002 AISC Seismic Provisions* permits limited yielding of the panel zone, but requires that the primary energy dissipation in moment frames still be provided by flexural plastic hinges in the beams.

2.4.4.4 Continuity Plates

Immediately after the Northridge Earthquake, concerns were raised about the accuracy of code formulas for continuity plate design. Consequently, *FEMA-267* recommended providing continuity plates at least equal to the thickness of the beam flange to all moment connections. *FEMA-267* also cautioned against the restraint introduced by overly thick continuity plates and associated large welds. Large scale tests by Ricles *et al.* (2002) and Dexter *et al.* (2004) subsequently indicated that the conservative continuity plate requirements by *FEMA-267* can be safely relaxed. *FEMA-350* provides updated formulas for computing the required thickness of continuity plates.

2.4.4.5 Web Connection

As discussed in Section 2.4.3.4, the welded web connection can transfer a significantly greater amount of moment and shear compared to bolted web connections, and thereby reduces the force demands at the beam flange welds. Unreinforced connections in SMFs are now required to be designed with a welded web connection (*FEMA-350*). Gross *et al.* (1999) cautions that RBS connections with bolted webs are more likely to fracture near the beam flange welds.

2.4.4.6 Composite Floor Slab

The presence of a concrete composite slab may potentially cause adverse effects on steel moment connections. As a result of composite action, the neutral axis can move depending on the loading direction. When the composite beam is subjected to a positive moment, the slab in compression would add to force resistance, and move the neutral axis closer to the slab. The larger strain demands at the bottom flange than at the beam top flange can cause premature fracture at the bottom flange weld. When the composite beam is subjected to a negative moment, the slab in tension would not contribute to force resistance. Composite slabs can also provide beneficial effects by preventing out-of-plane motion of the beams and torsional motion of the columns.

Leon *et al.* (1998) and Hajjar *et al.* (1998) observed significantly more extensive yielding and buckling in the bottom flange than in the top flange, and measured much higher strains. These results indicated that the composite slab effect may have been a contributing cause of premature fracture of the beam bottom flange welds in pre-Northridge connections (See Figure 2.14). Chen *et al.* (2001b) measured that composite beams developed 18% larger moment in the loading direction subjecting the slabs to compression, compared to the opposite loading direction. Civjan *et al.* (2001) observed the benefit of composite slabs in reducing the stresses at the top beam flange, delaying local and lateral torsional buckling of the beam, and thereby, delaying strength degradation of the moment connection. Similarly, Jones *et al.* (2002) noted that a composite slab can restrain lateral torsional buckling of RBS beams, while not causing early fracture of the connection.

Ricles *et al.* (2002) tested one specimen with a composite slab, which ultimately failed by fracture of the beam top flange initiating at a shear stud weld. The shear stud was placed near the column face, where the beam flange was subjected to significant plastic strains. Based on this observation, the *2002 AISC Seismic Provisions* prohibits placing welded shear studs in the region where large plastic strains are expected.

2.4.4.7 Material

Prior to the Northridge Earthquake, the permissive ASTM A36 and A572 Grade 50 specifications resulted in the production of “dual grade” steel (Dexter *et al.* 2000). Manufacturers typically produced steels that would meet both A36 and A572 Grade 50 specifications. As a result, beams designed according to A36 specifications frequently had properties of A572 Grade 50 steel. In cases where the elevated strength of the beams was not correctly accounted for, the strong column-weak beam balance might not be assured, the column panel zone might be weaker with respect to the beam than the design intended, and the beam flange welds might be subjected to higher stresses. Better estimation of material strength was required to achieve a more reliable design. Therefore, the *AISC Seismic Provisions* (1997, 2002) now specify using the expected yield strength instead of the specified minimum yield strength for evaluating member strengths when an adjoining element or connection is designed to develop the strength of the member. Moreover, a new structural steel specification, ASTM A992, has been introduced to provide better control of material strength. The ASTM A992 standard specifies a minimum yield stress of 50 ksi, a maximum yield stress of 65 ksi, and a maximum yield ratio (F_y/F_u) of 0.85. The ASTM A36 and A572 Grade 50 standards provided no upper limit on yield stress and no upper limit on yield ratio.

A number of the fractures observed after the Northridge Earthquake propagated through the column flange, raising suspicion that these failures were caused by inadequate through-thickness properties of the column flanges. However, based on pull-plate tests, Dexter *et al.* (2000) concluded that through-thickness fractures are not likely to occur in the column flanges at moment connections.

2.4.4.8 Beam Section Size

The size of the beam can have detrimental effects on the ductility of moment connections (Engelhardt and Sabol 1998). A beam with larger flange thickness would require larger weld heat input, and thereby increase the residual stresses induced by welding. The thicker flange may also introduce higher degrees of triaxial tension in the beam near the column and promote brittle fracture. A secondary effect of the beam section size is that if a deeper beam is used for the same span length, the span-to-beam depth ratio is reduced (Roeder and Foutch 1996). Many of the buildings damaged during the Northridge earthquake had W30, W33, and W36 beams (Youssef *et al.* 1995). Meanwhile, the experimental research which formed the basis of the pre-Northridge connection used much smaller sections, including W18, W21, and W24 beams. Noting that test data from smaller sections may not represent the same conditions realized in larger sections, *FEMA-350* specifies that prequalification tests on moment connections must use beams that are full-scale or nearly full-scale compared to those that will be used in the actual building.

2.4.4.9 Deep Columns

When column sizing is controlled primarily by code specified drift limits rather than code specified strength demands, a deep wide flange section is advantageous, compared to conventional heavy W12 or W14 sections. However, deep column sections have a smaller torsional stiffness and strength compared to heavy shallow sections. Column torsion is of special concern in cases where a deep column is used in an RBS connection. RBS beams are more prone to lateral torsional buckling than regular beams. A beam undergoing lateral motion applies torsional moment on the column about the column axis. Therefore, the combination of an RBS beam and a deep column can cause severe torsional motion of the column and impair the performance of the connection.

Chi and Uang (2002) tested connections of an RBS beam to a deep W27 column, and observed that twisting of the column can reduce the plastic rotation capacity of the connection. However, similar tests by Ricles *et al.* (2002) which also used W27 columns showed no detrimental effects of the columns. Based on these mixing results, *FEMA-355D — State of the Art Report on Connection Performance* (2000) recommended using deep columns with particular cautions in panel zone and continuity plate design, while *FEMA-350* limited prequalified connections to be used only with W12 and W14 columns. A more recent study by Zhang *et al.* (2004) involved large-scale testing of RBS beams connecting to deep columns. This study suggested that use of deep columns should not be detrimental to the performance of RBS connections.

2.4.4.10 Loading Rate

Since all moment connection tests prior to the Northridge earthquake were conducted under quasi-static loads, the effect of dynamic loading on these connections was largely unknown. Uang *et al.* (1998) compared the performance of moment connections tested under static and dynamic loads. Sinusoidal dynamic loading with a frequency of 1 Hz caused a change in the failure mode from that under static loading and appeared to slightly degrade the rotation capacity. A more comprehensive study on the effect of loading rate was conducted in Japanese research discussed in Section 2.5.5.

2.5 JAPANESE MOMENT CONNECTIONS

2.5.1 Japanese Design and Construction

Similar to the Northridge earthquake, the 1995 Kobe earthquake caused widespread damage to steel beam-to-column moment connections designed and constructed according to the latest standards (*FEMA-355E* 2000; Nakashima *et al.* 1994; *Reconnaissance Report* 1995). Therefore, significant research effort has been conducted in Japan in recent years to improve the performance of moment connections.

There are notable similarities and dissimilarities in the design, detailing, and construction of MRFs between the US and Japan. The similarities include the recent introduction of structural steel specifications, *e.g.*, ASTM A992 in the US and SN (Japanese Industry Standard) G 3136 in Japan. The dissimilarities include welding details (welding process, weld filler metal, welding details), frame design (typically, moment connections are provided only at selected perimeter frames in the US, while moment connections are provided at all beam-to-column joints in Japan, leading to greater redundancy in Japanese MRFs), column section (wide flange columns are typically used in the US, while square tube columns are common in Japan), connection configuration arising from the use of different column sections, and fabrication and construction procedure. The unique aspects of Japanese design and construction are discussed in Bruneau *et al.* (1998), Nakashima *et al.* (2000), *FEMA-355E* (2000), and Mele (2002), among others. The discussions are briefly summarized in the following.

The overwhelmingly dominant steel frame system in Japan uses square tube columns, often cold-formed, and adopts the so-called “through diaphragm” configuration for the beam-to-column joint. As illustrated in Figure 2.19, steel plates termed “diaphragms” are inserted in the column, and short beam stubs are

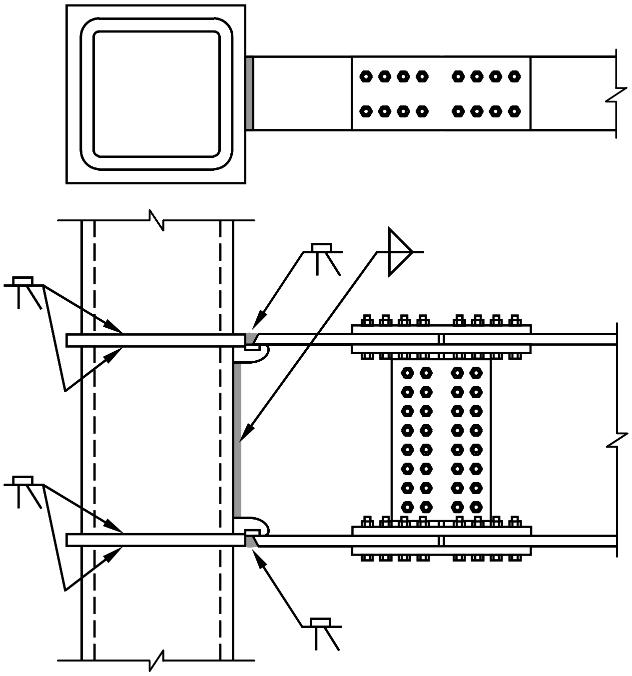

Figure 2.19 Through diaphragm connection

welded to the column in the shop, to construct a column tree. Construction of a column tree requires cutting the columns into segments, then welding the inserted diaphragms to the column segments. Beam stubs are connected to the column by placing a CJP groove weld between the diaphragm and the beam flange, and fillet welding the beam web to the column. The diaphragm functions as a device to allow smooth transmission of forces from the beam flanges to the column and also separates the beam flange welds from the beam web welds. At both the top and bottom beam flanges, a groove weld is placed continuously in a flat position, with the root of the weld located on the inner face of the flange. Instead of the FCAW process widely used in the US, the gas metal arc welding (GMAW) process with carbon dioxide (CO_2) shielding is most common. Shop fabrication of the column tree allows critical connection welds to be placed in the controlled shop environment. The column trees are transported to the site, and assembled into a moment frame. The middle portion of the beam is spliced to the column tree using high strength bolts.

Due to limitations in transportation, the construction process described above applies primarily to low to mid-rise buildings. In medium-high to high-rise buildings, where heavier and larger columns are used, the beam-to-column connections are constructed in the field. Built-up box columns are fabricated in the shop, and internal diaphragms are inserted where required. The moment connection is constructed in a manner very similar to the pre-Northridge US practice. The beam flanges are field welded to the column, and the beam web is bolted to a shear tab. As in the US practice, the root of the bottom flange weld is located on the outer side of the flange. However, even for field welds, the GMAW process is typically used.

2.5.2 Damages Observed After the Kobe Earthquake

As mentioned earlier, both the Northridge and Kobe Earthquakes caused wide spread damage in moment connections (*Reconnaissance Report* 1995; *FEMA-355E* 2000). However, unlike the pre-Northridge connections (Refer to Section 2.4.1), many of the fractured connections detected after the Kobe Earthquake showed signs that significant plastic deformation and local buckling took place before the fracture occurred. Following the earthquake, the preceding connection details were not entirely disqualified as were pre-Northridge connections. Nonetheless, very similar to pre-Northridge connections, fracture in shop-welded through diaphragm connections occurred primarily in the beam bottom flange.

As discussed in Section 2.4.2, the suspected causes of premature fracture in pre-Northridge connections were the combination of the notch effect introduced at the root of the bottom flange groove weld, lack of fracture toughness of the weld metal, high likelihood of weld defects at the weld root, and secondary bending that caused higher stresses at the root of the bottom flange. Many of these causes were not present in the Japanese shop welded connections where the root of the weld was located on the inner face of both the top and bottom flanges. In fact, observations from damaged connections (*Reconnaissance Report* 1995; *FEMA-355E* 2000) and from experiments (*Full-scale* 1997) suggest that the fracture of the bottom beam flanges typically initiated at the root of the weld access hole. In more rare occasions, the fracture initiated at the edge of the flange at the weld interface. The difference in damage observed after the two earthquakes raised suspicion that the significance of other factors beside the location of weld root, such as composite action of concrete floor slabs (Section 2.4.4.6) was the cause of more frequent fracture occurring in the bottom beam flange. Damage of the field-welded connections was less significant.

The frequent occurrence of fracture at the toe of the weld access hole in the base metal led Japanese researchers to focus on improving the weld access hole configuration and developing structural steel with improved ductility and fracture toughness (*FEMA-355E* 2000). Much less attention has been paid to the quality of welds. However, the mechanical and chemical properties of currently used structural steel (Matsumoto *et al.* 2004) and weld metal (Asai *et al.* 2004) are nearly equivalent in the US and Japan.

2.5.3 Improved-Weld-Access-Hole and No-Weld-Access-Hole Connections

As discussed in Section 2.4.3, the Northridge Earthquake led to drastic changes in connection configurations in the US. On the other hand, the Japanese research and construction community chose to refine the existing connection details, primarily by changing the size and configuration of the weld access holes.

As an immediate response to the Kobe Earthquake, a research program involving a large number of full-scale beam-column specimens was conducted (*Full-scale* 1997). The program was intended to develop improved details for Japanese connections that require minimal changes to existing design, fabrication, and erection procedures. One of the key improvement elements was the configuration of the weld access hole that could avoid fracture at the toe of the weld access hole. Three weld access hole configurations, including the conventional configuration and two modified configurations were examined. The tests demonstrated that the modified configurations can successfully mitigate the occurrence of fracture initiating at the toe of the weld access hole. However, it was also seen that this fracture could be prevented if the beam was made of steel with high fracture toughness. The majority of connections tested under ambient temperature, including connections with the conventional configuration, developed sufficiently large inelastic rotations.

Even before the Kobe Earthquake, Tateyama *et al.* (1988) and Nakagomi *et al.* (1992; 1994), among others, suggested that traditional connections which employ weld access holes could be dominated by fracture of the beam flange initiating near the weld access hole, and suggested no weld access hole (termed “non-scallop” in the Japanese literature) connections as a detail that mitigates occurrence of such a failure mode. Currently, the no weld access hole details are widely used in Japanese construction (*Structural Steelwork* 2000). However, some design elements are not well established. For example, the arrangements near the flange and web fillet where multiple weld passes meet requires further examination. It is also noted that the no weld access hole detail is used predominantly for shop fabricated column-tree type connections in Japan.

Caution is required when assessing the implication of the Japanese research to US moment connections. Since the through diaphragm connection relies on the out-of-plane bending stiffness of the column to transmit moment from the beam web, the through diaphragm connection has a relatively flexible web connection. On the other hand, moment connections in the US typically use wide flange columns, which results in very stiff web connections. It is quite likely that the local stress and strain environment at the through diaphragm connection is very different from that in typical US moment connections. Consequently, the modified weld access hole and no weld access hole details may not provide the same benefits to US connections. It is also noted that the improvements achieved by these details was much less pronounced compared to the improvements in rotation capacity seen in the US research on moment connections (Refer to Section 2.4).

2.5.4 Other New Connections

Tanaka *et al.* (1998) proposed a "horizontal haunch" connection, which uses a built-up beam with widened flanges near the column. This connection was developed based on a concept similar to the reinforced connections. The larger flanges near the column face were intended to force plastic hinge formation away from the vulnerable beam flange welds.

The uncertainty in assuring weld quality motivated the development of new connections which minimize the use of welds. One such example is the knee brace damper system proposed by Suita *et al.* (2001; 2003). The system intends to concentrate all inelastic deformation in ductile knee braces, which are bolted to the adjacent beams and columns.

2.5.5 Other Key Issues

2.5.5.1 Dynamic Loading

After the Northridge and Kobe Earthquakes, it was speculated that the high strain rates generated by strong ground motions can induce brittle behavior of steel, and consequently, reduce the rotation capacity of moment connections.

Nakashima *et al.* (1998) and Suita *et al.* (1998) compared the response of moment connections subjected to quasi-static and dynamic loading. The loading rate of the dynamic loading tests was comparable to the loading rate generated by strong ground motions (Suita *et al.* 1998). These tests demonstrated that dynamic loading is not detrimental to the rotation capacity of moment connections. During the dynamic loading tests, the temperature of steel rose significantly due to the rapid yielding of steel. The rise in temperature measured during the dynamic loading tests was found to offset the effective “temperature shift” in fracture toughness (Barsom and Rolfe 1999) caused by the high strain rate. The argument that the rise in temperature had a significant effect on specimen response was also supported by observations that dynamically loaded specimens tended to show a more ductile fracture mode than quasi-statically loaded specimens. The dynamic loading also caused increase in moment resistance by 5-10%, which is consistent with observations that higher loading rate causes increase in the strength of steel (SSRC 1998).

Suita *et al.* (1998) noted that the strain rate is highest at the first yielding when the stiffness of the connection changes abruptly. After first yielding, the transition from elastic response to inelastic response is more gradual due to the Bauschinger effect. Meanwhile, the rise in temperature requires repeated inelastic loading cycles. Therefore, it is quite possible that the adverse effect of dynamic loading is greatest at first yielding, and that the decrease in rotation capacity observed by Uang and Bondad (1998) was due to the connections failing before the beneficial temperature rise occurred.

2.5.5.2 Runoff Tabs

In the Japanese practice, either steel tabs or flux tabs are used for the CJP groove welds connecting the beam flanges to the diaphragm plates. The flux tabs are clamped in position during placement of the weld, and removed afterwards. When steel tabs are used, it is common practice in Japan, even after the Kobe Earthquake, to leave the tabs in place after completion of the weld.

Large-scale tests reported in *Full-scale* (1997) and Nakashima *et al.* (1998) suggested that the runoff tab is the most significant element affecting the performance of Japanese moment connections. Specimens that did not fail due to fracture at the toe of the weld access hole failed by fracture initiating at the edge of the beam flange. Strain gauge measurements indicated largest stress and strain at the edge of the beam flange. When steel tabs were used, the fracture initiated at the narrow gap formed between the steel tab and the beam flange. When flux tabs were used, the fracture initiated at the weld interface, either at the beam side or the diaphragm side of the weld. Moment connections with steel tabs generally achieved smaller rotation capacities than those with flux tabs. However, it was cautioned (*Full-scale* 1997) that appropriate workmanship is essential to benefit from the use of flux tabs. Tabuchi *et al.* (2002) suggested removing the steel tab entirely to mitigate occurrence of the fracture initiating at the edge of the beam flange.

2.5.6 RBS Connection versus No Weld Access Hole Connection

As discussed in Section 2.5.1, the US and Japanese construction differ in many respects. On the other hand, the developments after the Northridge and Kobe Earthquakes differ greatly between the US and Japan. While the RBS connection emerged as the most popular connection in the US due to its economy and insensitivity to weld quality, the Japanese connection configuration remained largely unchanged from before the Kobe Earthquake, except for changes in the weld access holes.

Suita *et al.* (1999) conducted a series of tests to directly compare the latest advances in Japan and the US. Beam-column specimens with the following three connection details were tested: (a) a connection with conventional weld access holes; (b) a no weld access hole connection; and (c) a radius cut-RBS connection with conventional weld access holes. All three connections employed square tube columns and the through-diaphragm configuration (See Figure 2.19). Connections (b) and (c) were chosen to represent the post-Kobe Japanese construction, and the post-Northridge US construction, respectively. The RBS connection design permitted yielding near the column face, and therefore, differed slightly from the prequalified US design (*FEMA-350*). Since the beam-column specimens were fabricated using identical materials in a Japanese fabrication shop according to Japanese practice, and subjected to the same Japanese loading protocol, the connection configuration was the sole test parameter in the study.

While the (a) type specimen failed prematurely, the (b) and (c) type specimens showed excellent cyclic behavior, and achieved inelastic rotations of roughly 0.055 rad. The (b) and (c) type specimens exhibited gradual degradation in strength due to local buckling. The (b) type specimens developed significant flange buckling before ultimately fracturing near the flange weld. The (c) type specimens fractured at locations of large concentrated deformations due to local buckling. This study suggests that the Japanese no weld access hole connection performs as well as the RBS connection, and merits further study for application to US construction.

2.6 LINK-TO-COLUMN CONNECTIONS

2.6.1 General

Some of the typical types of EBFs are arranged to have one end of the link connected to a column, as in arrangements (a) and (c) in Figure 2.1. In such EBFs, the integrity of the link-to-column connection is essential to the ductile performance of the link, and therefore, to the ductile performance and safety of the EBF.

Prior to the Northridge Earthquake, EBF link-to-column connections were designed, detailed, and constructed very similar to beam-to-column moment connections in special moment frames. Therefore, many of the design and construction practices responsible for the poor performance of moment connections during the 1994 Northridge Earthquake are also present in EBF link-to-column connections. Meanwhile, the force and deformation demands at EBF link-to-column connections are substantially different, and in many cases more severe than at moment connections.

2.6.2 Force and Deformation Demands at EBF link-to-Column Connections

A connection of a shear link to a column is required to resist a very large shear force and relatively less moment. The dominance of shear generates a force environment significantly different from moment connections. Meanwhile, the shear link-to-column connection is required to sustain inelastic link rotations of up to 0.08 rad. Such large inelastic rotations are not typically encountered in moment connections. Nonetheless, some insight into the behavior of link-to-column connections for shear links is obtained from the moment connections affected by large inelastic shear deformations of the adjoining column panel zone. Krawinkler (1978) and Popov (1987) observed that excessive panel zone deformation resulted in highly localized deformations, or kinks, in the beams and column flanges near the corners of the panel zone. The kinks imposed high strain demands near the beam flange groove welds, and eventually led to fracture of the beam flange weld. Although the yield mechanism of shear links is inherently different from that of the column panel zones, the large shear deformation of the link can also result in kinks in the link flanges near the flange welds. These kinks can impose high strain near the welds, and initiate fracture, similar to the observation by Krawinkler and Popov.

A connection of a moment link to a column is required to resist very large moment and relatively less shear. Moment links can develop end moments as large as or larger than in moment connections. Although the shear force in moment links may not be as large as in shear links, it is still much more substantial than in MRF beams. More importantly, the moment gradient in EBF links is typically much higher than in MRF beams. As discussed by Engelhardt and Popov (1989a), MRF beams with shorter length (and steeper moment gradient), confine yielding in a smaller region at the beam end, and therefore, generate higher bending strains to accommodate the same story drift. Moment links can be considered extremely short beams in MRFs. At a moment link-to-column connection, the significantly larger bending strain at the link end generates an environment more susceptible to fracture than at typical moment connections. Therefore, moment link-to-column connections present an environment significantly different from that at moment connections or at shear link-to-column connections.

The environment at an intermediate link-to-column connection is likely a combination of the two cases discussed above. The issues related to large shear, large inelastic deformation, high bending strain, and the short length of the flexural yielded region are all present, if not with the same severity as discussed above. In fact, a continuous spectrum of different force and deformation environments is expected between shear link-to-column connections and moment link-to-column connections.

2.6.3 Link-to-Column Connections Prior to the Northridge Earthquake

Roeder and Popov (1978a) suggested that bolted web connections are not suitable for transmitting the high shear force developed in the link, and hence a welded joint is required between the link web and column in the *AISC Seismic Provisions*. The requirement for a welded web connection was in place even before the Northridge Earthquake.

Malley and Popov (1983; 1984) investigated the performance of shear links (mostly of $e = 1.1M_p/V_p$) with different connection details employed at the ends. The connection details included the following: (a) flange and web provided with all-around fillet welds; (b) full penetration groove welds at the flanges, web fillet welded to a shear tab; (c) full penetration groove welds at the flanges, web bolted to a shear tab; and (d) link-to-column web configuration with full penetration groove welds at the flanges and web. For connections (a), (b), and (c), the link was connected to a heavy steel end plate. The majority of specimens adopted detail (a) for both link ends. This detail was similar to the end plate connections used for the current research (Refer to Appendix A). Detail (c) was used widely for seismic moment connections prior to the Northridge earthquake.

The connections that employed welding to both the web and flanges (connection details (a), (b) and (d)), generally showed excellent performance. Hjelmstad and Popov (1983a) also tested one specimen with connection detail (b), which exhibited excellent performance. On the other hand, the two specimens with detail (c) exhibited repetitive bolt slippage between the web and shear tab caused by the large link shear. The bolt slippage, in turn, transferred significant forces to the flange connections, eventually resulting in sudden failure in the flanges. These observations led to a recommendation that welded web connections should be used exclusively for EBF link-to-column connections.

Engelhardt and Popov (1989a; 1992) studied the behavior of long links (e > $1.6M_p/V_p$) attached to columns. Noting that shear is significantly larger in long links than in MRF beams, and bending strains higher (Refer to Section 2.6.2), welded flange-welded web details were deemed appropriate not only for shear link-to-column connections, but also for any link-to-column connection. Tests exhibited highly unpredictable failure of the link flange near the groove welds. These failures typically occurred prematurely, before significant inelastic link rotation was developed. Based on these results, it was recommended that long links of $e > 1.6M_p/V_p$ attached to columns should not be used in EBFs. The sections tested in this program were relatively small with W12 links and W10 columns. In addition, the welds were fabricated with a shielded metal arc weld (SMAW) process using an E7018 electrode. As such, the tests did not necessarily reflect the current US construction practices, where field welded connections are typically constructed using the self-shielded flux cored arc welding (FCAW) process. Nonetheless, this was among the first research to express concerns about the potentially poor performance of EBF link-to-column connections.

In order to prevent premature fracture, later specimens tested by Engelhardt and Popov (1989a; 1992) were provided with reinforcing elements, such as vertical ribs or triangular cover plates. These specimens, as well as a specimen attaching the link to the column flange with all around fillet welds, allowed the link to develop much greater inelastic rotation. Most notably, a specimen with triangular cover plates attached to the link flanges at the connection developed very significant link rotations. The addition of vertical ribs appeared to delay failure, but eventually led to flange fracture initiating at the tip of the ribs.

Two specimens tested by Engelhardt and Popov (1989a; 1992) were configured with the link ($e = 1.48M_p/V_p$ and $1.72M_p/V_p$) connecting to the column web. These specimens failed prematurely at small inelastic rotations due to fracture of the link flange at the groove weld to the continuity plate. Meanwhile, Malley and Popov (1983; 1984) noted little disadvantage in using a similar link-to-column web connection (detail (d) in earlier discussion in this section). The conflicting results combined with the questionable reliability observed in beam-to-column web connections for MRFs (*e.g.* Tsai and Popov 1988) led to the recommendation by Engelhardt and Popov that the use of link-to-column web connections should be restricted.

Figure 2.20 shows EBF shear link-to-column connections typically used prior to the Northridge Earthquake. The connections in this figure are intended for field construction and call for CJP groove welds between the link flanges and column flange. Popov *et al.* (1989b) provided the following design guidelines for EBF link-to-column connections. Bolted web connections were to be avoided.

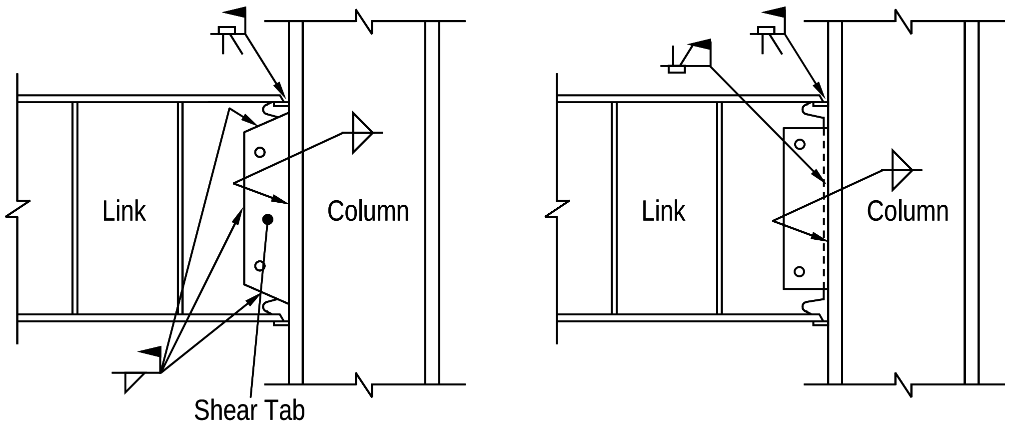

(a) EBF link-to-column connection with welded shear tab

(b) EBF link-to-column connection with web welded to column

Figure 2.20 Pre-Northridge connections

The link web was to be welded to the shear tab (Figure 2.20a), or connected directly to the column flange with a full penetration weld (Figure 2.20b). It is important to emphasize that the only significant difference between moment connections and EBF link-to-column connections prior to the Northridge Earthquake was the web connection detail. Moment connections typically used bolted web connections, whereas the link-to-column connections used welded web connections exclusively.

Large-scale link-to-box column connections tested in Taiwan (Engelhardt *et al.* 1992) exhibited premature failure of the connection due to fracture of the link flange welds. “Triangular wing plates” proved to be effective in reducing the stress concentration at the connection, and in precluding premature failure.

2.6.4 Post-Northridge Studies

Tsai *et al.* (2000) investigated the seismic performance of shear link-to-box column connections using construction practices typical in Taiwan. Prior to the current research program, this was the only series of tests of EBF link-to-column connections constructed to realistic scale and welding details. The link-column specimens had links of e = 0.9 and $1.5M_p/V_p$. Both types of welded flange-welded web connections shown in Figure 2.20 were examined. Some of the connections adopted the refined weld access hole configuration and groove weld backing details suggested by Ricles *et al.* (2002), while others followed common Taiwanese practice.

None of the six specimens developed the required link inelastic rotation of 0.08 rad, while links of $e = 0.9M_p/V_p$ developed greater rotation compared to links of $e = 1.5M_p/V_p$. The specimens typically failed at the link-to-column connection, by fracture of the link flange near the groove weld. Although the modification in weld access hole geometry and in flange weld backing details resulted in improved link rotation, the improvement was marginal. Overall, the tests highlighted the potentially poor performance of EBF link-to-column connections, and strongly suggested the need for further research.

2.6.5 Code Requirements

The *1992 AISC Seismic Provisions* discouraged attaching links of length e > $1.6M_p/V_p$ to columns. Configurations with the link connecting to the column web were restricted to cases where the design link inelastic rotation is limited to less than 0.015 rad. Exclusive use of welded flange-welded web details was mandated.

Following the Northridge earthquake, the *1997 AISC Seismic Provisions* discouraged the use of link-to-column configurations entirely. The provisions for link-to-column connections were completely revised. Similar to moment connections, cyclic test results were required for EBF link-to-column connections to demonstrate that the connection could satisfy the link rotation requirement. A qualifying cyclic test procedure for EBF link-to-column connections was first introduced in the supplement to the 1997 provisions issued in 2000. However, very limited experimental data is available for EBF link-to-column connections, and to date, there exists no prequalified EBF link-to-column connection design. Meanwhile, an exception was permitted for EBF link-to-column connections with sufficient reinforcement at the link end. A reinforced connection was permitted without testing if the reinforcement precluded yielding of the link end over the reinforcement length, if the link length excluding the reinforced length did not exceed $1.6M_p/V_p$, and if the design strength of the reinforced section and connection exceeded the required strength calculated based on the strain hardened link. There appears to be no research on link-to-column connections, however, that suggests a reinforced connection will provide satisfactory performance.

The *2002 AISC Seismic Provisions* remains mostly unchanged from the 1997 provisions including the *2000 Supplement*. A minor change in language was made in the acceptance criteria for the qualifying cyclic test procedure. Whereas the 1997 provisions required that an inelastic link rotation of 20% greater than the design demand be demonstrated by testing, the 2002 provisions require that the nominal shear strength, V_n, be maintained at the required link rotation angle.

2.7 DISCUSSION

This section discusses the scope of the current research program. Elements affecting the performance of EBF link-to-column connections are evaluated, referring to the discussion in the preceding sections of this chapter. The significance of each of the selected test parameters as well as the limitations of this program are discussed.

2.7.1 Link Length

As discussed in Section 2.6.2, the link length governs the link forces as well as the rotation capacity of the link. Therefore, the link length also governs the force and deformation environment at the EBF link-to-column connection. By altering the length of a link attached to a column, a continuous spectrum of different force and deformation environments can be realized at the link-to-column connection. Shear link-to-column connections are of primary interest, since short shear links are more desirable than long moment links (Refer to Section 2.2.4), and therefore, are used more frequently in design. Nonetheless, this program investigated EBF link-to-column connections with different link lengths, in shear, intermediate, and moment link range, to obtain a comprehensive data on the effect of link length on the performance of the connections.

2.7.2 Link Section

A wide range of wide flange sections can be used for link beams in EBFs. Figure 2.21 shows the relation between the section shape and non-dimensional length factor, $M_p/(V_p \cdot d)$, for all rolled wide flange shapes. The section shape is represented by two ratios: the depth to width ratio, d/b_f, (Figure 2.21a) and the flange to web area ratio, A_f/A_w, (Figure 2.21b). Here, $A_f = b_f \cdot t_f$ and $A_w = (d - 2t_f)\, t_w$, where b_f is the flange width, t_f is the flange thickness, d is the depth of the section, and t_w is the web thickness. The factor $M_p/(V_p \cdot d)$ relates the link length category with the link length to depth ratio, e/d, as follows:

$$\frac{e}{d} = \frac{\alpha \frac{M_p}{V_p}}{d} = \alpha\left(\frac{M_p}{V_p d}\right) \tag{2.6}$$

The above relation indicates that between links of the same length category, as $e = \alpha(M_p/V_p)$ with a constant α, a link with larger $M_p/(V_p \cdot d)$ has a proportionally larger length to depth ratio. Figure 2.21 shows that the value of $M_p/(V_p \cdot d)$ ranges between 1.0 and 3.4, depending on the section dimensions. Some representative sections are indicated to aid comparison of the section properties. The figure shows that the value of $M_p/(V_p \cdot d)$ is inversely proportional to the depth to width ratio, and linearly proportional to the flange to web area ratio.

It is acknowledged that the span to depth ratio of beams have a significant effect on the performance of moment connections (*FEMA-350*). A smaller span to depth ratio of the beam results in steeper moment gradient and a shorter plastic hinge. Therefore, in an excessively short beam, the plastic strain demand at the plastic hinge will be significantly larger than in longer beams. The length to depth

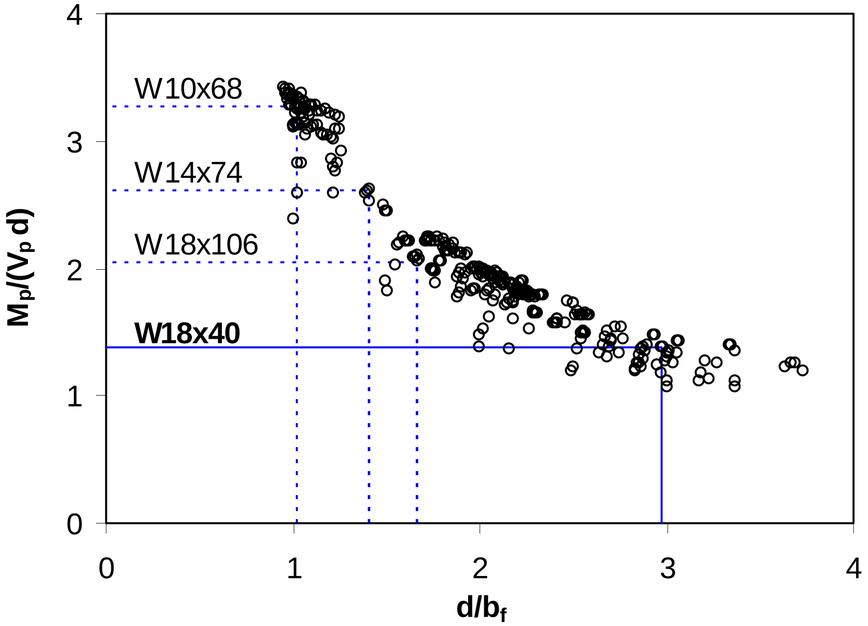

(a) Depth to Width Ratio vs. Length Factor

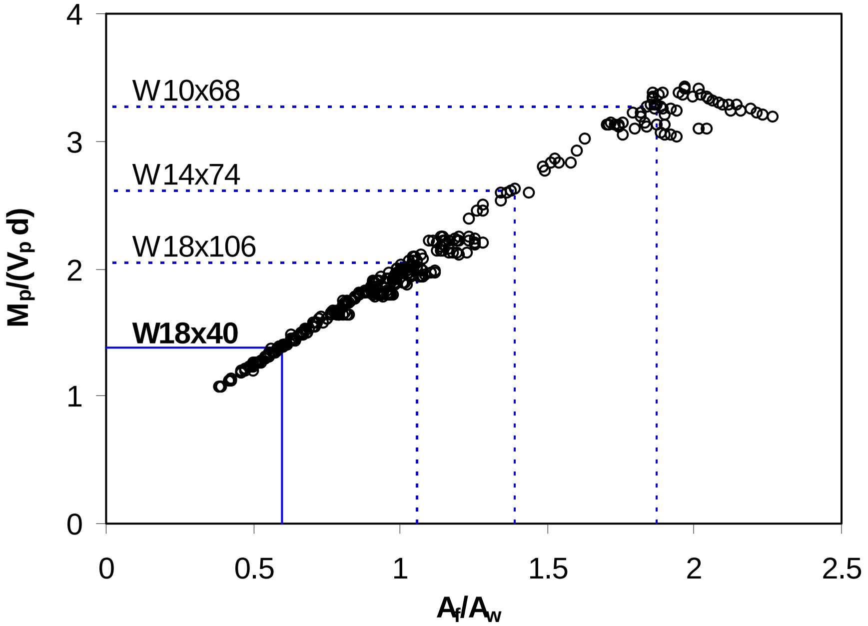

(b) Flange to Web Area Ratio vs. Length Factor

Figure 2.21 Non-dimensional link length factor ratio can have a similar effect on the flexural behavior of link-to-column connections. In a connection of a shear link to a column, the performance of the connection is dominated primarily by shear, and hence the moment gradient may have limited effect. However, in a connection of a moment link to a column, the connection is required to accommodate large plastic hinge rotation, similar to moment connections. The moment gradient can control the performance of such connections. The moment gradient can also affect a connection of a shear link to a column, in cases where the link end yields in flexure.

Depending on the section and length of the link, some EBF link-to-column connections meets all the conditions specified in *FEMA-350* for moment connections. *FEMA-350* typically requires the clear span (distance between the column faces at both ends) to depth ratio of beams in special moment frames to be greater than 8. A moment link constructed from a section with large $M_p/(V_p \cdot d)$ value can have a rather moderate length to depth ratio. For example, a W10x68 link, with $M_p/(V_p \cdot d) = 3.28$, of $e = 3M_p/V_p$ has a length to depth ratio of 9.5, which is greater than the minimum ratio allowed for MRFs. Therefore, for moment links constructed from column-like sections, with the depth nearly equal to the width, and large flange area compared to web area, the connection to a column might be designed and detailed according to a prequalified moment connection prescribed in *FEMA-350*.

On the other hand, a moment link constructed from a section with small $M_p/(V_p \cdot d)$ value can have very short length to depth ratios. For example, a W18x40 link, with $M_p/(V_p \cdot d) = 1.38$, of $e = 4M_p/V_p$ has a length to depth ratio of 5.5, much shorter than the minimum ratio allowed for MRFs. The W18x40 link selected for this research program has a relatively large depth to width ratio and a small ratio of flange to web area. Figure 2.21 shows that the $M_p/(V_p \cdot d)$ value for this section is near the lower bound for rolled wide-flange shapes likely to be used as links. Due to the very steep moment gradient that develops in such links, it was expected that the plastic strain demand generated at the link-to-column connection due to flexure would be very severe.

2.7.3 EBF Arrangement

The elastic-plastic moment distribution in an EBF link is dominated by the rotational restraints at the two ends of the link. The EBF arrangement and the relative sizing of the surrounding members can significantly alter the end restraints. As discussed in Section 2.2.6, a link-to-column joint produces a greater restraint than a link-to-beam/brace joint. Consequently, in the elastic range, the link-to-column connection is subjected to a larger moment than at the opposing beam/brace end of the link. Although moment redistribution tends to equalize end moments in the inelastic range, moment equalization may not be achieved, particularly in short shear links. Therefore, while the shear force in links is quite insensitive to end restraints, the moment developed at the face of the column can be significantly altered by unequal end restraints.

The effect of end restraints can be illustrated by a simple beam analysis. Figure 2.22 shows an isolated link under double curvature bending and shear, with rotational springs attached to each end. In this figure, the subscript “C” refers

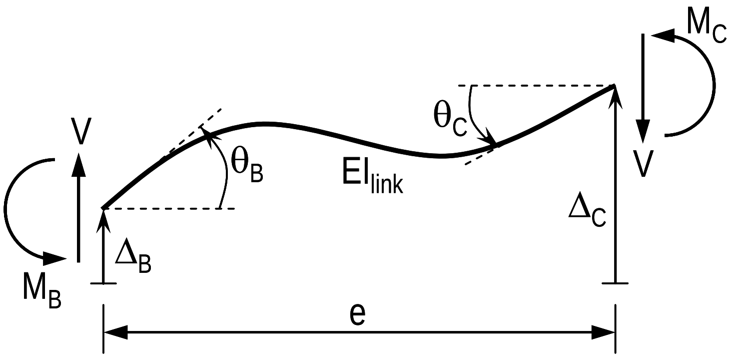

Figure 2.22 Isolated link model

to the column end of the link, while “B” refers to the beam end of the link. If the spring constants at each end of the link are taken as k_C and k_B, then:

$$M_C = -k_C\,\theta_C\,, \tag{2.7a}$$

$$M_B = -k_B\,\theta_B\,. \tag{2.7b}$$

Shear deformation is neglected for simplicity. A first order elastic analysis results in the following expression for the link end moment ratio:

$$\frac{M_C}{M_B} = \frac{\alpha(2+\beta)}{\beta(2+\alpha)}. \tag{2.8}$$

In the above equation, α and β are measures of the relative stiffness of the link and the rotational springs. These parameters are defined as follows:

$$\alpha = k_C \frac{e}{EI_{link}}, \tag{2.9a}$$

$$\beta = k_B \frac{e}{EI_{link}}. \tag{2.9a}$$

In the above equation, e is the link length and EI_{link} is the elastic flexural stiffness of the link section. Equations (2.8) and (2.9) show that the link end moment ratio, M_C/M_B, is a function of the end restraints and the flexural stiffness of the link itself. If the ratio of the spring stiffness to the flexural stiffness of the link is large at both ends, *i.e.*, α, $\beta \rightarrow \infty$, then the value of M_C/M_B will be close to unity. If α and β are of the order of unity to ten, as is typically the case, then the end restraints will have a large influence on the link end moment ratio. Moreover, as the link length increases, the values of both α and β increase, resulting in M_C/M_B values approaching unity.

A series of 2-D elastic frame analyses were conducted on sample EBFs to study the range of realistic link end moment ratios. In these analyses, rigid beams with length equal to half the depth of the column section were inserted between links and columns to represent the column panel zones. Lateral loads were applied at each story level, with magnitude increasing proportionally with height. All other loads were neglected. Results of the analyses are shown in Figure 2.23. The figure plots the end moment ratio for all links in the frames against their non-dimensional length. The notations, 3L, 3T, and 10, correspond to three frames, two three-story frames and one ten-story frame, presented by Richards and Uang (2003). All links in the original frame analyzed by Richards and Uang were shear links. The link length in each original frame was altered to generate three frames with intermediate links, and another three frames with all moment links. The

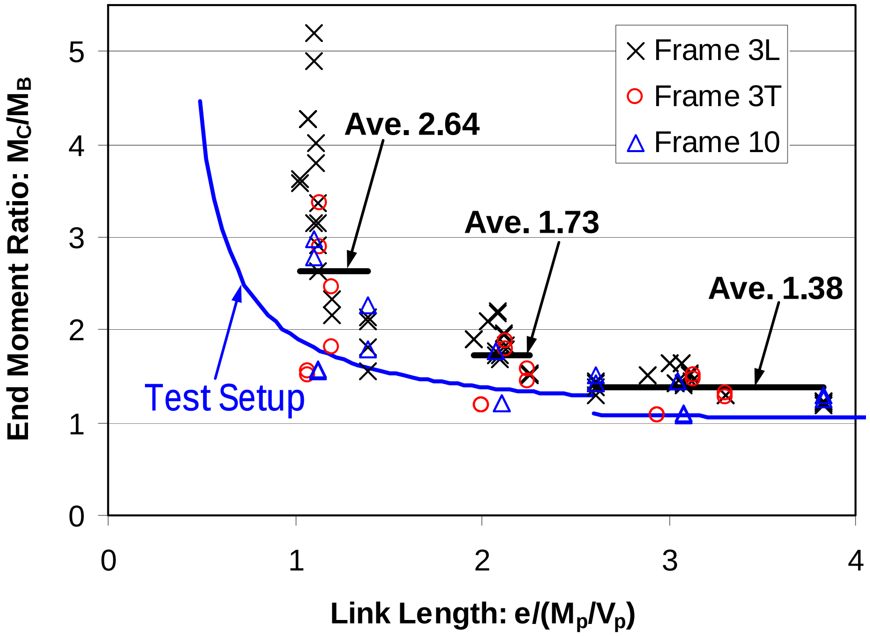

Figure 2.23 End moment ratios estimated from elastic frame analyses.

modified frames are indicated as 3L, 3T, and 10 in Figure 2.23, according to their original frames. Figure 2.23 shows significant variation in the end moment ratio, particularly for shear links. The variation diminishes rapidly with increase in link length. The significant dependence of force distribution on local and global frame arrangements is an aspect unique to links connecting to a column at one end. In beams in MRFs or links located at mid span of the beam between two diagonal braces, the end moment ratio is generally close to unity. It is also noted that the end moment ratio averaged at 2.6 in shear links, 1.7 in intermediate links, and 1.4 in moment links. The dependence of end moment ratio on link length was discussed earlier.

Figure 2.23 also shows the expected link end moment ratio supplied by the test setup devised for the experimental program (See Section 3.2.1). The theoretical values were derived based on linear beam theory, similar to the derivation of equations (2.8) and (2.9), and using the dimensions of the test setup. The figure suggests that the link end moment ratios produced by the test setupwas reasonable, although the ratios were somewhat lower than the average values obtained from the frame analyses. It is noted that the current program does not address the substantial dependence of the link end moment ratio on the EBF arrangement.

Although the capacity design procedure for EBFs requires all members outside of the link to remain essentially elastic, there are cases where limited inelastic action is expected in members adjacent to the link. Most notably, the use of a continuous member for the link and the beam outside of the link generally results in yielding and potentially instability in the brace connection panel (Refer to Section 2.2.8), particularly if the intersected angle between the diagonal brace and link is small (Section 2.2.3). The degradation in stiffness and strength of the brace connection panel can delay or prevent moment equalization (Section 2.2.6).

However, the test setup devised for the current program was designed to preclude yielding in the beam outside of the link, to enable repeated usage of the beam. Therefore, the degradation in stiffness and strength of the brace connection panel was not simulated in the tests.

2.7.4 Welding Details

The EBF link-to-column connections constructed prior to the Northridge earthquake likely possess the same welding related problems that contributed substantially to the widespread damage observed in moment connections. As discussed in Section 2.4.2, the factors include: the common use of the low toughness E70T-4 electrode for constructing the link flange groove welds; poor workmanship and quality control; the practice of leaving the backing bars and weld tabs after completion of the weld; and the detailing that resulted in interference with welding and inspection. Since the link flange welds in EBF link-to-column connections are subjected to high stress levels and large cyclic plastic strain, as in beam flange welds in moment connections, it is quite likely that the lack of fracture toughness and poor welding quality severely degrade the performance of EBF link-to-column connections.

Similar to pre-Northridge moment connections (*e.g.*, Engelhardt and Husain 1993), the EBF link-to-column connections with poor welding quality were expected to perform poorly, failing before exhibiting sufficient ductile deformation. In fact, because the force and deformation demands can be more severe at EBF link-to-column connections than at moment connections, it was expected that the welding quality can have a more detrimental effect on link-to-column connections. The connections tested in this program included a type which represented the pre-Northridge welding practice (PN-connection), as well as a type which adopted the modifications in welding recommended in *FEMA-*

350 discussed in Section 2.4.2 (MW-connection). The effect of welding quality could be studied by comparing the PN-connections with MW-connections. The welding modifications were followed for the other two connections (FF- and NA-connections), which featured modified connection configurations.

2.7.5 Connection Details

Among the various moment connection configurations developed from the extensive post-Northridge/Kobe research, the following types may be considered promising for application to EBF link-to-column connections:

- Reduced beam section (RBS);
- Reinforced connections, using haunches, ribs, cover plates, etc.;
- Free flange connection;
- Unreinforced connection;
- No-weld-access-hole connection; and
- Bolted connections.

The advantages and disadvantages of these connections are discussed in the following.

2.7.5.1 Reduced Beam Section

As discussed in Section 2.4.3.3, the radius cut RBS connection is quite insensitive to the quality of welds, and less costly compared to other post-Northridge connections. The reliable performance of the RBS connection has been demonstrated by a large number of tests. Therefore, in recent years, the RBS connection has emerged as the most popular choice for moment connections in the US. However, although the RBS approach proved to be extremely effective at moment connections, it may not be nearly as effective at EBF link-to-column connections.

The fundamental design intention of the RBS connection is to force plastic hinge formation away from the column face, and thereby, reduce the stress level near the groove welds connecting the beam/link flange to the column flange. The RBS connection may be suitable for long flexure yielding links which develop large moments near the link-to-column connection. However, it is not clear how the RBS would benefit shorter links, since the force and deformation environment is much different from that in moment connections. By promoting flexural yielding, the RBS can alter the post-yield behavior of the shear link to a more flexure dominated one, and thereby, reduce the rotation capacity of the link. Furthermore, the steeper moment gradient along the relatively short length of links and more substantial moment redistribution during inelastic response makes the RBS difficult if not impossible to implement for short links. Consequently, the RBS connection is not appealing for short shear links.

As discussed in Section 2.4.3.3, the trimmed segment of the radius cut RBS beam is prone to web buckling due to the reduced torsional properties of the section. In an EBF link, which develops much larger shear forces compared to beams in MRFs, the effect of web buckling can be even more significant. In fact, Engelhardt and Popov (1989a; 1992) and Arce (2002) observed intermediate links and moment links to be dominated by combined local flange and web buckling and lateral torsional buckling. Therefore, the reduction in sectional properties must be carefully considered when trimming the flanges of EBF links.

The procedure for sizing the radius cuts, as proposed by Engelhardt (1999), was found to be directly applicable to W10x68 links of the length range $e > 1.6M_p/V_p$. Figure 2.24a shows an example of radius cuts applied to a W10x68 link with $e = 2M_p/V_p$, where the design assumed equal and opposite end moments.

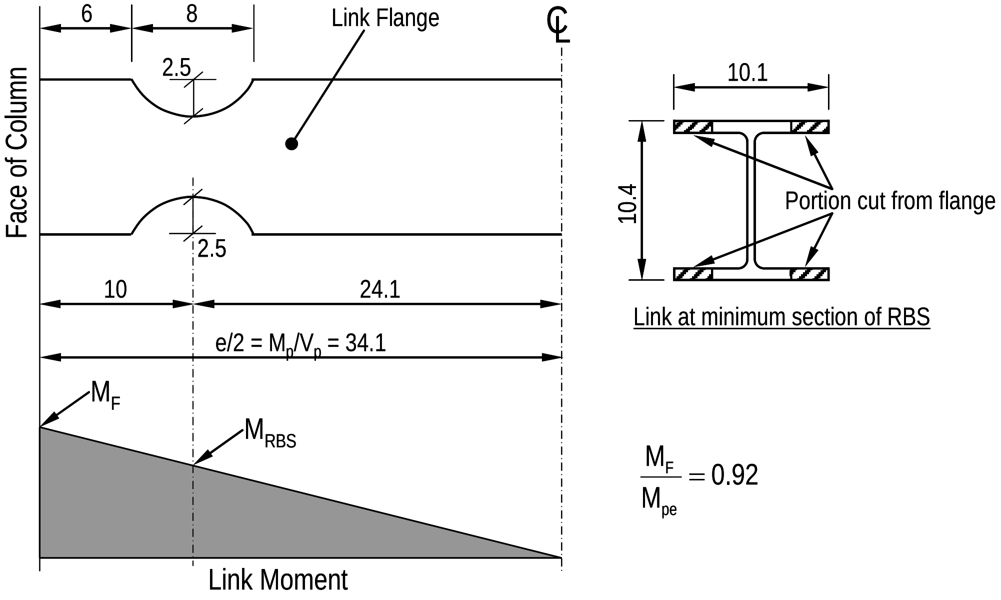

(a) W10x68 link

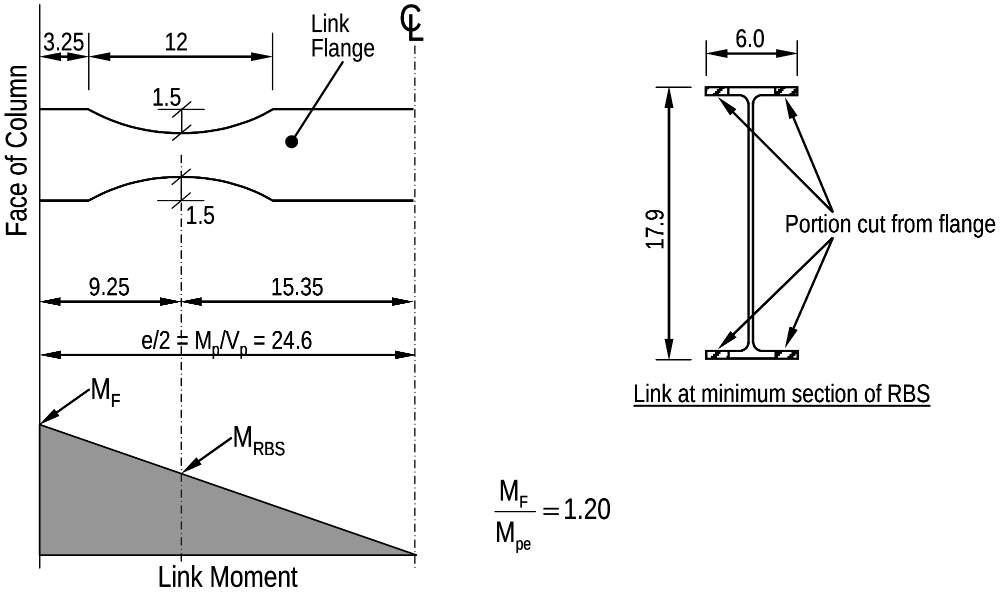

(b) W18x40 link

Figure 2.24 RBS applied to intermediate links of e = 2M_p/V_p

However, the same procedure could not size the radius cut for W18x40 links of the length range $e < 3M_p/V_p$. An example is shown in Figure 2.24b, where the procedure fails to limit the moment at the column face below the elastic limit. The figure also shows that the insufficient radius cut trims a substantial segment of the W18x40 link, and raises concern for stability issues. The wider flanges combined with the longer link length for a given link length category (Refer to Section 2.7.2) make the trimming easier for W10x68 links than for W18x40 links. Since sections with wider flanges are left with larger flanges, these sections retain more torsional stiffness after trimming. Therefore, the RBS connection may be more practical for shallower sections with small depth to width aspect ratios than for deeper sections with large depth to width ratios.

2.7.5.2 Reinforced Connections

As discussed in Section 2.4.3.2, the reinforced connections intend to force plastic hinge formation away from the column face and shield the beam/link flange groove welds from high stress levels. This primary intension can be equally as effective at EBF link-to-column connections as at moment connections. However, reinforcements can also significantly alter the behavior of the links, which in turn, may negate any beneficial effect provided by the reinforcement. Although Engelhardt and Popov (1989a) reported promising test results for reinforced EBF link-to-column connections, those specimens were of reduced scale, and did not realistically represent actual construction. In the following, various reinforcement methods are examined qualitatively for their applicability to EBF link-to-column connections.

Upstanding ribs (See Figure 2.15b) and welded haunches (See Figure 2.15d) can significantly increase both flexural and shear capacity of the link near the connection, and preclude yielding in the reinforced segment. Consequently, the effective link length would be reduced to the segment outside of the region reinforced with the rib or haunch. The reduction in link length can transform a moment link to an intermediate link, and an intermediate link to a shear link. Since shorter links generally perform better than longer links in terms of stiffness, strength, and ductility, such transformation in link length category can be favorable in many cases. Nonetheless, it is prudent that the reduction in link length be accounted for to properly size and detail the link and surrounding members. Meanwhile, both rib and haunch reinforcements require additional welds at locations of high stresses, and therefore, introduce new sources of potential fracture. For example, Engelhardt and Popov (1989a) tested four EBF link-to-column connections reinforced with upstanding ribs. Although the ribs appeared to delay failure of the connection, the connections ultimately failed due to fracture initiating at the tip of the rib. Engelhardt and Sabol (1994) discussed that the rib welds can be sensitive to the distortion of the column flange and to the quality of welds. At an EBF link-to-column connection, the large link rotation can cause a much more severe stress demand to the rib welds compared to a moment connection. Consequently, rib reinforcement may be much less suitable for shear links which are expected to develop the largest rotation.

Immediately after the Northridge Earthquake, some new EBF construction appeared to have adopted the coverplate reinforcement (See Figure 2.15a) for the link-to-column connection, reflecting the popularity of this reinforcement in MRF construction at the time. Figure 2.25 shows an example of such an EBF link-to-column connection with coverplates. Engelhardt and Popov (1989a) reported one EBF test specimen with triangular coverplates achieving promising performance. On the other hand, Engelhardt and Sabol (1998) discussed the mixed success of coverplate reinforcement in moment connections (Refer to Section 2.4.3.2). They noted that the thickness and length of cover plates should be well balanced to

Figure 2.25 Example of EBF link-to-column connection reinforced with coverplates.

preclude yielding of the beam at the face of the column. However, such balance is significantly more difficult to achieve in EBF links, where the moment gradient is higher than in beams in MRFs and significant moment redistribution is expected during inelastic response. Therefore, the cover plate reinforcement appears less promising for EBF link-to-column connections than demonstrated for moment connections.

Engelhardt *et al.* (1992) reported that triangular plates attached to the sides of the link flanges can effectively reduce stress concentrations at the link flange welds, and enhance the performance of the EBF link-to-column connection. A similar concept has been tested successfully by Tanaka *et al.* (1998) for moment connections.

The *2002 AISC Seismic Provisions* permits use of reinforced connections, provided that the reinforcement is designed to preclude yielding in the reinforced region. When such reinforcement is used, the link length, taken as the segment excluding the reinforced region, is required not to exceed $1.6M_p/V_p$. Upstanding ribs, haunches, and side plates (See Figure 2.15c) may be proportioned to satisfy such conditions. However, the discontinuity and additional welds required for placing the reinforcing elements can introduce a new source of potential fracture. Haunches may be better suited than upstanding ribs or side plates to achieve balanced reinforcement for both flexural and shear strength. As discussed above, ribs can be particularly disadvantageous due to the high stresses developed at the welds connecting the rib to the column flange and link flanges.

2.7.5.3 Unreinforced Connection

Even before the Northridge Earthquake, exclusive use of welded flange-welded web details was mandated for EBF link-to-column connections (Refer to Section 2.6.3). The detail illustrated in Figure 2.20a is nearly identical to the unreinforced welded flange-welded web connection for moment connections. As discussed in Section 2.4.3.4, the unreinforced connection is more sensitive to weld quality than the RBS connections, since the flange welds are not shielded from severe stress and strain. However, since only limited testing had been done to study the performance of this detail, the adequacy of this traditional EBF link-to-column connection was not clear prior to this research program. As in moment connections, the configuration of the weld access hole might have significant effect on the unreinforced connection.

2.7.5.4 Free Flange Connection

As discussed in Section 2.4.3.5, the free flange connection is designed to reduce the stress and strain demands at the flange welds by drawing the forces away to the link web. This goal is accomplished by the combined use of a heavy shear tab welded to the beam web and a selected free flange length.

A twofold advantage might be expected in applying this concept to EBF link-to-column connections. First, the shear force demand is more severe at EBF link-to-column connections than at moment connections, and hence the benefit of drawing shear forces away from the link flange welds should be significant. Second, the extreme local deformation demand in the link flanges near the column face, which is akin to the local deformation imposed on beam flanges in a moment connection adjoining a weak panel zone, can be relaxed. Meanwhile, the free flange connection precludes yielding in the link or beam web in the region adjacent to the column by significantly increasing the shear area of the section. The selective reinforcement of the web only and not the flanges can substantially affect the inelastic behavior of the links.

2.7.5.5 No Weld Access Hole Connection

As discussed in Section 2.5.3, the no weld access hole ("non-scallop") connection is a recommended detail for moment connections in Japan. Many Japanese sources (*e.g.*, Suita *et al.* 1999) report excellent performance of moment connections with this detail. The aim of this connection is to eliminate the source of stress and strain concentration surrounding the weld access hole by eliminating the weld access hole itself.

Engelhardt and Popov (1989a; 1992) tested one specimen with a moment link connected to a column with all-around fillet welds. This connection may be considered a variation of no weld access hole connection. The specimen achieved very large link rotation without developing notable damage at the connection.

Recent tests performed by Arce (2002) and Ryu *et al.* (2004) also support the development of connections that avoid using weld access holes. In the tests by

Arce and Ryu *et al.*, both ends of the links were fillet welded to heavy end plates, which in turn were bolted to the loading frame. The fillet welds were made by the submerged arc welding (SMAW) process using an E7018 electrode. The specimens either failed due to web fracture without exhibiting any damage at the welded ends, or failed at the welded ends after the link rotation far exceeded the required level. The latter case was common of specimens with long moment links. All specimens constructed for the current program had the beam end of the links attached to 2-inch thick steel plates using the same welding procedure used by Arce and Ryu *et al*. Further details of the weld between the link and the 2-inch plates are provided in Appendix A. Based on the above discussion, it may be concluded that the no weld access hole detail is promising for EBF link-to-column connections.

2.7.5.6 Bolted Connections

FEMA-350 lists several prequalified bolted connections for MRFs. Some of the fully restrained bolted connection designs may be applicable to EBF link-to-column connections with some modification. By enabling sensitive welds to be made in a well controlled shop environment, the bolted end plate connections have an advantage over field welded connections.

A variation of bolted unstiffened end plate connections (*FEMA-350*) has been tested in numerous link tests conducted in the past, as discussed in Section 2.7.5.5 and Appendix A. The end plate connections in link specimens differ from the prequalified unstiffened end plate connections in three respects: the overly conservative design for the thickness of the end plate, special weld detailing to prevent premature fracture, and the addition of a shear transferring lock mechanism to reduce the shear force developed in the bolts and to prevent repetitive bolt slippage during cyclic loading. The end plate and welding details used in this program are detailed in Appendix A, while the lock mechanism in the test setup is discussed in Section 3.2.2. Similar end plate connections have been used in previous link tests. However, although various different link sections have been tested, the sections tended to be of reduced scale. In order to develop practical design procedures for bolted unstiffened end plate connections in EBFs, practical plate thickness and welding details must be investigated. An alternative and more practical method to achieve the shear lock mechanism must be investigated.

The bolted stiffened end plate connection (*FEMA-350*) is supplied with upstanding ribs at the top and bottom flanges. The constraint introduced by the ribs discussed in Section 2.4.3.2, combined with large link rotation, can induce fracture in the welds connecting the rib to the end plate or link flange. Therefore, the benefit of ribs may be limited.

The bolted flange plate connection and double split tee connection are also included in *FEMA-350*. However, these bolted connections introduce potential problems with net section fracture at bolt holes, and have not been widely used for moment frame construction.

2.7.5.7 Other Connections

The proprietary slotted web connection and reduced web connection (*FEMA-350*) significantly reduce the shear strength of the beam or link. It is highly likely that the additional discontinuity would act as a source of fracture for shear links, where large inelastic deformation is expected in the web. The reduction in stiffness and strength of the link may significantly affect the overall design of the EBF. Nonetheless, provided that the reduction in shear strength does not severely affect the flexural strength of the link, the two connections may prove to be effective for some moment links.

2.7.5.8 Connections Selected for Investigation

Four connection types were investigated by large-scale tests in this research program. The first connection, denoted as the PN-connection, represents the pre-Northridge practice in detailing and construction of EBF link-to-column connections (Refer to Section 2.6.3). Similar to pre-Northridge moment connections, the PN-connection was expected to perform poorly, failing before exhibiting significant ductile deformation. In fact, because the force and deformation demands can be more severe in EBF link-to-column connections than in moment connections, it was expected that the PN-connections would perform poorly. Nonetheless, this connection type was included in the research program to provide baseline date on the expected performance of pre-Northridge link-to-column connections. No previous test program reported in the literature, either before or after the Northridge earthquake, tested the pre-Northridge link-to-column connection details using the E70T-4 electrode.

The second connection type, denoted as the MW-connection, was detailed similar to the PN-connection, but implemented the modifications in welding recommended in *FEMA-350*. The modifications included use of a weld filler metal with specified CVN-values and improved detailing (Refer to Section 2.4.2). As discussed in Section 2.7.5.3, the MW-connections is practically identical to the unreinforced welded flange-welded web connection.

The third and forth connection types were expected to achieve improved performance over the PN- and MW-connections. It was concluded that although the RBS connection (Refer to Section 2.7.5.1) and various reinforced connections (Section 2.4.3.2) hold promise for intermediate links and long moment links, they are not as suited for short shear links as for moment connections. As suggested by the *2002 AISC Seismic Provisions*, some reinforced connections may be utilized to transform longer links to shear links. The slotted web connection and reduced web connection (Section 2.7.5.7) are not appealing for short shear links. Since the West Coast practice prefers welded connections over bolted connections, the bolted connections (Section 2.7.5.6) hold less promise. Consequently, two types of promising connections were selected for detailed investigation in this research program: the free flange connection (Section 2.7.5.4) and the no weld access hole connection (Section 2.7.5.5).

2.7.6 Loading Protocol

It is widely acknowledged that the loading sequence can significantly affect the deformation capacity of structural members and connections. Although the *2002 AISC Seismic Provisions* provides a loading protocol for testing link-to-column connections in EBFs, this protocol was chosen somewhat arbitrarily by modifying the protocol for testing moment connections, and not developed on a rational basis. Recently, Richards and Uang (2003) developed a revised loading protocol for testing connections of a shear link to a column, using a methodology similar to that used for developing the protocol for testing moment connections (Krawinkler *et al.* 2000). The revised protocol, which is a more reasonable representation of seismic demands, is significantly less severe for shear links than the protocol provided in the *2002 AISC Seismic Provisions*. As discussed in Section 2.3.4, tests conducted alongside the current program by Arce (2002) and Ryu *et al.* (2004) have demonstrated that the loading protocol has a substantial effect on the rotation capacity of links. It is, therefore, prudent that the loading protocol represent the actual demands arising from earthquake ground motion, as is the case with the revised protocol developed by Richards and Uang.

Both the AISC loading protocol and revised loading protocol mentioned above were used in the experimental program.

2.7.7 Other Factors

2.7.7.1 Dynamic Loading

As discussed in Section 2.5.5.1, tests by Nakashima *et al.* (1998) suggest that dynamic loading has no detrimental effect on the performance of moment connections. It is speculated that the loading rate has a very similar effect on link-to-column connections as on moment connections. However, no research has been conducted on the effect of loading rate on EBF link-to-column connections. Since all tests in this research program were conducted by quasi-static loading, the dynamic loading effects were not considered in this program.

2.7.7.2 Composite Slabs

As discussed in Section 2.4.4.6 for moment connections, the presence of a composite concrete slab can have both beneficial as well as adverse effects on connection performance. Since EBF links tend to be smaller in dimension than MRF beams, it is quite possible that composite slabs have a more profound effect on EBF link-to-column connections than on moment connections. In fact, as discussed in Section 2.2.7, Ricles and Popov (1987b; 1989) observed that the ultimate shear forces and end moments can increase by as much as 25% due to composite action. The larger forces due to composite action indicate large shifts in the neutral axis location, which can subject the bottom link flange welds to higher stresses and strains. Therefore, composite slabs can potentially have detrimental effects on EBF link-to-column connections. Further research is needed to establish an adequate design procedure which accounts for composite slabs.

All test specimens in this research program were of bare steel elements with no composite concrete slab. Therefore, the composite slab effects were not considered.

2.7.7.3 Panel Zone Strength

Panel zone deformation can affect the link rotation for links connecting to a column. As in moment connections (Refer to Section 2.4.4.3), panel zone deformation is expected to have an impact on the performance of link-to-column connections. While inelastic panel zone deformation can contribute to link rotation, excessively large panel zone deformation can cause large localized deformation near the link flange welds, and cause premature fracture of the welds. Currently, limited research data are available for the design of column panel zones in EBF link-to-column joints. The commentary of the *2002 AISC Seismic Provisions* recommends sizing these panel zones according to the procedures provided for MRFs, with the flexural demand at the column end of the link evaluated based on the forces developed in a fully strain hardened link.

The design of column panel zones is largely unresolved for EBF link-to-column connections. Although the experimental program did not directly address this issue, the effect of panel zone strength was studied by finite element simulations in this research.

2.7.8 Summary

Section 2.7 discussed the significant factors that affect the performance of EBF link-to-column connections. Among the various factors, the following were selected as primary parameters in the current research program:

- Link length;
- Welding process and welding details;
- Connection details;
- Unequal link end moments;
- Loading protocol; and

- Panel zone strength.

The following factors are not explicitly addressed in this research program:

- Section shape and link length-to-depth ratio;
- Frame arrangement (range of elastic link end moment ratios);
- Yielding in the beam outside of the link;
- Dynamic loading; and
- Composite slabs.

The following four connection details were selected for detailed investigation:

- Connection representing Pre-Northridge practice;
- WUF-W connection with modified welding;
- Free flange connection; and
- No weld access hole connection.

CHAPTER 3

Test Program

3.1 INTRODUCTION

A series of large-scale cyclic loading tests was conducted as one of the key features of this research program on link-to-column connections. The tests were conducted in two phases. The first phase focused on the impact of two key parameters on the performance of EBF link-to-column connections: (1) the connection type, and (2) the link length, ranging from short shear links to long moment links. Four connection types and three different link lengths were selected to test a total of twelve link-column specimens. The second phase focused on EBF link-to-column connections with shear links only. Two connection types that demonstrated promising behavior in the first phase were reexamined using a modified cyclic loading protocol. For this second phase, two link lengths were selected within the shear yielding range. A total of four link-column specimens were tested in the second phase.

The links were designed following the *AISC Seismic Provisions* (1997, 2002). The specimens were constructed entirely from A992 steel, with W18x40 links and W12x120 columns. The test setup and test specimens were constructed at the Phil M. Ferguson Structural Engineering Laboratory (FSEL) at the University of Texas at Austin. The test procedure for this study was developed based on the qualifying cyclic test procedure for link-to-column connections provided in Appendix S of the *AISC Seismic Provisions* (2000, 2002).

This chapter describes the test program. Section 3.2 outlines the test plan, including the description of the test setup, the link-column specimens, the cyclic loading sequence, instrumentation, data reduction schemes, and the criterion to evaluate the performance of link-to-column connections. Section 3.3 discusses the material property of the steel sections and welds used for constructing the specimens. Section 3.4 discusses the design details and fabrication procedures for each of the four connection types.

3.2 TEST PLAN

3.2.1 Test Setup

A test setup was devised for this research, which consisted of the loading system shown in Figure 3.1 and Figure 3.2, and the lateral bracing system shown in Figure 3.3. Figure 3.4 shows photographs of the test setup.

3.2.1.1 Loading System

An overview of the loading system is shown in Figure 3.1, and a more detailed view is shown in Figure 3.2.

The loading system was designed to replicate the force and deformation environment in the link in an EBF arrangement where one end of the link is connected to a diagonal brace and a beam, and the other end is connected to a column. The column was oriented to resist in-plane moment by bending about the strong axis. Examples of such EBF arrangements are shown in Figure 2.1a and Figure 2.1c. For illustration, typical link forces in the arrangement in Figure 2.1a and those in the loading system are compared in Figure 3.5. When loaded, the link will yield under a combined action of shear and flexure. The shear force is constant along the length of the link. The two ends of the link have bending moments of opposite sense (*i.e.*, reverse curvature bending), typically greater at the column side end than at the beam side end due to greater rotational restraint at the column side. The loading system was designed based on the rigid-plastic

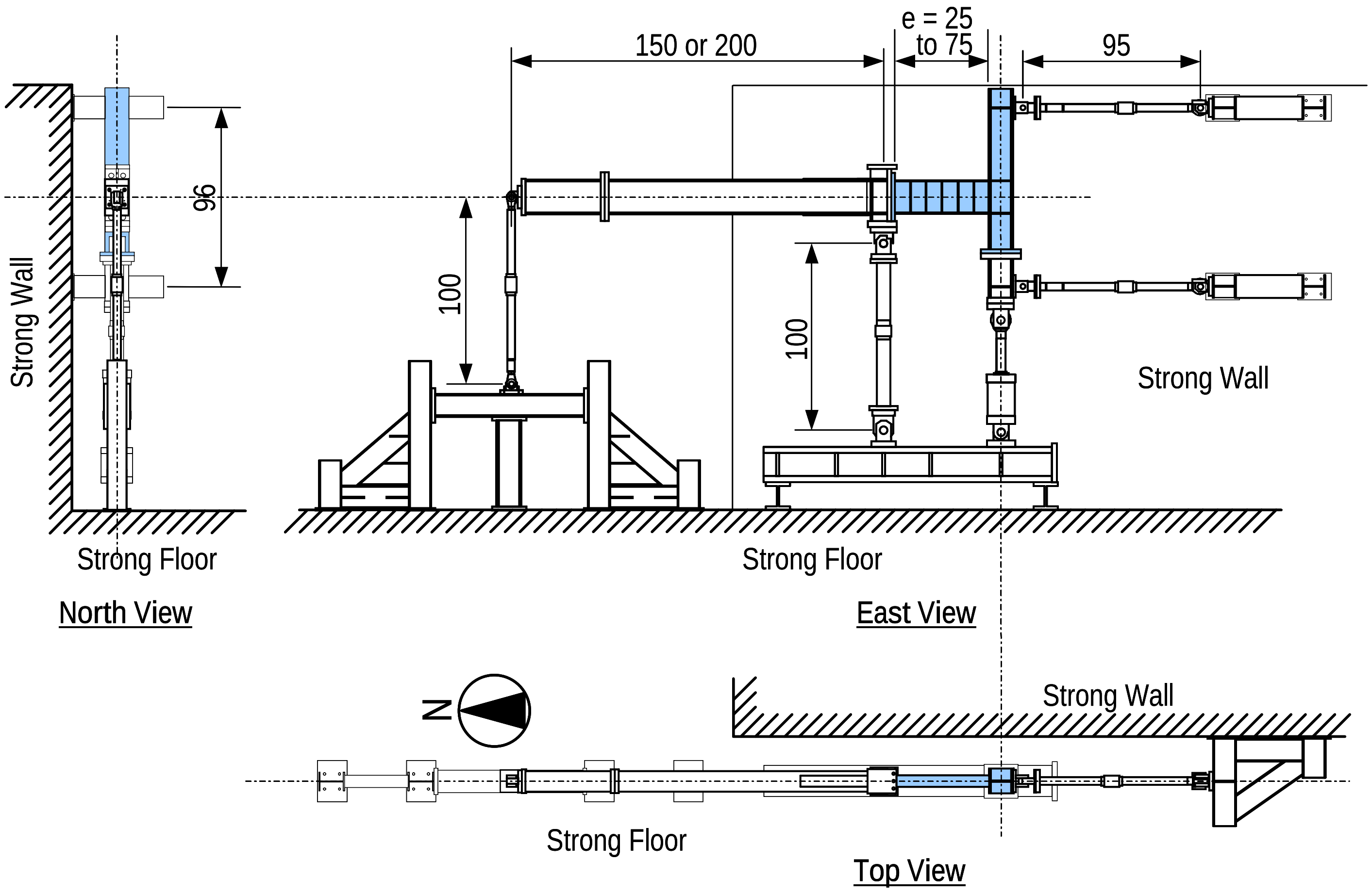

Figure 3.1 Loading system (Dimensions in inches)

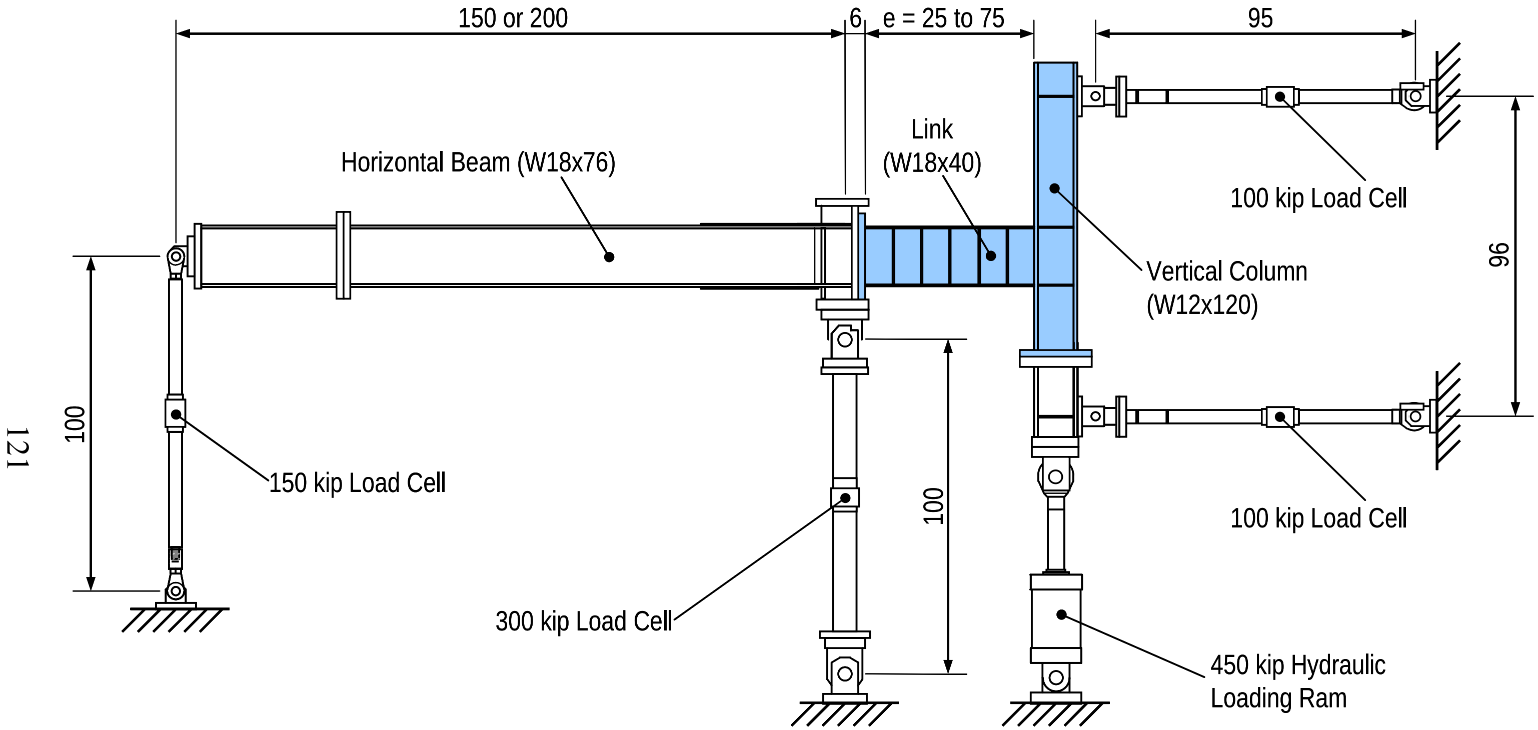

Figure 3.2 Details of the loading system (Dimensions in inches)

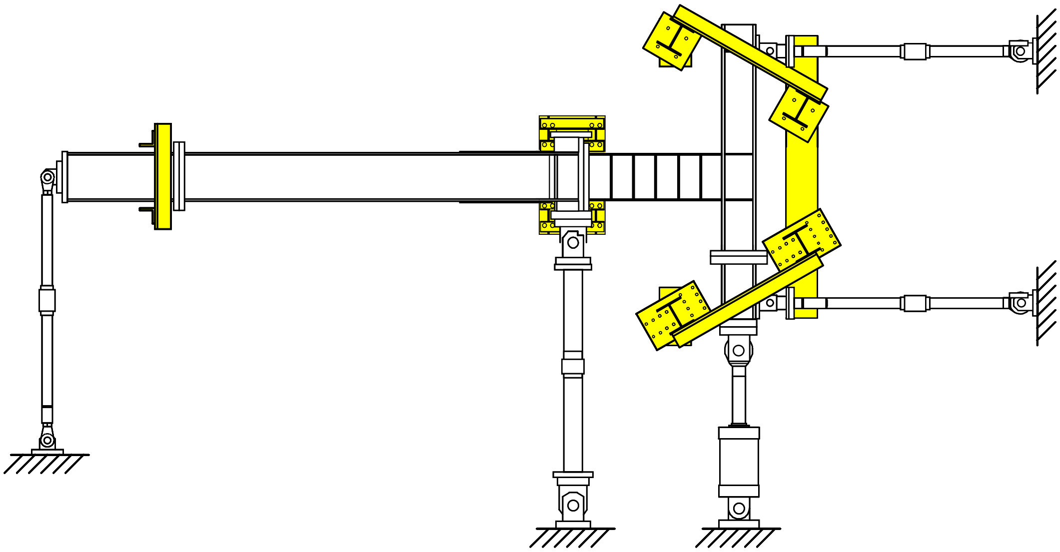

Figure 3.3 Lateral bracing system

Figure 3.4 Overall view of the test setup (Before testing Specimen PNI)

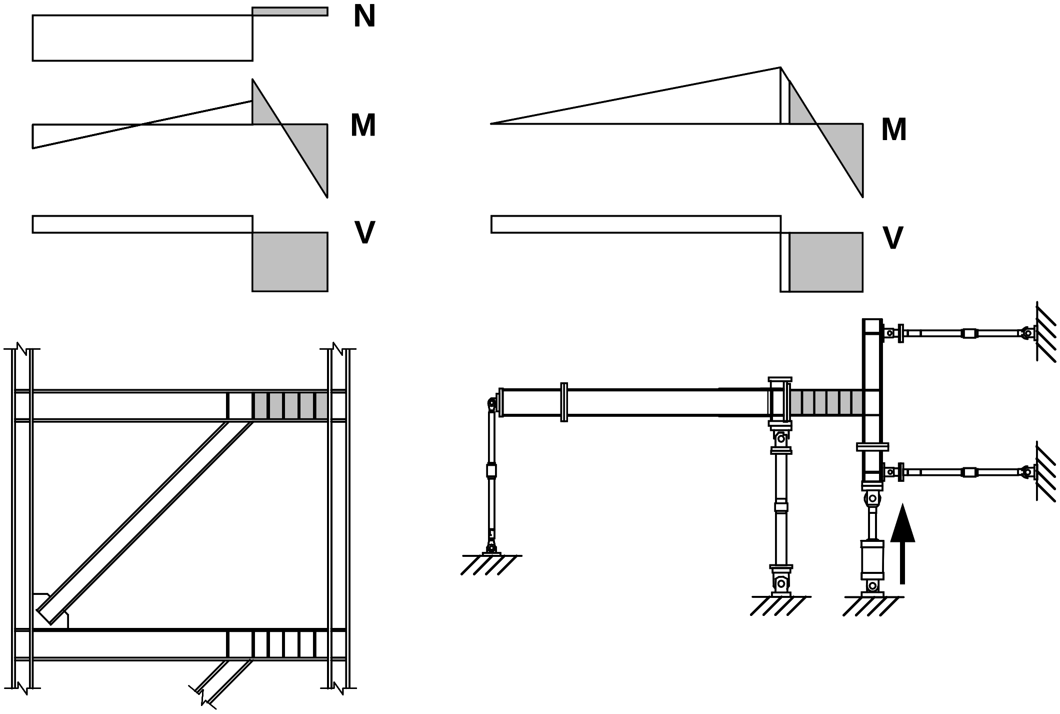

(a) Typical EBF *(b) Test setup*

Note: N, M, and V indicate axial force, bending moment, and shear force, respectively, in the link and horizontal beam. The link and the force distribution in the link are highlighted.

Figure 3.5 Link force distribution

energy dissipation mechanism of an EBF frame as shown in Figure 2.4. Figure 2.4 shows the rigid-plastic mechanism in which plastic deformation is strictly limited to the links and the column bases, while the remainder of the frame remains rigid. Similarly, the loading system was designed to restrict inelastic action in the link. The horizontal beam and vertical column in the loading system provide unequal elastic rotational restraints at each end of the link in a manner similar to that found in an actual EBF.

The loading system (see Figure 3.2) comprises a vertical column stub and a horizontal beam, each connecting to the link-column specimen; a 450-kip hydraulic loading ram which introduces vertical cyclic load and displacement to the column; and four reaction rods each attached to one end of the vertical column or horizontal beam. The sections selected for the link, the vertical column and the horizontal beam were W18x40, W12x120, and W18x76, respectively. The link and column sections as well as the column height of 8-ft were chosen to represent full or near full-scale dimensions in actual EBFs.

The region of the horizontal beam next to the link was reinforced with flange coverplates, a web doubler plate and rib stiffeners to prevent any yielding outside of the link. The length of the horizontal beam was varied depending on the link length of the test specimen. As shown in Figure 3.6, the pin-to-pin distance of the horizontal beam was 200-inches for shorter links (S-, SL- and I-links, as discussed in Section 3.2.2), and 150-inches for long links (M-links); The horizontal beam together with the attached vertical reaction rods could be moved in position to accommodate specimens with different link lengths.

Details of the link-column specimens are given in Section 3.2.2.

The far ends of each of the four reaction rods were fastened against the strong wall or strong floor (see Figure 3.1). The reaction rods simulate pin-rollers: the vertical reaction rods in the horizontal beam allow free motion in the horizontal direction, while preventing motion in the vertical direction; the horizontal reaction rods in the vertical column allow free motion in the vertical direction, while preventing motion in the horizontal direction.

The loading system introduces minimal axial force to the link. Although the presence of axial force can greatly affect the behavior of links (Kasai and Popov 1986b; 1986c), axial force effects were not of interest in this research program. The measured link axial force did not exceed 5 kips during any of the

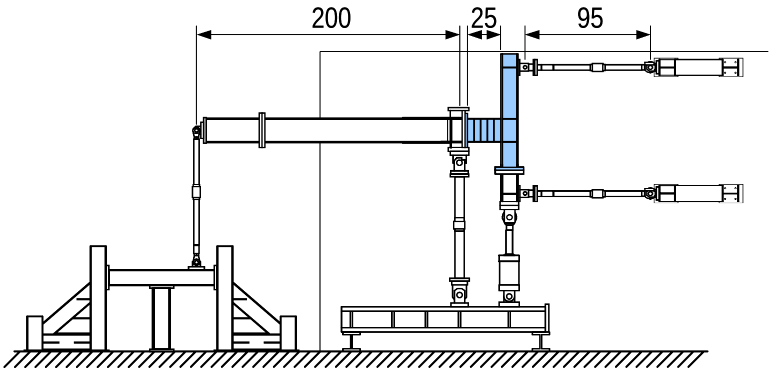

(a) S-Link

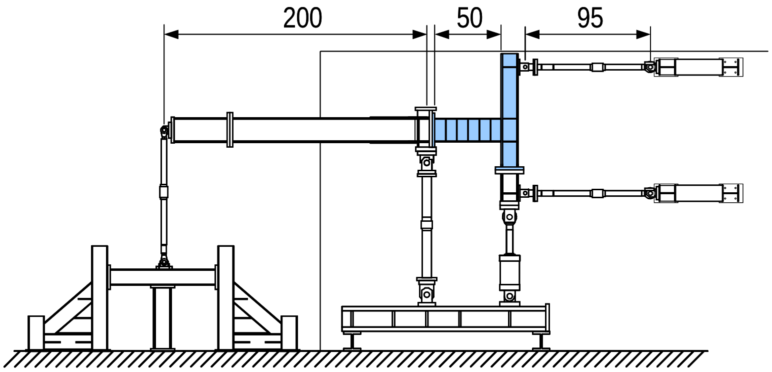

(b) I-Link

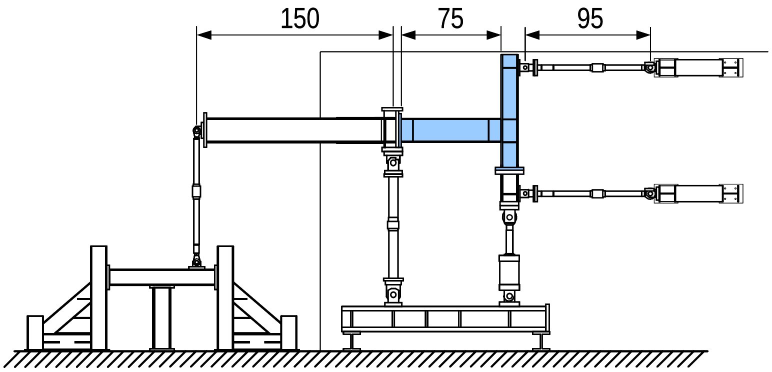

(c) M-Link

Figure 3.6 Arrangement of loading system with different link lengths (Dimensions in inches)

tests. This value corresponds to less than 1% of the axial yield force of the link section. Also note that the loading system does not simulate the large axial force developed in the upper portion of the column. The axial force introduced at the bottom of the column is transmitted through the link-to-column connection to the link as link shear force. Hence, only the bottom half of the column is subjected to significant axial force. The magnitude of this axial force was no more than one-fifth of the column axial yield strength. In actual EBFs, the frame overturning moment and the forces transmitted through braces and links under lateral load, in addition to gravity load, can result in significant column axial forces. Nonetheless, provided that the column is designed according to the capacity design procedure described in Section 2.2.3, the axial load in the column is believed to have limited impact on the behavior of the link-to-column connection.

3.2.1.2 Lateral Bracing System

As shown in Figure 3.3, lateral bracing was provided at four points of the loading frame to provide for the lateral stability of the test specimen. The four bracing points were located at: the top and bottom of the vertical column; in the horizontal beam near the link; and in the horizontal beam near the far end away from the link. The lateral bracing frames are also visible in the photograph shown in Figure 3.4.

At each of the bracing points, the loading system was braced through contact surfaces that allow free motion in the primary bending plane, while limiting motion out of the plane and torsion about the member axes. Teflon was glued to the two surfaces that contact each other in order to ensure minimal friction. The two bracing points at the two ends of the horizontal beam could be moved in position to accommodate to the different link length of the link-column specimens.

3.2.2 Test Specimen

A total of sixteen link-column specimens were tested in this program. All link-column specimens were constructed from a W18x40 link and a W12x120 column, both of A992 steel. The key variables in the specimens were the connection type, link length, and loading sequence. The test matrix is shown in

Table 3.1. The specifications of each specimen, including the main features of the connection type, link length, and link stiffener spacing, are summarized in Table 3.2. The names of the specimens represent the three test parameters: the first two letters (PN / MW / FF / NA) represent the connection type, and the next one or two letters (S / SL / I / M) represent the link length. An extension "-RLP" indicates that the specimen was tested using the revised loading protocol (described in Section 3.2.3), while the absence of this extension indicates the specimen was tested using the loading protocol specified in the *AISC Seismic Provisions* (2000; 2002).

Each test specimen was composed of a column and a link connected to the flange of the column, as shown in Figure 3.7. The three different links in the PN-specimens are illustrated in Figure 3.8. The specimen was attached to the test

Table 3.1 Test matrix

Loading Protocol	Connection Type	Link length			
		S-link	SL-link	I-link	M-link
AISC	Pre-Northridge	PNS		PNI	PNM
	Modified welding	MWS		MWI	MWM
	Free flange	FFS		FFI	FFM
	No weld access hole	NAS		NAI	NAM
Revised	Free flange	FFS-RLP	FFSL-RLP		
	No weld access hole	NAS-RLP	NASL-RLP		

Table 3.2 Specimen summary

Specimen	Connection features	Link length: $e/(M_p/V_p)$		Stiffener Spacing (in)(b)
		Nominal	Measured	
PNS	Pre-Northridge practice	1.02	1.11	5.0
PNI		2.03	2.22	8.33
PNM		3.05	3.34	(9.0)(c)
MWS	Modified welding practice; modified weld access hole	1.02	1.11	5.0
MWI		2.03	2.22	8.33
MWM		3.05	3.34	(9.0)(c)
FFS	Extended weld access hole; heavy shear tab; modified welding practice (a)	1.02	1.11	5.0(d)
FFI		2.03	2.22	7.25(d)
FFM		3.05	3.34	(9.0)(c) (d)
FFS-RLP		1.02	1.11	4.625(d)
FFSL-RLP		1.57	1.72	5.35(d)
NAS	No weld access hole; shop fabrication; modified welding practice	1.02	1.11	5.0
NAI		2.03	2.22	7.5
NAM		3.05	3.34	(9.0)(c)
NAS-RLP		1.02	1.11	5.0
NASL-RLP		1.57	1.72	5.35

Notes:

(a) The five FF-specimens had different shear tab geometries.

(b) The stiffener spacing is measured as the distance between the centers of each stiffener. For stiffeners adjacent to either link end, the spacing is measured as the distance between the center of the stiffener and the end of the link. See Figure 3.8 for example.

(c) For moment links, only one link stiffener was placed near each end. See Figure 3.8c for example.

(d) For FF-specimens, the link end at the column side was taken as the edge of the heavy shear tab, instead of at the column face.

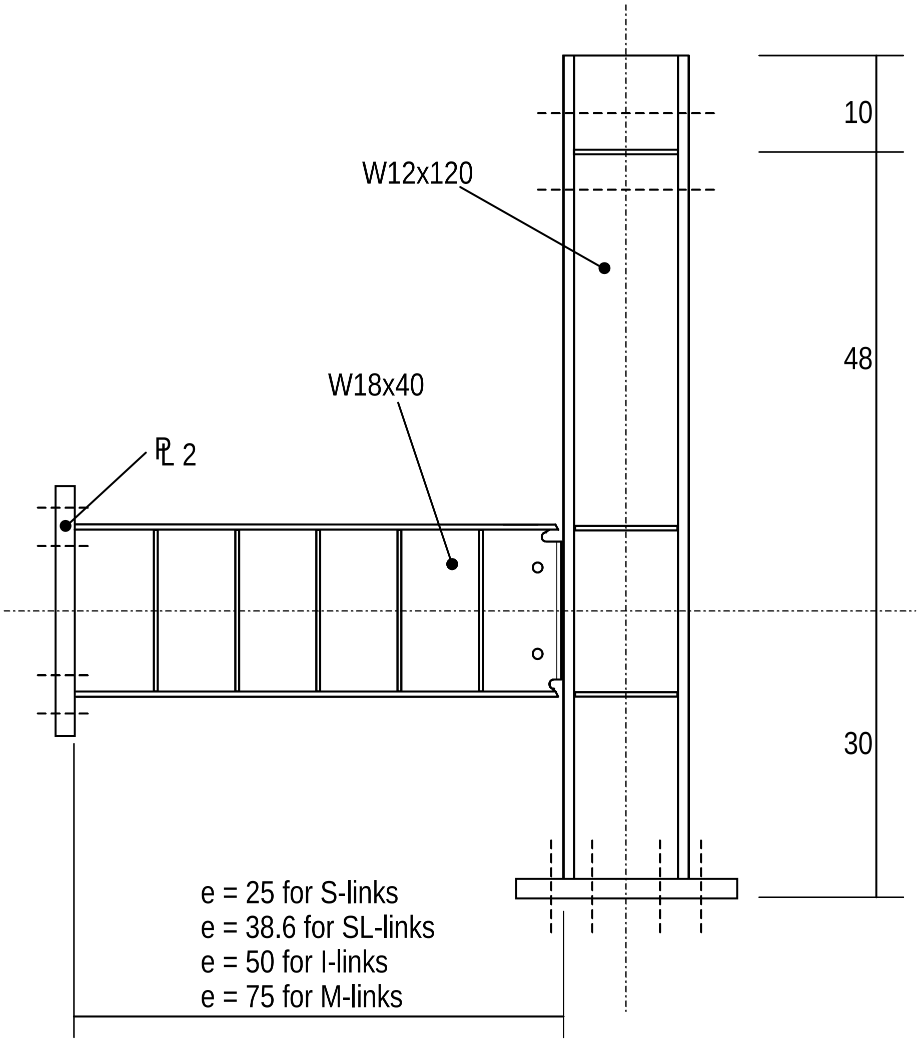

Figure 3.7 Example of test specimen. Specimen PNI is shown (Dimensions in inches)

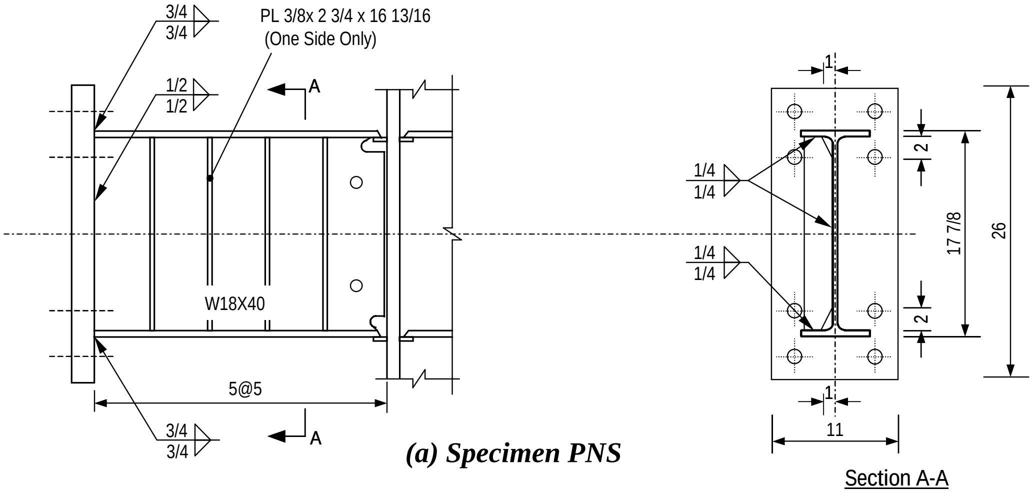

(a) Specimen PNS

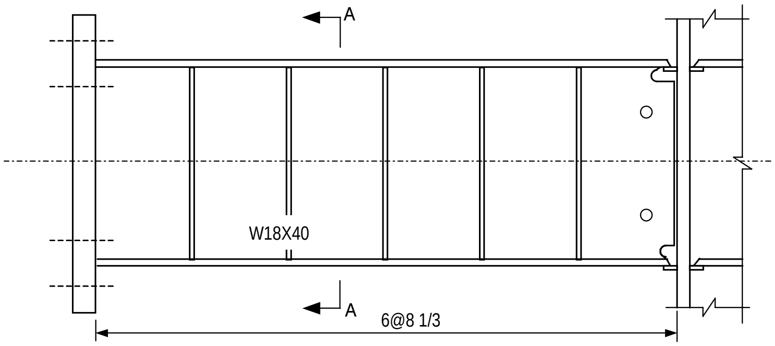

(b) Specimen PNI

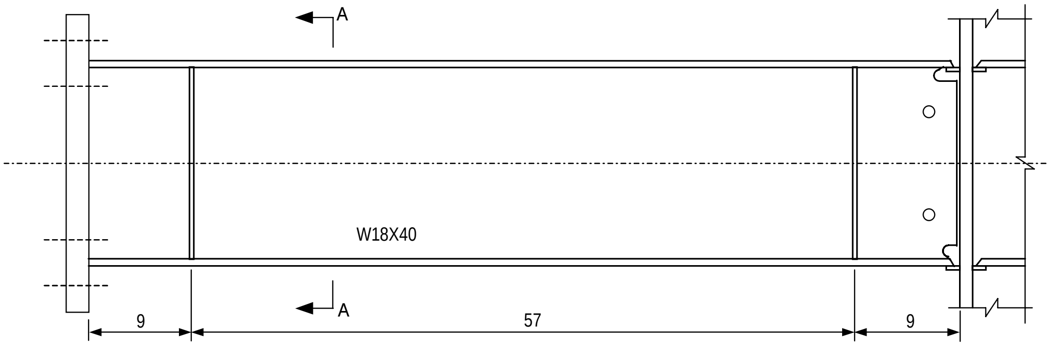

(c) Specimen PNM

Figure 3.8 Example of links (Dimensions in inches) setup through three bolted connections (see Figure 3.2). The link end was attached to the horizontal beam. The bottom of the column was attached to the column stub, which in turn connected to the hydraulic loading ram and to a horizontal reaction rod. The top of the column was attached to a horizontal reaction rod.

As indicated in Figure 3.7, 2-inch steel plates were fillet welded to the link end away from the column, and to the bottom of the column. Special care was taken for the welds between the link end and the steel end-plate, as described in Appendix A. The steel plate was, in turn, connected to the horizontal beam with eight 1-1/4-inch-diameter A490 bolts. The link-to-beam bolted connection was designed to resist the simultaneous action of moment and shear developed at the link end. Moment was resisted by the horizontal bolts in the end plate. An additional mechanism was provided to resist shear at the link end. As illustrated in Figure 3.9, the steel plate was fastened between a steel block and three 1-1/4-inch diameter A490 bolts placed in the vertical direction.

The three link lengths designated as S-link, I-link, and M-link were chosen to represent the different link length categories defined in the *AISC Seismic Provisions*. As discussed in Section 2.2.4, shear dominates the inelastic behavior of short shear links (link length of $e \leq 1.6M_p/V_p$), while flexure is dominant for long moment links ($e \geq 2.6M_p/V_p$). Links of intermediate length ($1.6M_p/V_p \leq e \leq 2.6M_p/V_p$) are affected significantly by both shear and flexure. Different link lengths will impose a variety of different force and deformation demands onto the link-to-column connection. The S-links were 25-inches long, corresponding to a nominal normalized link length of $e = M_p/V_p$, and represented shear links. I-links, with a length of 50-inches, and a nominal normalized length of $e = 2M_p/V_p$, represented intermediate links. M-links, with a length of 75-inches, and a nominal normalized length $e = 3M_p/V_p$, represented moment links. Finally, SL-links had a length of 38.6-inches, which corresponded to a nominal normalized length of e =

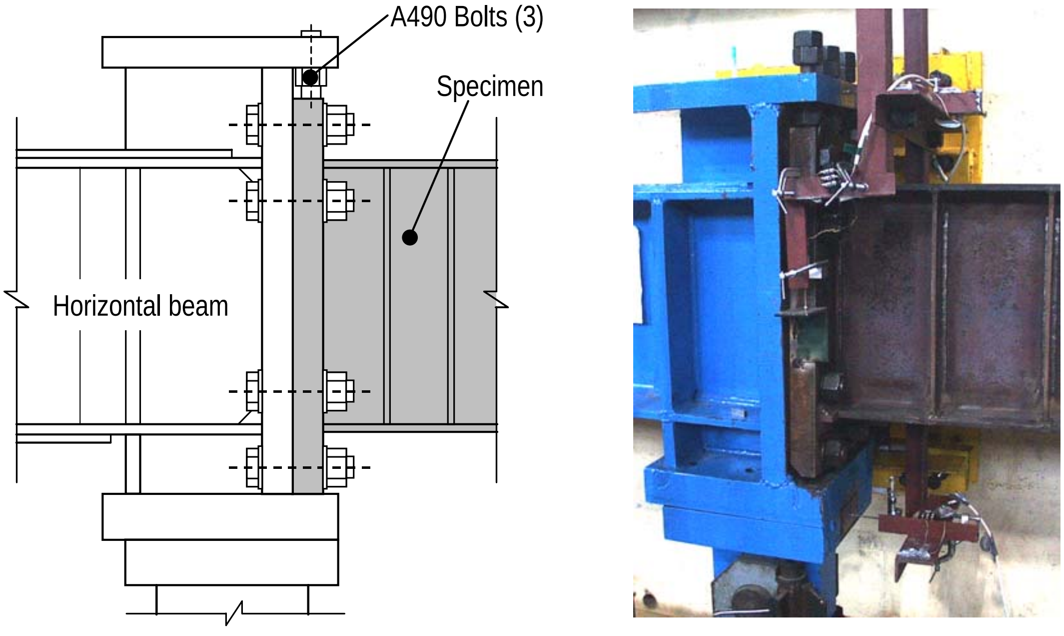

(a) Close-up details ***(b) Photograph***

Figure 3.9 Connection at link end-plate

$1.6M_p/V_p$. The SL-links represented the upper bound of the shear yielding length range, and was added to examine a boarder range of shear yielding links. The normalized link lengths given above were determined by using the nominal dimensions of the W18x40 section and assuming the yield strength is the same throughout the cross-section. All links were fabricated to within 1/4 inch of the target length.

The four connection types were designated the pre-Northridge (PN), modified welding (MW), free flange (FF), and no weld access hole (NA) types. Further discussion of the connection types and fabrication procedures are provided in Section 3.4.

The links were provided with intermediate web stiffeners per the *AISC Seismic Provisions*. Full-depth 3/8-inch thick stiffeners were attached to one side of the link. These stiffeners were fillet welded to the web as well as to the top and bottom flanges. The stiffener spacing for each link is summarized in Table 3.2.

The sixteen specimens were fabricated in six stages: (1) the PN-specimens; (2) the MW-specimens; (3) Specimen FFS; (4) Specimens FFI and NAS; (5) Specimens FFM, NAI, and NAM; and (6) Specimens FFS-RLP, FFSL-RLP, NAS-RLP, and NASL-RLP. The sequential fabrication enabled findings and experience from earlier tests to be reflected in the design details and welding procedures of later specimens.

3.2.3 Loading Sequence

The tests were conducted by applying increasing levels of cyclic link rotation angle, γ, which was computed as the relative displacement of one end of the link compared to the other, divided by the link length. The data reduction scheme is described in Section 3.2.5. The cyclic loading sequence followed one of two pre-determined protocols. One was the protocol specified in Appendix S of the *AISC Seismic Provisions* (2000; 2002), hereafter referred to as the "AISC protocol". The other was a revised loading protocol proposed by Richards and Uang (2003), hereafter referred to as the "revised protocol". The two loading protocols are summarized and compared in Table 3.3. The revised protocol was developed specifically for testing short shear links, based on a study involving extensive nonlinear dynamic analyses of EBFs subjected to strong ground motions. Richards and Uang developed the revised protocol in response to concerns that the AISC protocol was unrealistically too severe for testing short shear links (Refer to Section 2.3.3.3).

Table 3.3 Cyclic loading protocol

(a) AISC protocol

Amplitude: γ (rad)	Number of cycles
0.0025	3
0.005	3
0.01	3
0.02	2
0.03	2
0.04	2
0.05	2
0.06	2
0.07	2
0.08	2
0.09	2
0.10	2
0.11	2
Continue at increments of 0.01 rad with two cycles at each amplitude	

(b) Revised protocol

Amplitude: γ (rad)	Number of cycles
0.00375	6
0.005	6
0.0075	6
0.01	6
0.015	4
0.02	2
0.03	2
0.04	1
0.05	1
0.07	1
0.09	1
0.11	1
0.13	1
Continue at increments of 0.02 rad with one cycle at each amplitude	

After several initial elastic cycles, the AISC protocol requires increasing the link rotation in increments of 0.01 rad, with two cycles of loading applied at each increment of rotation, until failure is observed. The revised protocol requires a much larger number of small elastic cycles. Beyond 0.05 rad, the revised protocol requires the link rotation to be increased in increments of 0.02 rad, with one cycle of loading applied at each increment of rotation. In order to achieve large link rotations, such as approximately 0.10 rad required for shear yielding links, the AISC protocol requires nearly two times more inelastic cycles than does the revised protocol, and therefore, requires much greater accumulation of inelastic rotation. As discussed in Section 2.3.4, Ryu *et al.* (2004) found that the revised protocol allows shear links to achieve inelastic rotations of up to 50% greater than that allowed under the AISC protocol.

The designated loading protocols described above were strictly followed, except for a small deviation during the small amplitude cycles in Specimen MWS, discussed in Section 4.3.1. The loading history for each of the tested specimens is detailed in Chapter 4.

Link rotation was imposed by applying vertical motion at the bottom of the column (see Figure 3.2) in a quasi-static fashion. Whenever an appropriate increment in link rotation was achieved, further load application was stopped momentarily, and measurement readings were collected from the instruments. In the inelastic range, the strength of the specimen is somewhat load rate dependent, reflecting the fact that the yield stress of steel is load rate dependent (SSRC 1998). Load rate effects were apparent in the tests, in that whenever a specimen was in the inelastic range of behavior, the monitored load (reaction R_3 in Figure 3.12) of the specimen would typically drop after loading was stopped. The load drop typically stabilized within a matter of about 5 seconds after loading was stopped. The amount of load drop typically ranged between 5 and 10 kips. This load drop represents the difference between static and dynamic strengths. The effects of loading rate were mostly omitted from the acquired data by pausing load application for several seconds, and collecting the readings after the monitored load came to rest. Consequently, link shear and moment values reported herein largely represent static strength values.

3.2.4 Instrumentation

As shown in Figure 3.2, load cells were installed within the four reaction rods in such a way that the internal forces in the loading system can be completely determined from statics. Displacement and rotation transducers were placed at the two ends of the link (see Figure 3.10a), and in the column (Figure 3.10b), in order to monitor the deformation history of the link and of the column panel zone. Additional displacement transducers were placed to monitor the inclination of reaction rods (Figure 3.10c).

Prior to testing, each specimen was white washed on the front side of the link, the column flange facing the link, and the front side of the column panel zone. The white wash aided qualitative visual observation of progressive yielding.

As shown in Figure 3.11, strain gauges were placed in the MW-specimens to monitor the strain distribution. Uniaxial gauges were placed to monitor the bending strain in the link flanges near the column face and rosette gauges were placed to monitor the strain in the web.

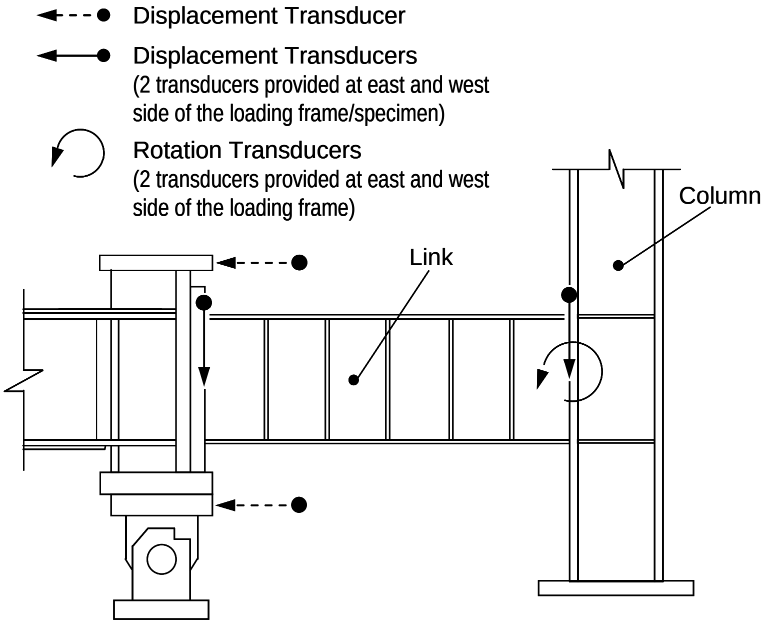

(a) Transducers to monitor link deformation

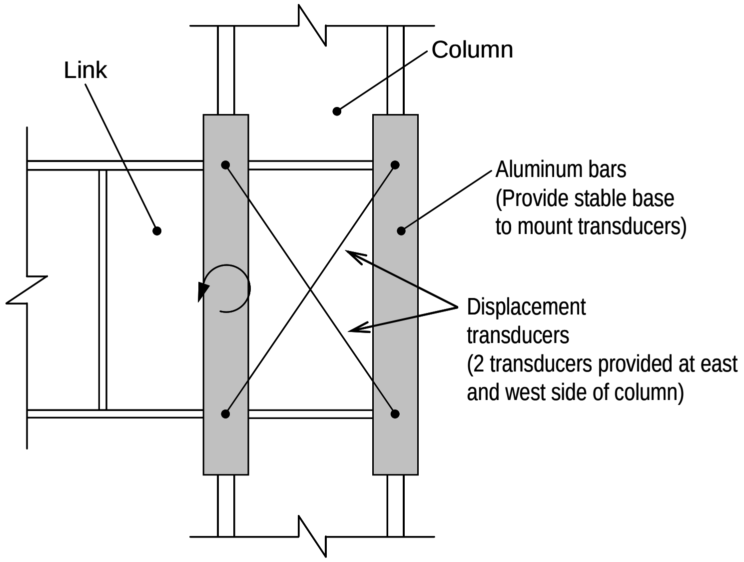

(b) Transducers to monitor panel zone deformation

Figure 3.10 Location of displacement and rotation transducers

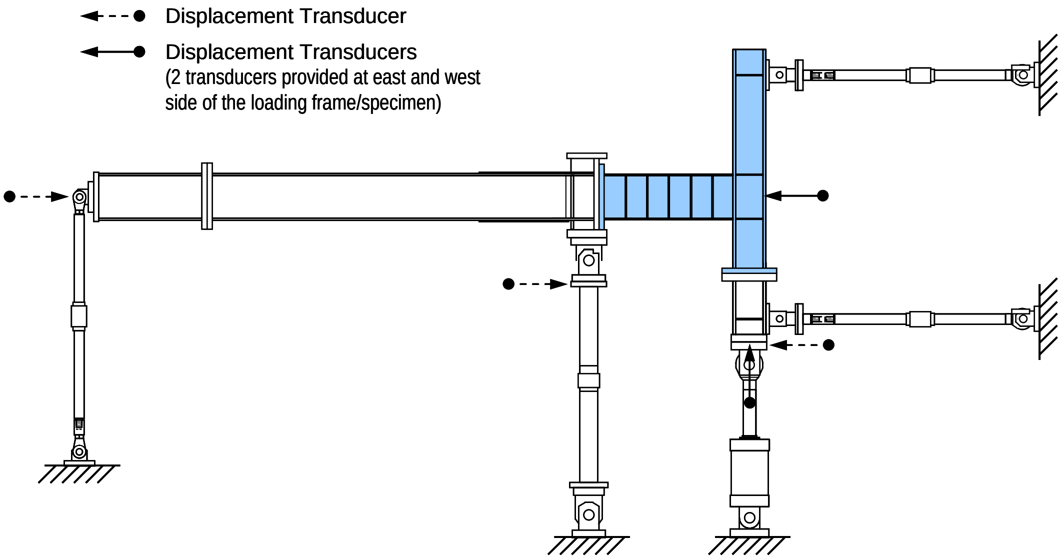

(c) Transducers to monitor overall motion of test frame

Figure 3.10 Location of displacement and rotation transducers (Continued)

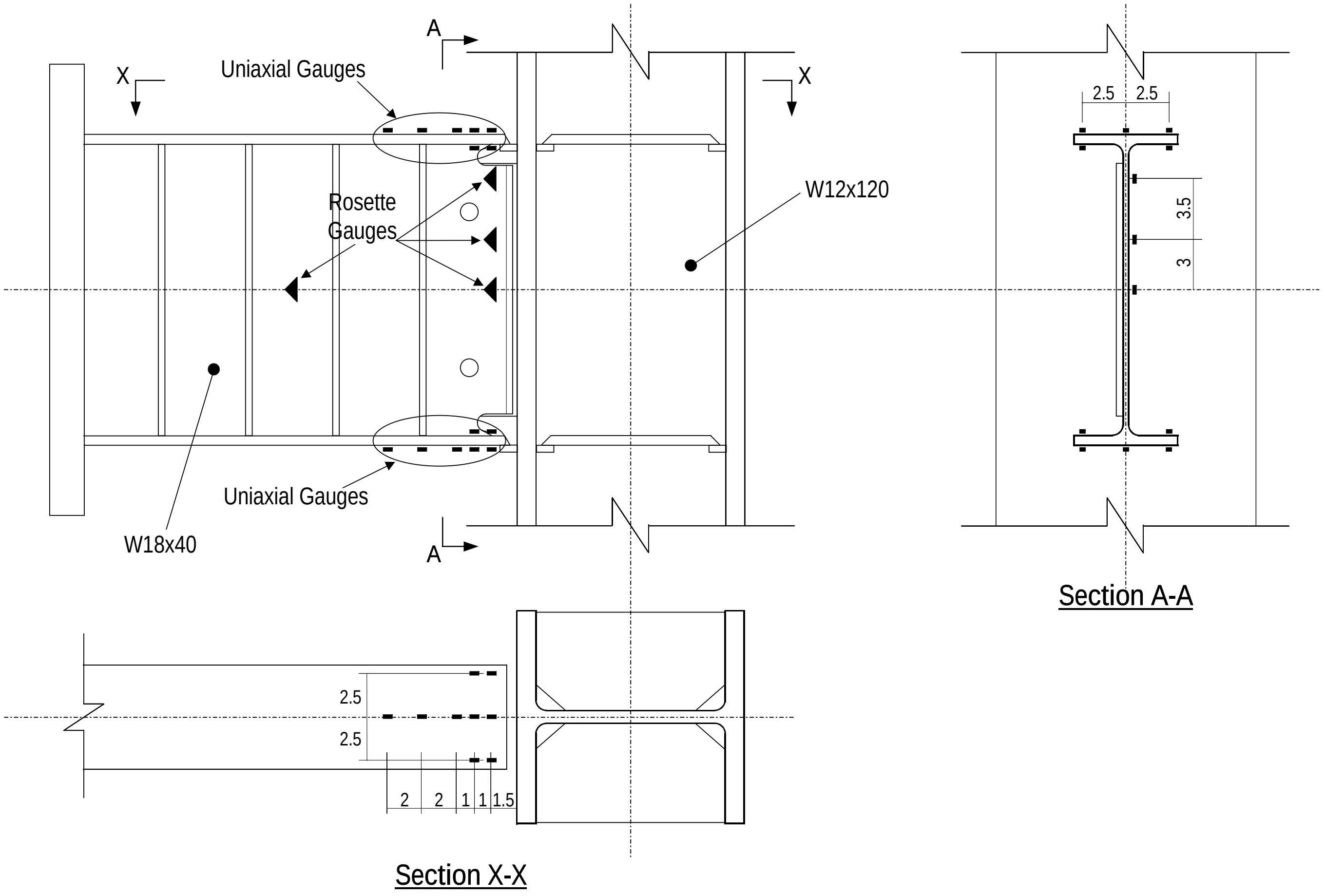

Figure 3.11 Strain gauge location for MWS

3.2.5 Data Reduction

The relationships between the instrument measurements and the quantities of interest are summarized in Figure 3.12 and Figure 3.13. Reactions R_1 to R_4, load induced by the hydraulic loading ram, P, as well as reaction rod inclination angles Θ_1 to Θ_4 are defined as shown in Figure 3.12a. Angles Θ_1 to Θ_4 are evaluated by dividing the movement of a clevis-hinge point by the length of the corresponding reaction rod. Since Θ_2, Θ_3, and Θ_4 were very small, they were taken as zero in the following calculations. The link forces V, M_C, M_B, and N were computed from the diagram shown in Figure 3.12b, based on static equilibrium. The link forces can alternatively be evaluated through the diagram shown in Figure 3.12c. The values obtained from the two independent procedures were compared for the entire loading history to confirm accurate evaluation of link forces. The definition of link rotation angle γ and link end rotations θ_C and θ_B are illustrated in Figure 3.13a. The column panel zone deformation Γ was evaluated from the relations shown Figure 3.13b. Also note that the diagrams in Figure 3.12 and Figure 3.13 follow the adopted sign conventions. The arrows in the figures indicate the positive direction for the forces or displacements.

In these tests, the primary interest is in the relationships between the link shear force V, column face bending moment M_C, and the link rotation angle γ. γ is defined as positive when the column is displaced upward relative to the original position. V is defined as positive when the hydraulic loading ram introduces compression. Positive M_C introduces tensile bending stress in the link top flange, and compressive bending stress in the link bottom flange.

The link rotation γ consists of components attributed to the rotation at the two ends of the link, in addition to the elastic-plastic deformation of the link. The rotation at the column side end of the link arises from the column panel zone deformation and from the flexural deformation of the column, while the rotation at the beam side end arises from the flexural deformation of the horizontal beam.

The *AISC Seismic Provisions* evaluate the performance of the link in terms of the inelastic component of the link rotation angle, γ_p. In this research, γ_p is evaluated as follows:

$$\gamma_p = \gamma - \frac{V}{K_e}. \tag{3.1}$$

In the above equation, K_e is the ratio V/γ evaluated from the initial elastic loading cycles.

The loading system for these tests was designed so that plastic deformation is limited primarily within the link. However, limited yielding was observed in the column panel zone of Specimens FFI and FFM. Therefore, for these two specimens, the γ_p evaluated according to equation (3.1) is affected by inelastic panel zone deformation. This issue is discussed in Section 5.7. No sign of inelastic deformation was detected in any element outside of the link and column panel zone during the tests.

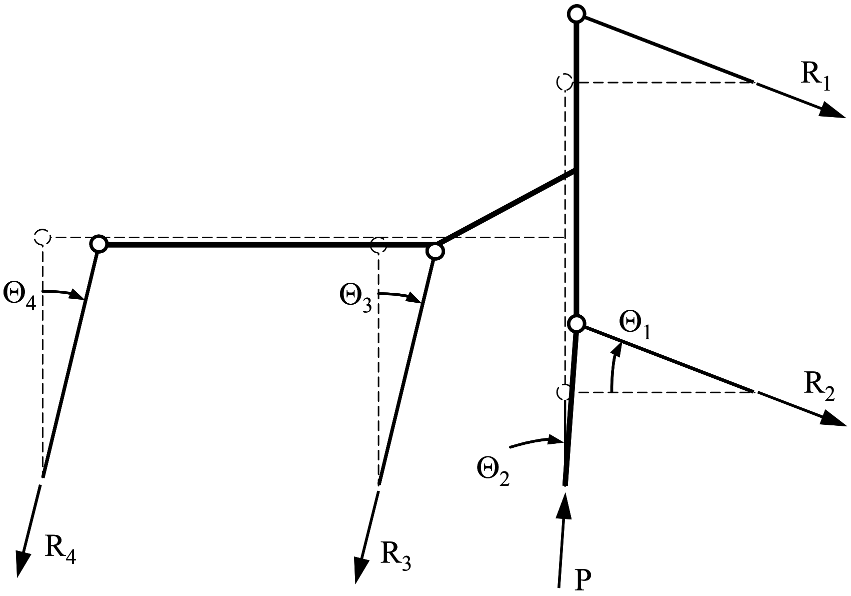

(a) Measured reactions and movement of reaction rods

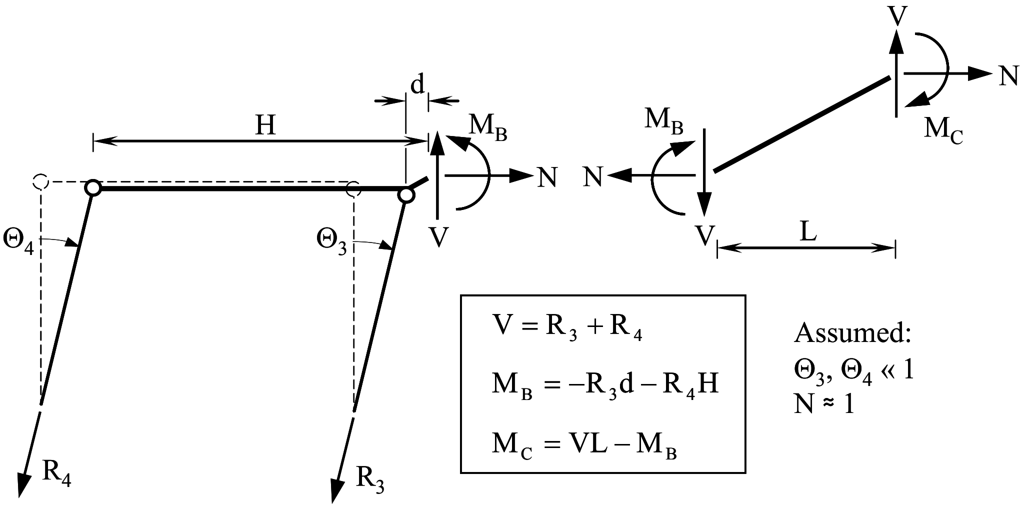

(b) Link force evaluated from beam side end

Figure 3.12 Data reduction to evaluate internal forces

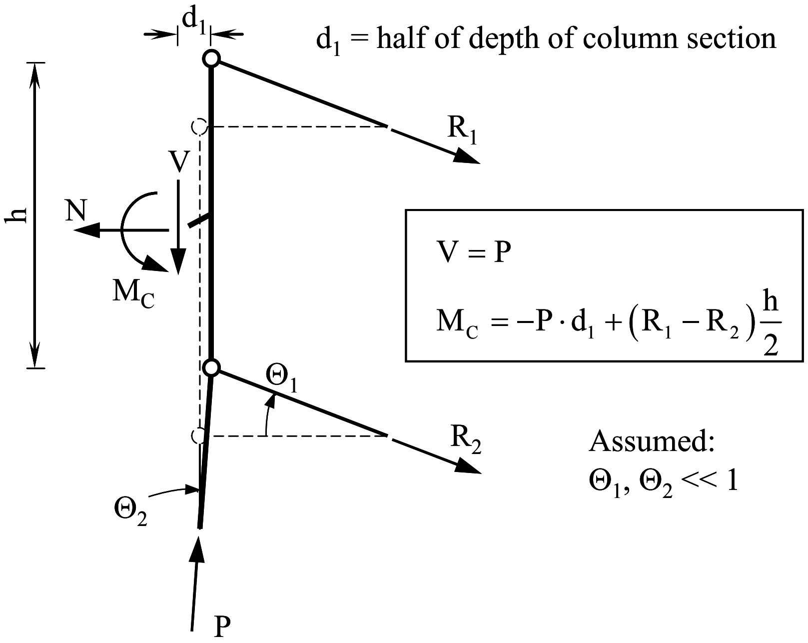

$$V = P$$

$$M_C = -P \cdot d_1 + (R_1 - R_2)\frac{h}{2}$$

(c) Link forces evaluated from column side end

Figure 3.12 Data reduction to evaluate internal forces (Continued)

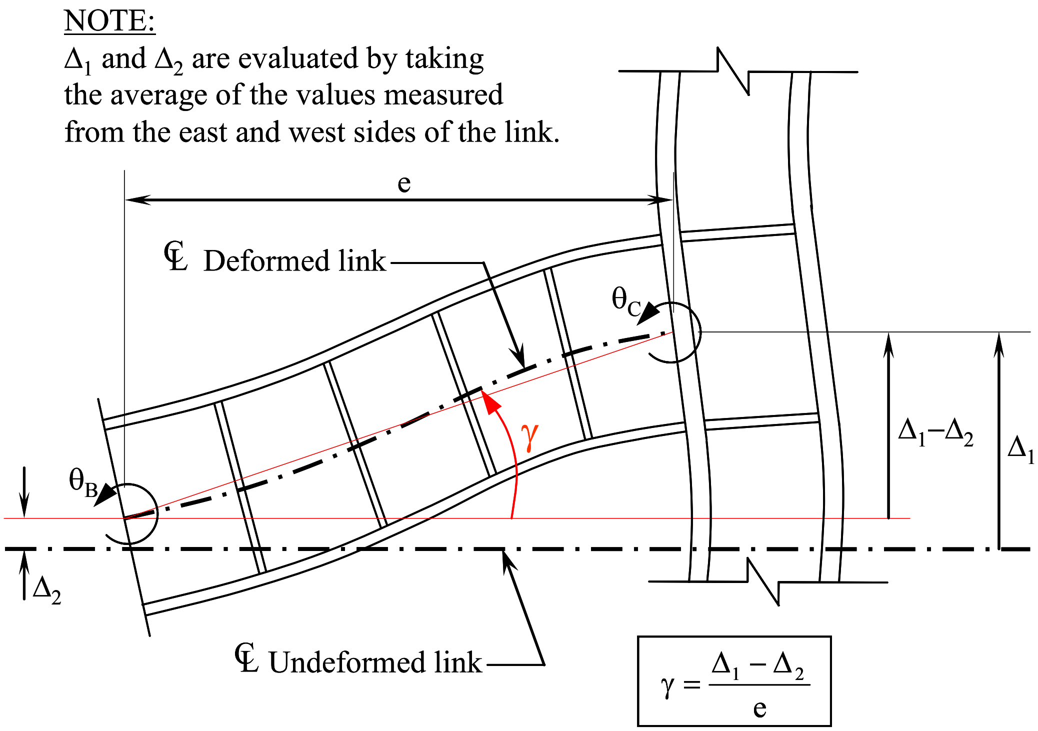

NOTE:
Δ_1 and Δ_2 are evaluated by taking the average of the values measured from the east and west sides of the link.

$$\boxed{\gamma = \frac{\Delta_1 - \Delta_2}{e}}$$

(a) Link deformation

Figure 3.13 Data reduction to evaluate deformations

NOTE:

L_1 and L_2 are evaluated by taking the average of the values measured from the east and west sides of the link.

$$\boxed{\Gamma = \text{average}(\Gamma_1, \Gamma_2)}$$

where:

$$\Gamma_1 = \sin^{-1}\left(\frac{L_1{}^2 - L^2}{2(d_c - t_{cf})(d - t_f)}\right)$$

$$\Gamma_2 = \sin^{-1}\left(\frac{L_2{}^2 - L^2}{2(d_c - t_{cf})(d - t_f)}\right)$$

$$L = \sqrt{(d_c - t_{cf})^2 + (d - t_f)^2}$$

and:

d = overall link depth, in

t_f = thickness of link flange, in

d_c = overall column depth, in.

t_{cf} = thickness of column flange, in.

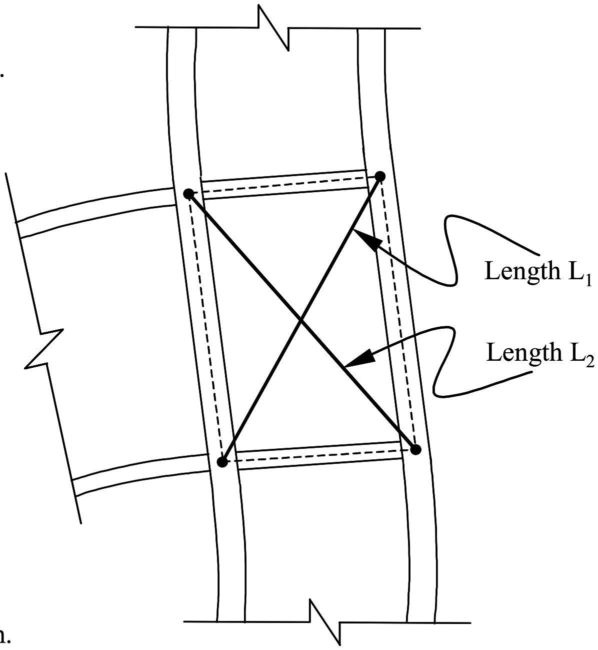

(b) Column panel zone deformation

Figure 3.13 Data reduction to evaluate deformations (Continued)

3.2.6 Evaluation Criteria

The *AISC Seismic Provisions* (2002) define the acceptance criteria for link-to-column connections in qualifying cyclic tests as follows. The test specimen subjected to the AISC loading protocol (described in Section 3.2.3) must sustain the link inelastic rotation amplitude greater than or equal to the required level for at least one complete loading cycle. The required inelastic rotation varies depending on the link length: shear links should be capable of developing inelastic rotation of 0.08 radians; moment links should be capable of developing inelastic rotation of 0.02 radians. The required inelastic rotation for links of intermediate lengths is determined by linear interpolation between 0.08 and 0.02 radians.

For this program, the inelastic rotation capacity of a specimen was defined as the maximum inelastic rotation amplitude sustained for at least one complete loading cycle, including one positive and one negative excursion, prior to loss of strength of the specimen. The loss of strength was defined as the stage when either the link shear strength, V, or the flexural strength at the column face, M_C, dropped to below 80% of their respective maximum magnitudes attained during the test. The inelastic rotation capacity was compared with the required inelastic rotation in order to evaluate the performance of the specimen. As discussed in Section 2.3.2, recent tests (McDaniel *et al.* 2003; Arce 2002) have demonstrated that shear links constructed of grade 50 steel and loaded according to the AISC protocol (See Table 3.3.a) typically do not achieve the inelastic rotation requirement specified in the *AISC Seismic Provisions*.

3.3 MATERIALS

3.3.1 General

The W18x40 links for all specimens were fabricated from the same heat of A992 steel. Similarly, the W12x120 columns for all specimens were fabricated from the same heat of A992 steel. The mill test reports are shown in Appendix C. The measured dimensions of the steel members are listed in Table 3.4 with comparison to their nominal values provided in *ASTM A6* (2002). Distortion of the cross-section and reduction in thickness of the web was visible near the k-area. Material properties of the W18x40 and W12x120 sections were characterized by hardness tests and by tensile coupon tests. The complete joint penetration (CJP) groove welds between the link flange and the column flange (hereafter referred to as link flange groove welds) were characterized by Charpy V-Notch (CVN) tests.

3.3.2 Hardness Tests

Figure 3.14 shows the results from Rockwell B hardness tests performed

Table 3.4 Dimensions of link and column sections

Section	**Dimension**	**Measured (in)**	**Nominal (in)**
W18x40	d	17.82	17.90
	b_f	6.094	6.015
	t_f	0.500	0.525
	t_w	0.310	0.315
W12x120	d	13.25	13.12
	b_f	12.51	12.32
	t_f	1.080	1.105
	t_w	0.708	0.710

per *ASTM E18* (2000) on sections of the W18x40 and W12x120 steel. These tests were conducted using an Instron Series 2000 machine. The hardness test provides an indication of uniformity, or conversely non-uniformity, of the material strength across the cross section. Figure 3.14 indicates that, in both sections, there existed a small region in the web with notably different properties. This region in the web near the flange-to-web fillet is generally referred to as the k-area. The distribution of hardness in the W18x40 section, along the two dashed lines A-A and B-B in Figure 3.14a, is shown in Figure 3.15. This figure further illustrates that the hardness was quite uniform across the cross section with values between 80 and

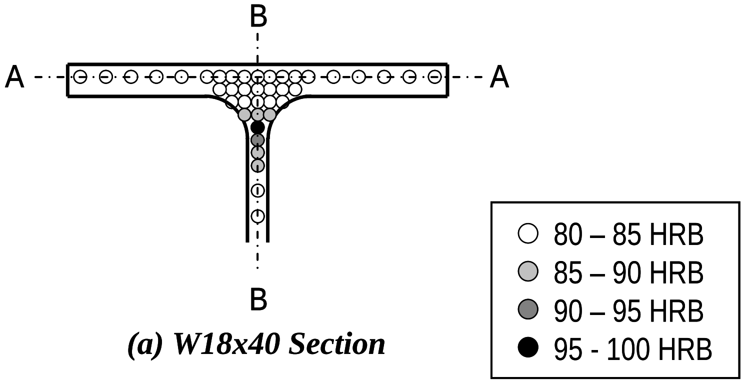

(a) W18x40 Section

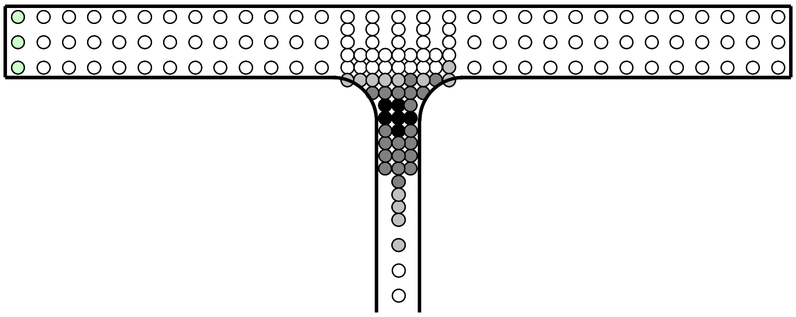

(b) W12x120 Section

Figure 3.14 Hardness test results

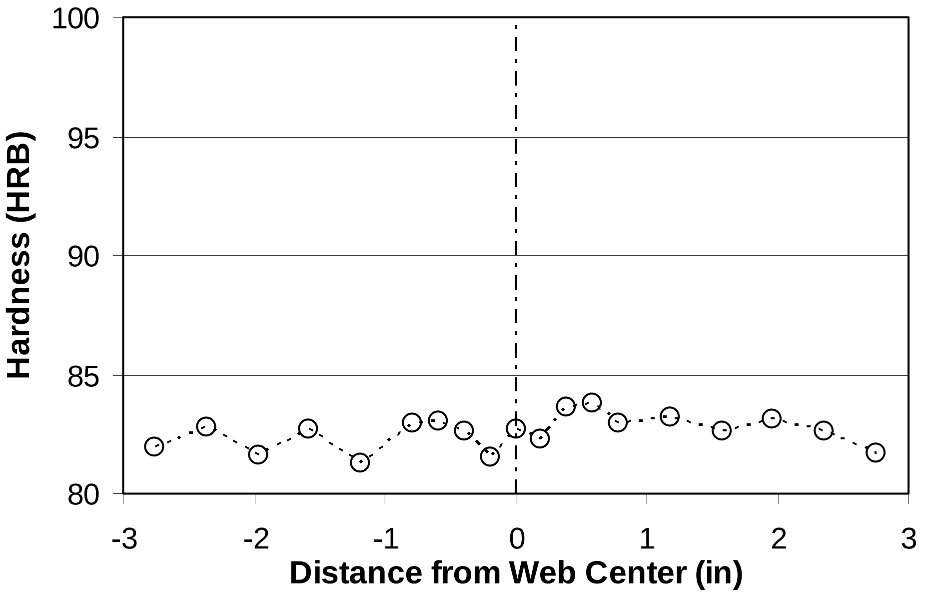

(a) Across width of flange (line A-A)

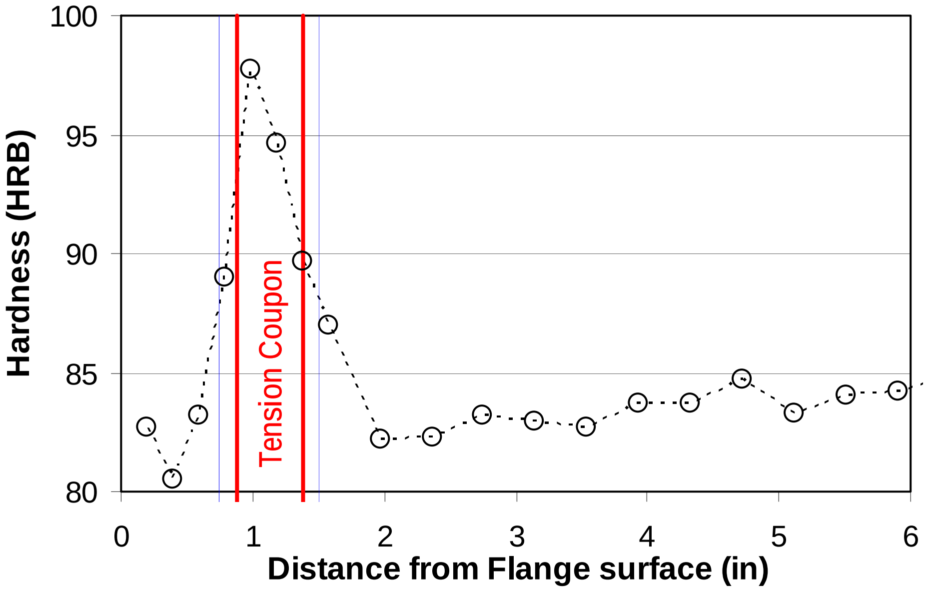

(b) Across depth of section along web center (line B-B)

Figure 3.15 Distribution of hardness in W18x40 section

85 HRB, except in the k-area, where the measured hardness values were between 90 and 98 HRB.

As discussed in Section 2.4.2, recent studies by Arce (2002) report fracture in EBF links that may be related to poor material properties in the k-area of the link section.

3.3.3 Tension Coupon Tests

Tension coupon tests were performed per *ASTM E8* (2001) for the W18x40 and W12x120 sections. As shown in Figure 3.16a, tension coupons for the W18x40 section were sampled from six locations in the cross section: two edges of one flange (coupon LF1 and LF2); and two edges of the other flange (coupon LF3 and LF4); mid-depth of the web (coupon LW); and the k-area region of the web (coupon LK). The location of coupon LK was carefully selected by studying the results of the hardness tests (See Figure 3.15b), to properly include the material with elevated HRB rating. The coupon test results are summarized in Table 3.5, alongside the corresponding values provided in the mill test report. The properties of the flange were evaluated by taking the average values of coupons LF1, LF2, LF3 and LF4.

Coupon LK exhibited significantly higher yield strength and significantly reduced ductility compared to the other five coupons. The high level of hardness in the k-area appeared to correlate to the low material ductility in this area. Comparison of the measured stress versus strain curves in Figure 3.17 illustrates the significant difference in material properties between the k-area and the remainder of the cross-section. The dynamic yield strength was 78.8 ksi in coupon LK, compared to 54.9 ksi in coupon LF1, and 60.8 ksi in coupon LW. Elongation at fracture was only 15% in coupon LK, while it was 34% in coupon LF1, and 31% in coupon LW. The yield-to-strength ratio was 0.88 in coupon LK, 0.76 in

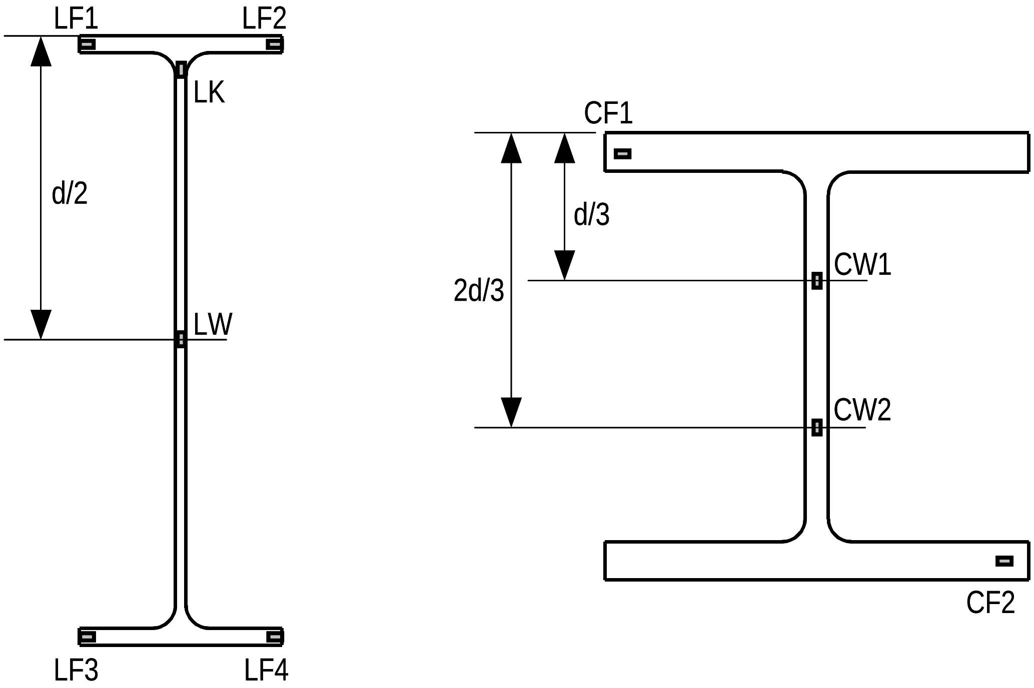

(a) W18x40 Section ***(b) W12x120 Section***

Figure 3.16 Tension coupon locations

coupon LF1, and 0.80 in coupon LW.

As shown in Figure 3.16b, tension coupons for the W12x120 steel were sampled from four locations in the cross section: an edge of one flange (coupon CF1); diagonal opposite edge of the other flange (coupon CF2); and two from two third-points along the depth of the web (coupons CW1 and CW2). Since the primary objective was to evaluate the panel zone shear strength and column flexural strength, k-area properties did not pose special interest for the W12x120. The coupon test results are summarized in Table 3.5, alongside the corresponding values provided in the mill test report. The properties of the flange and web were evaluated by taking the averaged values of coupons CF1 and CF2, and of coupons

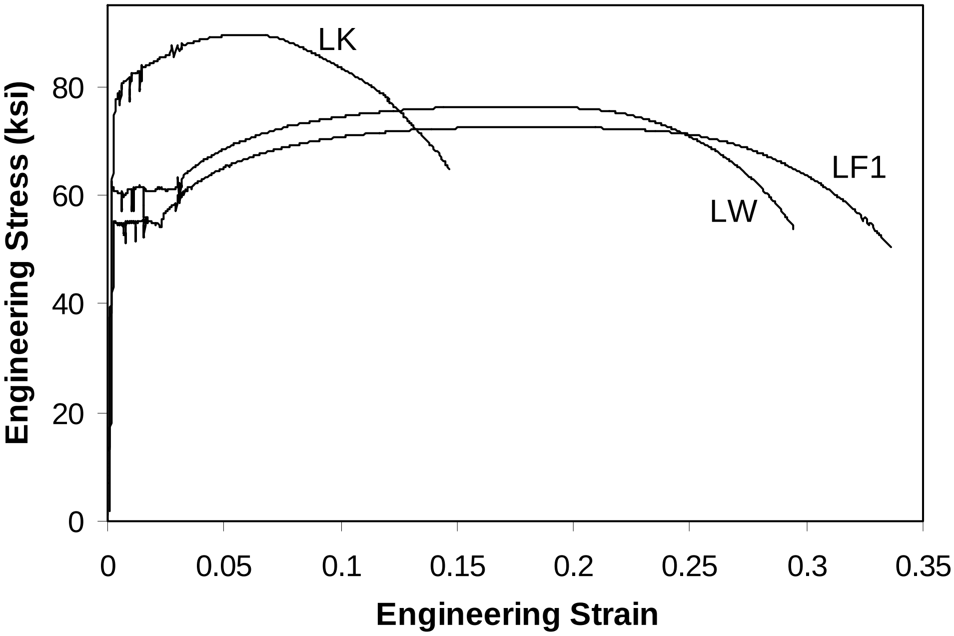

Figure 3.17 Stress-strain curves for W18x40 section

Table 3.5 Tension test results

Section	Location	Laboratory Test			Mill Test		
		F_y[(a)] (ksi)	F_u[(b)] (ksi)	Elong. (%)	F_y (ksi)	F_u (ksi)	Elong. (%)
W18x40	Flange	51.0	72.4	34	55.4	72.9	26
	Web	57.0	76.4	31			
	k-area	75.6	89.6	15			
W12x120	Flange	46.9	66.0	29	53.0	85.5	20
	Web	51.2	70.4	33			

Note:

(a) The tabulated F_y is a static yield stress value, measured with the test machine cross-heads stationary. For Further details, refer to Appendix B.

(b) The tabulated F_u is a dynamic ultimate strength, measured with the test machine cross-heads in motion. For Further details, refer to Appendix B.

CW1 and CW2, respectively. It is interesting to note that the measured tensile strength of the W12x120 steel was 20% lower than the tensile strength value provided in the mill test report. The measured elongation at fracture was 50% greater than the value provided in the mill test report.

Further details of the tension coupon tests are provided in Appendix B.

The key section properties evaluated from the measured dimensions and yield strengths are summarized in Table 3.6, alongside their nominal values. The nominal values are evaluated by using the nominal section dimensions per *ASTM A6* and the minimum required yield strength of A992 steel, 50 ksi. Note that because of the higher yield strength of the web compared to the flanges, the measured value of $e_0 = M_p/V_p$ for the W18x40 section was smaller than its nominal value. Therefore, the actual measures of link length e/e_0 were larger compared to their nominal values: 1.11 instead of unity for S-links, 2.22 instead of 2 for I-links, 1.72 instead of 1.6 for SL-links, and 3.34 instead of 3 for M-links.

3.3.4 Weld Metal CVN Tests

The link flange groove weld is one of the most critical factors affecting the performance of EBF link-to-column connections. In this research, the link flange groove welds were made by the self-shielded flux cored arc welding (SS-FCAW) process using two different types of electrodes, an E70T-4 (Lincoln Electric

Table 3.6 Section properties

Section		N_y (kip)	V_p (kip)	M_p (kip-in)	M_p/V_p (in)
W18x40	Measured	618	178	4008	22.48
	Nominal	590	159	3920	24.62
W12x120	Measured	1669	241	8893	-
	Nominal	1765	232	9300	-

product NS-3M) with 0.120-inch diameter, and an E70T-6 (Lincoln Electric product NR-305) with 3/32-inch diameter. The E70T-4 electrode was used for the PN-connections. The E70T-6 electrode was used for the MW-, FF-, and NA-connections.

The E70T-4 electrode, which has no specified toughness requirement, was chosen to represent pre-Northridge welding practice. The E70T-6 electrode was chosen because it is currently being widely used by West-Coast structural steel erectors following the introduction of weld metal toughness requirements in the *AISC Seismic Provisions*. In addition, it has been established through extensive beam-to-column connection tests that the E70T-6 electrode generally conforms to the minimum CVN values of 20 ft-lb at –20 degrees F and 40 ft-lb at 70 degrees F suggested by *FEMA-350* (2000) and the *AISC Seismic Provisions* (Johnson *et al.* 2000). It is noted that the *AWS A5.20* requires only the CVN rating of 20 ft-lbs at –20 degrees F for the E70T-6.

The two weld filler metals were examined by CVN tests. One sample complete joint penetration (CJP) groove weld as shown in Figure 3.18 was made using each of the two electrodes: E70T-4 and E70T-6. The sample groove welds were made by the same welder who made the welds in the link-to-column connections, using the same welding procedure detailed in Appendix E. WPS # PNEBF3 (See Figure E.7) was used for the E70T-4 electrode; WPS # MWEBF4 (See Figure E.8) was used for the E70T-6 electrode. The 1-inch thick steel plates were restrained during welding to prevent excessive warping. From each of the two sample groove welds, 9 CVN specimens were fabricated. The 10 mm by 10 mm specimen were oriented within the weld as shown in Figure 3.18. The specimens were tested under three different temperatures: –20 degrees F, 0 degrees F, and 70 degrees F. Three specimens were tested for each of the three temperatures. Copies of the CVN test reports are provided in Appendix D.

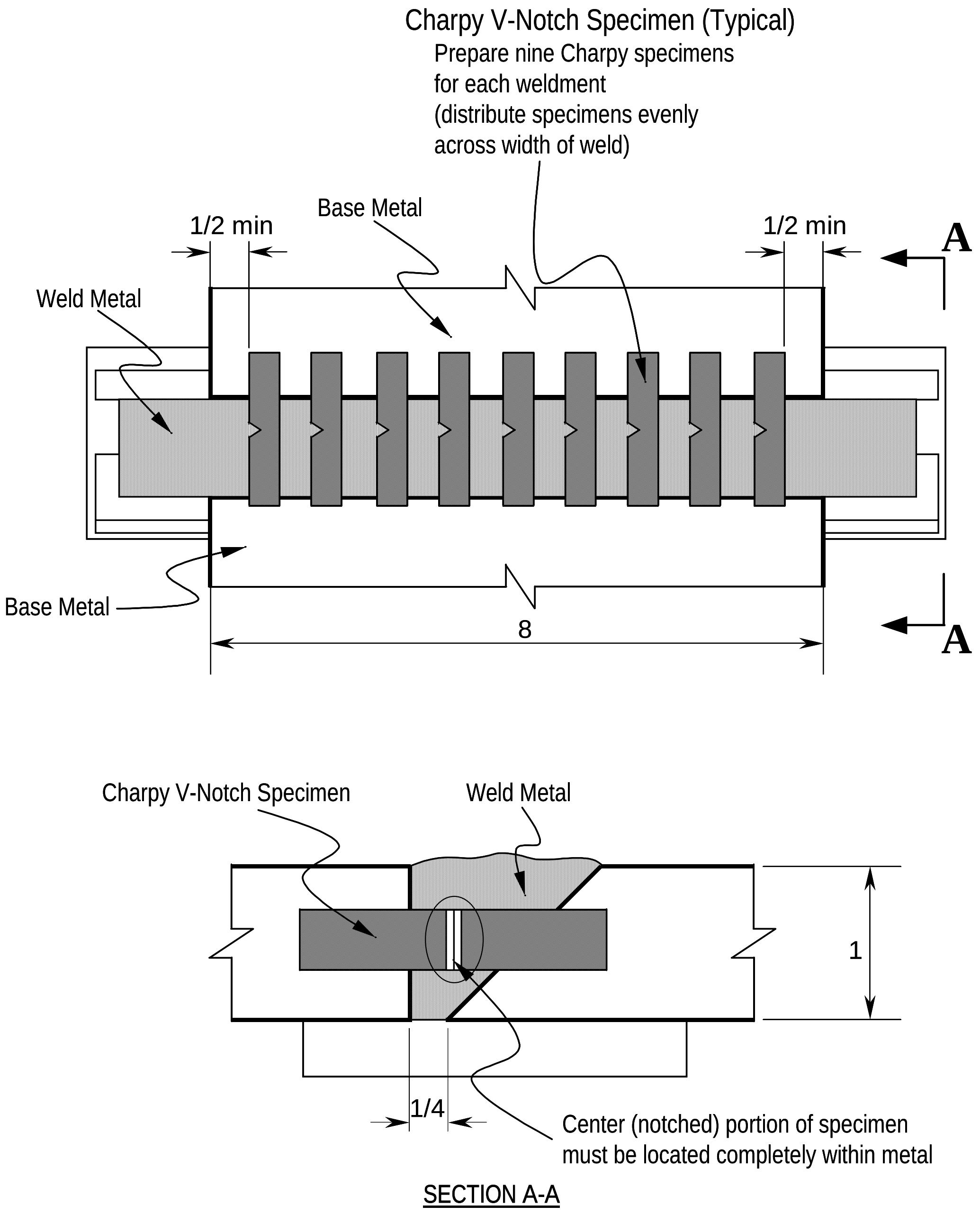

Figure 3.18 CVN Coupons sampling scheme (Dimensions in inches)

The CVN test results are presented in Figure 3.19. This figure shows that the E70T-6 weld had CVN toughness of approximately 30 ft-lbs at –20 degrees F and 50 ft-lb or higher at 70 degrees F. These values exceed the minimum values suggested by *FEMA-350* (2000). Meanwhile, the E70T-4 weld had CVN toughness of below 10 ft-lb at -20 degrees F and between 20 ft-lb and 25 ft-lb at 70 degrees F. These values fall below the minimum rating required in *FEMA-350* (2000), although they are greater than the 5 ft-lb to 10ft-lb at 70 degrees F as reported by Kauffman (1997). The close adherence to the pre-qualified welding procedure is believed to have contributed to the relatively high CVN values of the E70T-4 weld. Comparison of the two sample welds clarify the superior notch toughness of the weld made from E70T-6 over that made from E70T-4. It should be noted here that the laboratory temperature during the large-scale cyclic tests ranged roughly between 70 and 90 degrees F.

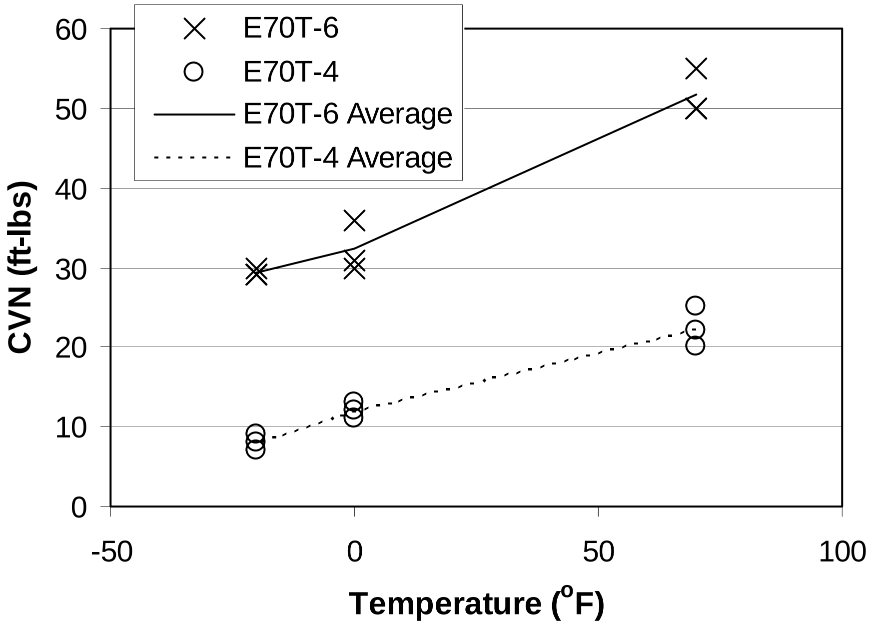

Figure 3.19 CVN test results

3.4 DESIGN DETAILS AND FABRICATION PROCEDURES OF SPECIMENS

3.4.1 General

As discussed in section 3.2.2, four different connection types were tested in this study. Detailed drawings of the connections are provided in Figure 3.20 to Figure 3.25. The links and columns were fabricated separately at the laboratory. The link-to-column connections were welded and finished by a commercial structural steel welder. Detailed welding procedures and welding records are reported in Appendix E.

The welding procedures were strictly controlled following the description provided in this section. In order to simulate field conditions, the column was orientated in an up-right position while welds were being placed at the link-to-column connection. The CJP groove welds between the link top flange and the column flange (link top flange weld), as well the CJP groove welds between the link bottom flange and column flange (link bottom flange weld) were placed in the flat position. The CJP groove welds between the link web and column flange (link web weld) were placed in the vertical position. The link flange CJP groove welds typically made with four or five weld beads (See Figure E10).

Welding inspection and ultrasonic testing were performed by a commercial welding inspection and testing firm. Ultrasonic testing of link flange groove welds and link web groove welds (where accessible) were performed per Table 6.2, Chapter 6 of *AWS D.1-1* (2002). The link top flange welds in Specimens MWS and FFS-RLP were rejected due to discontinuities in the weld. After removing the discontinuities and repairing the welds, both specimens passed the inspection and ultrasonic testing. No other weld was rejected. Copies of the ultrasonic test reports are reproduced in Appendix F.

In the following sections, design details and fabrication procedures are discussed for each of the four connection types.

3.4.2 PN-Specimens

Details of the PN-connection are shown in Figure 3.20. The PN-connection was developed to represent the common design and fabrication practices prior to the Northridge earthquake. Practicing engineers were consulted before this design was finalized to assure that the detailing was representative of pre-Northridge practice.

3.4.2.1 Fabrication Procedure

Prior to placing the welds, the link was connected to the shear tab by erection bolts. First the link top flange weld was placed. Second, the link bottom flange weld was placed. Finally, the link web weld was placed. A detailed description of the procedure is provided in Figure E7.

3.4.2.2 Weld Access Hole

The configuration of the weld access hole conformed to the *AISC ASD Manual* (1989), and was chosen to represent a geometry commonly used in pre-Northridge construction. The dimensions of the top and bottom weld access holes are given in Figure 3.26a. Among the fundamental issues concerning pre-Northridge practice was the fact that little care was taken for the configuration or the fabrication of weld access holes. However, no attempt was made in this program to introduce an intentionally ill-designed or poorly fabricated weld access hole. The drilled and saw-cut surfaces were ground smooth, so that no notches were introduced.

3.4.2.3 Link Flange Welds

The link flange welds were made using the SS-FCAW process using an E70T-4 electrode (Lincoln Electric product NS-3M) with 0.120-inch diameter. This particular electrode was widely used in West-Coast steel erection practice prior to the Northridge Earthquake. Consequently, the link flange welds in EBFs would likely have been made with this electrode in pre-Northridge practice. In the PN-specimens, the link top flange weld was placed with continuous passes along the width of the flange. In the link bottom flange, the weld passes were interrupted by the link web. Backup bars and weld tabs were left in place after completion of the weld, and no reinforcing fillet weld was placed.

3.4.2.4 Shear Tab and Link Web Weld

Two distinct approaches are possible in the design of welded web connections (Popov *et. al* 1989). One approach is to use a heavy welded shear tab. With this approach, the shear tab is shop welded to the column. In the field, the web of the link is then fillet welded to the shear tab. In the second approach, the link web is welded directly to the face of the column using a CJP groove weld. With this approach, the shear tab merely serves as an erection device and as backing for the groove weld between the link web and column flange. The second approach was adopted for the PN-connection, since it was believed to be more common in practice. The FF-connection, detailed in Section 3.4.4, can be regarded as an extension of the first approach.

The shear tab was fillet welded to the column flange in a position that would permit the link web to align with the column web. The SS-FCAW process using an E70T-7 electrode (Lincoln Electric product NR-311) with 3/32-inch diameter was used for these fillet welds. The E70T-7 electrode was widely used prior to the Northridge earthquake for shop welding, but does not have specified

CVN toughness requirements. A detailed description of the procedure is provided in Figure E3.

After the flange groove welds were completed, the link web weld was made by the SS-FCAW process using the all position electrode E71T-8 (Lincoln Electric product NR-232) with 0.072-inch diameter.

During the fabrication of Specimen PNS, the fillet weld between the shear tab and column flange was mistakenly made with a shielded metal arc welding (SMAW) process using an E7018 electrode, rather than using the procedure described above. However, this error is believed to have had no impact on the overall performance of Specimen PNS, since the specimen experienced no recognizable yielding near this weld during the test.

3.4.2.5 Column and Link

The SS-FCAW process using an E70T-7 electrode with 3/32-inch diameter was used for the welds connecting the continuity plates to the column. First, CJP groove welds were placed between the continuity plate and the two inner faces of the column flanges. Subsequently, fillet welds were placed between the continuity plate and the column web. A detailed description of the procedure is provided in Figure E1.

The fillet welds between the link web stiffeners and the link were also made using the SS-FCAW process with an E70T-7 electrode with 3/32-inch diameter. After observing premature failure of the link due to web fracture (Arce 2002), it was realized that the stiffener fillet welds in the link web should be placed a larger distance from the link flanges, to keep these welds away from the k-area. Figure 3.15b indicates that the high hardness region of the web of the W18x40 section extends to a point that is approximately one inch beyond the inner face of the flange. Consequently, the distance between the flange inner face and the termination of stiffener fillet welds was taken as two inches, as shown in Figure 3.8. This treatment was applied to all links fabricated for this program.

3.4.3 MW-Specimens

Details of the MW-connection are shown in Figure 3.21. The main feature of the MW-connection was the use of modified welding procedures adopted following the Northridge earthquake. An additional feature was the modification in the configuration of the link bottom weld access hole to comply with *FEMA-350*.

3.4.3.1 Fabrication Procedure

The fabrication procedure was identical to that used in the PN-connection, except for changes in the welding procedures. A detailed description of the procedures is provided in Figure E8.

3.4.3.2 Weld Access Hole

In order to comply with the requirements in *FEMA-350*, minor changes were made from the PN-connection in the configuration of the weld access hole. The dimensions of the top and bottom weld access holes are given in Figure 3.26b. For the bottom flange, a longer length was introduced between the column face and the root of the weld access hole. Choi *et al.* (2000) and Ricles *et al.* (2000) demonstrated that this distance plays a critical role in relaxing the stress concentration in the link flanges. The shallow intersection angle between the weld access hole and the link flange contributes to a reduction in stress concentration (Barsom *et al.* 2002). The top flange weld access hole remained unchanged from the PN-connection, and was identical in configuration to the bottom weld access hole. The drilled and saw-cut surfaces were carefully ground smooth, so that no notches were introduced.

3.4.3.3 Link Flange Welds

The requirements for the weld metal and welding details recommended in *FEMA-350* (2000) were used for the link flange welds. The welding recommendations in *FEMA-350* have been widely adopted for beam-to-column moment connections following the Northridge earthquake.

Modifications in the link flange welds in the MW-connections, as compared to the PN-connections included: the use of weld metal with specified notch-toughness; removal of the backing bar at the link bottom flange weld, followed by the placement of a supplemental reinforcing fillet weld; placement of a fillet weld connecting the backing bar to the face of the column at the link top flange; and removal of weld tabs at both top and bottom link flange welds.

The SS-FCAW process using an E70T-6 electrode (Lincoln Electric product NR-305) with 3/32-inch diameter was used for placing the CJP groove welds between the link flanges and the column flange. The replacement of the E70T-4 electrode with an E70T-6 electrode was one of the key upgrade features from the PN-connection to the MW-connection. Comparison of CVN-ratings (see Section 0) indicates the higher fracture toughness of E70T-6 weld metal as compared to E70T-4 weld metal. Research efforts following the Northridge earthquake revealed that the use of high deposition, low notch toughness weld electrode such as the E70T-4 was among the primary causes of the widespread damage in moment connections (e.g., *FEMA-355E* 2000). The E70T-6 electrode is one of the most popular electrodes in current use for field welding, and generally complies with the CVN toughness requirement introduced in the *AISC Seismic Provisions* following the post-Northridge studies.

Following advice provided by the welder, the backing bars were extended 2-inches beyond the edge of the flanges (see Figure E8) in the modified flange weld procedure. For the PN-connections, the backing bars were extended only 1-

inch beyond the edge of the flanges (see Figure E7). The 2-inch extension was used for the FF- and NA-connections as well.

3.4.3.4 Shear Tab and Link Web Weld

The MW-connection used the same link web to column connection detail as was used for the PN-connection. That is, the link web was connected to the column flange using a CJP groove weld, with the shear tab acting as an erection aid and as a backing bar. However, the fillet welds between the shear tab and the column flange were made with an E71T-8 electrode. The CJP groove weld for the link flange was made with the E71T-8, and this groove weld overlays one of the fillet welds joining the shear tab to the column flange. Consequently, the E71T-8 electrode was also used for the shear tab to column flange fillet welds to avoid intermixing of dissimilar welds metals (*FEMA-267* 1995). A detailed description of the procedure is provided in Figure E4. The same welding procedure used for the PN-connection was used for the link web CJP groove weld.

3.4.3.5 Column and Link

The columns fabricated for the PN-specimens were reused for the MW-specimens. A new link was welded to the fresh column flange, opposite the flange where the link was welded for the PN-specimen. The weld between the continuity plates and the column, made using the E70T-7 electrode, did not necessarily reflect post-Northridge practice. Instead of an E70T-7 electrode, an E70T-6 is more commonly used after the Northridge earthquake. However, no panel zone deformation or damage between the continuity plates and column was observed in the PN-specimens. Consequently, it was assumed that the continuity plate welds were not a critical aspect of the test specimens. It is to be noted that this observation may not hold true for designs that intend extensive panel zone yielding.

The fillet welds between the link stiffeners and link were made with an E70T-6 electrode instead of an E70T-7 electrode used for the PN-specimens.

3.4.4 FF-Specimens

Details of the FF-connections are shown in Figure 3.22, Figure 3.23, and Figure 3.24. This connection features the combined use of extended weld access holes and a heavy shear tab welded to the link web.

The three specimens tested in the first phase, Specimens FFS, FFI, and FFM had different shear tab geometries. Modifications were made for the web connection of the two specimens tested in the second phase, Specimens FFS-RLP and FFSL-RLP.

3.4.4.1 Fabrication Procedure

The fabrication procedure for the connections was similar to that in the MW-connection except for the additional fillet welds placed between the heavy shear tab and link web. All modifications in welding procedure developed for the MW-connection were adopted for the FF-connections. A detailed description of the procedure is provided in Figure E9.

3.4.4.2 Weld Access Hole

The dimensions of the weld access hole are given in Figure 3.26c. The selected free flange length (distance between the root of the weld access hole and column face) was taken as 2.5 inches, equal to five times the flange thickness, following the suggestion by Choi *et al.* (2000). The drilled and saw-cut surfaces were carefully ground smooth, so that no notches were introduced.

3.4.4.3 Link Flange Welds

The link flange welds were made using the same procedure used for the MW-connection. For details, refer to Section 3.4.3.3.

3.4.4.4 Shear Tab and Link Web Weld

The geometry of the shear tabs was selected based on preliminary finite element analyses. The welded shear tab increased the stiffness of the link web near the column face and draws the shear force away from the link flanges. A different geometry was developed for each of Specimens FFS, FFI, and FFM, as shown in Figure 3.22 and Figure 3.23. The shear tabs for Specimens FFS-RLP and FFSL-RLP were chosen based on observations from testing Specimens FFS, FFI, and FFM.

It is important to note that the region of the link web welded to the shear tab does not participate in the inelastic shear deformation mechanism, because of the increased cross-sectional area of the combined web and shear tab. As a result, the link is effectively shortened by as the distance that the shear tab extends from the column face. This shortened link length will result in as increase in deformation demand. A rectangular shear tab was chosen for Specimen FFS, to minimize the extent of link shortening (see Figure 3.22). Trapezoidal shear tabs, similar to those developed by Choi *et al.* (2000) were chosen for Specimens FFI, FFM (see Figure 3.23), FFS-RLP, and FFSL-RLP (see Figure 3.24). The shear tab in Specimen FFM extended 7.5 inches away from the column face, while the shear tab in Specimens FFI, FFS-RLP, and FFSL-RLP extended 6.5 inches.

The shear tab for all FF-specimens was groove welded in a flat position to the column flange. A detailed description of the procedure is provided in Figure E6.

After completion of link flange welds, the link web weld was made. In Specimens FFS, FFI, and FFM, the link web was groove welded directly to the column face, as in the MW-connections. In Specimens FFS-RLP and FFSL-RLP, the link web was cut short from the column face, and was fillet welded to the shear tab, as suggested by Choi et al. (2000).

After completing the link flange and web welds, a fillet weld was placed between the edge of the shear tab and the link web. The weld wrapping at the corners of the shear tabs are shown in Figure 3.27. In Specimen FFS (see Figure 3.27a), the weld wrapped around the corner of the shear tab, extending approximately 1-inch in the horizontal direction, and stopping just short of the weld access hole. In Specimens FFI, FFS-RLP, and FFSL-RLP, the weld was terminated within the inclined portion of the shear tab, stopping just short of the top and bottom corners. In Specimen FFM (see Figure 3.27b), the weld was terminated at the top and bottom corner of the inclined edge of the shear tab.

3.4.4.5 Column and Link

The same design and welding procedure developed for the PN-specimens was used for the fabrication of columns and links, except that the E70T-7 electrode replaced the E70T-6 electrode to reflect the post-Northridge practice. A detailed description of the procedure is provided in Figure E2.

Specimen FFS was constructed using a new column section. Specimens FFI and FFM shared a column. Specimen FFS-RLP shared a column with Specimen NAS-RLP, and Specimen FFSL-RLP with Specimen NAI.

As described above, the link is effectively shorter in the FF-specimens, compared to in other specimens with the same nominal link length. Therefore, the link stiffener spacing was altered from those in the other specimens as indicated in Table 3.2.

3.4.5 NA-Specimens

Details of the NA-connection are shown in Figure 3.25. This connection features the elimination of weld access holes. As is the case in Japanese practice, the NA-connection was intended for fabrication in the shop. Both the top and bottom link flange groove welds were placed continuously across the width of the flange in a flat position, the outer face of the link flange facing upward.

Another feature of the NA-connection was the elimination of the shear tab. The primary function of the shear tab as an erection device is not needed for shop fabrication. Further, the presence of the shear tab would complicate the welding procedure for the web to column connection, at the transition between the web and flange welds. The use of through-diaphragms as in the Japanese practice (see Figure 2.19), separate the flange welds and web welds, and avoids interaction of multiple weld lines. This was not the case with the NA-connection. A fabrication procedure was developed in order to minimize the interaction of welds, and to simplify fabrication.

3.4.5.1 Fabrication Procedure

The welding procedure for the NA-connections differed significantly from the other three connections due to the fact that it is intended to be shop fabricated. First, the column was laid horizontally so that the column flange to be welded to the link faced upward. The link was positioned vertically with the section to be welded facing downward and in contact to the column flange. Then, a fillet weld was placed between the link web and the column flange near the centroid of the link section. Second, the specimen was repositioned so that the outer face of the top flange faced upward. The link top flange weld was made in the flat position. Third, the specimen was repositioned upside-down so that the outer face of the bottom flange faced upward, and the link bottom flange weld was made. Finally, a reinforcing fillet weld was placed between the backing bar and the column flange. This fillet weld was continued to a location between the link web and column flange. A detailed description of the procedure is provided in Figure E10.

3.4.5.2 Link Flange Welds

The link flange welds differed from those in the PN-, MW- and FF-connections in two respects. First, the groove bevel extended beyond the link flange into the link web as shown in Figure 3.26d and Figure 3.28. Second, the welding procedure was identical for both the link top flange and link bottom flange, so that the link bottom flange weld was not interrupted by the link web, and the root of both welds were positioned at the inner face of the flange.

In order to accommodate this special welding procedure, customized backing bars, as shown in Figure 3.28a, were prepared. The backing bars, together with the link flange groove bevel and column flange, formed a closed surface as shown in Figure 3.28b. This surface was filled with weld metal, prior to placing the CJP groove welds. Note that the backing bar, which was split into two pieces with a separation at the link web, did not conform to the full-length backing required by *AWS D1.1*.

Other than the two aspects mentioned above, the link flange welds were made using the same welding procedure used for the MW-connection (Refer to Section 3.4.3.3).

3.4.5.3 Link Web Weld

The link web was fillet welded to the column flange. This fillet weld was made in two separate procedures. Prior to placing the link flange welds, the mid-depth region of the link web was fillet welded to the column flange. After the link flange welds were completed, a continuous fillet weld was placed between the backing bar and column flange, and between the remainder of the link web and column flange.

3.4.5.4 Column and Link

The columns were identical to those fabricated for the FF-connections. Refer to Section 3.4.4.5 for further details. No shear tab was used for the NA-connection. The link stiffener spacing was identical to that in the PN-specimens.

Specimen NAS shared a column with Specimen FFS. Specimens NAI and NAM were constructed using new column sections. Specimen NAS shared a column with Specimen FFS-RLP; Specimen NASL-RLP and Specimen NAM.

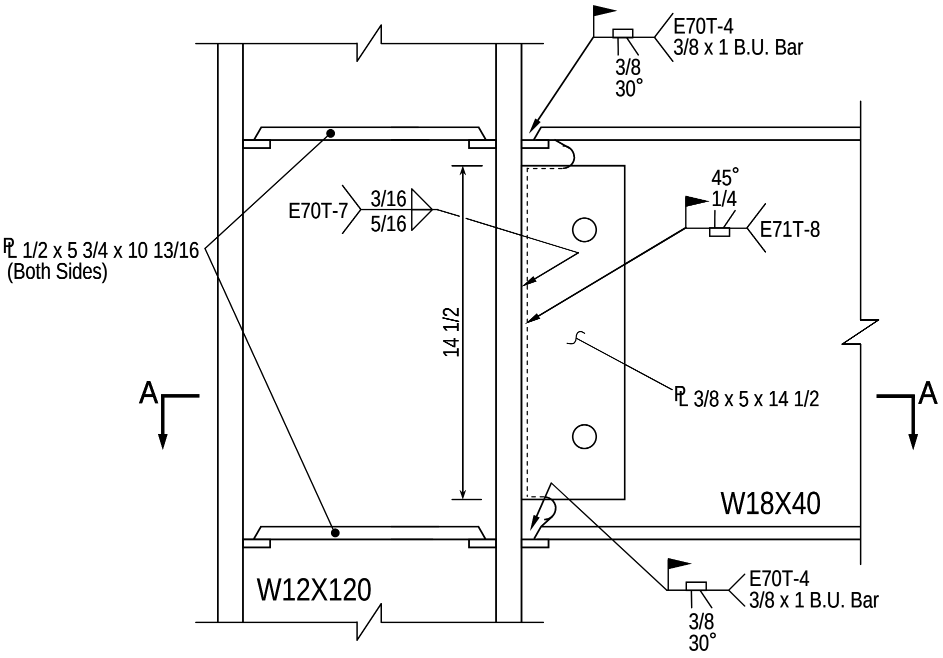

East View

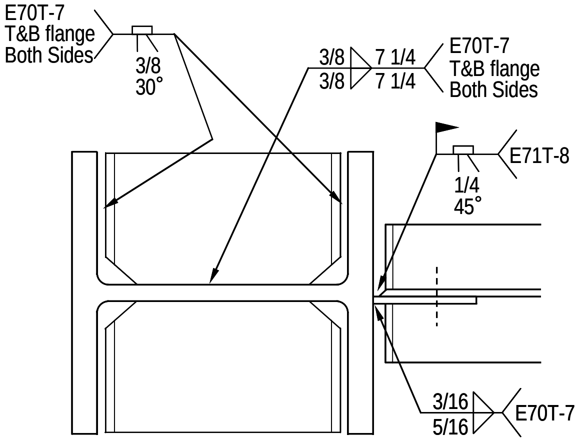

Section A-A

Figure 3.20 PN-connection (Dimensions in inches)

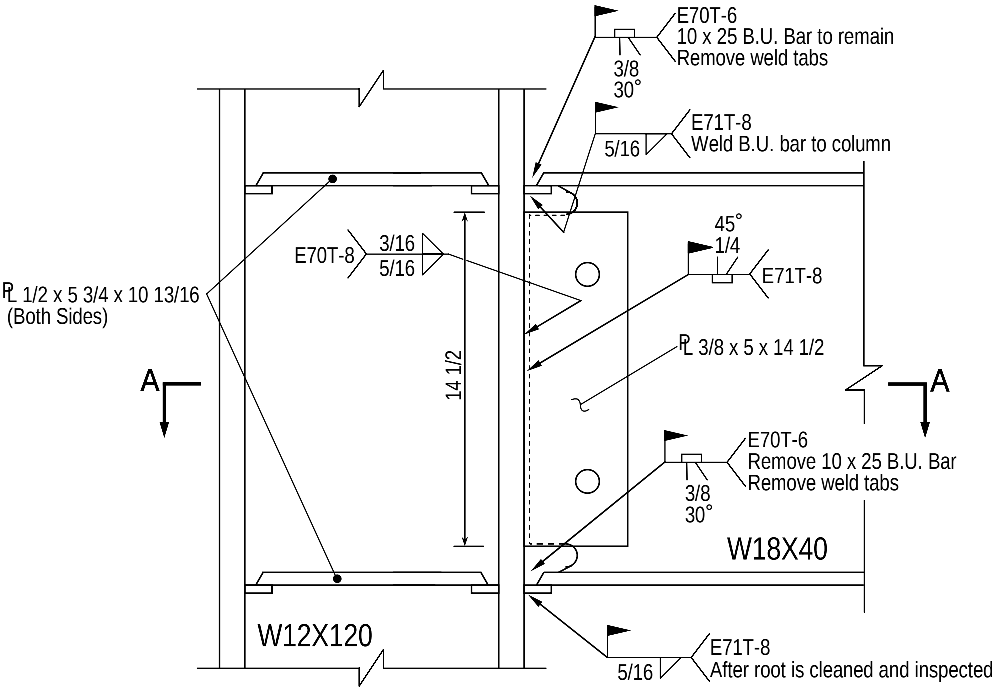

East View

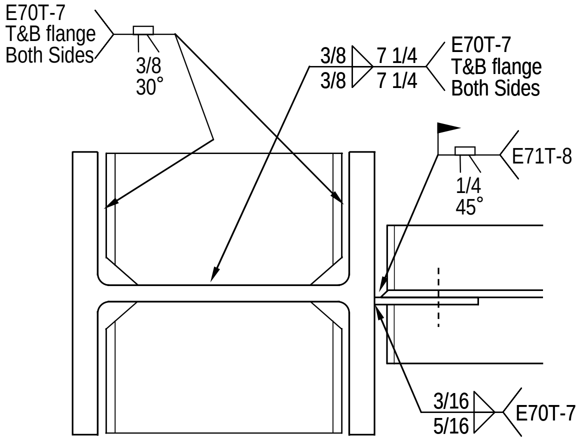

Section A-A

Figure 3.21 MW-connection (Dimensions in inches)

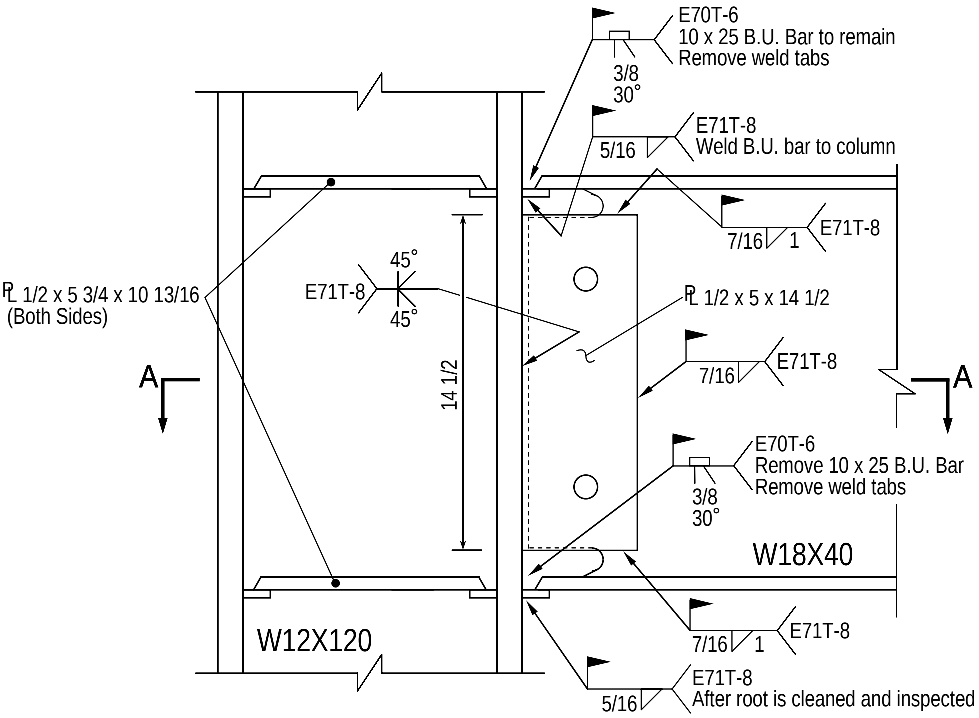

East View

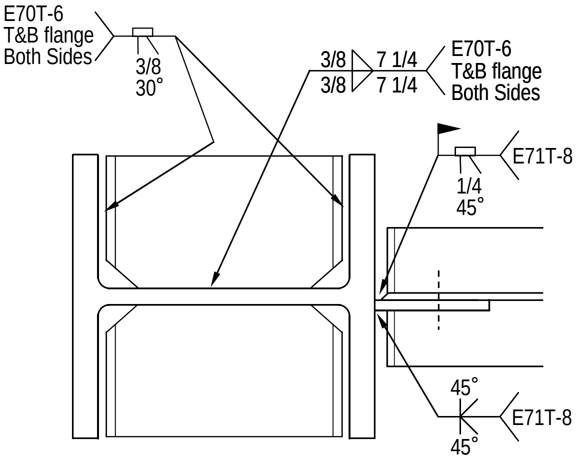

Section A-A

Figure 3.22 Connection FFS (Dimensions in inches)

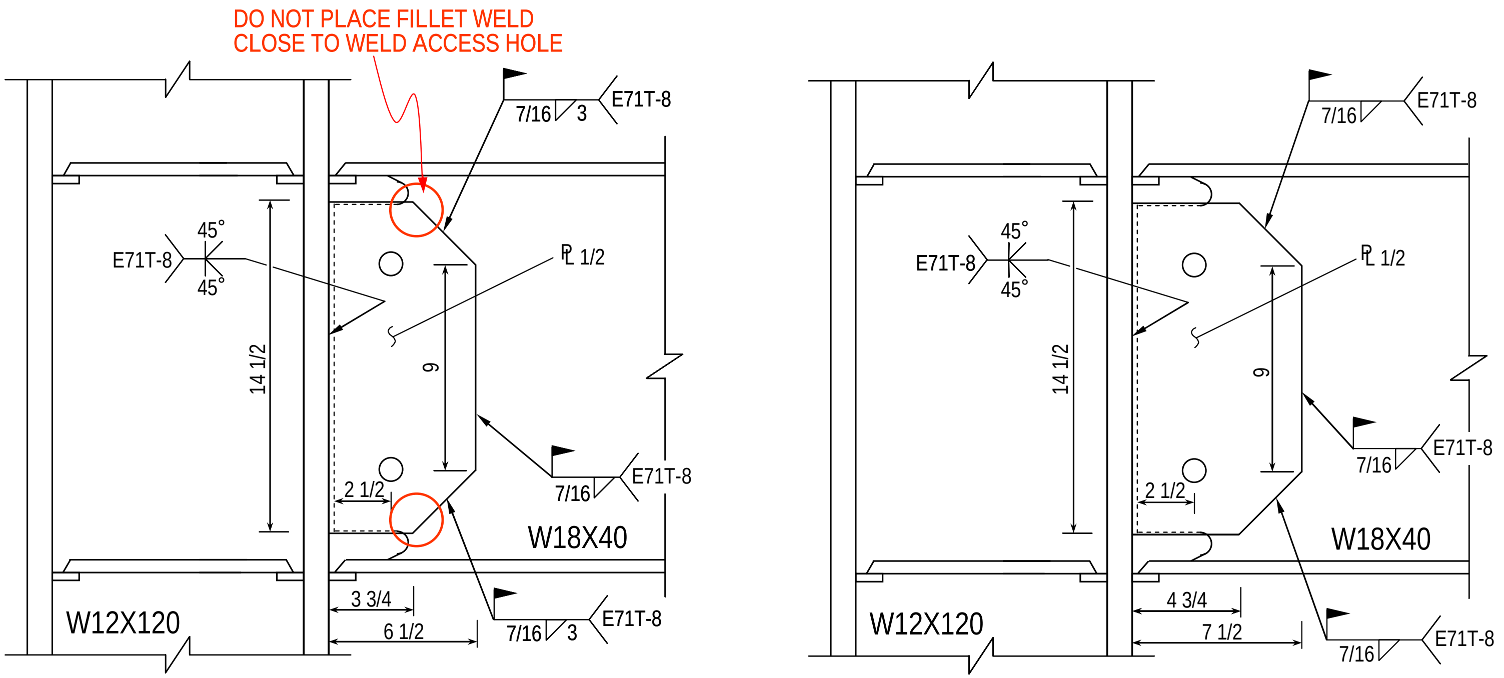

Connection FFI East View

Connection FFM East View

Figure 3.23 Connections FFI and FFM (Dimensions in inches)

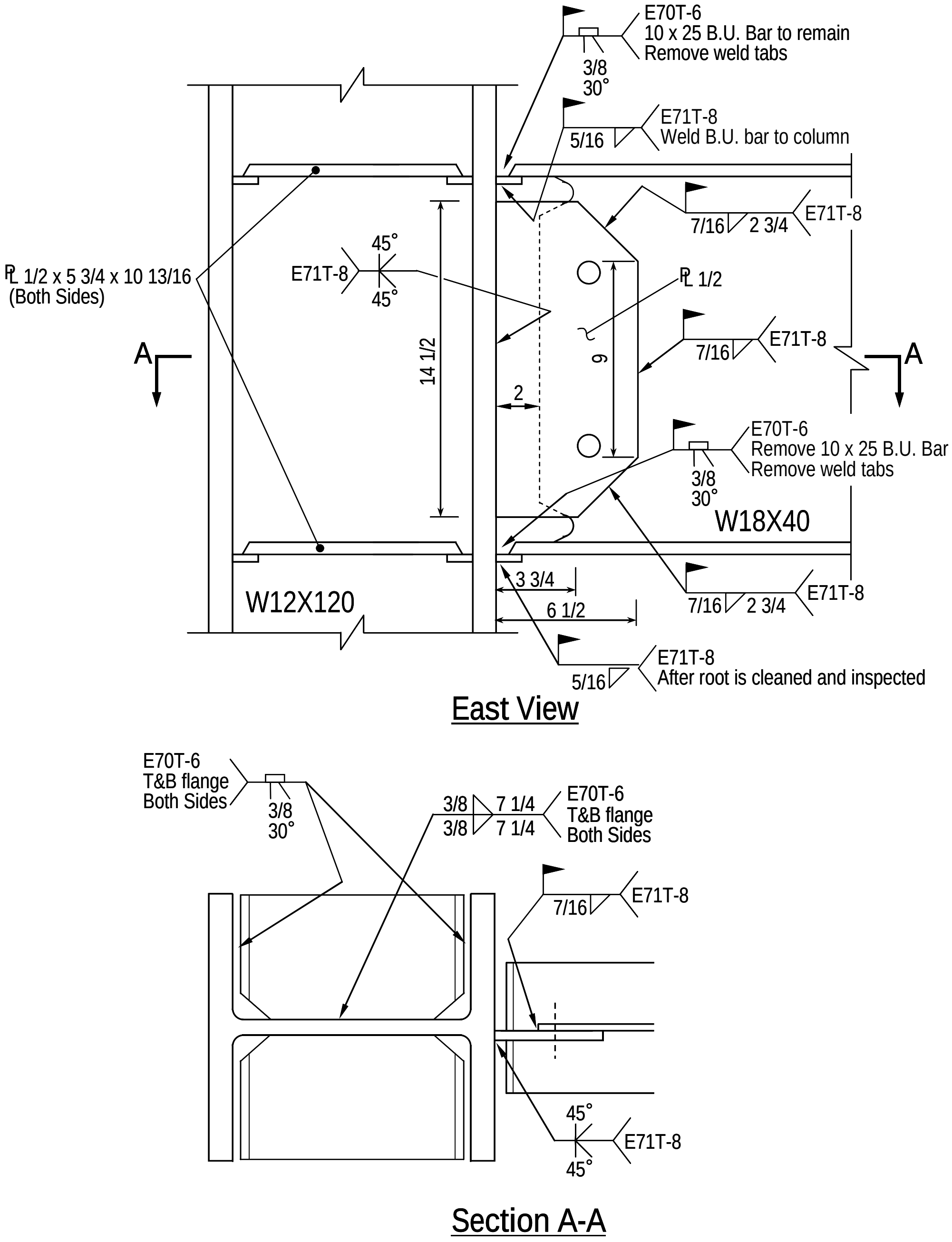

Figure 3.24 Connections FFS-RLP and FFSL-RLP (Dimensions in inches)

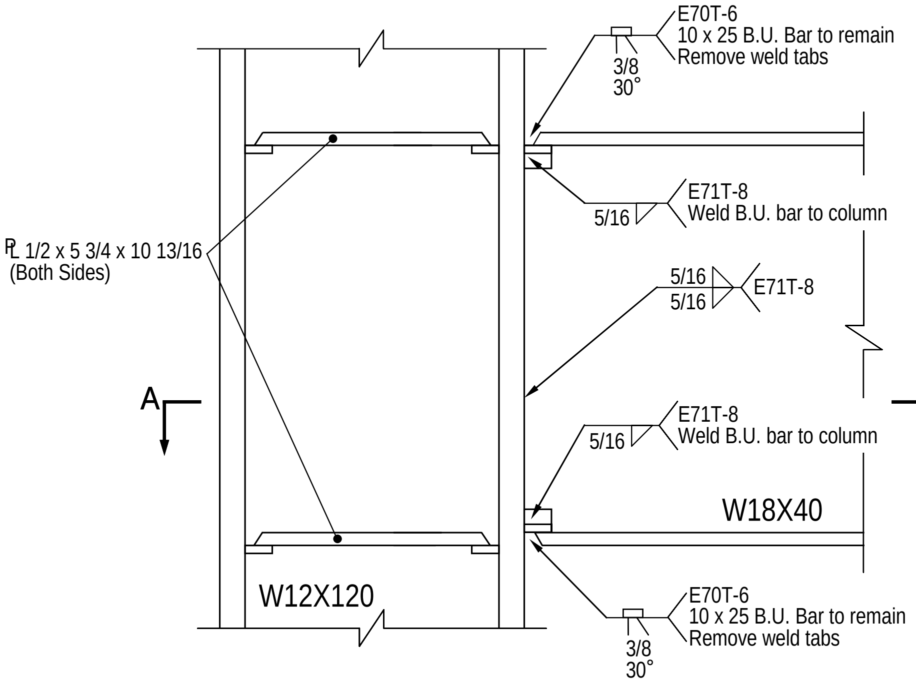

East View

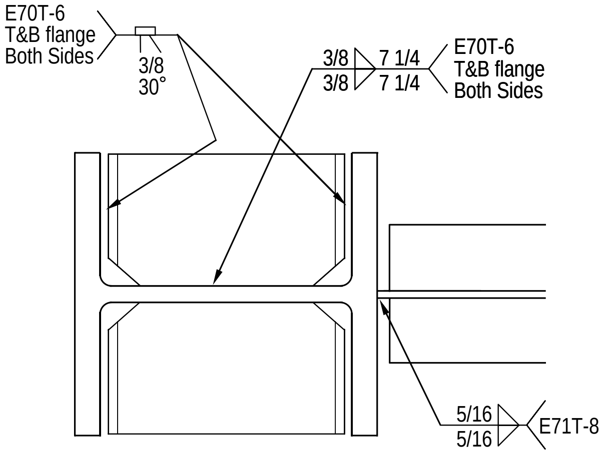

Section A-A

Figure 3.25 NA-connection (Dimensions in inches)

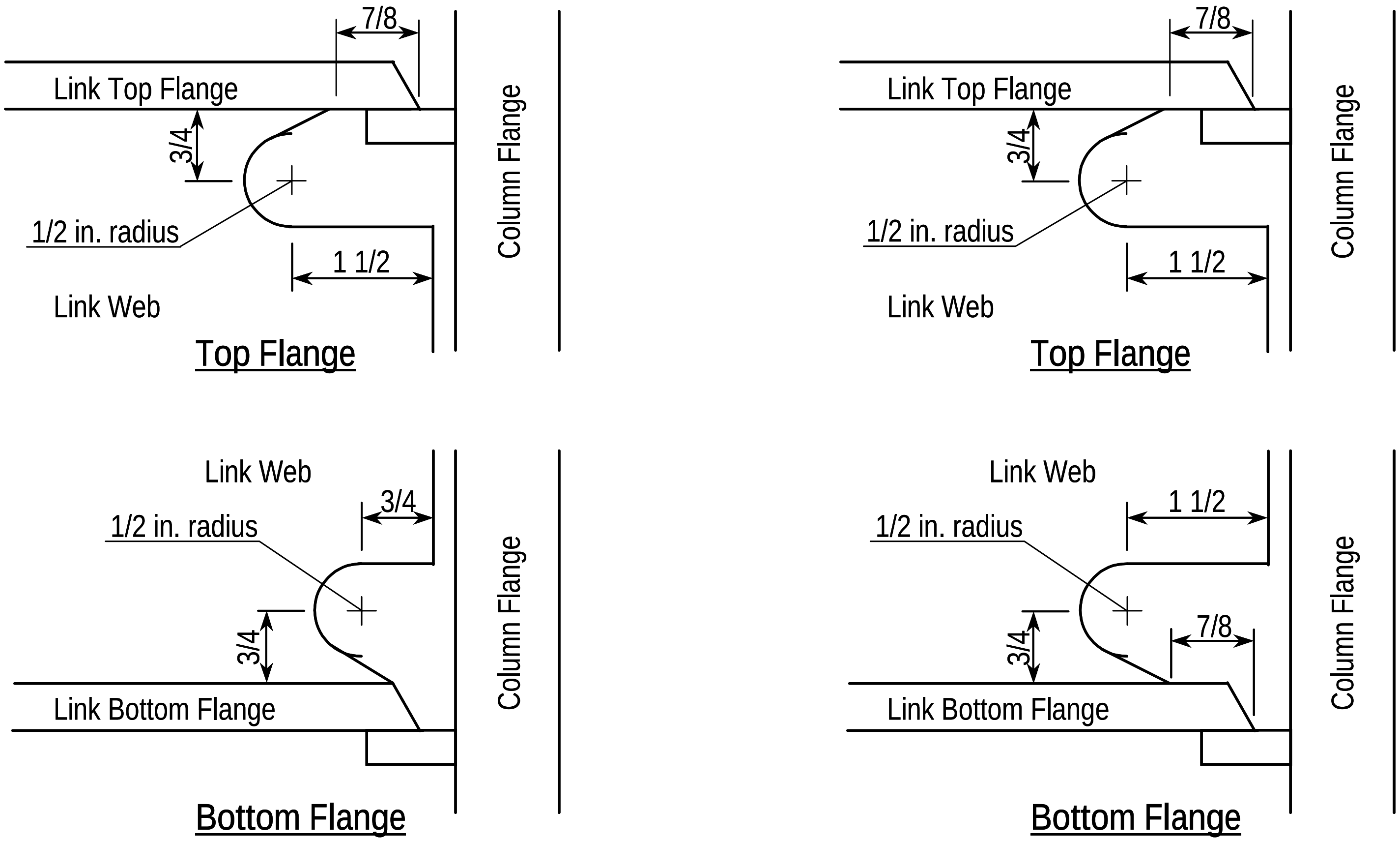

(a) PN-connections ***(b) MW-connections***

Figure 3.26 Weld access hole and flange bevel (Dimension in inches)

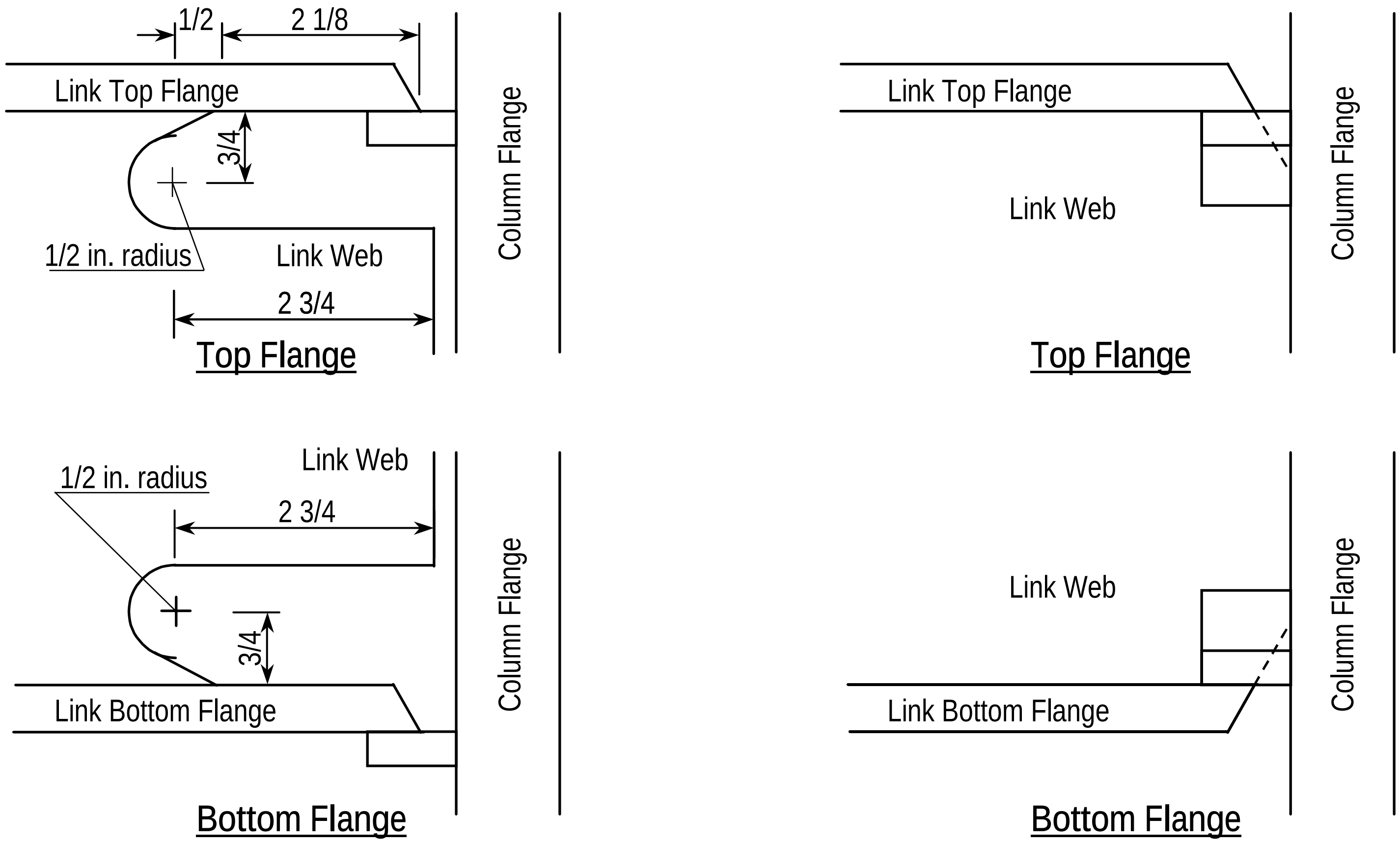

(c) FF-connections ***(d) NA-connections***

Figure 3.26 Weld access hole and flange bevel (Dimension in inches) (Continued)

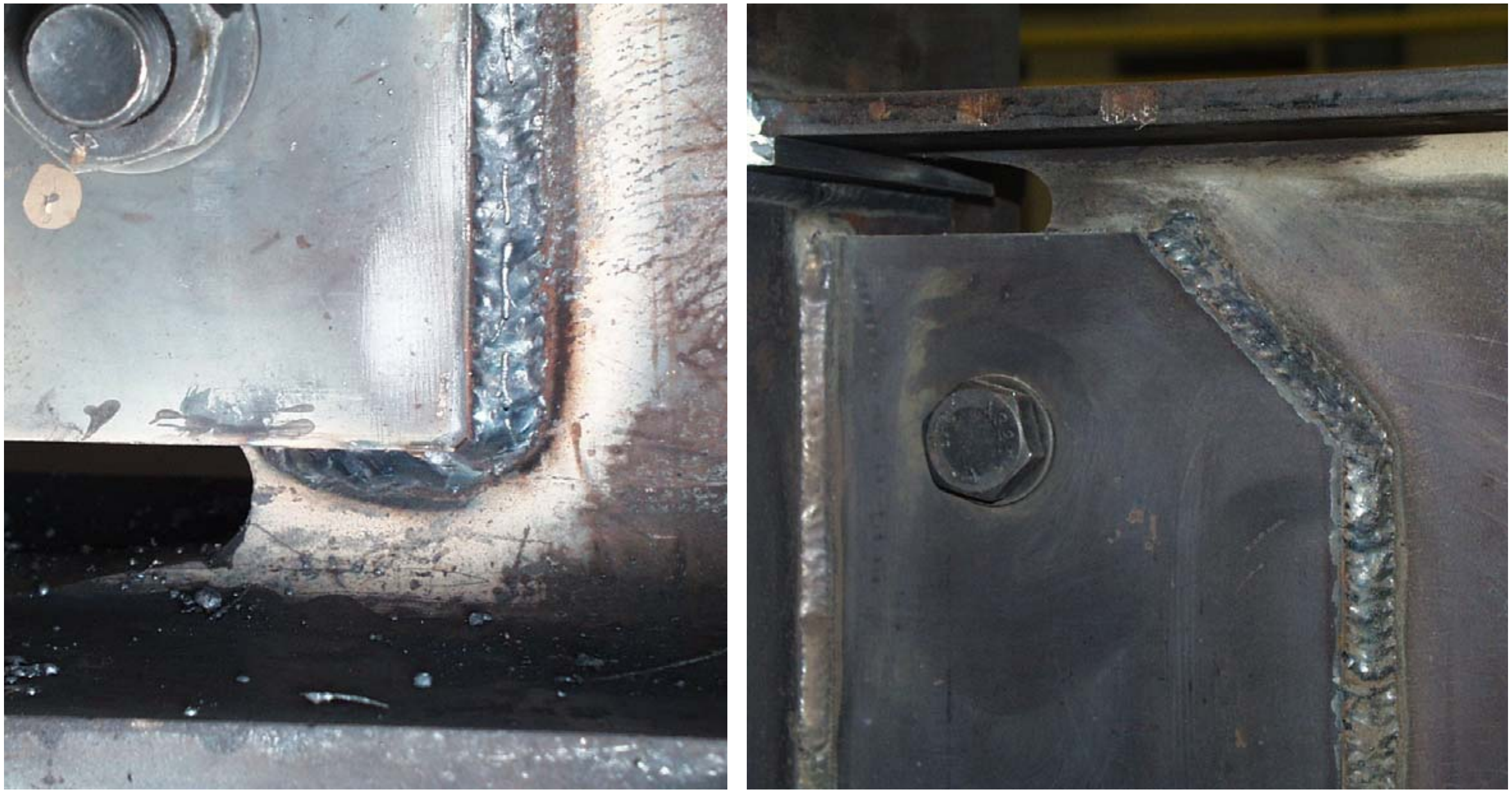

(a) FFS shear tab bottom *(b) FFM shear tab top*

Figure 3.27 Weld wrapping around corners of shear tab

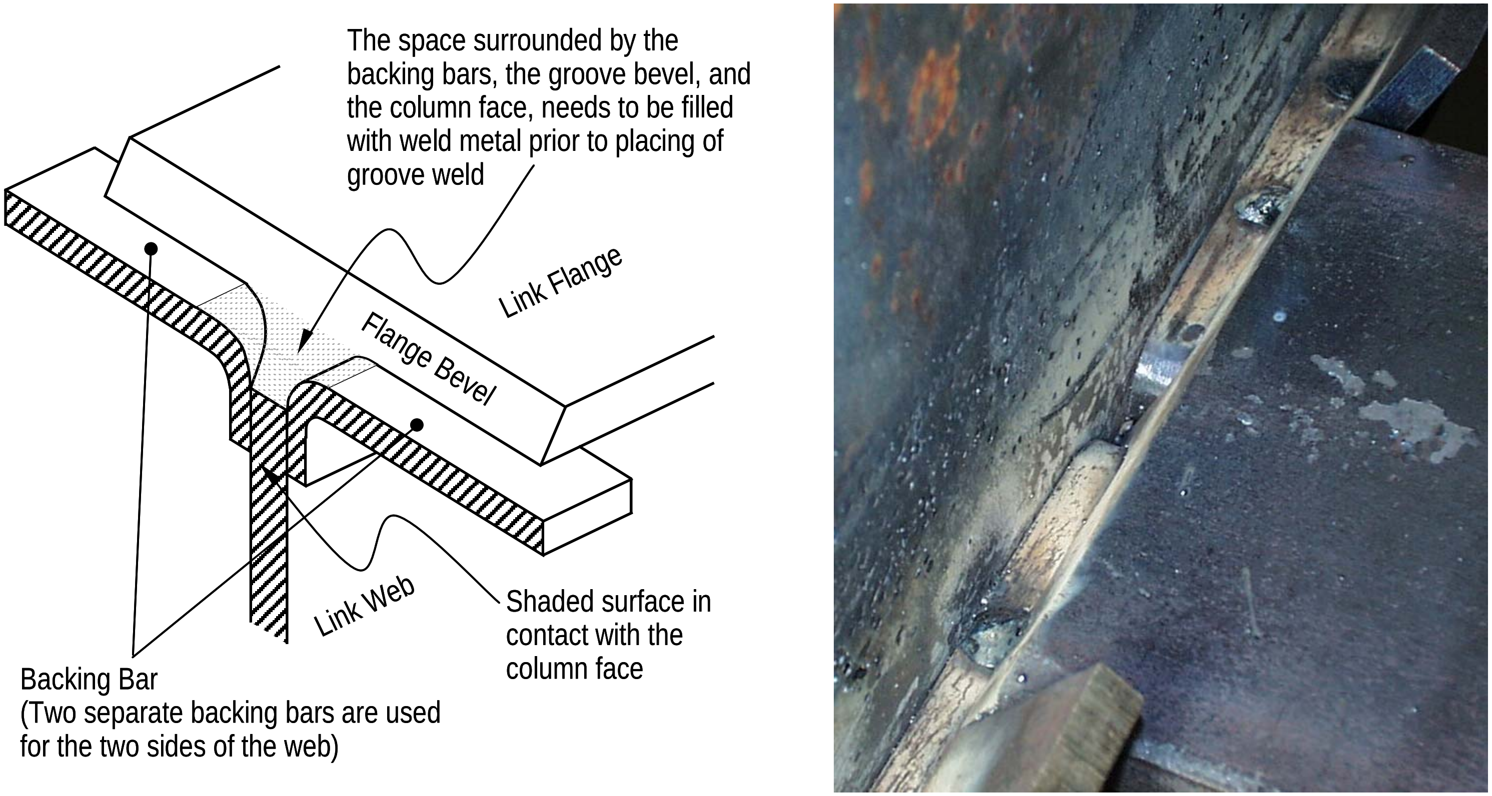

(a) Customized backing bar for NA-connections

(b) Fabrication of Specimen NAI. Backing bar tack welded

Figure 3.28 Backing bars used for NA-connections

CHAPTER 4

Test Results

4.1 INTRODUCTION

This chapter describes the principal results obtained from the large-scale tests of link-column specimens. Further analysis and discussion of the test results are provided in Chapter 5.

During each test, loading was interrupted at key points, such as when all loading cycles at a specified link rotation amplitude were completed, or when a significant drop in the monitored link shear force was noticed. At these points, the loading was stopped, and visual inspection of the specimen was performed. Although the east side of the specimen (link web panels facing the reaction wall) was not easily accessible for visual inspection, the remainder of the specimen surfaces was carefully examined during each load stop. The observations of various failure phenomena described for each specimen later in this chapter, such as buckling or fracture, were not necessarily detected immediately upon their initial occurrence. Detection of fracture at its initiation stage, which is generally difficult to recognize due to the small size of many fractures at this stage, relied heavily on visual observations. Visual inspections of the specimens were not made frequently enough to assure early detection of all fractures. More obvious failure conditions, such as separation of the link flange or the link web from the column flange were immediately noticed, since large drops in the monitored link shear force typically accompanied these events. In general, the reader of this chapter should understand that the actual events may have taken place earlier than their reported detection.

Of primary interest of these tests is in the relation between link shear force, V, bending moment at the column face, M_C, and link rotation angle, γ. Link rotation γ consists of components arising from the rotation at the two link ends, in addition to the elastic-plastic deformation of the link. The inelastic component of link rotation, γ_p, was computed based on equation (3.1). γ_p is the key measure by which the performance of the EBF link-to-column connection is evaluated. The sign conventions are defined in Section 3.2.5: During initial elastic cycles, γ, V, and M_C took positive values when the link top flange adjacent to the column was in tension. As discussed in Section 3.2.5, the inelastic link rotation capacity was evaluated at the last cyclic rotation amplitude in which at least one full cycle was completed prior to loss of strength of the specimen. Upon completion of each positive or negative half cycle, the link shear force and column face moment must retain 80% or more of their respective maximum values achieved in earlier cycles. Otherwise, all following loading sequences including the just completed half cycle will be discarded from evaluation of the link rotation capacity.

To aid discussion of this chapter, a set of figures is presented for each specimen. Each set of figures comprises a diagram showing the loading sequence alongside observed damage; three plots representing the hysteretic response of the connection, notably the γ-V, γ_p-V and γ-M_C relations (the observed damage is indicated in these plots); and photographs of the specimen taken during the test at key stages and after the test. The loading stages at which these photographs were taken are indicated in the three plots. The stage of loading is abbreviated in the discussion, for example, as 0.07-2. This notation indicates the second cycle (2) at link rotation amplitude γ = 0.07 rad (0.07). 0.07-2P indicates the positive excursion (P) of cycle 0.07-2, while 0.07-2N indicates the negative excursion (N) immediately following the positive excursion 0.07-2P.

The main test results are summarized in Table 4.1, Table 4.2, and Table 4.3. Table 4.1 lists the link length, e, required inelastic link rotation, $\gamma_{p\text{-}max}$, last completed half cycle prior to loss of strength of the link-to-column connection (using the abbreviation described above), and primary deformation parameters obtained from the test, including the maximum achieved link rotation, γ_{max}, inelastic link rotation capacity, $\gamma_{p\text{-}max}$, and maximum inelastic deformation of the column panel zone, $\Gamma_{p\text{-}max}$. Table 4.2 lists the initial elastic end moment ratio, $(M_C/M_B)_e$, and nominal link shear strength, V_n, alongside the maximum link shear force, V_{max}, maximum column face moment, M_{max}, and link overstrength, V_{max}/V_n, (both positive and negative values) developed during the test. Table 4.3 summarizes key observations.

Sections 4.2 through 4.5 discuss the test results categorized by the four different connections types; namely, the PN- (Section 4.2), MW- (Section 4.3), FF- (Section 4.4), and NA-connections (Section 4.5). The PN- and MW-connections were each tested with three specimens of different link lengths: an S-link, I-link, and M-link. These six specimens were tested under the AISC loading protocol. The FF- and NA-connections were each tested with five specimens: three specimens with an S-link, I-link, and M-link, respectively, each tested under the AISC loading protocol; and two specimens with an S-link and SL-link, respectively, tested under the revised loading protocol. The test matrix is shown in Table.3.1. The key features of the test specimens are summarized in Table 3.2. The principal results are summarized and discussed in Section 4.6. Additional analyses of the test results are provided in Chapter 5.

4.2 PN-SPECIMENS

Specimens PNS, PNI, and PNM had the PN-link-to-column connection with link lengths of e = 1.1, 2.2, and $3.3M_p/V_p$, respectively. Design details and fabrication procedures of the PN-specimens are discussed in Section 3.4.2. The PN-connection features the pre-Northridge practice in detailing and construction of EBF link-to-column connections. Figure 4.1 shows the link-to-column connection of Specimen PNI before testing. This figure depicts aspects of the pre-Northridge practice in welding, such as leaving the backing bars and weld tabs in place after completion of the link flange groove welds.

All three specimens were tested up to complete separation of the link from the column flange.

4.2.1 Specimen PNS

The loading history and response of Specimen PNS is illustrated in Figure 4.2. Specimen PNS achieved inelastic link rotation of 0.041 rad, which is 51% of the 0.08 rad required for S-links.

Specimen PNS underwent erroneous loading cycles during the third link rotation amplitude: at a larger rotation of $\gamma = \pm 0.014$ rad, instead of $\gamma = \pm 0.01$ rad, two cycles were repeated instead of the designated three cycles. However, the impact of this error on the overall performance of the specimen is believed to have been minimal, since the inelastic link rotation accumulated during these erroneous cycles was insignificant compared to those from later cycles.

At completion of 0.014-2N, flaking of the whitewash indicated yielding in all link web panels, and in the link flanges in the region immediately adjacent to the column face. Upon further loading, very significant yielding developed in the link web panels. Yielding of the link flanges spread in the region farther away from the column face.

Specimen PNS exhibited ductile behavior until a slight drop in link shear force was noted during 0.05-2N (indicated by unfilled circle in Figure 4.2). A fracture was detected in the link bottom flange weld, running between the toe of the weld access hole (mid-width of the flange) and the west edge of the flange. At this stage, the column face moment was 60% of its maximum value. Therefore, the previous half cycle, 0.05-2P, was the last half cycle completed prior to loss of strength of the link-to-column connection. At completion of 0.05-2N, the weld fracture in the link bottom flange ran through roughly two-thirds of the flange width, as shown in Figure 4.3a. The figure shows the fracture running primarily in the weld, but at the interface of the flange base metal and weld metal at the toe of the weld access hole. Yielding in the link flanges spread in the region within five inches from the column face. At this stage, the column face moment was 58% of its maximum value, while the link shear force was close to its maximum value.

At completion of 0.06-1P, the link top flange was separated from the column flange (indicated by filled triangle in Figure 4.2). No fracture in the link top flange was noticed prior to this stage. This fracture initiated and propagated at the interface of the flange base metal and weld metal. The column face moment was 63% of its maximum value, while the link shear force was close to the maximum value. The link bottom flange separated from the column flange during 0.06-1N, leading to further degradation of moment resistance of the link-to-column connection. At completion of 0.06-1N, a horizontal fracture was detected in the link web in the radius zone of the top weld access hole. Flaking of the whitewash indicated wide spread yielding in the link flanges near the beam end, which corresponded to the drastic redistribution of the link moment from the column end to the beam end following the separation of the link top and bottom flanges from the column flange.

During 0.06-2, fractures were detected near the bottom and top edges of the link web at the groove weld (indicated by diamond and rectangle in Figure 4.2), at the interface of the web base metal and weld metal. During 0.07-1, these web fractures grew in the vertical direction, parallel to the column face, while slip of the erection bolts became apparent. At completion of 0.07-1, the column face moment at both positive and negative loading were merely 20% of their respective maximum values. The link web separated from the column flange during 0.07-2P, when the two vertical web fractures met each other, and the bottom erection bolt failed in shear. Before completing 0.07-2P, the specimen was unloaded and the test was terminated. Figure 4.3b shows the link and the column panel zone after the test. The figure indicates extensive yielding in the link web panels, and no yielding in the column panel zone. Large fractures are visible in the link web panel adjacent to the column. Figure 4.3c shows a close up view of the failed link-to-column connection. Large dislocation of the link with respect to the column face, large dislocation of the bottom bolt hole, and fracture running vertically through the link web panel is visible.

The shear strength of the link-to-column connection was largely maintained throughout the failure process until completion of 0.07-1N. As failure propagated, the relative stiffness of the beam end restraint to the column end restraint increased, and therefore, increasingly larger moment was attracted to the beam end. Since the beam end was capable of developing quite large moment, the shear strength was maintained until the link-to-column connection lost its ability to transmit shear force.

4.2.2 Specimen PNI

The loading history and response of Specimen PNI is illustrated in Figure 4.4. Specimen PNI achieved inelastic link rotation of 0.018 rad, which is 42% of the 0.043 rad required for I-links.

At completion of 0.01-3N, flaking of the whitewash indicated yielding of the outer face of the link top flange in the region within three inches from the column face. Yielding of the outer face of the link bottom flange was skewed, spreading farther from the column face at the east edge than at the west edge. At completion of 0.02-2N, yielding of the outer faces of the link flanges spread in the region within six inches from the column face. In the link top flange, yielding spread farther away from the column face at the west edge than at the east edge, whereas in the link bottom flange, yielding spread farther away at the east edge. The skewed distribution of flange yielding may be attributed to torsional action in the link. Yielding of the link flanges did not spread much farther at the column end during subsequent loading cycles. Yielding of the link web panels appeared to gradually spread from near the centroidal axis towards the flanges upon further increase in link rotation.

Specimen PNI exhibited ductile behavior until a significant crack was noted during 0.03-2P extending from the west edge of the link top flange, at the interface of the link flange base metal and weld metal. The location of this fracture reflected the distribution of yielding in the link top flange, which implied that the bending stress was highest at the west edge of the flange. At completion of 0.03-2P, the column face moment was 70% of the maximum value, while the link shear force was close to the maximum value. Load step 0.03-1N was marked as the last half cycle completed prior to loss of strength of the link-to-column connection. At this stage, the fracture in the link top flange extended at the weld interface for approximately four inches, as shown in Figure 4.5a. This figure shows the fracture growing along the weld interface, and a crack opening of approximately half inch at the west edge of the flange.

The link top flange separated from the column flange during 0.04-1P, as shown in Figure 4.5b, accompanied by a drastic drop in column face moment. At completion of 0.04-1P, a vertical fracture was detected in the link web near the radius zone of the top weld access hole. Large local deformation of the web in the vicinity of the top weld access hole, and a large slip of the top erection bolt were also noted. During 0.04-1N, the link bottom flange separated from the column flange. The vertical fracture at the top edge of the link web extended to and rested at the top bolt hole. A large slip of the bottom erection bolt was noted. At completion of 0.04-1N, the link shear force and column face moment were 70% and 25% of their respective maximum values.

At completion of 0.04-2P, the column face moment was almost negligible, while the link shear force was 70% of the maximum value. At completion of 0.04-2N, a fracture was noted at the bottom edge of the link web, extending from near the radius zone of the bottom weld access hole. Local buckling of the link flanges was apparent near the beam end of the link, indicating the presence of large moment at the beam end. Similar to Specimen PNS, link moment was redistributed from the column end to the beam end once the link top and bottom flanges separated from the column flange. During 0.05-1 and 0.05-2, the shear strength of the link-to-column connection gradually degraded as the vertical fractures at the top and bottom edges of the link web grew towards the centroid of the section. The link web separated from the column flange during 0.06-1P, when the two vertical web fractures met each other, and the bottom erection bolt failed in shear. The test was terminated before completion of 0.06-1P upon unloading. Figure 4.5c shows the link and link-to-column connection after the test. Significant local flange buckling at the beam end of the link, and large dislocation of the link with respect to the column face is visible in the figure. Yielding of the link web was not wide spread as in Specimen PNS (Compare Figure 4.5c with Figure 4.3b).

4.2.3 Specimen PNM

The loading history and response of Specimen PNM is illustrated in Figure 4.6. Specimen PNM achieved an inelastic link rotation of 0.008 rad, which is 40% of the 0.02 rad required for M-links.

At completion of 0.01-3N, flaking of the whitewash indicated yielding in the outer faces of the link flanges, in the region within two inches from the column face. No yielding was apparent in the link web. A fracture was noted in the link bottom flange during 0.02-2N, as shown in Figure 4.7a. This figure shows the fracture running between the west edge of the flange and the toe of the weld access hole (mid-width of the flange), along the interface of the flange base metal and weld metal. The location of fracture initiation was unclear. At completion of 0.02-2N, the fracture in the link bottom flange ran farther along the weld interface. The link shear force and column face moment were 78% and 48% of their respective maximum values. Load step 0.02-2P was marked as the last half cycle completed prior to loss of strength of the link-to-column connection. At this stage, yielding was apparent in the link web near both ends. Yielding of the link flanges spread in the region within approximately nine inches from the column face.

A fracture was detected in the link top flange during 0.03-1P. This fracture ran along the interface of the flange base metal and weld metal, for approximately four inches (two thirds of the flange width) from the east edge of the flange. The link top flange separated from the column flange before completion of 0.03-1P. At completion of 0.03-1P, the link shear force and column face moment were 80% and 50% of their respective maximum values. Upon load reversal, during 0.03-1N, the link bottom flange separated from the column flange. At completion of 0.03-1N, the link shear force and column face moment were 80% and 45% of their respective maximum values.

At completion of 0.03-2P, a fracture was detected in the link web extending from near the radius zone of the top weld access hole to the top bolt hole. The link shear force and column face moment were 65% and 16% of their respective maximum values. At completion of 0.03-2N, another fracture was detected in the link web, running from near the radius zone of the bottom weld access hole to the bottom bolt hole. The link shear force and column face moment were 65% and 20% of their respective maximum values.

During 0.04-1 and 0.04-2, the two fractures in the link web ran through the bolt holes and extended diagonally towards the column face. The link web separated from the column flange during 0.05-1N, when the two fractures met each other at mid-depth of the web. The test was terminated upon unloading. Figure 4.7b shows the link-to-column connection after the test. Large dislocation of the link with respect to the column face, and the growth path of the link web cracks described above are visible in the figure.

4.2.4 Discussion of PN-specimens

The PN-connection featured the pre-Northridge practices in detailing and construction of EBF link-to-column connections. None of the three PN-specimens achieved their required link rotations. Specimens PNS, PNI, and PNM achieved inelastic link rotations of 0.041, 0.017, and 0.008 rad, respectively. These rotations correspond to roughly half the inelastic link rotations required in the *2002 AISC Seismic Provisions*.

As discussed in Section 2.4, the failure of links constructed of A992 steel and detailed according to the current provisions is typically controlled by link web fracture initiating at the stiffener welds if the link is of $e < 1.7M_p/V_p$ and by a combination of local flange bucking, local web buckling, and lateral torsional buckling if the link is of $e \geq 1.7M_p/V_p$. Such failure modes were not observed in the PN-specimens. The absence of the expected failure modes indicates that the links could have achieved greater rotation had the link-to-column connections not failed prematurely. In fact, test results from other specimen types discussed later in this chapter suggest that the links are capable of developing much greater rotation. Therefore, EBF link-to-column connections constructed prior to the pre-Northridge earthquake, or constructed according to the pre-Northridge practice, are not likely to allow the links to develop their intended inelastic rotation.

The controlling failure mode for all three specimens was fracture of the link flange at the groove weld. The initiation point of flange fracture was not clear for most cases, partly because the backing bar overlaid the bottom side (root side) of the groove welds. Nonetheless, it appeared that the fracture of the top flange typically initiated at the edge of the flange, while fracture of the bottom flange initiated either at the toe of the weld access hole (mid-width of the flange) or at the edge of the flange. With the exception of the bottom flange of Specimen PNS, the flange fracture initiated and developed primarily at the interface of the link flange base metal and weld metal. The bottom flange of Specimen PNS fractured primarily in the weld metal. In all three specimens, once a flange fracture developed to a noticeable size, the fracture propagated rapidly. Typically within completion of one more loading cycle, the link flange separated from the column flange. After the flange in tension separated or nearly separated from the column flange, the specimen was not capable of developing a column face moment of 80% of the maximum value. Hence the strength of the link-to-column connection was exhausted by that stage.

The most characteristic failure mode observed in pre-Northridge moment connections was not replicated in any of the PN-specimens. As discussed in Section 2.4.1, studies have shown that the dominant failure mode of pre-Northridge moment connections is brittle fracture initiating at the root of the groove weld between the beam bottom flange and column flange. Many of the factors that are believed to be responsible for this failure mode (Engelhardt *et al.* 1997a) were also present in the PN-connections, notably the use of weld metal with high deposition rate and no specified fracture toughness, interruption of the placement of the bottom flange groove weld at the link web, leaving the backing bar and weld tabs after completing the link flange groove welds, and the configuration of the connection that leads to high overstress at the link flanges. Nonetheless, none of the PN-connections failed due to fracture initiating at the root of the link bottom flange groove weld. The absence of the particular failure mode may be attributed to the adherence to the specified welding procedure, and to the relatively high CVN values of the E70T-4 metal in these test specimens (Refer to Section 3.3.4). In fact, Engelhardt *et al.* (1993) reported that efforts to improve the weld quality shifted the dominant failure mode of moment connections from the aforementioned fracture of the beam bottom flange to fracture initiating at the weld interface at either the top or bottom beam flange. It is also possible that the relative significance of shear force in EBF link-to-column connections generates an environment quite different from that in MRF beam-to-column connections, where the effect of flexure is dominant. Therefore, the force and deformation environment that drives fracture from the lack of fusion or notch at the root of the groove welds may not have been realized in the link-to-column connections.

Although the observed failure mode of the PN-connection was somewhat different from that of pre-Northridge moment connections, it is likely that the poor quality of welding played a significant role in the premature fracture of the link flanges. As discussed in Section 5.5.1, many weld defects were present in the fracture surfaces studied after the tests, even though the welds passed ultrasonic testing. These defects may have contributed to the flange fractures. The PN-specimens might have exhibited better performance, and failed in different modes if the welding was better in quality.

Prior to the tests, it was expected that fracture was more likely to occur in the link bottom flange than in the link top flange. Besides the practices that typically produce inferior welding quality at the bottom flange, the weld access hole at the bottom flange violated the geometric requirements in the *2002 AISC Seismic Provisions*, while the weld access hole at the top flange met those requirements. The bottom flange was expected to suffer from a more severe stress and strain environment surrounding the inappropriate weld access hole. However, the test results suggest that both the top and bottom flanges were equally susceptible to fracture at the groove weld. In Specimens PNS and PNM, fracture of one flange was immediately followed by fracture of the other flange upon load reversal. In Specimen PNI, the link top flange separated from the column flange before any fracture was detected in the bottom flange.

All three PN-specimens were tested well beyond the point where significant strength deterioration occurred to study link behavior after failure of the link-to-column connection. Separation of the link flange from the column flange was immediately followed by appearance of fractures in the link web. Rapid redistribution of bending stress from the link flanges to the link web was the likely cause of fracture of the link web initiating at the top and bottom edges of the weld interface and/or surrounding the weld access holes. After both link flanges separated from the column flange, the link-to-column connection functioned effectively as a hinge, maintaining significant shear strength, but very limited flexural strength.

4.3 MW-SPECIMENS

Specimens MWS, MWI, and MWM had the MW-link-to-column connection with link lengths of e = 1.1, 2.2, and $3.3M_p/V_p$, respectively. Design details and fabrication procedures of the specimens are discussed in Section 3.4.3. The MW-connections feature post-Northridge modifications in welding that are widely accepted for MRF beam-to-column connections. Figure 4.8 shows the link-to-column connection of Specimen MWI before testing. Some of the modifications over the PN-connection are apparent by comparing Figure 4.10 with Figure 4.1. Weld tabs were removed and ground smooth; the backing bar was removed at the bottom flange; the weld access hole at the bottom flange was extended farther away from the column face; and at the top flange, a reinforcement fillet weld was placed between the backing bar and the column flange.

Specimen MWS was tested up to separation of the link from the column flange. Specimen MWI was tested beyond its link rotation capacity, until severe lateral torsional deformation of the link began to interfere with the measurement of link rotation. Specimen MWM was tested until the link bottom flange separated from the column flange.

4.3.1 Specimen MWS

The loading history and response of Specimen MWS is illustrated in Figure 4.9. Specimen MWS achieved an inelastic link rotation of 0.051 rad, which is 64% of the 0.08 rad required for S-links.

At completion of 0.01-3N, flaking of the whitewash indicated yielding in all link web panels. At completion of 0.02-2N, yielding in the outer face of the flanges (bottom face of bottom flange and upper face of top flange) spread in the region within one and one-half inches from the column face. Upon further increase in link rotation, yielding in the link flanges gradually spread to the region of up to four inches away from the column face.

Specimen MWS exhibited ductile behavior until a fracture was detected in the outer face of the link bottom flange at completion of 0.06-2N, as shown in Figure 4.10a. This figure shows a crack opening in the circled area, centered at mid-width of the flange. The fracture is running for two inches (one-third of the width of link flange) along the interface of the link flange base metal and weld metal. Another fracture was detected at the bottom edge of the link web, at the interface of the web base metal and weld metal. A small crack opening seemed to exist in the link top flange along the toe of the link flange groove weld, although it was barely visible, as the top flange was in compression when the observation was made. No degradation in strength of the link-to-column connection was noted at this stage.

At completion of 0.07-1N, the fracture in the link bottom flange ran farther along the toe of the groove weld, reaching almost four inches in length. Horizontal fractures were detected in the web near the radius zone of both the top and bottom weld access holes. The vertical fracture at the bottom edge of the link web weld reached over one inch in length. The fractures in the link web surrounding the bottom weld access hole as described above are shown in Figure 4.10b. The link shear force and column face moment were 97% and 65% of their respective maximum values. 0.07-1P was marked as the last half cycle completed prior to loss of strength of the link-to-column connection.

Short of completing 0.07-2P, the link top flange separated from the column flange, as shown in Figure 4.10c. Study of the fracture surface made after the test (refer to Section 5.5.2) indicated that fracture of the top flange initiated at the east edge of the flange, at the interface of the link flange base metal and weld metal. The location of fracture also matched the location of the suspected crack opening noted earlier at completion of 0.06-2N. At completion of 0.07-2P, the link shear force and column face moment were 87% and 25% of their respective maximum values. The vertical fracture at the top edge of the link web ran for over one inch in length. Upon load reversal, during 0.07-2N, the link bottom flange separated from the column flange. The development of the multiple fractures in the link web led to disintegration of the link web panel adjacent to the column face. By completion of 0.07-2N, the link web fractures had extended through the entire depth of the link web. At this stage, the link shear force was 35% of its maximum value, while the column face moment was negligible. After completing 0.08-1, during which the measured link shear force and column face moment were negligible, the test was terminated. Figure 4.10d shows the link after the test. This figure shows extensive yielding of the link web panels, the severely damaged link web panel adjacent to the column face, and large dislocation of the link with respect to the column face.

By the end of the test, small fractures had formed in the link web at the top and bottom terminations of the fillet welds connecting the stiffeners to the link web. As discussed in Section 2.4, these fractures were typically observed in shear link specimens tested by Arce (2002). In the tests by Arce, these web cracks propagated in the horizontal direction, and ultimately grew large enough to cause severe degradation in the strength of the link. The reduction in link forces following the progressive failure of the link-to-column connection prohibited further development of web fractures in Specimen MWS.

4.3.2 Specimen MWI

The loading history and response of Specimen MWI is illustrated in Figure 4.11. Specimen MWI achieved an inelastic link rotation of 0.018 rad, which is 43% of the 0.043 rad required for I-links.

The fabricated Specimen MWI had a large initial imperfection. As shown in Figure 4.12a, the beam end of the link was rotated as much as 0.06 rad about the link longitudinal axis with respect to the column end. It was expected that this initial imperfection could promote bending and torsional action, and therefore, affect the overall response of the specimen. However, since such an imperfection can likely be present in actual construction, the data provided by this specimen was expected to still be valuable.

At completion of 0.01-3N, flaking of the whitewash indicated yielding of the outer face of the link flanges in the region within three inches from the column face. At completion of 0.02-2N, yielding was noted in the link web panels. Yielding of the outer face of the link top flange spread in the region within six inches from the column face at the west edge of the flange, while at the east edge, yielding was contained within three inches from the column face. The skewed distribution of yielding in the link flange might have been caused by torsional action in the link. Yielding in the flanges did not appear to spread much farther away from the column face upon further increase in link rotation, while yielding in the link web panels gradually extended from near the centroid axis towards the flanges.

Specimen MWI exhibited ductile behavior until small fractures were detected at the top and bottom edges of the link web at completion of 0.03-2N. These fractures initiated and propagated along the interface of the web base metal and weld metal. At this stage, no fracture was noted in the link flanges.

During 0.04-1P, a significant drop in the link shear force was noted, when a fracture was detected in the link top flange, as shown in Figure 4.12b. This figure shows the fracture running from the west edge of the link flange for more than four inches (two-thirds of the flange width), along the interface of the link flange base metal and weld metal. A crack opening in the weld interface of approximately one-quarter inch is visible at the west edge of the flange. The much larger crack opening at the west edge suggests that the fracture initiated at the west edge of the flange. This agrees with the distribution of yielding discussed earlier, which suggested that bending stress was highest at the west edge of the flange. The link top flange was almost separated from the column flange at completion of 0.04-1P. The link shear force and column face moment were 85% and 50% of their respective maximum values. Load step 0.03-2N was marked as the last half cycle completed prior to loss of strength of the link-to-column connection. At this stage, the vertical fractures at the top and bottom edges of the link web each extended over one inch in length. During the following negative cycle, 0.04-1N, the link-to-column connection retained its strength developed during 0.03-2N.

During 0.04-2P, the link top flange separated from the column flange. The fracture at the top edge of the link web grew rapidly along the weld interface; and the top erection bolt failed in shear. At completion of 0.04-2P, the top half of the link was separated from the column flange, which led to large torsional deformation of the link. The column face moment was almost negligible. Upon load reversal, the torsional deformation of the link developed even further. The test was terminated before completion of 0.04-2N, when the large distortion of the link at the column end, as shown in Figure 4.12c, began to interfere with the measurement of link rotation. Figure 4.12c shows the link top flange displaced as much as four inches (two-thirds of the flange width) to the west with respect to the column due to torsional deformation. The initial imperfection might have played a role in this very large torsional deformation. No fracture was detected in the link bottom flange at the end of the test, although a horizontal fracture was noted in the link web in the radius zone of the bottom weld access hole, as shown in Figure 4.12d. The figure also shows the vertical fracture in the web weld interface, which extended along the entire depth of the web.

4.3.3 Specimen MWM

The loading history and response of Specimen MWM is illustrated in Figure 4.13. Specimen MWM achieved an inelastic link rotation of 0.008 rad, which is 40% of the 0.02 rad required for M-links.

At completion of 0.02-2N, flaking of the whitewash indicated yielding in the link web near the two ends of the link. Yielding in the link flanges spread in the region within seven inches from the column face. A significant drop in link shear force was noted just short of completing 0.03-1N, when a fracture was found in the link bottom flange, as shown in Figure 4.14a. This figure shows a crack opening of one-quarter inch along the interface of the link flange base metal and weld metal, extending from the west edge of the flange for approximately four inches (two-thirds of the flange width). At completion of 0.03-1N, the link shear force and column face moment were 84% and 68% of their respective maximum values. Load step 0.03-1P was marked as the last half cycle completed prior to loss of strength of the link-to-column connection.

At completion of the following positive half cycle, 0.03-2P, a fracture was noted in the link top flange, running four inches from the east edge of the flange. At the east edge of the flange, the fracture formed at the interface of the link flange base metal and weld metal. Apart from the east edge, the fracture propagated largely in the flange base metal away from the weld interface. Another fracture was detected at the top edge of the link web, at the interface of the web base metal and weld metal. At this stage, the link shear force and column face moment were 84% and 62% of their respective maximum values. Local buckling was apparent in the almost fractured link bottom flange, as it was compressed. At completion of 0.03-2N, the link bottom flange separated from the column flange. Very large distortion of the link web near the link bottom flange, and a large slip of the bottom erection bolt were noted. At this stage, the link shear force and column face moment were 68% and 32% of their respective maximum values. The test was terminated upon unloading. Figure 4.14b shows the connection after the test. In this figure, the bottom flange is separated from the column flange. Yielding in the link web is limited to the region immediately adjacent to the column face. As noted above, the local buckling of the bottom flange visible in Figure 4.14b occurred during 0.03-2P.

4.3.4 Discussion of MW-specimens

The MW-connection featured modifications in welding from that used for the PN-connection. The welding and the configuration of the weld access holes in the MW-connection comply with the requirements in *FEMA-350* (2000). Comparison of the MW-specimens with the PN-specimens highlights the effect of welding and welding details on the performance of EBF link-to-column connections.

Some improvement in performance was noted in the MW-specimens over the PN-specimens. Specimen MWS survived three more loading cycles than did Specimen PNS before the link-to-column connection lost its strength. Specimen MWI survived one more loading cycle than Specimen PNI, and Specimen MWM survived one-half more loading cycle than Specimen PNM. Specimen MWI performed better then Specimen PNI despite the significant initial imperfection that may have had a negative influence on the performance. However, these improvements in connection performance are marginal when considered in terms of link inelastic rotations. Specimen MWS achieved a link inelastic rotation of 0.051 rad opposed to 0.041 rad achieved by Specimen PNS. Specimens MWI and

PNI both achieved 0.018 rad. Specimens MWM and PNI both achieved 0.008 rad. While Specimen MWS achieved a 20% improvement over Specimen PNS, Specimens MWI and MWM achieved virtually no improvement over Specimens PNI and PNM in terms of link inelastic rotation. The inelastic link rotations achieved by the MW-specimens fell well below the level required by the *2002 AISC Seismic Provisions*.

Similar to the PN-specimens, the MW-specimens failed by fracture of the link flanges. As in the PN-specimens, the link flange fracture appeared to typically initiate at the interface of the link flange base metal and groove weld metal. In Specimen MWS, fracture of the top flange was immediately followed by fracture of the bottom flange upon load reversal. The fracture in the bottom flange initiated at mid-width of the flange. Study of the fracture surface suggests that the fracture of the top flange initiated at the east edge of the flange. In Specimen MWI, fractures appeared at the top and bottom edges of the link web groove weld before any fracture was noted at the flange groove welds. Specimen MWI failed due to fracture of the top flange, which likely initiated at the west edge of the flange. No fracture was noted in the bottom flange after the test, even after the top flange and the entire link web separated from the column flange. The significant initial imperfection of Specimen MWI might have affected the failure by promoting torsional deformation of the link. In Specimen MWM, fractures were observed in both the top and bottom flanges. The fracture in the bottom flange likely initiated either at the west edge or at mid-width of the flange. The fracture in the top flange likely initiated at the east edge of the flange.

As summarized above, link flange fracture occurred equally in both the top and bottom flanges. The fractures in the bottom flanges of Specimen MWS and also possibly Specimen MWM initiated at mid width of the flange. On the other hand, in all three specimens, fracture of the top flange was rather clearly seen to initiate at the edge of the flange. Since the bottom flange was vulnerable to fracture at mid width of the flange, while the top flange was not, the benefit of modifying the configuration of the bottom weld access hole may have been limited.

The MW-specimens gained a marginal increase in link rotation capacity over the PN-specimens, but failed in a very similar mode. This suggests that while the modifications in welding are beneficial, they are not nearly sufficient to improve the performance of link-to-column connections to the required level. More importantly, conventional link-to-column connection configurations may not be suited for seismic design, regardless of the quality of welding. The premature failure by link flange fracture can occur not only in connections of a long link ($e > 1.6M_p/V_p$) to a column, as noted by Engelhardt and Popov (1989a; 1992), but equally as frequently in connections with a short shear link, such as a link of $e = 1.1M_p/V_p$.

4.4 FF-SPECIMENS

Specimens FFS, FFI, and FFM had the FF-link-to-column connection with link lengths of $e = 1.1$, 2.2, and $3.3M_p/V_p$, respectively. Specimens FFS-RLP and FFSL-RLP had a modified FF-connection with link lengths of $e = 1.1$ and $1.7M_p/V_p$, respectively. Design details and fabrication procedures of the FF-specimens are discussed in Section 3.4.4. The two key aspects of the FF-connections were the extended free flange length (distance between the toe of the weld access hole and column face) and the use of a heavy shear tab welded to the link web. The free flange length was identical for all five specimens. The shape of the shear tab was customized for each specimen to account for the different force and deformation environment arising from different link lengths. The same welding procedure as in the MW-specimens was used in the FF-specimens.

Figure 4.15 shows Specimen FFI before testing. The extended free flange length is clearly noticeable by comparing Figure 4.15 with Figure 4.8. As in the MW-connection, weld tabs were removed and ground smooth, the backing bar was removed at the bottom flange, and a reinforcement fillet weld was placed between the backing bar and column flange at the top flange. Figure 4.15a indicates that heat input from welding combined with large restraint in the web panel caused mild yielding of the web panel during the fabrication process. Specimens FFS and FFM had the same connection configurations as Specimen FFI, except for the geometry of the shear tab. Figure 4.16 shows Specimen FFS-RLP before testing. Specimens FFS-RLP and FFSL-RLP had identical connection configurations. Unlike in Specimen FFI, the link web of Specimen FFS-RLP was not directly welded to the column flange. Instead, the link web was cut short of reaching the column flange. The link web was fillet welded to the shear tab, which was in turn, welded to the column flange.

4.4.1 Specimen FFS

The loading history and response of Specimen FFS is illustrated in Figure 4.17. Specimen FFS achieved an inelastic link rotation of 0.06 rad, which is 75% of the 0.08 rad required for S-links.

An important aspect of the FF-connections is that because the heavy shear tab significantly increases the cross sectional area of the link web, the region of link web welded to the shear tab does not participate in the inelastic deformation of the link. Consequently, the effective length of the link is shortened by the distance between the end of the shear tab and the column face, as illustrated by Figure 4.18a. The whitewash remaining on the link web panel clearly suggests that the segment of the link web welded to the rectangular shear tab did not participate in inelastic action. The link length was effectively shortened from 25 inches to 20 inches for Specimen FFS. Therefore, the inelastic rotation imposed on the link was effectively magnified by 25% during the entire loading process. The magnified rotation demand on the link might have penalized the performance of Specimen FFS.

At completion of 0.01-3N, flanking of the whitewash indicated yielding in the link web panels. Slight yielding in the outer faces of the link flanges was noted at five inches away from the column face, indicating that inelastic bending action was forced to occur beyond the end of the shear tab. Yielding in the link flanges gradually spread closer to the column face upon further increase in link rotation.

At completion of 0.06-2N, a fracture was detected in the link web near the bottom corner of the shear tab, along the toe of the fillet weld connecting the shear tab to the link web. Nonetheless, the strength of the specimen was maintained throughout 0.07-1. During 0.07-2P, the web fracture grew rapidly in two perpendicular directions along the toe of the fillet weld, as shown in Figure 4.18b, causing a gradual decrease in the column face moment. The link shear force was affected little by the propagation of this fracture. At completion of 0.07-2P, the column face moment was 80% of the maximum value. Load step 0.07-1N was marked as the last half cycle completed prior to loss of strength of the specimen.

At completion of 0.07-2N, a fracture was noted in the link web around the top corner of the shear tab, also along the toe of the fillet weld. The column face moment was almost negligible; the link shear force was 30% of the maximum value. The fracture ran around the shear tab, almost separating the link web from the shear tab. Even at this stage, no fracture was detected in the link top and the bottom flanges. During 0.08-1P, the link web separated from the shear tab. The test was terminated after completion of 0.08-2. At the end of the test, only the link flanges were connected to the column flange, as shown in Figure 4.18c. This figure also shows the extensive yielding in the link web panels except for the segment welded to the shear tab. The large deformation and yielding in the link flanges occurred after the link web had separated from the shear tab, when the link flanges supplied much of link rotation. Figure 4.18d shows the bottom corner of the shear tab after the test. It is clearly visible in this figure that the link web fracture developed along the toe of the fillet weld connecting the shear tab to the link web. The fracture was observed to initiate within the area circled in the figure.

4.4.2 Specimen FFI

The loading history and response of Specimen FFI is illustrated in Figure 4.19. Specimen FFI achieved inelastic an link rotation of 0.046 rad, which is 107% of the 0.043 rad required for I-links.

Specimen FFI was largely free from the design elements that caused fracture of the link web in Specimen FFS. Magnification in rotation demand resulting from the effective shortening of link length was 14% in Specimen FFI, opposed to 25% in Specimen FFS. The shear tab was tapered in order to reduce the restraint near the corner of the shear tab (Compare Figure 3.22 with Figure 3.23). Moreover, the required link rotation is smaller for I-links than for S-links. Therefore, Specimen FFI was much less likely to induce fracture in the link web at the edges of the shear tab, as seen in Specimen FFS.

At completion of 0.01-3N, flaking of the whitewash indicated yielding in the link flanges near the column face. Flange yielding gradually spread farther away from the column face upon further increase in link rotation. In the top flange, the yielded region spread farther away from the column face at the east edge than at the west edge. In the bottom flange, the yielded region spread farther away at the west edge. The skewed spreading of flange yielding indicated torsional action in the link. Yielding appeared to spread equally on the inner and outer faces of the link flanges. At completion of 0.02-2N, yielding was clearly noted in the link web. At completion of 0.04-2N, the flanges yielded in the region extending ten inches from the column face. Figure 4.20a shows the link near the column face at this stage. Very mild local buckling of the link top flange, and mild yielding in the column panel zone is visible in this figure. The segment of link web welded to the shear tab did not participate in inelastic action. Although not clearly visible in Figure 4.20a, localized yielding was noted near the bottom edge of the link web near the groove weld.

At completion of 0.05-2N, a fracture was detected at the east edge of the link top flange at the interface of the link flange base metal and groove weld metal. At completion of 0.06-1P, the fracture ran two inches (one-third of the flange width) along the flange-weld interface. Local buckling was noted in the link bottom flange. The column face moment was 90% of its maximum value, while the link shear force was near the level in the previous cycle. At completion of 0.06-1N, a fracture was detected at the bottom edge of the shear tab in the double bevel groove weld, as shown in Figure 4.20b. Since the shear tab functioned as backing to the link web groove weld, and the link web weld overlayed the shear tab groove weld, the fracture in the shear tab weld caused a fracture at the bottom edge of the link web weld. A fracture was suspected to have formed at the west edge of the link bottom flange. No loss in strength of the link-to-column connection was noted at this stage.

During 0.06-2P, the link top flange separated from the column flange, as shown in Figure 4.20c. Study of the fracture surface indicates that the fracture propagated in a ductile fashion along the weld interface until it reached the mid-width of the flange, and afterwards progressed in a sudden and brittle fashion into the link flange base metal away from the weld interface (Refer to Section 5.5.3). The rapid development of flange fracture was reflected in the sudden drop in column face moment, as shown in Figure 4.20d. Load step 0.06-1N was marked as the last half cycle completed prior to loss of strength of the link-to-column connection. At completion of 0.06-2P, the link shear force and column face moment was 65% and 35% of their respective maximum values. The top half of the link web was separated from the column flange, due to fractures that propagated at the interface of the link web metal and weld metal. A longitudinal crack extended in the fillet weld connecting the shear tab to the link web, tearing the link web off from the shear tab. During 0.06-2N, the link web separated from the column flange, giving rise to severe torsional deformation of the link web panel. At completion of 0.06-2N, the column face moment was almost negligible. The test was terminated at this stage. Figure 4.20d shows the link-to-column connection after the test. The figure shows large dislocation of the link with respect to the column face, large distortion of the link web panel resulting from torsional deformation of the link web, and mild yielding in the column panel zone. The link bottom flange remained intact to the column flange at the end of the test.

4.4.3 Specimen FFM

The loading history and response of Specimen FFM is illustrated in Figure 4.21. Specimen FFM achieved an inelastic link rotation of 0.016 rad, which is 80% of the 0.02 rad required for M-links.

At completion of 0.01-1N, flaking of the whitewash indicated yielding in the link flanges, in the region immediately adjacent to the column face and near the end of the shear tab. At completion of 0.02-2N, yielding in the link web spread in a two-inch wide band along the periphery of the shear tab. Fractures were detected at the bottom edge of the shear tab, in the double bevel groove weld connecting the shear tab to the column flange. Another small fracture was detected at the bottom edge of the link web, at the interface of the web base metal and weld metal. Since the shear tab functioned as backing to the link web groove weld, and the link web weld overlayed the shear tab groove weld, it is likely that the fracture at the link web weld developed simultaneously with the fracture in the shear tab weld. Localized yielding was noted at the top and bottom edges of the link web near the groove weld. At completion of 0.03-2N, mild local buckling was noted in the link top flange. As shown in Figure 4.22a, yielding spread in the entire web panel between the periphery of the shear tab and the first link stiffener, and slightly beyond the stiffener. Flange yielding spread in the region extending approximately ten inches from the column face. Although not visible in this figure, the vertical fracture in the shear tab weld was more than three inches in length. Mild yielding was noted in the column panel zone, which developed further during 0.04-1 and 0.04-2. A small crack opening was detected at the east edge of the link bottom flange at the groove weld interface.

At completion of 0.04-1N, the column face moment was 76% of its maximum value. Load step 0.04-1P was marked as the last half cycle completed prior to loss of strength of the link-to-column connection. The fracture in the link bottom flange ran from the east edge to the mid-width of the flange, with a crack opening of one-quarter inch at the east edge of the flange. This fracture initiated at the east edge of the flange, propagated for approximately one inch along the interface of the flange base metal and weld metal, then propagated away from the weld interface into the flange base metal. Vertical fractures in the shear tab weld left no more than half of the shear tab connected to the column flange. The fracture at the top edge of the link web weld interface was two inches long. Another fracture was noted at the bottom edge of the link web weld interface.

During 0.04-2P, the link top flange separated from the column flange, as shown in Figure 4.22b. Although no fracture was detected in the link top flange prior to this stage, study of the fracture surface (Refer to Section 5.5.3) indicates that the fracture initiated at the east edge of the flange. Figure 4.22b shows a crack opening extending along the width of the top flange near the toe of the groove weld. At completion of 0.04-2P, the shear tab was completely separated from the column flange. The link shear force and column face moment were 55% and 8% of their respective maximum values. The test was terminated after unloading. Figure 4.22c shows the link-to-column connection after the test. This figure indicates yielding in the link flanges and web, and in the column panel zone in the region close to the link. Yielding of the link web near the column face was a result of the separation of the shear tab and link web from the column flange. As the fracture of the shear tab and link web propagated, the increasingly smaller link web area was required to transmit link forces, and thus led to yielding of the link web near the column face.

4.4.4 Specimen FFS-RLP

The loading history and response of Specimen FFS-RLP is illustrated in Figure 4.23. Specimen FFS-RLP achieved an inelastic link rotation of 0.031 rad, which is 39% of the 0.08 rad required for S-links, and only 52% of the 0.60 rad achieved by Specimen FFS. Specimen FFS-RLP had the same link length as Specimen FFS, and a slightly different connection configuration.

At completion of 0.01-6N, flaking of the whitewash indicated yielding in the link web panels, excluding the segment welded to the shear tab. At completion of 0.015-6N, yielding became apparent in the link flanges near the end of the shear tab, indicating that inelastic bending action was forced to occur beyond the end of the shear tab. At completion of 0.03-2N, a fracture was noticed at the bottom edge of the double bevel groove weld connecting the shear tab to the column flange. Figure 4.24a shows the link at this stage. No indication of yielding is visible in the shear tab exposed beyond the link web or in the segment of link web welded to the shear tab. At completion of 0.04-1N, the fracture in the shear tab weld ran two inches long in the longitudinal direction of the weld, as shown in Figure 4.24c. This figure also indicates that no significant yielding had occurred in the link bottom flange near the groove weld. Figure 4.24b shows the link at this stage. Comparison of Figure 4.24b with Figure 4.24a clarifies the effect of the fracture in the shear tab weld on the response of the link. Although the two figures show similar extent of yielding in the link web, the progression of fracture in the shear tab weld caused yielding in the exposed shear tab as shown in Figure 4.24b. It appeared that redistribution of stresses within an effectively smaller shear tab area caused yielding in the exposed shear tab apart from near the bottom edge, where the fracture was present. At this stage, the strength of the link-to-column connection was still maintained.

At completion of 0.05-1N, the shear tab was separated from the column flange. It appeared that the fracture at the bottom edge of the shear tab weld propagated through the entire length of the weld. A fracture was noted at the east edge of the link bottom flange at the interface of the flange base metal and weld metal. The column face moment was 45% of its maximum value. Load step 0.05-1P was marked as the last half cycle completed prior to loss of strength of the link-to-column connection. The link-to-column connection was able to develop significant link shear force due to bearing of the shear tab against the link top flange. Therefore, at this stage, the link forces shown in Figure 4.24 may not correctly represent the strength of the link-to-column connection for 0.05-1N. Upon reverse of loading direction, the specimen was not able to develop significant forces. The test was terminated upon unloading.

Figure 4.24d shows the link-to-column connection after the test. The figure shows fracture in the shear tab weld, and extensive yielding in the segment of the shear tab exposed beyond the link web. The horizontal fractures in the link web extending from the weld access holes appeared after the link web separated from the column flange. No fracture was present in the link web near the corners of the shear tab, as seen in Specimen FFS.

4.4.5 Specimen FFSL-RLP

The loading history and response of Specimen FFSL-RLP is illustrated in Figure 4.25. Specimen FFS-RLP achieved an inelastic link rotation of 0.019 rad, which is 26% of the 0.073 rad required for SL-links.

At completion of 0.01-6N, flaking of the whitewash indicated yielding in the link web panels, excluding the segment welded to the shear tab. Yielding spread in the link flanges in the region between the column face and the end of the shear tab. At completion of 0.02-2N, a small fracture was noticed at the bottom edge of the double bevel groove weld connecting the shear tab to the column flange. Figure 4.26a shows the link near the column face at this stage. This figure shows that the shear tab and the segment of the link web welded to the shear tab are excluded from yielding.

At completion of 0.03-1N, yielding was noted at the top and bottom edges of the shear tab near the column face, as shown in Figure 4.26b. The fracture at the bottom end of shear tab weld reached one inch in length. At completion of 0.03-2P, the top half of the shear tab was separated from the column flange. Correspondingly, the bottom half of the shear tab exposed beyond the link web yielded extensively, as shown in Figure 4.26c. The link shear force and column face moment were 94% and 73% of their respective maximum values. Therefore, 0.03-1N was marked as the last half cycle completed prior to loss of strength of the link-to-column connection. Before completion of 0.03-2N, the link web separated from the column flange. The test was terminated before completing 0.03-2N.

Figure 4.26a-c illustrates the relation between the fracture of the shear tab groove weld and yielding of the exposed shear tab. As a fracture first appeared at the bottom edge of the shear tab weld, yielding was noted in the region immediately surrounding the fracture (Figure 4.26a). As the fracture grew at the bottom edge of the shear tab, yielding spread around the fracture. Simultaneously, redistribution of the link forces likely caused yielding in the top half of the shear tab (Figure 4.26b). As another fracture emerged at the top edge of the shear tab weld, and quickly grew along the weld, yielding spread in the bottom half of the shear tab (Figure 4.26c). Figure 4.26d shows the link after the test. The limited extent of yielding in the link web panels suggests that the SL-link whose behavior was dominated primarily by shear was capable of developing much greater rotation had the link-to-column connection not failed prematurely. Figure 4.26e shows clearly that the fracture of the shear tab initiated and propagated entirely in the throat of the groove weld.

4.4.6 Discussion of FF-specimens

The FF-connections were developed based on the free flange moment connection developed and proposed by Choi *et al.* (2000; 2003). By the combined use of an extended free flange length and a heavy shear tab, the FF-connections aimed to reduce the shear force transmitted by the link flanges, and consequently relax the local stress demands at the link flange groove welds.

Specimen FFS, FFI, and FFM performed significantly better than the PN- and MW-specimens. Specimen FFS survived one and a half more loading cycles than did Specimen MWS before the link-to-column connection lost its strength.

Specimen FFI survived five more loading cycles than Specimen MWI and Specimen FFM survived one-half more loading cycle than Specimen MWM. In terms of inelastic link rotations, Specimen FFS achieved 0.060 rad, a 20% increase over Specimen MWS; Specimen FFI achieved 0.046 rad, a 155% increase over Specimen MWI; and Specimen FFM achieved 0.016 rad, a 106% increase over Specimen MWM. Although Specimens FFS and FFM failed to meet their link rotation requirements, Specimen FFI achieved 107% of its required inelastic link rotation. The improvement over the corresponding MW specimen with the same link length was most significant for Specimen FFI, and least significant for Specimen FFS.

The shear tab welded to the link web was instrumental in significantly altering the behavior of the link. First, the shear tab increased the sectional area of the web, and created a region of the link web that does not participate in inelastic deformation. Consequently, inelastic rotation was magnified in the remaining segment of the link by approximately 25%, 20%, 15%, and 11%, respectively, for S-, SL-, I-, and M-links. Shorter links were more severely penalized by the effective shortening of the link. Secondly, the shear tab added to the plastic flexural strength of the link by as much as 30%. For S- and SL-links, this resulted in moving the section of large inelastic bending deformation, or kink, away from the column flange, shielding the link flange groove welds from large inelastic strain demands. The benefit of the increased flexural strength was more limited for the I-link and even more limited for the M-link. In Specimens FFI and FFM, the added flexural stiffness near the column resulted in yielding in the link flanges spreading over a much larger region, extending farther away from the column face, compared to other I-link and M-link specimens. However, the shear tab and link web were prone to fracture at the top and bottom edges of the welds, and these fractures appeared to accelerate failure of the specimen.

Specimen FFS failed due to fracture of the link web along the toe of the fillet weld connecting the shear tab to the link web. It is believed that the large restraint imposed on the link web material between the shear tab and the link flange combined with large cyclic link rotation generated severe cyclic inelastic strain demands near the corner of the shear tab, and induced fracture at this location. In order to relax such local strain demand, it may be preferable to use a shear tab with tapered corners. However, tapering the corner of the shear tab may conflict with other design considerations. As cautioned by Engelhardt and Popov (1989a) and Choi *et al.* (2000), the fillet weld connecting the shear tab to the link/beam web should be placed well apart from the weld access hole, not to draw severe stress and strain near this sensitive area. To secure a distance between the fillet weld and the weld access hole, a shear tab with tapered corners must extend farther away from the column face. This would cause further shortening of the effective link length, and further magnify the rotation demand on the link. On the other hand, shortening of the link length is especially penalizing to short shear links. Considering the above discussion, the FF-connection may not be suited for use with very short links.

The web fracture around the shear tab was not observed in any of the other four FF-specimens, which were provided with tapered shear tabs, instead of a rectangular shear tab as in Specimen FFS. Although these specimens developed a smaller link shear force and link rotation compared to Specimen FFS, they demonstrated to some extent the benefit of the tapering the corners of the shear tab.

Unlike the other FF-specimens, Specimens FFS-RLP and FFSL-RLP did not have the link web welded directly to the column flange. Instead, the link web was welded to the shear tab, which in turn was welded to the column flange (See Figure 3.24). The inferior performance of Specimens FFS-RLP and FFSL-RLP compared to Specimens FFS and FFI was likely caused by this design alteration. Specimens FFS-RLP and FFSL-RLP failed due to fracture of the groove weld connecting the shear tab to the column flange, initiating at the top and/or bottom edges of the shear tab. As the fracture propagated, the segment of the shear tab extending beyond the link web yielded. This failure mode was not observed in Specimens FFS, FFI, and FFM. More importantly, Specimen FFS developed much greater link rotation than Specimen FFS-RLP, which had the same link length but tested under a more relaxed loading protocol than that used for Specimen FFS. Therefore, it is believed that the top and bottom edges of the shear tab welds in Specimens FFS-RLP and FFSL-RLP would not have been so sensitive to fracture had the link web been welded directly to the column flange. In Specimens FFI and FFM, a lag was noted in the development of fracture in the shear tab weld and in the link web weld, with the shear tab fracture constantly preceding the link web weld fracture. It appeared that the development of shear tab fracture was delayed due to the fracture resistance of the link web weld. In Specimens FFS-RLP and FFSL-RLP, the shear tab fracture did not have the benefit of such an additional fracture resistance mechanism. Another possibly disadvantageous factor was the eccentricity of the shear tab with respect to the primary bending plane of the link (centerline of the link web). Choi *et al.* (2000; 2003) noted that the eccentricity gives rise to out-of-plane bending in the shear tab. The torsional moment equal to the eccentricity multiplied by the link/beam shear force is considerably greater in EBF link-to-column connections than in moment connections due to the greater shear force.

Specimen FFM nearly completed the first loading cycle (0.04-1) that would have credited the specimen with the inelastic link rotation capacity of 0.026 rad, which is beyond the required 0.02 rad. However, short of completing 0.04-1N, the flexural strength of the link-to-column connection degraded due to fracture of the link bottom flange. Even before fracture initiated in the link bottom flange, fractures were present in the shear tab weld and link web weld. It is quite possible that the reduction in flexural resistance of the shear tab and link web redistributed bending stress from the link web and shear tab to the link flanges, and thus triggered fracture of the link bottom flange.

Specimen FFI achieved an inelastic link rotation of 0.046 rad, which is greater than the required 0.043 rad. However, fractures were already present when the first loading cycle (0.06-1) exceeding the required inelastic link rotation requirement was completed. At that stage, fractures were noted at the edge of the top flange groove weld and at the bottom edge of the shear tab weld and link web weld. The link-to-column connection failed due to fracture of the top flange during the immediately following half cycle (0.06-2P). Therefore, Specimen FFI exceeded the rotation requirement by only a small margin.

Although the FF-specimens were not quite capable of meeting the link rotation requirements, observation suggests that their performance might be improved by refining the design details of the link-to-column connection. The FF-connections appeared to be sensitive to fracture in the shear tab weld and the link web weld. Such fractures caused the very early failure of Specimens FFS-RLP and FFSL-RLP. In Specimens FFI and FFM, fractures in the link web weld and shear tab weld likely interacted with and accelerated the fracture of link flanges. Should the fracture of shear tab weld and link web weld have been prevented, these four specimens could have developed greater link rotation.

4.5 NA-SPECIMENS

Specimens NAS, NAI, NAM, NAS-RLP, and NASL-RLP had the NA-link-to-column connection with link length of e = 1.1, 2.2, 3.3, 1.1, and $1.7M_p/V_p$, respectively. Design details and fabrication procedures of the NA-specimen are discussed in Section 3.4.5. The NA-connection eliminates the geometric discontinuity typically introduced in field-welded connections due to the presence of weld access holes. In addition, the CJP groove weld at the bottom flange was placed continuously in a flat position, without interruption by the link web. The same welding procedure used in the MW- and FF-connections was used in the NA-connection.

Figure 4.27 shows the NA-connection before testing. Unlike in the PN-, MW-, and FF-connections, the bottom flange groove weld was oriented to have the root of the groove located at the inner face of the flange. Therefore, the backing bar at the bottom flange is placed on top of the flange instead of below the flange (Compare Figure 4.27a with Figure 4.1a). Figure 4.27b shows the backing bar fit around the flange-web fillet of the link. Weld tabs were removed and ground smooth, and reinforcement fillet welds were placed between the backing bars and column flange. No shear tab was used in the NA-connection.

4.5.1 Specimen NAS

The loading history and response of Specimen NAS is illustrated in Figure 4.28. Specimen NAS achieved an inelastic link rotation of 0.071 rad, which is 88% of the 0.08 rad required for S-links.

At completion of 0.01-3N, flaking of the whitewash indicated yielding in the link web panels. At completion of 0.02-2N, yielding in the link flanges spread over the region extending approximately two inches from the column face. Upon further increase in link rotation, yielding in the link flanges gradually spread over the region extending to four inches from the column face.

Specimen NAS exhibited stable response until completion of 0.05-2N, when multiple fractures were detected in the link web at the bottom terminations of the fillet welds connecting the link stiffeners to the link web. This fracture was very similar to that shown in Figure 2.12. At completion of 0.07-2N, a fracture was noted at the outer face of the link bottom flange, along the toe of the groove weld metal, centered at mid-width of the flange. At completion of 0.08-2N, the fractures in the link web were notably larger than in earlier stages. A crack opening of approximately one-eighth inch was noted in one of these link web fractures. A fracture along the toe of the top flange groove weld, similar to the fracture in the bottom flange was noted.

At completion of 0.09-1P, the fractures in the link web ran in the horizontal direction, parallel to the link flanges. As shown in Figure 4.29a, two fractures initiating from different stiffener edges connected to form a ten-inch long horizontal fracture in the link web. The horizontal fracture is visible near the bottom link flange, running across the two middle stiffeners. At this stage, the link shear force and column face moment were 95% and 88% of their respective maximum values. Before completion of 0.09-1N, a drastic drop in link shear force was noted. At this stage, the link shear force and column face moment were 78% and 81% of their respective maximum values. As 0.09-1N was continued, the link shear force and column face moment decreased constantly. 0.09-1P was marked as the last half cycle completed prior to loss of strength of the link.

It should be emphasized that the strength of Specimen NAS degraded due to fracture of the link web, and not due to the fractures at the link-to-column connection. However, fractures were present in the link top and bottom flanges along the toe of the groove welds. Figure 4.29b shows a small crack opening running along the entire width of the link top flange viewed after the test. The crack opening was somewhat greater near the mid-width of the flange than at the edges. It is possible that the fractures in the link flanges would have developed further, and led to loss of strength of the link-to-column connection had the link forces not been degraded due to fracture of the web.

The test was terminated after 0.09-1N was completed. Figure 4.29c shows the link after the test. The figure shows the link still completely attached to the column flange. A large horizontal fracture is visible in the middle of the link near the bottom flange, separating a large segment of the web from the bottom flange. The bending deformation of the link stiffeners was caused after the link web fracture developed to a large size, as the link forces were supplied by bending of the stiffeners. The failure mode shown in Figure 4.29c agrees with the observation by Arce (2002) that shear links are dominated by fracture of the link web (Refer to Section 2.4.2). Therefore, it is very likely that the rotation capacity of the link of Specimen NAS was fully exhausted.

4.5.2 Specimen NAI

The loading history and response of Specimen NAI is illustrated in Figure 4.30. Specimen NAI achieved inelastic link rotation of 0.024 rad, which is 56% of the 0.043 rad required for I-links.

At completion of 0.02-2N, flaking of the whitewash indicated that yielding in the link web was more severe in the panel next to the column than in the other link web panels. Yielding in the link flanges extended over a region within approximately seven inches from the column face. Upon further increase in link rotation, yielding of the link flanges did not extend much farther from the column face. Figure 4.31a shows that at completion of 0.04-2N, yielding spread evenly across the width of the link bottom flange, with no skews as observed in the other I-link specimens, PNI, MWI, and FFI.

At completion of 0.04-2N, mild local buckling was noted in the compressed link top flange. Near completion of 0.05-1P, the link top flange separated from the column flange, as shown in Figure 4.31b. No fracture was noted in the link top flange prior to this stage. Study of the fracture surface (Refer to Section 5.5.4) suggests that the fracture initiated at the east edge of the flange at the interface of the link flange base metal and weld metal, and extended along the width of the flange. Figure 4.31b shows the fracture running in the flange base metal away from the weld interface in the west half of the flange. When the fracture propagated beyond mid-width of the link flange, it also propagated continuously into the link web. Local buckling of the link bottom flange was noted at this stage. The link shear force and column face moment were 72% and 39% of their respective maximum values. Load step 0.04-2N was marked as the last half cycle completed prior to loss of strength of the link-to-column connection.

At completion of the following negative cycle, 0.05-1N, the link shear force and column face moment retained the value achieved in the previous cycle, 0.04-2N. During 0.05-2P, as the column face moment became positive, the fracture in the link web propagated rapidly downwards beyond the centroid of the link section, and led to complete loss of flexural strength of the link-to-column connection. At this stage, a fracture was noted in the link bottom flange at the groove weld, although closer observation of this fracture was obscured by the presence of the backing bar. Further continuation of 0.05-2P led to excessive torsional deformation of the link. The link top flange was displaced by approximately three inches (half the width of the link flange) to the west when the test was terminated.

Figure 4.31c shows the link-to-column connection after the test. The figure shows that the link top flange and almost the entire link web were separated from the column flange. The large torsional deformation of the link that developed during 0.05-2P is visible. Figure 4.31d shows a close-up view of the link top flange after the test. The figure shows the fracture that separated the link top flange from the column flange propagated continuously into the link web, and reached the fillet weld connecting the link web to the column flange. Below that point, the crack runs vertically along the throat of the fillet weld.

4.5.3 Specimen NAM

The loading history and response of Specimen NAM is illustrated in Figure 4.32. Specimen NAM achieved an inelastic link rotation of 0.017 rad, which is 85% of the 0.02 rad required for M-links.

At completion of 0.01-3N, flaking of the whitewash indicated yielding in the link flanges in the region immediately adjacent to the column face. At completion of 0.02-2N, yielding was noted in the link web panels at the two ends. Yielding in the link flanges spread over the region extending nine inches from the column face. Upon further increase in link rotation, yielding in the link web spread a little farther away from the two ends. Yielding in the link flanges spread farther away from the column face at the east edge than at the west edge in the top flange, and at the west edge of the flange in the bottom flange. The skewed distribution of link flange yielding indicated torsional action in the link. During 0.03-2, local buckling was noted in the compressed link flange near the column face. Figure 4.33a shows the link near the column face at completion of 0.04-1P. Yielding in the link web spreading in the end panel and beyond the stiffener, local buckling of the link bottom flange, and yielding in the link flanges in the region within roughly ten inches from the column face is visible.

At completion of 0.03-2P, a small fracture was detected at the east edge of the link top flange, at the interface of the link flange base metal and weld metal. The crack opening was one-eighth inch at the east edge of the flange. Shortly before the completion of 0.04-1P, the link top flange separated from the column flange, as shown in Figure 4.33b. Apart from the east edge, where the fracture appeared to have initiated, the fracture propagated in the link flange base metal, away from the weld interface. As the fracture propagated beyond mid-width of the link flange, it also propagated continuously into the link web. At completion of 0.04-1P, the link shear force and column face moment were 74% and 43% of their respective maximum values. Load step 0.03-2N was marked as the last half cycle completed prior to loss of strength of the link-to-column connection.

At completion of 0.04-1N, the link shear force and column face moment were 94% and 90% of their respective maximum values. A fracture was detected at the east edge of the link bottom flange. Apart from the east edge of the flange, where the fracture formed at the interface of the flange base metal and weld metal, the one-inch long fracture ran primarily in the link flange base metal. During 0.04-2P, the fracture at the top of the link web propagated downwards, and caused a drastic degradation in the strength of the link-to-column connection. The test was terminated after 0.04-2P. Figure 4.33c shows the connection after the test. The figure shows the fracture separating the link top flange from the column flange running vertically into the link web for four inches, reaching the fillet weld connecting the link web to the column flange, and then running along the throat of the fillet weld.

4.5.4 Specimen NAS-RLP

The loading history and response of Specimen NAS-RLP is illustrated in Figure 4.34. Specimen NAS-RLP achieved an inelastic link rotation capacity of 0.119 rad, which is 149% of the 0.08 rad required for S-links. Specimen NAS-RLP was identical to Specimen NAS, but was tested under the revised loading protocol instead of the AISC protocol. The use of the more relaxed loading sequence resulted in a 68% increase in inelastic link rotation over Specimen NAS.

At completion of 0.01-6N, flaking of the whitewash indicated yielding in all link web panels. At completion of 0.015-4N, yielding in the link flanges was noted in the region immediately adjacent to the column face. As link rotation was further increased, yielding in the link flanges gradually spread to the region extending four inches from the column face.

At completion of 0.07-1N, it was suspected that small fractures were present at both edges of both the top and bottom link flanges. At completion of 0.09-1N, a fracture was noticed in the link web, at the bottom termination of the weld connecting the stiffener closest to the column to the link web. This fracture was very similar to that shown in Figure 2.12. At completion of 0.11-1N, similar link web fractures were noted at the other stiffeners. Figure 4.35a shows the link at completion of 0.13-1P. The large link rotation shown in this figure exemplifies the excellent ductility developed by a properly designed EBF link. Figure 4.35b shows a fracture forming at the west edge of the link top flange at this stage. A small crack opening is visible along the thickness of the flange at the interface of the link flange base metal and weld metal. A similar development of fracture was noted at the other edges of the top and bottom link flanges. At completion of 0.13-1N, some of the link web fractures had an opening of nearly one-quarter inch. A small crack opening was noted along the entire width of the link bottom flange along the toe of the groove weld. The crack opening at the west edge of the link top flange (location shown in Figure 4.35b) grew to one-eighth inch. The strength of the link-to-column connection was still maintained.

At completion of 0.15-1P, the link top flange was nearly separated from the column flange. A fracture extended along the entire width of the top flange at the toe of the groove weld, with a crack opening of one-eighth inch between the east edge and mid-width of the flange. The link shear force and column face moment were 100% and 91% of their respective maximum values. At completion of 0.15-1N, the link bottom flange was separated from the column flange. The link shear force was 80% of its maximum value. The column face moment was negligible. The test was terminated upon unloading. Load step 0.15-1P was marked as the last half cycle completed prior to loss of strength of the link-to-column connection.

Figure 4.35c shows a side view of the link after the test. Extensive yielding in all link web panels and the crack opening in the bottom link flange are visible. Figure 4.35d shows a close-up view of the bottom of the stiffener closest to the column. A fracture is visible in the link web, running in the horizontal direction for roughly two inches through the bottom termination of the stiffener weld. Unlike Specimen NAS, Specimen NAS-RLP failed by fracture of the link flange before the link web fractures grew large enough to cause degradation in link forces. Figure 4.35e shows the link bottom flange separated from the column flange. The figure shows that although the fracture ran along the toe of the groove weld, as observed during earlier stages, the fracture propagated primarily in the flange base metal.

4.5.5 Specimen NASL-RLP

The loading history and response of Specimen NASL-RLP is illustrated in Figure 4.36 Specimen NASL-RLP achieved an inelastic link rotation of 0.058 rad, which is 83% of the 0.073 rad required for SL-links.

At completion of 0.01-6N, flaking of the whitewash indicated yielding in the link flanges in the region immediately adjacent to the column face. At completion of 0.02-2N, yielding in the link web panels was noted. Yielding in the link top flange spread farther away from the column face at the east edge than at the west edge, while at the link bottom flange, yielding spread farther away at the west edge. Upon further increase in link rotation, the distribution of flange yielding became more uniform across the width of the flange, and spread in the region extending up to six inches from the column face.

At completion of 0.07-1N, a small crack opening was noted in the link bottom flange along the toe of the groove weld, as shown in Figure 4.37a. Short of completing 0.09-1P, a significant drop in link shear force was noted. A fracture was noted running from the east edge of the link top flange to mid-width of the flange. The crack opening was as much as one-half inch at the east edge. Observation suggested that the fracture initiated at the east edge of the flange at the interface of the flange base metal and weld metal. At completion of 0.09-1P, the link shear force and column face moment were 70% and 36% of their respective maximum values. 0.07-1N was marked as the last half cycle completed prior to loss of strength of the link-to-column connection. Figure 4.37b shows the fractured link top flange at completion of 0.09-1P. The fracture propagated primarily in the flange base metal, as shown in this figure. As the fracture propagated beyond mid-width of the link flange, it also propagated continuously into the link web. The test was terminated upon unloading, during which the link bottom flange separated from the column flange.

Figure 4.37c shows a side view of link after the test. The local buckling of the link bottom flange, visible in the figure, developed during 0.09-1P as fracture developed rapidly in link top flange. Figure 4.37c shows extensive yielding in all link web panels and yielding in the link flanges near the ends. Figure 4.37d shows the fractured bottom flange. The figure shows that although the fracture ran along the toe of the groove weld, as observed during earlier stages, the fracture developed primarily in the flange base metal.

4.5.6 Discussion of NA-specimens

The NA-connections featured elimination of the weld access hole and a fabrication procedure that enables continuous placement of the CJP groove weld at the link bottom flange. These features were expected to reduce local stress concentrations associated with the access hole and eliminate the need to weld through the access hole at the bottom flange, thereby promoting better weld quality at the link bottom flange.

The five NA-specimens exhibited significant improvement in performance over the MW-specimens. Specimen NAS survived three and one-half more loading cycles than did Specimen MWS before the specimen lost its strength. Specimen NAI survived two more loading cycles than Specimen MWI and Specimen NAM survived one and one-half more loading cycles than Specimen MWM. In terms of inelastic link rotations, Specimen NAS achieved 0.071 rad, a 39% increase over Specimen MWS; Specimen NAI achieved 0.027 rad, a 50% increase over Specimen MWI; and Specimen NAM achieved 0.017 rad, a 113% increase over Specimen MWM. Specimens NAS, NAI, and NAM failed to meet their link rotation requirements. However, Specimen NAS failed due to fracture of the link web away from the link ends, and not due to damage at the link-to-column connection. Therefore, although the failure occurred before the required link rotation was reached, the link-to-column connection of Specimen NAS allowed the link to develop its inherent rotation capacity. Based on the inelastic link rotations, Specimen NAS performed better than Specimen FFS, and Specimen NAM performed the same as Specimen FFM. However, Specimen NAI performed significantly worse than Specimen FFI.

Noting that the AISC loading protocol is overly severe for shear links, two more specimens with shear links, Specimens NAS-RLP and NASL-RLP, were subsequently tested under the revised loading protocol. The effect of loading sequence on the performance of the link-to-column connection can be studied by comparing two practically identical specimens, Specimen NAS and Specimen NAS-RLP. The former was tested under the AISC loading protocol, the latter under the revised protocol. Specimen NAS-RLP achieved an inelastic link rotation of 0.119 rad, a 68% increase over the 0.071 rad achieved by Specimen NAS. Specimen NAS-RLP failed due to fracture of the link flange before the link web fractures grew large enough to cause degradation of link strength. In contrast, in Specimen NAS, fracture of the link web occurred before the fractures in the link flanges fully developed. This comparison suggests that the cyclic loading sequence has a significant effect on the inelastic link rotation capacity, and possibly some lesser effect on the failure mode of the link-column specimen.

Although Specimen NAS-RLP exceeded the inelastic link rotation requirement by as much as 49%, Specimen NASL-RLP, which was also tested under the revised loading protocol, developed an inelastic link rotation of 0.058 rad, which is only 80% of the requirement for SL-links. It is also to be noted here that the improvement of Specimen NAI over Specimen MWI was limited compared to the improvement of Specimen NAS over Specimen MWS, and that Specimen NAI performed significantly worse than Specimen FFI. These comparisons indicate that although the NA-connection showed excellent performance with short shear links, such as links of $e = 1.1M_p/V_p$, it may not be suited for intermediate links, such as links of $e = 1.7$ or $2.2M_p/V_p$. The large difference in performance between Specimen NAS-RLP (with $e = 1.1M_p/V_p$) and Specimen NASL-RLP (with $e = 1.7M_p/V_p$) suggests that the NA-connection may be suited only for a limited range of shear links.

Except for Specimen NAS, which failed by fracture of the link web away from the link-to-column connection, all NA-specimens failed due to fracture of the link flange. Observations during the tests and examinations of the fracture surface (Refer to Section 5.5.4) suggest that these fractures generally initiated at the edge of the flange at the interface of the link flange base metal and weld metal. The absence of the weld access holes allowed the link flange fractures to propagated continuously into the link web as it propagated beyond mid-width of the flange. After the link flange separated from the column flange, the fracture in the link web propagated rapidly in the vertical direction parallel to the column face. Unlike the PN- and MW-specimens, no fracture in the NA-specimens was seen to initiate at the mid-width of the link bottom flange. Therefore, it appears that the NA-connection successfully prevented such fractures of the link bottom flange. However, it is not clear from the current tests whether this was because of the absence of the weld access holes, or because of the continuous placement of the groove weld at the link bottom flange, or both.

One clear advantage of eliminating the weld access hole was that no fracture developed in the link web until the fracture in the link flanges propagated into the link web. It is possible that elimination of the weld access hole allows a more smooth bending stress distribution in the link web near the flange-web fillet of the link section. No interaction was suspected between the link flange fracture and the link web/shear tab fracture, as in Specimens MWI, FFI, and FFM.

The welding procedure of the NA-connection calls for filling the bevel extending into the link web before the flange groove weld is placed (Refer to Section 3.4.5.2). The small size of this extended bevel can cause lack of fusion, which, in turn, may induce fracture initiation at this location. However, detailed study of the fracture (Refer to Section 5.5.4) suggests that the bevel was typically completely filled with weld metal, and that no fracture initiated in the vicinity of the extended bevel. In fact, even in cases when the extended bevel was not completely filled, no fractures developed in the link web near this bevel. This suggests that connection performance is not highly sensitive to such deficiencies at the bevel.

4.6 DISCUSSION OF TEST RESULTS

4.6.1 Overview

The *2002 AISC Seismic Provisions* require the performance of EBF link-to-column connections to be evaluated in terms of the inelastic rotation developed by the link. As described in Section 3.2.6, the required inelastic rotation varies depending on the link length. Figure 4.38 summarizes the performance of the sixteen specimens tested in this program, plotting the inelastic link rotation capacity against the link length. Specimens tested under the revised loading protocol instead of the AISC protocol are separately indicated. The inelastic rotation required in the *2002 AISC Seismic Provisions* is indicated by a solid line. Figure 4.38 shows that only Specimens FFI and NAS-RLP successfully met their link rotation requirements. Specimen FFI achieved an inelastic link rotation of 0.046 rad, which is merely 0.003 rad greater than the 0.043 rad required for I-links. Specimen NAS-RLP achieved inelastic link rotation of 0.119 rad, which is 0.039 rad or 49% greater than the 0.080 rad required for S-links. Therefore, out of the sixteen specimens, Specimen NAS-RLP was the only specimen that met the requirement with a comfortable margin. The data plotted in Figure 4.38 strongly suggest that the performance of the specimens depended on the connection type as well as on the link length. With increase in link length, the link-column specimens developed smaller inelastic link rotation. This trend is similar to that seen in isolated link specimens summarized in Figure 2.5. Whereas the PN- and MW-specimens performed poorly, developing only about half of the required inelastic link rotations, the FF- and MW-specimens achieved greater rotations, although generally still falling short of the required rotation levels.

4.6.2 Connection Type

Four different connection types, as described in Section 3.4, were examined in this experimental program. These connection types included the PN-, MW-, FF-, and NA-connections. Figure 4.38 suggests that the connection type had a significant effect on the performance of the link-column specimens. It should also be stressed that all specimens except for Specimen NAS failed at the link-to-column connection. Therefore, it was clear that the majority of specimens did not develop the rotation capacity inherent in the link.

The PN-connection was designed to represent the pre-Northridge practice in detailing and welding of EBF link-to-column connections. The three PN-specimens achieved no more than half of their required inelastic link rotations, and failed due to fracture at the link flange groove welds. Fracture initiating at the root of the bottom flange groove weld, which was observed in many pre-Northridge moment connections (e.g. Engelhardt *et al.* 1993), was not observed in any of the three PN-specimens. The absence of this particular failure mode may be attributed to the adherence to the specified welding procedure, and to the difference in the fore and deformation environment between EBF link-to-column connections and moment connections. The poor performance of the PN-specimens suggests that link-to-column connections in existing EBFs constructed prior to the Northridge Earthquake may not perform as intended, and therefore, raises questions concerning the safety of those EBFs.

The MW-connection used weld metal with a specified notch toughness requirement, and incorporated modified welding details which have been widely adopted in MRF beam-to-column connections following the Northridge earthquake. By comparing the MW-specimens with the PN-specimens, the effect of welding on the performance of link-to-column connections can be studied. Specimen MWS achieved a 20% improvement in inelastic link rotation over

Specimen PNS. However, Specimen MWI achieved no improvement in inelastic link rotation over Specimen PNI, nor did Specimen MWM over Specimen PNM. Similar to the PN-connections, the MW-connections failed due to fracture of the link flanges. These results suggest that although the modifications in welding may be somewhat beneficial, they are not nearly sufficient to improve the connection performance to the required level. More importantly, the conventional EBF link-to-column connection configuration may not be suited for seismic design, regardless of the quality of welding. Premature failure due to link flange fracture can occur not only in connection of a long link ($e > 1.6M_p/V_p$) to a column, as noted by Engelhardt and Popov (1989a, 1992), but also in connections with short shear links, such as links of $e = 1.1M_p/V_p$.

The FF-connections were configured to relax the force and deformation environment near the link flange groove welds. More specifically, the FF-connections aimed to draw the link shear force away from the link flange groove welds by decreasing the relative stiffness of the link flange-to-column connection with respect to the link web-to-column connection. The FF-specimens were successful in preventing or delaying fracture of the link flange. Specimens FFS, FFS-RLP, and FFSL-RLP had no fractures in the link flange until after the link web separated from the column flange. Although Specimens FFI and FFM failed due to fracture of the link flange, the occurrence of link flange fracture was delayed compared to Specimens MWI and MWM, and the specimens were allowed to develop greater link rotation.

The restraint provided by the shear tab welded to the link web had a significant effect on the link behavior in the FF-specimens. A direct effect of the shear tab was that yielding was precluded from the segment of the link web welded to the shear tab, as shown in Figure 4.18a, Figure 4.20a, and Figure 4.22a, and thus, inelastic rotation was amplified within an effectively shortened link. The shortening of the link had a more prominent effect on the shorter links. The link length measured from the end of the shear tab to the beam end was 80%, 87%, and 90% of the full link length, respectively, for the S-link, I-link, and M-link. Correspondingly, the inelastic link rotation was magnified by roughly 25%, 15%, and 10%, for the respective links.

Specimen FFS failed by fracture of the link web along the toe of the fillet weld connecting the shear tab to the link web (See Figure 4.18c, d). It is believed that the cause of this fracture was the significant magnification in link rotation demand and the high restraint in the link web material near the right-angled corners of the shear tab. After noting the disadvantage of rectangular shear tabs, the remaining four FF-specimens were provided with tapered shear tabs. The failure mode of Specimen FFS was not reproduced in any of the other FF-specimens.

In Specimens FFI and FFM, fractures were noted at the top and bottom edges of the shear tab and link web, simultaneous to or prior to fractures in the link flange. As a fracture propagated in the double bevel groove weld connecting the shear tab to the column flange (See Figure 4.20b), another fracture propagated at the interface of the link web base metal and groove weld metal. Since the shear tab weld was located at the root of the link web weld, the two fractures developed simultaneously, interacting with each other. In Specimen FFM, it was clearly observed that noticeable development of the fractures in the shear tab weld and link web weld preceded fracture initiation in the link flange. Although Specimens FFI and FFM ultimately failed due to fracture of the link flange, it is quite likely that the progression of fractures in the shear tab and link web caused redistribution of bending stress from the link web to the link flanges, and consequently accelerated fracture of the link flange.

Specimens FFS-RLP and FFSL-RLP failed due to fracture in the groove weld between the shear tab and column flange, initiating at the top and bottom edges of the shear tab. These two specimens achieved very limited link rotation although they were tested under the more relaxed revised loading protocol. The poor performance of Specimens FFS-RLP and FFSL-RLP was likely caused by the alteration in the connection configuration from the other three FF-specimens. Whereas the other FF-specimens had the link web directly welded to the column flange, Specimens FFS-RLP and FFSL-RLP had the link web cut short of reaching the column flange, and fillet welded to the shear tab. This alteration resulted in a smaller web section near the column face, with the greater eccentricity of the shear tab with respect to the link web generating greater torsion about the longitudinal axis of the link. It is possible that these factors affected the shear tab welds in a severely detrimental manner.

The above discussion of Specimens FFI, FFM, FFS-RLP, and FFSL-RLP suggests that the FF-connections were very sensitive to fracture initiating at the top and bottom edges of the link web weld and shear tab weld.

The NA-connection featured the elimination of the weld access hole and a fabrication procedure that enables continuous placement of the CJP groove weld at the link bottom flange. Specimens NAI, NAM, NAS-RLP, and NASL-RLP failed due to fracture of the link flanges. Although Specimen NAS failed due to fracture of the link web away from the link ends, at the end of the test, crack openings were noted at both the top and bottom link flanges along the toe of the groove weld. Had the link forces not reduced due to link web fracture, the fractures in the link flange could have continued to propagate. Therefore, it is believed that fracture of the link flanges was the dominant failure mode of the NA-connection regardless of the link length.

Specimen NAS achieved an inelastic link rotation of 0.071 rad before the link forces drastically reduced, at which point the link-to-column connection likely still maintained its strength. This specimen failed due to fracture of the link web at the stiffener welds. Arce (2002) and Ryu *et al.* (2004) observed that such a failure mode dominates links of $e < 1.7M_p/V_p$. Judging from isolated link tests by Ryu *et al.*, the link web fracture in Specimen NAS might have been delayed had the specimen been tested under the revised loading protocol instead of the AISC protocol. In fact, Specimen NAS-RLP, which was identical to Specimen NAS but tested under the revised protocol, achieved an inelastic link rotation of 0.119 rad, which exceeds the link rotation requirement by as much as 49%. This rotation level is similar to that achieved by shear link specimens tested by Ryu *et al.* In fact, a specimen (Specimen 12-RLP) with similar length as Specimen NAS-RLP ($e = 1.0M_p/V_p$ opposed to $1.1M_p/V_p$), constructed from the same W18x40 steel, and tested under the same revised loading protocol, achieved an inelastic rotation of 0.12 rad. Also since link web fracture was developing significantly near the end of the test, it is likely that Specimen NAS-RLP exhausted much of the rotation capacity inherent in the link. The results from Specimens NAS and NAS-RLP suggest that the NA-connection is quite suited for use with S-links.

However, the three other specimens with longer links, Specimens NAI, NAM, and NASL-RLP, failed prematurely, falling short of their inelastic link rotation requirement by 17 to 37%. Therefore, the NA-connection may be suited only for shear links of limited length range around $e = 1.1M_p/V_p$.

4.6.3 Link Length

As stated in Section 3.2.2, links of nominal $e = M_p/V_p$, $1.6M_p/V_p$, $2M_p/V_p$, and $3M_p/V_p$ are designated as S-links, SL-links, I-links, and M-links, respectively, in this research program. The four link lengths were selected to study the performance of link-to-column connections subjected to a wide range of possible force and deformation environments.

Figure 4.38 suggests that the performance of the link-column specimens depended significantly on the link length. This statement applies directly to the performance of link-to-column connections, since all specimens except Specimen NAS failed at the link-to-column connection. Table 4.2 indicates that the force environment at the link-to-column connection differed significantly depending on the link length. For example, for the MW-specimens, the maximum link shear force ranged between 235 kips in Specimen MWS and 130 kips in Specimen MWM; the maximum column face moment ranged between 3250 kip-in in Specimen MWS and 4600 kip-in in Specimen MWM. Meanwhile, the link-to-column connection was required to accommodate different levels of link rotation in accordance with the link length, as indicated by the solid line in Figure 4.38. It is natural to believe that the very significant difference in force and deformation environment had a significant influence on the performance of the link-to-column connection.

Despite their very short length, flexural yielding was observed in the S-links. In Specimens PNS, MWS, NAS, and NAS-RLP, yielding in the link flanges spread over a region extending up to four inches from the column face. This was due to the unequal end restraints causing significantly larger moment at the column end than at the beam end, and more significantly due to moment-shear interaction. Table 4.2 indicates that the column face moment was considerably smaller than the plastic flexural capacity of the link section of 4008 kip-in. However, shear yielding in the link web led to significant reduction in the flexural strength of the link web. Note that the plastic flexural capacity of the W18x40 section consisting of only the flanges was 2691 kip-in. This reduced capacity was exceeded in all S-link specimens over a region extending roughly three inches from the column end, which matches the flaking of whitewash observed during the tests. In Specimens FFS and FFS-RLP, the shear tab increased the flexural capacity of the link near the column face, and therefore, precluded yielding of the link flanges near the groove welds.

Specimens PNS, MWS, and NAS-RLP failed due to fracture of the link flange. The significant bending stress acting near the groove welds, as discussed above, was a likely cause of this fracture. Specimen FFS failed due to fracture of the link web around shear tab, while Specimen FFS-RLP failed due to fracture of the shear tab in the groove weld. The failure modes of Specimens FFS and FFS-RLP were likely caused by the unique configuration of the FF-connections. Although Specimen NAS ultimately failed by fracture of the link web, fractures were developing at the toe of the link flange groove welds during the test. These results indicate that, with the exception of the FF-connections, failure of a connection of as S-link to a column is controlled primarily by fracture of the link flange. The inelastic link rotation developed by Specimens PNS, MWS, FFS, and NAS were 51%, 63%, 75%, and 88%, respectively, of the required 0.08 rad. Specimens NAS and NAS-RLP exhibited very promising performance, suggesting the adequacy of the NA-connection for use with S-links.

Specimens PNM, MWM, FFM, and NAM failed due to fracture of the link flange at the groove welds. All four specimens failed to meet the link rotation requirement. Specimens PNM and MWM achieved 40% of the required inelastic link rotation of 0.02 rad, while Specimens FFM and NAM achieved 80% of 0.02 rad. Engelhardt and Popov (1989a; 1992) observed that moment links typically exhibit severe local flange buckling and lateral torsional buckling prior to fracture at the link ends. However, the four specimens with M-links fractured at the link flanges without exhibiting degradation in link forces due to instability. Therefore, it appears that these specimens failed well before the link developed its inherent rotation capacity. As discussed in Section 2.3.2, a connection of a moment link to a column is subjected to very severe bending strains, much more severe than in typical MRF beam-to-column connections. It is believed that this severe environment made the specimens quite susceptible to fracture at the link flange groove welds.

Specimens PNI, MWI, FFI, and NAI failed due to fracture of the link flange groove weld metal, similar to specimens with M-links discussed above. Specimens PNI and MWI both achieved 42% of the required inelastic link rotation of 0.043 rad, while Specimens FFI and NAI achieved 108% and 63%, respectively, of 0.043 rad. Whereas Specimen FFI displayed a significant improvement in link rotation over Specimens PNI and MWI, Specimen NAI achieved a much smaller improvement. This indicates that the FF-connection is the most suited among the four connections for use with I-links. However, Specimen FFI failed immediately after completing the first loading cycle with inelastic link rotation greater than 0.043 rad. Therefore, Specimen FFI just barely exceeded the link rotation requirement.

The results from eight specimens with I-links and M-links agree with earlier observations by Engelhardt and Popov (1989a; 1992) that the performance of a connection of a long link ($e > 1.6M_p/V_p$) to a column is dominated by fracture of the link flange.

Whereas Specimens NAS-RLP with a link of $e = 1.1M_p/V_p$ achieved an inelastic rotation of 0.119 rad, Specimen NASL-RLP with a link of $e = 1.7M_p/V_p$ achieved only 0.070 rad. The large difference in performance between these two specimens of identical connection type tested under the same loading protocol suggests that the force environment at the link-to-column connection changes quite significantly in the range of link length between $e = 1.1M_p/V_p$ and $e = 1.7M_p/V_p$.

While the FF- and NA-connections generally performed better than the PN-and MW-connections, the comparison between the FF- and NA-connections is not straightforward. In terms of inelastic link rotation, Specimen FFS performed 14% better than Specimen NAS; Specimen FFI performed 60% better then Specimen NAI; Specimens FFM and NAM performed similarly. This suggests that the optimum configuration for ENF link-to-column connections may differ depending on the link length.

4.6.4 Loading Sequence

As discussed in Section 2.4.4, the revised protocol developed by Richards and Uang (2003) is based on a more rational basis than the AISC protocol, and therefore, should be more realistic to represent the demands arising from earthquake ground motion. Meanwhile, the revised protocol, which was developed specifically for testing shear link specimens, is more relaxed compared to the AISC protocol, and would therefore be expected to result in greater link rotation capacity for shear links. In fact, tests by Ryu *et al.* (2004) showed that the use of the revised protocol could increase the inelastic rotation as much as 50% from the inelastic rotation obtained under the AISC protocol. In this program, twelve specimens were tested under the AISC protocol; four specimens were tested under the revised protocol.

The effect of loading sequence is most clearly seen in the comparison between Specimens NAS and NAS-RLP. These two specimens were constructed using the same material, design, and construction procedure, with the only significant difference being the loading protocol used for testing. Specimen NAS used the AISC protocol, while Specimen NAS-RLP used the revised protocol. Specimen NAS-RLP achieved an inelastic link rotation of 0.119 rad, which is 49% greater than the 0.071 rad achieved by Specimen NAS. Although Specimen

NAS failed due to fracture of the link web away from the link-to-column connection, crack openings were noted along the toe of the link flange groove welds during the test. Although Specimen NAS-RLP failed due to fracture of the link flange, fractures in the link web, very similar to the fractures that caused failure of Specimen NAS, were developing during the test. Therefore, either of the two failure modes could have occurred in both specimens. Based on this comparison, it appears that the choice of loading sequence had a very large effect on the inelastic link rotation achieved by the specimens. It is quite likely that Specimen NAS was penalized by the use of the overly severe AISC protocol, and that this same specimen could have achieved greater link rotations had it been tested using the more realistic revised protocol. The effect of the loading sequence on the failure modes appeared to be more limited.

Little information on the effect of loading sequence can be deduced from the comparison between Specimens FFS and FFS-RLP. Specimen FFS had a rectangular shear tab, with the link web welded directly to the column flange. Specimen FFS-RLP had a tapered shear tab, but with the link web cut short of reaching the column flange. The difference in design resulted in significant difference in the behavior of the two specimens. It is especially interesting to note that Specimen FFS-RLP, which was tested under the more relaxed revised loading protocol, developed much smaller link rotation compared to Specimen FFS, which was tested under the more severe AISC protocol. As discussed in Section 4.4.6, it rather clear that the use of a tapered shear tab instead of the rectangular shear tab is beneficial. Therefore, the comparison of Specimens FFS and FFS-RLP emphasizes the extent of the detrimental effect caused by not extending the link web to the column flange.

4.6.5 Failure Modes

4.6.5.1 *Dominant Failure Modes*

The primary failure modes observed in the tests are summarized in Table 4.3. Failure of the specimens was dominated by the following four modes: (a) fracture of the link flange initiating at the groove weld; (b) fracture of the link web initiating at the toe of the top and bottom terminations of the stiffener welds; (c) fracture of the link web along the toe of the fillet weld connecting the shear tab to the link web; and (d) fracture of the groove weld connecting the shear tab to the column flange. Failure mode (a) was observed in the majority of the specimens. Failure mode (b) was unique to S-links, and did not directly involve damage at the link-to-column connection. Failure mode (c) was unique to Specimen FFS, whereas (d) was unique to Specimens FFS-RLP and FFSL-RLP, which adopted a slightly altered design from the other three FF-specimens.

4.6.5.2 *Fracture of Link Flange*

Of the sixteen specimens tested in this program, twelve specimens failed due to fracture of the link flange initiating at the groove weld. Among the four specimens that did not fail due to this mode, Specimen NAS failed by fracture of the link web away from the link ends, but fractures were developing at the link flange groove welds during the test. Specimens FFS, FFS-RLP, and FFSL-RLP exhibited a unique failure mode, which is likely due to their unique connection configuration. Therefore, with the exception of FF-specimens with short shear links, link flange fracture was the dominant failure observed in the link-column specimens.

Link flange fracture typically initiated at the interface of the link flange base metal and groove weld metal. One possible exception was seen in Specimen PNS. It was unclear whether the fracture of the bottom flange of Specimen PNS initiated at the toe of the weld access hole (mid-width of the flange) at the weld interface or at the edge of the flange in the weld metal. In all specimens, fracture of the top flange was rather clearly seen to initiate at the edge of the flange. Fracture of the bottom flange initiated either at the edge or at mid-width of the flange. In Specimen MWS, the fracture of the bottom flange was clearly seen to initiate at mid-width of the flange. In three specimens, PNS, PNM, and MWM, the initiation point of bottom flange fracture was unclear, but it appeared to be either the edge or mid-width of the flange. A detailed study of the fracture surfaces is provided in Section 5.5.

Link flange fracture typically propagated rapidly, leading to separation of the link flange from the column flange within at most two loading cycles after the fracture was first detected. The progression of fracture appeared to be slower in Specimens NAS and NAS-RLP than in other specimens. In Specimens PNS, PNM, and MWM, a fracture ran between one of the edges and mid-width of the flange, near two-thirds of the flange width, when the fracture was first detected. As fracture propagated in the link flange, the column face moment decreased dramatically, and led to failure of the specimen.

Among the twelve specimens that failed due to link flange fracture, four specimens, PNS, PNM, MWS, and MWM, lost their strength due to fracture of the bottom flange. The remaining eight specimens, PNI, MWI, FFI, FFM, NAI, NAM, NAS-RLP, and NASL-RLP, lost their strength due to fracture of the top flange. In Specimens PNS, PNM, MWS, MWM, FFM, NAS-RLP, and NASL-RLP, fracture developed simultaneously in both the top and bottom link flanges.

During the fabrication of the PN-, MW-, and FF-specimens, the link web interrupted placing of the CJP groove weld in the link bottom flange. Since this increases the likelihood of weld defects at the point of interruption, the bottom flange was more susceptible to fracture initiating at this location. In fact, Specimen MWS, and possibly Specimens PNS, PNM, and MWM exhibited fracture initiating at this location. Nonetheless, the test specimens fractured more frequently at the top flange than at the bottom flange. Therefore, the welding practice mentioned above appeared to have little influence on the performance of the link-to-column connection.

Specimens FFS, FFS-RLP, and FFSL-RLP did not exhibit fracture in the link flanges until the link web completely separated from the column flange. The limited extent of yielding seen in the link flange near the groove welds also suggests that the FF-connection is beneficial in relaxing the force and deformation demands imposed on the groove welds, especially for short shear links.

4.6.5.3 Fracture of Link Web at the Stiffener Welds

As discussed in Section 2.4, recent tests on isolated link specimens suggest that links of $e < 1.7M_p/V_p$ constructed of A992 steel and detailed according to the current provisions typically fail due to fracture of the link web at the stiffener welds. This type of fracture was observed in Specimens MWS, NAS, and NAS-RLP. While Specimen NAS failed due to link web fracture, Specimens MWS and NAS-RLP failed by fracture of the link flange before the link web fracture fully developed. It is believed that fracture at the link-to-column connection caused degradation in link forces, and therefore prevented full development of the link web fractures in Specimens MWS and NAS-RL.

As discussed in Section 2.4, the link web fracture may be associated with the proximity of the weld termination to the K-area of the link section. In order to avoid this fracture, the stiffener welds were terminated at approximately three times the web thickness away from the k-line of the link section in all sixteen specimens. Tests by Arce (2002) and Ryu *et al.* (2004) demonstrated that moving the weld termination as much as five times away from the k-line could delay the occurrence of link web fracture. Moving the weld terminations farther away from the k-line than done in the current specimens could have increased the link rotation capacity of the specimen. However, if the link forces had not degraded due to the link web fractures, the fracture developing in the link flange could have caused failure of specimen. Therefore, it is not clear whether moving the weld terminations farther away from the k-line than done in the current specimens could have allowed the specimen to meet the link rotation requirement.

4.6.5.4 Failure Modes Unique to FF-Connections

Specimen FFS failed due to fractures of the link web initiating at the two corners of the rectangular shear tab. The fracture initiated and propagated along the toe of the fillet weld connecting the shear tab to the link web. It is believed that the large restraint imposed on the link web material between the shear tab and the link flange combined with the large cyclic link rotation generated severe cyclic inelastic strain demands near the right-angled corners of the shear tab, and induced fracture at these locations by low cycle fatigue. The fractures rapidly propagated around the entire periphery of the shear tab, and eventually separated the link web from the shear tab. A tapered shear tab without right-angled corners would likely relieve the local strain demands. In fact, no fracture was observed in the link web in the other four FF-specimens, which were provided with tapered shear tabs. Although these four specimens developed smaller link shear forces and link rotations compared to Specimen FFS, they demonstrated to some extent the benefit of tapering the corners of the shear tab in the FF-connections.

The FF-connections were very sensitive to fracture initiating at the top and bottom edges of the link web and shear tab. In Specimens FFI and FFM, fractures were noted at the top and bottom edge of the shear tab and link web simultaneous to or prior to fracture of the link flange. Fracture in the shear tab initiated and propagated in the groove weld metal, while fracture in the link web initiated and propagated along the interface of the web base metal and weld metal. Since the shear tab weld was located at the root of the link web weld, these two fractures developed simultaneously, interacting with each other. It is quite likely that the propagation of fractures in the shear tab weld and link web weld caused redistribution of bending stress and shear from the link web to the link flange, and therefore, accelerated fracture of the link flange.

Specimens FFS-RLP and FFSL-RLP failed by fracture in the groove weld connecting the shear tab to the column flange. Unlike the other three FF-specimens, Specimens FFS-RLP and FFSL-RLP did not have the link web welded directly to the column flange. Comparison among the five FF-specimens suggests that this alteration in connection configuration was the primary cause of the poor performance of Specimens FFS-RLP and FFSL-RLP.

4.6.6 Additional Comments

The stiffener spacing for the FF-specimens was measured by taking the end of the shear tab as one end of the link. Therefore, the link flanges in the FF-specimens were left with a rather long unstiffened length near the face of the column. This long unstiffened length did not appear to promote local flange buckling in the FF-specimens, at least within the range of link rotation achieved by the specimens. It appeared that the shear tab provided sufficient restraint to prevent local buckling of the link web and thereby helped to prevent flange buckling.

Specimens MWI, FFI, NAI, and NAM exhibited significant lateral-torsional deformation in the link after the link top flange separated from the column flange. This instability led to a drastic reduction in link forces, and therefore, arrested the development of fracture in the link bottom flange. Whereas

Specimens MWI was likely influenced by initial imperfection, Specimens FFI, NAI, and NAM developed rather large link rotations, and exhibited benign local buckling in the link flanges. It is likely that the unsymmetrical form of the local flange buckling promoted torsional deformation of the link.

4.7 SUMMARY

A total of sixteen large-scale link-column specimens were tested to investigate the influence of the connection type, link length, and loading sequence on the performance of EBF link-to-column connections. Four different link lengths (S-link, SL-link, I-link, and M-link), four connection types (PN, MW, FF, and NA-connections), and two loading protocols (AISC protocol and revised protocol) were examined. Details of the test parameters are provided in Chapter 3. This chapter discussed the behavior of the specimens and key observations made during the tests. The discussions are summarized in the following:

- The PN-specimens, which featured the pre-Northridge practice in design, detailing, and welding of EBF link-to-column connections, performed poorly for a wide range of link lengths, achieving no more than half of the inelastic link rotation required in the *2002 AISC Seismic Provisions*. The PN-connections typically failed due to fracture of the link flange initiating at the groove weld. The poor performance of the PN-specimens raises questions concerning the safety of existing EBFs.

- Fracture initiating at the root of the beam bottom flange groove weld, which was observed in a large number of pre-Northridge moment connections, was not observed in any of the PN-specimens. The absence of this particular failure mode may be attributed to the adherence to the specified welding procedure during the fabrication of the specimen, and to the difference in the force and deformation environment between EBF link-to-column connections and MRF beam-to-column connections.

- The MW-specimens, which featured the use of weld metal with specified notch toughness and modifications in welding details, showed marginal improvement over the PN-specimens. This suggests that modifications in welding alone are not sufficient to improve the performance of EBF link-to-column connections to the required level. Similar to the PN-connections, failure of the MW-connections was typically controlled by fracture of the link flange initiating at the groove weld. Fracture occurred at either the top flange or bottom flange, or in both flanges. Premature fracture of the link flanges is a major concern not only for connections of a long link ($e > 1.6M_p/V_p$) to a column, as previously recognized, but also for connections with a short shear link, such as a link of $e = 1.1M_p/V_p$.

- The FF-connections configured with a shear tab welded to the link web and an extended weld access hole aims to relax the force and deformation environment at the link flange groove welds. The FF-specimens achieved significantly greater link rotations compared to the PN- and MW-specimens. Nonetheless, the FF-specimens failed to meet their link rotation requirements, except for one specimen with a link of $e = 2.2M_p/V_p$. However, this specimen exceeded its link rotation requirement by only a small margin.

- The shear tab welded to the link web had a significant effect on link behavior in the FF-specimens, as well as on the failure of the FF-connection. The failure modes of the FF-connections were significantly different from the failures observed in the PN- and MW-connections, and ranged from fracture of the link web around the shear tab, to fracture in the groove weld connecting the shear tab to the column flange. Overall, the FF-connections were very sensitive to fracture initiating at the top and bottom edges of the link web and shear tab.

- Two FF-specimens with links of e = 1.1 and $1.7_p/V_p$ demonstrated that cutting of the link web short of reaching the column flange is disadvantageous. Considerably better performance was demonstrated by FF-specimens with the link web welded directly to the column flange.

- The FF-specimen with a link of e = $1.1M_p/V_p$ failed due to fracture of the link web around the shear tab welded to the link web. It is believed that the large restraint imposed on the link web material between the shear tab and the link flange combined with large cyclic deformation demand on the link generated severe cyclic inelastic strain demands near the right-angled corners of the shear tab, and induced fracture at this location. The fractures propagated around the shear tab, and eventually separated the link web from the shear tab.

- In two FF-specimens with e = 2.2 and $3.3M_p/V_p$, fractures were detected at the top and bottom edges of the welds connecting the shear tab and link web to the column flange prior to or simultaneous with fracture of the link flanges. It is likely that the propagation of fracture in the link web weld and shear tab weld accelerated the development of the link flange fractures.

- The NA-specimens featured the elimination of the weld access holes and a fabrication procedure that enables continuous placement of the bottom flange groove weld. The performance of the NA-specimens strongly depended on the link length. One specimen with a link of e = $1.1M_p/V_p$ achieved an inelastic link rotation 49% greater than the required 0.08 rad. However, all NA-specimens with longer links (e = 1.7, 2.2, and $3.3M_p/V_p$) fell short of the inelastic link rotation requirement by 17 to 37%. Fracture of the link flange initiating at the groove weld was the dominant failure mode of the NA-connection.

- An NA-specimen with a link of e = $1.1M_p/V_p$ failed due to fracture of the link web initiating at the terminations of the fillet welds connecting the stiffeners to the link web. Eventually, this link web fracture caused a drastic reduction in link forces, which in turn, arrested development of fractures in the link flanges. Similar link web fractures were also observed in two other specimens in this program which also had links of e = $1.1M_p/V_p$, although these two specimens ultimately failed due to fracture of the link flanges. The three specimens demonstrated that short shear links can fail due to fracture of the web at the stiffener welds.

- Two practically identical NA-specimens with shear links were tested under different loading protocols. Comparison of these two tests shows that the cyclic loading sequence can have a very large effect on the inelastic link rotation capacity of the link-column specimen. Therefore, it is important to select a loading sequence that realistically represents the demands caused by earthquake ground motion, as does the revised loading protocol developed and proposed by Richards and Uang (2003). It should be cautioned that except for four specimens that used the revised protocol, the current program used the

AISC loading protocol, which may not necessarily be representative of seismic demands.

- The performance of the link-to-column connection depended strongly on the link length, with the inelastic link rotation decreasing significantly with increase in the link length. The effect of the link length was reflected in the substantial difference in link shear force and column face moment. The maximum link shear force ranged between 130 and 250 kips depending on the link length, while the maximum column face moment ranged between 3250 and 5000 kip-in.

- Link flange yielding was observed even in short shear links of $e = 1.1M_p/V_p$ that did not develop moment beyond the flexural strength of the section. Moment-shear interaction can cause a substantial decrease in flexural strength. It should also be noted that link moment is typically greater at the column end than at the beam/brace end. Therefore, inelastic stress and strain should be expected near the link flange groove weld even in very short links.

- The test results from the current program suggest that premature failure of the link-to-column connection can occur not only in connections of a long link ($e > 1.6M_p/V_p$) to a column, as previously recognized, but also in connections with a short shear link, such as a link of $e = 1.1M_p/V_p$.

Table 4.1 Summary of test results

Specimen	Link Length $e/(M_p/V_p)$	Required $\gamma_{p\text{-max}}$ (rad)	Last Completed Half-Cycle	Measured Deformation		
				γ_{max} (rad)	$\gamma_{p\text{-max}}$ (rad)	$\Gamma_{p\text{-max}}$ (rad)
PNS	1.11	0.08	0.05-2P	0.050	0.041	0.0
PNI	2.22	0.043	0.03-1N	0.030	0.018	0.0
PNM	3.34	0.02	0.02-2P	0.020	0.008	0.0
MWS	1.11	0.08	0.07-1P	0.060	0.051	0.0
MWI	2.22	0.043	0.03-2N	0.030	0.018	0.0
MWM	3.34	0.02	0.03-1P	0.020	0.008	0.0
FFS	1.11	0.08	0.07-1N	0.070	0.060	0.0
FFI	2.22	0.043	0.06-1N	0.060	0.046	0.003
FFM	3.34	0.02	0.04-1P	0.030	0.016	0.004
FFS-RLP	1.11	0.08	0.05-1P	0.040	0.031	0.0
FFSL-RLP	1.72	0.073	0.03-1N	0.030	0.019	0.0
NAS	1.11	0.08	0.09-1P	0.080	0.071	0.0
NAI	2.22	0.043	0.04-2N	0.040	0.027	0.0
NAM	3.34	0.02	0.03-2N	0.030	0.017	0.001
NAS-RLP	1.11	0.08	0.15-1P	0.130	0.119	0.0
NASL-RLP	1.72	0.073	0.07-1N	0.070	0.058	0.0

Table 4.2 Connection forces

Specimen	Link Length $e/(M_p/V_p)$	Nominal Link Shear Strength V_n (kips)	Maximum Shear V_{max} (kips)	Maximum Moment M_{max} (kip-in)	Link Overstrength V_{max}/V_n
PNS	1.11	178	230.5 / -224.7	3228 / -3124	1.29 / -1.26
PNI	2.22	160	168.3 / -181.4	4285 / -4405	1.05 / -1.13
PNM	3.34	107	127.6 / -121.3	4472 / -4651	1.19 / -1.13
MWS	1.11	178	234.5 / -236.2	3255 / -3078	1.32 / -1.32
MWI	2.22	160	172.6 / -178.7	3957 / -4192	1.08 / -1.11
MWM	3.34	107	130.6 / -129.6	4634 / -4537	1.22 / -1.21
FFS	1.11	178	244.5 / -245.7	3501 / -3450	1.37 / -1.38
FFI	2.22	160	202.1 / -199.9	5136 / -4851	1.26 / -1.25
FFM	3.34	107	146.3 / -134.3	5022 / -5024	1.37 / -1.26
FFS-RLP	1.11	178	226.4 / -224.4	3343 / -2964	1.27 / -1.26
FFSL-RLP	1.72	178	194.4 / -189.2	3859 / -3606	1.09 / -1.06
NAS	1.11	178	253.3 / -247.3	3535 / -3422	1.42 / -1.39
NAI	2.22	160	185.7 / -193.9	4688 / -4505	1.16 / -1.21
NAM	3.34	107	134.2 / -134.9	4932 / -4698	1.26 / -1.26
NAS-RLP	1.11	178	256.3 / -261.9	3517 / -3297	1.44 / -1.47
NASL-RLP	1.72	178	224.1 / -216.4	4120 / -3909	1.26 / -1.21

Table 4.3 Key observations

Specimen	Controlling Failure Mode	Other Observations
PNS	Fracture of link bottom flange in groove weld. Initiating point unclear.	Fracture of link top flange along weld interface. Initiating point unclear.
PNI	Fracture of link top flange along weld interface, initiating at west edge.	Fracture of link bottom flange initiated after failure of the top flange.
PNM	Fracture of link bottom flange along weld interface, initiating either at west edge or at root of weld access hole.	Fracture of link top flange along weld interface, likely initiating at east edge.
MWS	Fracture of link bottom flange initiating at mid-width in weld interface.	Fracture of link top flange initiating at east edge in weld interface(a). / Fractures at bottom edge of link web.
MWI	Fracture of link top flange initiating at west edge in weld interface.	Fractures at top and bottom edges of link web prior to fracture of link top flange. / No fracture in link bottom flange at completion of test.
MWM	Fracture of link bottom flange. Initiating point unclear.	Fracture of link top flange initiating at east edge of flange in weld interface.
FFS	Fracture of link web surrounding toe of fillet weld between shear tab and link web, initiating at corners of shear tab.	No fracture in either top or bottom link flange at completion of test.
FFI	Fracture of link top flange initiating at the east edge in weld interface.	Shear tab detaching from column face at bottom edge. / No fracture in link bottom flange at completion of test.

(a) Location of fracture initiation was not based on observation during the test, but based on study of fracture surface discussed in Section 5.5.

Table 4.3 Key observations (Continued)

Specimen	Controlling Failure Mode	Other Observations
FFM	Fracture of link bottom flange initiating at the east edge in weld interface[(a)]. Fracture of link top flange initiating at east edge in weld interface.	Shear tab detaching from column face at top and bottom edges. / Fracture initiation in link top flange from weld interface, initiating at west edge of flange.
FFS-RLP	Fracture of weld between shear tab and column flange	No fracture in either link flanges until shear tab separated from column flange.
FFSL-RLP	Fracture of weld between shear tab and column flange	No fracture in either link top or bottom flange at completion of test.
NAS	Fracture of link web initiating at terminations of stiffener welds, at root of fillet weld.	Possible fractures in link top and bottom flanges visible along toe of groove weld.
NAI	Fracture of link top flange initiating at the east edge in weld interface.	Fracture initiated in link bottom flange after failure of the link top flange.
NAM	Fracture of link top flange initiating at the east edge in weld interface.	Fracture initiated in link bottom flange after failure of the link top flange.
NAS-RLP	Fracture of link top flange simultaneously developing along entire width of flange in weld interface.	Fracture of link bottom flange along entire width of flange in weld interface. / Fracture of link web initiating at terminations of stiffener welds, at root of fillet weld.
NASL-RLP	Fracture of link top flange initiating at the east edge in weld interface.	Fracture of link bottom flange initiating at the east edge in weld interface.

(a) Location of fracture initiation was not based on observation during the test, but based on study of fracture surface discussed in Section 5.5.

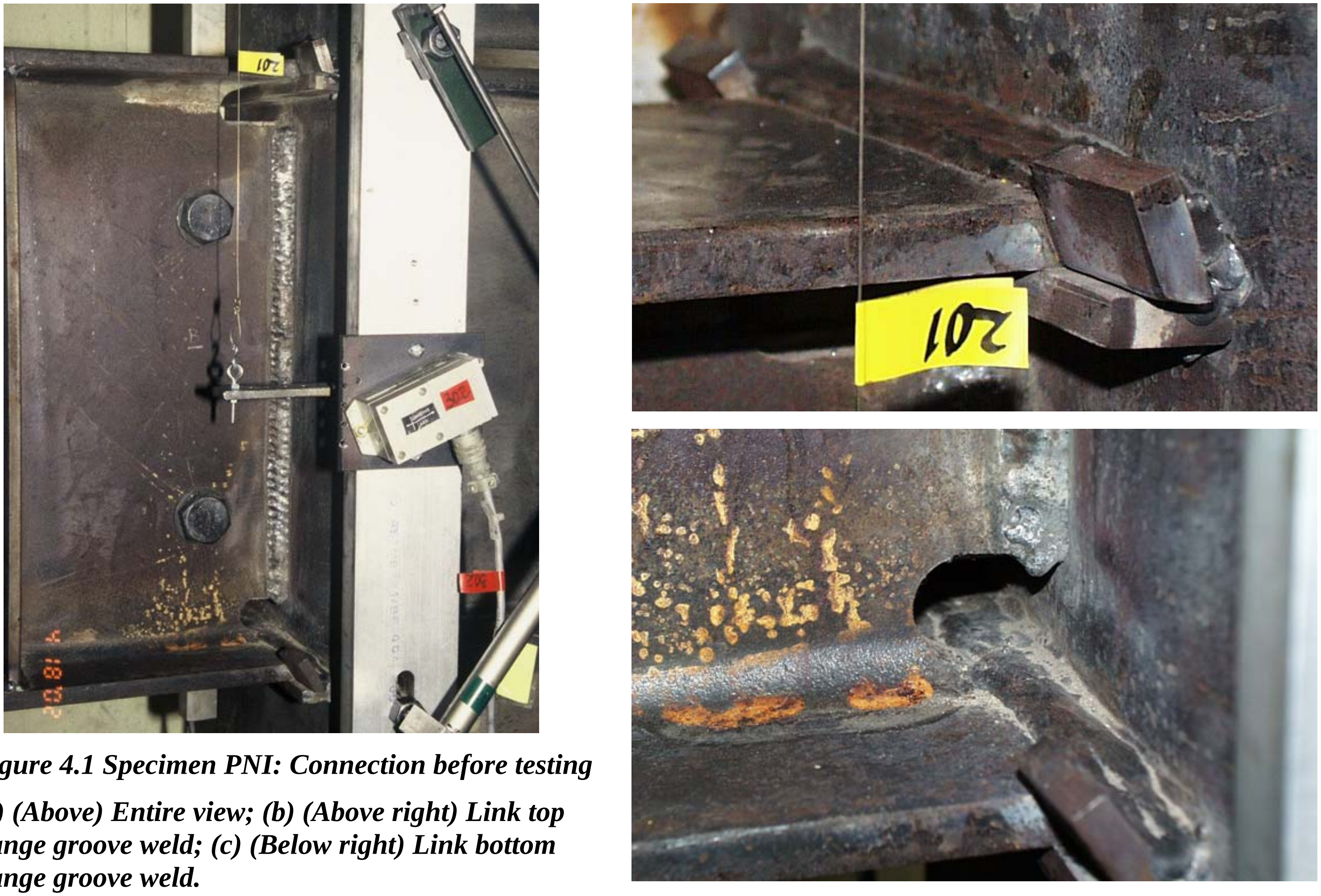

Figure 4.1 Specimen PNI: Connection before testing

(a) (Above) Entire view; (b) (Above right) Link top flange groove weld; (c) (Below right) Link bottom flange groove weld.

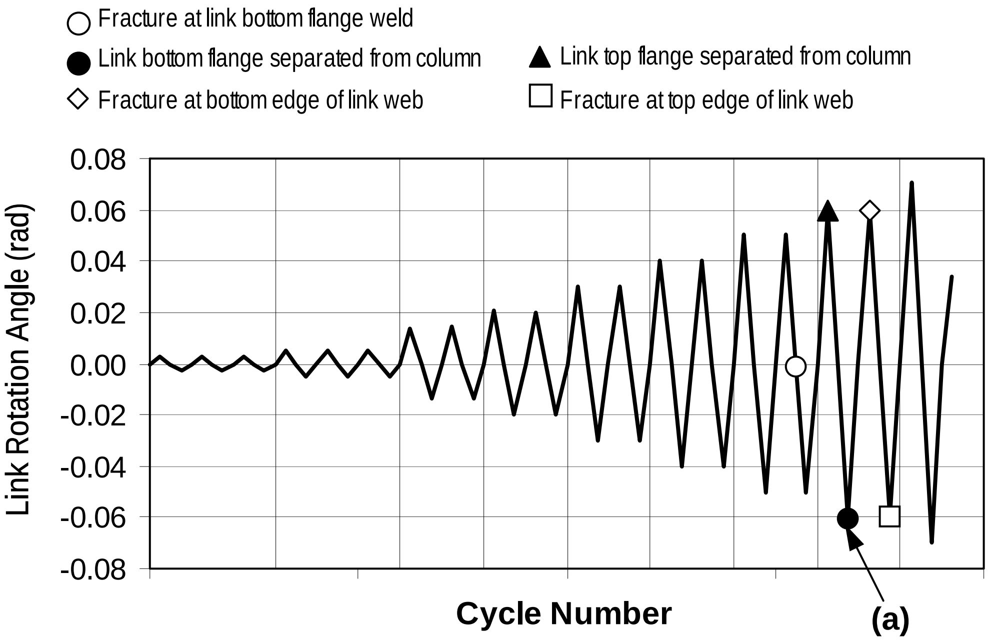

(a) Loading History

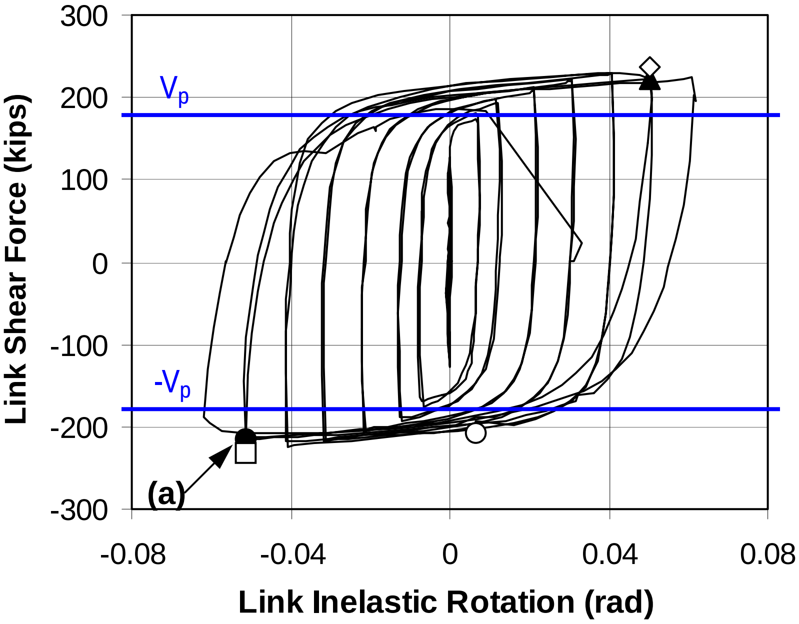

(b) Link Shear vs. Inelastic Rotation Angle

Figure 4.2 Response of Specimen PNS

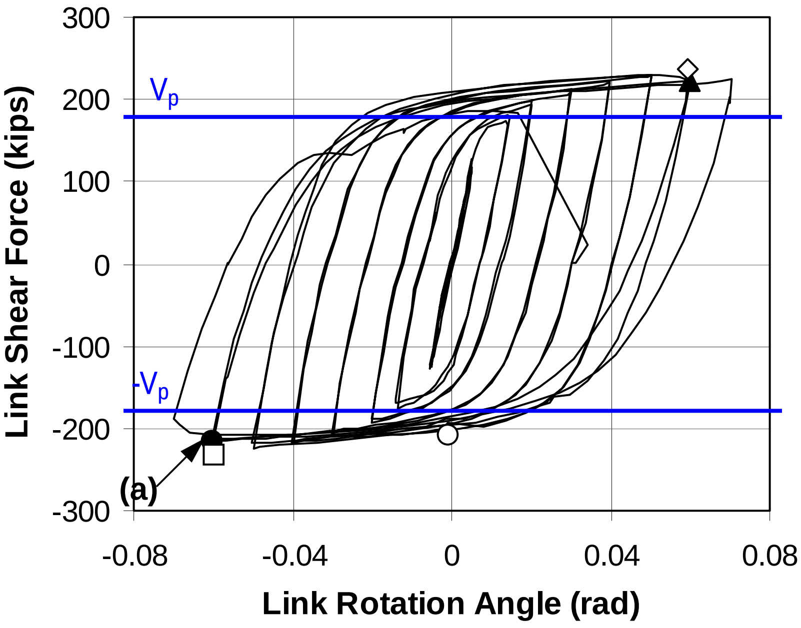

(c) Link Shear vs. Rotation Angle

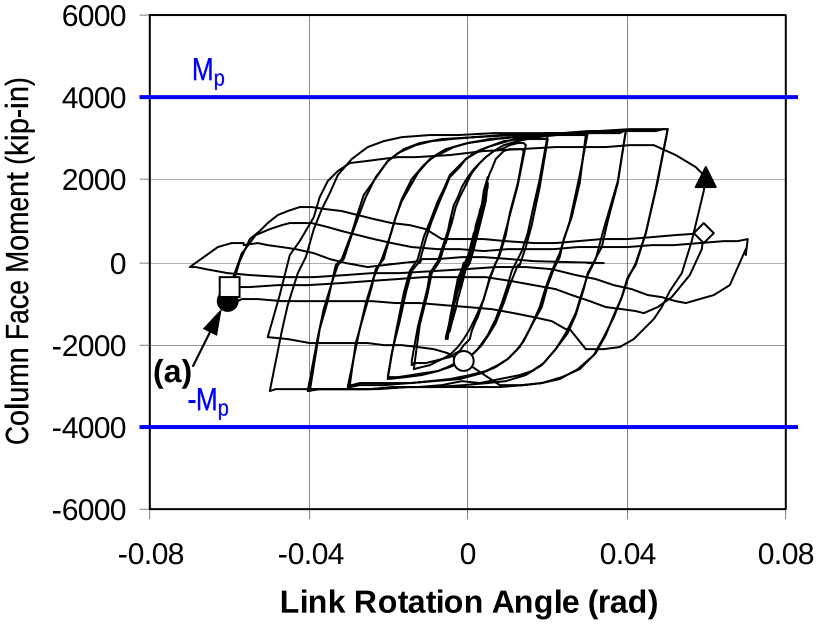

(d) Column Face Moment vs. Rotation Angle

Figure 4.2 Response of Specimen PNS (Continued)

(a) Fracture in link bottom flange weld (0.05-2N)

(b) Link and panel zone after test

Figure 4.3 Photographs of Specimen PNS

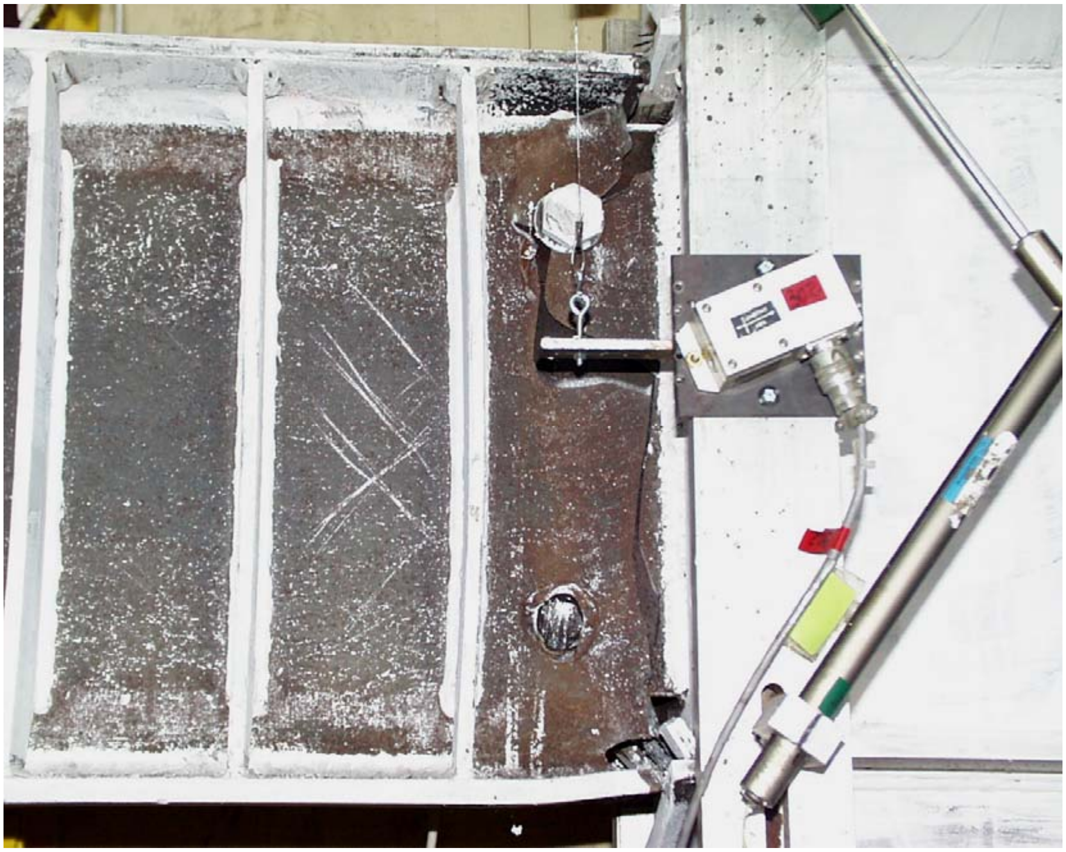

(c) Link-to-column connection after test

Figure 4.3 Photographs of Specimen PNS (Continued)

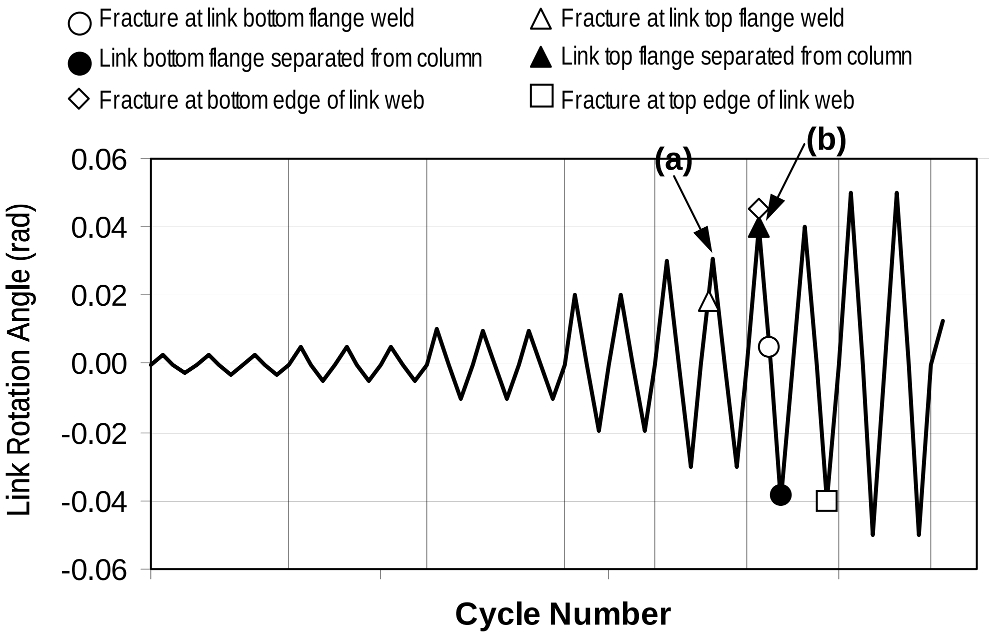

(a) Loading History

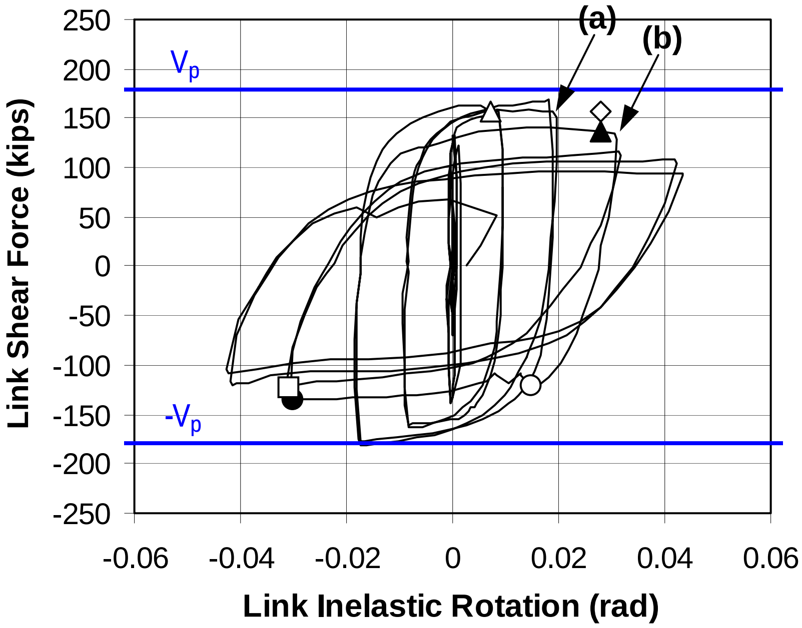

(b) Link Shear vs. Inelastic Rotation Angle

Figure 4.4 Response of Specimen PNI

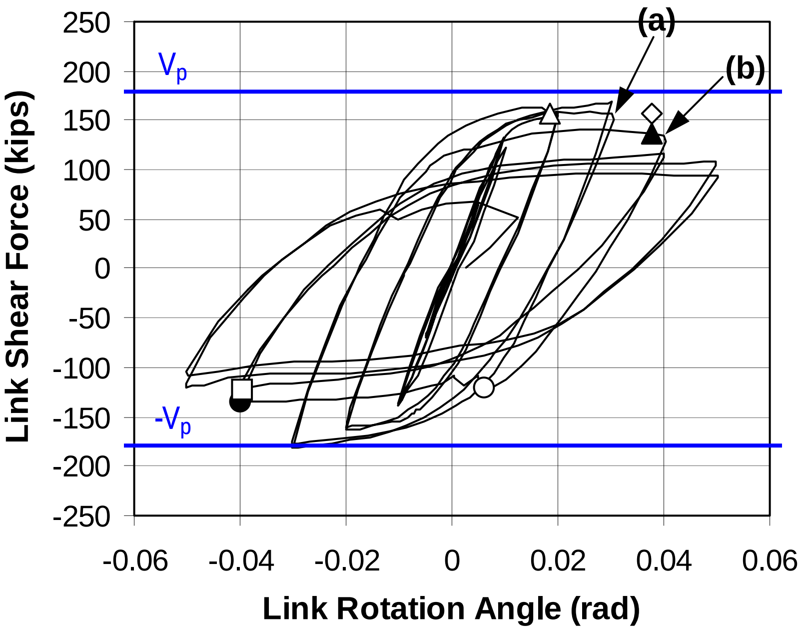

(c) Link Shear vs. Rotation Angle

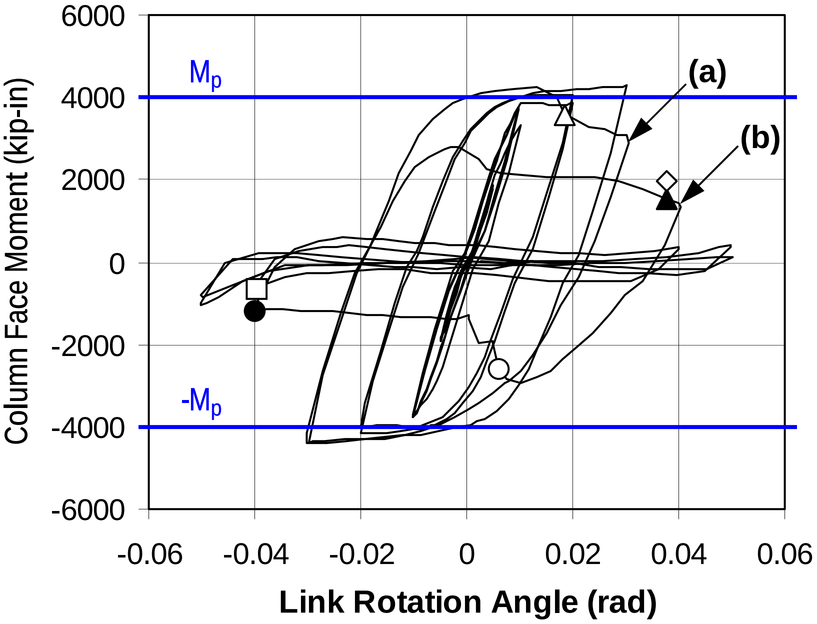

(d) Column Face Moment vs. Rotation Angle

Figure 4.4 Response of Specimen PNI (Continued)

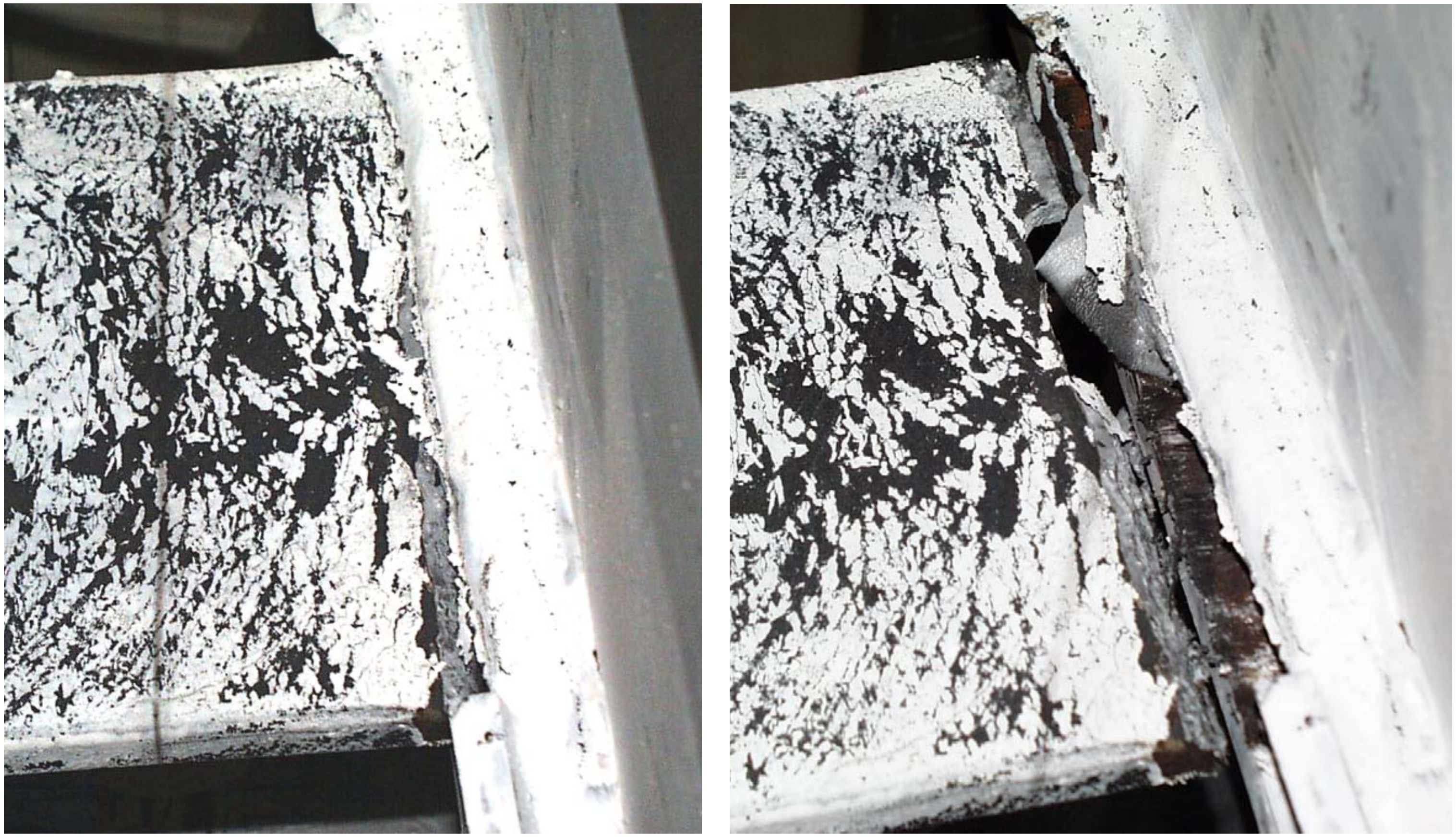

(a) Fracture in link top flange (0.03-2P)

(b) Link top flange separated from column flange (0.04-1P)

Figure 4.5 Photographs of Specimen PNI

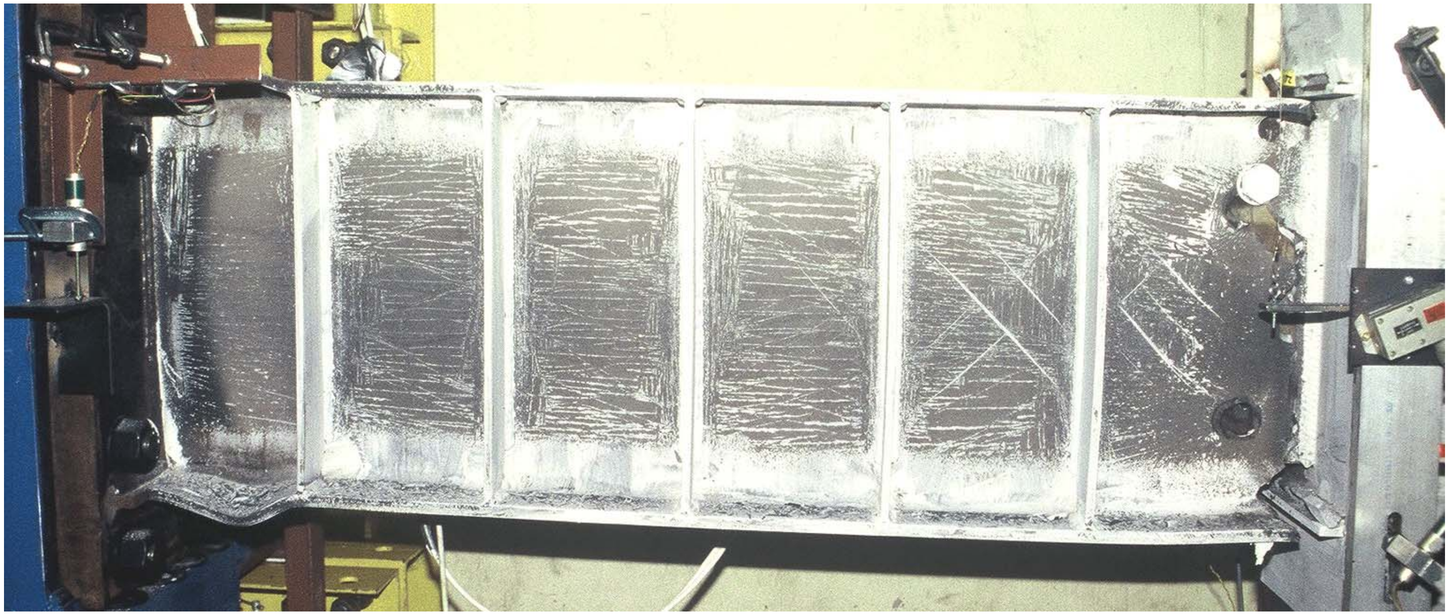

(c) Link after test

Figure 4.5 Photographs of Specimen PNI (Continued)

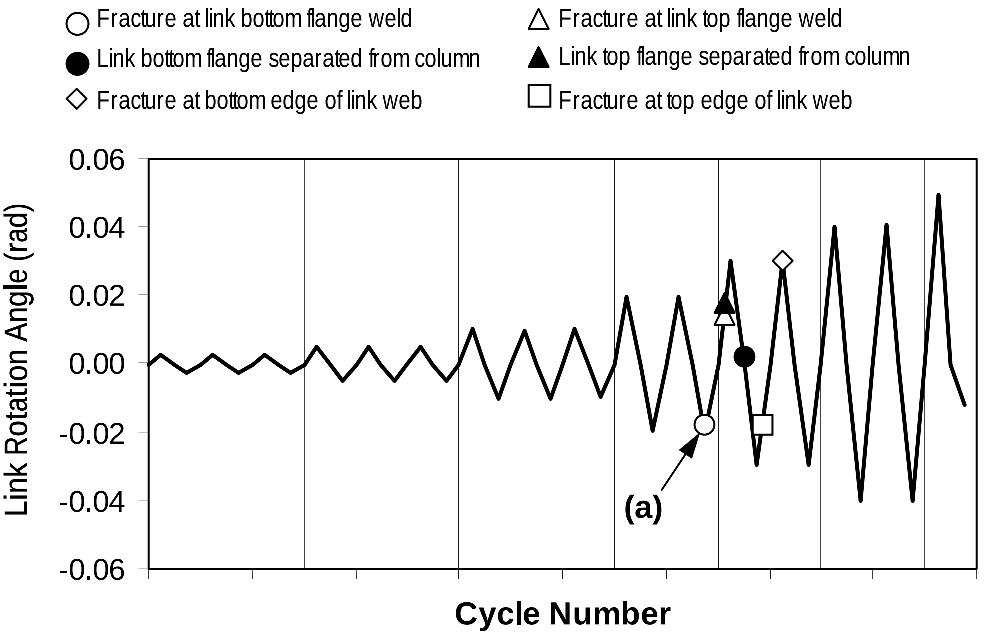

(a) Loading History

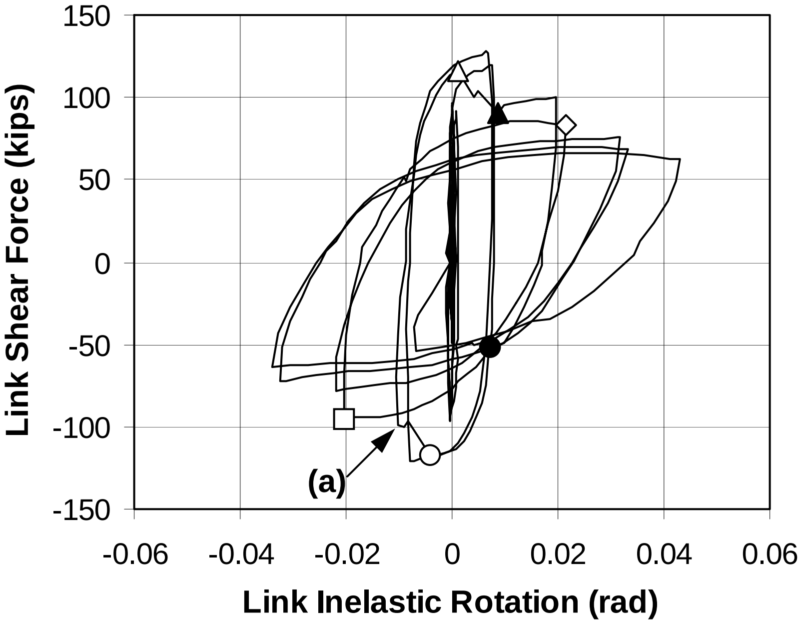

(b) Link Shear vs. Inelastic Rotation Angle

Figure 4.6 Response of Specimen PNM

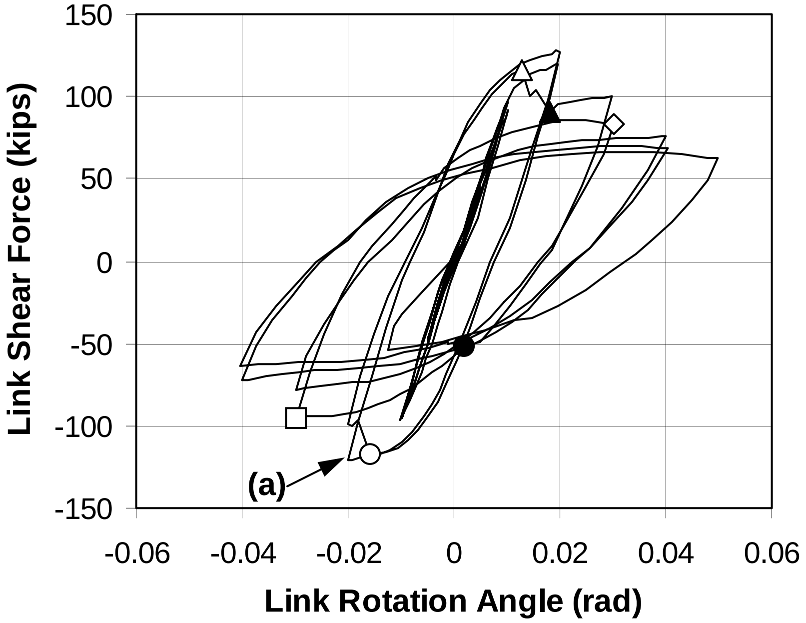

(c) Link Shear vs. Rotation Angle

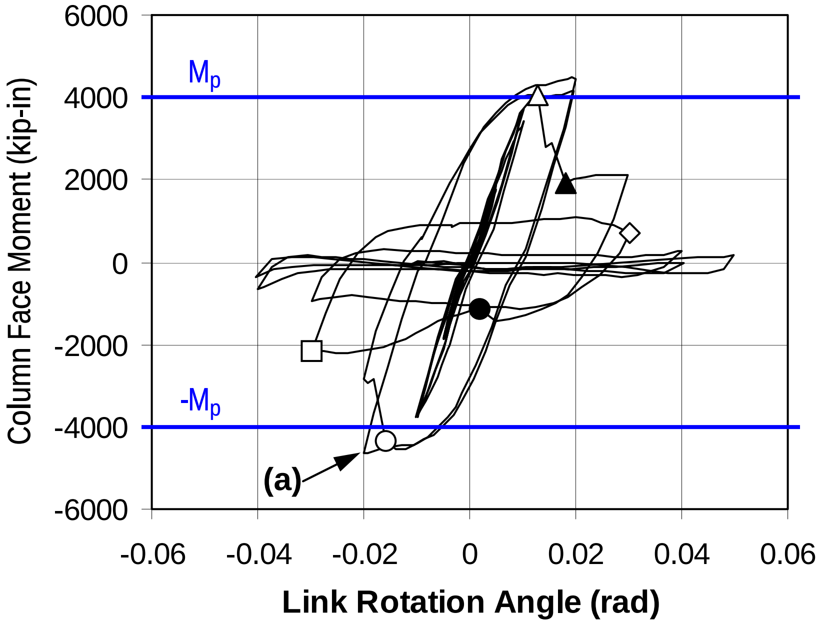

(d) Column Face Moment vs. Rotation Angle

Figure 4.6 Response of Specimen PNM (Continued)

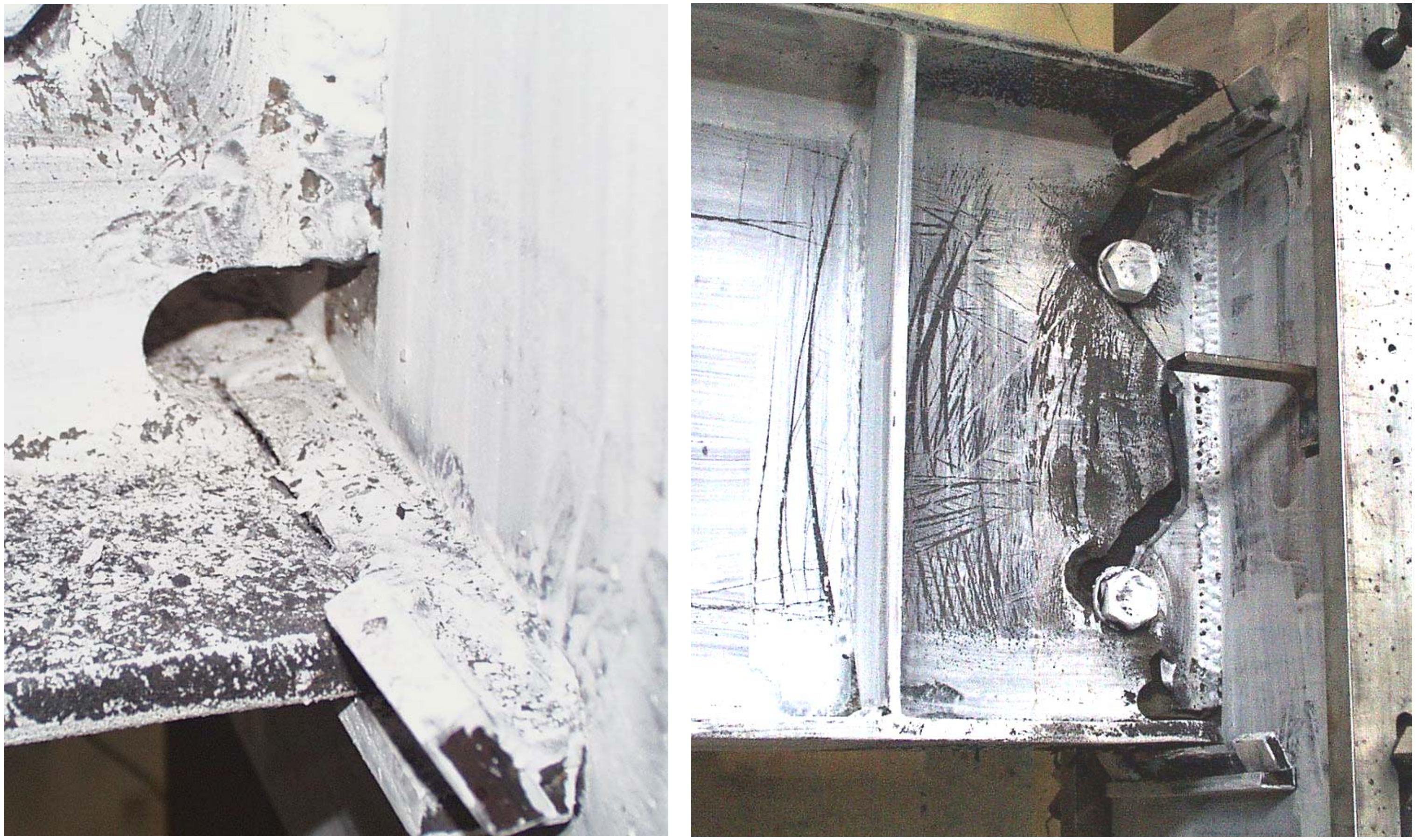

(a) Fracture in link bottom flange (0.02-2N)

(b) Link-to-column connection after test

Figure 4.7 Photographs of Specimen PNM.

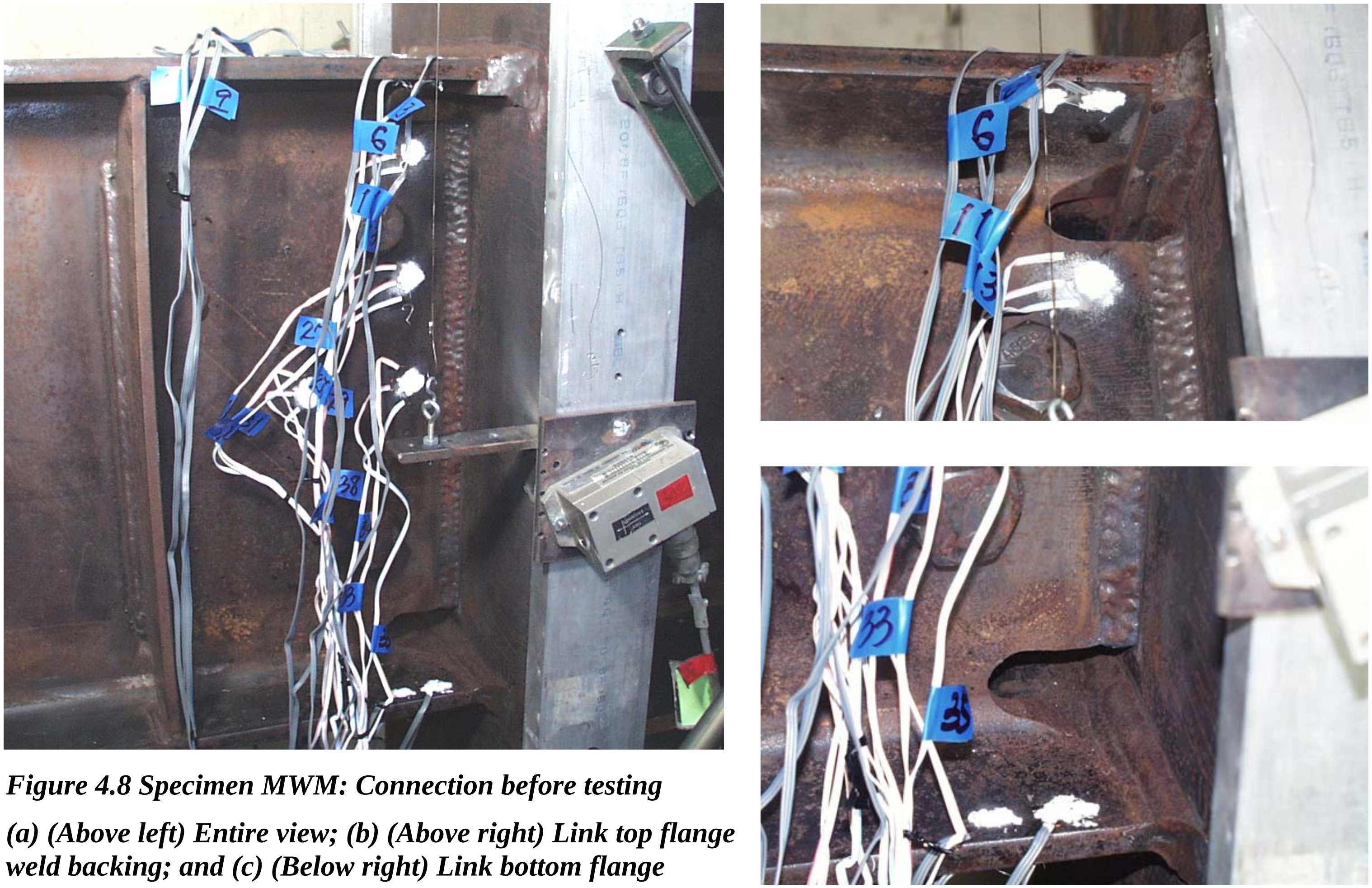

Figure 4.8 Specimen MWM: Connection before testing

(a) (Above left) Entire view; (b) (Above right) Link top flange weld backing; and (c) (Below right) Link bottom flange groove weld.

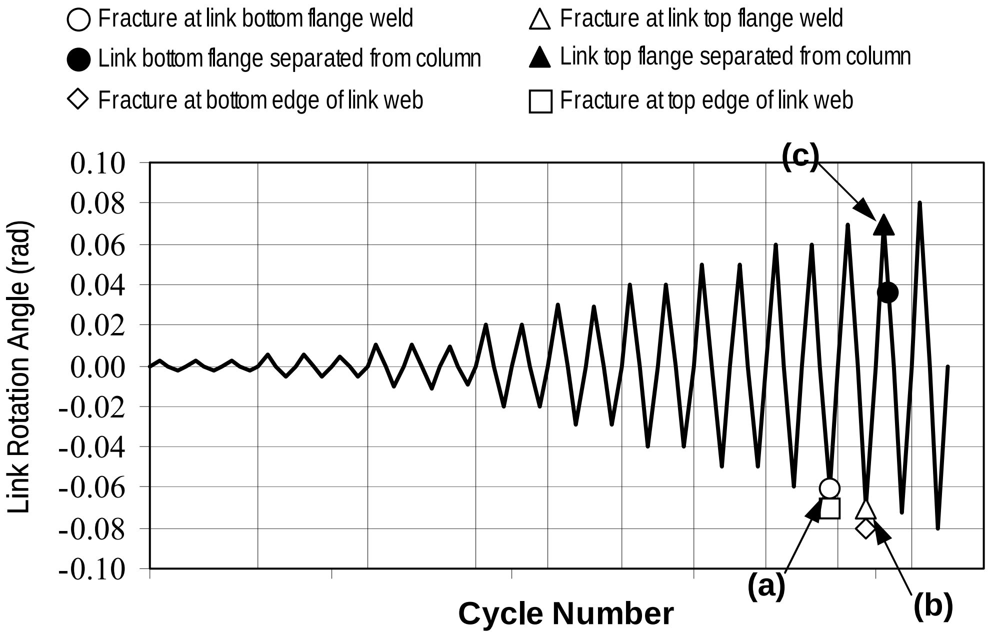

(a) Loading History

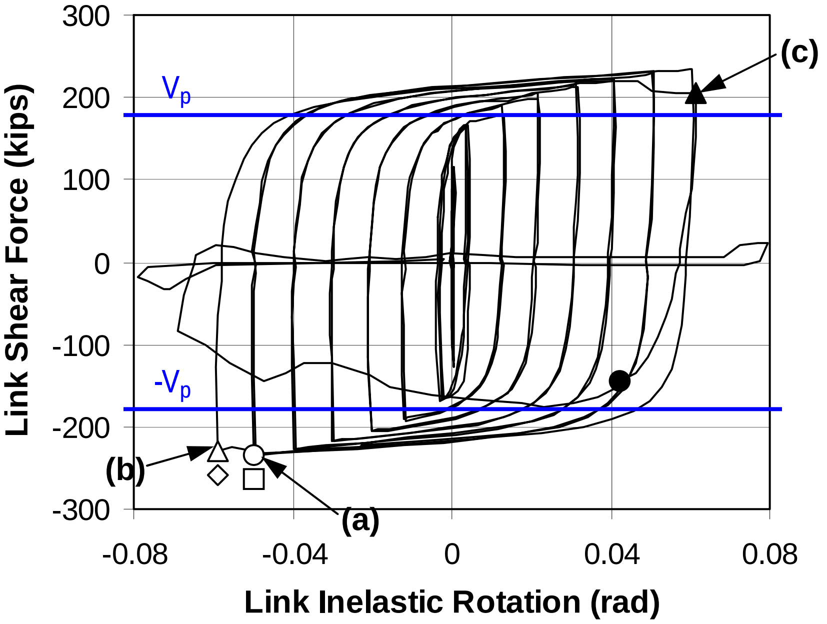

(b) Link Shear vs. Inelastic Rotation Angle

Figure 4.9 Response of Specimen MWS

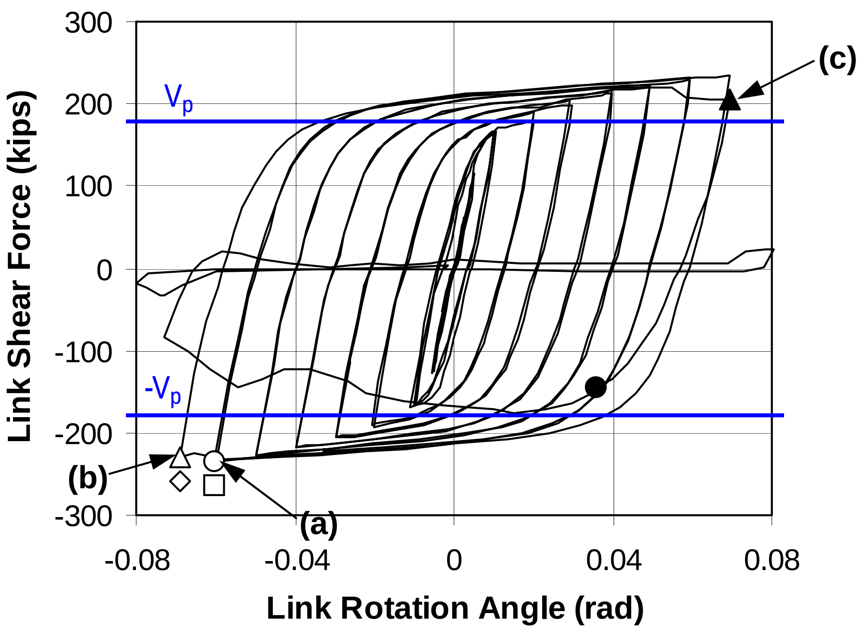

(c) Link Shear vs. Rotation Angle

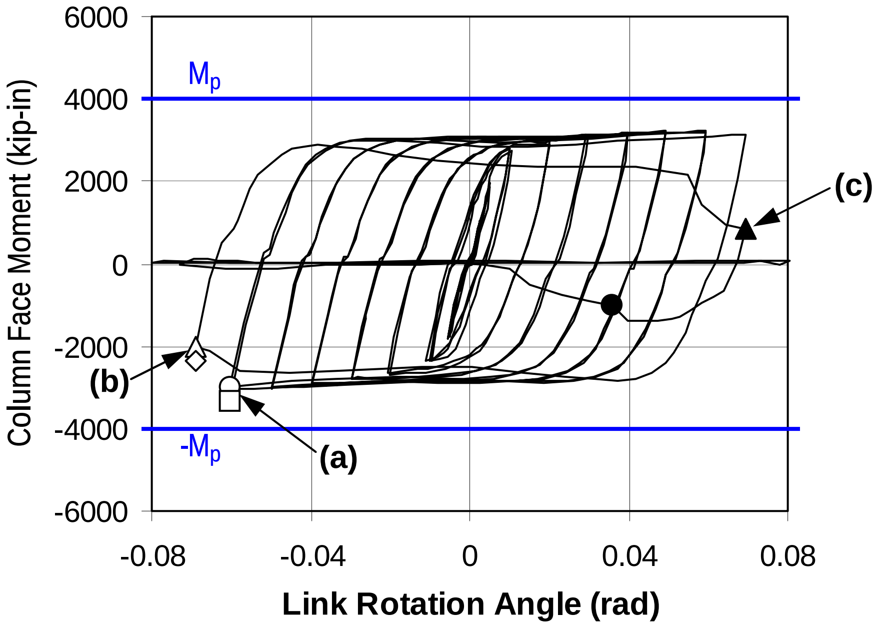

(d) Column Face Moment vs. Rotation Angle

Figure 4.9 Response of Specimen MWS (Continued)

(a) Fracture in link bottom flange (0.06-2N)

(b) Fracture at bottom edge of link web (0.07-1N)

Figure 4.10 Photographs of Specimen MWS

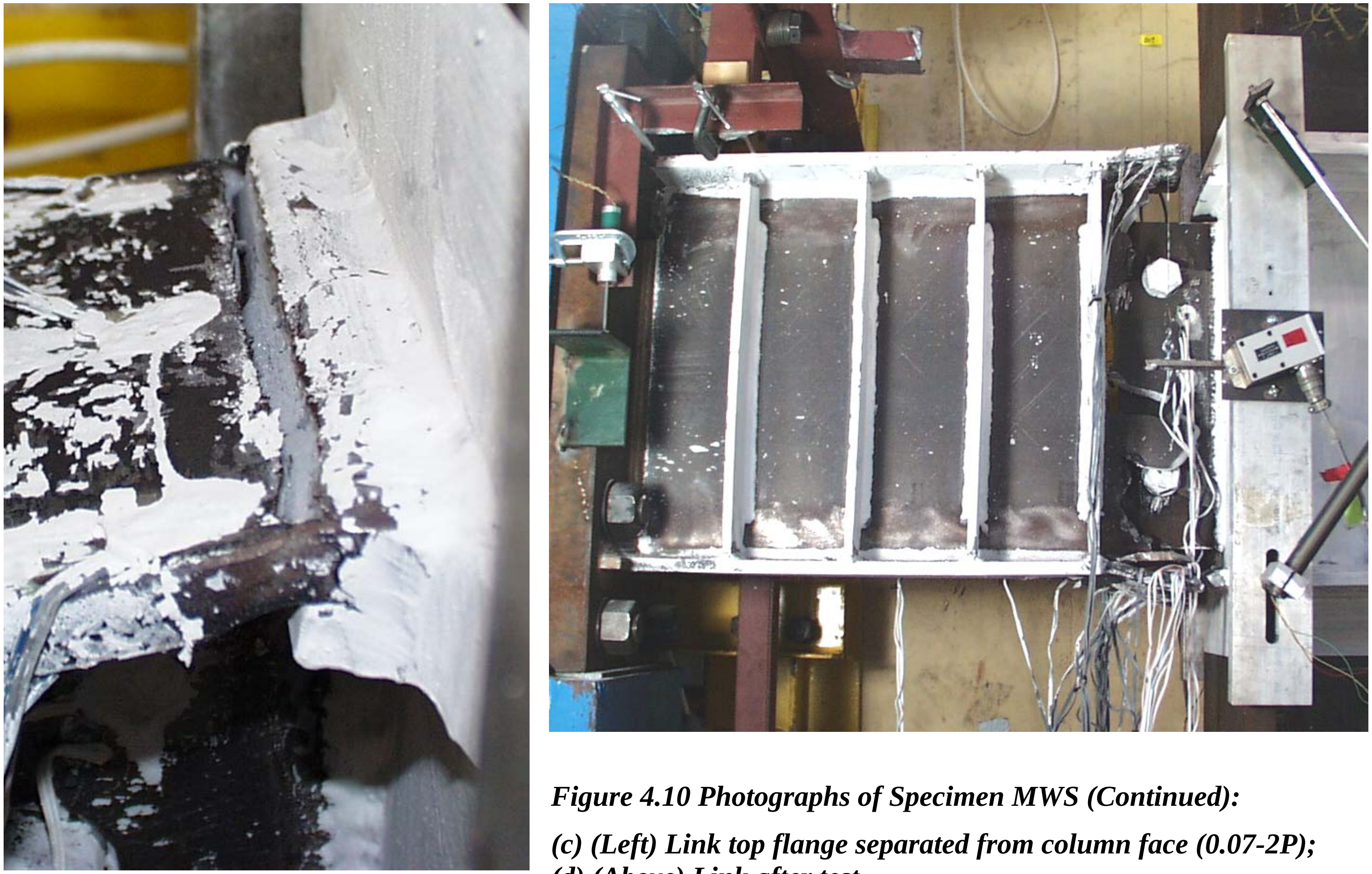

Figure 4.10 Photographs of Specimen MWS (Continued):

(c) (Left) Link top flange separated from column face (0.07-2P);
(d) (Above) Link after test.

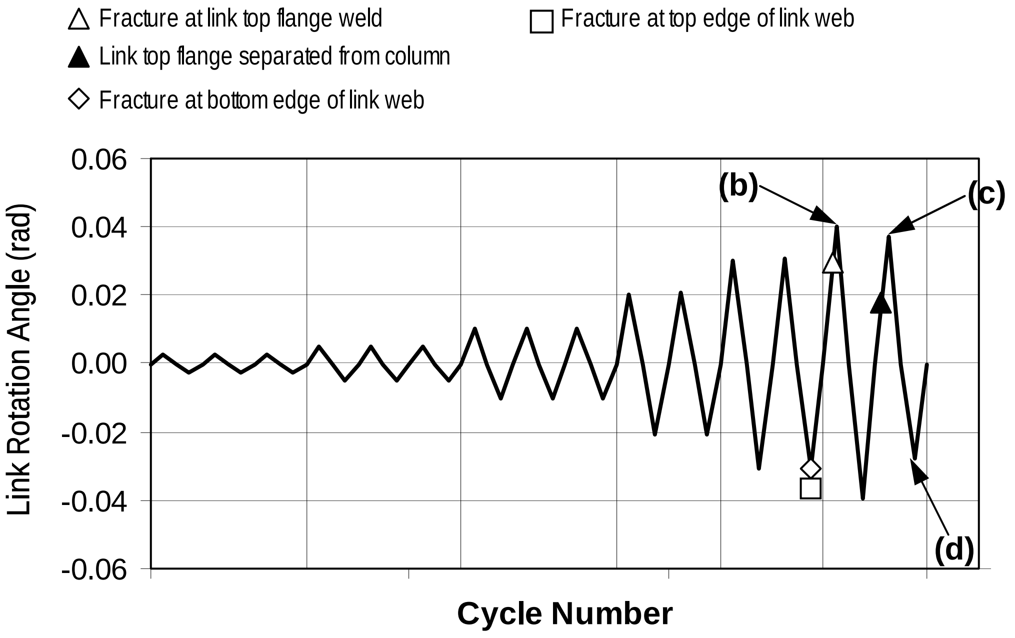

(a) Loading History

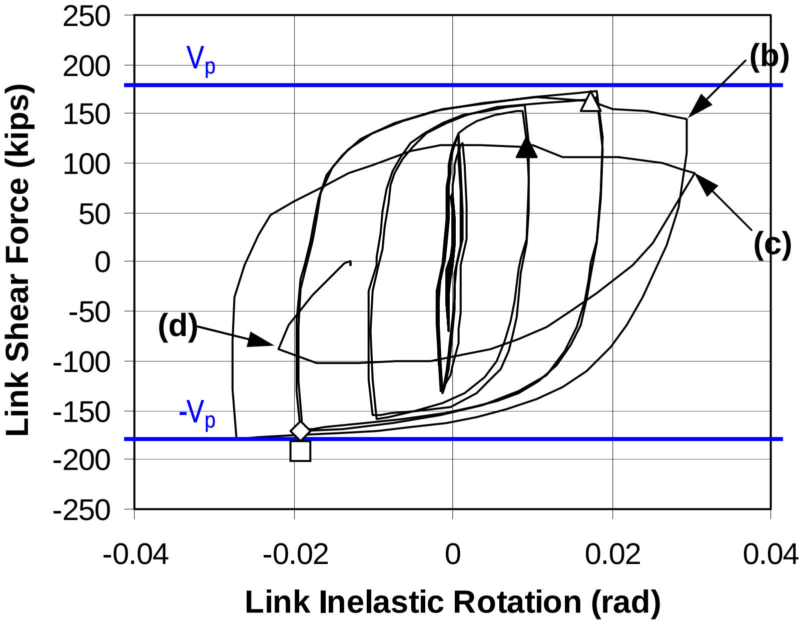

(b) Link Shear vs. Inelastic Rotation Angle

Figure 4.11 Response of Specimen MWI

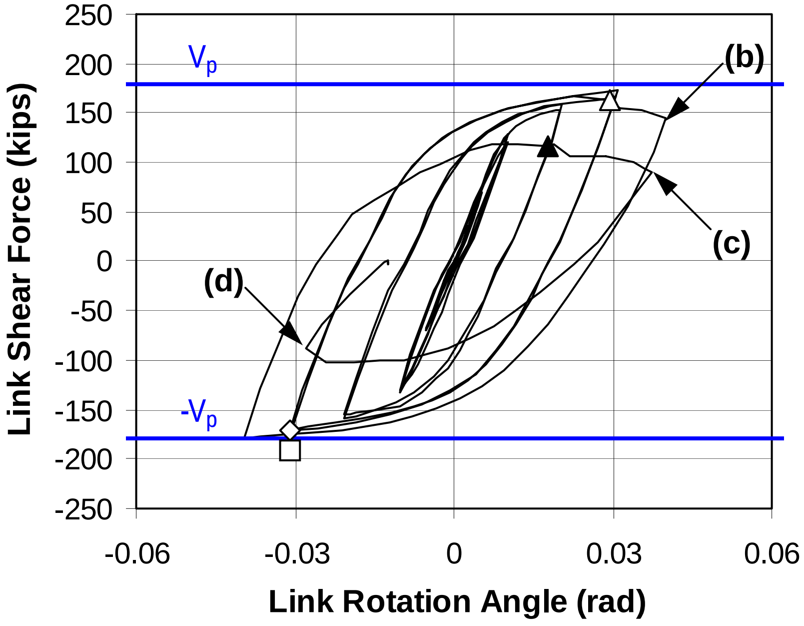

(c) Link Shear vs. Rotation Angle

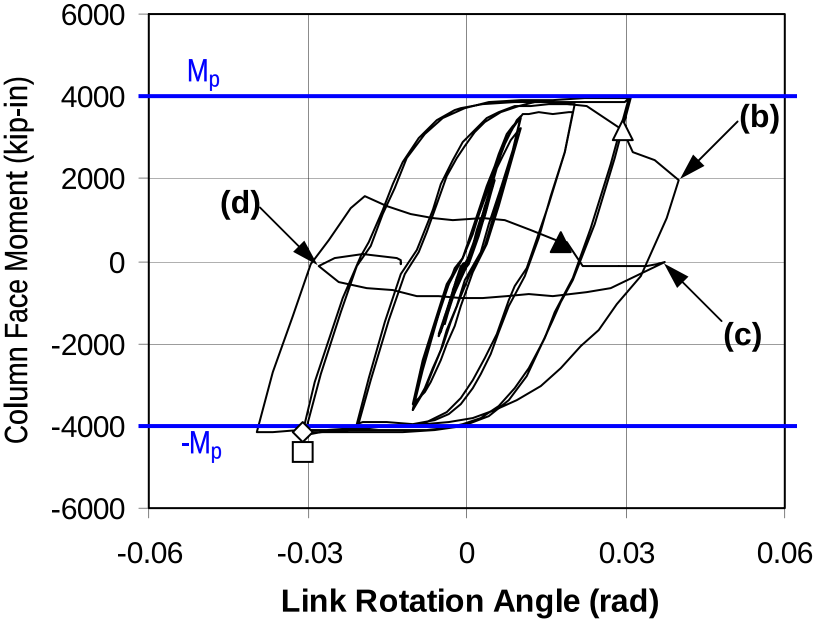

(d) Column Face Moment vs. Rotation Angle

Figure 4.11 Response of Specimen MWI (Continued)

(a) Initial imperfection visible at beam end of link

(b) Fracture in link top flange (0.04-1P)

Figure 4.12 Photographs from MWI

(c) Torsional deformation of link viewed from above the link (0.04-2N).

(d) Fracture in link web surrounding bottom weld access hole (0.04-2N).

Figure 4.12 Photographs from MWI (Continued)

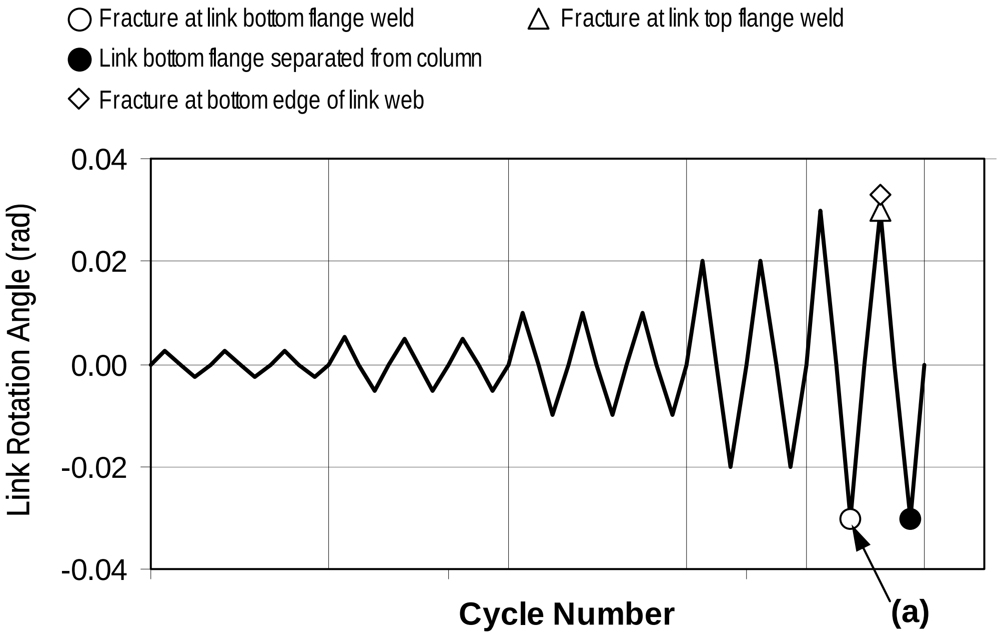

(a) Loading History

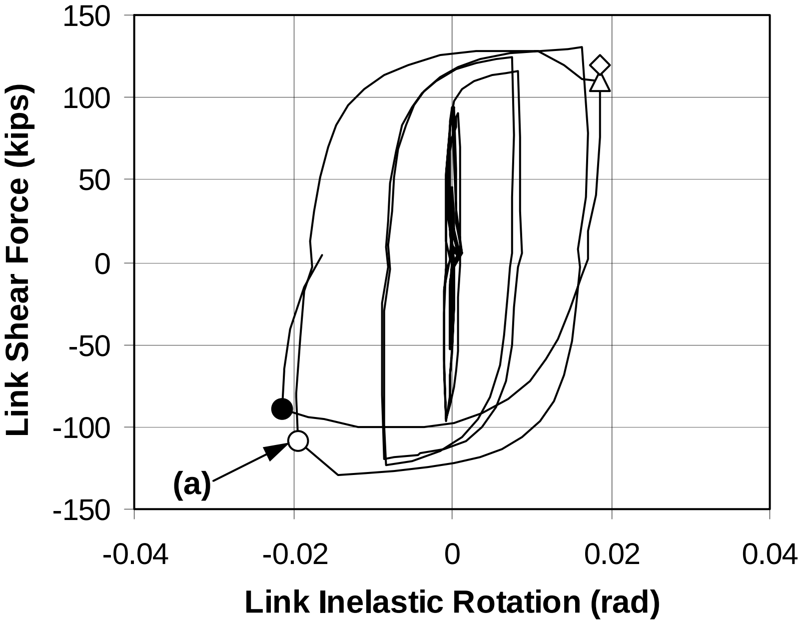

(b) Link Shear vs. Inelastic Rotation Angle

Figure 4.13 Response of Specimen MWM

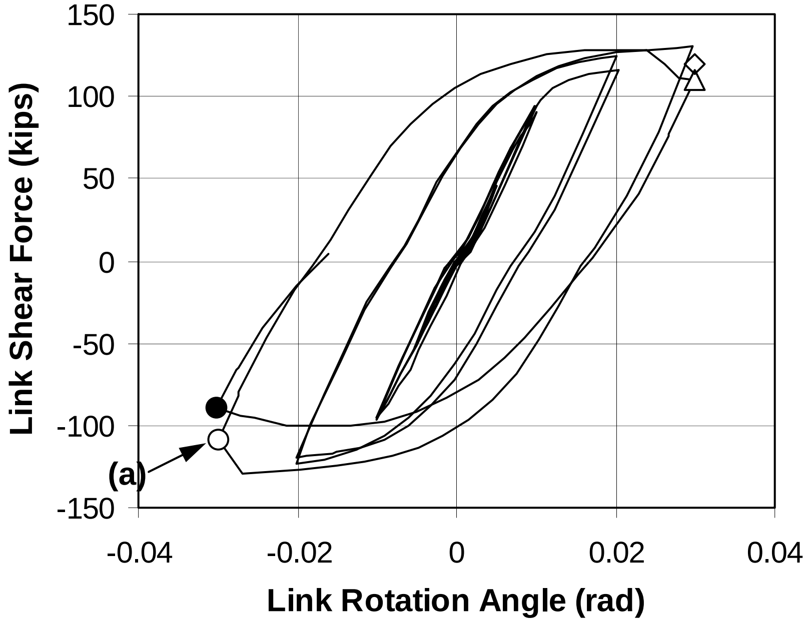

(c) Link Shear vs. Rotation Angle

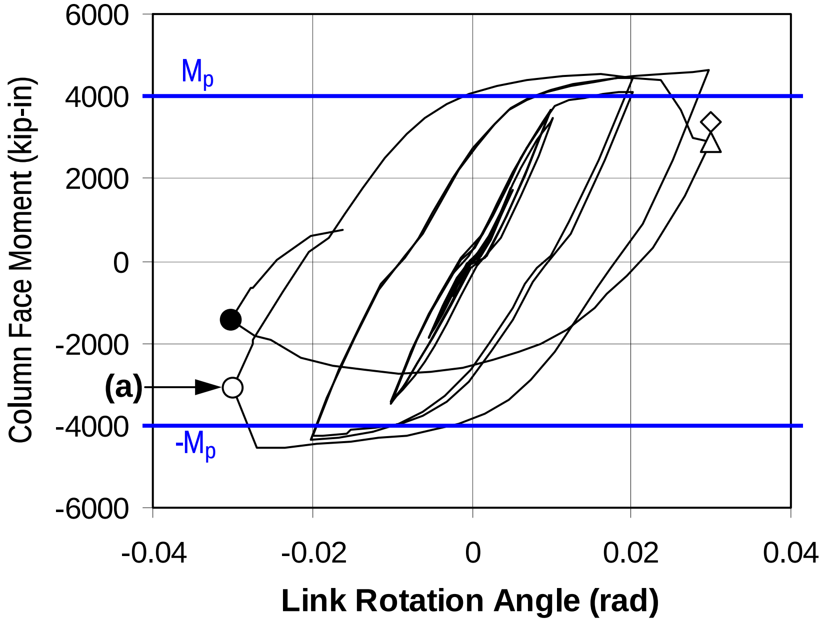

(d) Column Face Moment vs. Rotation Angle

Figure 4.13 Response of Specimen MWM (Continued)

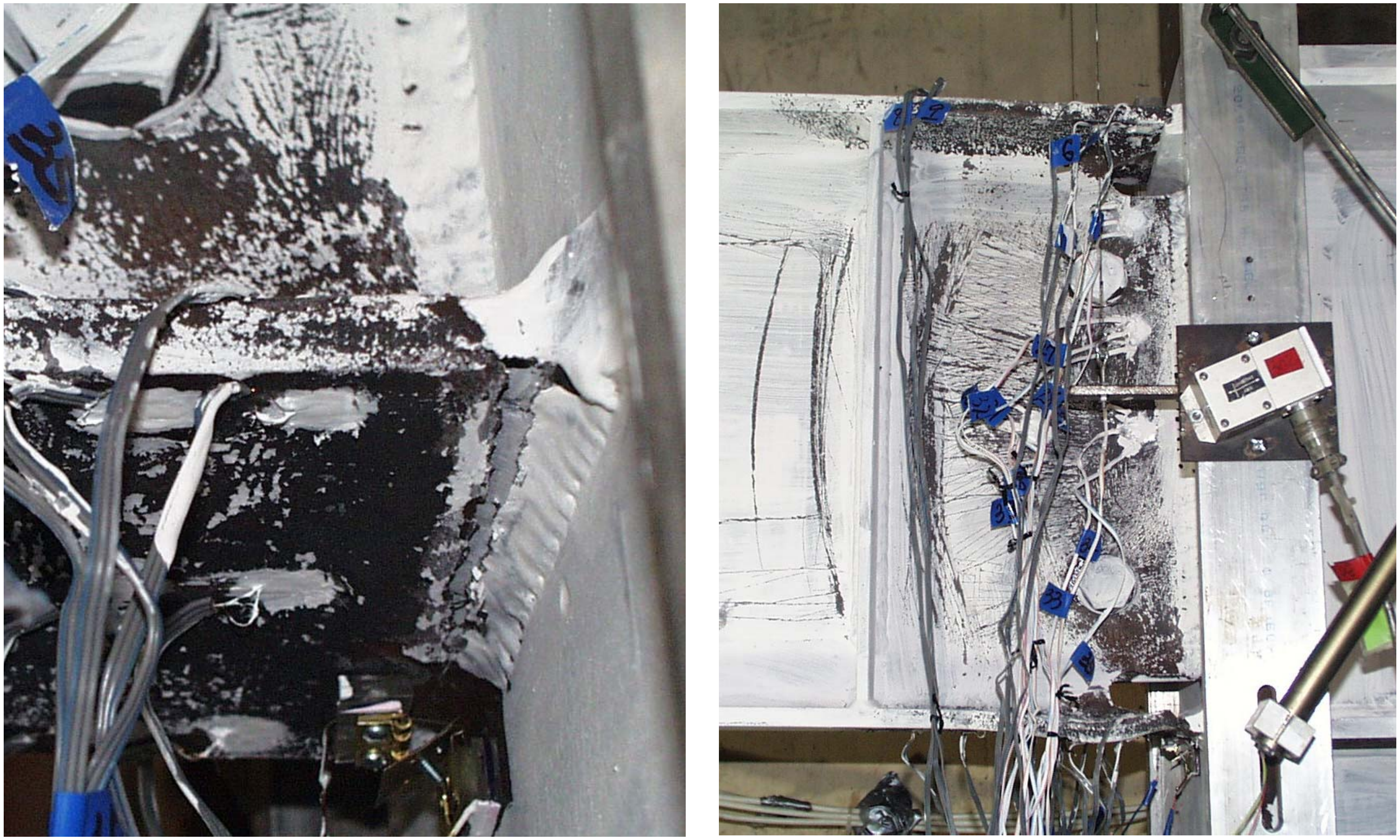

(a) Fracture in link bottom flange (0.03-1N) ***(b) Link-to-column connection after test***

Figure 4.14 Photographs of Specimen MWM

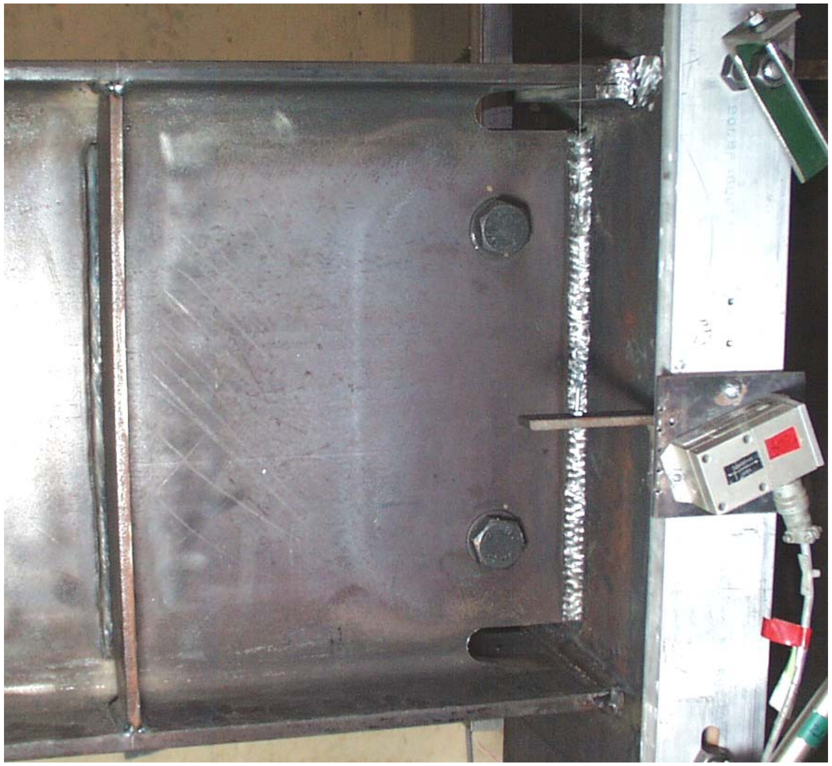

Figure 4.15 Specimen FFI before testing

(a) (Above left) Entire view; (b) (Above right) Link top flange weld backing and reinforcement; and (c) (Below right) link bottom flange groove weld.

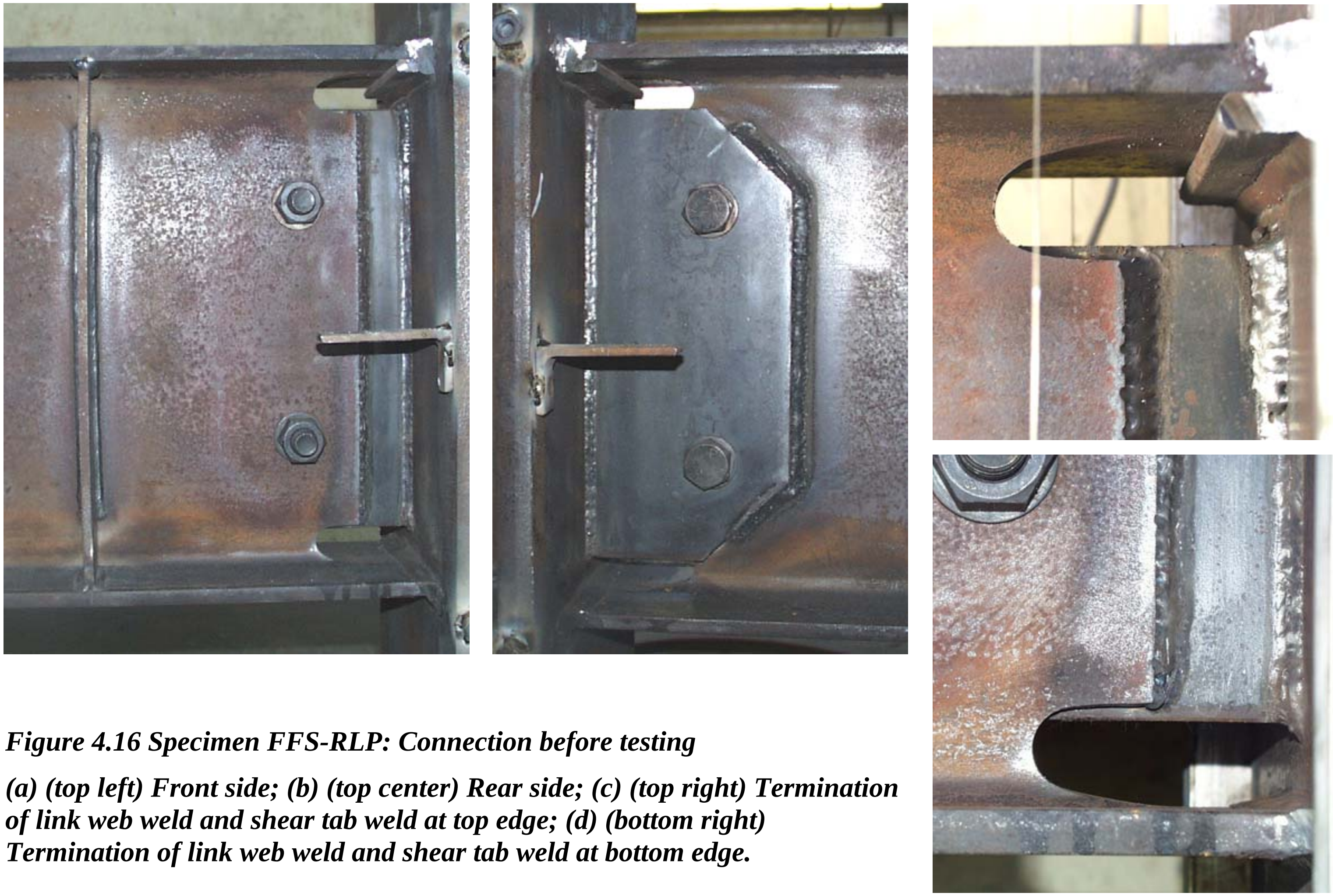

Figure 4.16 Specimen FFS-RLP: Connection before testing

(a) (top left) Front side; (b) (top center) Rear side; (c) (top right) Termination of link web weld and shear tab weld at top edge; (d) (bottom right) Termination of link web weld and shear tab weld at bottom edge.

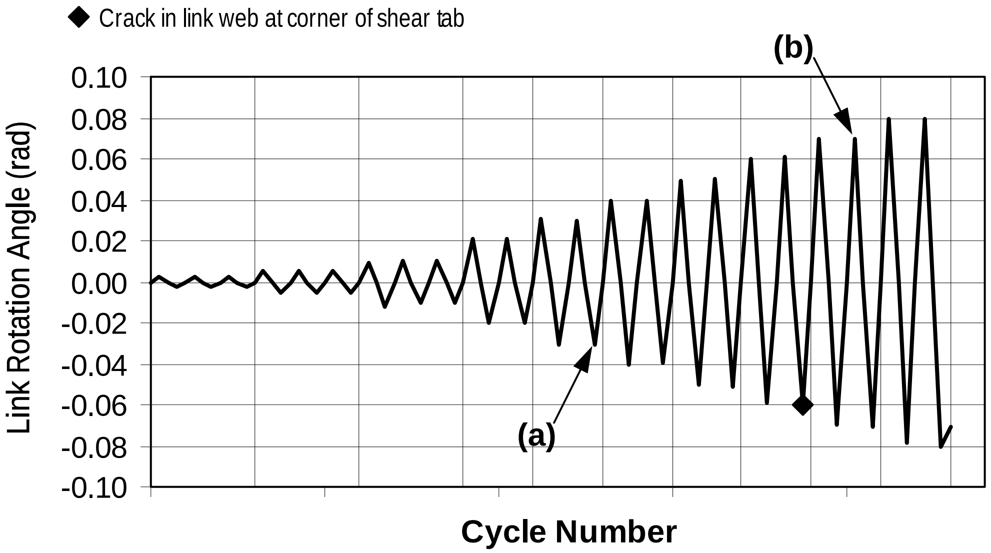

(a) Loading History

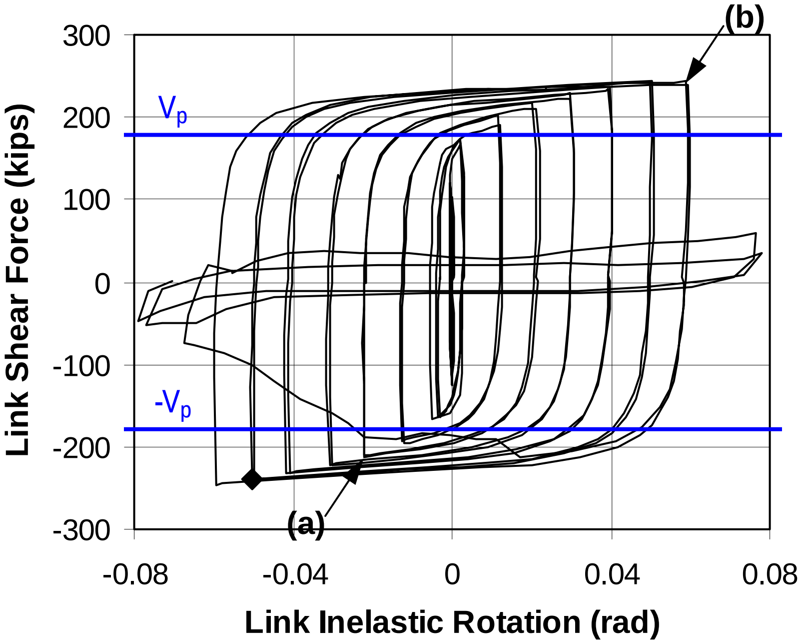

(b) Link Shear vs. Inelastic Rotation Angle

Figure 4.17 Response of Specimen FFS

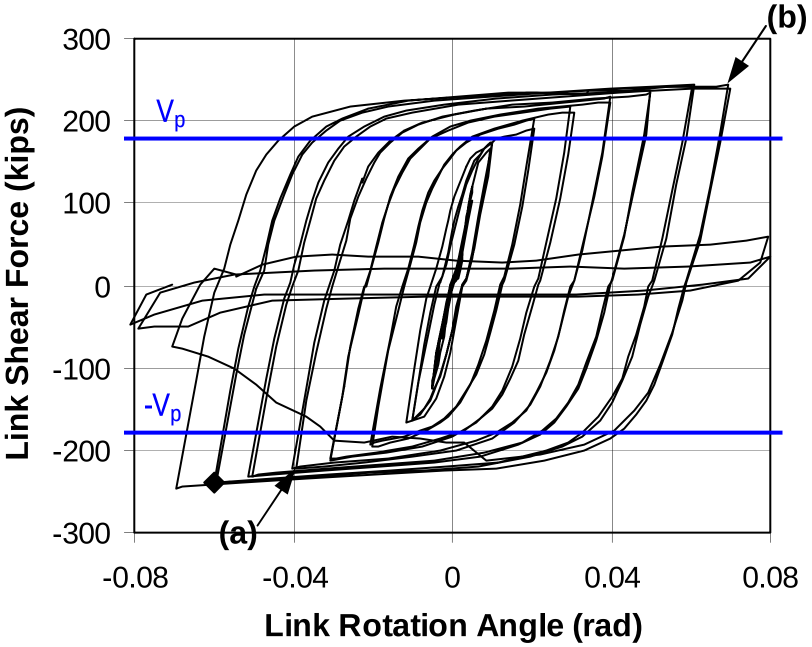

(c) Link Shear vs. Rotation Angle

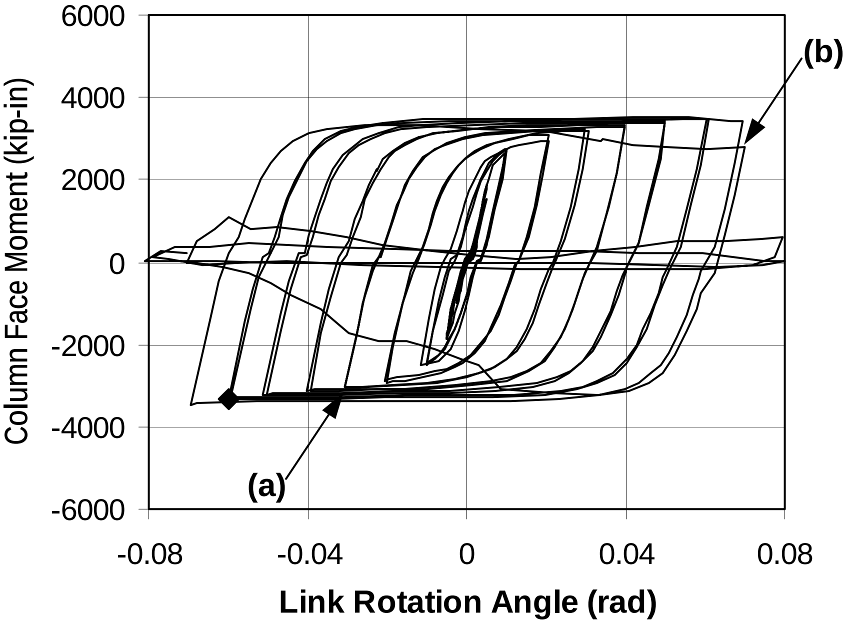

(d) Column Face Moment vs. Rotation Angle

Figure 4.17 Response of Specimen FFS (Continued)

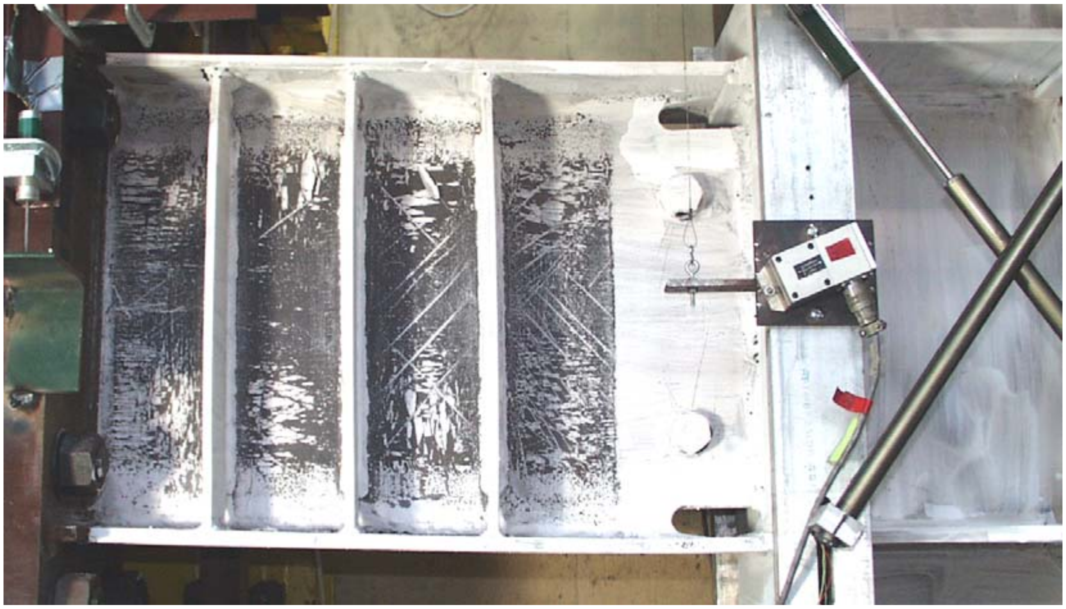

(a) Yielding in link web panels (0.03-2N)

(b) Fracture in link web initiated at corner of shear tab (0.07-2P)

Figure 4.18 Photographs of Specimen FFS

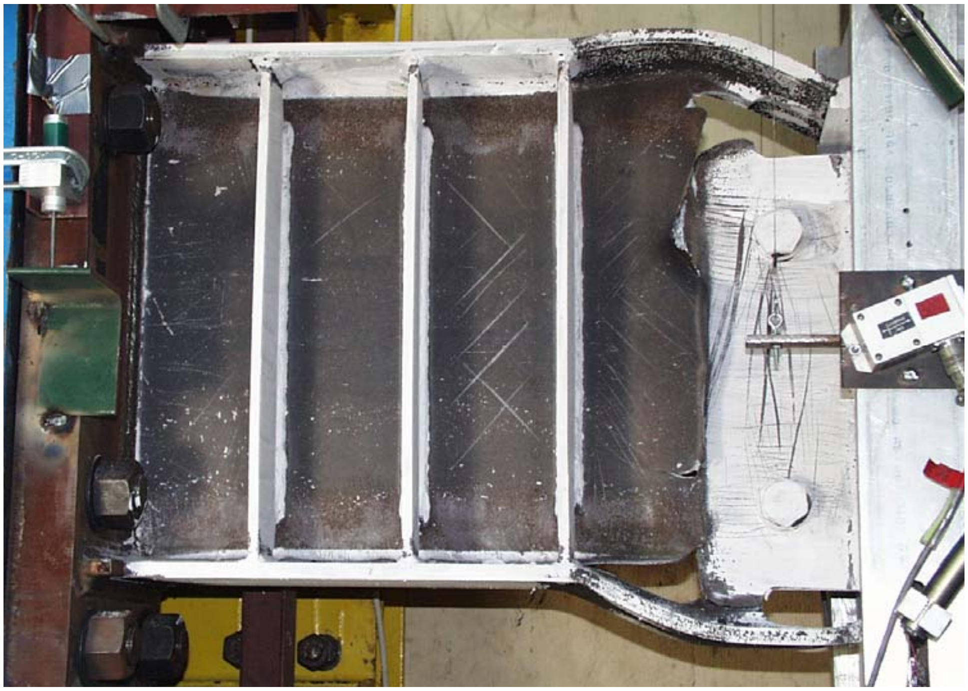

(c) Link after test

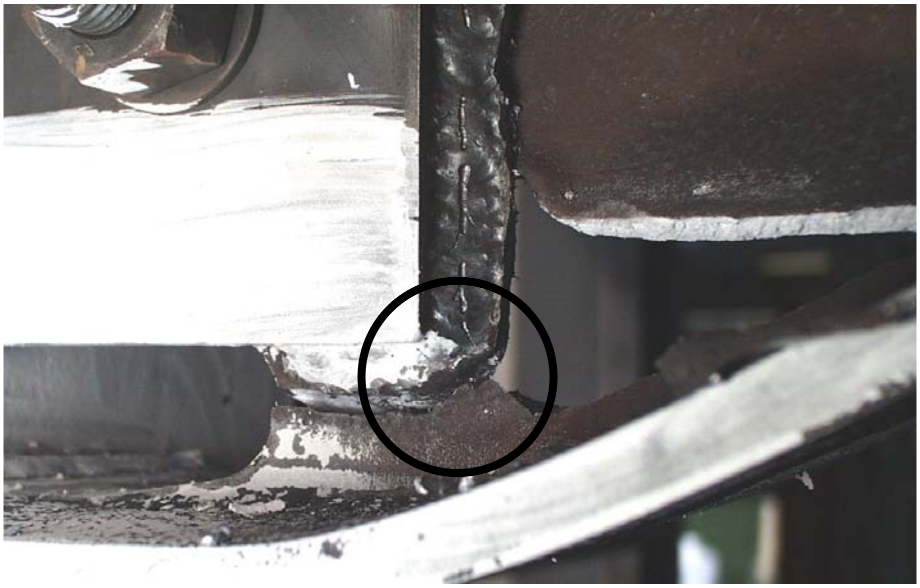

(d) Initiation point of link web fracture (after test)

Figure 4.18 Photographs of Specimen FFS (Continued)

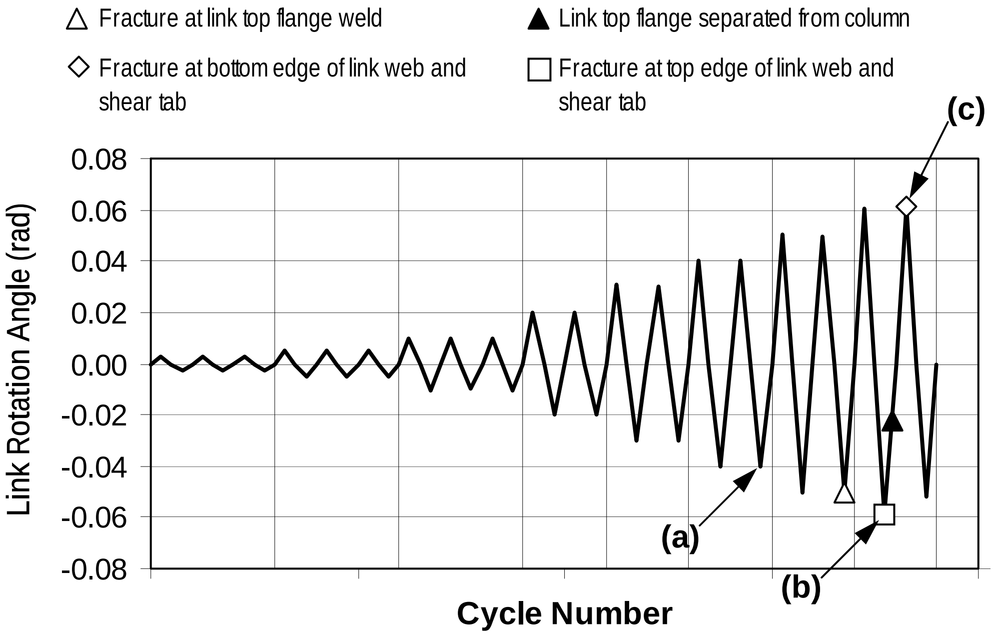

(a) Loading History

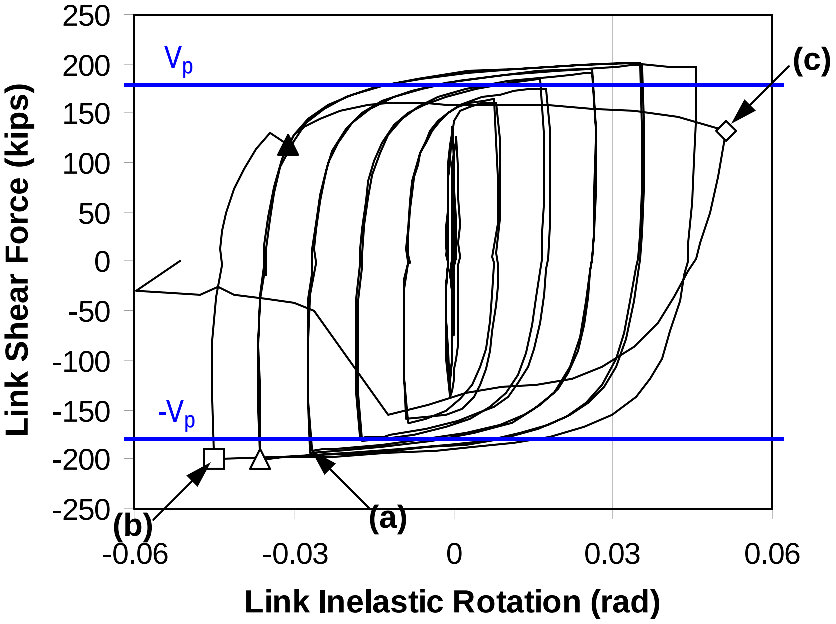

(b) Link Shear vs. Inelastic Rotation Angle

Figure 4.19 Response of Specimen FFI

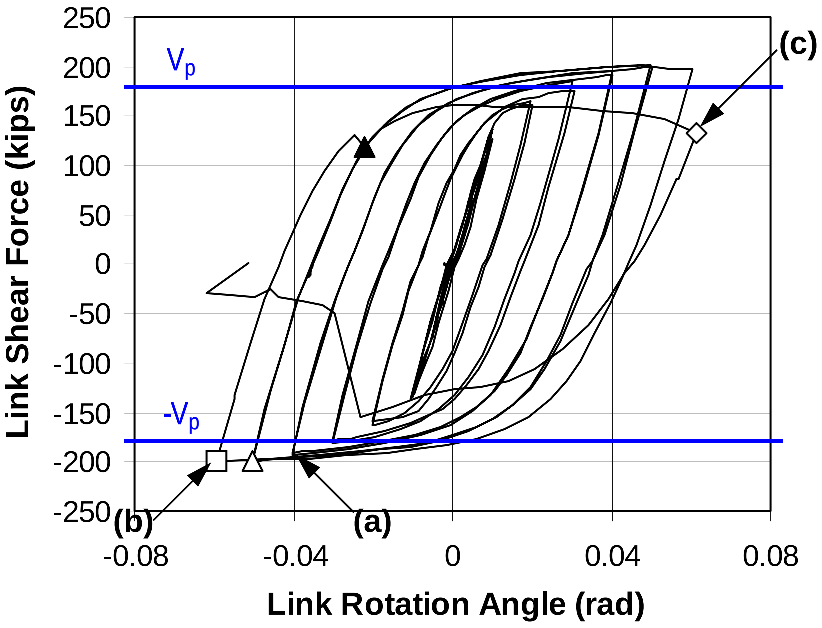

(c) Link Shear vs. Rotation Angle

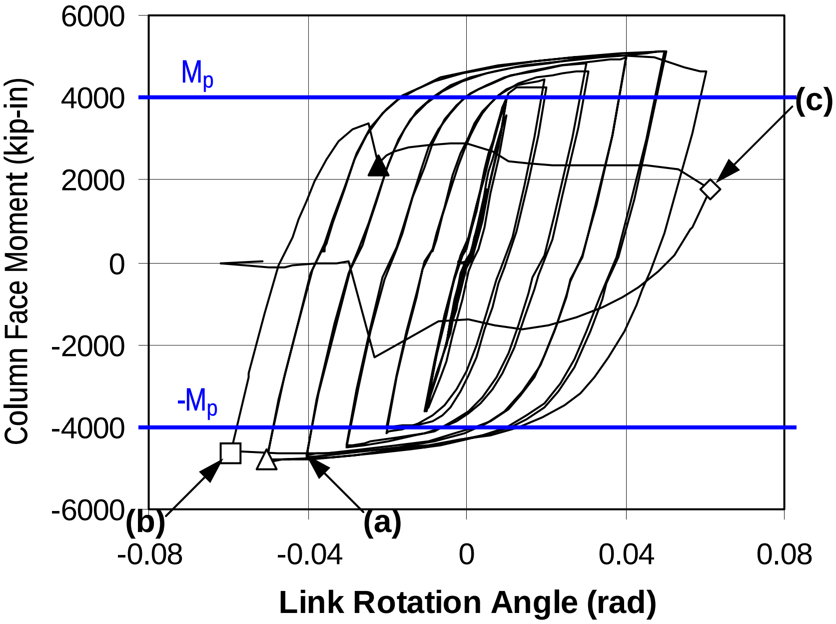

(d) Column Face Moment vs. Rotation Angle

Figure 4.19 Response of Specimen FFI (Continued)

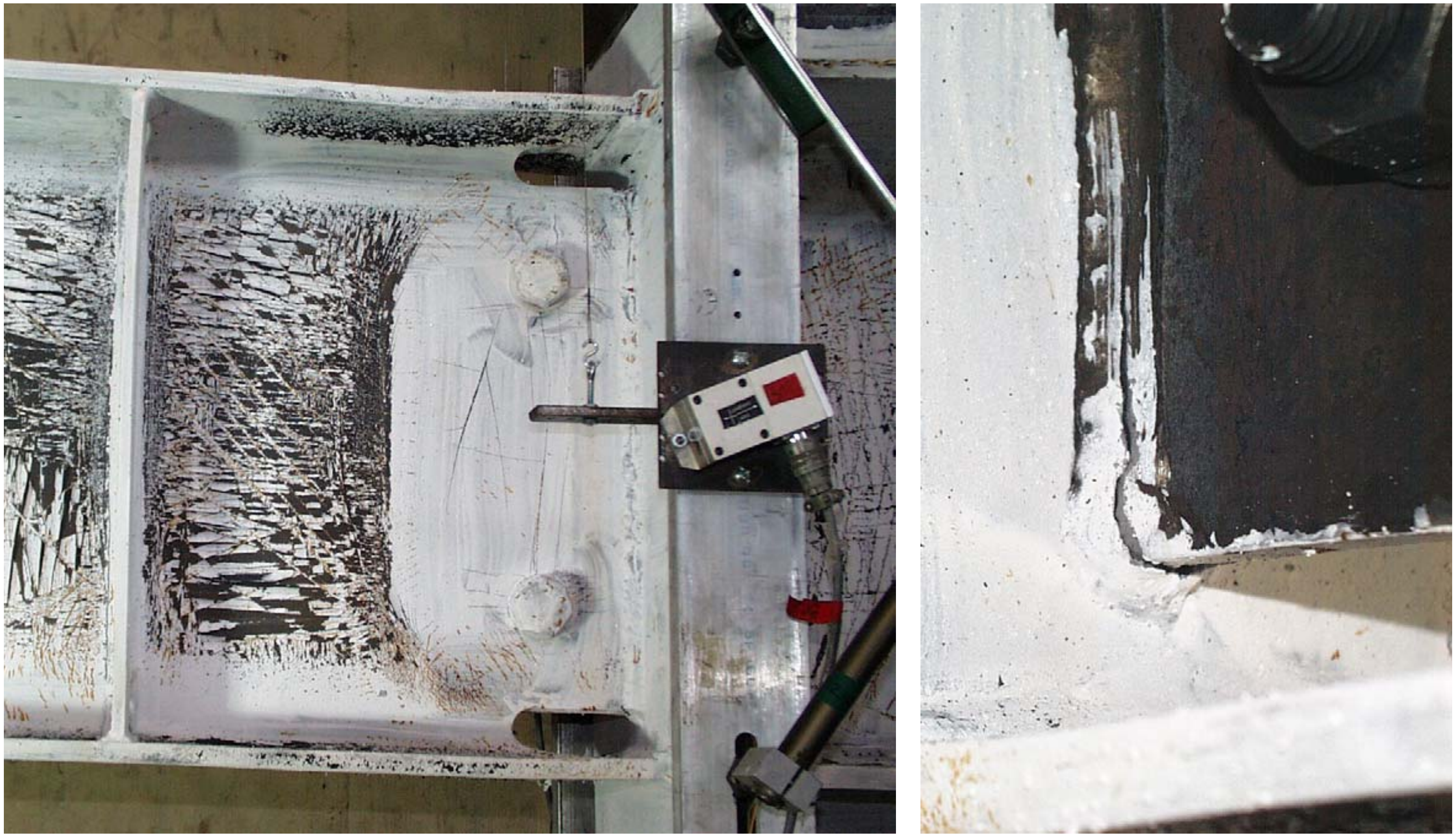

(a) Yielding around shear tab (0.04-2N)

(b) Fracture in bottom edge of shear tab weld (0.06-1N)

Figure 4.20 Photographs of Specimen FFI

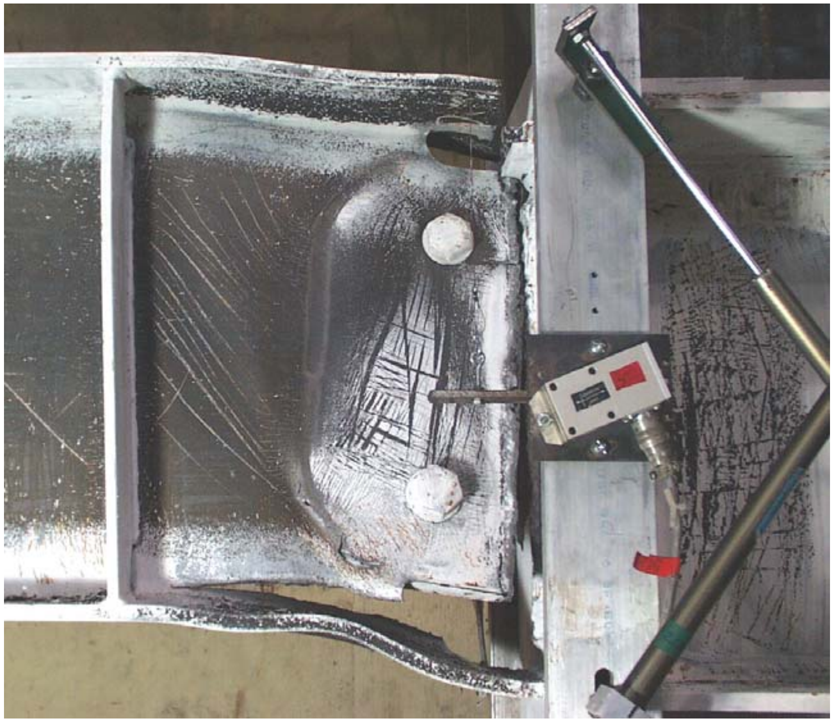

Figure 4.20 Photographs of Specimen FFI (Continued):

(c) (Left) Link top flange separated from column flange (0.06-2P); (d) (Above) Link-to-column connection after test.

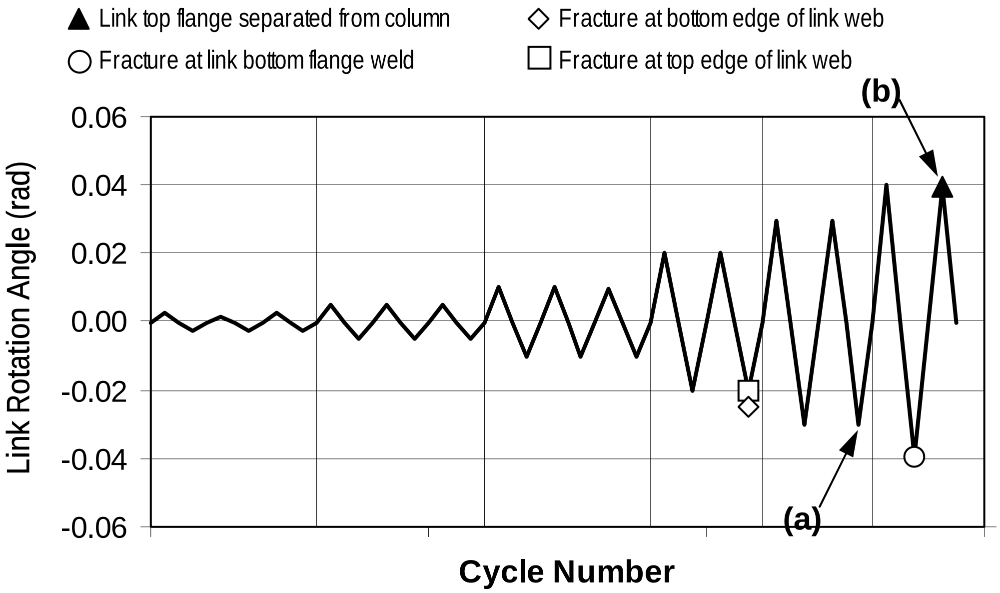

(a) Loading History

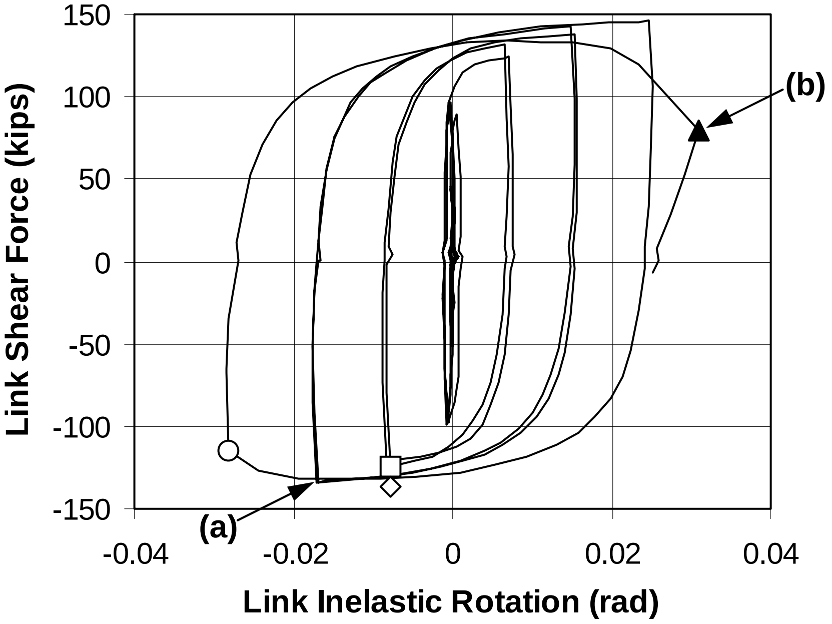

(b) Link Shear vs. Inelastic Rotation Angle

Figure 4.21 Response of Specimen FFM

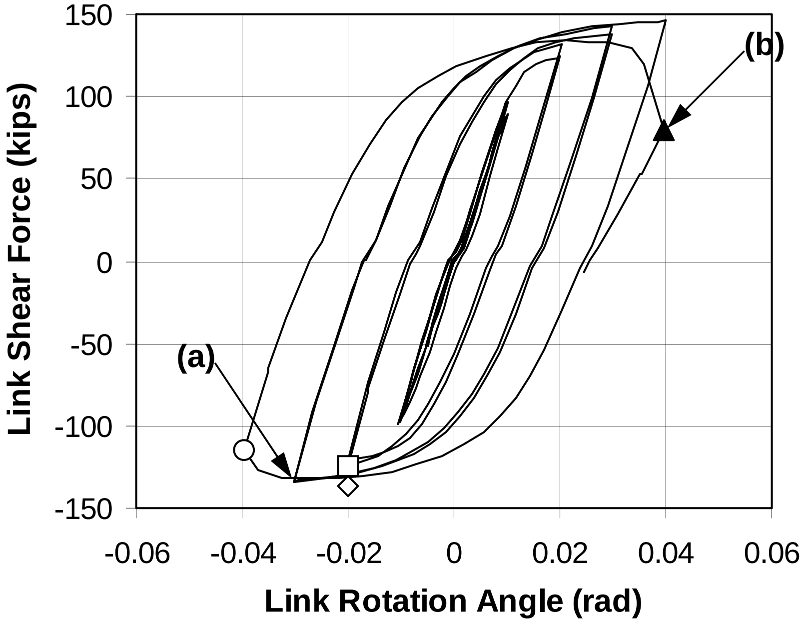

(c) Link Shear vs. Rotation Angle

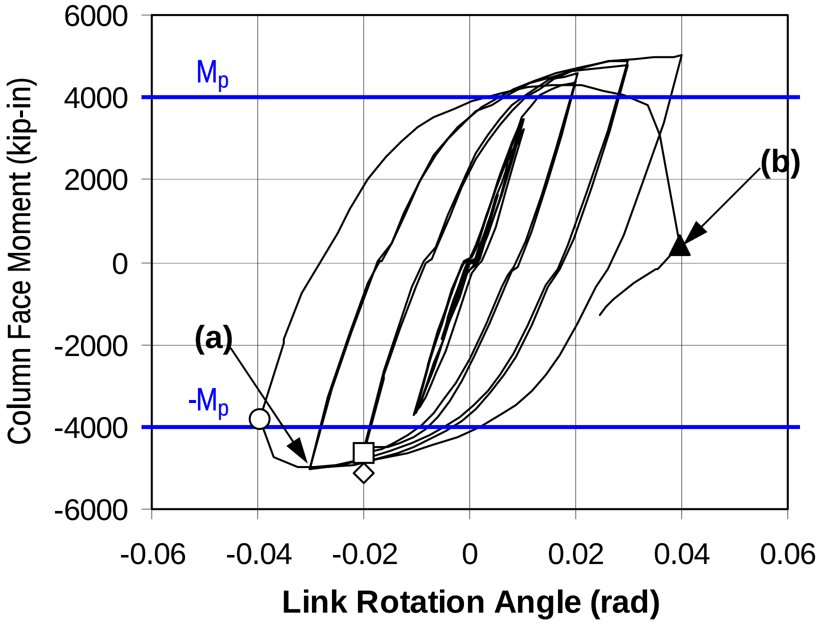

(d) Column Face Moment vs. Rotation Angle

Figure 4.21 Response of Specimen FFM (Continued)

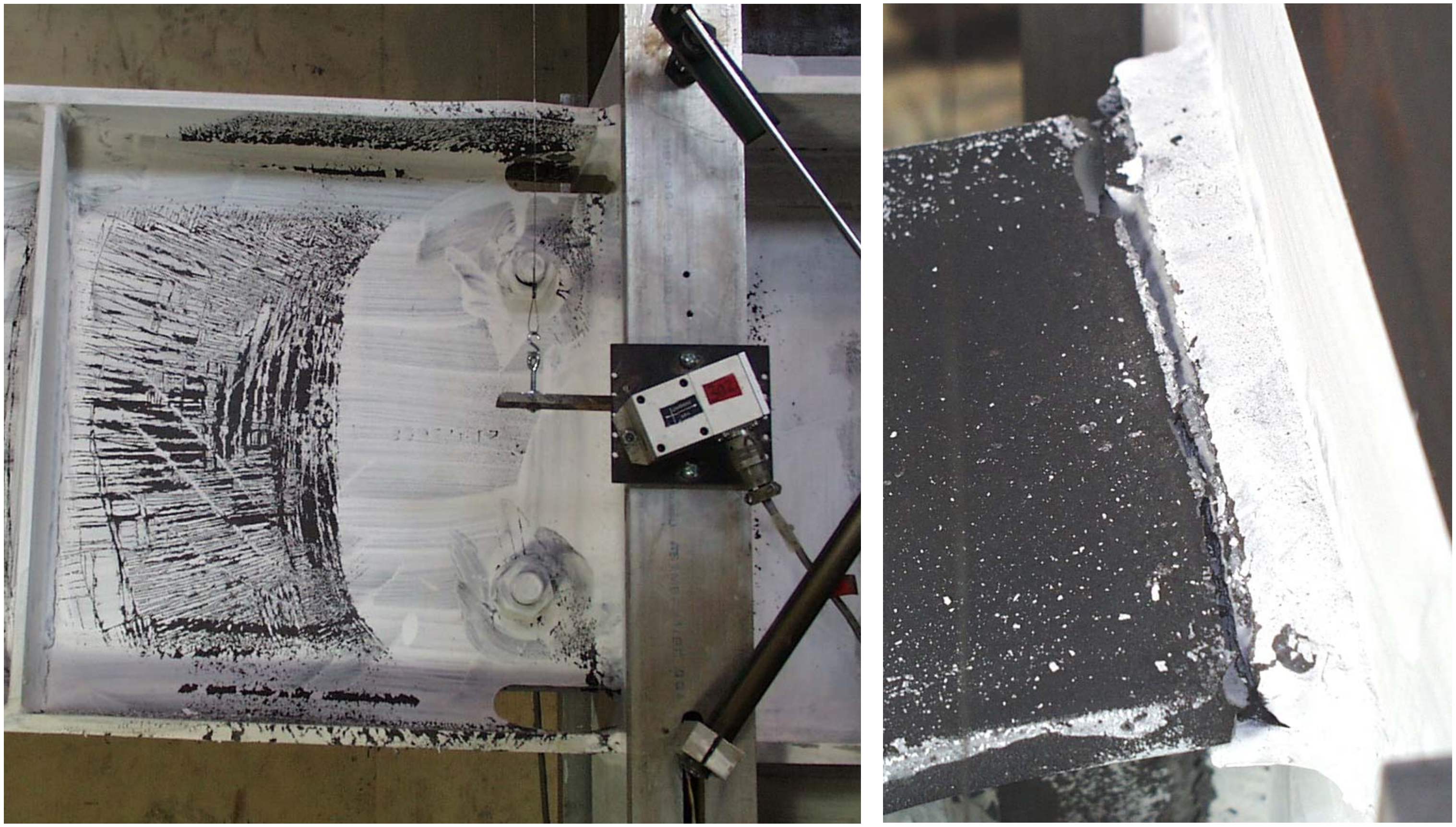

(a) Yielding around shear tab (0.03-2N) ***(b) Fractured link top flange after test***

Figure 4.22 Photographs of Specimen FFM

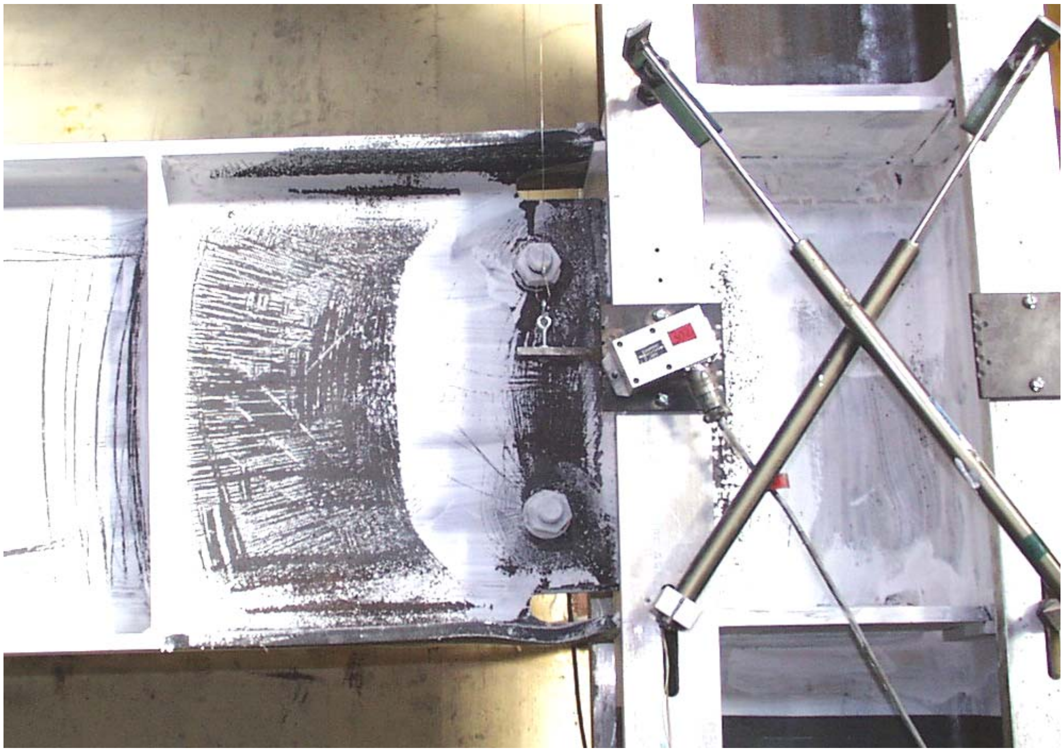

(c) Link-to-column connection after test

Figure 4.22 Photographs of Specimen FFM (Continued)

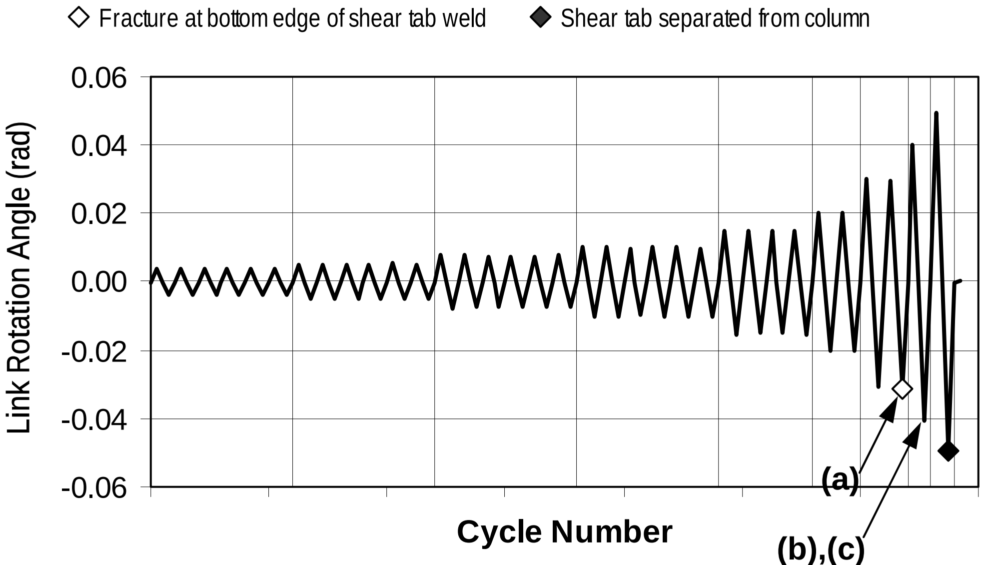

(a) Loading History

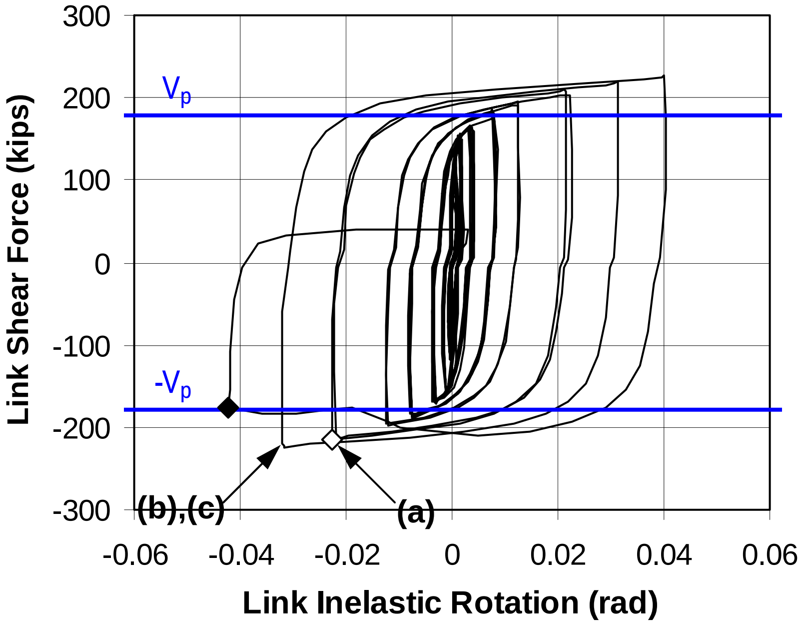

(b) Link Shear vs. Inelastic Rotation Angle

Figure 4.23 Response of Specimen FFS-RLP

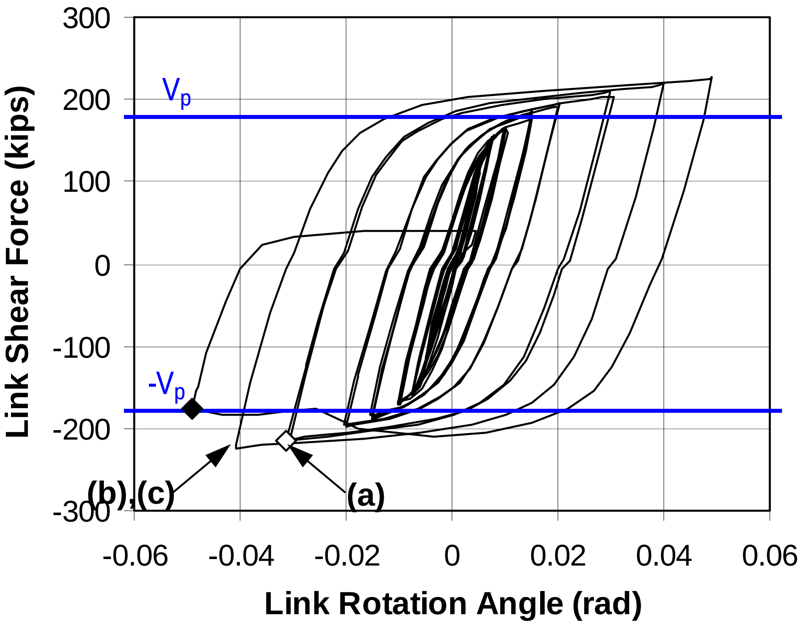

(c) Link Shear vs. Rotation Angle

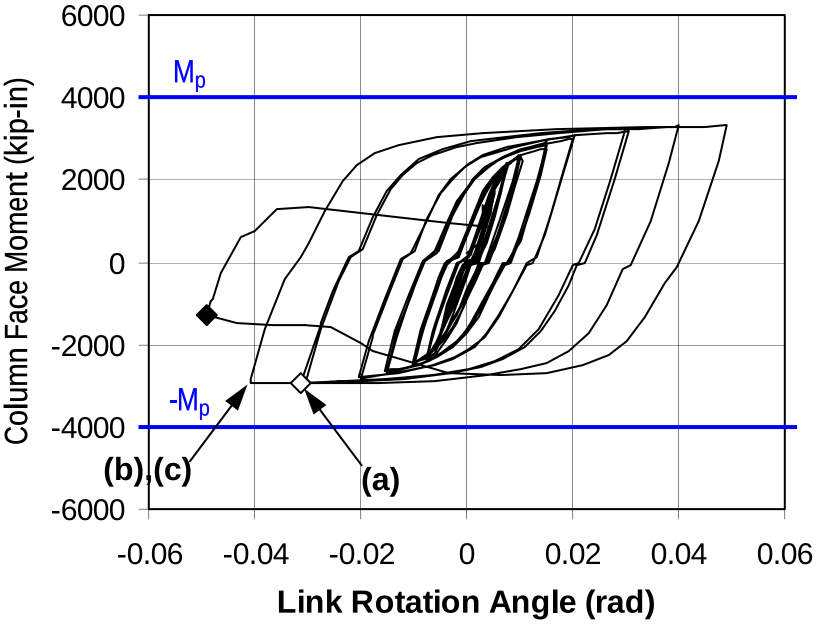

(d) Column Face Moment vs. Rotation Angle

Figure 4.23 Response of Specimen FFS-RLP (Continued)

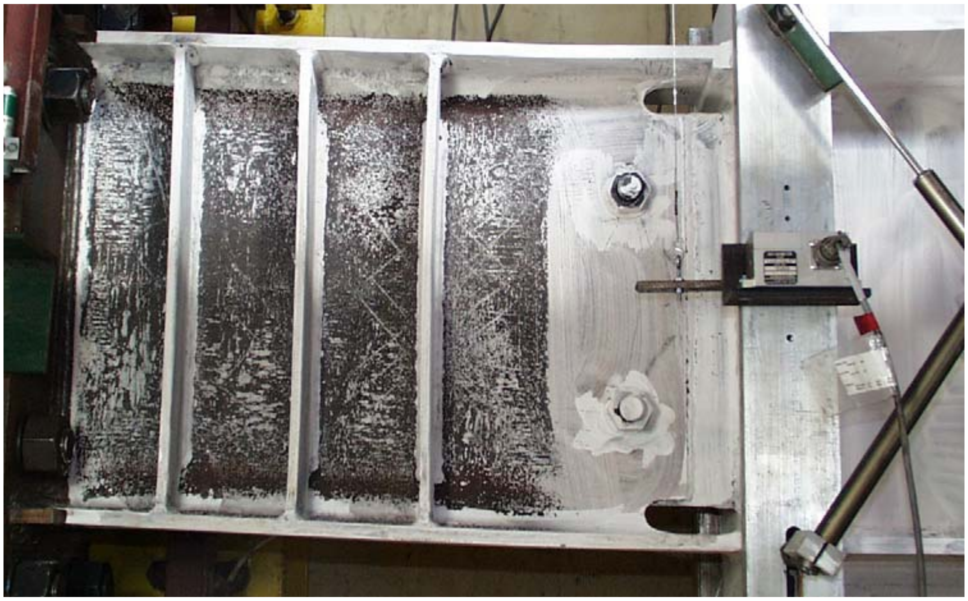

(a) Yielding in link web panels (0.03-2N)

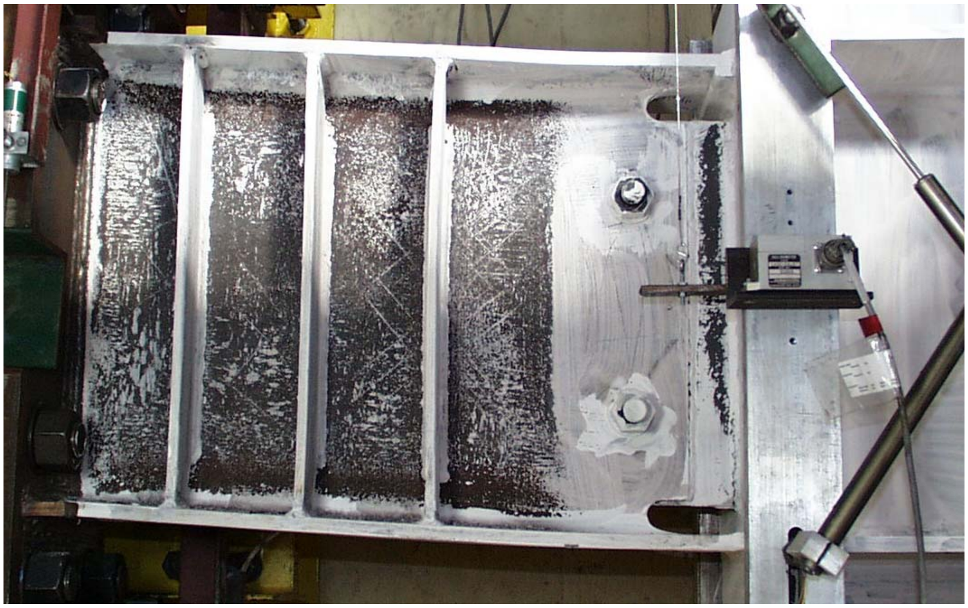

(b) Yielding in shear tabe near column face (0.04-1N)

Figure 4.24 Photographs of Specimen FFS-RLP

Figure 4.24 Photographs of Specimen FFS-RLP (Continued)
(c) (Above) Fracture in bottom edge of shear tab weld (0.04-1N); and (d) (Right) Link-to-column connection after test.

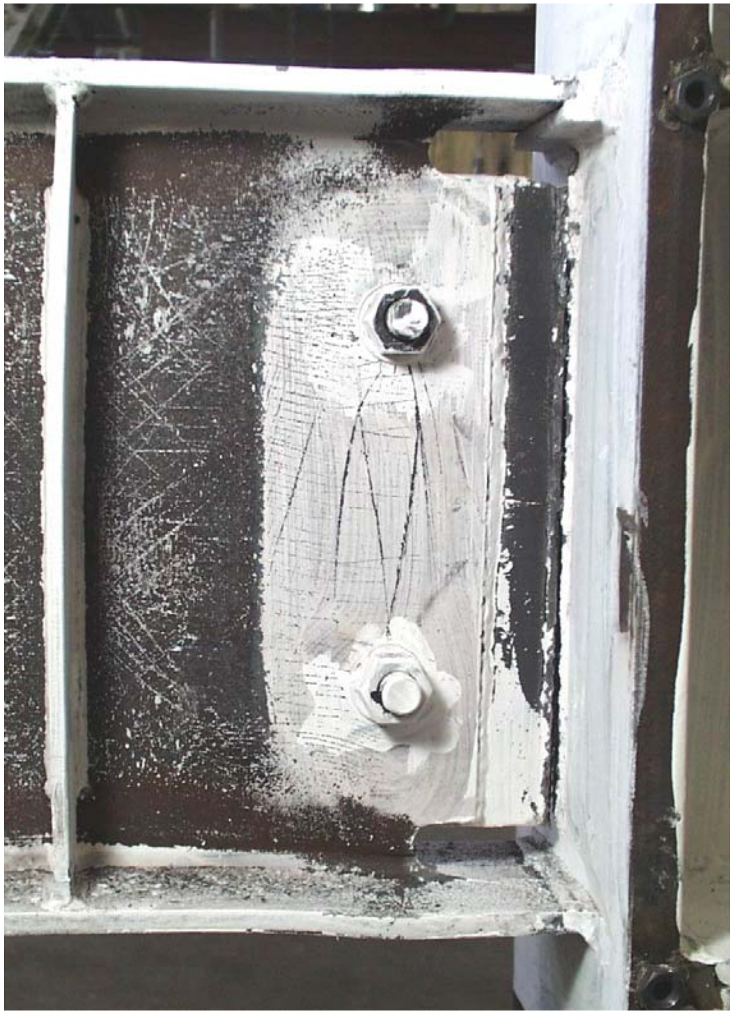

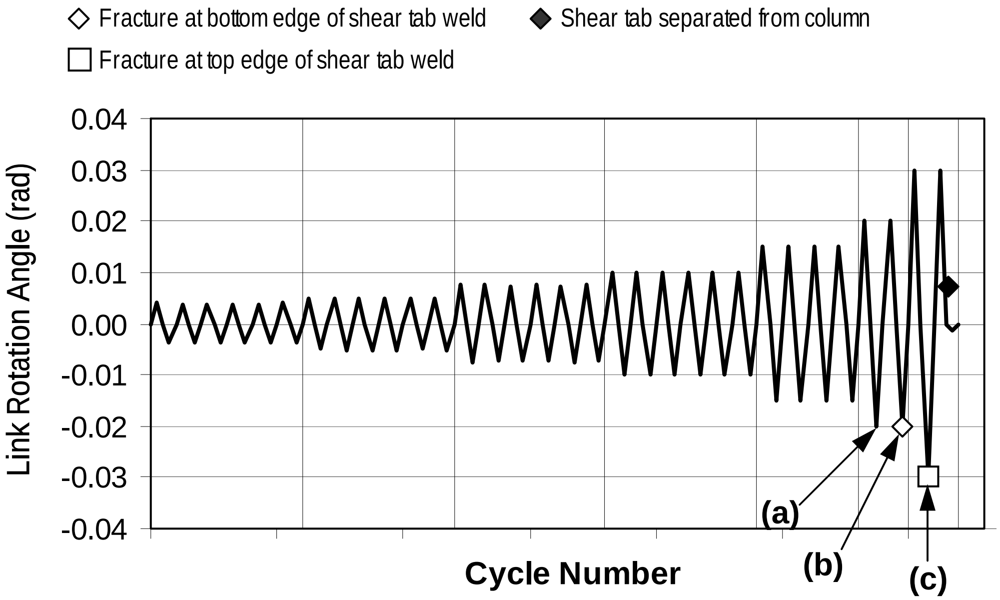

(a) Loading History

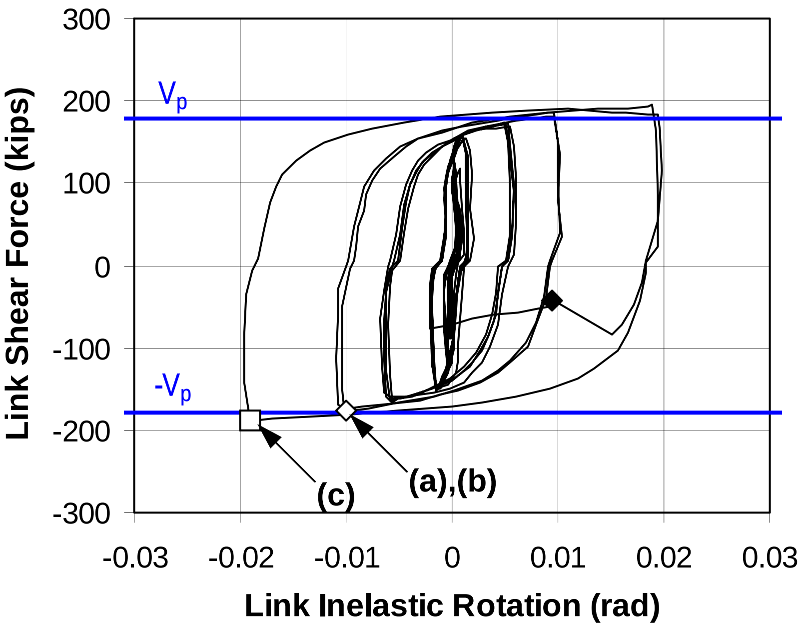

(b) Link Shear vs. Inelastic Rotation Angle

Figure 4.25 Response of Specimen FFSL-RLP

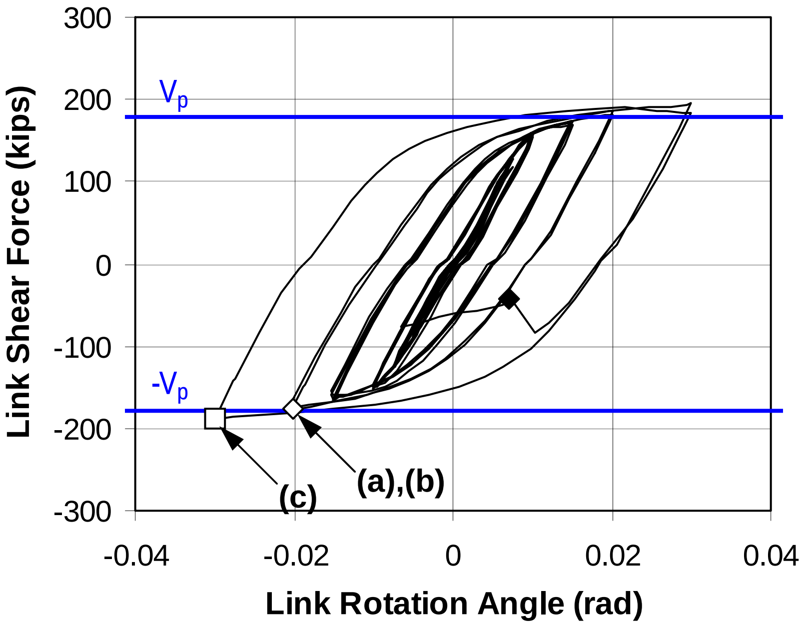

(c) Link Shear vs. Rotation Angle

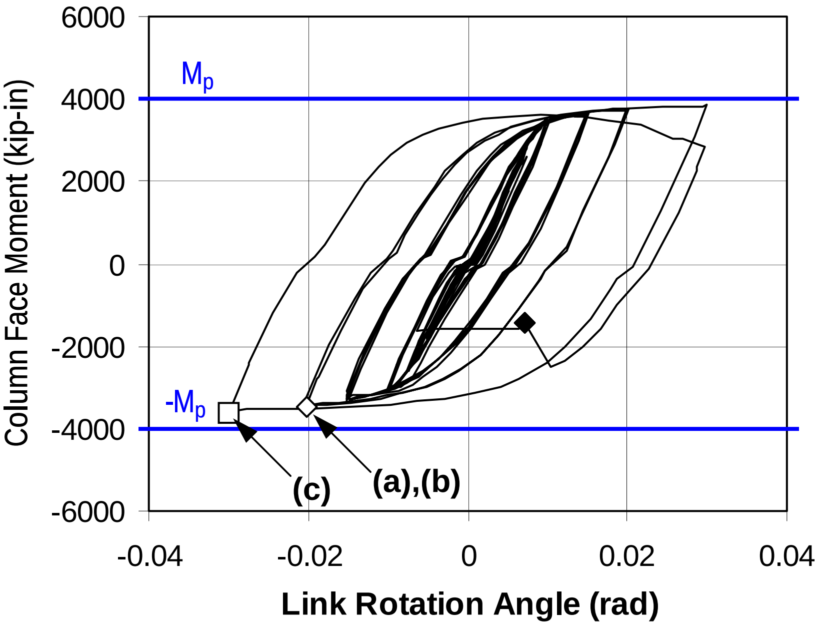

(d) Column Face Moment vs. Rotation Angle

Figure 4.25 Response of Specimen FFSL-RLP (Continued)

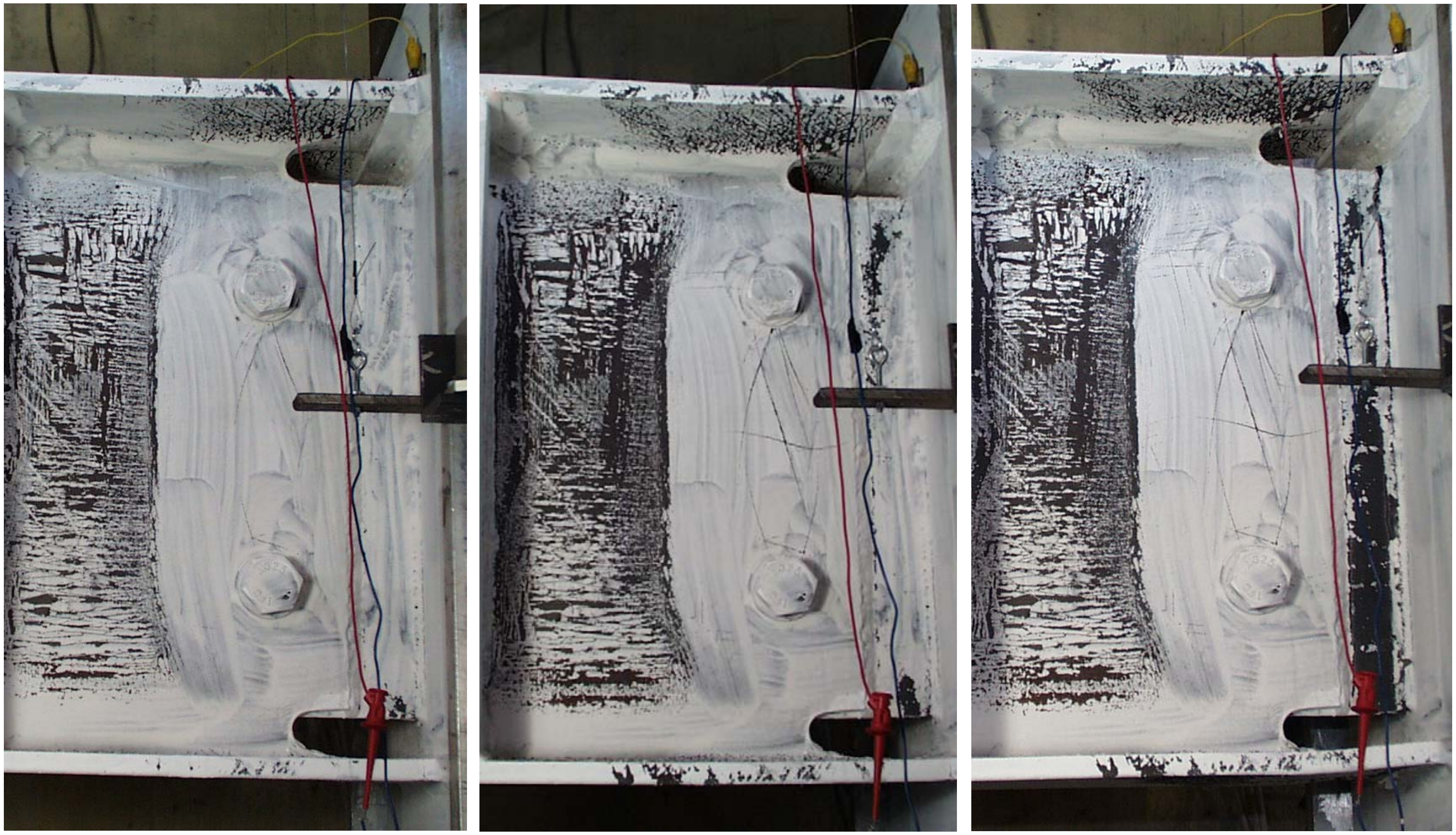

Figure 4.26 Photographs of Specimen FFSL-RLP

Progressive yielding near web weld: (a)(Left) At completion of 0.02-2N; (b) (Center) At completion of 0.03-1N; and (c) (Right) During 0.03-2N after link web separated from column flange.

(d) Link after test

(e) Bottom edge of shear tab weld (after test)

Figure 4.26 Photographs of Specimen FFSL-RLP (Continued)

Figure 4.27 NA-Connection before testing

(a) (Left) Connection of Specimen NASL-RLP; and (b) (Above) Backing bar and reinforcement weld at link bottom flange (from Specimen NAM).

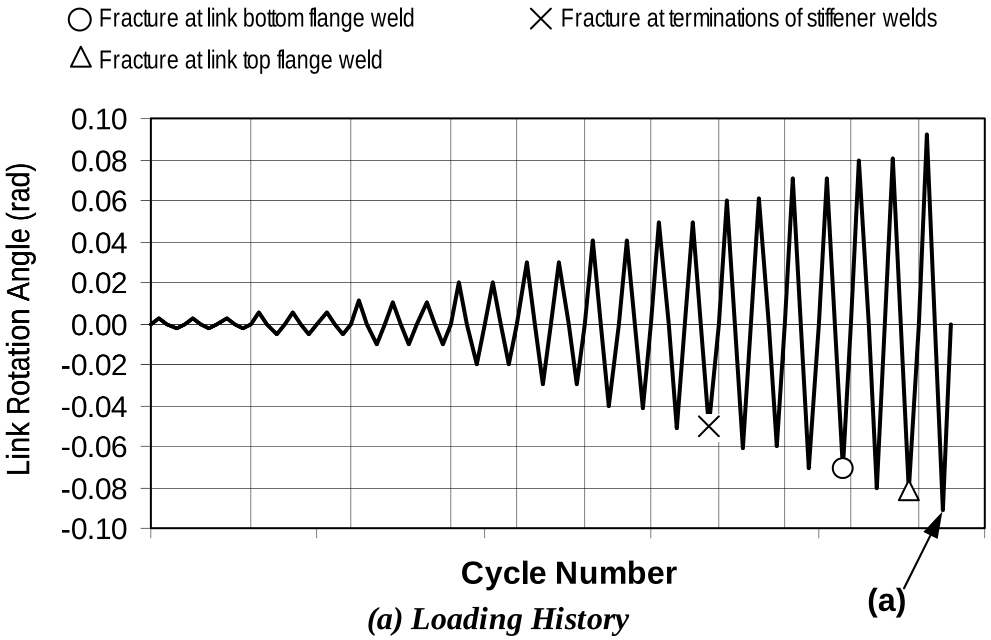

(a) Loading History

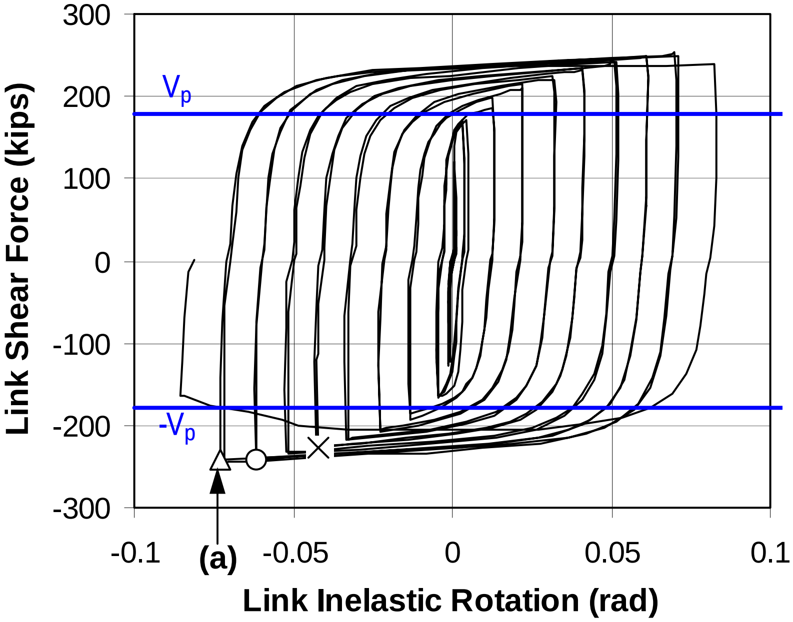

(b) Link Shear vs. Inelastic Rotation Angle

Figure 4.28 Response of Specimen NAS

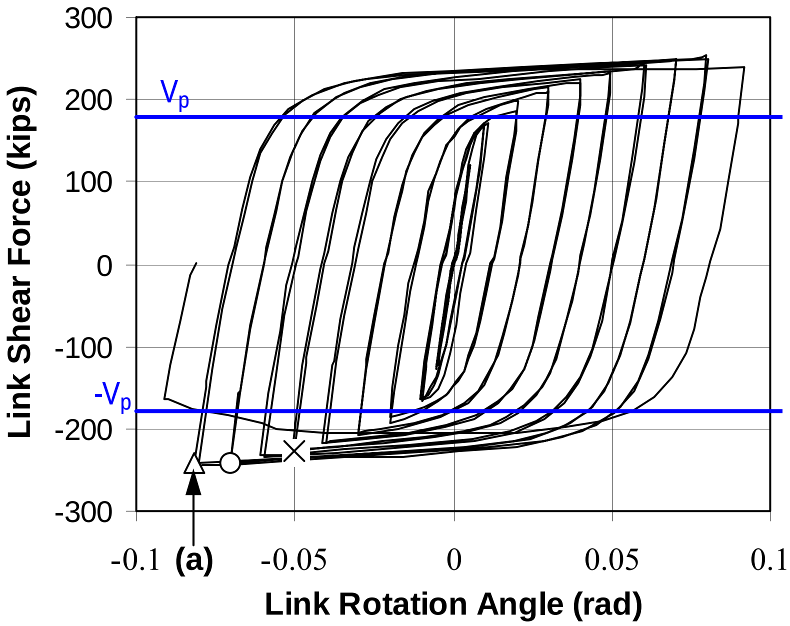

(c) Link Shear vs. Rotation Angle

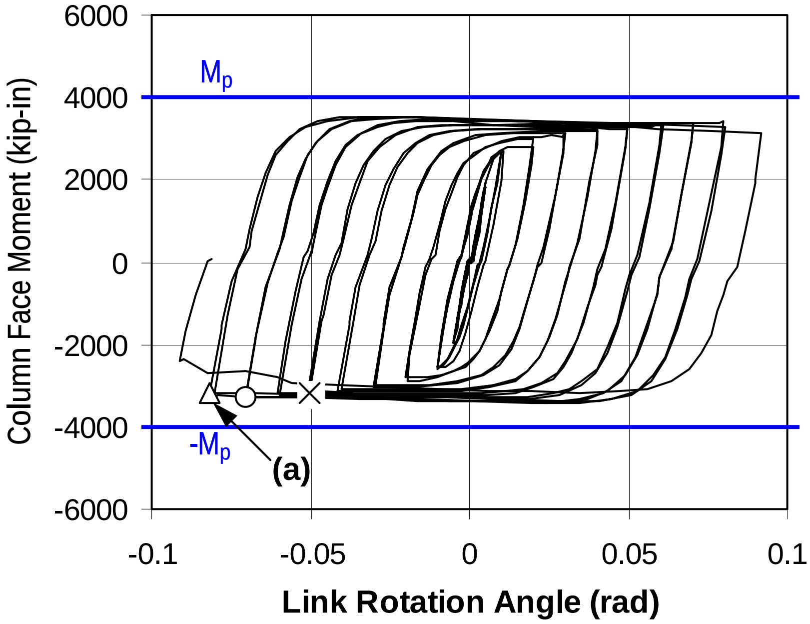

(d) Column Face Moment vs. Rotation Angle

Figure 4.28 Response of Specimen NAS (Continued)

(a) Horizontal fracture in link web (0.09-1P)

(b) Fracture in link top flange (after test)

Figure 4.29 Photographs of Specimen NAS

(c) Link after test

Figure 4.29 Photographs of Specimen NAS (Continued)

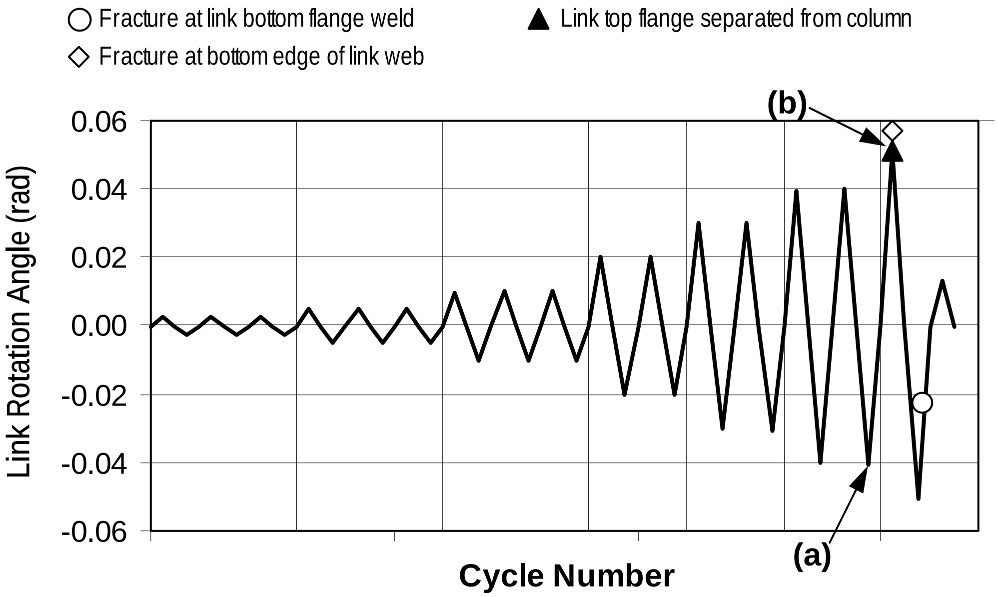

(a) Loading History

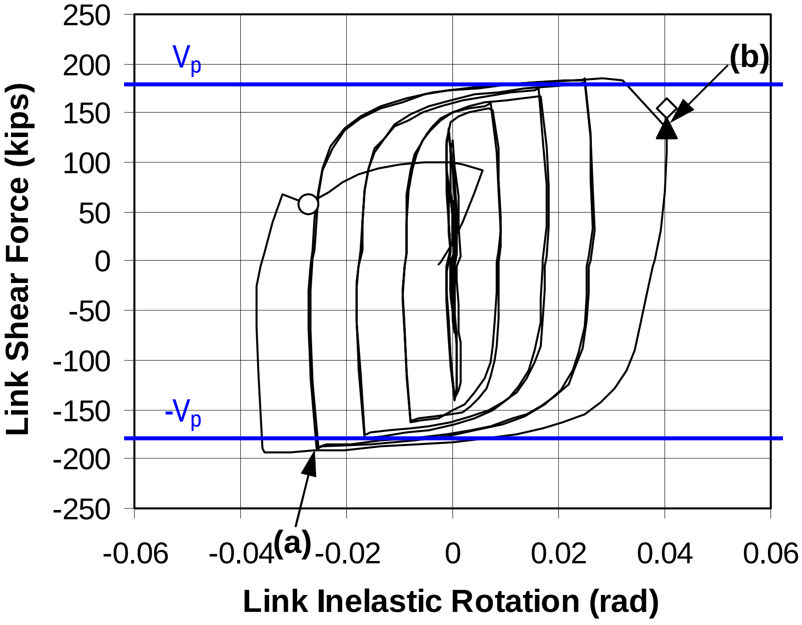

(b) Link Shear vs. Inelastic Rotation Angle

Figure 4.30 Response of Specimen NAI

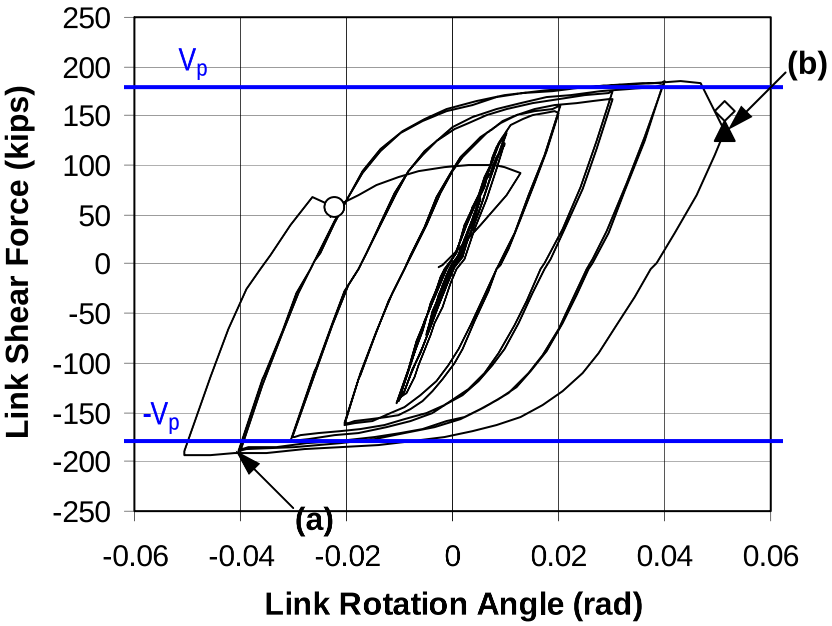

(c) Link Shear vs. Rotation Angle

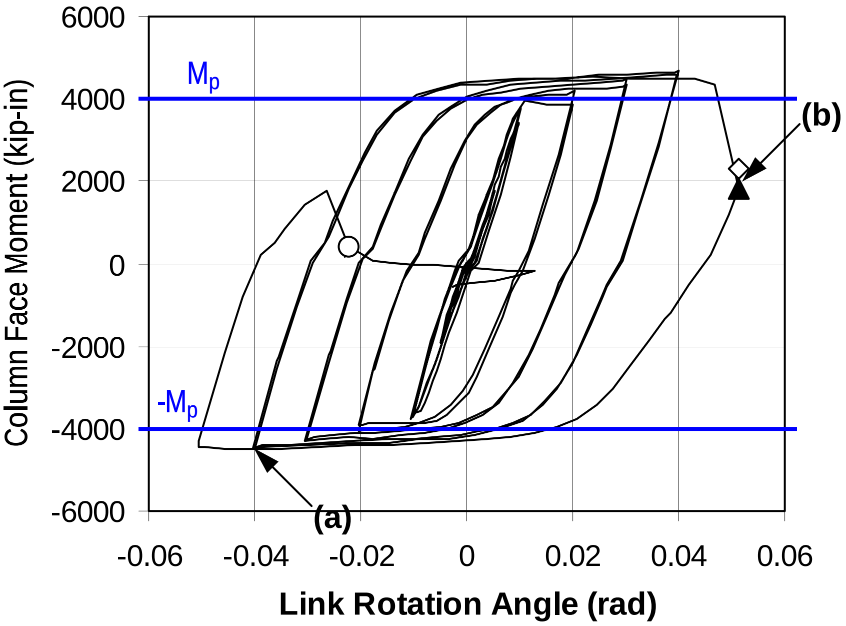

(d) Column Face Moment vs. Rotation Angle

Figure 4.30 Response of Specimen NAI (Continued)

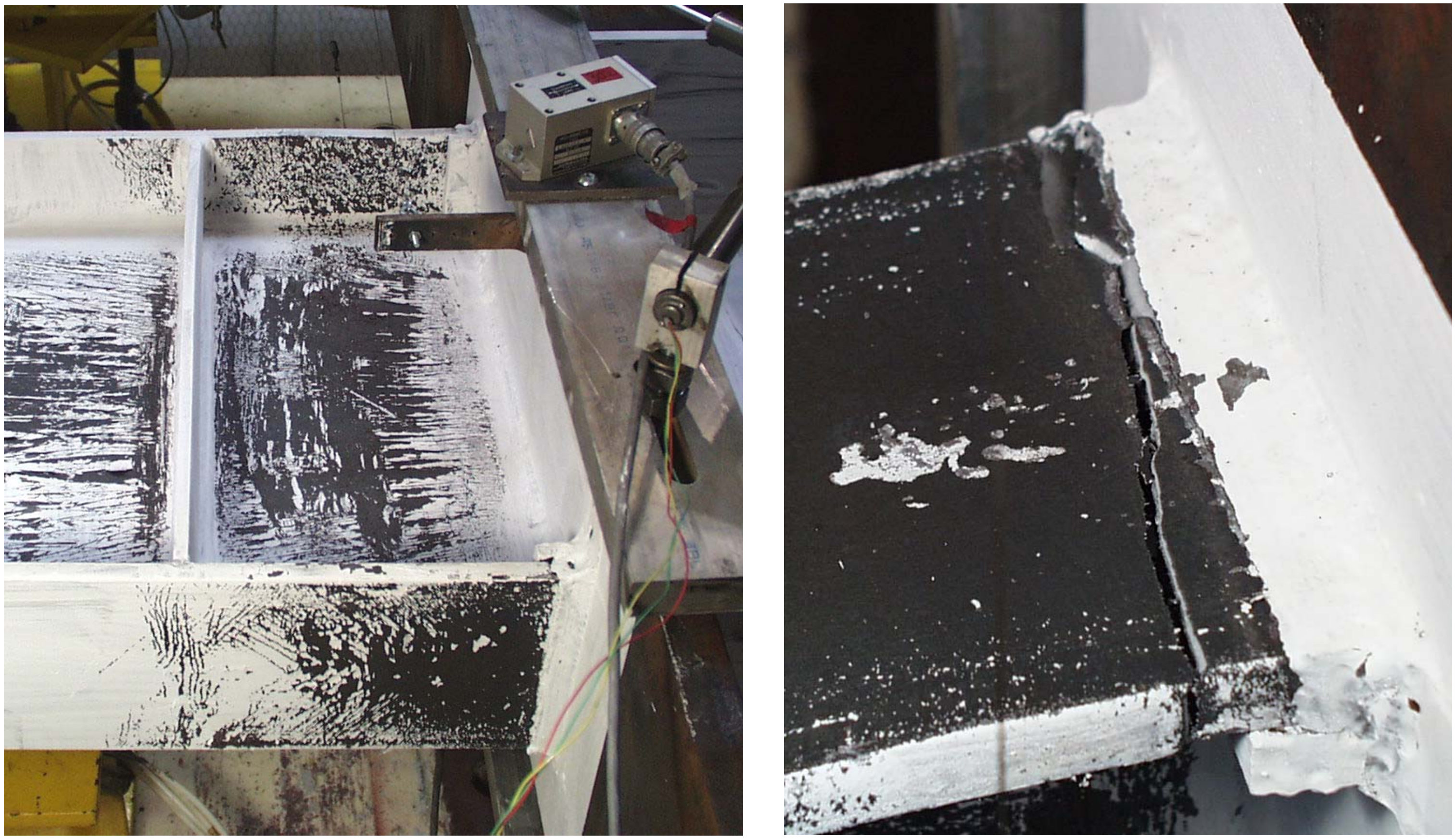

(a) Yielding in link near column face (0.04-2N)

(b) Link top flange separated from column flange (0.05-1P)

Figure 4.31 Photographs of Specimen NAI

(c) Link-to-column connection after test

(d) Side view of link top flange separated from column flange (after test)

Figure 4.31 Photographs of Specimen NAI (Continued)

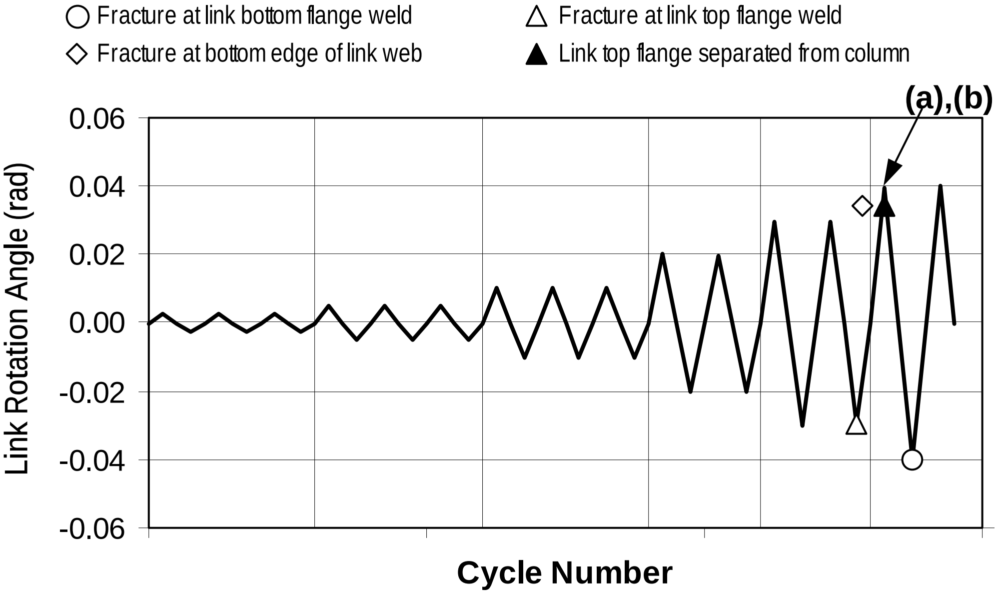

(a) Loading History

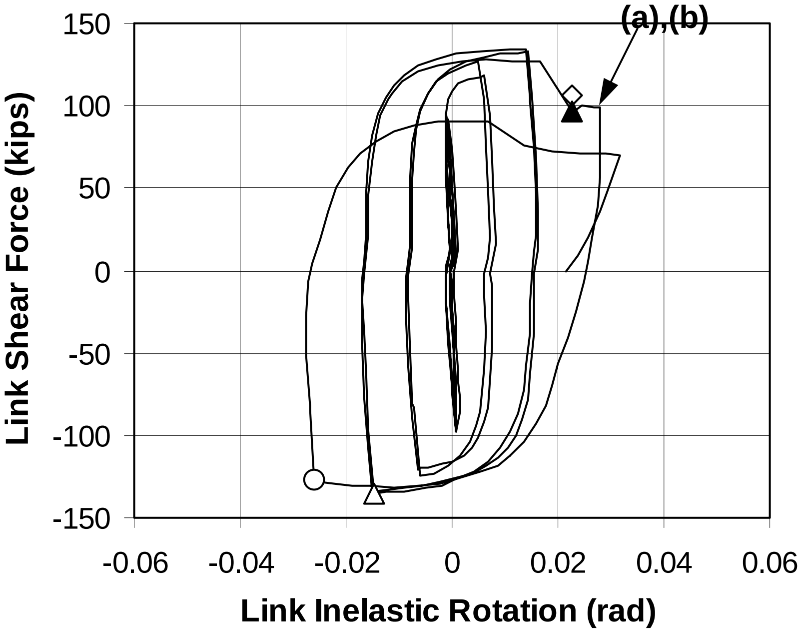

(b) Link Shear vs. Inelastic Rotation Angle

Figure 4.32 Response of Specimen NAM

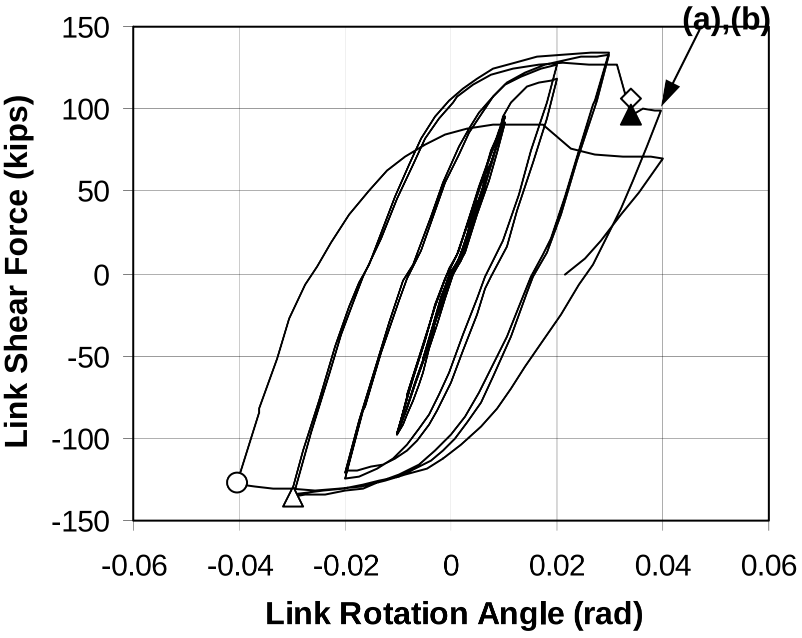

(c) Link Shear vs. Rotation Angle

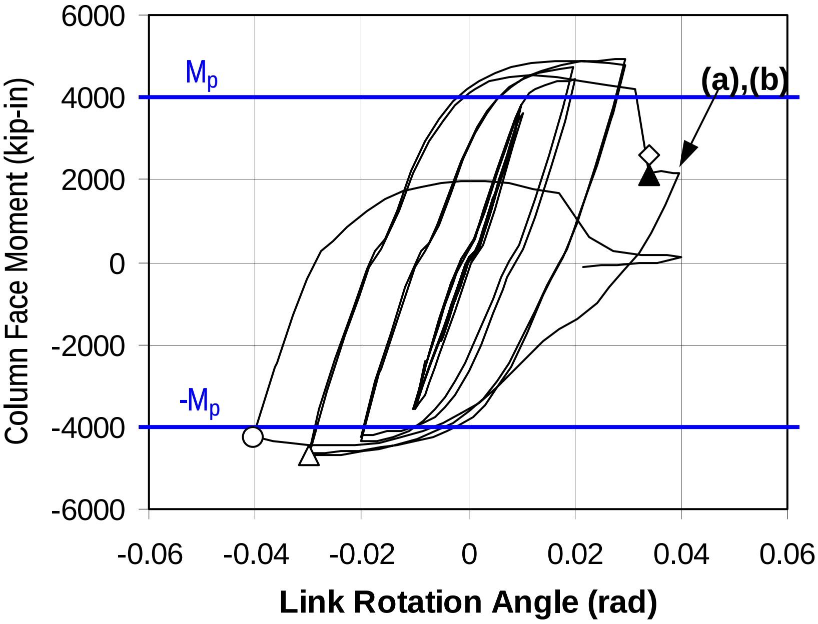

(d) Column Face Moment vs. Rotation Angle

Figure 4.32 Response of Specimen NAM (Continued)

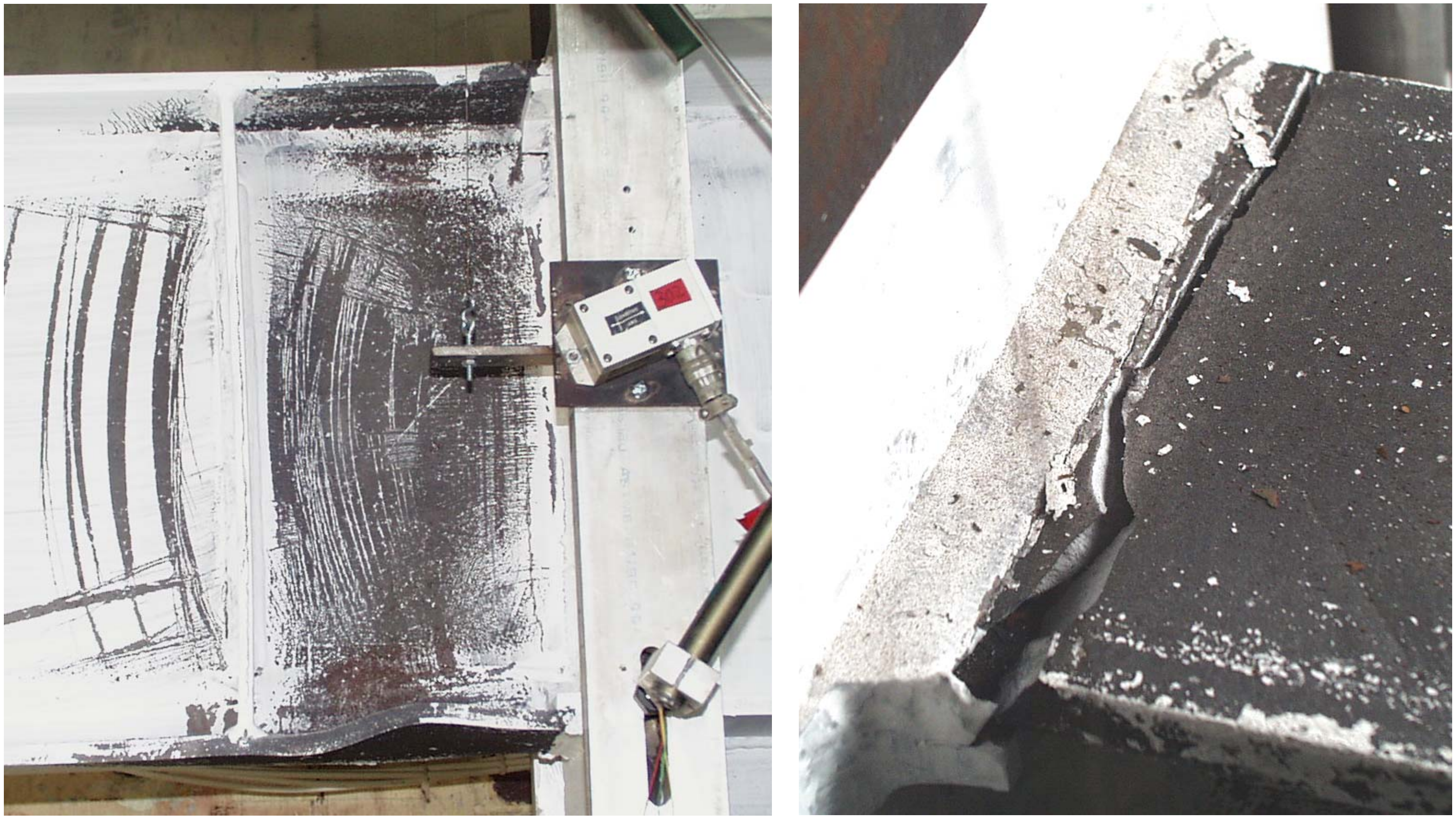

(a) Yielding and local buckling in link near column face (0.04-1P)

(b) Link top flange separated from column flange (0.04-1P)

Figure 4.33 Photographs of Specimen NAM

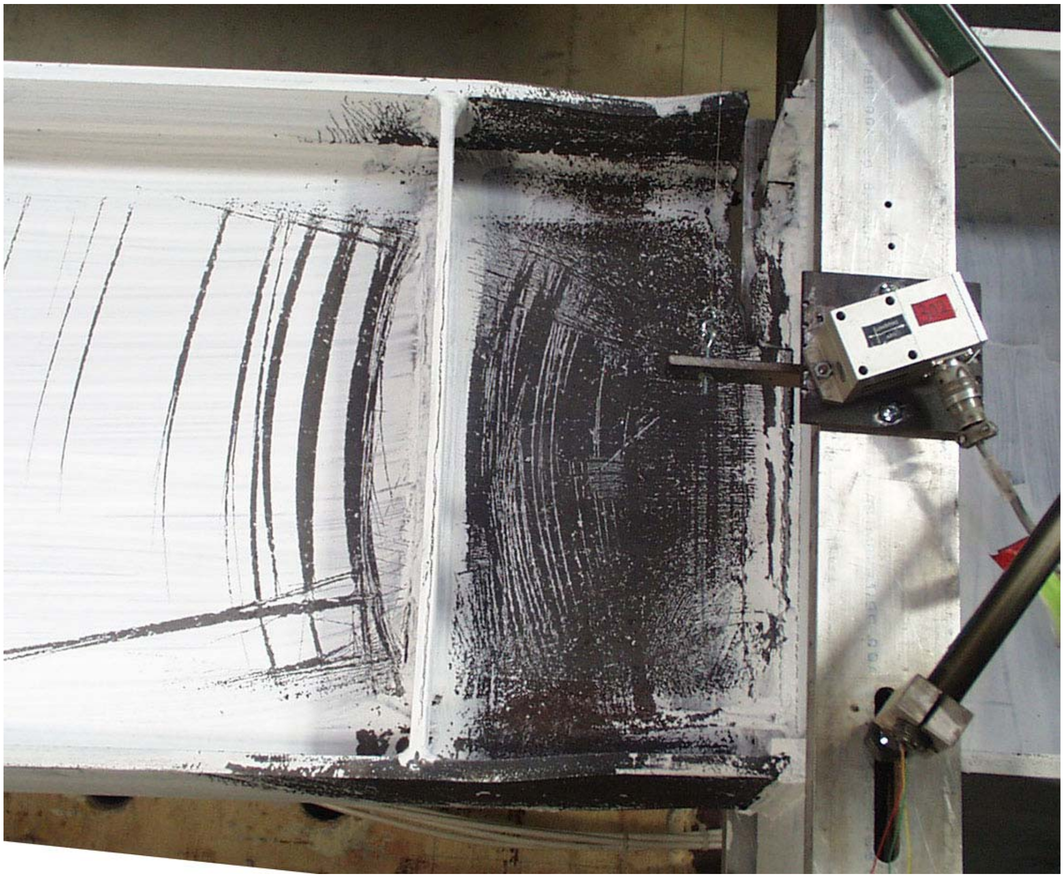

(c) Link-to-column connection after test

Figure 4.33 Photographs of Specimen NAM (Continued)

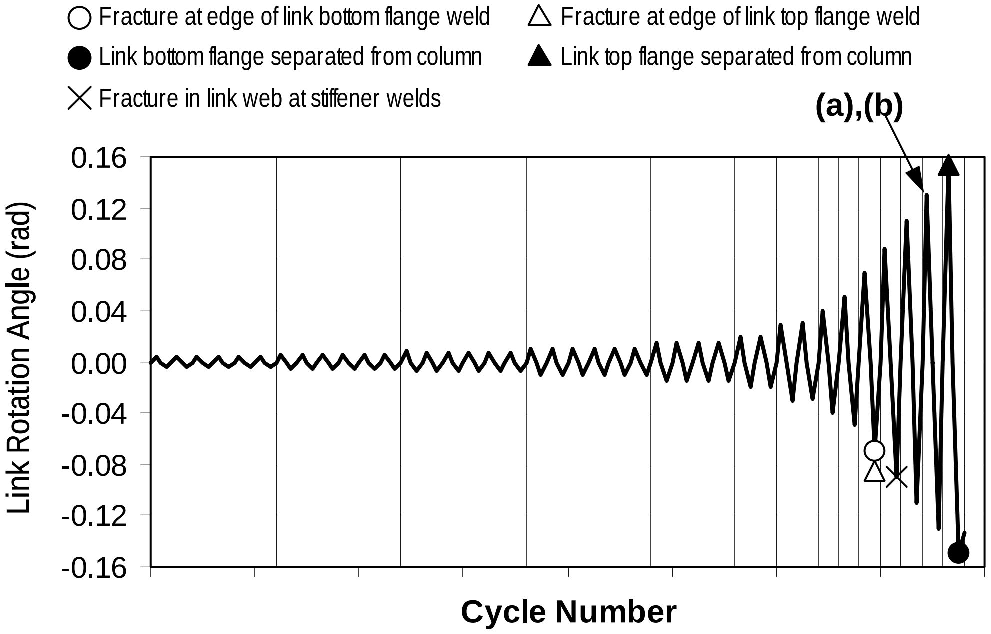

(a) Loading History

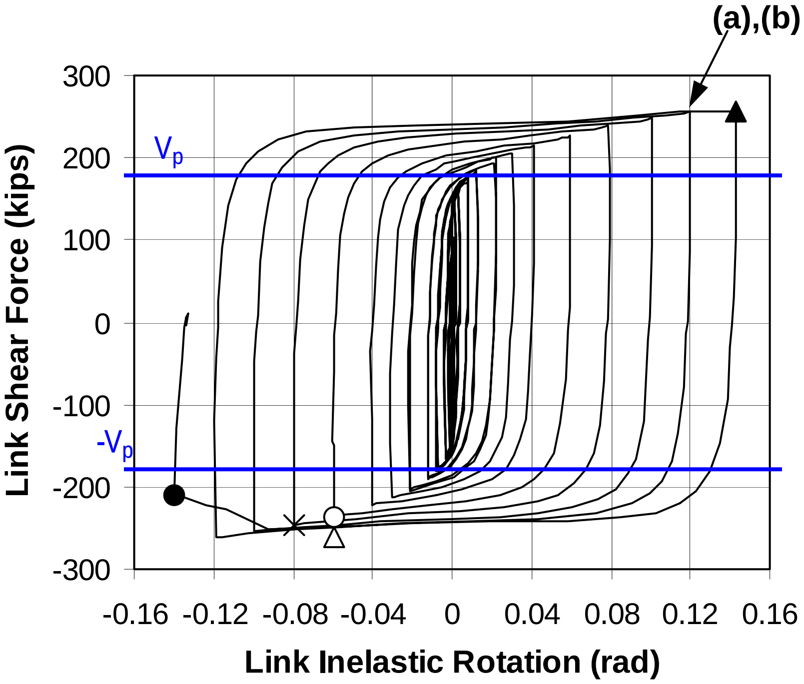

(b) Link Shear vs. Inelastic Rotation Angle

Figure 4.34 Response of Specimen NAS-RLP

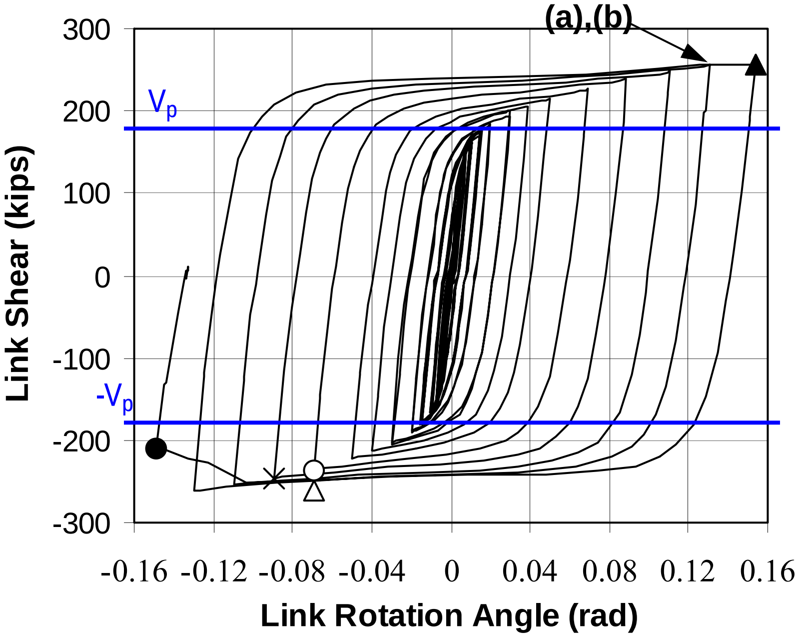

(c) Link Shear vs. Rotation Angle

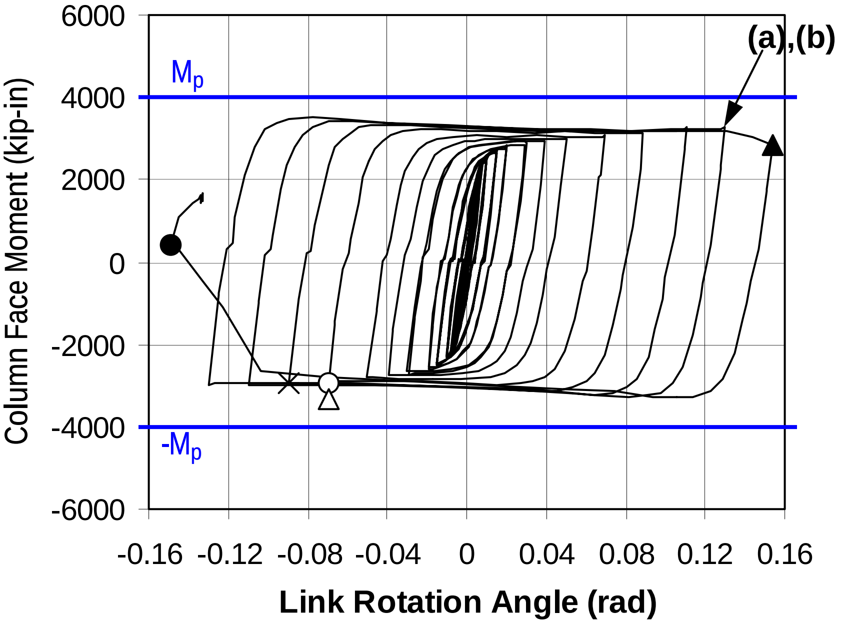

(d) Column Face Moment vs. Rotation Angle

Figure 4.34 Response of Specimen NAS-RLP (Continued)

(a) Link deformation (0.13-1P)

(b) Fracture initiation at west edge of top flange (0.13-1P)

Figure 4.35 Photographs of Specimen NAS-RLP

Figure 4.35 Photographs of Specimen NAS-RLP (Continued)

(c) (Above left) Link after test; (d) (Above right) Fracture in link web (after test); and (e) (Below right) Link bottom flange separated from column flange (after test).

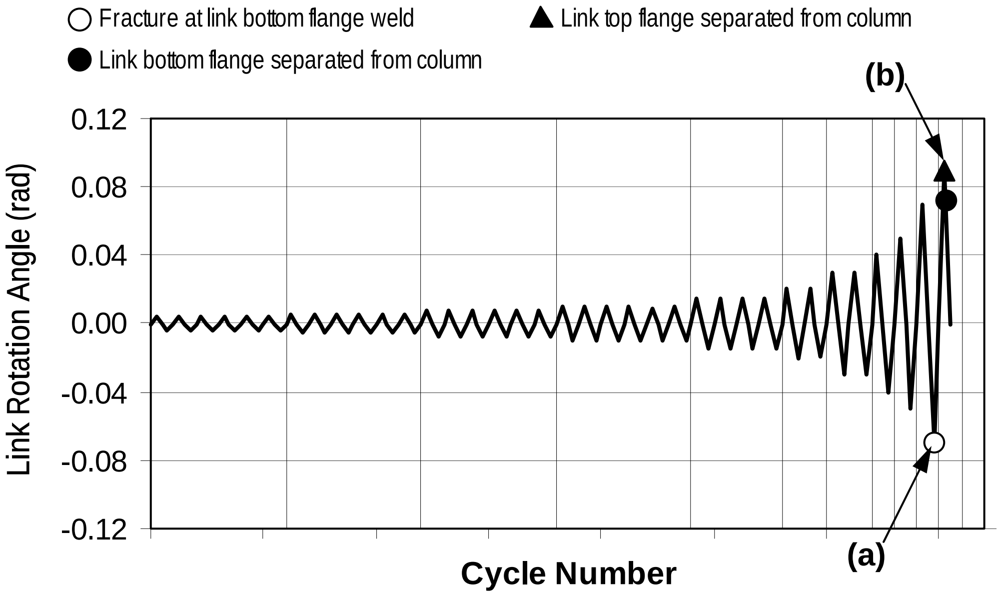

(a) Loading History

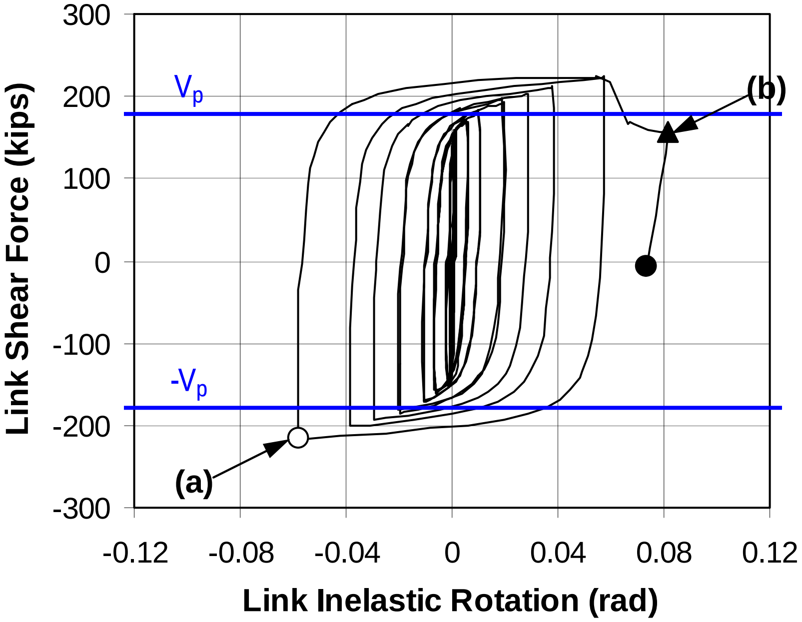

(b) Link Shear vs. Inelastic Rotation Angle

Figure 4.36 Response of Specimen NASL-RLP

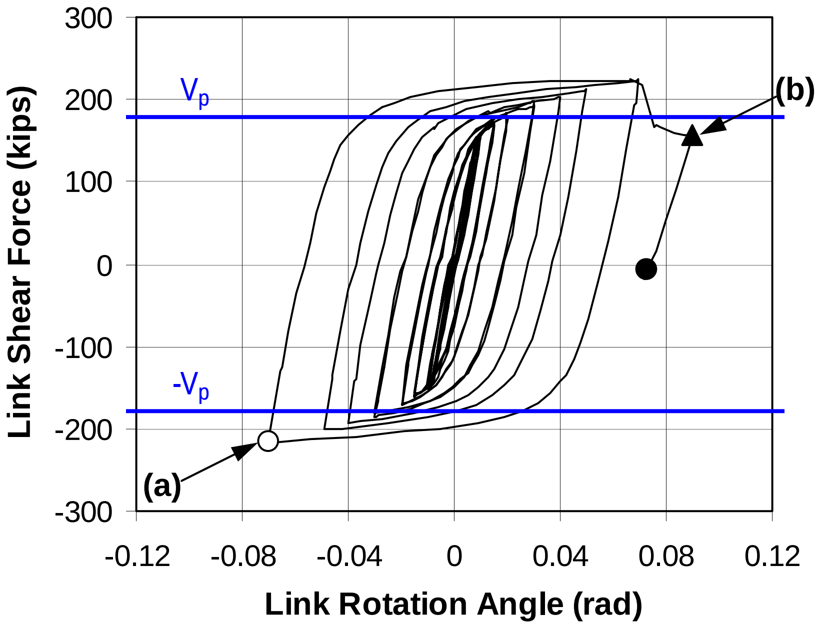

(c) Link Shear vs. Rotation Angle

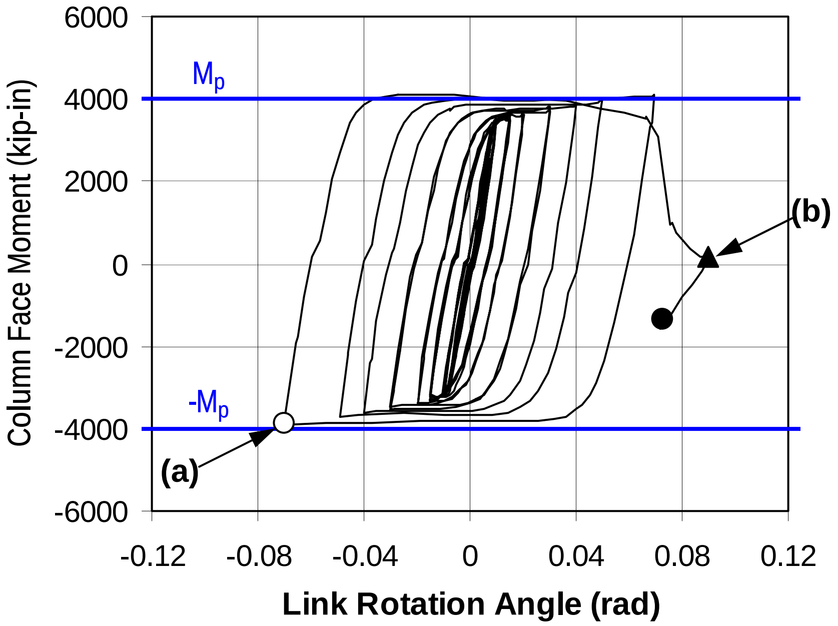

(d) Column Face Moment vs. Rotation Angle

Figure 4.36 Response of Specimen NASL-RLP (Continued)

Figure 4.37 Photographs of Specimen NASL-RLP

(a) (Above) Fracture across link bottom flange (0.07-1N); and (b) (Right) Link top flange separated from column flange (0.09-1P).

(c) Link after test

(d) Link bottom flange separated from column flange (after test)

Figure 4.37 Photographs of Specimen NASL-RLP (Continued)

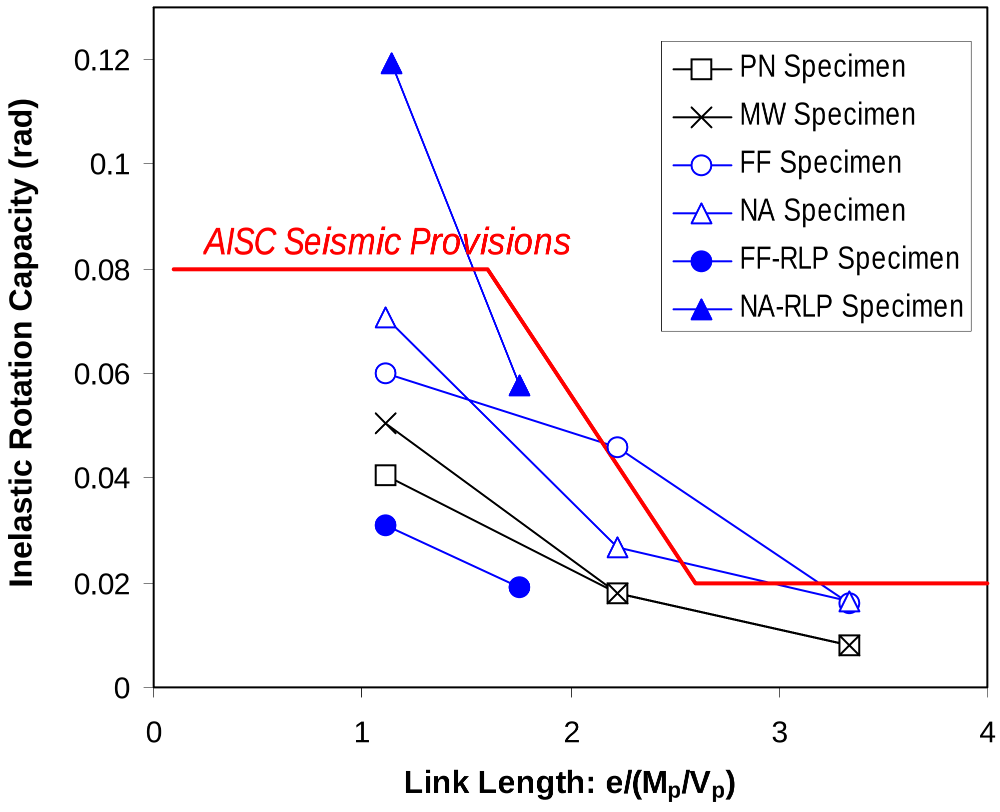

Figure 4.38 Link Rotation Capacity

CHAPTER 5

Further Discussion of Test Results

5.1 INTRODUCTION

Further analyses and discussion of the results of the link-to-column connection tests are presented in this chapter. Section 5.2 discusses the performance characteristics of the test setup. Section 5.3 discusses the performance of the specimens based on a variety of different performance measures. Section 5.4 details and analyzes the forces developed in the specimens. Section 5.5 discusses the evaluation of fracture surfaces. Section 5.6 analyzes the strain gauge data. Section 5.7 discusses panel zone deformations. Finally, Section 5.8 summarizes the discussions in this chapter.

5.2 EVALUATION OF TEST SETUP

5.2.1 Initial Elastic Response

All specimens exhibited linear elastic response during the initial loading cycles up to $\gamma = \pm 0.005$ rad. Table 5.1 lists the stiffness of the system, $K_e = V/\gamma$, and the ratio of the moment at the column face to the moment at the beam end, $(M_C/M_B)_e$, both measured during these initial elastic cycles. K_e was essential to the evaluation of inelastic link rotation using equation (3.1). Table 5.1 also lists the link rotation at the elastic limit, evaluated as V_n/K_e, where V_n is the nominal shear strength.

The end moment ratio, $(M_C/M_B)_e$ provide basic information on the rotational restraints imposed at both ends of the link. As is typically the case in actual EBFs, the link end restraints in the test setup were essentially elastic. These

Table 5.1 Elastic Response

Specimen	Measured			Finite Element Simulation		
	K_e (kips)	$(M_C/M_B)_e$	V_n/K_e (rad)	K_e (kips)	$(M_C/M_B)_e$	V_n/K_e (rad)
PNS	24,352	1.83	0.0073	27,032	2.05	0.0061
PNI	14,301	1.33	0.0112	16,611	1.48	0.0098
PNM	10,324	1.14	0.0104	12,017	1.18	0.0091
MWS	24,735	1.85	0.0072	26,916	2.04	0.0062
MWI	14,350	1.29	0.0112	16,572	1.48	0.0099
MWM	10,443	1.02	0.0102	11,997	1.17	0.0091
FFS	24,312	1.76	0.0073	28,212	2.04	0.0059
FFI	14,239	1.34	0.0113	16,903	1.49	0.0097
FFM	10,158	0.99	0.0105	12,160	1.18	0.0090
FFS-RLP	24,851	1.72	0.0072	28,000	2.04	0.0059
FFSL-RLP	17,592	1.31	0.0101	20,819	1.63	0.0080
NAS	25,948	1.93	0.0069	27,948	1.91	0.0059
NAI	14,327	1.25	0.0112	17,142	1.42	0.0095
NAM	10,027	1.03	0.0107	12,397	1.14	0.0088
NAS-RLP	23,784	1.64	0.0075	27,948	1.91	0.0059
NASL-RLP	18,182	1.34	0.0098	21,148	1.55	0.0078

restraints dominate the link moment distribution during elastic response and the moment redistribution process during inelastic response. K_e and $(M_C/M_B)_e$ are functions of the stiffness of the link as well as of the rotational restraint at the link ends. The value of K_e decreases with increase in link length, primarily due to the decrease in the bending stiffness of the link. The greater rotational restraint at the column end of the link than at the beam end results in values of $(M_C/M_B)_e$ greater than unity. The value of $(M_C/M_B)_e$ decreases and approaches unity with increase in link length, as the bending stiffness of the link relative to the end restraints decreases. The link rotation at the elastic limit, V_n/K_e, was roughly 0.01 rad, regardless of the connection type and link length.

Table 5.1 also lists the elastic properties evaluated from finite element simulation. The elastic response of the global finite element models discussed in

Section 6.3 was used for this evaluation. Comparison between the measured response and the numerically simulated response shows reasonable agreement. The system stiffness, K_e, measured from the test was generally 10 to 20% smaller than the value evaluated from the finite element simulation. The end moment ratio, $(M_C/M_B)_e$, measured from the test was also 10 to 20% smaller than the value obtained from the finite element simulation.

The finite element simulations show that greater rotational restraint at the link-to-column connection causes a minor increase in system stiffness, K_e. The PN-connection provided slightly greater restraint than the MW-connection due to the smaller size of the weld access hole. The FF-connection provided greater restraint than the PN- and MW-connections due to the shear tab welded to the link web. The NA-connections provided greater restraint than the PN- and MW-connections due to the absence of the weld access hole. While Specimen FFS was stiffer than Specimen NAS, Specimen FFI was less stiff than Specimen NAI, and Specimen FFM was less stiff than Specimen NAM. Although not as clear, a similar trend was seen in the values of K_e measured from the tests. Both the test measurements and finite element simulations suggest that the difference in system stiffness caused by the connection type was at most on the order of 5%. The connection type had a similarly minor effect on the end moment ratio.

5.2.2 Beam End of the Link

Although the force and deformation environment at actual EBF link-to-column connections was realistically reproduced in the link-column specimens, the environment near the link-brace-beam joint was less accurately represented in the specimens.

In actual EBFs, the brace connection panel (region of the beam in the link-brace-beam joint) is subjected to severe axial forces transferred to the beam by the diagonal brace in addition to the flexure transferred to the beam by the link (Refer to Section 2.2.8). Therefore, if a continuous section is used for the link and the beam outside of the link, as is typically the case, yielding in the brace connection panel is difficult to avoid. The *AISC Seismic Provisions* recognize this difficulty, and permit limited yielding in the brace connection panel. Therefore, the beam is expected to experience limited yielding in the region immediately outside of the link.

In an EBF link with one end connecting to a column, the rotational restraint is higher at the column end than at the beam-brace end (Refer to Section 2.2.6). Therefore, greater moment initially develops at the column end of the link than at the beam-brace end, and yielding will occur first at the column end. Upon loading beyond the elastic limit, the moment will increase more rapidly at the beam-brace end of the link than at the column end, as long as the restraints at both ends remain constant. However, as noted above, it is quite likely that yielding would occur in the beam connection panel in an actual EBF during this moment equalization process. The resulting degradation of end restraint at the beam-brace end can delay moment equalization. Additionally, yielding in the beam connection panel can limit the maximum moment at the beam end of the link, and thereby prevent moment equalization beyond that limit.

In the test setup, the restraint at the beam end of the link might have been higher than what is reasonably expected in actual EBFs. Greater restraint at the beam end can lower the elastic end moment ratio. As listed in Table 5.1, the end moment ratio, $(M_C/M_B)_e$, measured from the test ranged from 2.0 for shear links to 1.0 for moment links. On the other hand, the elastic analyses of EBF frames discussed in Section 2.7.3 provided widely varying values for $(M_C/M_B)_e$, ranging from 1.5 to 5.2 for shear links, and from 1.0 to 1.7 for moment links. This variation in end moment ratio depending on the frame arrangement is a factor not explicitly represented by the test setup.

While the maximum moment measured at the column face was $1.25M_p$, the maximum moment measured at the beam end was as much as $1.45M_p$. Such large flexural strength at the beam end of the link may not be realized in an actual EBF, where the link end is not provided with as high rotational restraint, and inelastic behavior in the brace connection panel is expected. Although the large moment at the beam end was developed after the link shear force degraded, the difference in the flexural capacity between the two ends also suggests that the flexural capacity at the column face was reduced due to the detailing at the link-to-column connection.

5.2.3 Rigid-Plastic Mechanisms

Figure 5.1 illustrates the rigid-plastic mechanisms that the link-column specimens can form under the loading and boundary conditions supplied by the test setup. Figure 5.1a shows the forces in the specimen when loading is applied in the direction to increase link rotation, according to the sign convention defined in Section 3.2.5. Figure 5.1b illustrates mechanisms that can generate motion of the link-to-column joint in the same direction as the load applied. Included are the following four independent base mechanisms:

(1) Plastic rotation of the link;
(2) Plastic panel zone deformation, accompanied by plastic hinge formation in the column;
(3) Rigid body motion of the panel zone, accompanied by plastic hinge formation in the link at the column face and in the column; and

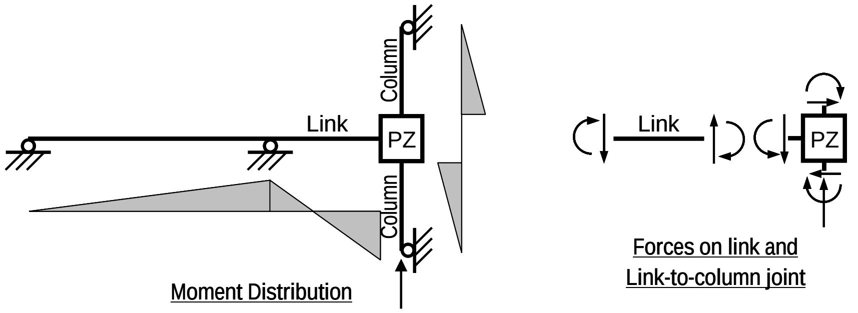

(a) Forces in link-column specimens

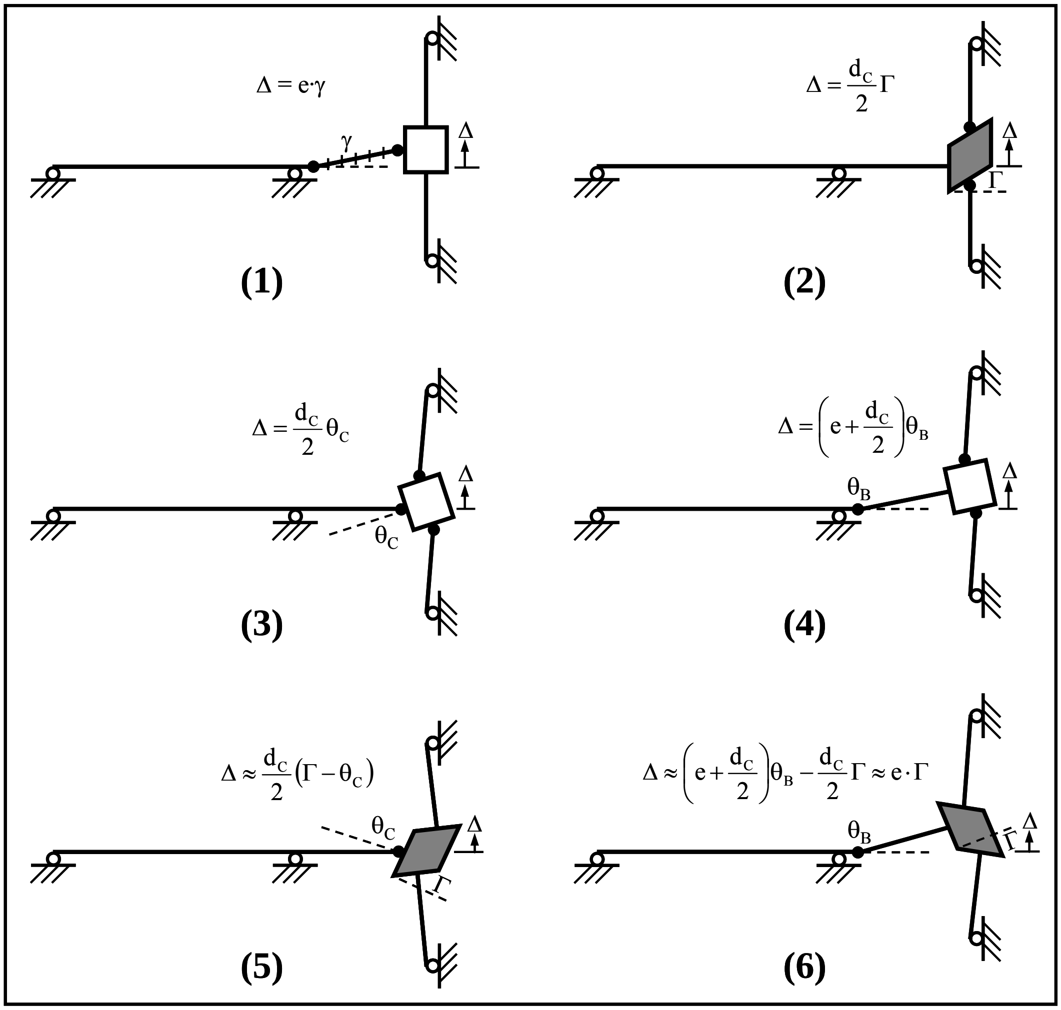

(b) Rigid-plastic mechanisms

Figure 5.1 Energy dissipation mechanisms of link-column specimen

(4) Rigid body motion of the panel zone, accompanied by plastic hinge formation in the link at the beam end and in the column.

Important characteristics of the plastic behavior of the link-column specimen can be deduced from Figure 5.1b. If capacity design principles were strictly adhered to, mechanism (1) is the only mechanism that can be realized. Mechanism (4) cannot be realized independently if yielding in the column were prevented. It should also be noted that the directions of the panel zone deformation in mechanism (2) and the plastic hinge rotation in the link in mechanism (3) are opposed to the direction of internal forces illustrated in Figure 5.1a, and therefore, these two mechanisms will not be realized independently. On the other hand, plastic panel zone deformation cannot take place without being joined by plastic hinge formation either in the link or in the column. However, panel zone deformation can take place, for example, in mechanism (5), which can be considered as a combination of mechanisms (2) and (3), and also in mechanism (6), which can be considered as a combination of mechanisms (2) and (4). Notice that these two mechanisms do not include yielding in the column. Mechanism (5) cannot be configured to generate motion in the direction of load application while complying with the internal forces. In the figure, the panel zone is deformed in the direction opposite to that expected from the link end moment. Mechanism (6), as shown in the figure, completely complies with the direction of internal forces.

Consequently, should yielding in the column be precluded, mechanisms (1) and (6) are the only admissible mechanisms. If yielding were to occur in the column, it would be by activation of mechanism (4). Since it was observed during the tests that plastic action was strictly limited to the link and the column panel zone, the measured deformation of the specimens can be considered as combinations of mechanisms (1) and (6). As discussed in Section 2.2, a properly designed EBF restricts formation of any other mechanism but mechanism (1).

Mechanism (6) involves plastic panel zone deformation, rigid body motion of the panel zone, and plastic hinge formation in the link at the beam end. The rigid body motion of the panel zone is negligible compared to the other rotation components. The link rotation angle supplied by this mechanism is equal to the plastic hinge rotation in the link, and to the shear deformation of the panel zone, if the rigid body motion were neglected. Since mechanism (6) requires plastic hinge formation only at the beam end of the link and not at the column face, participation of this mechanism can be beneficial to the link-to-column connection in reducing the inelastic flexural deformation demand.

Mechanism (6) also suggests that simultaneous yielding in the column panel zone and brace connection panel can generate plastic link rotation without involving yielding in the link or in the column. However, it should be recalled that instability in the brace connection panel can lead to significant reduction in strength of the EBF and limit its ductility (Engelhardt and Popov 1989a; 1992). Therefore, mechanisms relying on the plastic rotation in the brace panel zone should be avoided.

5.3 ALTERNATIVE MEASURES OF PERFORMANCE

5.3.1 General

In Chapter 4, the performance of the specimens was evaluated in terms of the inelastic link rotation angle, per the acceptance criteria of the *2002 AISC Seismic Provisions*. The inelastic rotation capacity measured for each specimen is summarized in Table 4.1. In this section, the performance of the specimens is further examined by various alternative measures besides the inelastic rotation angle, such as: (a) dissipated energy; (b) skeleton rotation capacity; (c) skeleton energy; (d) Bauchinger energy; and (e) cumulative inelastic rotation. The quantities evaluated from each test are summarized in Table 5.2. The physical significance, the correlation with inelastic link rotation, and the implications of each of these measures are described.

5.3.2 Dissipated Energy

Dissipated energy is a useful measure to evaluate the comparative performance of the test specimens, since a basic function of link in EBFs is to dissipate energy input into the frame by earthquake ground motions. The total energy dissipated by a specimen, E_T, was computed by summing the area enclosed by the hysteretic curve of the relative link end displacement, $\Delta = \gamma e$, versus link shear, V. The hysteretic curve was included up to the point where the loss of link strength, as defined in Section 3.2.6 occurred. For Specimen FFI, which completed 0.06-1N but did not develop 80% of the maximum strength during 0.06-2P, the curve was included up to unloading after completion of 0.06-1N.

Figure 5.2 plots the relationship between the inelastic link rotation capacity, $\gamma_{p\text{-}max}$, and dissipated energy, E_T. The trend line shown in the figure is a

Table 5.2 Alternative measures of connection performance

Specimen	$\gamma_{p\text{-max}}$ (rad)	γ_{Sp} (rad)		$\Sigma\gamma_p$ (rad)	E_T (kip-in)	E_S (kip-in)	E_B (kip-in)
PNS	0.041	+0.075	-0.081	0.417	3771	832	2939
PNI	0.018	+0.028	-0.037	0.083	1156	664	491
PNM	0.008	+0.016	-0.014	0.034	509	350	159
MWS	0.051	+0.093	-0.102	0.744	6985	1060	5926
MWI	0.018	+0.033	-0.035	0.133	1741	834	907
MWM	0.008	+0.028	-0.022	0.070	1033	591	441
FFS	0.060	+0.110	-0.124	0.793	8001	1329	6672
FFI	0.046	+0.080	-0.080	0.414	7050	1584	5466
FFM	0.016	+0.048	-0.033	0.130	2403	924	1478
FFS-RLP	0.031	+0.058	-0.059	0.358	3002	631	2370
FFSL-RLP	0.019	+0.026	-0.029	0.145	1679	449	1230
NAS	0.071	+0.137	-0.154	1.292	13287	1654	11633
NAI	0.027	+0.058	-0.055	0.253	3633	1258	2375
NAM	0.017	+0.037	-0.041	0.101	1826	848	978
NAS-RLP	0.119	+0.228	-0.237	1.346	13520	2555	10966
NASL-RLP	0.058	+0.129	-0.131	0.374	6120	2099	4021

Notation

$\gamma_{p\text{-max}}$: inelastic link rotation capacity
γ_{Sp} : inelastic skeleton rotation capacity
$\Sigma\gamma_p$: accumulative inelastic link rotation

E_T : total dissipated energy
E_S : skeleton energy
E_B : Bauschinger energy

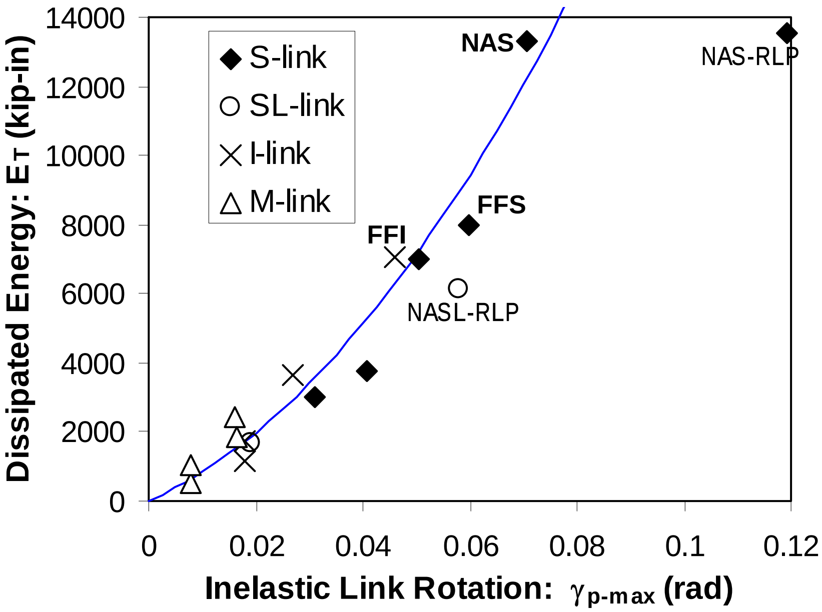

Figure 5.2 Inelastic link rotation capacity versus dissipated energy

polynomial curve of the second degree, fitted to the twelve specimens tested under the AISC loading protocol (Refer to Section 3.2.3 for loading protocols). The trend line reflects the fact that following the AISC loading protocol, the rate of energy dissipation increases as the link rotation amplitude is increased, and that specimens with inferior link rotation capacity are severely penalized for lacking the later loading cycles, which would have added increasingly greater energy dissipation.

The specimens tested under the revised loading protocol do not follow the same trend, suggesting the dependency of the $\gamma_{p\text{-max}}$-E_T relation on the loading protocol. Specimens NAS-RLP and NASL-RLP, which achieved large inelastic link rotations, fall further away from the trend line compared to Specimens FFS-RLP and FFSL-RLP, primarily because the revised protocol is much less severe than the AISC protocol for larger rotation amplitudes. More specifically, for link rotations beyond $\gamma = \pm 0.05$ rad (roughly $\gamma_p = \pm 0.04$ rad), the revised protocol requires one loading cycle per increment in rotation of 0.02 rad, as opposed to two loading cycles per increment in rotation of 0.01 rad required by the AISC protocol.

The effect of the loading protocol on the dissipated energy is illustrated by Figure 5.3, which shows the hysteretic relation between the inelastic link rotation and dissipated energy for Specimens NAS and NAS-RLP. The figure shows that the ratio E_T/γ_p remains essentially constant throughout the entire loading history, although the sign alternates with loading direction. Therefore, the energy dissipated during one loading cycle is linearly dependent on the inelastic link rotation amplitude. Although the energy dissipated per loading cycle were similar at similar rotation amplitudes, Specimen NAS underwent a much larger number of inelastic cycles, while Specimen NAS-RLP dissipated much of the energy during the last five loading cycles. In both specimens, the later loading cycles dissipated increasingly greater amounts of energy, although the increase was

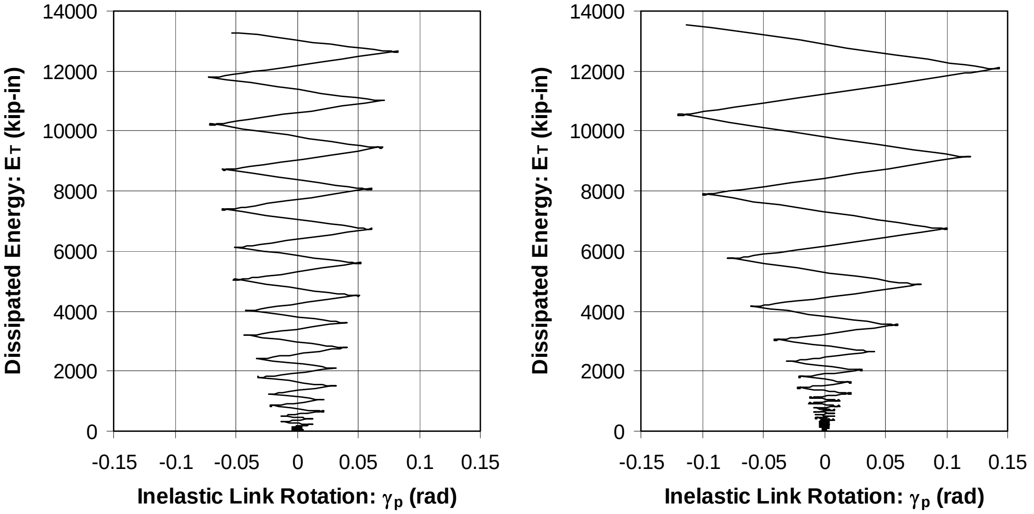

(a) Specimen NAS ***(b) Specimen NAS-RLP***

Figure 5.3 Inelastic link rotation vs. dissipated energy

significantly more rapid in Specimen NAS-RLP, owing to the characteristics of the loading protocol.

The significant variation about the trend line of the twelve specimens tested under the AISC loading protocol in Figure 5.2 is caused by specimens failing at different stages qualifying for the same link rotation capacity. For example, Specimen NAS, which failed during 0.09-1N, completed one and one half cycles beyond the minimum requirement to achieve $\gamma_p = 0.071$ rad. Because of the energy dissipated during the extra loading cycles, the data point for this specimen lies above the trend line. Specimen FFS, which failed during 0.07-2P, completed little more than the minimum requirement to achieve $\gamma_p = 0.060$ rad. The lack of additional loading cycles is reflected by the data point for this specimen lying beneath the trend line. In other words, by accounting for the loading cycles which were rounded down in the evaluation of link rotation capacity, the dissipated energy enhances the difference in performance expressed by link rotation capacity.

Figure 5.4 illustrates the relation between the link length and dissipated energy, E_T. Only the twelve specimens tested under the AISC loading protocol are included in this figure. The figure indicates that shorter shear links are significantly more efficient energy dissipating elements than longer moment links. S-links dissipated roughly twice the energy dissipated by I-links with the same connection type; I-links dissipated twice the energy dissipated by M-links with the same connection type. In terms of dissipated energy, Specimen NAS performed the best for S-links, out-performing the other specimens by 70 to 250%. Specimen FFI performed the best for I-links, out-performing the other specimens by 90 to 500%. For M-links, Specimen FFM performed somewhat better than Specimen NAM. The PN-specimens performed the poorest for all link lengths, dissipating only a quarter or less energy of the best performing specimen.

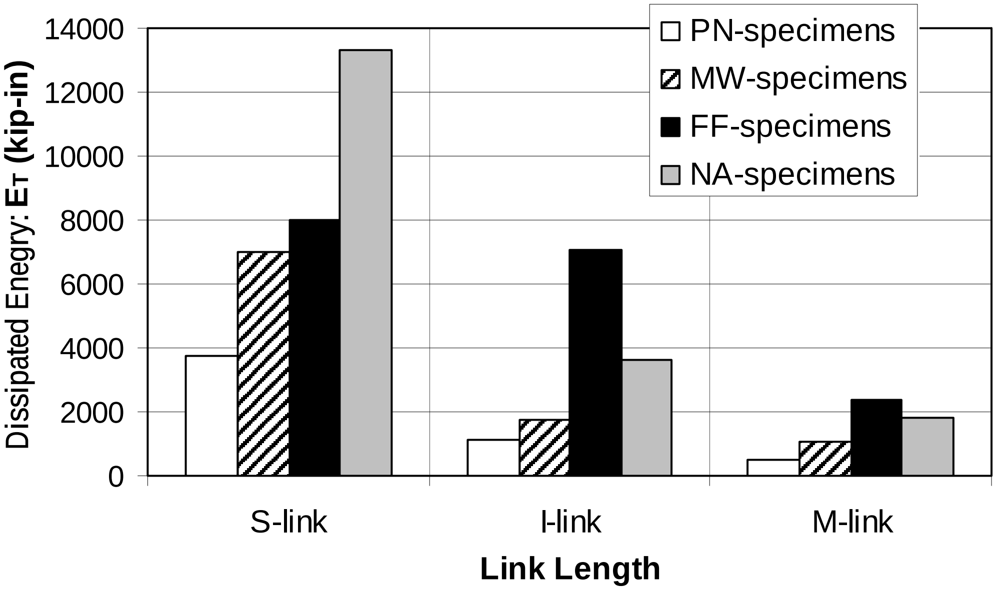

Figure 5.4 Dissipated energy

The MW-specimens dissipated roughly twice the energy dissipated by the PN-specimens with the same link lengths. With the exception of Specimen FFS, all FF- and NA-specimens dissipated twice or more energy than the corresponding PN- and MW- specimen with the same link lengths.

5.3.3 Skeleton Curve

The skeleton curve, introduced by Akiyama and Kato (1968), has been used extensively in Japanese research (*e.g. Full-scale* 1997; Suita *et al.* 1998) to evaluate the performance of ductile steel connections. The skeleton curve provides a rational basis for comparing test results using different loading sequences, since previous investigations (Akiyama 1985) suggest that the skeleton curve closely represents the response under monotonic loading, as long as significant buckling or fracture is avoided.

In this research, skeleton curves are constructed from the hysteretic curve of the link rotation, γ, versus link shear, V, by the following procedure. The portion of the γ-V curve with the shear force exceeding the maximum shear force from previous loading cycles is extracted as a new portion of the skeleton curve. The new portion is added to the skeleton curve constructed from previous loading cycles, with its origin of γ coinciding to the maximum γ of the already constructed curve. This procedure is repeated until the maximum link shear is reached. It should be stressed that although some researchers include the softening portion of the hysteretic curve, only the hardening portion is included to construct the skeleton curve in this research. The skeleton curve described above was constructed from both the positive and negative excursions of the γ-V curves. During positive excursions, both link rotation and link shear force increase monotonically; during negative excursions, both link rotation and link force decrease monotonically. Figure 5.5 illustrates the construction of skeleton curves from the γ-V hysteretic curve of Specimen MWI.

Figure 5.6 shows examples of skeleton curves constructed from the I-link specimens. Only the positive skeleton curves are shown. The four skeleton curves constructed from the hysteretic responses of Specimens PNI, MWI, FFI, and NAI follow a very similar trend, although the curve for Specimens FFI showed elevated strength compared to the other three curves. This figure illustrates that the skeleton curves resemble the response of specimens subjected to monotonic loading, where the strength of the specimen continuously increases with increase in link rotation until fracture or buckling causes strength degradation. A similar observation can be made for the positive and negative skeleton curves constructed from all sixteen specimens shown in Figure 5.7. In this figure, the inelastic skeleton rotation, evaluated by removing the elastic contribution from the total skeleton rotation, is taken for the abscissa instead of the total skeleton rotation.

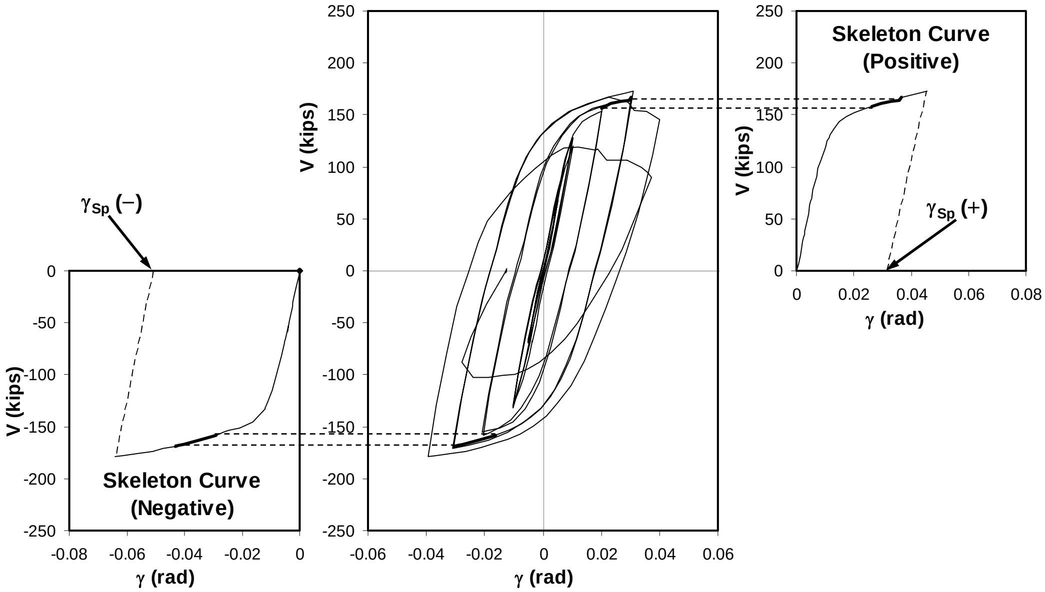

Figure 5.5 Skeleton curve constructed for Specimen MWI.

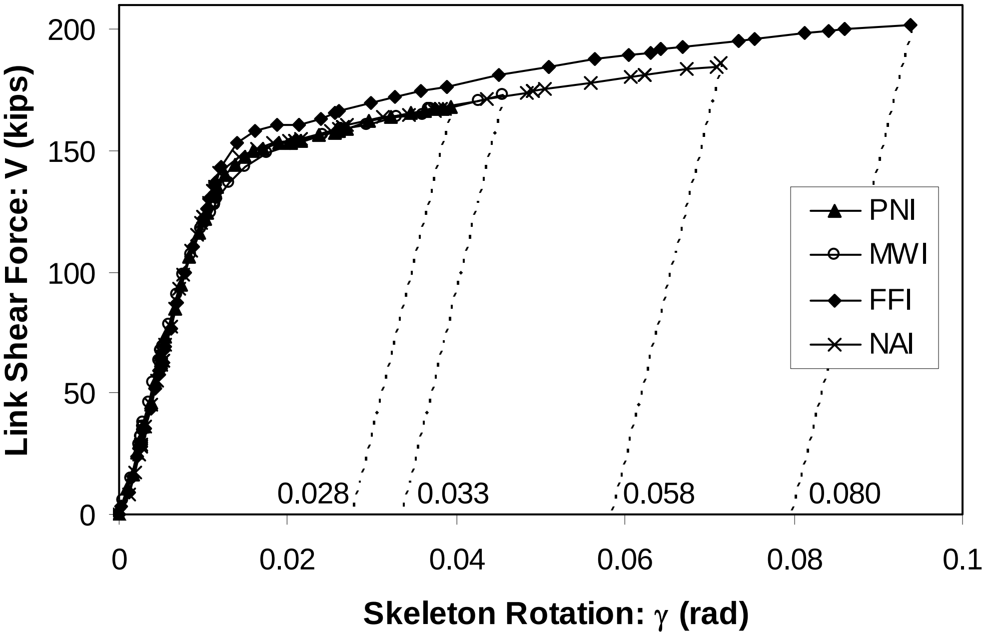

Figure 5.6 Positive skeleton curves for specimens with I-links

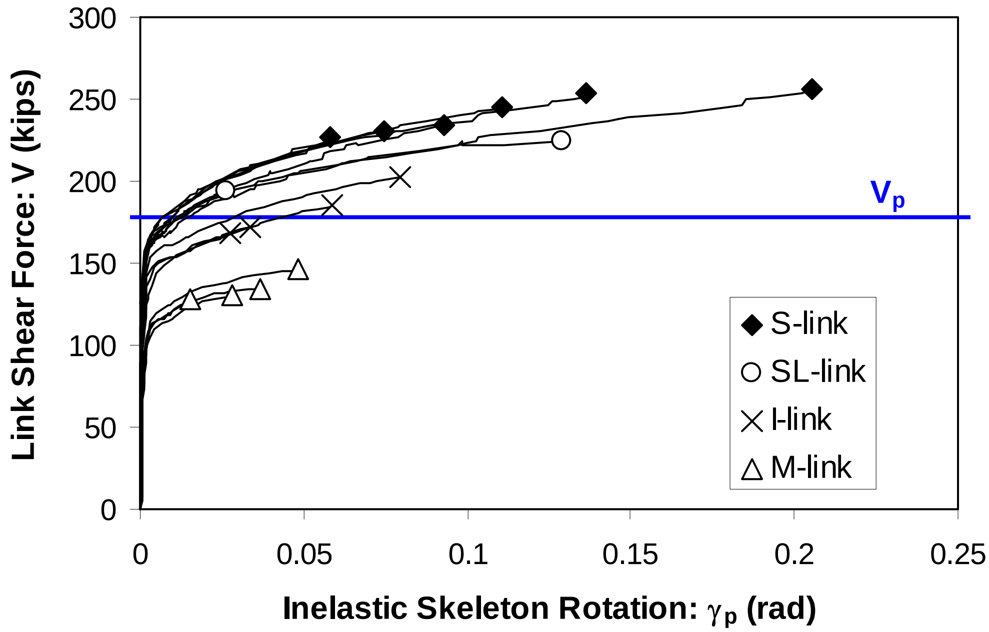

(a) Positive Skeleton Curve

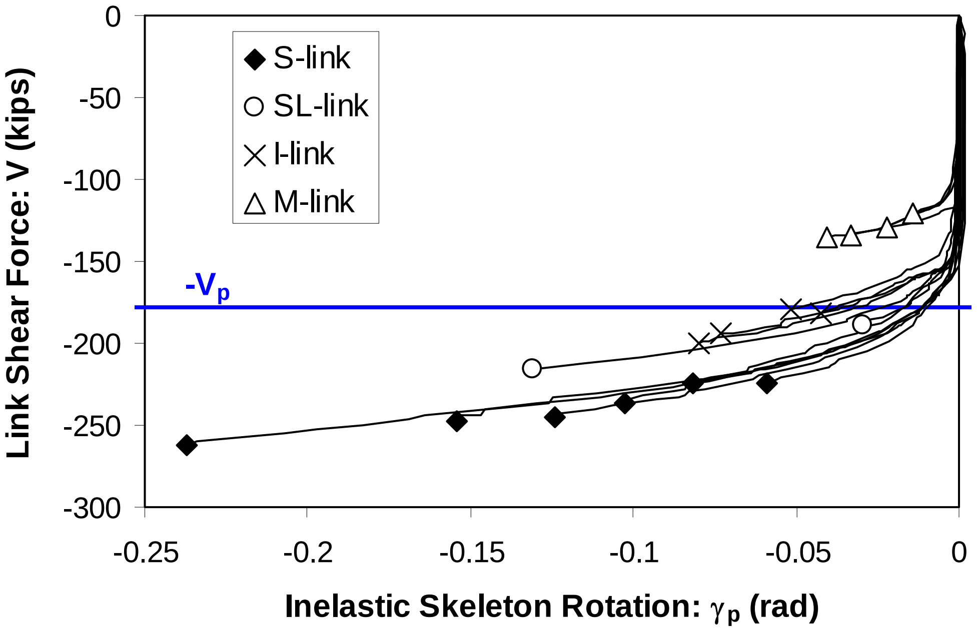

(b) Negative Skeleton Curve

Figure 5.7 Inelastic skeleton rotation vs. maximum link shear

The dependency of the skeleton curve on link length, and the resemblance to monotonic response, as recognized in Figure 5.6, is also clearly seen in Figure 5.7.

Since the skeleton curve omits fatigue effects due to cyclic loading, it provides a reasonable lower-bound prediction of the deformation capacity and strength of the same specimen had it been subjected to monotonic loading. Multiple performance measures with unique physical significance can be deduced from the skeleton curve, as described in the following.

In this research, the maximum rotation obtained by the skeleton curve is defined as the inelastic skeleton rotation capacity, γ_{Sp}. As illustrated in Figure 5.5, the positive and negative skeletons each produce a distinct skeleton rotation capacity. Figure 5.7 indicates the points where the values of γ_{Sp} were measured. Because the skeleton curve is a reasonable representation of the monotonic loading curve, the inelastic skeleton rotation also indicates the extent of strain hardening developed by the specimen.

The skeleton energy E_S is evaluated by taking the product of the link length, e, and the sum of two areas: one enclosed by the positive skeleton curve, the abscissa, and the elastic unloading line; the other enclosed by the negative skeleton curve, the abscissa, and the elastic unloading line (See Figure 5.5). The skeleton energy represents the amount of energy required to produce the strain hardening developed in the specimen. The energy dissipated by the specimen, E_T, as defined in Section 5.3.2, can be decomposed into two components: the skeleton energy, E_S, and the Bauschinger energy, E_B, as follows:

$$E_T = E_S + E_B \ . \tag{5.1}$$

The Bauschinger energy thus defined represents the portion of the dissipated energy that was not accompanied by strain hardening, and was purely used to generate low cycle fatigue effects (Kuwamura and Takagi 2004; Ichinohe and Kuwamura 2000). Furthermore, the ratio E_B/E_T or E_B/E_S may be regarded as a parameter representing the relative significance of low cycle fatigue in the response of the specimen.

The values of γ_{Sp}, E_S, and E_B computed for each specimen are summarized in Table 5.2. Values evaluated from both the positive (+) and negative (-) skeleton curves are listed for γ_{Sp}. The table shows that the difference between the absolute values of the positive and negative γ_{Sp}'s ranged between 2 and 32%.

Figure 5.8 illustrates the correlation between the inelastic link rotation capacity, $\gamma_{p\text{-max}}$, and the skeleton inelastic rotation capacity, γ_{Sp}. In this figure, the smaller absolute value of the positive and negative inelastic skeleton rotations is used. A linear trend line is fitted to all sixteen test data points. Figure 5.8 suggests that for all specimens, regardless of the link length, connection type, or loading protocol, the skeleton inelastic rotation was approximately twice the inelastic link rotation capacity.

Figure 5.9 illustrates the inelastic skeleton rotation achieved by all sixteen specimens. As discussed earlier, the skeleton rotation capacity is a lower bound estimate for rotation capacity under monotonic loading. However, the 35% difference between Specimens NAS and NAS-RLP indicates the dependency of the estimation on the loading protocol. The decrease in skeleton rotation capacity with link length simply reflects the decrease in link rotation capacity with link length. The inelastic skeleton rotation capacities of Specimens PNS, PNI, PNM, MWI, FFS-RLP, and FFSL-RLP were smaller than the required inelastic rotations indicated in the figure. Therefore, these specimens may not have achieved the rotation requirements even under monotonic loading. On the other hand, the remaining ten specimens with inelastic skeleton rotation capacities greater than their required inelastic rotations would most likely exceed the same rotation requirement under monotonic loading. Nonetheless, only two of those ten

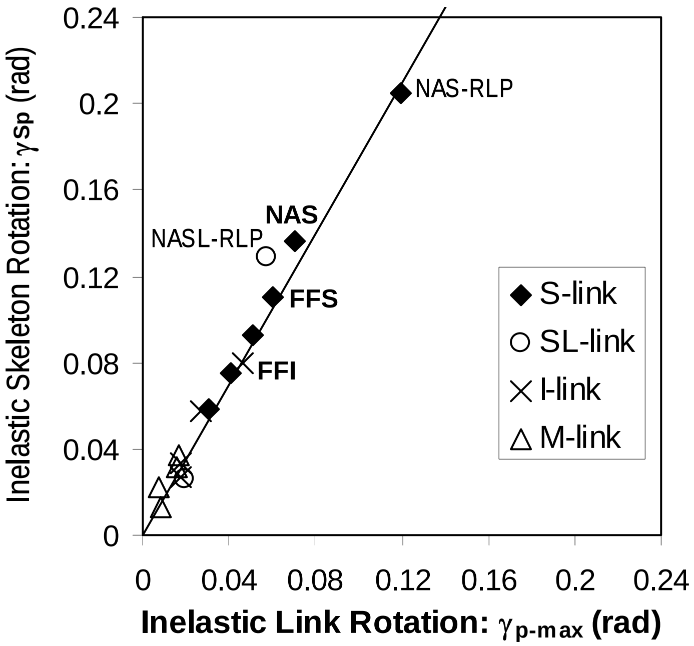

Figure 5.8 Inelastic link rotation vs. inelastic skeleton rotation.

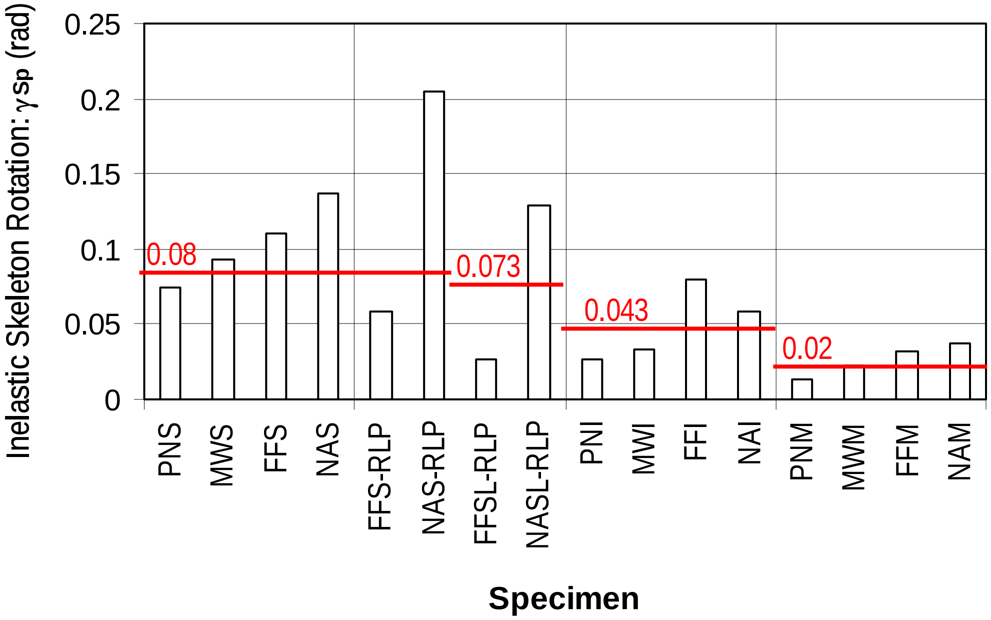

Figure 5.9 Inelastic skeleton rotation

specimens, FFI and NAS-RLP, satisfied the acceptance criteria per the *AISC Seismic Provisions*. Since the inelastic skeleton rotations of Specimens NAS, NASL-RLP, and NAM exceeded their required inelastic link rotations by significant margins, these specimens may have achieved the rotation requirements had they been subjected to less severe loading sequences.

Figure 5.10 illustrates the dissipated energy decomposed into the skeleton and Bauschinger components. The skeleton energy represents the energy dissipated by an equivalent monotonic loading curve, while the Bauschinger energy represents the energy dissipated through fatigue cycles, without generating any strain hardening. For a monotonic loading case, $E_B = 0$, and hence, $E_T = E_S$. Figure 5.10 shows that the Bauschinger energy decreases drastically with link length, and increases moderately with dissipated energy. The skeleton energy

Figure 5.10 Skeleton energy and Bauschinger energy

dominated the energy dissipation in Specimens PNI, PNM, and MWM, which had either an I- or M-link, and failed very prematurely, achieving only 40% of the required inelastic link rotation. In all eight specimens with either an S- or SL-link, the Bauschinger energy accounted for roughly 80% of the total energy dissipation, regardless of the large variation in dissipated energy. Therefore, it appears that the effect of strain hardening is more limited for shorter shear yielding links than for longer flexure yielding links, or conversely, low cycle fatigue effects are more significant in short shear links than in longer links.

5.3.4 Cumulative Inelastic Rotation

The cumulative inelastic rotation, $\Sigma\gamma_p$, is defined as the sum of the increments in inelastic link rotation associated with each half loading cycle. Figure 5.11 illustrates the computation of cumulative inelastic rotation based on the hysteretic relation between the link rotation, γ, and link shear, V, of Specimen MWI. Similar to the dissipated energy, the γ-V curve was included up to the point where the strength of the specimen was lost. The cumulative energy is a reasonable basis for comparing tests conducted under different loading histories, similar to the dissipated energy.

Figure 5.12 shows the relation between the inelastic link rotation capacity, $\gamma_{p\text{-}max}$, and cumulative inelastic rotation, $\Sigma\gamma_p$. The trend line shown in the figure is a polynomial curve of the second degree, fitted to the twelve specimens tested under the AISC loading protocol. A similar polynomial trend was recognized between the inelastic link rotation capacity and dissipated energy, as discussed in Section 5.3.2. The specimens tested under the revised loading protocol, notably Specimens NAS-RLP and NASL-RLP, fall far away from the trend line. Similar to the dissipated energy, the cumulative inelastic rotation is sensitive to the loading history.

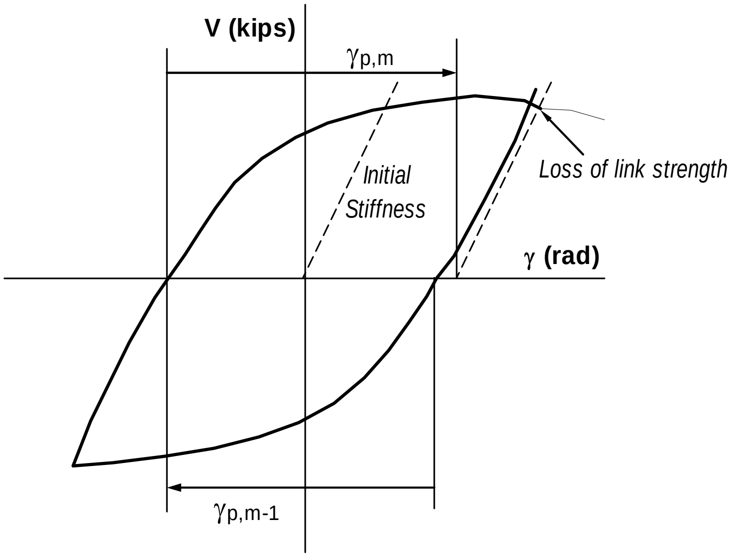

$$\sum \gamma_{\mathrm{p}} = \gamma_{\mathrm{p},1} + \gamma_{\mathrm{p},2} + \cdots + \gamma_{\mathrm{p},\mathrm{m}-1} + \gamma_{\mathrm{p},\mathrm{m}}$$

Figure 5.11 Computation of cumulative inelastic rotation (example shown for specimen MWI)

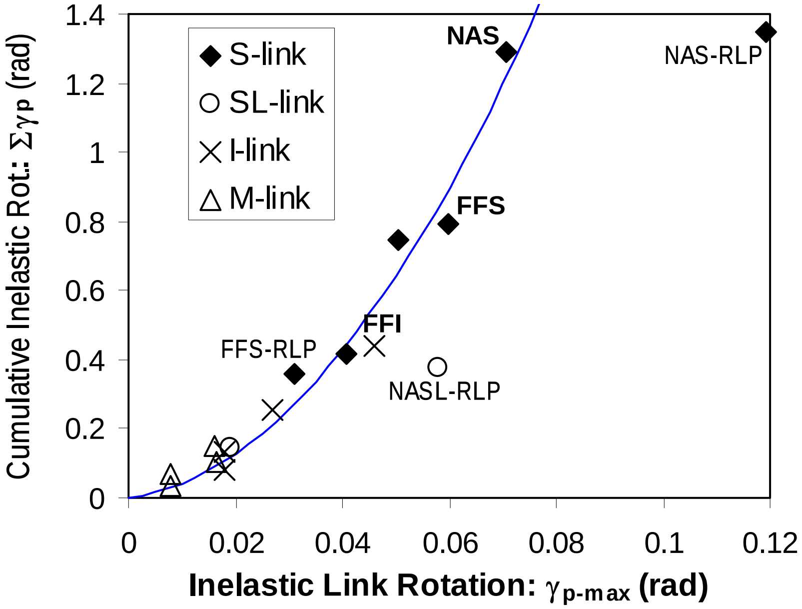

Figure 5.12 Inelastic link rotation vs. cumulative inelastic link rotation

Figure 5.13 shows the relation between the cumulative inelastic rotation, $\Sigma\gamma_p$, and dissipated energy, E_T. The figure clearly indicates that the $\Sigma\gamma_p$-E_T relation depends strongly on link length. Longer links dissipated energy more rapidly with accumulation of inelastic rotation, but ultimately developed smaller values of $\Sigma\gamma_p$ and E_T, while shorter links dissipated energy less rapidly with accumulation of inelastic rotation, but ultimately developed greater values of $\Sigma\gamma_p$ and E_T. The effect of link length on the dissipated energy is twofold: a greater link length results in a proportionally greater energy dissipation for a given γ-V hysteresis; on the other hand, since longer links tend to develop smaller shear forces, the area enclosed in the γ-V loop tends to be smaller. Dependency on link length is present in the $\gamma_{p\text{-max}}$–E_T relation (See Figure 5.3) and $\gamma_{p\text{-max}}$–$\Sigma\gamma_p$ relation (See Figure 5.12), although not as clearly noticeable as in the $\Sigma\gamma_p$–E_T relation (Figure 5.13). A linear correlation is noted between the cumulative inelastic rotation and dissipated

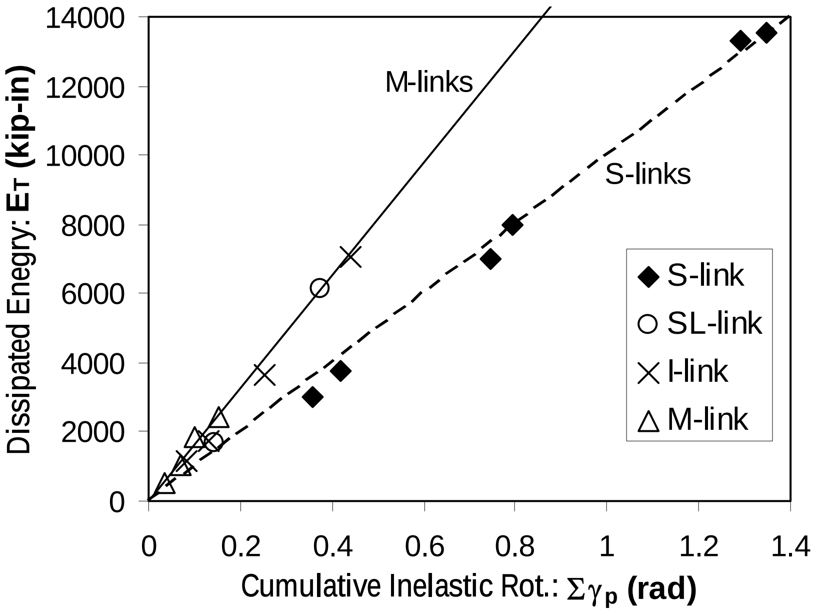

Figure 5.13 Cumulative inelastic link rotation vs. dissipated energy

energy for any given link length. The loading protocol appears to have limited influence on the $\Sigma\gamma_p$–E_T relation.

Figure 5.14 shows the cumulative inelastic rotation normalized by the required inelastic rotation for all sixteen specimens. Similar to the dissipated energy, the cumulative inelastic rotation is expected to provide a basis for comparing specimens tested under different loading sequences. As indicated by Figure 5.13, among specimens with the same link length, the cumulative inelastic rotation is approximately proportional to the dissipated energy. Therefore, the same observations made in Section 5.3.2 from Figure 5.4 can be made from Figure 5.14.

Specimens NAS, FFI, and FFM, which nearly or barely achieved the required inelastic rotation, exemplify the cumulative rotations that develop under the AISC loading protocol with respect to the required inelastic link rotation. The

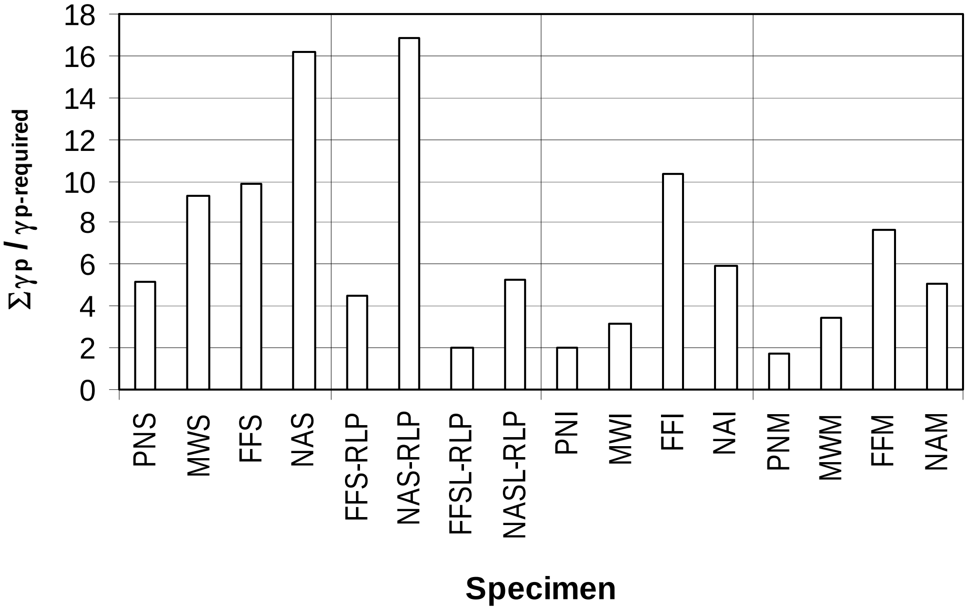

Figure 5.14 Cumulative inelastic rotation

S-links develop normalized cumulative inelastic rotations of over fifteen, while I-links develop roughly ten, and M-links develop below ten. Furthermore, despite the 50% difference in inelastic rotation capacity between Specimens NAS and NAS-RLP, the two specimens underwent very similar cumulative inelastic rotation. These comparisons might indicate that the AISC loading protocol was unduly penalizing to shorter links.

5.3.5 Discussion

The alternative measures for performance evaluation can highlight aspects of specimen response that are not well reflected in the inelastic link rotation. The dissipated energy and cumulative inelastic link rotation have the advantage of being less sensitive to the loading history. For example, Specimens NAS and NAS-RLP, which are virtually identical specimens tested under different loading protocols, achieved very similar dissipated energy and cumulative inelastic deformation. The skeleton rotation maps the response history to an equivalent monotonic loading curve, and thereby represents the extent of strain hardening developed over the loading history. On the other hand, the skeleton rotation and skeleton energy completely omits the low cycle fatigue effects. The Bauschinger energy is an indicator for the severity of fatigue effects.

Overall, the alternative measures correlate well with each other, except in their dependency to the loading history. Comparison between the measures illustrates that the inelastic link rotation is quite sensitive to the loading history. The Bauschinger energy strongly suggests that AISC loading protocol was increasingly severe to shorter links. It is worth noting that these issues are taken into consideration in the revised loading protocol for short shear links developed by Richards and Uang (2003). Moreover, since the revised loading protocol was developed based on a rational basis to represent the seismic demands under realistic ground motions, the revised loading protocol should be used instead of the AISC protocol to evaluate the performance of connections of shear links to columns.

The different measures combined may shed some light into the cause of different failure modes in Specimens NAS and NAS-RLP (Refer to Section 4.6.4). As stated above, the dissipated energy and cumulative inelastic link rotation were very similar for these two virtually identical specimens. However, Specimen NAS-RLP developed greater strain hardening than Specimen NAS, as evidenced by its greater skeleton rotation (γ_{Sp} = 0.23 rad as opposed to 0.14 rad) and greater shear force (V_{max} = 262 kips as opposed to 253 kips). On the other hand, the Bauchinger energy was greater in Specimen NAS ($E_B = 0.88E_T$ as opposed to $0.81E_T$ in Specimen NAS-RLP). The greater strain hardening effect in Specimen NAS-RLP may have imposed a more severe stress and strain environment near the flange welds, and allowed fracture to occur in the link flanges before at the link web stiffeners. The greater fatigue effects in Specimen NAS may have caused the fractures at the link web stiffeners to grow more rapidly than in Specimen NAS-RLP.

5.4 LINK FORCES

5.4.1 Maximum Link Forces

The measured link forces are of principal interest in two respects. First, the maximum forces developed in the link are important information for the capacity design procedure of EBFs (Refer to Section 2.2.2). Secondly, the link forces represent the force environment at the link-to-column connection.

Table 5.3 summarizes the maximum link forces measured from the tests, listing the link overstrength factor, V_{max}/V_n, alongside the normalized maximum shear force, V_{max}/V_p, and the normalized maximum moment at the column face,

M_{max}/M_p. Here, V_n, is the nominal shear strength of the link defined as the smaller of V_p and $2M_p/e$ (AISC 2002), and V_p and M_p are the shear strength and full plastic moment of the link section, evaluated based on measured dimensions and tension coupon tests. V_n is controlled by either shear yielding or flexure yielding, depending on the link length. Both positive and negative values of the forces are separately listed in Table 5.3.

Table 5.3 shows that the link forces varied quite significantly between specimens, with the absolute value of V_{max}/V_p varying between 0.68 and 1.42, M_{max}/M_p between 0.77 and 1.28, and V_{max}/V_n between 1.05 and 1.47. The link

Table 5.3 Normalized maximum link forces

Specimen	V_{max}/V_p		M_{max}/M_p		V_{max}/V_n	
PNS	-1.26	+1.29	-0.78	+0.81	-1.26	+1.29
PNI	-1.02	+0.94	-1.10	+1.07	-1.13	+1.05
PNM	-0.68	+0.72	-1.16	+1.12	-1.13	+1.19
MWS	-1.32	+1.32	-0.77	+0.81	-1.32	+1.32
MWI	-1.00	+0.97	-1.05	+0.99	-1.11	+1.08
MWM	-0.73	+0.73	-1.13	+1.16	-1.21	+1.22
FFS	-1.38	+1.37	-0.86	+0.87	-1.38	+1.37
FFI	-1.12	+1.13	-1.21	+1.28	-1.25	+1.26
FFM	-0.75	+0.82	-1.25	+1.25	-1.26	+1.37
FFS-RLP	-1.26	+1.27	-0.74	+0.83	-1.26	+1.27
FFSL-RLP	-1.06	+1.09	-0.90	+0.96	-1.06	+1.09
NAS	-1.39	+1.42	-0.85	+0.88	-1.39	+1.42
NAI	-1.09	+1.04	-1.12	+1.17	-1.21	+1.16
NAM	-0.76	+0.75	-1.17	+1.23	-1.26	+1.26
NAS-RLP	-1.47	+1.44	-0.82	+0.88	-1.47	+1.44
NASL-RLP	-1.21	+1.26	-0.98	+1.03	-1.21	+1.26

Note: The following values were used for the evaluation summarized in this table: V_p = 178.3 kips; M_p = 4008 kip-in; V_n = 178.3, 178.3, 160.3, and 106.9 kips for S-, SL-, I-, and M-links, respectively. The positive and negative values for V_{max} and M_{max} are reported in Table.4.2.

forces were governed primarily by three factors: (a) the link length, (b) the geometry of the link-to-column connection, and (c) the extent of strain hardening.

As discussed in Section 2.2.1, the link length has significant influence on forces developed in the link. Shear links ($e \leq 1.6M_p/V_p$) yield primarily in shear and develops shear forces significantly greater than the nominal shear strength. In shear links, the shear strength bounds the moments that can be developed at the link ends. On the contrary, in moment links ($e \geq 2.6M_p/V_p$), which yield primarily in flexure, the shear strength is bounded by the flexural strength. The strength of intermediate links ($1.6M_p/V_p \leq e \leq 2.6M_p/V_p$), which are governed by both shear and flexural behavior, is significantly influenced by moment-shear interaction. Therefore, shorter links generally develop greater shear forces, while longer links develop greater end moments. Table 5.3 shows that the absolute value of the maximum link shear force ranged from 1.26 to $1.47V_p$ for S-links, from 0.94 to $1.13V_p$ for I-links, and from 0.68 to $0.82V_p$ for M-links. The absolute value of the maximum column face moment ranged from 0.77 to $0.88M_p$ for S-links, from 1.05 to $1.28M_p$ for I-links, and from 1.12 to $1.25M_p$ for M-links.

For S-links, in which the web develops very high shear stress, the flexural capacity might be more accurately estimated by omitting the contribution of the web, as discussed in Section 4.6.3. The plastic flexural capacity of the link section based on only the flanges, $M_{p\text{-flanges}}$, was evaluated as 2691 kip-in. The maximum column face moment values normalized by $M_{p\text{-flanges}}$ are listed in Table 5.4. The $M_{max}/M_{p\text{-flanges}}$ value for S-links varied from 1.15 to 1.3, which is similar in magnitude to the M_{max}/M_p values for I- and M-links listed in Table 5.3. Therefore, the S-links may have developed very large bending stresses at the flanges, comparable in magnitude to those in longer I- and M-links.

The rotational restraint and the force and deformation capacity of the link-to-column connection have a direct influence on the link forces. A higher

Table 5.4 Normalized maximum moment

Specimen	$M_{max}/M_{p\text{-flanges}}$
PNS	-1.16 +1.20
MWS	-1.14 +1.21
FFS	-1.28 +1.30
FFS-RLP	-1.10 +1.24
FFSL-RLP	-1.34 +1.43
NAS	-1.27 +1.31
NAS-RLP	-1.23 +1.31
NASL-RLP	-1.45 +1.53

Note: In this table: $M_{p\text{-flanges}}$ = 2691 kip-in. The positive and negative values for M_{max} are reported in Table.4.2.

rotational restraint supplied by the link-to-column connection results in larger moment at the column face for the same link shear force. Meanwhile, the link forces are inevitably limited by the strength of the link-to-column connection. The specimens which developed greater link rotation also developed greater link forces.

The primary cause of a link developing greater forces as it undergoes greater rotation is strain hardening. Due to strain hardening, a link can develop forces much greater than the nominal level. The relation between link rotation, connection performance, and strain hardening is discussed in Section 5.3.3. Figure 5.7 indicates that all specimens were strain hardening when failure occurred, and that had the specimens failed in a later stage, they could have developed larger forces.

On the other hand, the factor of M_{max}/M_p and V_{max}/V_p in the range of 1.3 to 1.5 cannot be explained by the yield ratio F_y/F_u of 0.74 in the flanges and 0.80 in the web of the W18x40 link section obtained from tension coupon tests (See Table B1). This may be evidence that the strength of steel can change significantly as it undergoes inelastic deformation. In fact, Figure 3.17 suggests that the same W18x40 section had much higher tensile strength in the k-area, where the roller straightening process imposes locally severe strains. However, the relation between the material properties and inelastic deformation history is not well known.

5.4.2 Link Overstrength

As discussed in Section 2.2.4, EBF links develop significant overstrength primarily due to strain hardening of the material. An appropriate estimation of link overstrength is essential to the capacity design procedure adopted in the *AISC Seismic Provisions*.

As shown in Table 5.3, the link overstrength factor, V_{max}/V_n, computed for S-links averaged at 1.36, ranging from 1.27 in Specimens PNS and FFS-RLP to 1.47 in Specimen NAS-RLP. The overstrength factor for I-links averaged at 1.18, ranging from 1.11 in Specimen MWI to 1.26 in Specimen FFI. The overstrength factor for M-links averaged at 1.26, ranging from 1.19 in Specimen PNM to 1.37 in Specimen FFM. These values are slightly lower than the values measured in isolated links tested by Arce (2002) and Ryu *et al.* (2004). Arce and Ryu *et al.* measured an average overstrength of 1.42 for shear links, and 1.21 for intermediate links and moment links, all constructed of A992 steel (Refer to Section 2.4.5).

Besides Specimens NAS which failed due to fracture of the link web, all specimens failed by fracture at the link-to-column connection. Many of the specimens failed to develop the inelastic link rotation required in the *2002 AISC Seismic Provisions*. Had the link-to-column connection not failed prematurely, these specimens could have developed greater forces in the link.

In light of the above, the link overstrength factor measured in the current program is in fair agreement with those measured by Arce (2002) and Ryu *et al.* (2004), although the overstrength factor measured in the current tests tended to be somewhat smaller for short shear links. Therefore, the overstrength factor of 1.5 implied in the current provisions is reasonable.

5.4.3 Moment-Shear Interaction

Figure 5.15 shows the moment-shear history at the column face. The sixteen specimens are separated into six groups depending on the connection type and loading protocol used for testing. Each of the six figures compares two or three specimens with the same connection type but with different link length. The hysteretic response is included up to the stage when the strength of the specimen was lost (Refer to Section 3.2.6).

Figure 5.15 indicates that the moment-to-shear ratio is controlled by the link length. The moment-to-shear ratio remained constant through the initial elastic loading cycles. The decline in gradient of the hysteretic curves near the turning points (corresponding to peak link rotation) corresponds to inelastic action, during when the rate of increase of shear force was greater than the rate of increase of column face moment. The moment-shear hysteretic curves grew increasingly thicker during later inelastic cycles, as the link rotation amplitude increased. The connection type appears to have little influence on the moment-shear relation, except that the FF-connections were capable of developing slightly greater forces than the other connections.

Another interesting observation from Figure 5.15 is that the decline in the gradient of the hysteretic curves was increasingly severe for shorter links. In Specimens NAS and NAS-RLP, the gradient decreased to below zero near the turning points in later loading cycles. In Specimen MWS, the gradient decreased, and then, increased near the turning points. This behavior is further illustrated in Figure 5.16, which follows the relation between link rotation, link shear force, column face moment, and beam end moment in Specimen NAS during the loading cycle 0.07-1. The numbers “1” through “4” in the figure denotes common load steps. The moment-shear relation shown in Figure 5.16c is roughly linear during 1-2-3, including the duration 2-3 when Figure 5.16a and Figure 5.16b clearly indicates yielding of the link. During 3-4, when the link underwent large inelastic rotation, the gradient of the moment-shear curve shown in Figure 5.16c dropped to below zero. Figure 5.16b shows that the column face moment actually decreased during this time. Figure 5.16d shows that very significant moment redistribution took place, as the beam end moment increased while the column end moment slightly decreased. The decrease in column face moment with increase in link rotation is also observed in Figure 4.9d, Figure 4.28d, and Figure 4.34d.

Figures 4.2d, 4.9d, 4.17d, 4.23d 4.28d, and 4.34d suggest that the link moment at the column end reached a peak magnitude at a link inelastic rotation of roughly γ_p = 0.04 rad. In Specimens MWS, NAS, and NAS-RLP, the column end moment reduced with an increase of link rotation at rotations beyond γ_p = 0.04 rad. It is possible that these three specimens developed their full flexural strength at the column end of the link. As discussed in Section 5.4.1, due to the severe shear in the link web, the flexural capacity of the link was significantly reduced, and very severe bending stresses developed in the link flanges. Therefore, even for connections of a short shear link to a column, where the effect of shear may be regarded dominant, the level of bending stresses can be the controlling factor for connection performance.

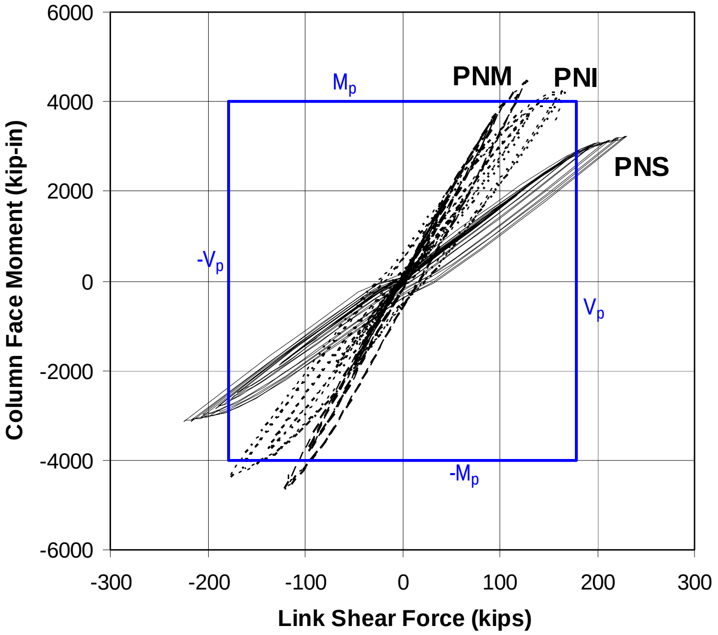

(a) PN-specimens tested under AISC protocol

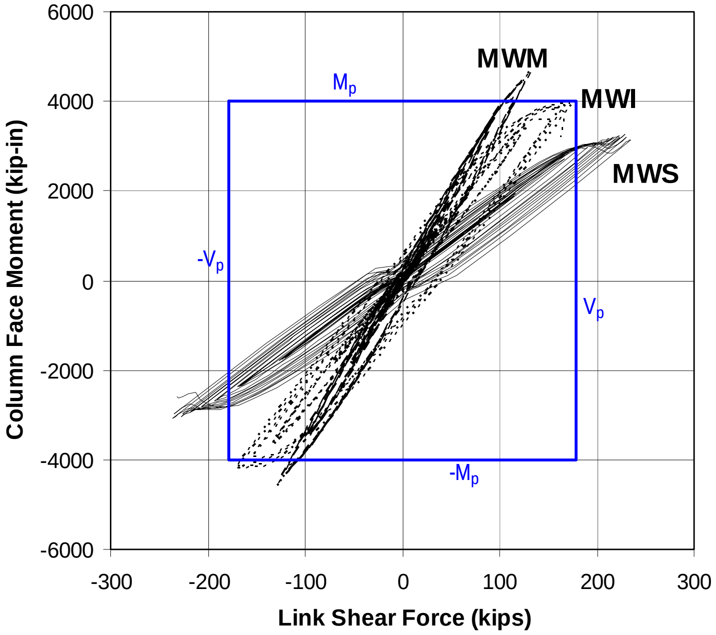

(b) MW-specimens tested under AISC protocol

Figure 5.15 Shear force vs. column face moment

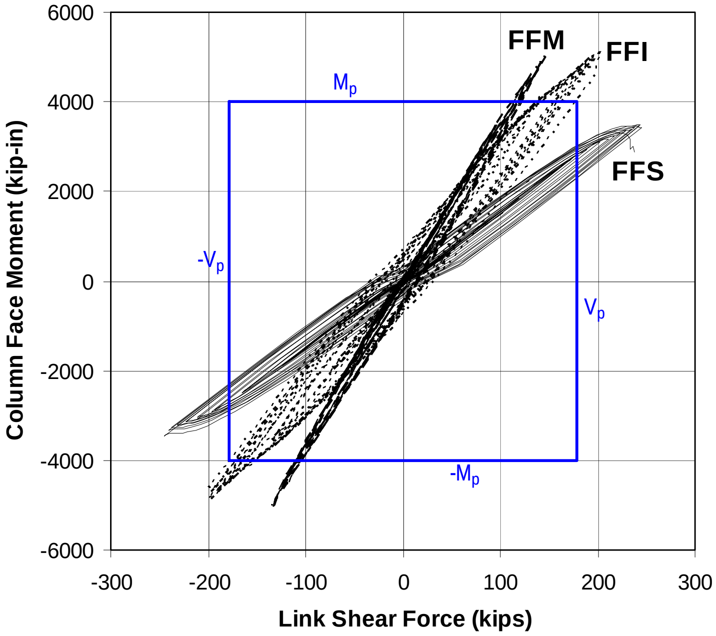

(c) FF-specimens tested under AISC protocol

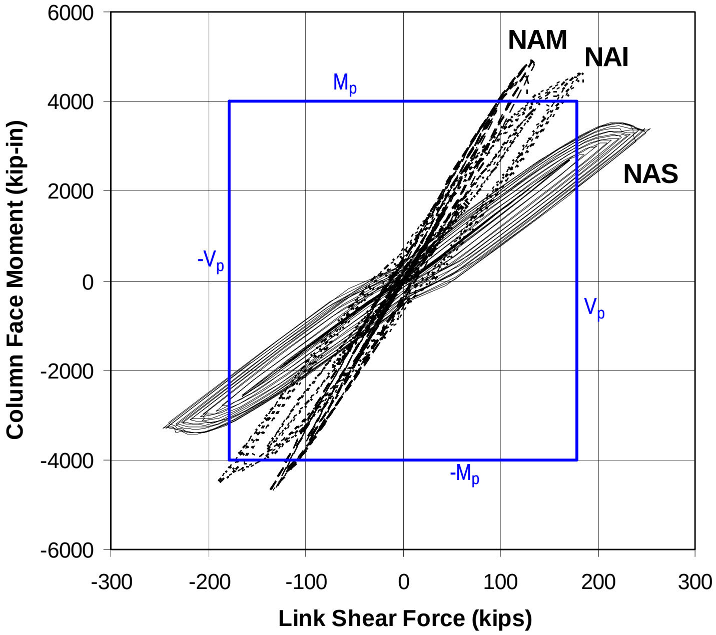

(d) NA-specimens tested under AISC protocol

Figure 5.15 Shear force vs. column face moment (Continued)

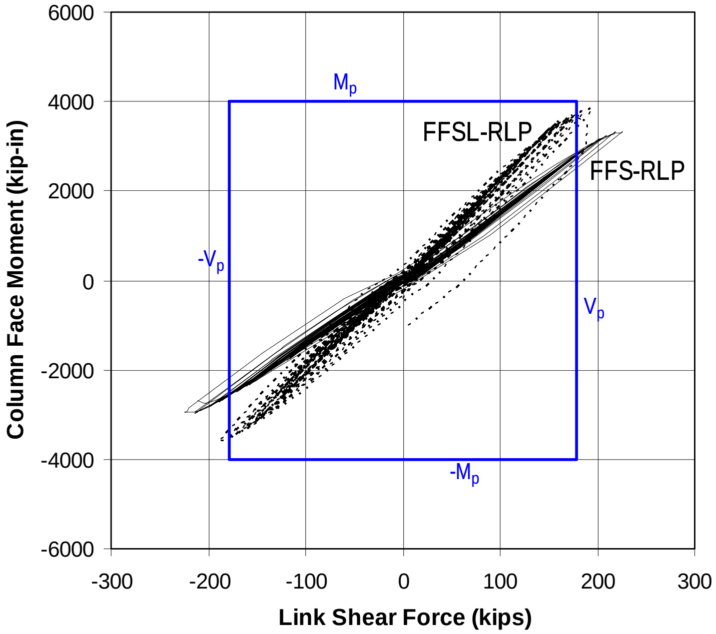

(e) FF-specimens tested under revised protocol

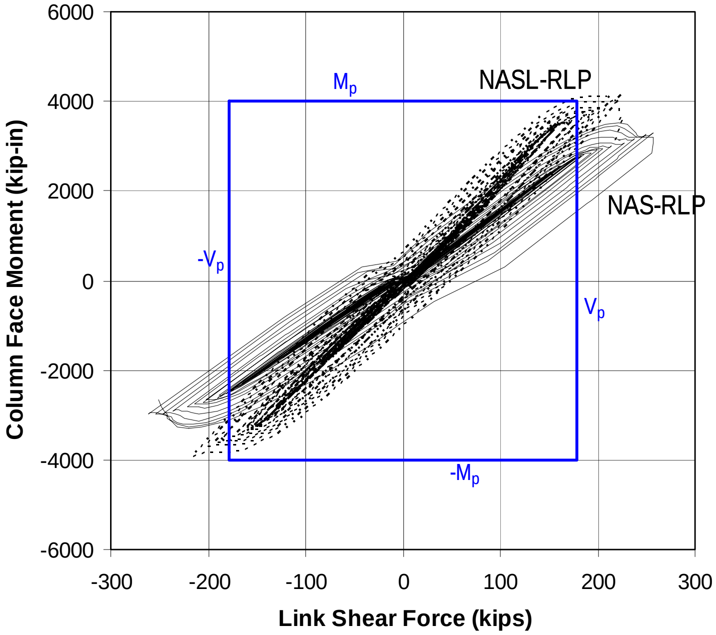

(f) NA-specimens tested under revised protocol

Figure 5.15 Shear force vs. column face moment (Continued)

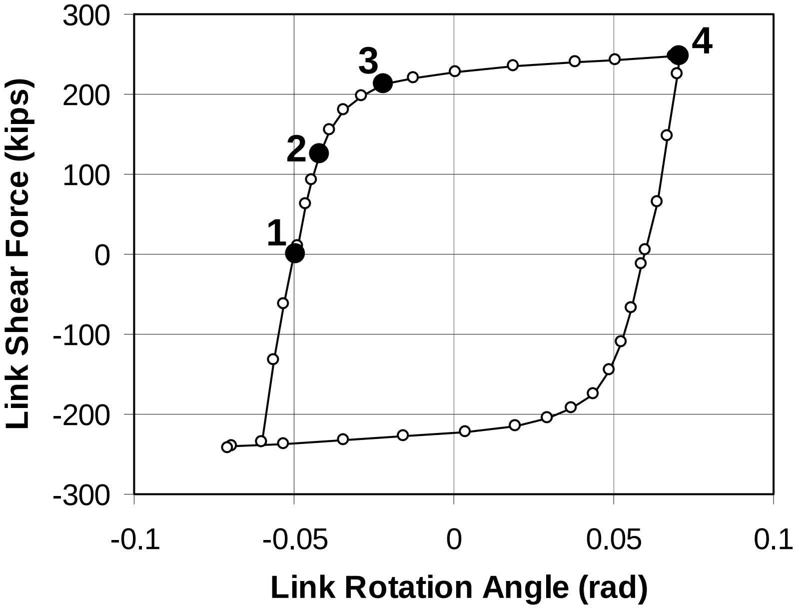

(a) Link Shear vs. Link Rotation

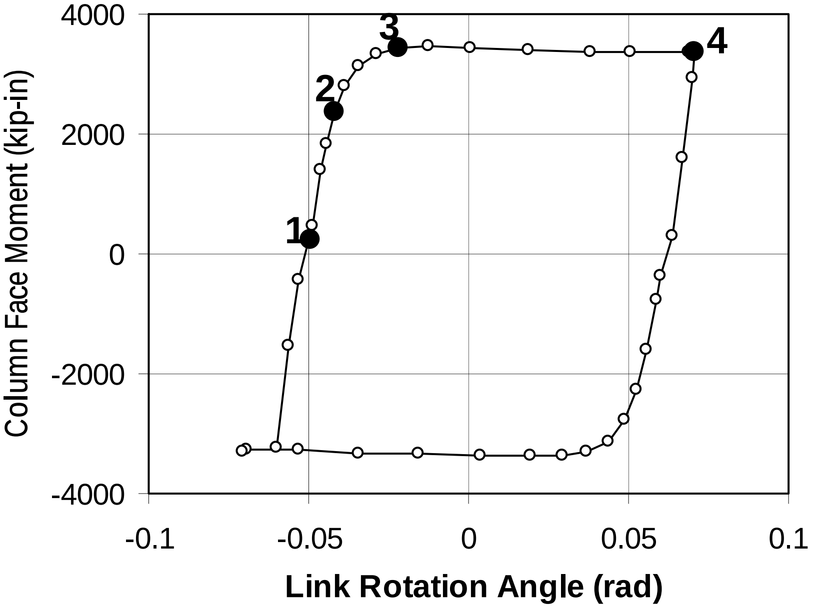

(b) Column Face Moment vs. Link Rotation

Figure 5.16 Detailed behavior of Specimen NAS

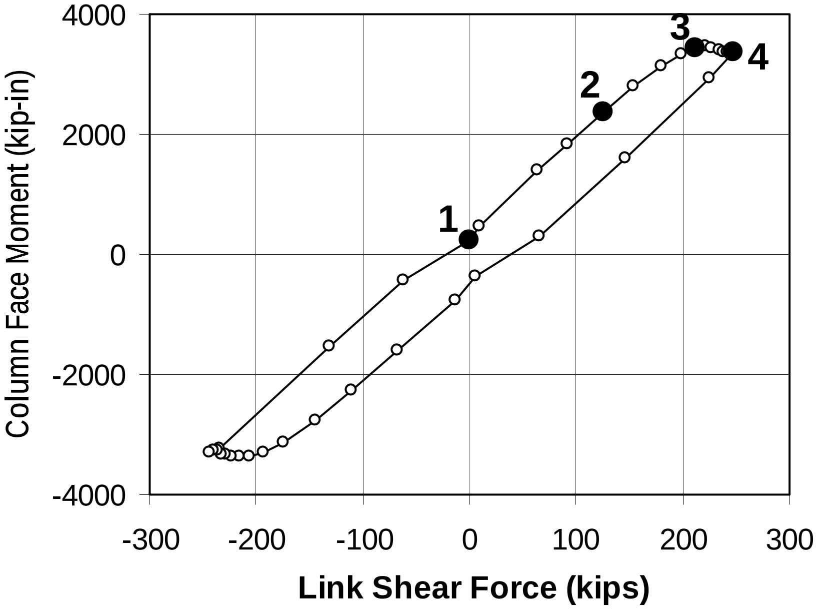

(c) Column Face Moment vs. Link Shear

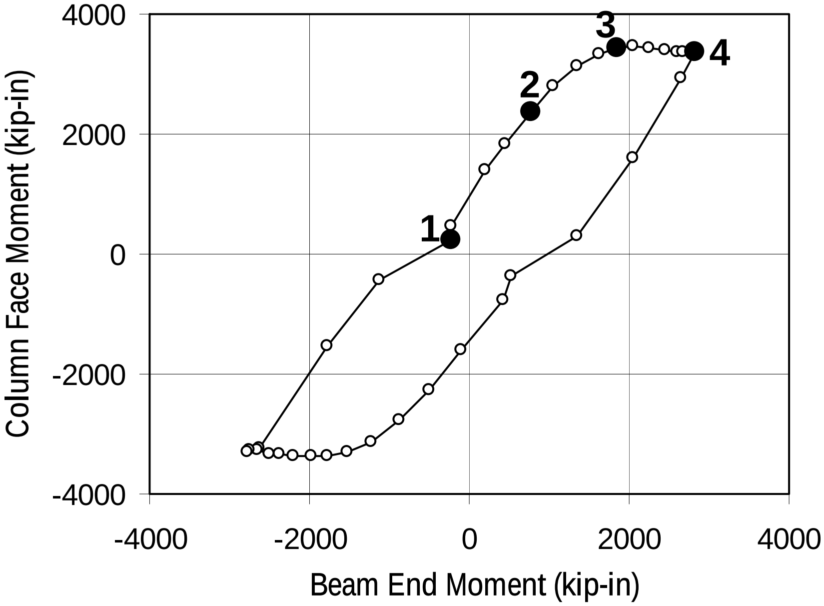

(d) Column Face Moment vs. Link Shear

Figure 5.16 Detailed behavior of Specimen NAS (Continued)

5.4.4 Moment Redistribution

The current test setup was designed to supply greater rotational restraint at the column end of the link than at the beam end of the link, and thereby develop greater moment at the column end of the link. As expected, it was observed during the tests that, as yielding progressed near the column end, the link moment was redistributed from the column end to the beam end. Moment redistribution progressed more dramatically, as fracture developed in the link flange and the strength of the link-to-column connection quickly diminished.

Figure 5.17 shows the hysteretic relation between the column face moment (M_C) and the beam end moment (M_B) for all sixteen specimens. The figure clearly indicates the reduction in initial end moment ratio, M_C/M_B, with link length, as discussed in Section 5.2.1. The decrease in gradient of the hysteretic curves near the turning points (corresponding to peak link rotation) indicates that moment redistribution is taking place, as the beam end moment increased at a higher rate than the column face moment. In general, the decrease in gradient was more rapid for shorter links and less rapid for longer links, indicating that the rate of moment redistribution was greater for shorter links. As a result of the nonlinear behavior near the turning points, the hysteretic curves gradually opened upon increase in link rotation amplitude and accumulation of plastic deformation. Similar observations were made earlier on the hysteretic relation between link shear force and column face moment (Refer to Section 5.4.3).

The M_B-M_C hysteresis was altered drastically by the occurrence of fracture at the link-to-column connection. As fracture developed in the link flanges, the flexural stiffness and strength of the connection reduced dramatically, causing rapid moment redistribution from the column face to the beam end. Figure 5.17 indicates that within one or two full loading cycles, the flexural resistance at the link-to-column connection reduced to near zero. Meanwhile, as a result of moment redistribution, the beam end of the link developed very large moment. The largest moment measured at the beam end was 5,980 kip-in, or $1.48M_p$, which is much greater than the moment measured at the column face. In Specimen PNI, which was subjected to a large number of loading cycles after the link-to-column connection failed, the link developed severe flange buckling near the beam end, as shown in Figure 4.5. Even under such extreme forces and deformation, no deterioration in flexural strength occurred at the beam end. No fracture was observed at the beam end of the link in any of the specimens.

In links of $e = 1.1$ and $1.7M_p/V_p$, the large moment at the beam end developed only after fracture started to develop at the link-to-column connection. In some links of $e = 2.2$ and $3.3M_p/V_p$, the end moment had equalized even before the stage when fracture was noted at the link-to-column connection. Beyond that point, those links developed greater moment at the beam end than at the column end even prior to occurrence of fracture at the link-to-column connection. As noted in Section 5.2.2, the beam end of the link was capable of sustaining moment of up to $1.45M_p$ without exhibiting any fracture at the welds connecting the link to the end plate. On the other hand, the maximum column face moment ranged from 1.12 to $1.25M_p$. The significant difference in flexural capacity between the beam end and column end of the link indicates that the fillet welded end plate connection at the beam end had higher flexural capacity than the link-to-column connection. The beam end moment was also bound to diminish towards the end of the test, as fracture developed in the link web near the column, and the link became incapable of the developing shear force.

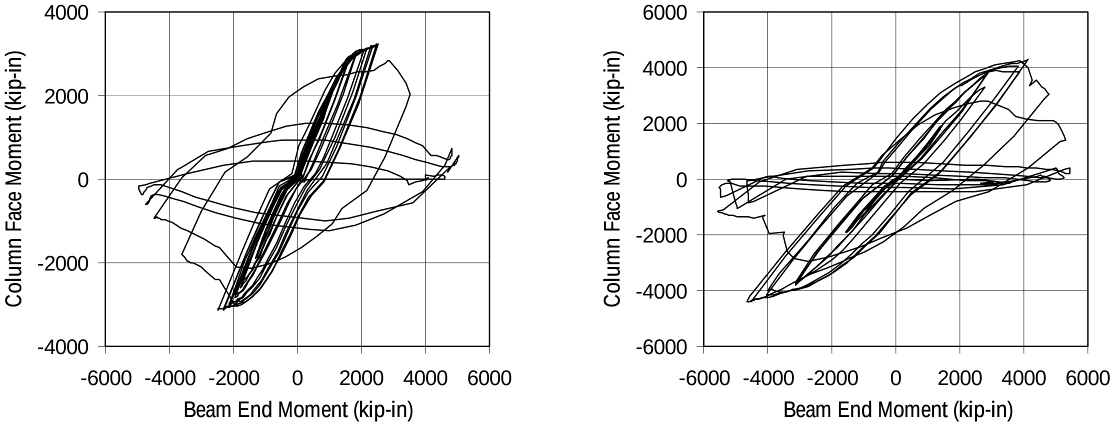

(a) Specimen PNS

(b) Specimen PNI

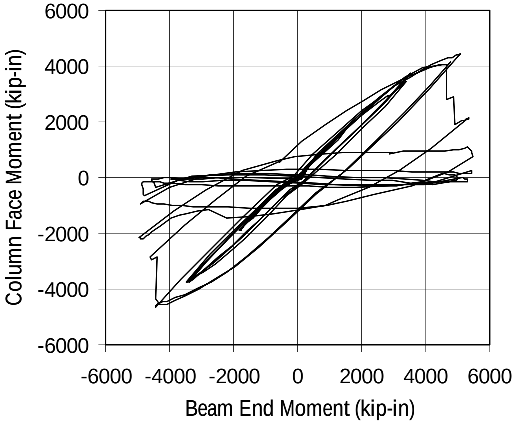

(c) Specimen PNM

Figure 5.17 Moment redistribution

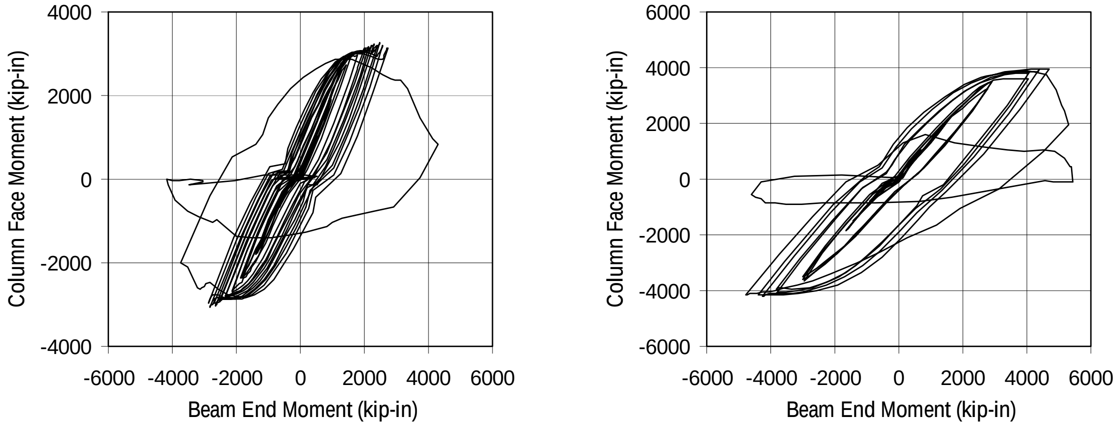

(d) Specimen MWS

(e) Specimen MWI

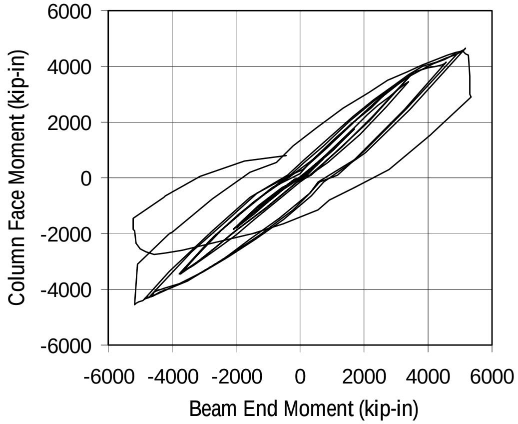

(f) Specimen MWM

Figure 5.17 Moment redistribution (Continued)

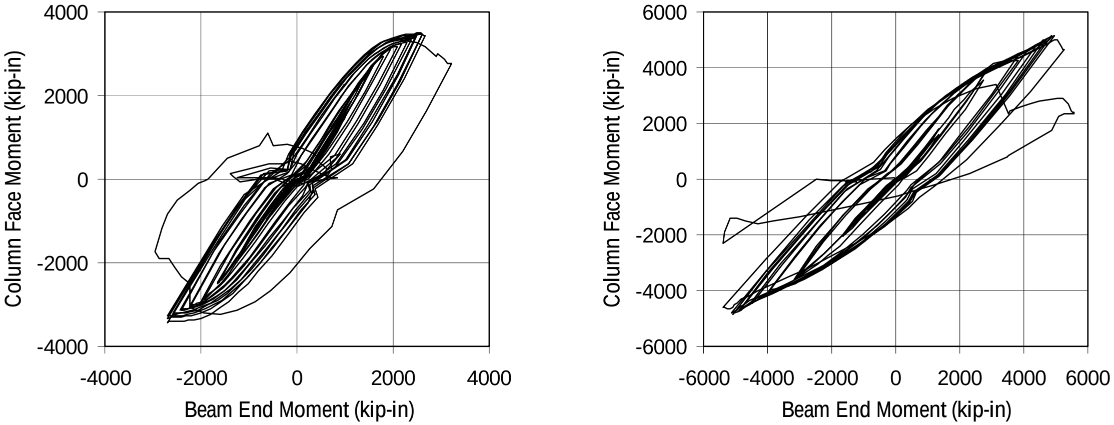

(g) Specimen FFS

(h) Specimen FFI

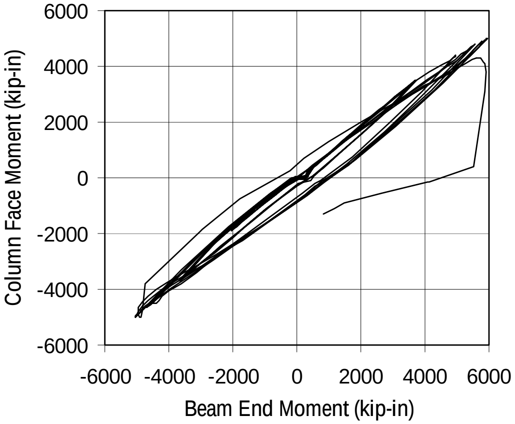

(i) Specimen FFM

Figure 5.17 Moment redistribution (Continued)

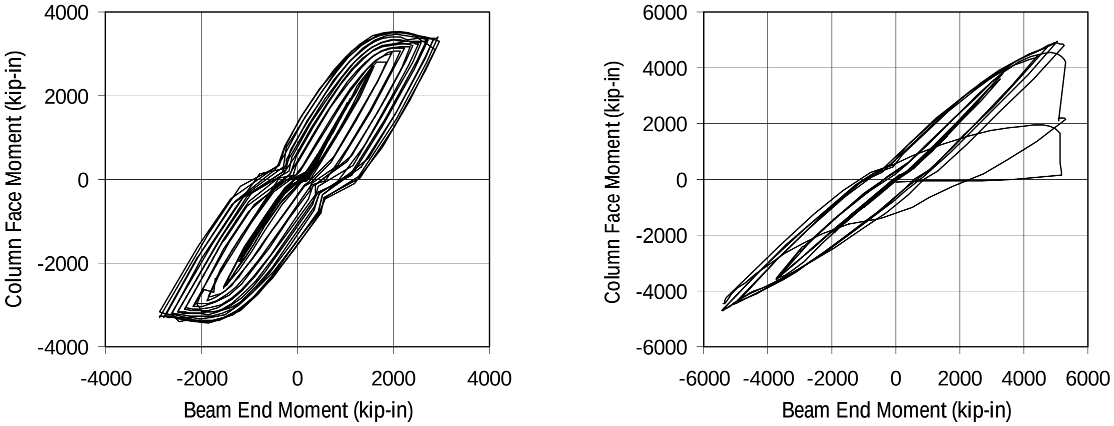

(j) Specimen NAS

(k) Specimen NAM

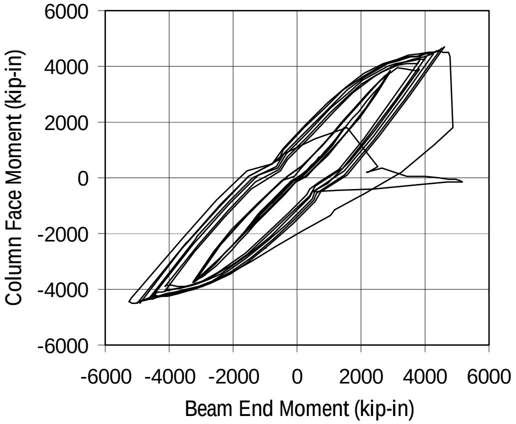

(l) Specimen NAI

Figure 5.17 Moment redistribution (Continued)

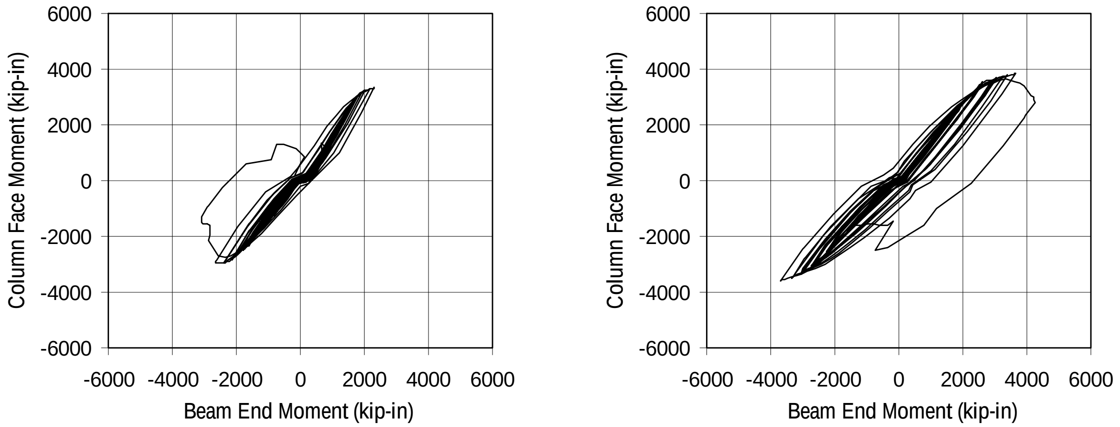

(m) Specimen FFS-RLP ***(n) Specimen FFSL-RLP***

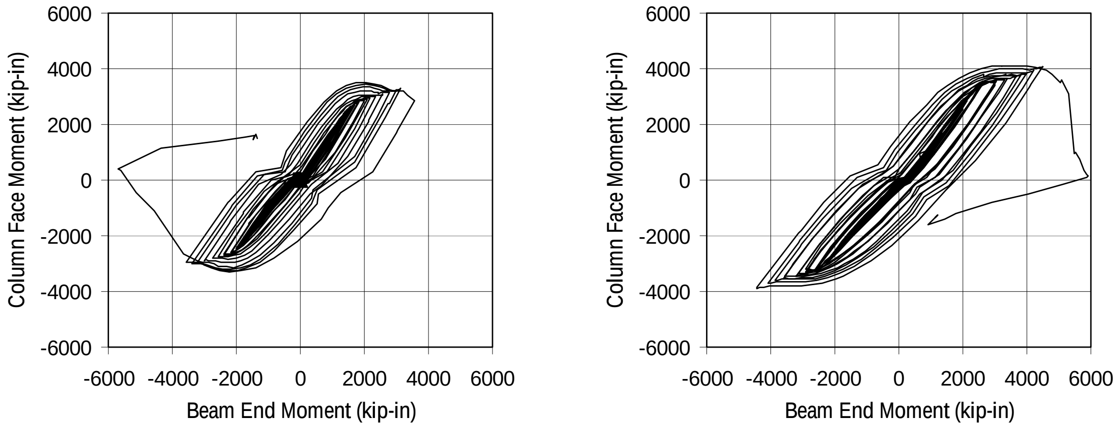

(o) Specimen NAS-RLP ***(p) Specimen NASL-RLP***

Figure 5.17 Moment redistribution (Continued)

5.5 FRACTURE SURFACE EXAMINATION

The surfaces of the link flange fractures are studied in this section. The fracture surfaces shown in Figure 5.18 through Figure 5.21 are associated with the fracture that controlled failure of the specimen, unless otherwise indicated. The circles in the photographs indicate the suspected locations of fracture initiation, based on the observations made during the test.

5.5.1 PN-Connections

Specimen PNS failed due to fracture of the top and bottom link flanges. The initiation point of the bottom flange fracture, which occurred before the top flange fracture, was not clearly recognized during the test. Specimen PNI failed due to fracture of the link top flange initiating at the west edge of the flange. Specimen PNM failed due to fracture of the link bottom flange, likely initiating either at the west edge or root of the weld access hole. Figure 5.18 shows the fracture in the bottom flange of Specimen PNS, top flange of Specimen PNI, and bottom and top flanges of Specimen PNM.

Countless holes are visible in all four photographs in Figure 5.18, along with a layered feature parallel to the weld-longitudinal direction, which appear to correspond to the interface of overlaid weld beads. Such indications of weld defects are scattered across the entire fracture surface. The fractures developed almost entirely at the interface of the link flange base metal and weld metal, where many weld defects were present. Therefore, it is very likely that the flange fractures of the PN-specimens were affected and promoted by weld defects. These specimens passed inspection and ultrasonic testing, as discussed in Section 3.4.1. The rough surfaces provide little indication of ductile tearing, and chevron patterns cannot be recognized along any segment of the surface. Figure 5.18b shows ductile tearing in Specimen PNI near mid-width of the flange. However, this ductile distortion occurred after the flange was nearly separated from the column flange. Due to its homogeneity, the surfaces shown in Figure 5.18 provide little indication of the fracture initiation point or direction of fracture propagation.

5.5.2 MW-Connections

Specimen MWS failed due to fracture of the top and bottom link flanges. Although fracture of the link bottom flange was observed to initiate at mid-width of the flange, the fracture initiation point in the link top flange was not clearly recognized during the test. Specimen MWI failed due to fracture of the link top flange, which initiated at the west edge of the flange. Specimen MWM failed due to fracture of the link bottom flange, although the fracture initiation point was not clearly recognized during the test. Figure 5.19 shows the fracture in the bottom and top flanges of Specimen MWS, top flange of Specimen MWI, and bottom flange of Specimen MWM.

The flange fractures of the MW-specimens, shown in Figure 5.19, have very different characteristics from those of the PN-specimens. The large number of holes visible in Figure 5.18 are not present in Figure 5.19. Distinction between the initial ductile and stable fracture propagation and the subsequent rapid brittle fracture propagation is clearly visible in Figure 5.19.

Figure 5.19a shows slag inclusion in the bottom flange weld of Specimen MWS, at the mid-width of the flange. Failure of specimen MWS was controlled by fracture initiating precisely at this location (see Figure 4.8b). It is quite likely that the inclusion affected the fracture initiation observed during the test. Shear lips are visible in the segment between the east edge and mid-width of the flange, while the chevron pattern near the west edge of the flange indicates that, within this segment, brittle fracture propagated from left (east) to right (west) in the photograph. It is not entirely clear from the surface study whether the ductile segment of the fracture propagated from the mid-width toward the east edge, or a separate fracture initiated at the left edge of the flange and propagated westward to mid-width of the flange.

Figure 5.19b shows the fracture of the top link flange of Specimen MWS, which initiated at the west edge of the flange, at the interface of the weld metal and flange base metal, and propagated towards the east edge. Signs of plastic work are visible along the entire width of the fracture surface, suggesting that the fracture developed in a stable and ductile fashion. Apart from the initiation point at the west edge, the fracture formed in the flange base metal, away from the weld interface.

Figure 5.19c shows the fracture of the top link flange of Specimen MWI. Near the two edges of the flange, the fracture developed at the interface of the weld metal and flange base metal, while near the mid-width of the flange, ductile tearing occurred in the flange base metal. During the test, it was observed that the fracture initiated at the west edge of the flange. However, Figure 5.19c suggests that two separate fractures may have initiated from the two edges of the flange, and propagated simultaneously toward mid-width of the flange.

Figure 5.19d shows the fracture of the top flange of Specimen MWM. When first noted during the test, the fracture extended between the west edge and mid-width of the flange. The photograph shows a slag inclusion near mid-width of the flange. At the west edge of the flange, the fracture formed at the interface of the weld metal and flange base metal. To the east edge of the flange beyond the slag inclusion, the fracture formed in the flange base metal. Since evidence of extensive plastic work is visible along the entire fracture surface, the entire fracture likely developed in a ductile fashion.

5.5.3 FF-Connections

Specimen FFS failed due to fracture in the link web, and showed no fracture in the link flanges. Specimen FFI failed due to fracture of the link top flange, which initiated at the east edge of the flange. When testing was terminated after the link top flange separated from the column, no fracture had occurred in the link bottom flange. Specimen FFM exhibited fracture in both top and bottom link flanges. However, when testing was terminated after the top flange separated from the column, the fracture in the bottom flange had not extended through the entire width of the flange. Specimens FFS-RLP and FFSL-RLP failed due to fracture of the shear tab, and showed no fracture in the link flanges. Figure 5.20 shows the fractures in the top flanges of Specimens FFI and FFM.

The link top flanges of Specimens FFI and FFM exhibited a similar fracture. The fracture initiated at the east edge of the flange, and propagated in a ductile fashion until reaching the mid-width of the flange. The fracture initiation point was at the interface of the flange base metal and weld metal. In Specimen FFI, the fracture propagated to the mid-width of the flange along the weld interface (See Figure 5.20a). In Specimen FFM, apart from the initiation point, the fracture diverted away from the weld interface into the flange base metal (See Figure 5.20b). Horizontally distributed dimples and a small number of holes are visible in the segment of the fracture which formed along the weld interface. These signs of weld defects are particularly evident in Figure 5.20a. In both Specimens FFI and FFM, after reaching mid-width of the flange, the fracture propagated in a brittle and rapid fashion towards the west edge, and separated the link flange from the column flange. Figure 5.20 clearly shows the chevron pattern in the west half of the fracture surface, suggesting that the fracture propagated from the left (east) towards the right (west) of the photograph in that segment.

In Specimen FFM, another fracture was noted near the west edge, although not clearly visible in Figure 5.20b. It is believed that, as the fracture from the east edge grew in size, the energy release rate associated with this larger east fracture became increasingly greater than energy release rate associated with the smaller west fracture, and thus prevented further development of the west fracture.

5.5.4 NA-Connections

Specimen NAS failed due to fracture of the link web away from the link-to-column connection. Although fracture was noted in the top and bottom link flanges near the groove weld, those fractures did not appear to affect the strength of the specimen. Specimens NAI and NAM failed in a very similar mode, driven by fracture of the link top flange which initiated at the east edge. Fracture of the link bottom flange occurred after the top flange had already failed. In Specimens NAS-RLP and NASL-RLP, link top flange fractured first, shortly followed by fracture of the link bottom flange. Figure 5.19 shows the fractures of the top flanges of Specimens NAI and NAM.

The photographs in Figure 5.19 indicate that the fractures initiated at the east edge of the flange, at the interface of the weld metal and flange base metal. Until it reached the link web, the fractures propagated in the flange base metal in a ductile fashion, as evidenced by the plastic shear deformation. Propagation beyond the link web occurred in a rapid and brittle fashion, as evidenced by the flat cleavage surface. The chevron pattern in the west half of the surface suggests that the fracture propagated from the left (east) towards the right (west) in this segment. It is possible that the brittle fracture propagation in the west half of the flange was triggered by the sudden loss of restraint caused by the fracture propagating into the web, which likely caused a sudden rise in energy release rate.

Other fractures are visible along the toe of the weld in both photographs in Figure 5.19. These fractures did not fully develop, likely due to the same reason discussed in Section 5.5.3.

5.5.5 Further Discussions

Slag inclusion are visible in the fracture surfaces of Specimens MWS (See Figure 5.19a) and MWM (See Figure 5.19d). These defects may have had a significant influence on the fractures. The slag inclusions were located near mid-width of the bottom flange at the interface of the flange base metal and weld metal. This is a location highly susceptible to defects since weld placement must be terminated or initiated at this location. Since similar inclusions were not detected in the FF- and NA-specimens, the FF- and NA-connection details may be effective in limiting the occurrence of weld defects in the link bottom flange. Recall that the FF-connection is detailed with an extended weld access hole, which may ease weld placement at the bottom flange. The NA-connection enables continuous weld placement at both the top and bottom flanges.

Flange fracture of the FF- and NA-specimens typically initiated at the edge of the flange at the interface of the link flange base metal and weld metal. As the fracture propagated across the width of the flange, the fracture either formed in the weld interface or deviated away from the weld interface into the link flange base metal. Horizontally distributed dimples and a small number of pin holes are visible in the segment of the fracture which formed along the weld interface, which may suggest that initiation of these fractures were influenced by the presence of weld defects. In the PN-specimens, where the link flange welds were constructed using an E70T-4 electrode instead of an E70T-6 electrode used for the MW-, FF, and NA-specimens, the fracture formed almost entirely along the weld interface. The interface fractures in the FF-and NA-specimens had a shiny and smooth surface, while those in the PN-specimens had a rough surface. The defects in the PN-specimens were more clearly evident compared to those in the FF- and NA-specimens. In all fracture surfaces studied in this section, it was clearly seen that the fracture forming away from the weld interface in the link flange base metal involved more plastic deformation than fracture forming at the interface. Therefore, it is suspected that either (a) defects in the weld interface, (b) material properties in the weld interface, particularly near the heat affected zone, or (c) the combination of (a) and (b), had a significant effect on the fracture initiation process. The occurrence of fracture may be delayed, if not prevented, by improving the weld quality to decrease defects, and controlling the material property at the weld interface.

(a) PNS Bottom Flange

(b) PNI Top Flange

Figure 5.18 Photographs of fracture surfaces of PN-connections

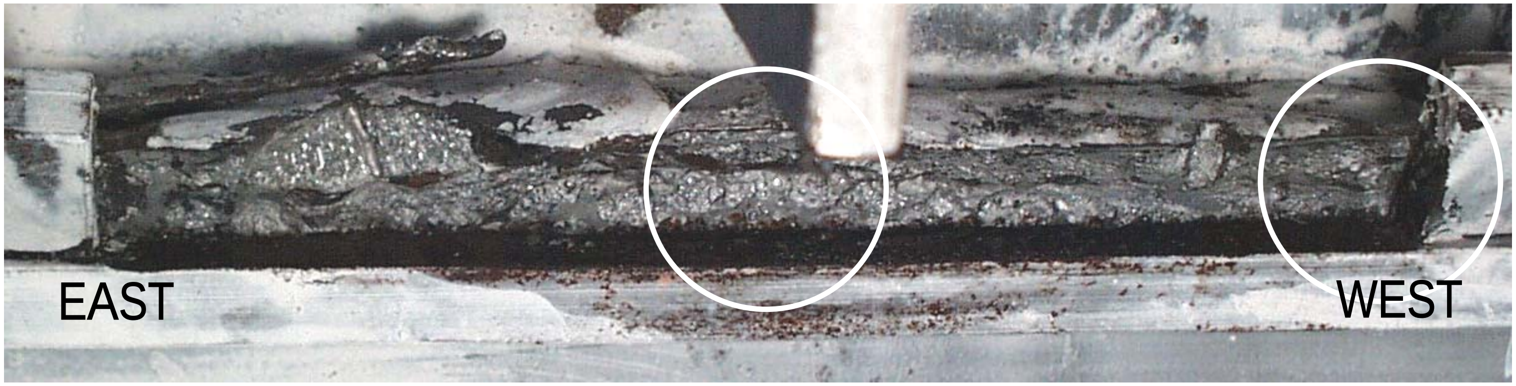

(c) *PNM Bottom Flange*

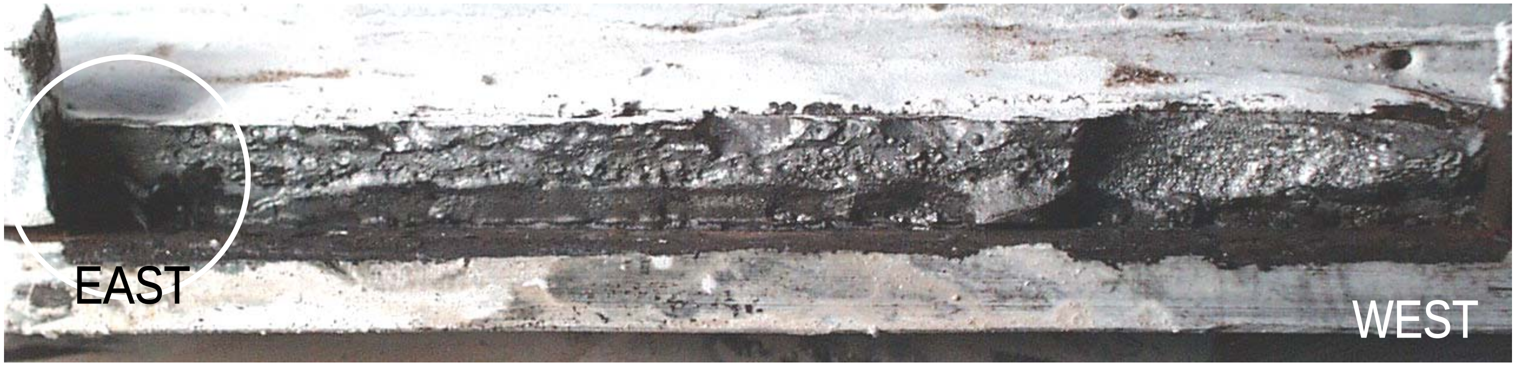

(d) PNM Top Flange (Not controlling failure mode)

Figure 5.18 Photographs of fracture surfaces of PN-connections (Continued)

(a) MWS Bottom Flange

(b) MWS Top Flange (Not controlling failure mode)

Figure 5.19 Photographs of fracture surfaces of MW-connections

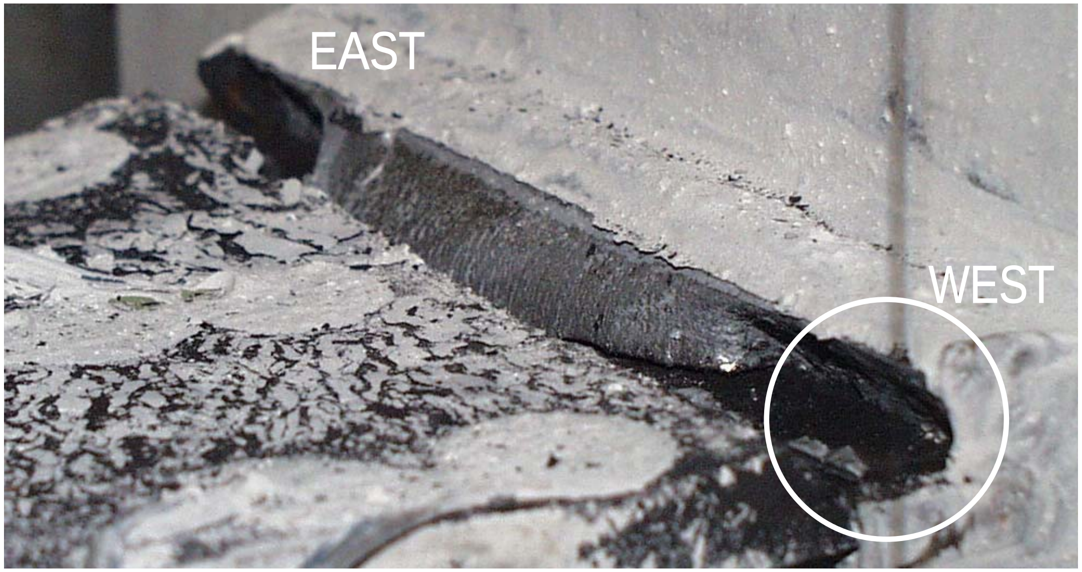

Figure 5.19 Photographs of fracture surfaces of MW-connections (Continued): (c) (Left) Top flange of Specimen MWI; and (d) (Below) Bottom flange of Specimen MWM.

(a) Top Flange of Specimen FFI

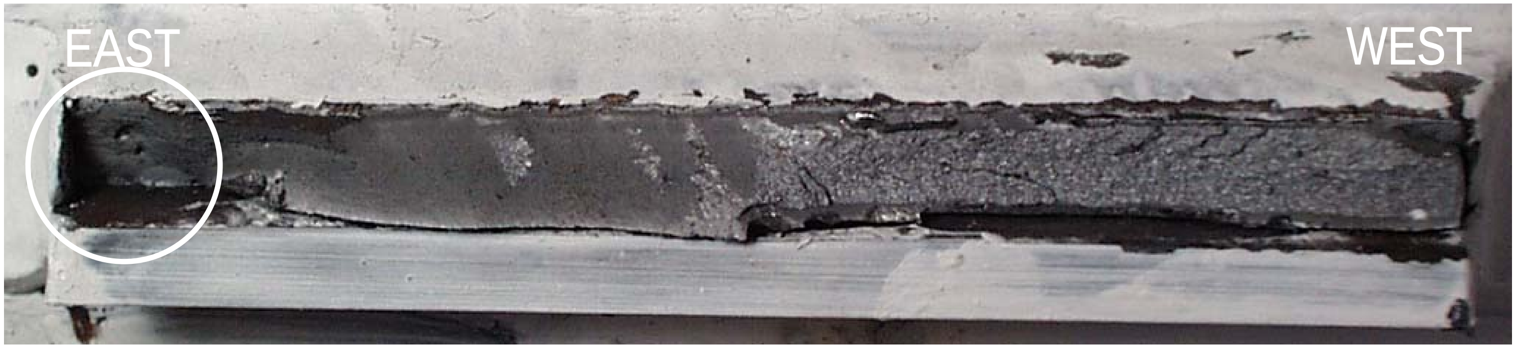

(b) Top Flange of Specimen FFM

Figure 5.20 Photographs of fracture surfaces of FF-connections

(a) Top Flange of Specimen NAI

(b) Top Flange of Specimen NAM

Figure 5.21 Photographs of fracture surfaces of NA-connections

5.5.6 Hardness Measurements near the Fusion Line

The frequent occurrence of fracture initiating at the interface of the weld metal and link flange base metal was discussed above. This observation motivated further study of material properties near the weld interface, particularly in the heat affected zone. A mockup NA-connection was constructed following the same welding procedure as the NA-specimens, except that one of the two link flange welds was made with a SMAW process using an E7018 electrode and the other was made using a SS-FCAW process using an E70T-6 electrode. The weld records are provided in Table E.2 and Table E.3. Ultrasonic testing was not performed for this connection. Hardness test specimens were taken from each of two flange welds, to examine the cross section perpendicular to the welds at a distance of approximately 1/2-inch from the flange edge. Vickers hardness tests were made at a test force of 10 kgf in the region near the weld interface.

As shown in Figure 5.22a and Figure 5.22c for the E70T-6 weld and E7018 weld, respectively, the variation in hardness was measured along two lines in a direction parallel to the link axis and perpendicular to the weld, near the top and bottom faces of the link flange. The photographs clearly show the fusion lines and heat affected zones, as well as the weld pass boundaries. While the E70T-6 weld was completed with only three passes, the E7018 weld required ten passes. The heat affected zone was significantly smaller in the E7018 weld. Weld defects are visible in both photographs, either between weld passes or at the weld root. The hardness measurements shown in Figure 5.22b (E70T-6 weld) and Figure 5.22d (E7018 weld) were centered at the fusion line. The following observations were made based on these measurements.

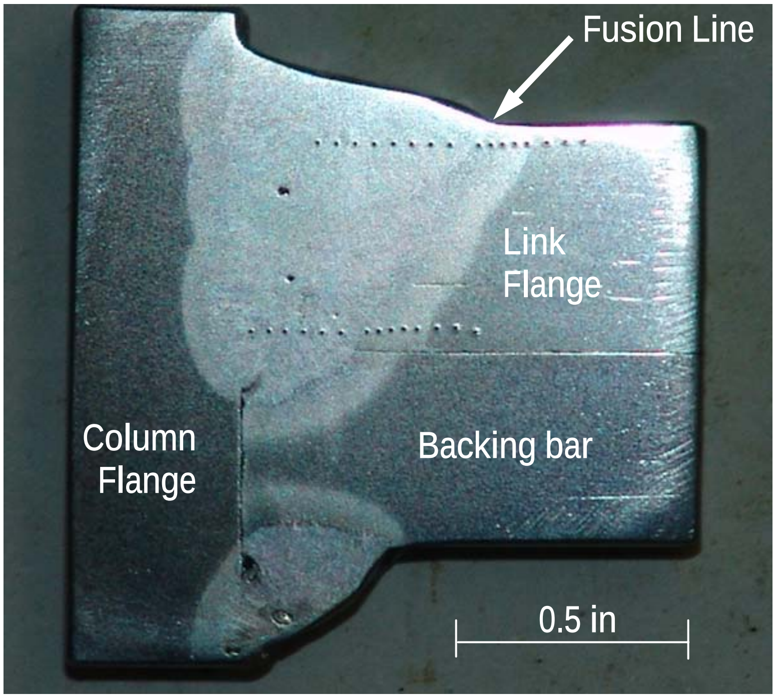

(a) Acid-etched E70T-6 weld

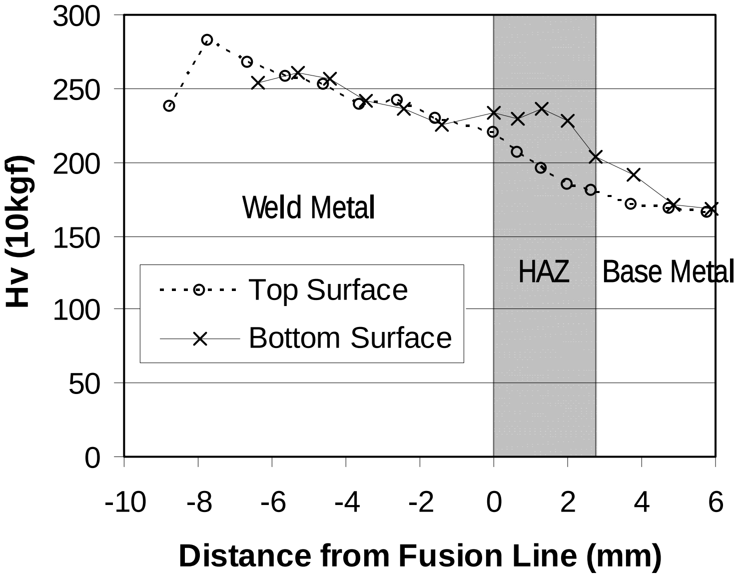

(b) Hardness distribution in E70T-6 weld

Figure 5.22 Vickers hardness test results of CJP groove welds

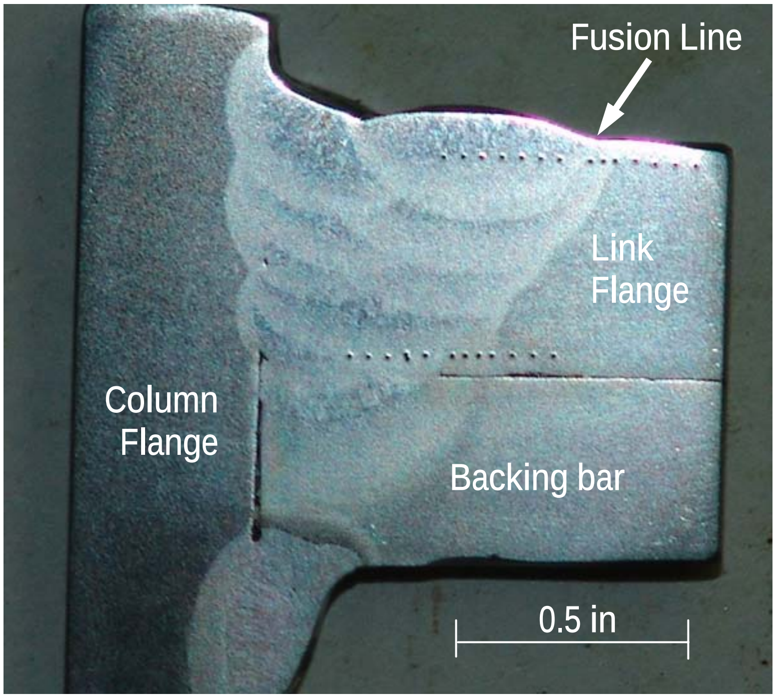

(c) Acid etched E7018 weld

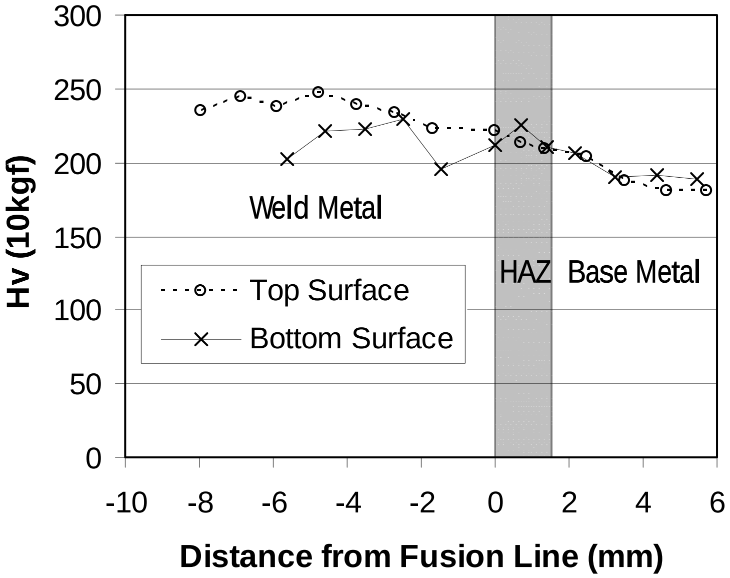

(d) Hardness distribution in E7018 weld

Figure 5.22 Vickers hardness test results of CJP groove welds (Continued)

- The hardness value, Hv, ranged between 225 and 280 in the E70T-6 metal and between 200 and 250 in the E7018 metal. The hardness measurement was roughly 10-percent higher in the E70T-6 metal.
- Within the heat affected zone, the Hv value ranged between 180 and 235 in the E70T-6 weld and between 215 and 225 in the E7018 weld. The much smaller variation in the E7018 weld was likely due to the smaller size of the heat affected zone, smaller heat input per weld pass, and to the annealing effect caused by the larger number of weld overlays.
- The Hv value increased gradually from the link flange base metal, through the heat affected zone, and well into the weld metal. Due to the larger value in the weld metal, the increase was greater in the E70T-6 weld than in the E7018 weld.
- No discontinuity or rapid transition in Hv value is seen across the heat affected zone and fusion line in the E70T-6 weld. Therefore, it is possible that the mechanical properties did not have any detrimental effect on the occurrence of fracture observed in the tests. However, it is not clear whether hardness is an appropriate property to represent the resistance to fracture. It was typically observed that the fracture developed in a ductile fashion in the initiation stage (Refer to Section 5.5). Hardness may not correlate well with the likelihood of ductile fracture initiation.
- The Hv value dropped notably near the boundaries between different weld passes.

Figure 5.22 clearly presents the transition in material properties across the weld interface. However, as stated above, it is not clear whether the hardness distribution provides evidence of correlation between material property near the weld interface and the fracture observed in the tests.

5.6 STRAIN GAUGE DATA

Post-yield strain gauges were placed on the three MW-Specimens within the link, as discussed in Section 3.2.4. Selected data collected from these strain gauges are discussed in this section. Further details of the strain gauge data are provided in Appendix G.

5.6.1 Longitudinal Strain History

Figure 5.23 shows examples of the hysteretic relation between the moment at the column face and longitudinal strain in the link top flange. The strain gauge was located at 1.5-inches from the column face at the middle of the link top flange, as indicated in the figure. This flange was subjected to accumulated elongation as the column face moment increased. Note that at the section where the strain measurements were made, the moment was slightly smaller than at the column face, with the difference between the two moments being greater for shorter links. Figure 5.23 includes the hysteresis up to the last completed half cycle.

Figure 5.23 indicates that the strain developed gradually with increase in link rotation in Specimen MWS. On the contrary, in Specimens MWI and MWM, the strain developed increasingly rapidly during later loading cycles, with increase in link rotation. The maximum column face moments measured in Specimens MWS, MWI, and MWM were $0.81M_p$, $1.05M_p$, and $1.16M_p$, respectively. Although Specimen MWS did not develop the plastic moment of the section, significant yielding occurred in its link flanges. It appears that the flexural capacity of the S-link is well represented by the plastic flexural capacity considering only the flanges, $M_{p\text{-flanges}}$. The three figures clearly indicate that the flexural capacity of the link increased with link length.

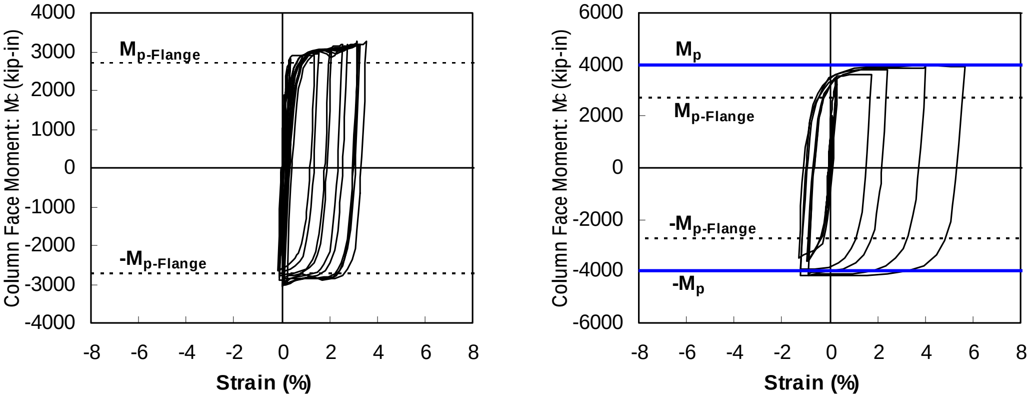

(a) Specimen MWS *(b) Specimen MWI*

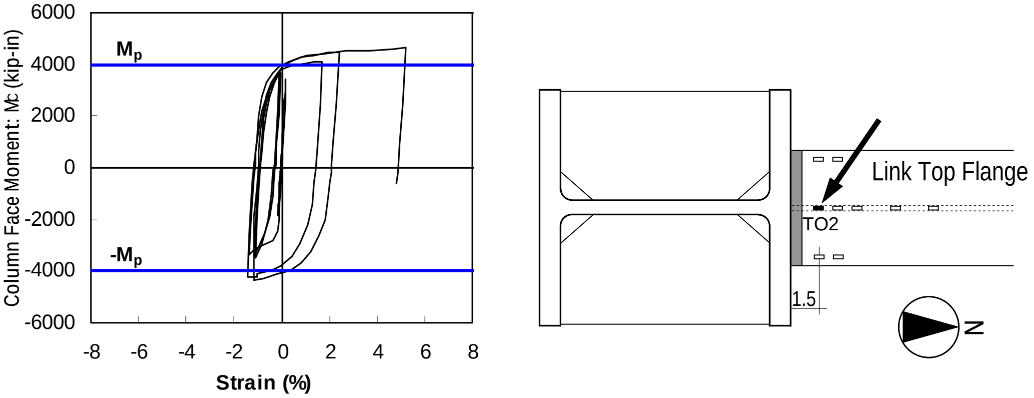

(c) Specimen MWM

Figure 5.23 Longitudinal strain history

Figure 5.24 plots longitudinal strains against the column face moment, measured in Specimen MWS. Strain was measured by three gauges near the column face: in the link flange, at top edge of the link web, and at the centroid of the section. The limited plastic longitudinal strain in the link web suggests that the link web had limited contribution to bending resistance. This observation provides strong evidence to the postulate in Section 5.4.3, that the flexural strength of the section might be better evaluated by neglecting the contribution of the web, since the large shear limits the flexural strength of the web.

5.6.2 Shear Strain History

Figure 5.25 shows the hysteretic relation between the link rotation angle, γ, and shear strain measured at three locations in the link web of Specimen MWS. The three strain gauges are indicated in the figure. Should the link deform solely in shear, and shear deformation be distributed uniformly in the entire depth of the link web, the shear strain measured at any point in the link web would be equal to the link rotation angle. The solid line in the figure corresponds to such uniform shear. The hysteresis is included up to the last completed half cycle.

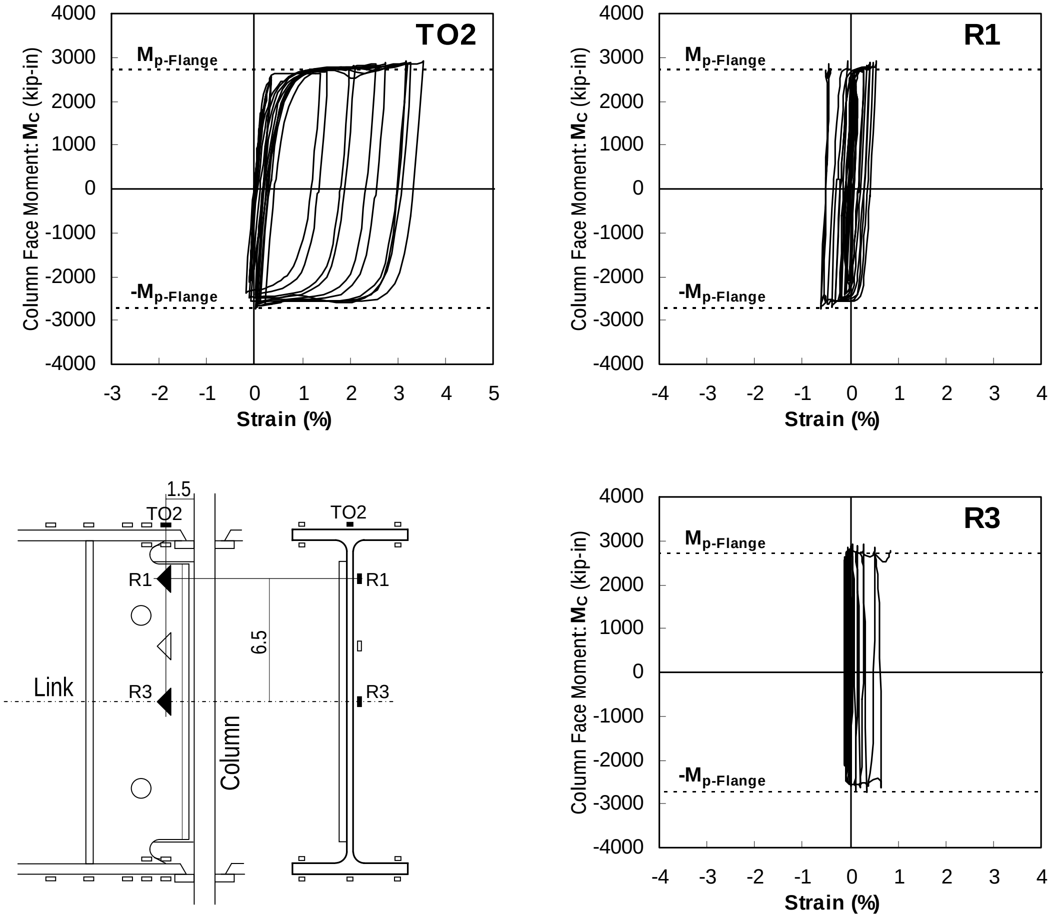

Figure 5.24 Longitudinal strain history in Specimens MWS

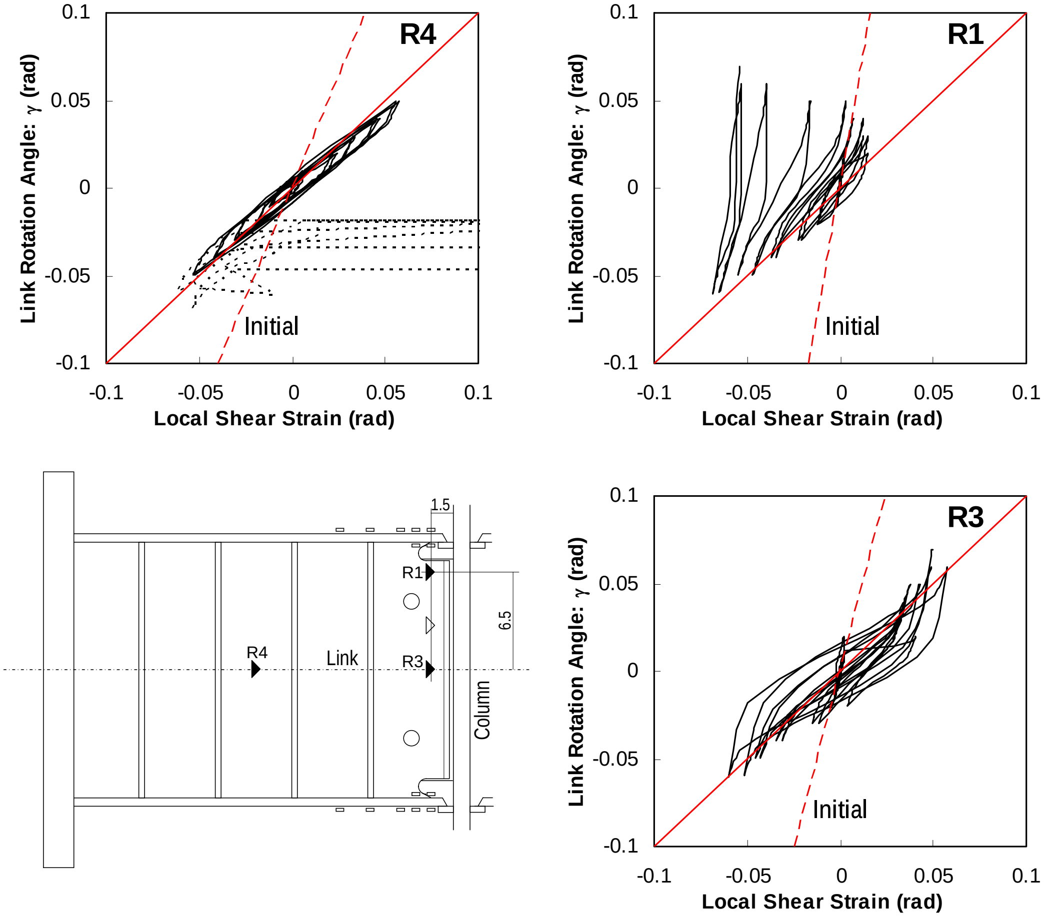

Figure 5.25 Shear strain history in Specimen MWS

The broken lines in the figure are fitted to the response during the initial elastic cycles. The difference in slope between the broken lines and the solid line indicates the significant contribution of factors beside the shear deformation of the link web to the elastic link rotation, such as rotation of the link ends, and bending of the link. Inaccuracy in measuring small link rotations may also partly account for differences between the two slopes. The slope of the broken line is greater at gauge R1 than at gauge R3, indicating that the edge of the link web drew greater shear stress than mid-depth of the link web. The smaller slope of the broken line at gauge R4 than at gauges R1 or R3 may indicate that the influence of the link end restraints and bending of the link is smaller at mid-length of the link. Similar observations for the elastic response were made for the shear strain measurements from Specimens MWI and MWM.

As the link web yielded, and the inelastic shear deformation of the link web accounted for an increasingly greater proportion of link rotation, the shear strain became closer to the link rotation. During this stage, the shear strain amplitude at gauges R3 and R4 tended to be greater than at gauge R1, suggesting that the link web developed greater shear deformation near the centroid of the section. During large link rotation cycles, the hysteresis diverted away from the uniform shear line near the turning points of the curve, near peak link rotation prior to load reverse. The alteration in hysteretic behavior was significant at gauges R1 and R3, whereas at gauge R4, the hysteresis remained stable. The primary cause of the divergence from uniform shear was likely the formation of plastic flexural hinges at the link ends, which relieved further fluctuation in inelastic shear deformation. Gauge R1 grew insensitive to the link rotation angle during later loading cycles, which might be attributed to the development of plastic deformation in the adjacent link top flange, and partly to the development of fracture near the top edge of the link web.

The general inelastic response in Specimens MWI and MWM was similar to that in Specimen MWS discussed above, except that much smaller inelastic shear strain was developed in Specimens MWI and MWM.

5.6.3 Longitudinal Strain Distribution in Link Flange

Figure 5.26 plots the amplitude of normal strain measured at the outer fibers of both the top and bottom flanges, at five locations near the column face indicated in the figure. The strain amplitude was evaluated as half of the

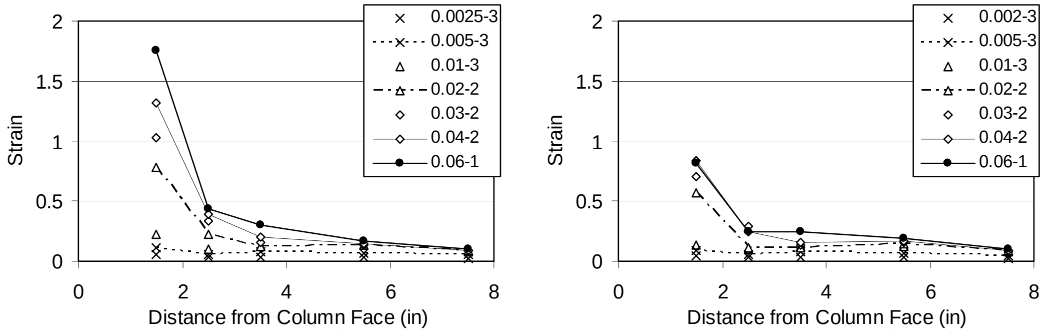

(a) Specimen MWS: Top flange *(b) Specimen MWS: Bottom flange*

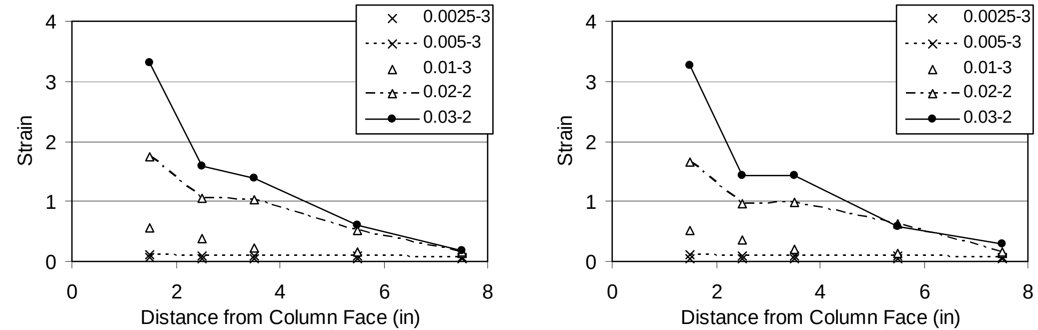

(c) Specimen MWI: Top flange *(d) Specimen MWI: Bottom flange*

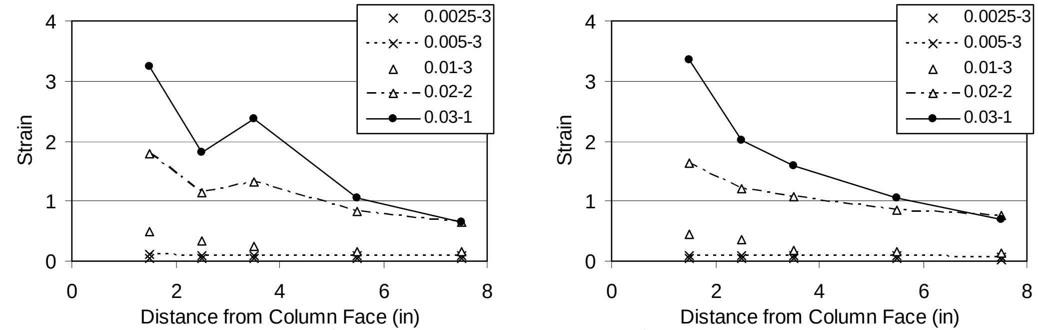

(e) Specimen MWM: Top flange *(f) Specimen MWM: Bottom flange*

Figure 5.26 Strain distribution along link longitudinal direction in link flange

<u>NOTE:</u> Strain gauge location indicated in the following figure:

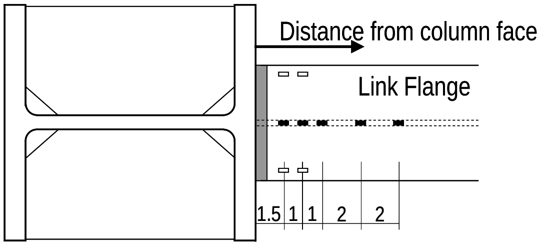

difference between the maximum and minimum strain measured during the loading cycle. The longitudinal distribution of the normal strain is plotted for different loading cycles. The loading cycles are indicated using the convention defined in Section 4.1.

Keeping in mind that the yield strain is of the order of 0.2% for grade 50 steel under uniaxial tension, Figure 5.26 suggests that yielding of the link flanges in Specimen MWS was contained in the region within three inches from the column face. The yielded region appeared to spread in a wider region as the link length increased. In Specimen MWI, the yielded region spread to seven inches from the column face, while in Specimen MWM, the yielded region spread even further away from the column face. The yielded region deduced from the strain measurements generally matches well with the region where the whitewash flaked off (Refer to Section 4.3.1).

Figure 5.26 also indicates that the rate of increase in strain amplitude with link rotation was much greater in Specimens MWI and MWM than in Specimen MWS. The maximum strain plotted in the figure was also much greater in Specimens MWI and MWM than in Specimen MWS. The rise in strain seen in Figure 5.26e, at roughly four inches away from the column face, coincides with the location where flange buckling caused locally concentrated deformation.

5.6.4 Strain Distribution through Thickness of Link Flange

Figure 5.27 plots the distribution of strain amplitude along the width of both the top and bottom link flanges at a distance of 1.5-inches from the column face. The strain amplitude was evaluated as half of the difference between the maximum and minimum strain measured during the loading cycle. Measurements were taken at three locations on the outer face and at two locations on the inner face of the link flange, as indicated in the figure. The distribution at the outer face

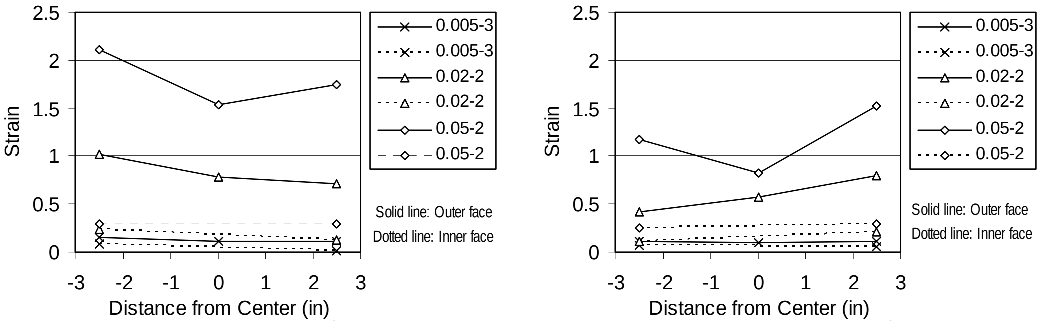

(a) Specimen MWS: Top flange

(b) Specimen MWS: Bottom flange

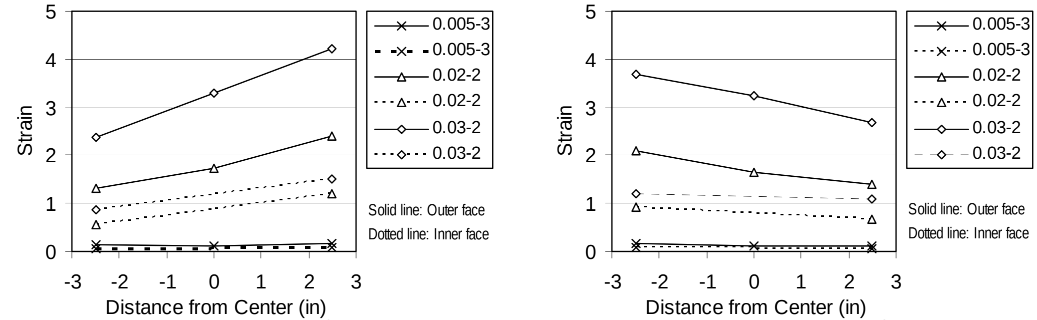

(c) Specimen MWI: Top flange

(d) Specimen MWI: Bottom flange

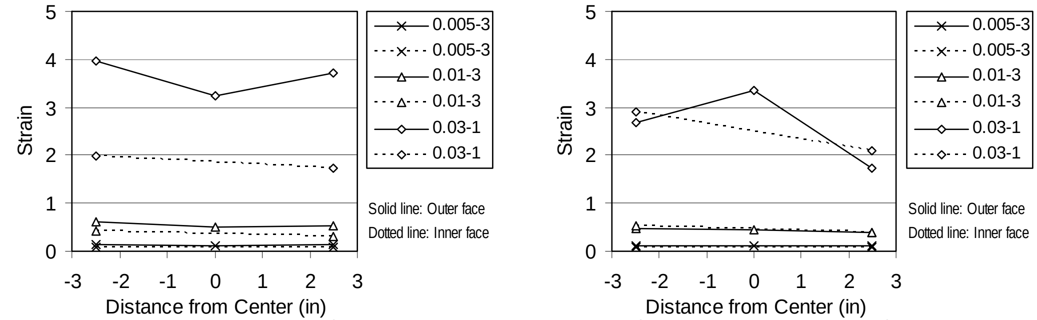

(e) Specimen MWM: Top flange

(f) Specimen MWM: Bottom flange

Figure 5.27 Strain distribution along width of flange

<u>NOTE:</u> Strain gauge location indicated in the following figure:

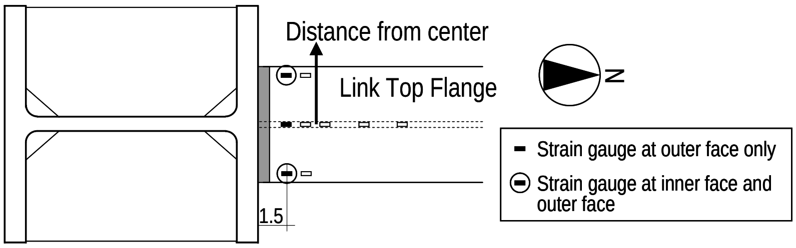

is indicated by a solid line, while the distribution at the inner face is indicated by a dotted line. The figure illustrates the increase in strain as the loading history progressed. The distance from the center of the flange was measured taking the direction to the west as positive. The skewed distribution of strain across the width of the flange in Specimen MWI corresponds well with the flaking pattern of the whitewash observed during the test

It is clearly seen in the figure that, with the exception of the bottom flange of Specimen MWM, the strain level differs significantly between the two faces of the flanges, with higher strain measured at the outer face of the flange (top face of the top flange and bottom face of the bottom flange). The difference in strain level between the two faces of the flanges tended to be greater as the link shortened. The variation through the thickness of the flanges was likely due to the large portion of the shear force transferred to the column through the flanges, which generated secondary bending in the flanges near the column face. Since shorter links developed greater shear force than longer links, it is likely that the secondary bending in the flanges was also more significant in shorter links, and therefore, resulted in greater variation in strain through the thickness of the flanges.

5.7 PANEL ZONE DEFORMATION AND PANEL ZONE STRENGTH

5.7.1 Test Data

Flaking of the white wash observed during the tests indicated small but notable inelastic deformation in the panel zones of Specimens FFI and FFM. As shown in Figures 4.20d and 4.22c, yielding was noted in the column web in the region close to the link. Although the measured data suggested small panel zone yielding in Specimen NAM, no flaking of the white wash was observed during the test.

The relations between panel zone deformation, Γ, and column face moment, M_C, in Specimens FFS, FFI, and FFM are shown in Figure 5.28. Although Specimen FFS showed no panel zone deformation, it is shown in the figure for the purpose of comparison. Specimen FFM reused the column previously used for Specimen FFI, welding the link to the fresh flange face. Therefore, the column of Specimen FFM had already experienced minor inelastic deformation in the panel zone prior to testing. Comparison of Figure 5.28c with Figure 5.28b indicates that the influence of this prior inelastic deformation was negligible.

Figure 5.28 shows that the elastic stiffness of the panel zone and the column face moment at onset of panel zone yielding are predicted reasonably well by K_{PZ} and M_{PZy}, respectively, evaluated as follows:

$$K_{PZ} = G\,(d_c - t_{cf})\,t_p\,(d_b - t_{bf})\ , \tag{5.1}$$

$$M_{PZy} = 0.6\,F_y\,(d_c - t_{cf})\,t_p\,(d_b - t_{bf})\ . \tag{5.2}$$

In the above equation,

G = shear modulus, ksi. G = 29,000/2.6 ksi.

d_c = overall column depth, in.

t_{cf} = thickness of the column flange, in.

t_p = total thickness of panel-zone including doubler plate(s), in.

d_b = overall link depth, in.

F_y = specified minimum yield strength of panel-zone steel, ksi.

Equations (5.1) and (5.2) assume uniform distribution of shear stress across the depth of the panel zone, and no participation of the surrounding elements. Using the measured dimensions and $F_y = 51.2$ ksi, $K_{PZ} = 1.67 \times 10^6$ kip-in and M_{PZy} = 4,606 kip-in. The panel zone deformation at onset of yield, $M_{PZy}/K_{PZ} = 0.6F_y/G$ is evaluated as 0.0028 radians, which also agrees well with the response shown in Figure 5.28.

The commentary to the *2002 AISC Seismic Provisions* recommends that the shear strength of the panel zone in EBF link-to-column joints, ϕR_v, be evaluated by the following equation (equation (9-1) in the provisions), provided that the effect of axial force in the column is negligible:

$$\phi R_v = 0.6F_y d_c t_p \left(1 + \frac{3b_{cf} t_{cf}{}^2}{d_b d_c t_p} \right). \tag{5.3}$$

In the above equation, b_{cf} = width of the column flange, in.

Equation (5.3) accounts for the effects of flexural stiffness of the column flanges and the geometric aspect ratio of the panel zone, and represents the shear strength developed when the panel zone deformation exceeds three times the yield strain in shear (Krawinkler 1978).

In an EBF link-to-column connection, the shear strength, ϕR_v, obtained from equation (5.3) is required to be greater than the demand arising from the moment at the column face. In other words, the strength requirement of the panel zone can be expressed in terms of the flexural strength, evaluated as follows:

$$\phi M_v = \phi R_v \left(d_b - t_{bf}\right) = 0.6F_y d_c t_p \left(d_b - t_{bf}\right)\left(1 + \frac{3b_{cf} t_{cf}^{\;2}}{d_b d_c t_p}\right). \quad (5.4)$$

As indicated in Figure 5.28, ϕM_v = 6,321 kip-in provides an upper bound estimate for the strength of the panel zone below which stable and controlled inelastic deformation is assured. The maximum measured moment at the column face was 55, 81, and 80% of ϕM_v for Specimens FFS, FFI, and FFM, respectively. This observation supports the recommendation provided in the commentary to the provisions that the panel zone at EBF link-to-column connections should be designed using the shear strength of the panel zone evaluated from equation (5.3) with the flexural demand at the column end of the link.

Figure 5.29 shows the correlation between the link shear force, V, and panel zone deformation, Γ. A strong dependency of the panel zone stiffness on link length is noted, since the stiffness increased as the link length shortened. This observation corresponds to the fact that the ratio of the column face moment over the link shear, M_C/V, remained fairly constant throughout the loading history, until fracture occurred in the link-to-column connection (Refer to Section 5.4.3). Therefore, panel zone deformation was controlled primarily by the column face moment, and link shear force played a minor role.

5.7.2 Discussion

As discussed in Section 5.2.3, in the absence of inelastic panel zone deformation, the specimens dissipated energy solely through mechanism (1) in Figure 5.1b. When the panel zone participated, a secondary mechanism (6) in Figure 5.1b was activated. The motion in the direction of applied load associated with the secondary mechanism can be approximated as the product of the link length and inelastic panel deformation, $e \cdot \Gamma$, as indicated in Figure 5.1b.

Based on the $(e \cdot \Gamma)$-V relation, the energy dissipated by the secondary mechanism was evaluated as 451 kip-in for Specimen FFI and 294 kip-in for Specimen FFM. This energy amounted to 6 and 12% of the total dissipated energy for Specimens FFI and FFM, respectively. Based on the Γ-M_C relation, the energy dissipated by the panel zone alone was evaluated as 252 kip-in for Specimen FFI and 206 kip-in for Specimen FFM. Since they did not appear to significantly promote fracture of link flanges, it is believed that the panel zone deformation had beneficial effects on the performance of the two specimens.

It is well known (Krawinkler 1978; El-Tawil 2000) that excessive panel zone deformation can form locations of highly concentrated deformation in the surrounding beams and columns. Based on past research (*e.g.* Krawinkler 1978; Ricles 2002; Jones *et al.* 2002), 0.01 rad may be a rough but reasonable limit for the inelastic panel zone deformation before it can induce severe potential of fracture at the link flange groove weld. While the inelastic panel zone deformation of 0.01 rad can constitute half of the inelastic link rotation of 0.02 rad required for moment links, this provides much less contribution to the inelastic link rotation of 0.08 rad required for shear links. Therefore, while panel zone deformation might be beneficial to moment links and possibly longer intermediate link, it can provide much less benefit to shear links and shorter intermediate links.

The maximum panel zone deformations developed by Specimens FFI and FFM were 0.003 and 0.004 rad, respectively, which are easily within the limit of 0.01 rad mentioned above.

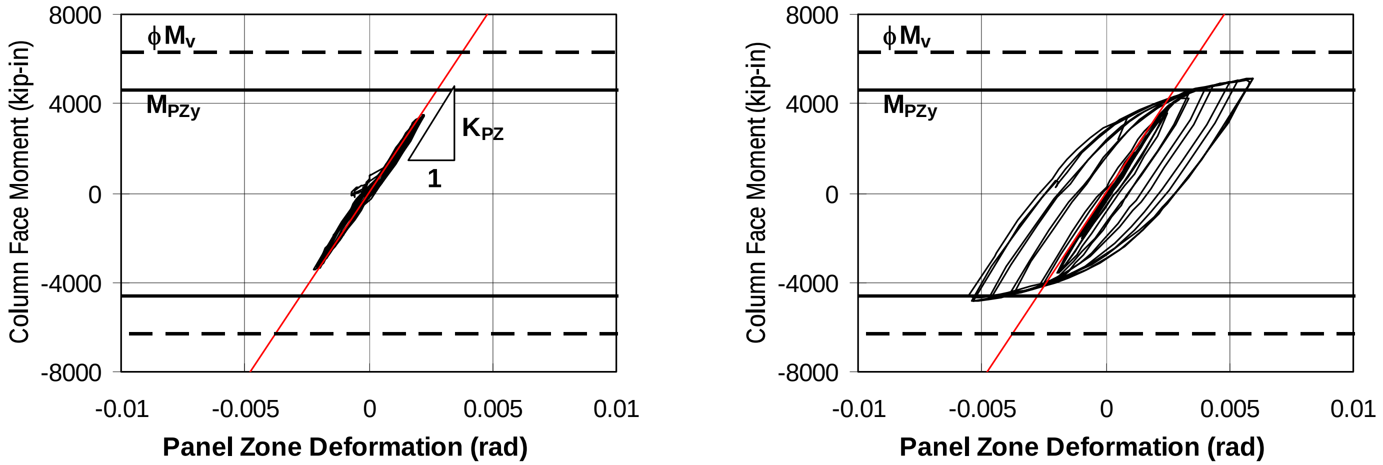

(a) Specimen FFS

(b) Specimen FFI

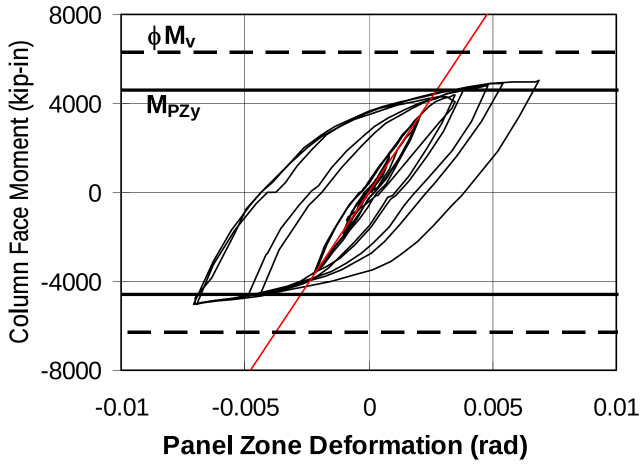

(c) Specimen FFM

Figure 5.28 Panel zone deformation vs. column face moment

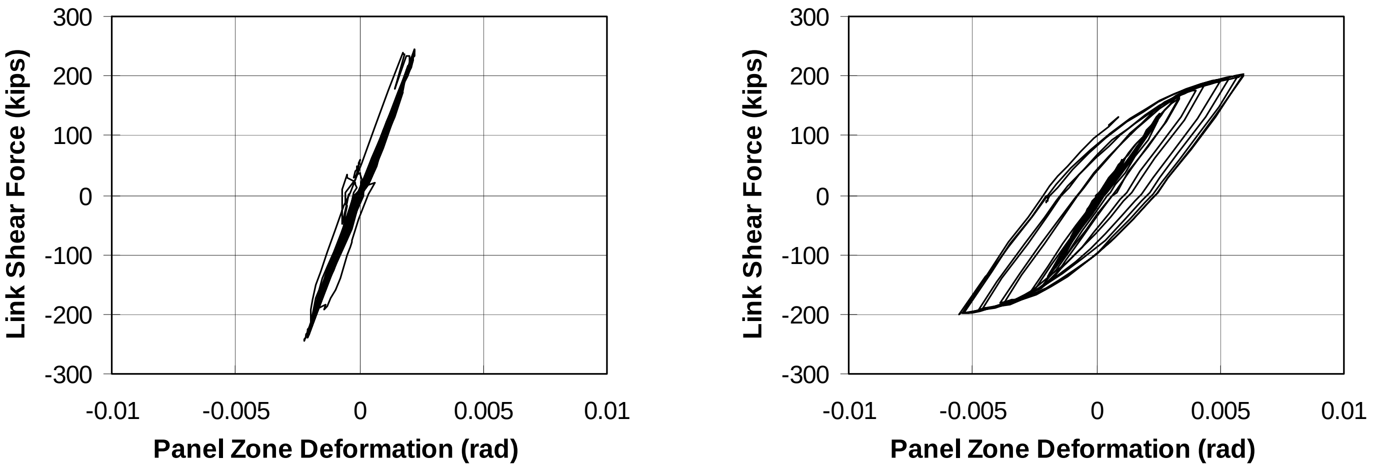

(a) Specimen FFS

(b) Specimen FFI

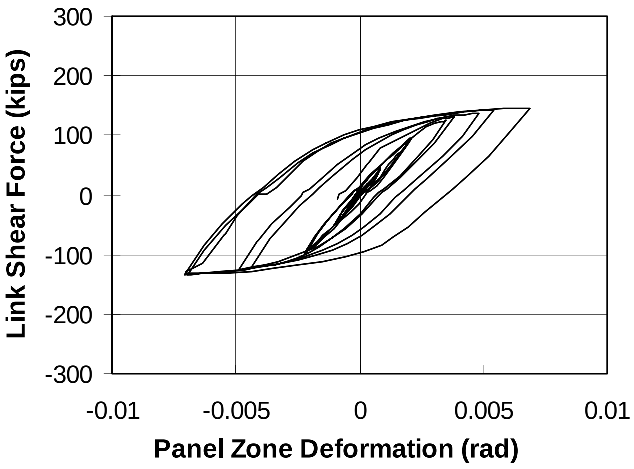

(c) Specimen FFM

Figure 5.29 Panel zone deformation vs. link shear

5.8 SUMMARY

This chapter has provided further analyses and discussion of the test data obtained from the sixteen link-column specimens. Key observations in this chapter are summarized in the following:

- The performance of the specimens was examined through measures besides the inelastic link rotation. The dissipated energy and cumulative inelastic deformation have the advantage of being less insensitive to the loading history. The skeleton rotation and skeleton energy are rational measures to represent the extent of strain hardening. Comparison among the different measures underscores the importance of using a rational loading protocol so that the measured inelastic link rotation will adequately reflect the ductile capacity of the link.

- The welds constructed using an E70T-4 electrode introduced many weld defects at the interface of the link flange base metal and weld metal. These defects were not rejected by ultrasonic testing. Since the fractures propagated almost entirely along the weld interface where weld defects were present, it is likely that the fractures were influenced by the defects. Typical characteristics of ductile and brittle fracture were not recognized along the fracture surface.

- Compared to those constructed using an E70T-4 electrode, weld defects were much less perceptible in the fracture surfaces of flange connections constructed using an E70T-6 electrode. Traces of plastic work and chevron patterns were clearly visible along the surfaces. Examination of the surfaces suggested that the fractures typically initiated at the edge of the flange at the interface of the flange base metal and weld metal.

- In two of the three MW-specimens, which were constructed using an E70T-6 electrode, weld inclusions were present in the fractured bottom flange near the root of the weld access hole. This is a location susceptible to weld defects since weld placement is interrupted by the link web. Since such inclusions were not noted in the FF- and NA-specimens, the FF- and NA-connections may be effective in reducing the incidence of weld defects in the link bottom flange at the root of the weld access hole.

- Most fractures of the link flange appeared to initiate at the interface of the link flange base metal and weld metal, either at the edge or at mid-width of the flange. In some cases, the fracture propagated in the interface along the entire width of the flange. In other cases, the fracture formed at the edge of the flange, then diverted away from the interface into the link flange base metal. Therefore, it is likely that the material properties at the weld interface including the heat affected zone had a significant influence on the flange fractures.

- Microhardness was measured to study the transition in material properties near the weld interface. A gradual transition in hardness was noted across the weld interface. However, it was not clear whether the hardness distribution provided evidence of correlation between material properties near the weld interface and the fracture observed in the tests.

- The link overstrength factors evaluated from the sixteen tests averaged at 1.25, ranging from 1.05 to 1.47. For S-links, the overstrength factor averaged at 1.36, ranging from 1.27 to 1.47. The overstrength factor for I-links averaged at 1.18, ranging from 1.11 to 1.26; the overstrength factor for M-links averaged at 1.26, ranging from 1.19 to 1.37. Considering that the majority of specimens failed prematurely, and could have developed somewhat greater forces if they have developed their required link rotation, these overstrength factors are in reasonable agreement with those measured from previous tests. Therefore, the factor of 1.5 assumed in the *2002 AISC Seismic Provisions* is reasonable.

- In links of $e = 1.1M_p/V_p$, the moment at the column face reached a peak magnitude at link rotation of roughly $\gamma_p = 0.04$ rad, and reduced with further increase of link rotation. The link shear force continued to increase even as the column face moment decreased, causing rapid moment redistribution from the column end to the beam end of the link. This response indicates that these specimens developed their full flexural strength at the column face.

- In specimens of all link lengths, the beam end of the link was capable of sustaining moments of up to $1.45M_p$ without exhibiting fracture. On the other hand, the maximum moment measured at the column end of the link ranged from 0.74 to $1.28M_p$. In short links of $e = 1.1$ and $1.6M_p/V_p$, the large moment at the beam end developed only after failure had occurred at the link-to-column connection, and the moment gradient had reduced significantly. Nonetheless, the significant difference in flexural capacity between the beam end and column end of the link indicates that the beam end connection had higher flexural capacity than the link-to-column connection.

- The plastic flexural capacity of short shear links may be better estimated by removing the contribution of the link web. Strain gauge data indicate that significant plastic strain developed in the link flanges of a shear link specimen as the column face moment exceeded this reduced flexural capacity. The strain gauge data also indicate that the link web of this specimen developed limited bending strain, and hence contributed little to the flexural strength of the link.

- Strain gauge data from the three MW-specimens suggests that significantly greater strain developed at the outer faces of the flanges (top face of top flange and bottom face of bottom flange) than at the inner faces of the flanges. The variation in strain through the thickness of the flange tended to be greater for shorter links. This variation may be caused by the large portion of shear force transmitted through the link flanges, which generated secondary bending in the flanges near the column face.

- The energy dissipation mechanism involving panel zone deformation requires associated plastic hinge rotation at the beam end of the link (or at the beam connection panel). Participation of this mechanism can reduce the plastic rotation demand at the column face, and thereby provide significant benefit to long moment links. However, the plastic link rotation generated by this mechanism is much less appreciable for short shear links.

- In the two specimens that exhibited notable panel zone deformation, the maximum moment developed at the column end of the link was 80% of the strength of the panel zone evaluated from equation (9-1) of the *2002 AISC*

Seismic Provisions. The specimens underwent ductile inelastic deformation in the panel zone, while not significantly promoting fracture of the link flanges. This observation supports the recommendation provided in the commentary to the provisions that the panel zone at EBF link-to-column connections should be designed using the shear strength of the panel zone evaluated from equation (9-1) with the flexural demand at the column end of the link.

CHAPTER 6

Finite Element Simulation of Link-to-Column Connections

6.1 OVERVIEW

The behavior of EBF link-to-column connections was studied by finite element simulations. The primary objectives of this analytical study were: (a) to investigate the effect of the two test parameters, the connection type and link length, on the stress and strain environment at the locations where fracture initiated in the test specimens; (b) to study the effectiveness of finite element simulation to evaluate the performance of the connection; (c) to investigate the effects of other variables which were not considered in the experimental program; and (d) to aid in the development of further improved connections.

The correlation between simulations and experimental observations was a primary interest of this study. As discussed in Section 4.6.5, the majority of link-column specimens failed due to fracture of the link flanges near the groove welds. Finite element simulation of the specimens provided detailed information on the complex stress and strain environment at local regions of concern. Therefore, although the initiation and propagation of fracture was not modeled, the likelihood of fracture was considered based on the computed stress and strain distribution. The primary focus of this study was the effect of geometric configurations on the performance of EBF link-to-column connections.

Section 6.2 outlines the finite element analysis procedure. Section 6.3 compares the simulated global response of the link-column specimens with the experimental response. Section 6.4 discusses the submodeling analysis procedure to sample the stress and strain values at critical locations. Section 6.5 discusses the correlation between the simulated stress and strain environment and the occurrence of fracture observed in the test specimens. Section 6.6 presents an additional set of simulations to study the effect of panel zone strength on the behavior of link-to-column connections. Panel zone strength was one of the design factors which were not explicitly studied in the experimental program. Section 6.7 summarizes the key findings of this chapter and discusses their design implications.

6.2 DESCRIPTION OF THE FINITE ELEMENT ANALYSES

6.2.1 Finite Element Models

The general-purpose finite element analysis program ABAQUS Version 6.4-1 (ABAQUS 2003) was used to perform nonlinear three-dimensional (3-D) finite element simulations of link-column test specimens. ABAQUS was run on a Dell workstation PWS530 using Microsoft Windows XP as the operating system.

Each finite element simulation was performed in two stages. First, a “global model” including the entire link-column test specimen was analyzed. Subsequently, a more detailed “submodel” including a limited region of the link and column near the weld access hole and groove weld at the link bottom flange was analyzed. The results from the “submodeling” analyses were used for the detailed study of stress and strain environment.

Nonlinear 3-D finite element global models were developed to represent the link-column specimen and loading beam described in Sections 3.2.1 and 3.2.2. Figure 6.1 shows an example of such a global model. As shown in this figure, the global model included details such as link stiffeners, continuity plates in the column, and cover plates and doubler plate in the loading beam. The weld access

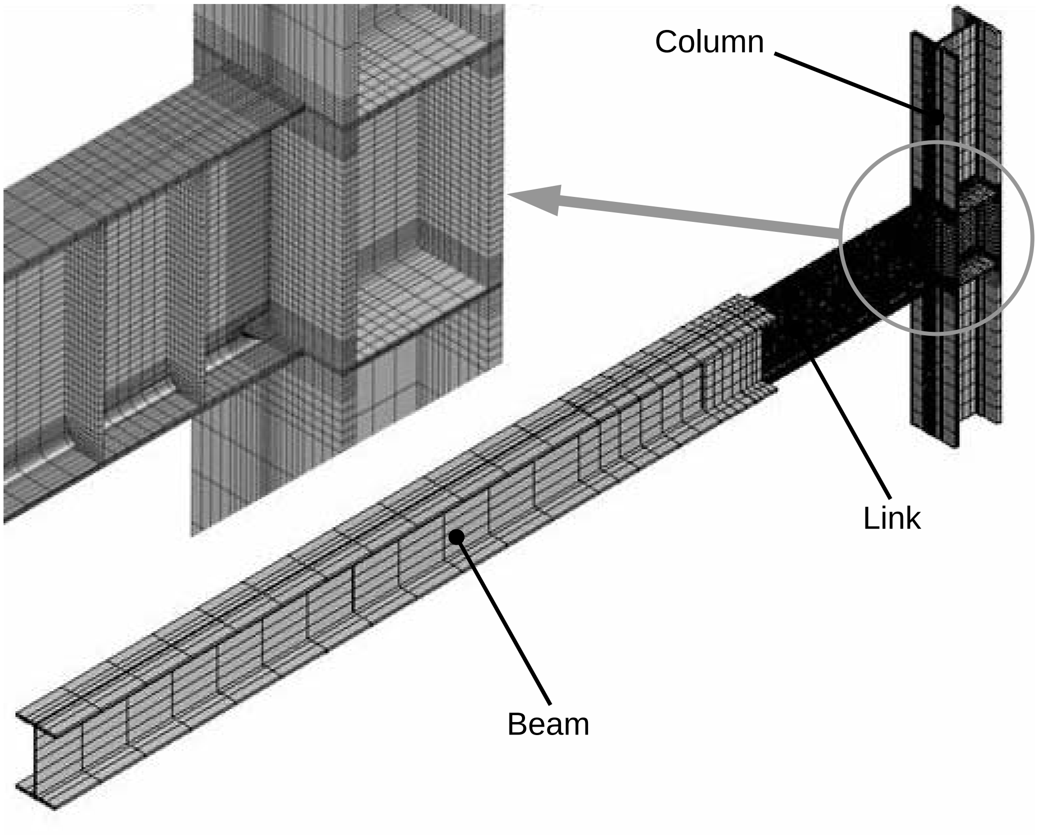

Figure 6.1 Global model for Specimen MWI and enlarged view of joint region

holes, the fillet at the flange-web junction of the link section, and corner cutoff of link stiffeners were also modeled. The welds at the link-to-column connection were provided with different material property definitions from that of the base metal, as described later. The bolted connection between the shear tab and the link web, which primarily serves for erection purposes, was not modeled. The backing bars for the link flange groove welds were not included in the global models of the PN-, MW-, and FF-specimens. The global models of the FF-specimens included the fillet welds connecting the shear tab to the link web and the groove welds between the shear tab and column flange. The global models of the NA-specimens included the backing bars for the link flange groove welds, as well as the fillet welds connecting the backing bars and link web to the column flange.

The boundary and loading conditions for the global model are illustrated in Figure 6.2. For each connection type, a beam-column subassemblage model with a W18x40 beam and a W12x120 column was analyzed in addition to link-column-beam models with varying link lengths. The length of the beam measured from the face of the column was 90-inches, providing a span-to-depth ratio of 10 for the beam-column subassemblage. The beam-column models were denoted, for example, as MWB for the model with an MW-beam-to-column connection.

The link-column-beam models were supplied with pin roller supports at four nodal points. Lateral restraints were provided at the same sections where the pin rollers were located. At these four locations, the flanges of the beam or column sections were restrained against motion out of the principal bending plane. Loading was applied as a monotonically increasing static point load, acting at the bottom of the column at the centroid of the section, in the direction subjecting the link bottom flange adjacent to the column to tension. For convenience, the sign convention for link rotation, link shear, and column face moment are altered from the definition in Section 3.2.5 to omit the repetition of the negative sign. Similarly, the beam-column models were supplied with three pin roller supports at the top and bottom of the column and at the end of the beam. Lateral restraints were provided at the three support points and at the end of the beam plastic hinge zone.

The submodels included a limited region of the link and column near the weld access hole and groove weld at the link bottom flange, as shown in Figure 6.3. The submodels were significantly more detailed compared to the global models, and were intended to achieve increased resolution and accuracy for the stress and strain distributions in the region included. Loading was applied by imposing displacement fields obtained from the corresponding global analysis on

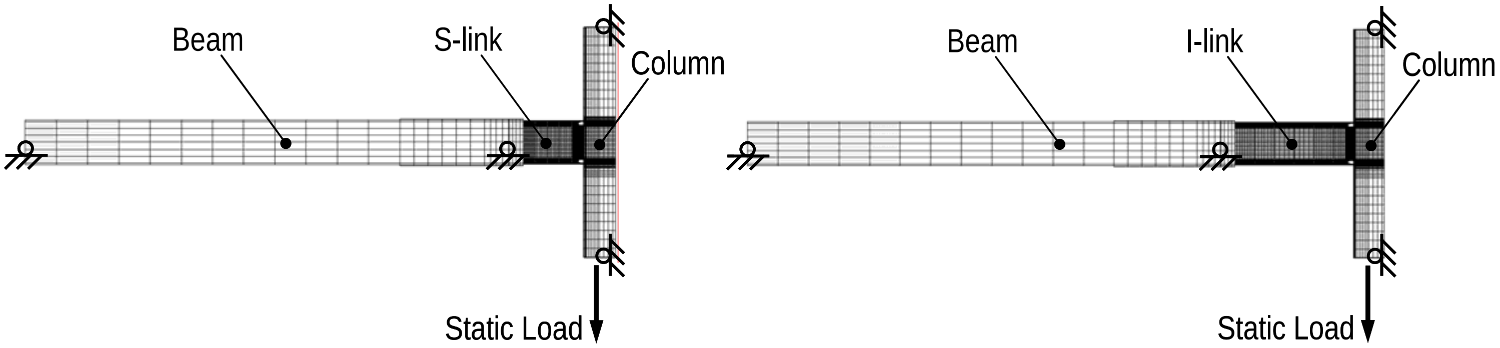

(a) Global Model MWS *(b) Global Model MWI*

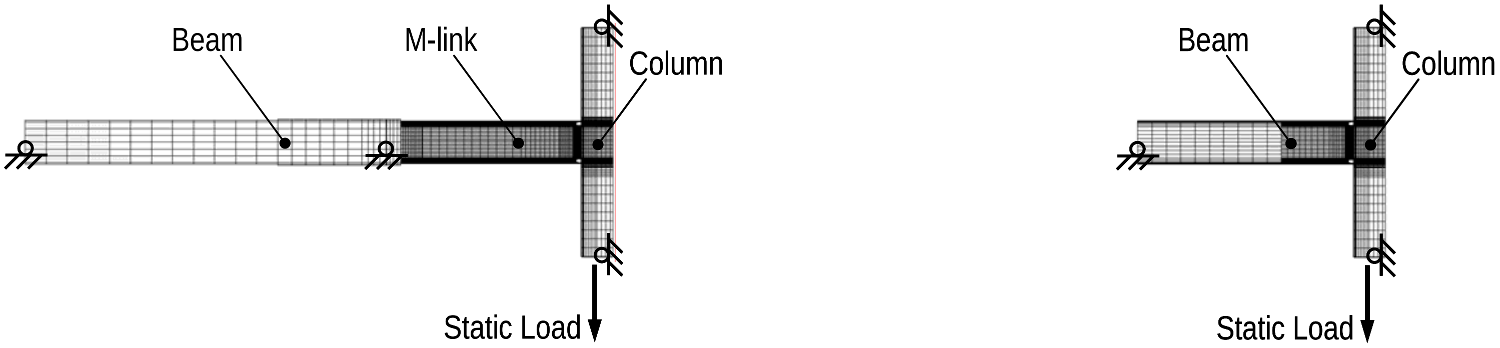

(c) Global Model MWM *(d) Global Model MWB*

Figure 6.2 Boundary and loading conditions

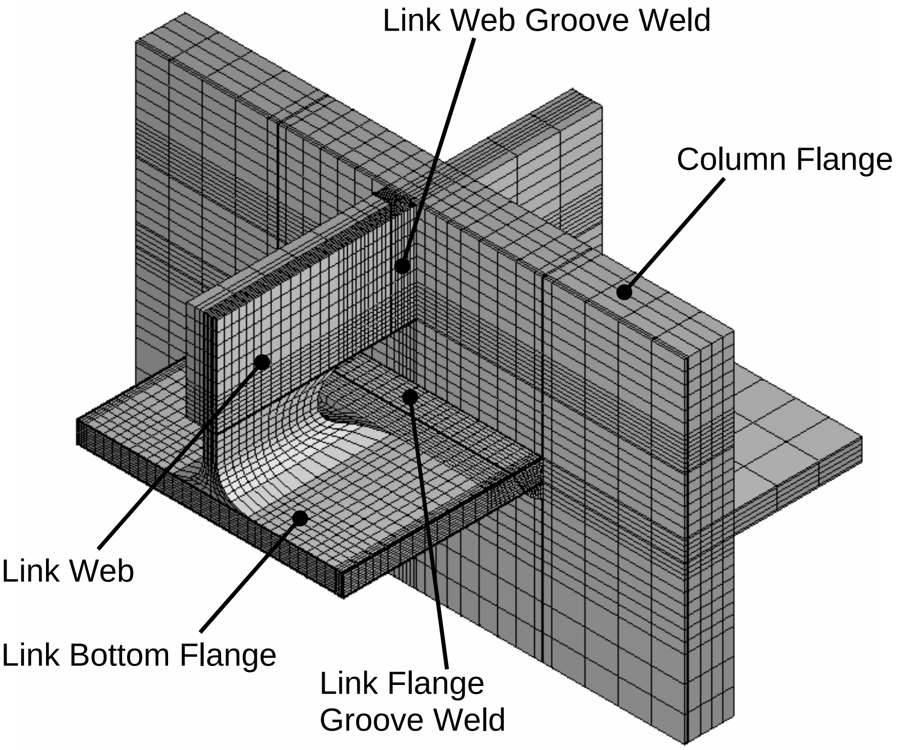

Figure 6.3 Submodel for Specimen MWI

the peripheral boundary of the submodel.

Eight node first-order isoparametric brick elements with standard integration points, designated as C3D8 in the ABAQUS element library, were used for the entire body of the global models and submodels. The global models consisted of between 50,000 and 90,000 nodes. The elements in the link flange near the groove weld had dimensions of approximately 1/8 by 1/8 by 1/4-inch. The submodels consisted of between 35,000 and 70,000 nodes. The smallest elements in the link bottom flange near the groove weld had dimensions of 0.02 by 0.02 by 0.02-inches. The assigned material properties were consistent between the global models and submodels. The link, weld metal, shear tab, backing bars (when included), and a limited region of the column including the panel zone were provided with nonlinear material properties. The beam connecting to the link as well as the region of the column outside of the panel zone, where no yielding was expected, was provided with linear elastic properties. The beam and column sections in the immediate vicinity of the reaction, loading, and lateral bracing points were provided with very stiff linear elastic properties.

6.2.2 Nonlinear Analysis

Material nonlinearity was considered using the von Mises yield criterion and the associative flow rule, which are the default options adopted by ABAQUS. Hardening was modeled by an isotropic hardening rule. The constitutive rule of the isotropic hardening material was modeled by a tri-linear rule, as shown in Figure 6.4. The figures compares the A992 steel model, which was used for the link, column panel zone, shear tab, and backing bars (when included), with selected tension coupon test results (Refer to Section 3.3.3). The A992 steel model represented the flange of the W18x40 section and the web of the W12x120 section reasonably well. The variation in material property across the cross section (Refer to Sections 3.3.2 and 3.3.3) and residual stresses arising from the steel manufacturing process and fabrication process were not accounted for in material modeling.

Since no test data were available, the weld metal was modeled by an arbitrary tri-linear rule, as shown in Figure 6.4. The same model was assigned to all welds in the link-to-column connection, including the welds made with an E70T-4, E70T-6, and E71T-8 electrode. The weld metal model had yield strength of 65 ksi, representing an overmatched weld. Kauffman (1997) states that the E70T-4 weld typically has a yield strength ranging between 60 and 70 ksi, and ultimate strength between 80 and 95 ksi, while the E70T-6 weld typically has yield strength ranging between 65 and 75 ksi, and ultimate strength between 70

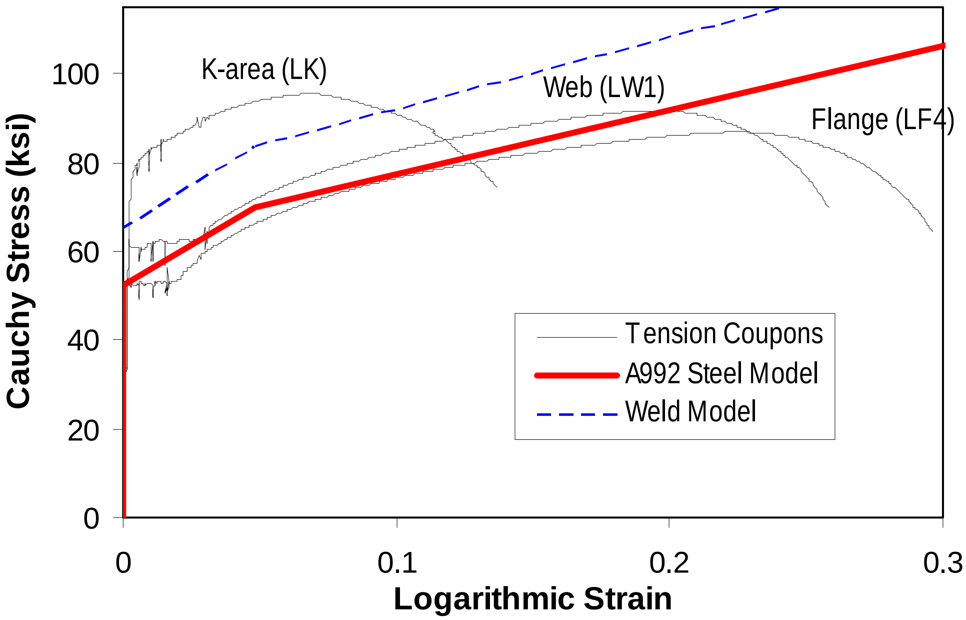

(a) W18x40 (Link) Section

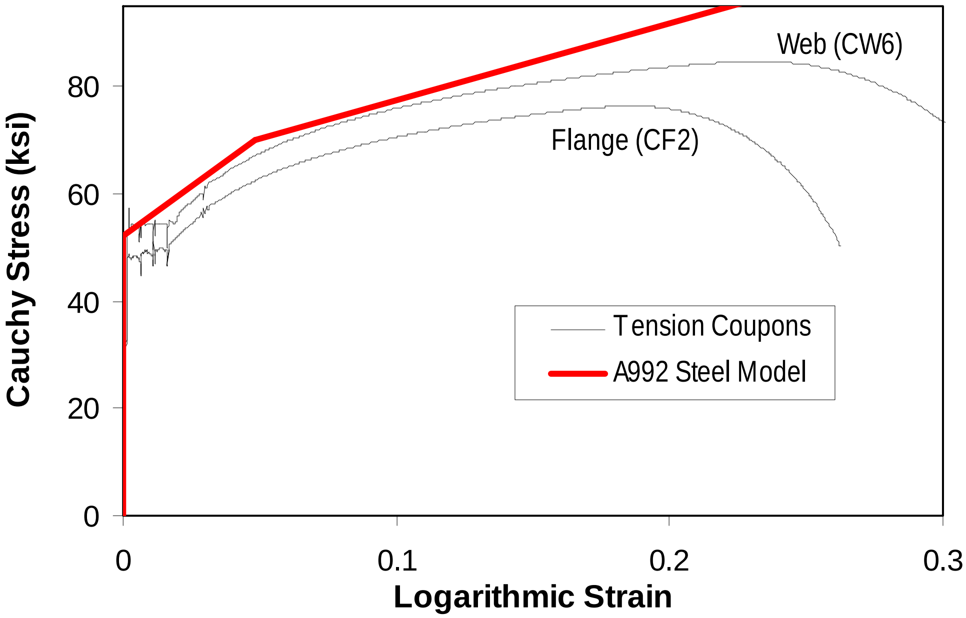

(b) W12x120 (Column) Section

Figure 6.4 Material models

and 90 ksi. Figure 6.4 shows that the selected tri-linear model roughly follows the properties suggested by Kauffman.

The input command lines for the material models in ABAQUS are shown in Figure 6.5

```
*Material, name=Column
*Elastic
29000., 0.3
*Plastic
  52.09,      0.
  69.94, 0.04808
125.70, 0.43508
*Material, name=Linear
*Elastic
29000., 0.3
*Material, name=Link
*Elastic
29000., 0.3
*Plastic
  52.09,      0.
  69.94, 0.04808
 125.70, 0.43508
*Material, name=Rigid
*Elastic
 2.9e+06, 0.3
*Material, name=Weld
*Elastic
29000., 0.3
*Plastic
  65.15,      0.
  83.65, 0.04804
 145.91, 0.43467
```

COMMENTS

Column: Tri-linear stress-strain model

Column outside of panel zone and horizontal beam: Linear elastic model

Link: Tri-linear stress-strain model

Column and beam section near reaction points: Linear elastic model

Weld metal: Tri-linear stress-strain model

Figure 6.5 Command lines for material properties

Geometric nonlinearity was considered in all analyses by a large strain-large displacement formulation. ABAQUS adopts a large strain formulation for 3-D solid elements by default. When the optional parameter “nlgeom” is activated, the locations of all nodes are updated after each analysis step. The “nlgeom” was activated for all global and submodel analyses so that local instability and large deformation effects could be captured. No initial imperfection was introduced in the analyses.

The default Newton algorithm in ABAQUS was used to perform iteration calculations.

6.2.3 Material Model Verification

Tension coupon tests were simulated to verify the material models. As shown in Figure 6.6, the tension coupons discussed in Section 3.3.3 were modeled as a prismatic rectangular bar. Taking advantage of symmetries, one-eighth of the coupon was modeled. Axial force was applied as a point load at the centroid of the end section. In order to assure uniform stress distribution within the gauge length, the region near the end section was provided with a large stiffness, and an extended loading arm was attached between the gauge length and the end section. Engineering stress was computed by dividing the point load by the original cross sectional area. Engineering strain was evaluated by dividing the extension in gauge length by the original gauge length. Except for the stiff region near the end section, the coupon model was assigned the A992 steel material model discussed in Section 6.2.1. Figure 6.7 compares the engineering stress-engineering strain curves constructed from the finite element simulation with the A992 steel model. Note that the A992 steel model, which was defined by a tri-linear Cauchy stress-logarithmic strain relationship, is converted to an engineering stress-engineering strain curve in the figure. The figure shows complete agreement between the

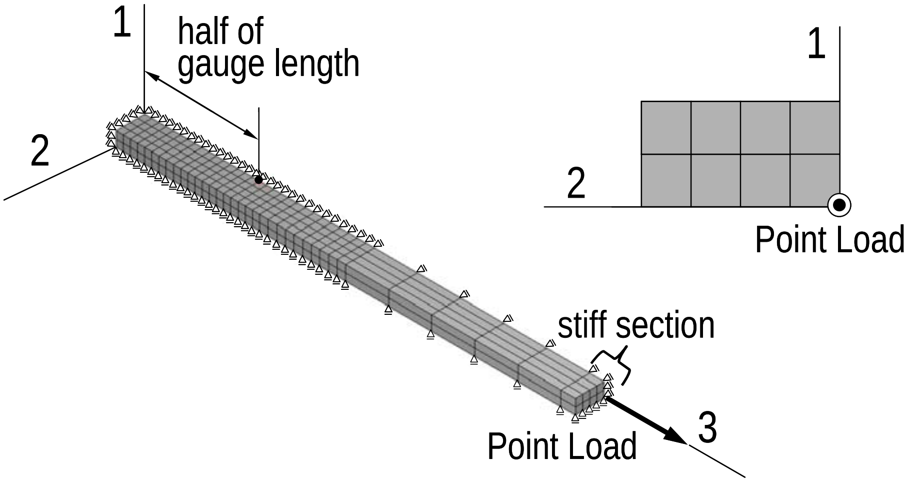

NOTE: Symmetry planes 1-2, 2-3, and 3-1 restrain motion in the 3, 1, and 2-direction, respectively.

Figure 6.6 Tension coupon model

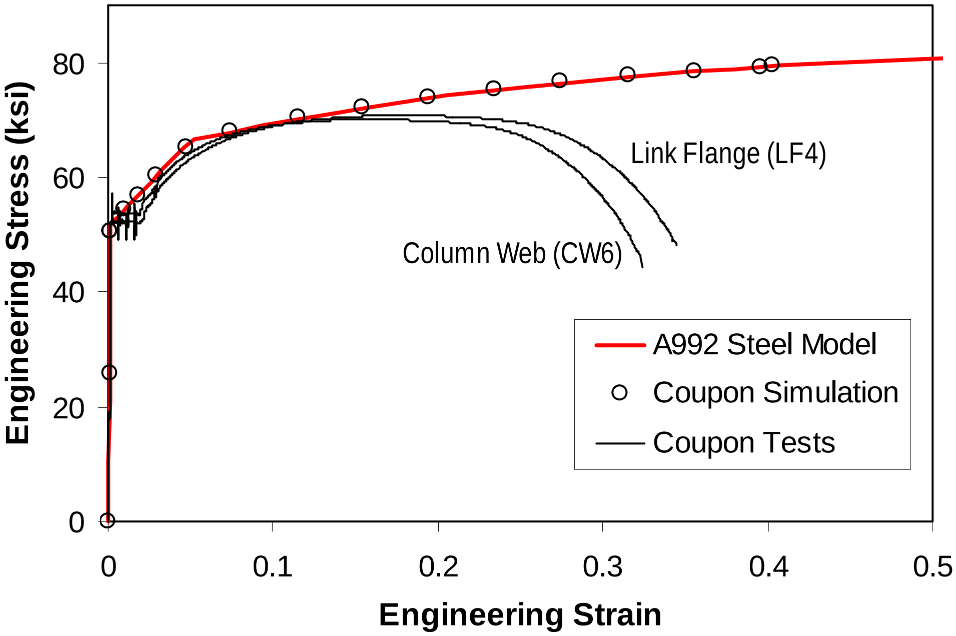

Figure 6.7 Comparison of stress-strain relationships

stress-strain relationship obtained from coupon simulation and the assigned A992 steel model. Further analyses, which are not discussed here, showed that the simulation was insensitive to further mesh refinement.

Figure 6.7 also shows tension coupon tests results. The figure indicates that the coupon simulation does not agree with the tension coupon tests in the range of engineering strain greater than 15%, and engineering stress greater than 70 ksi. Beyond an engineering strain of 20%, the tension coupons softened with increasing strain due to necking. On the other hand, the coupon simulation was not capable of capturing necking. Since the cross sectional area remained relatively constant throughout the simulation, the coupon hardened until the end of the simulation.

Stress-strain relationships compensated for necking (*e.g.* Hancock and Mackenzie 1976; Kuwamura *et al.* 1994; An *et al.* 2003) show strain hardening with a reasonably constant modulus until ultimate failure occurs. Therefore, the model with a constant strain hardening modulus up to large strain levels should be reasonable to represent the response of ductile steel subjected to large plastic strains. Under uniaxial tension, the A992 steel model defined in Figure 6.5 strain hardens up to a strain of 0.55 in engineering strain, or 0.43 in logarithmic strain, and a stress of 81 ksi in engineering stress, or 126 ksi in Cauchy stress. Beyond the point of largest defined strain, ABAQUS allows perfectly plastic behavior, *i.e.*, plastic strain increases with the Mises stress maintained at the largest defined stress level.

The Mises stress and equivalent plastic strain are important invariants that govern the nonlinear material behavior of the finite element model. The Mises stress is defined as follows:

$$\sigma_{\mathrm{Mises}} = \sqrt{\frac{2}{3} s_{ij} s_{ij}} \qquad (6.1)$$

In the above equation, s_{ij} are the deviatoric stress components, and the summation convention is applied over i, j = 1, 2, 3. The equivalent plastic strain, named "PEEQ" in ABAQUS, is evaluated as follows:

$$\varepsilon_{\mathrm{PEEQ}} = \int \sqrt{\frac{2}{3} d\varepsilon_{ij}^{p} d\varepsilon_{ij}^{p}} \qquad (6.2)$$

In the above equation, ε_{ij}^{p} are the plastic strain components, and the summation convention is applied over i, j = 1, 2, 3. The integration is applied over the loading history. Since the von Mises criterion is used in the analysis, the σ_{Mises}- $\varepsilon_{\mathrm{PEEQ}}$ relationship follows the same tri-linear model defined in Figure 6.5. Note that under uniaxial tension, σ_{Mises} equals the tensile stress (Cauchy stress) and $\varepsilon_{\mathrm{PEEQ}}$ equals the plastic tensile strain (plastic Logarithmic strain).

6.3 GLOBAL MODEL ANALYSIS

6.3.1 Global Response

The elastic response of the specimen is represented by the elastic system stiffness, $K_e = V/\gamma$, and the elastic end moment ratio, $(M_C/M_B)_e$. Table 5.1 lists the values of K_e and $(M_C/M_B)_e$ measured from the experimental response and finite element simulations. The values of K_e and $(M_C/M_B)_e$ were constantly 10 to 20% smaller in the experiments than in corresponding finite element simulations. The smaller experimental stiffness may be due to flexibility at the boundary supports of the specimen.

Skeleton curves constructed from the experimental cyclic loading curves were compared with corresponding simulated monotonic loading curves. As discussed in Section 5.3.3, skeleton curves can be considered as equivalent monotonic loading curves. Figure 6.8 compares the positive and negative skeleton curves for all sixteen specimens in the experimental program with corresponding simulated monotonic loading curves. The figure plots the link shear against the rotation or skeleton rotation. The absolute values are taken for the rotation and link shear of the negative skeleton curve. The filled and hollow triangles indicate the point of maximum rotation of the positive and negative skeleton curves, respectively. Figure 6.8 shows excellent agreement between the skeleton curves and the simulated responses for all specimens with the exception of Specimen NAS-RLP. For Specimen NAS-RLP, the skeleton curves showed a notably smaller secondary slope compared to the simulated loading curve. The discrepancy between the skeleton curve and the simulated curve is attributed primarily to the difference in elastic stiffness K_e discussed above. The agreement between experiment and ABAQUS simulation may appear to decrease with link length, due to the decreased contribution of inelastic deformation, as compared to elastic deformation, in longer links. Nevertheless, the simulation captures all important features of the skeleton curve, such as the progressive yielding following the initial linear behavior, and the steady hardening behavior in the inelastic range.

The agreement between the skeleton curves and the monotonic loading simulation curves implies that the force and deformation environment predicted by the simulation is equivalent to the environment developed in the test specimens when the skeleton rotation was equal to that simulated monotonic rotation.

6.3.2 Link Deformation

Two specimens were selected to compare the simulated and experimental deformation of the link.

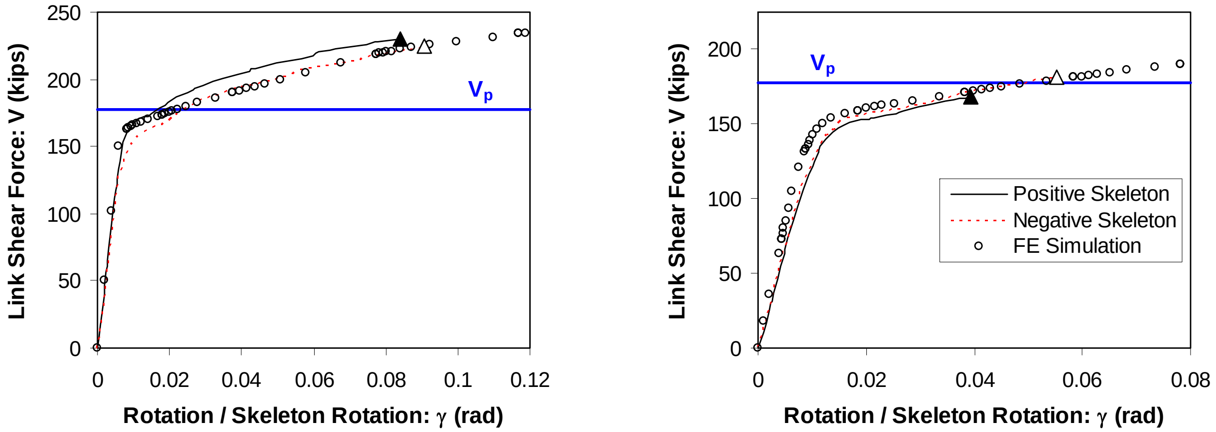

(a) Specimen PNS

(b) Specimen PNI

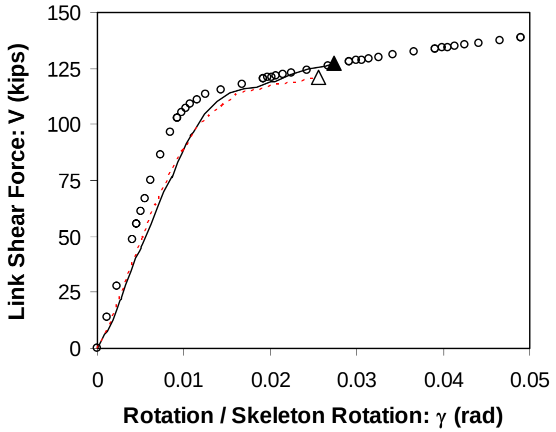

(c) Specimen PNM

Figure 6.8 Simulated loading curve vs. skeleton curves

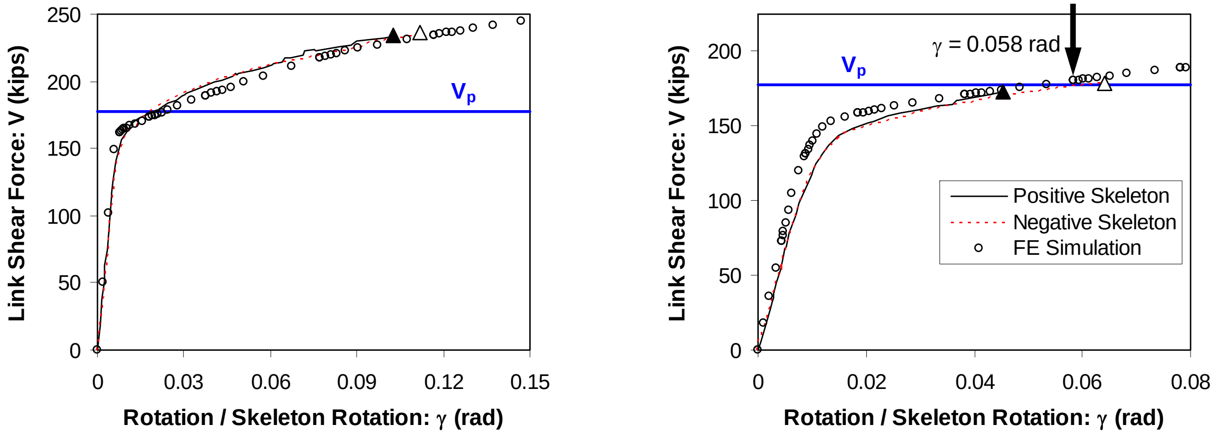

(d) Specimen MWS

(e) Specimen MWI

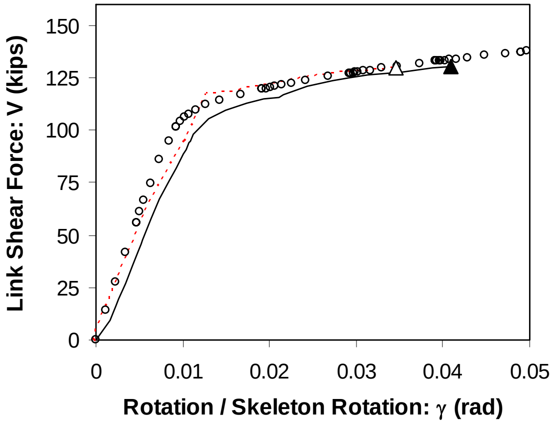

(f) Specimen MWM

Figure 6.8 Simulated loading curve vs. skeleton curves (Continued)

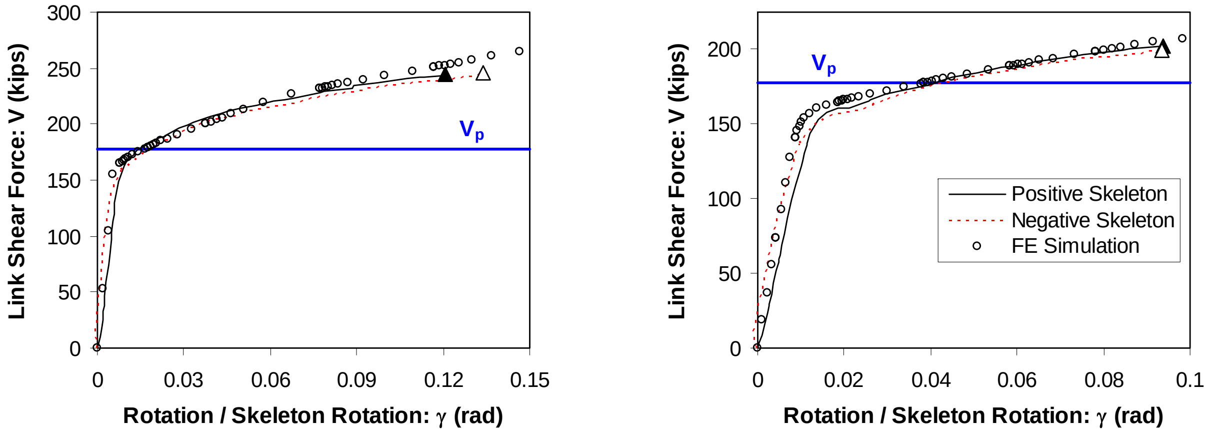

(g) Specimen FFS

(h) Specimen FFI

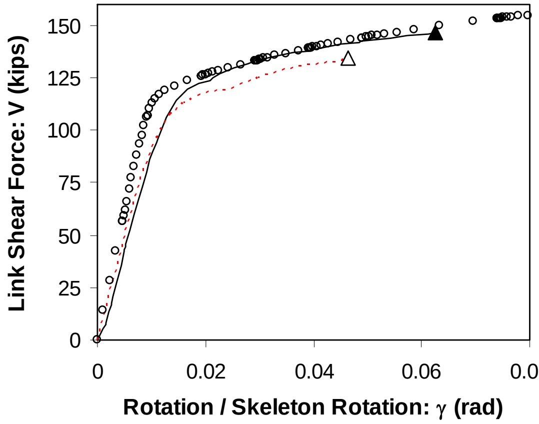

(i) Specimen FFM

Figure 6.8 Simulated loading curve vs. skeleton curves (Continued)

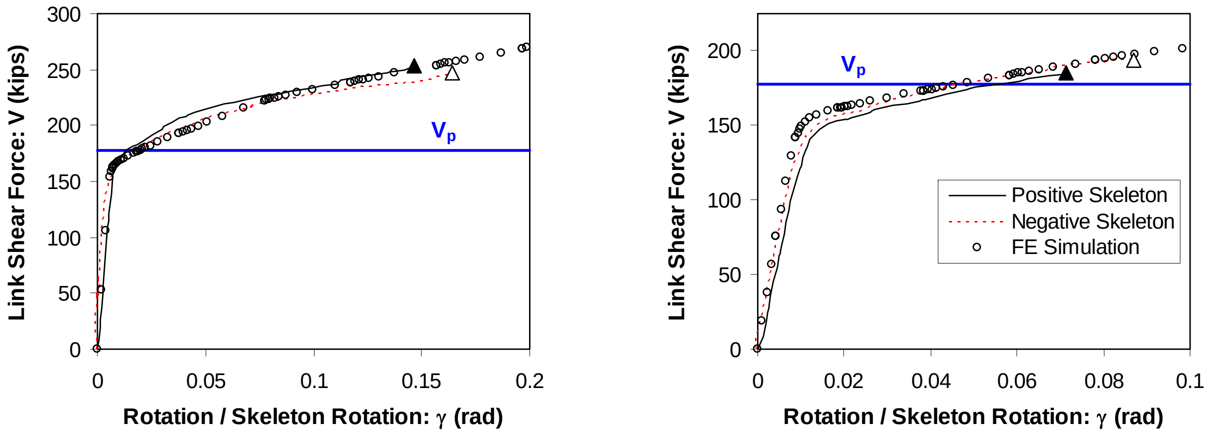

(j) Specimen NAS　　*(k) Specimen NAI*

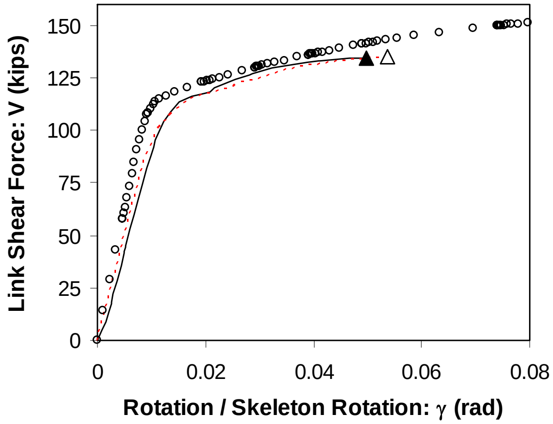

(l) Specimen NAM

Figure 6.8 Simulated loading curve vs. skeleton curves (Continued)

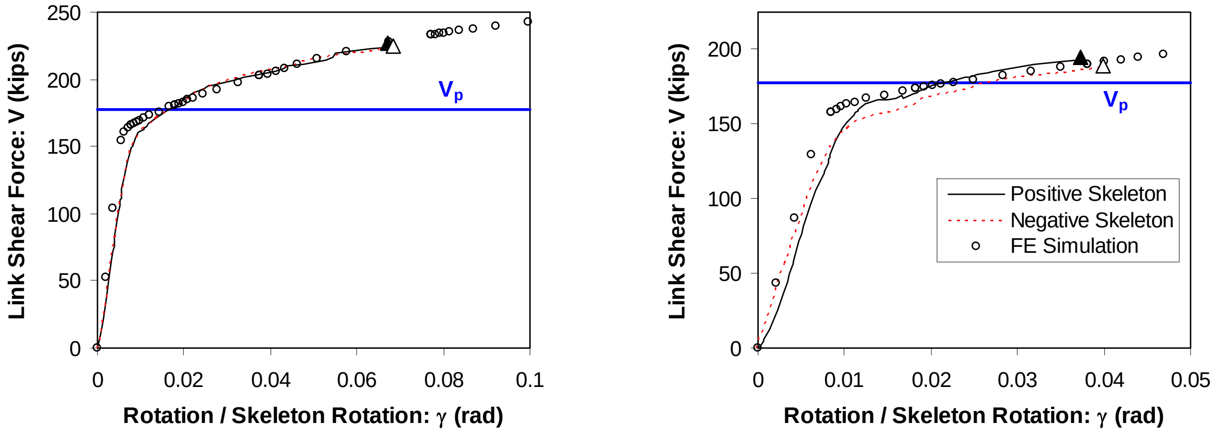

(m) Specimen FFS-RLP

(n) Specimen FFSL-RLP

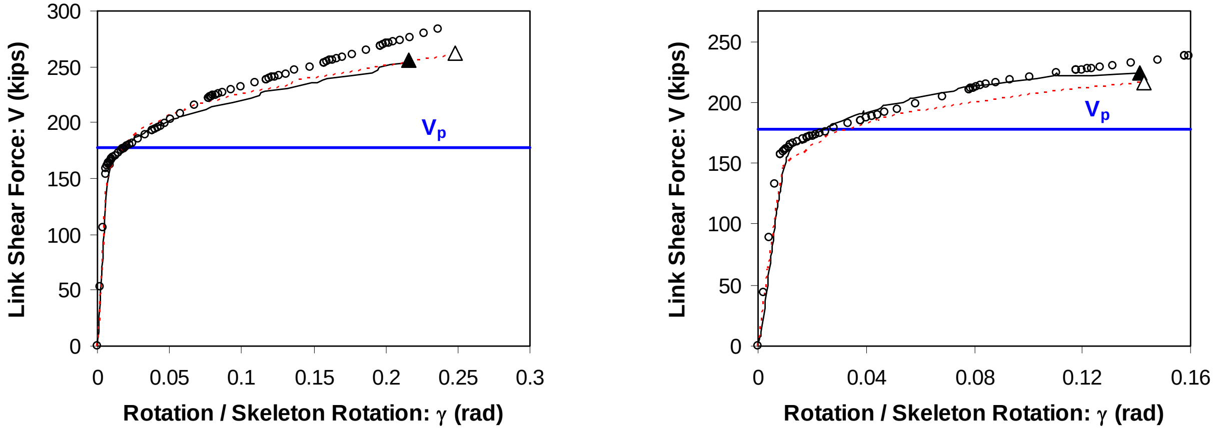

(o) Specimen NAS-RLP

(p) Specimen NASL-RLP

Figure 6.8 Simulated loading curve vs. skeleton curves (Continued)

Figure 6.9 compares the simulated link of Specimen FFS with the tested link. Specimen FFS had an S-link, whose inelastic behavior is dominated by shear yielding of the link web. The Mises stress distribution shown in Figure 6.9a as well the flaking of whitewash shown in Figure 6.9b imply that yielding was precluded from the segment of the link web welded to the shear tab. The overall link deformation agreed well between the simulation and experiment, both showing significant inelastic shear deformation of the link web panels. Figure 6.9a shows the simulated link under a large rotation of $\gamma = 0.117$ rad, with a kink formed in the link top flange near the corner of the shear tab. The kink in the top flange is also recognized in the test specimen, shown at a much smaller rotation of $\gamma = -0.06$ rad. The negative skeleton rotation at this loading stage was $\gamma = -0.12$ rad, which is roughly equivalent to the rotation level of the monotonic loading simulation. It is believed that the large local deformation imposed on the link web between the corner of the shear tab and kink in the flange, indicated by the elevated Mises stress values in the circled region in Figure 6.9a, combined with low cycle fatigue effects, caused fracture in Specimen FFS at the corner of the shear tab (Refer to Section 4.4.1). Overall, the simulated link behavior of Specimen FFS agreed well with the experimental observations.

Figure 6.10 compares the simulated and experimental behavior of Specimen NAM. Specimen NAM had an M-link, whose inelastic behavior is controlled primarily by flexural yielding near the link ends. The simulated link shown in Figure 6.10a was at a link rotation of $\gamma = 0.049$ rad. At the stage shown in Figure 6.10b, the specimen had already fractured at the link top flange near the groove weld. The negative skeleton rotation capacity of the test specimen was $\gamma = -0.054$ rad. Figure 6.10a shows the largest plastic strain values near the link flange groove welds, which may correspond to the occurrence of fracture at this location in the test specimen. The region where the whitewash flaked off in the test

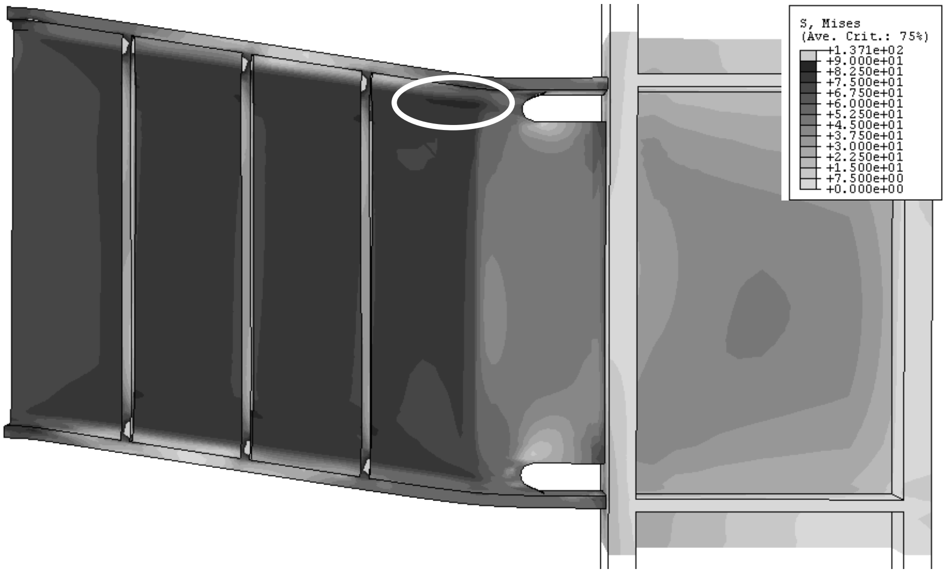

(a) Simulated link and panel zone at $\gamma = 0.117$ rad

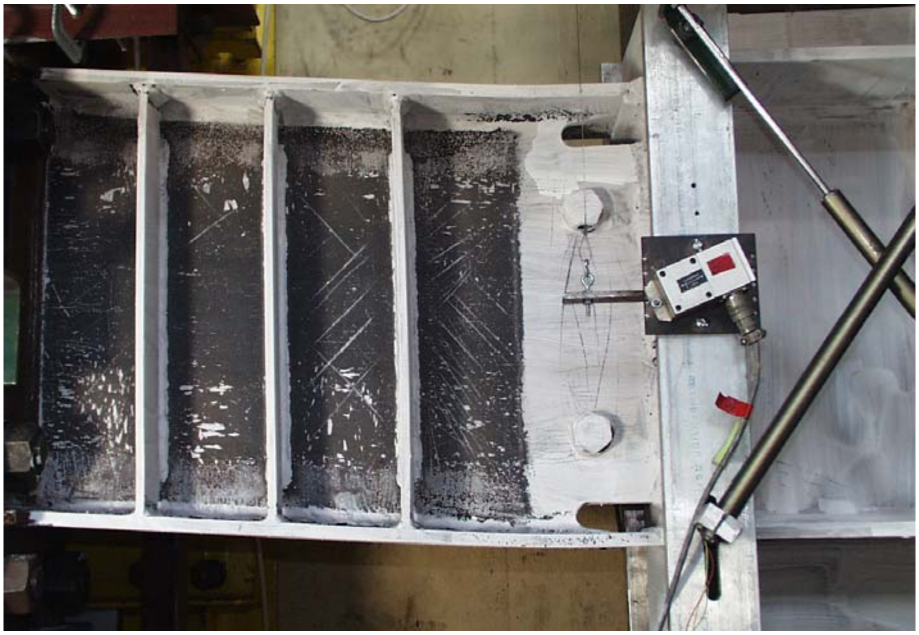

(b) Tested link and panel zone at $\gamma = 0.06$ rad

Figure 6.9 Comparison of link deformation in Specimen FFS

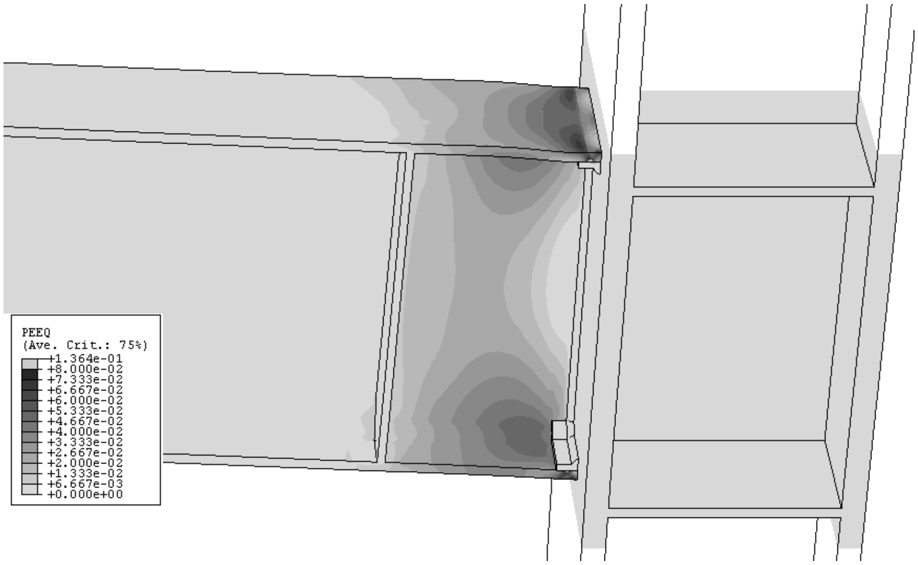

(a) Simulated link and panel zone at $\gamma = 0.075$ rad

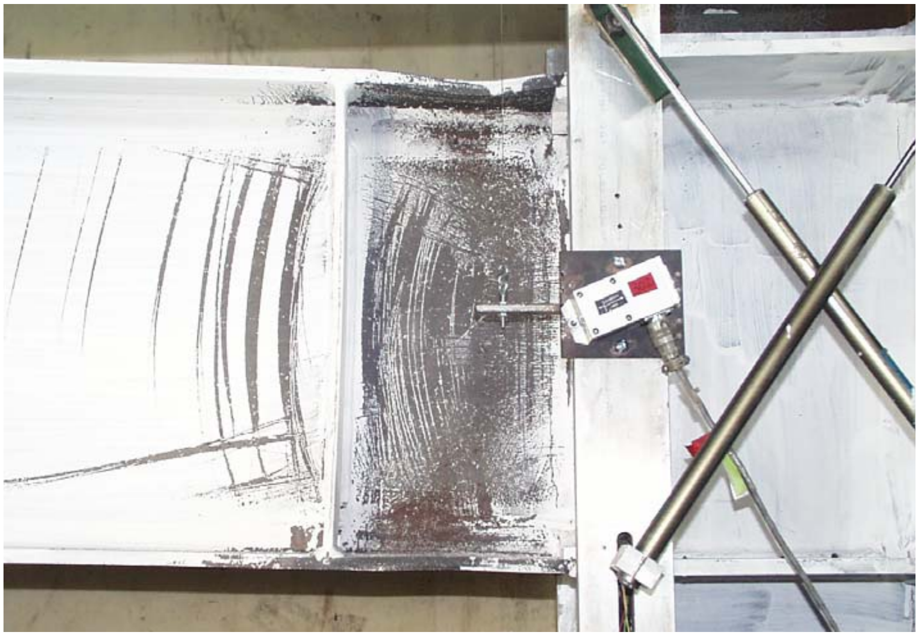

(b) Tested link and panel zone at $\gamma = 0.04$ rad

Figure 6.10 Comparison of link deformation in Specimen NAM

specimen, shown in Figure 6.10b, roughly agreed with the plastic strain distribution in Figure 6.10a. A small local buckle can be recognized in the compressed link top flange in Figure 6.10a. Figure 6.10b shows that the tested specimen subjected to cyclic loading developed local buckling in both the top and bottom link flanges. Therefore, the simulated Specimen NAM reproduced the experimental observations with reasonable accuracy.

As suggested by the above examples, the simulated links developed significant local flange deformation under large rotation levels. Although the local deformations led to small lateral deformations, none of the simulated specimens exhibited strength degradation caused by instability of the link, such as lateral torsional buckling or local buckling. Instability also played minimal effects on the test specimens. It is also noted that while a monotonically loaded link is subjected to larger absolute rotation compared to a cyclically loaded link at the same skeleton rotation, the difference in absolute rotation has little effect on the force and deformation environment until large deformation effects become significant. At large link rotations levels, such as that shown in Figure 6.9, of the order of γ = 0.15 rad or larger, large deformation effects cannot be neglected. Therefore, caution is required in correlating the monotonic loading simulation with the experimental behavior.

Further study showed that the response and deformation of the specimen global models was quite insensitive to further mesh refinement. Therefore, it was concluded that reasonable mesh convergence was obtained by the global models used in the current program. As stated before, the results from the global model analyses were used to perform submodeling analyses. The force and deformation environment predicted in the region included in the submodels was expected to agree well with the actual environment realized in the test specimens, as long as the influence of large deformation effects was limited.

6.3.3 Global Model Analysis Results

For each connection type, a beam-column model was analyzed along with models of link-column test specimens. The beam-column models, hereinafter referred to as the B-models (for example, FFB refers to a beam-column model with the FF-beam-to-column connection), were used to confirm the consistency between observations from this study and previous studies on steel moment frame connections. Figure 6.11 shows the simulated link deformation for the sixteen test specimens and beam deformation for the four beam-column models. The figure also shows the distribution of equivalent plastic strain. The S-link and SL-link models were at $\gamma = 0.117$ rad ($\gamma_p = 0.108$ rad), I-link models at $\gamma = 0.058$ rad ($\gamma_p = 0.047$ rad), M-models at $\gamma = 0.039$ rad ($\gamma_p = 0.028$ rad), and beam-column models at $\theta = 0.060$ rad ($\theta_p = 0.046$ rad). In the above, θ is the beam rotation angle and θ_p is the plastic beam rotation angle. These rotations are 1.1 times the skeleton rotations achieved by the MW-specimens (excluding Model MWB), and 1.35, 1.1, 1.4, and 1.55 times the plastic rotation required in the *2005 AISC Seismic Provisions* for the S, I, M-link and beam, respectively.

Figure 6.11 illustrates the different yielding mechanism predicted by the simulations. The S-links yielded primarily in the web panels. While the I-links also yielded in the web panels, the plastic strain was much greater in the end panels than in other panels, suggesting significant influence of flexure-shear interaction. The M-link yielded only near the link ends. Yielding of the flanges was spread in a much larger region of the beam flanges in the beam-column models compared to the I or M-link models. The difference in flexural yielding behavior might be attributed to the significantly different moment gradient (Refer to Sections 2.7.1 and 2.7.2). As discussed in Section 6.3.2, good agreement was generally found between the simulated and experimental link deformation. The deformation and yielding behavior of the beam-column model agree well with

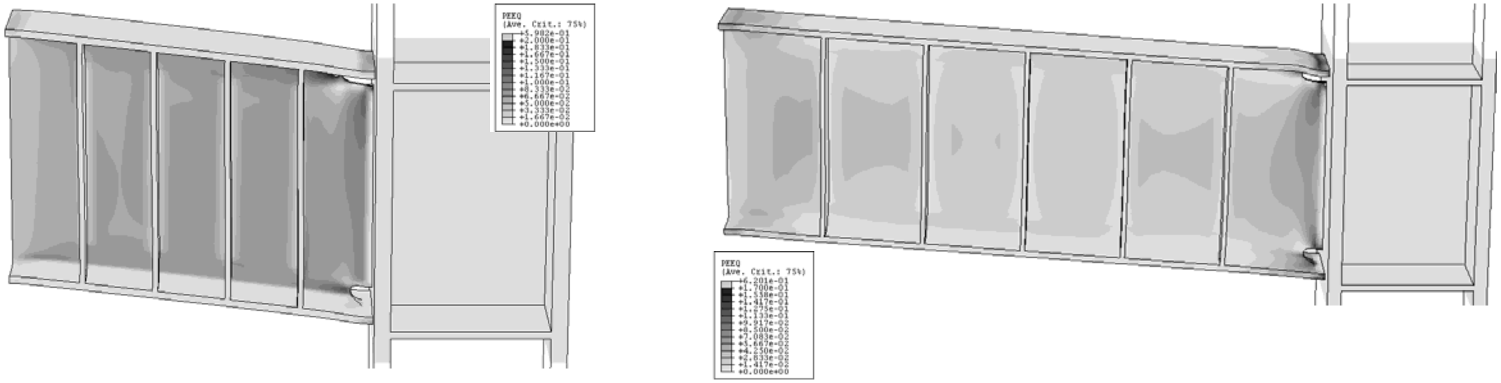

(a) Model PNS

(b) Model PNI

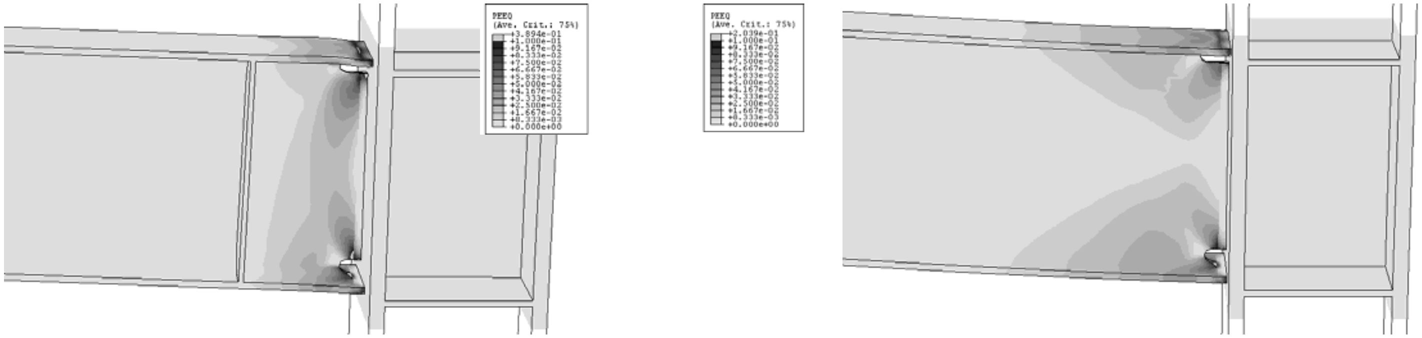

(c) Model PNM

(d) Model PNB

Figure 6.11 Simulated link deformation

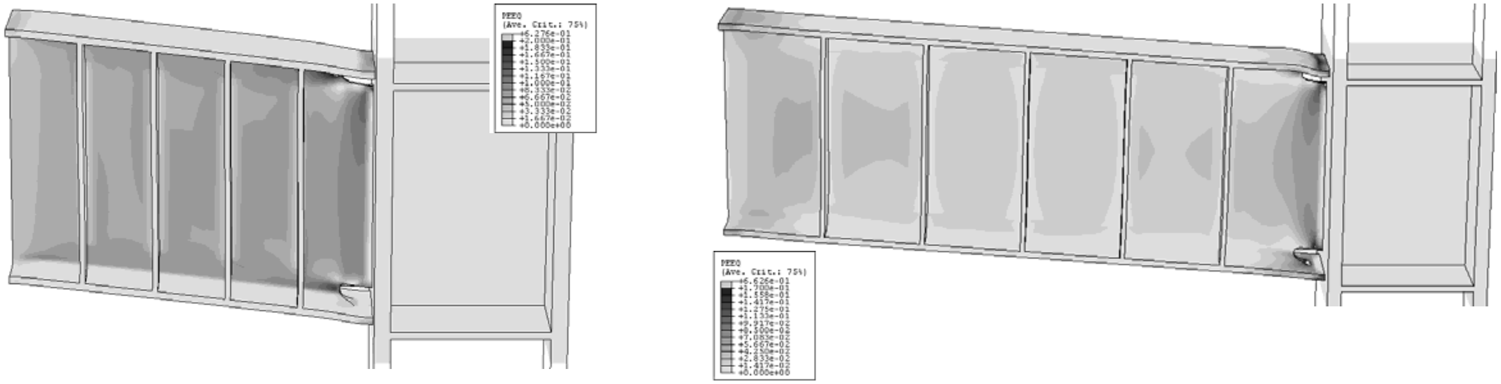

(e) Model MWS

(f) Model MWI

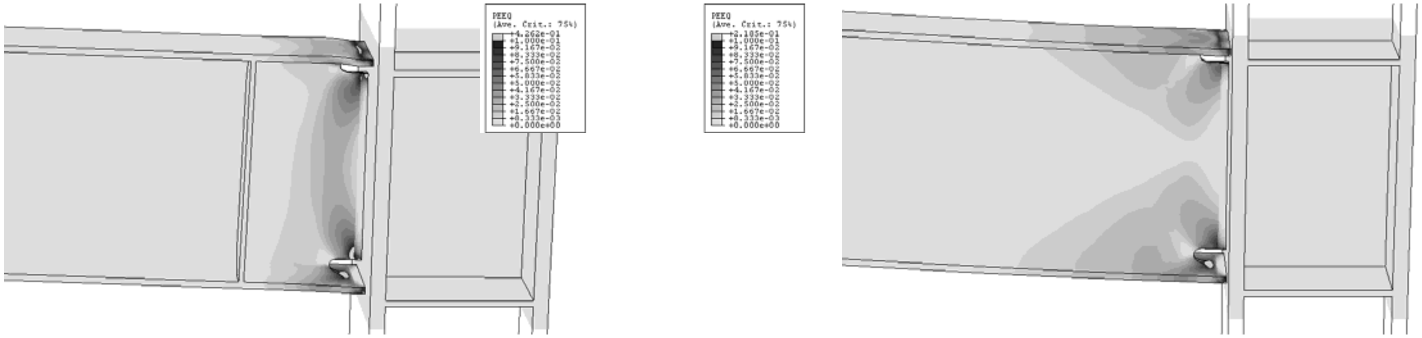

(g) Model MWM

(h) Model MWB

Figure 6.11 Simulated link deformation (Continued)

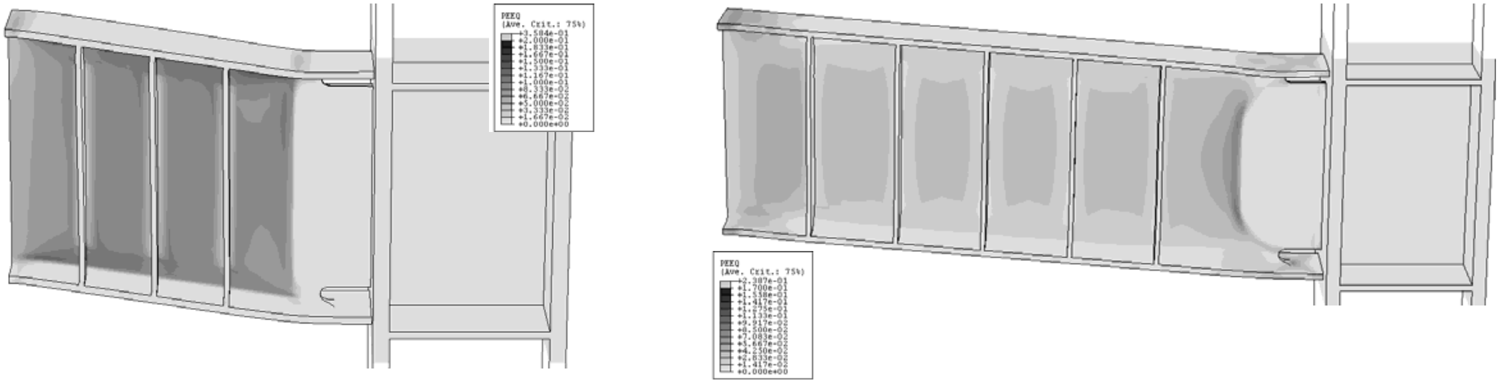

(i) Model FFS

(j) Model FFI

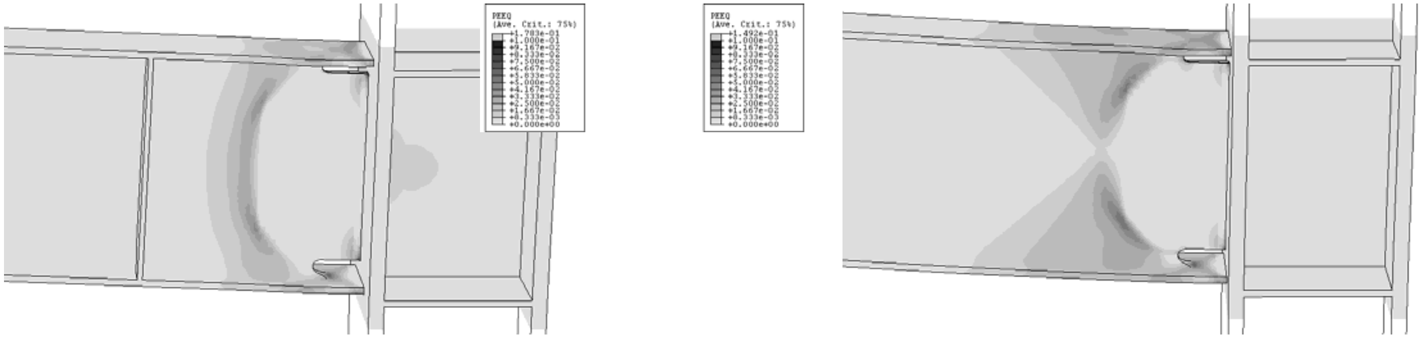

(k) Model FFM

(l) Model FFB

Figure 6.11 Simulated link deformation (Continued)

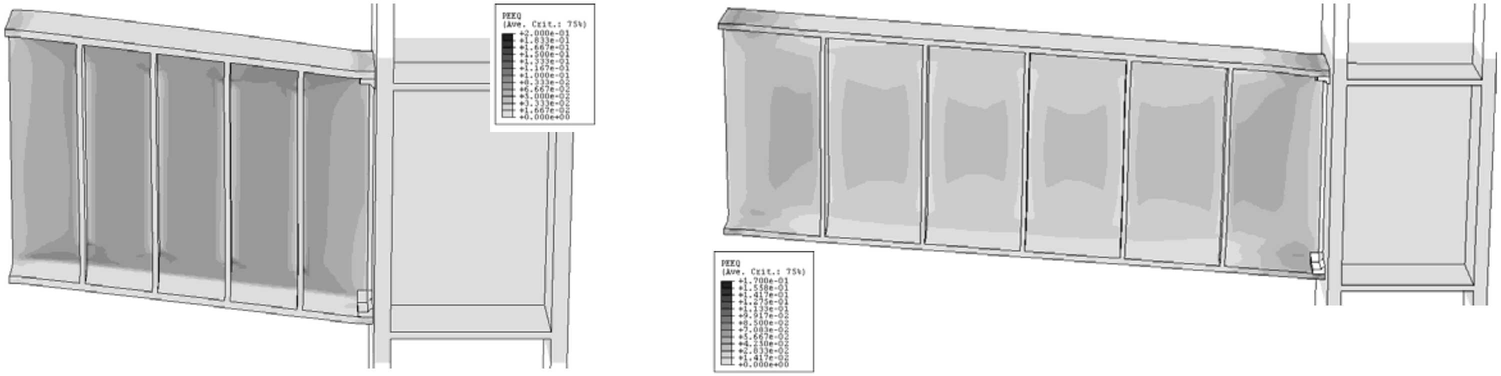

(m) Model NAS

(n) Model NAI

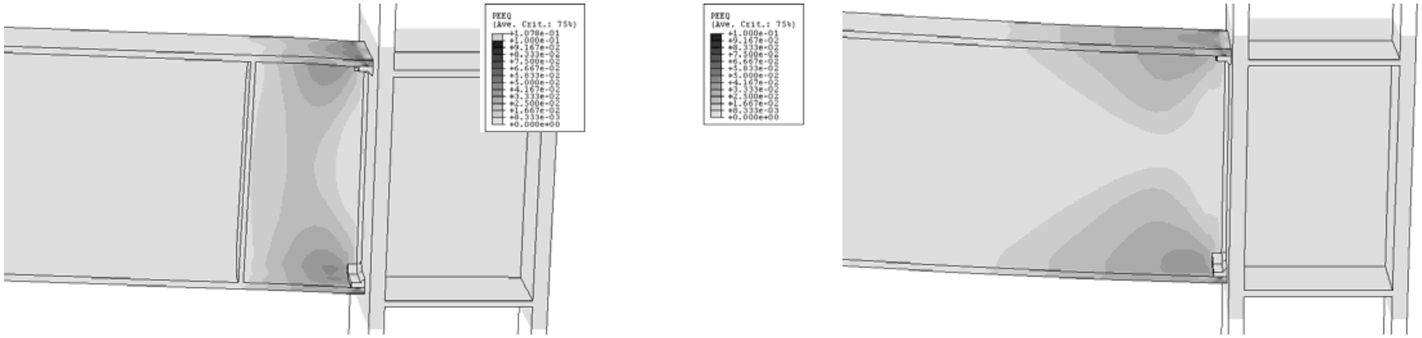

(o) Model NAM

(p) Model NAB

Figure 6.11 Simulated link deformation (Continued)

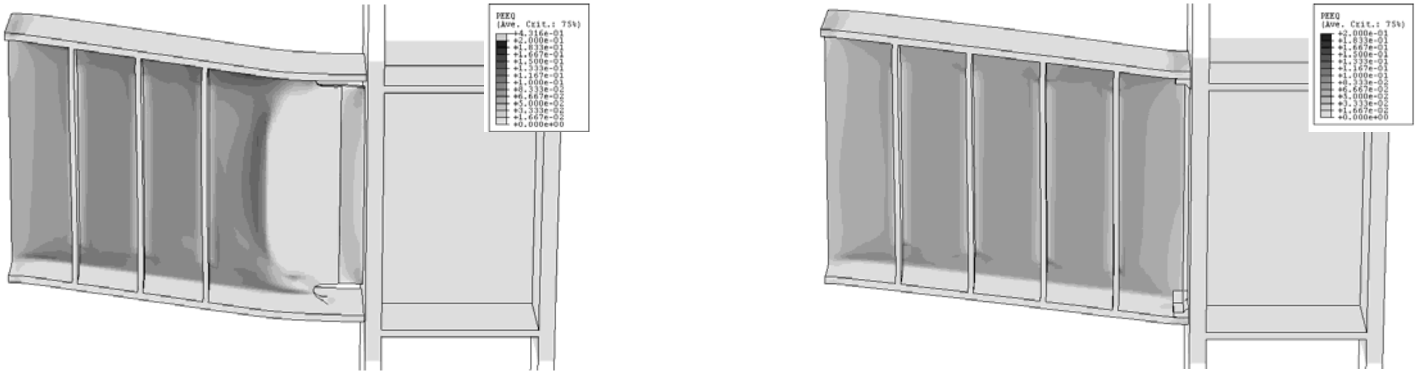

(q) Model FFS-RLP

(r) Model NAS-RLP
(Identical to Model NAS)

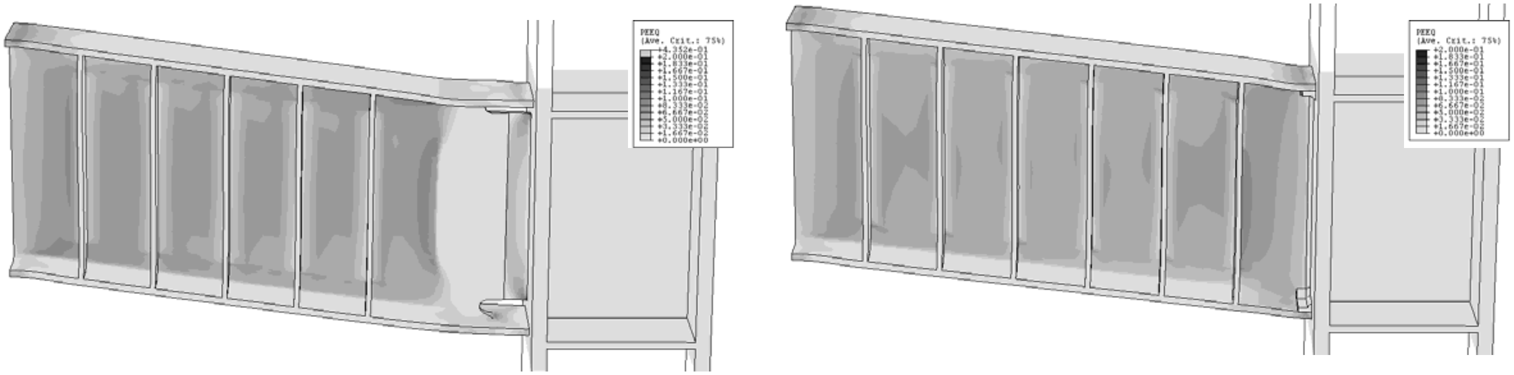

(s) Model FFSL-RLP

(t) Model NASL-RLP

Figure 6.11 Simulated link deformation (Continued)

past experimental and analytical studies.

The connection type had very significant influence on the deformation and yielding behavior of the link and beam. Little difference was found between the PN and MW-models of the same link lengths. The PN and MW models with S, I, and M-links developed large concentration of plastic strains near the link flange groove welds, and at the top and bottom edges of the link web. It appears that the reduced cross-sectional stiffness combined with severe flexure and shear force caused local deformation in this region, and the imposed deformation in turn, generated additional plastic strains.

The shear tab welded to the link web in the FF-models had a significant influence on the yielding mechanism. Due to the cross-sectional shear area added by the shear tab, yielding of the link or beam web was precluded in the segment welded to the shear tab. Instead of the concentrated inelastic flange and web deformation near the face of the column as in the PN and MW-models, the FF-models had yielding spread around the perimeter of the shear tab. The extent of yielding was substantially reduced near the link/beam flange groove weld in the FF-models compared to the PN and MW-models. The plastic strain around the perimeter of the shear tab concentrated near mid-depth of the link web in Model FFI, agreeing with previous observations that shear yielding spreads from mid depth of the link web towards the link flanges (Hjelmstad and Popov 1983a; 1983b). Meanwhile, Models FFM and FFB developed the largest plastic strain adjacent to the tapered portion of the shear tab. This behavior agrees with considerations by Choi (2000) that the tapered portion of the shear tab functions most efficiently in transmitting forces from the link/beam web to the shear tab in the free flange connection. While yielding in Model FFB spread from the beam flanges into the web, as also demonstrated in experiments (Choi 2000), yielding in

Model FFM developed simultaneously in the link flanges and web around the perimeter of the shear tab.

The NA-models generally developed the smallest inelastic deformation and plastic strains for the same link rotation. The higher restraint provided at the face of the column precluded the large local deformation near the face of the column found in the PN and MW-models.

Figure 6.11 also shows concentrated plastic strain at the top and bottom edges of the shear tab in Models FFS-RLP and FFSL-RLP. The other four FF-models do not show such high plastic strains at these locations. The difference in yielding behavior was caused by the Models FFS-RLP and FFSL-RLP having the link web cut short of reaching the column flange, while the other FF-models having the link web connected directly to the column flange. It appears that Models FFS-RLP and FFSL-RLP are disadvantaged by the smaller shear area of the link-to-column connection. Meanwhile, Figure 6.12 compares the deformed shape of the link in Models FFS and FFS-RLP, at a link rotation of $\gamma = 0.157$ rad. The large distortion of the link web in Model FFS-RLP was caused by torsion generated in the link web-to-shear tab connection, a product of the link shear force and the eccentricity between the link web and shear tab. Model FFS developed much less distortion of the link web compared to Model FFS-RLP. Since the torsion is proportional to the shear force developed in the link or beam, the FF-connection with the link web cut short of reaching the column flange is significantly more disadvantageous to link-to-column connections than to moment connections. Therefore, Figure 6.11 and Figure 6.12 suggest that FF-connections can achieve better performance with the link web directly welded to the column flange. The free-flange connection design for moment connections, which detaches the beam web from the column flange (*FEMA-350*), may not be suited for EBF link-to-column connections.

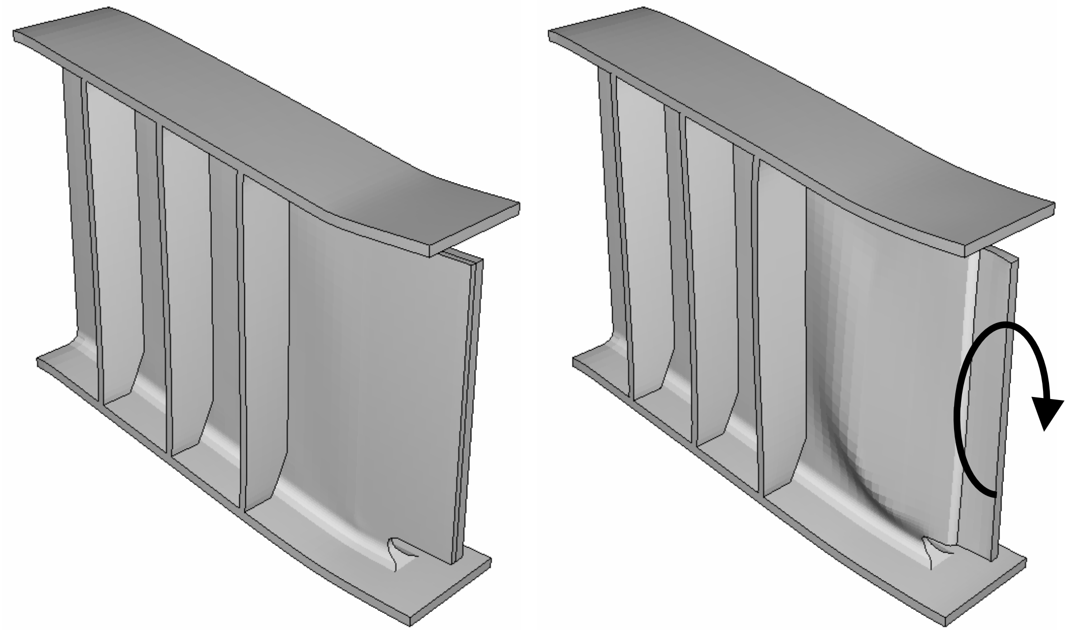

(a) Model FFS

(b) Model FFS-RLP

Figure 6.12 Link deformation in Models FFS and FFS-RLP

6.4 SUBMODELING ANALYSIS AND SAMPLING METHOD

6.4.1 Submodeling Analysis

A study of the submodeling analysis using models of specimen MWI is presented in this section. As shown in Figure 6.3, the submodel included the weld access hole and the groove weld at the link bottom flange. This region experiences the most severe stress and strain demand within the entire link-column assemblage, and test observations indicated that failure of the link-to-column connection was typically controlled by fracture of the link flange initiating at the groove weld. As discussed in Section 4.6.5.2, fracture occurred more frequently in the link top flange than at the link bottom flange. However, since the geometric and loading conditions at the link top flange is reasonably similar to that at the link bottom flange, and there are no apparent reasons for the more frequent occurrence of fracture in the top flange other than the loading sequence that subjected the top flange to tension before the bottom flange, only the bottom flange was considered in the submodeling analysis.

Past studies by El-Tawil *et al.* (1998) and Ricles *et al.* (2000) suggest that the C3D8 element is adequate for submodeling analysis of moment connections, which share similar geometric and loading features with EBF link-to-column connections. Analyses discussed herein also implicitly confirmed that the C3D8 element is adequate for the current program, where meshing was significantly more refined compared to the above mentioned studies.

Figure 6.13 shows the link segment of the global model and submodel. The submodel was much more detailed than the global model, particularly at the edges of the link flange and in the region near the weld interface in the link flange and link web. The global model did not include the reinforcing fillet weld at the root of the link flange groove weld, while the submodel included the reinforcing fillet weld.

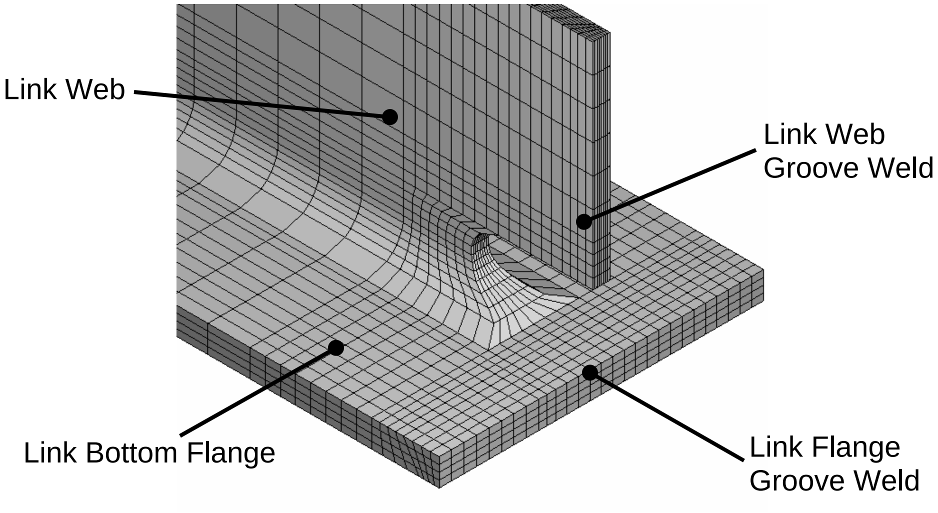

(a) Global Model

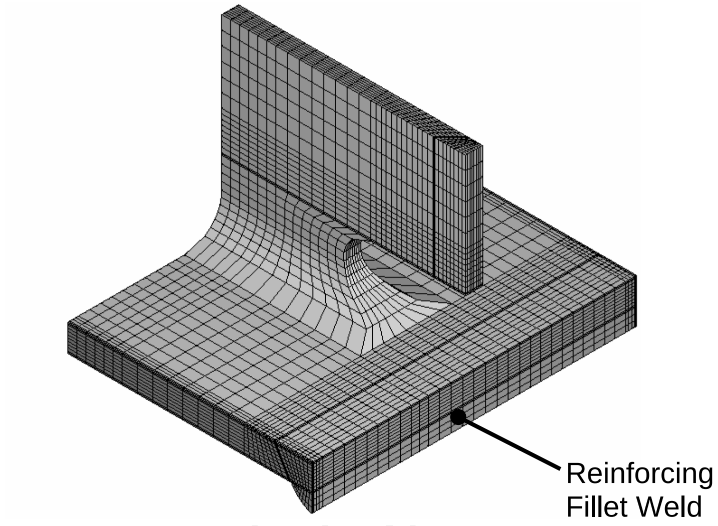

(b) Submodel

Figure 6.13 Link in global model and submodel

6.4.2 Validity of Submodeling Analysis

The submodeling analysis is justified by the assumption that detailed modeling of the local region included in the submodel has negligible effect on the response of the global model (ABAQUS 2003). Therefore, in order to confirm the validity of the submodeling analysis, the results from submodeling analyses were compared with the global model analysis results used to drive the submodeling analysis.

Figure 6.14 compares the Mises stress distribution obtained from the global model analysis and submodeling analysis. The results are shown for a link rotation of $\gamma = 0.058$ rad. This rotation is between the $\gamma = 0.064$ rad achieved by the negative skeleton curve and $\gamma = 0.045$ rad achieved by the positive skeleton curve for Specimen MWI (See Figure 6.8e). The Mises stress distribution is shown in a section parallel to the link web and including the centroid axis of the link section. The boundary that drove loading of the submodel is indicated in the global model (See Figure 6.14a) by solid lines. Although the difference in meshing and geometry (See Figure 6.13) resulted in different stress distribution in regions away from the boundary of the submodel, the stress distribution near the boundary was quite consistent between the global model and the submodel.

6.4.3 Identification of Critical Locations

Figure 6.15 compares the Mises stress distribution between the global model and submodel at $\gamma = 0.058$ rad. The stress distribution is shown on the surfaces of the link segment cut by a plane parallel to the link web. The boundary that drove loading of the submodel is indicated in the global model (See Figure 6.15a) by solid lines. As in Figure 6.14, the Mises stress distribution near the driving boundary agreed well between the submodel and the global model. In all models, elevated Mises stress values are found at the following locations: (a) near

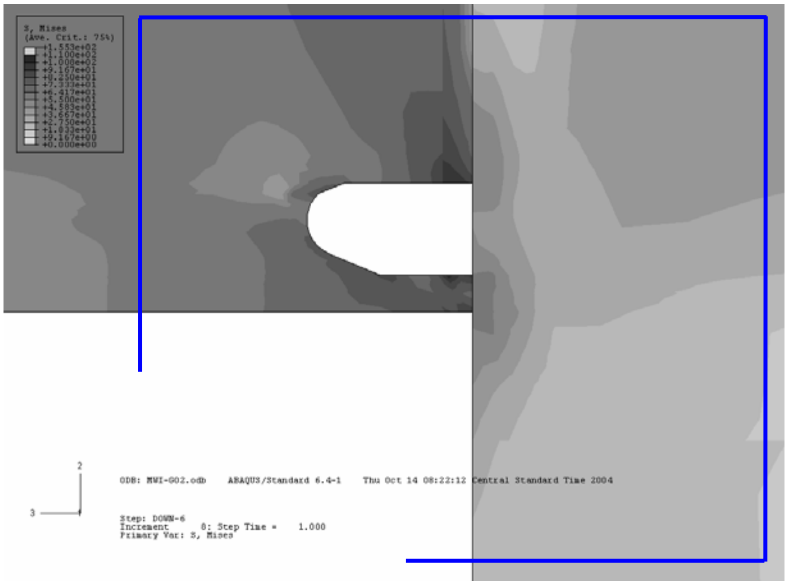

(a) Global Model

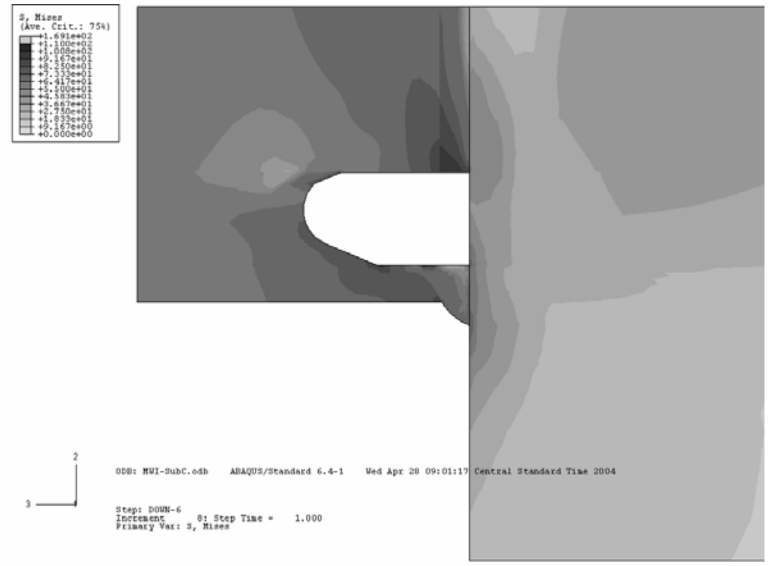

(b) Submodel

Figure 6.14 Check of driving boundaries in submodel the interface of the link flange and the groove weld; (b) the toe of the weld access hole; and (c) the bottom edge of the link web near the interface of the link web and the groove weld. Since fracture of test specimens was frequently observed at these locations, the Mises stress distribution is in line with the test observations. The Mises stress distribution differed significantly between the global model and submodel in the link flange near the face of the column. The submodel, which included the fillet weld (See Figure 6.15b) shows regions with notably lower Mises stresses in the groove weld. The global model (See Figure 6.15a) shows high Mises stresses in the entire groove weld. This difference was likely caused by the presence and absence of the reinforcing fillet weld at the root of the link flange groove weld. Both models show a region of very low Mises stresses near the radius zone of the weld access hole. In this region, the Mises stress was roughly 30 ksi lower than in the surrounding region.

.

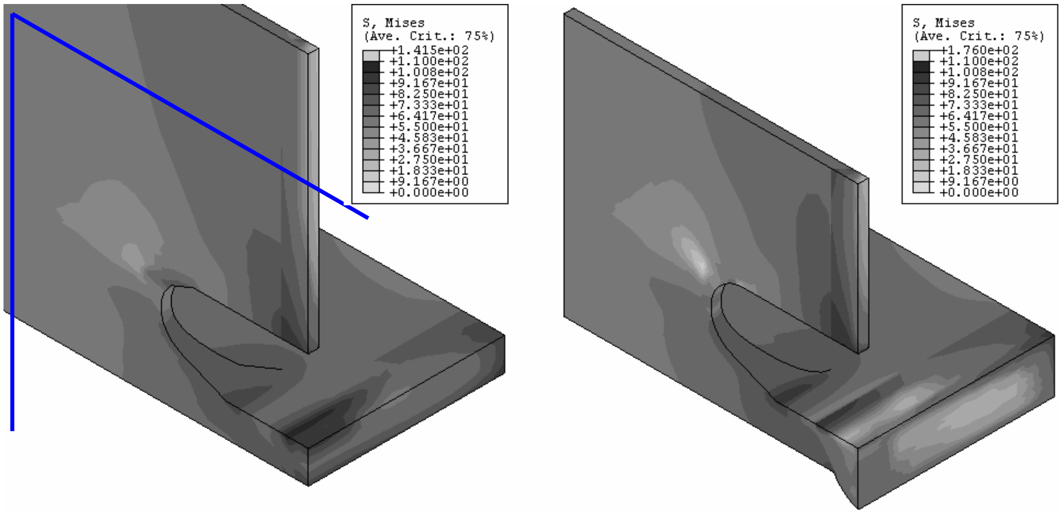

(a) Global model ***(b) Submodel***

Figure 6.15 Mises stress distribution in global model and submodel

Figure 6.16 shows the distribution of discontinuities in Mises stress at γ = 0.058 rad on the same surfaces of the link as in Figure 6.15. The discontinuities are the greatest difference in the nodal values of Mises stress evaluated from more than two elements sharing the node. The figure shows very large discontinuities in the range of 30 to 60 ksi at the following locations: (a) near the radius zone of the weld access hole, surrounded by a circle in the figure; (b) the toe of the weld access hole, also surrounded by a circle; (c) in the flange and web groove welds; and (d) near the weld interface of the flange groove weld, pointed to by an arrow in the figure. These four locations coincide either with geometrical discontinuities or material discontinuities. The Mises stress discontinuities at (a) and (b) were also likely caused by the distorted shape of elements at the fillet of the link section at the flange-web junction, particularly near the toe of the weld access hole (See Figure 6.13).

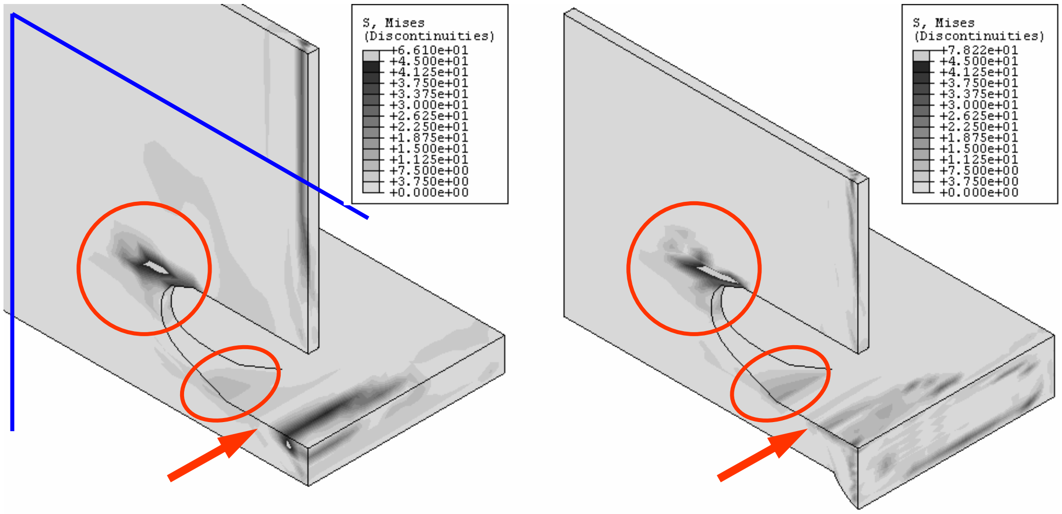

(a) Global model ***(b) Submodel***

Figure 6.16 Discontinuities in Mises stress

Caution is required in interpreting the stress and strain values near the four locations described above. However, the stress and strain values at location (d) are essential to study the fractures in the link flanges observed in the experiments. In the following section, the factors that affect the local convergence of the solution at important locations are discussed through comparison of the stress and strain distribution obtained from different finite element models.

6.4.4 Stress and Strain near Link Flange Groove Weld

Figure 6.17 compares the longitudinal distribution of equivalent plastic strain and Mises stress in the global model and submodel. The two longitudinal lines indicated in the figure as Lines-1 and 2 were chosen to study the stress and strain environment near the link flange groove weld. Line-1 lies on the top of the flange at mid-width, while Line 2 is at the bottom edge of the flange. Two sets of analysis results are presented, one analysis using the A992 steel properties for the entire body, and a second analysis that introduced the weld models for the link flange and web groove welds. The figure indicates the former as the “Uniform” material analysis. The second material distribution was used for the simulations presented in subsequent sections. The effect of modeling refinements and material discontinuity can be studied by comparing the four analysis results.

Figure 6.17 shows significant disagreement between the four solutions in Mises stress values along Line-1 near the toe of the weld access hole and along both Lines-1 and 2 near and in the groove weld. As discussed before, the locations of disagreement coincided with where elevated Mises stresses were obtained. On the other hand, the discrepancy between the four solutions was contained in small regions near the locations of geometric or material discontinuities. The good agreement between the global model and submodel outside of the small regions support the submodeling analysis procedure used in this study.

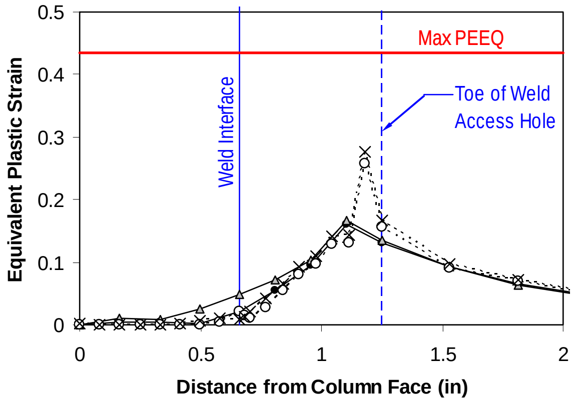

(a) Plastic Strain along Line-1 (γ = 0.058 rad)

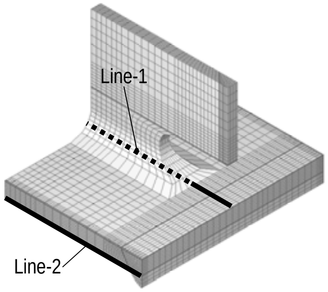

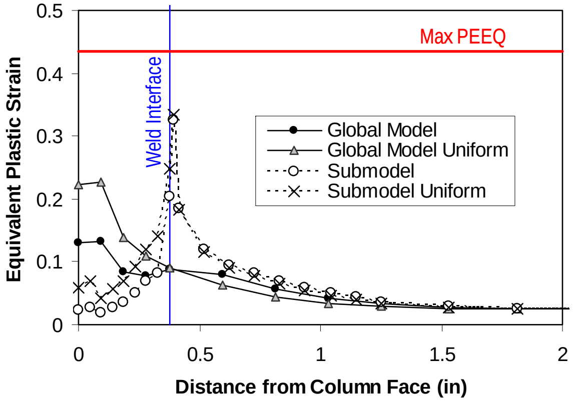

(c) Plastic Strain along Line-2 (γ = 0.058 rad)

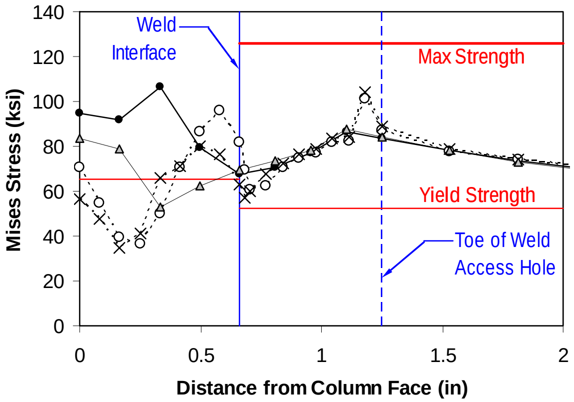

(b) Mises Stress along Line-1 (γ = 0.058 rad)

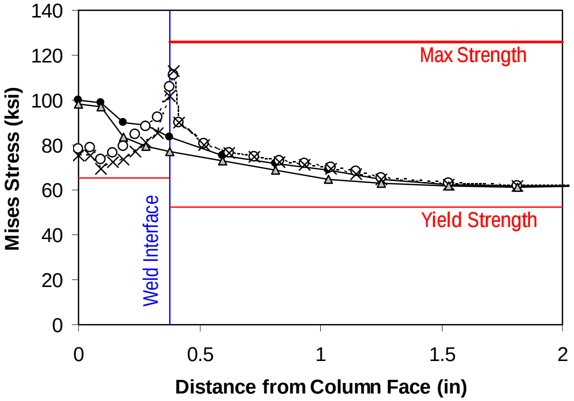

(d) Mises Stress along Line-2 (γ = 0.058 rad)

Figure 6.17 Comparison between global model and submodel

The difference in the weld metal material model caused notable differences in the stress and strain distribution within the groove weld. Comparison of the global model or submodel solutions show that higher yield strength of the weld metal model caused higher stresses but smaller plastic strains in the groove weld. However, the Mises stress and plastic strain values outside of the groove weld were insensitive to the weld metal models.

The reinforcing fillet weld at the root of the flange groove weld altered the stress and strain environment in the groove weld. Figure 6.17 shows that along Line-2, the presence of the reinforcing fillet weld shifted the location of elevated Mises stress and plastic strain from the face of the column in the global model to the end of the fillet weld in the submodel. The very significant difference in Mises stress distribution between the submodel and global model corresponds to the previous observation made from Figure 6.15. Therefore, the geometrical effect of the reinforcing fillet weld is significant, and the reinforcing fillet weld should be included in the model to evaluate accurately the stress and strain environment near the weld interface. Tabuchi *et al.* (2002) demonstrated that the presence of steel welds tabs and the geometry of the weld metal after removal of the weld tabs can significantly alter the stress and strain environment at the flange edge, with the gap between a steel weld tab and the flange edge acting as a fracture initiating notch. However, the current study did not consider the weld tabs or non-regular geometrical details other than the reinforcing fillet weld.

In the submodel, the end of the fillet weld intersected with the weld interface at the bottom of the flange. The two submodel solutions in Figure 6.17 suggest that the stress and strain elevation at the weld interface was caused primarily by the presence of the fillet weld, while the material discontinuity was less influential. Nonetheless, it is noted that the material discontinuity assigned to the models does not correctly represent the properties of actual welds. As shown in Figure 5.22, the material near the weld fusion line is characterized by a gradual transition of properties from the base metal, heat affected zone, weld interface, to the weld metal. The sharp discontinuity of material properties in the finite element model can introduce artificial stress and strain concentrations.

6.4.5 Sampling Method

The above discussion suggests that the critical locations of interest lie at geometrical and material discontinuities, where the stress and strain values may be affected by the modeling parameters.

Figure 6.18 illustrates the locations where the critical stress and strain values were sampled to represent the environment near the link flange-weld interface. The figure shows the longitudinal distribution of the equivalent plastic strain and Mises stress along Lines-1 and 2 in the global model and submodel. In addition to the averaged nodal values, which was also used in Figure 6.17, the values at the integration points are also plotted for the submodel. The finite element method provides higher accuracy for the stress and plastic strain values at integration points. Therefore, good agreement of the nodal values with the integration point values would suggest that the solution has converged. Figure 6.18 shows that excellent agreement between the nodal values and integration point values immediately outside of the weld interface line. The bold arrows in the figure point to the nodal values used to represent the stress and strain environment at the weld interface at Lines-1 and 2. The nodal values at this location agreed very well with the integration point values, and the points were a sufficient distance from artificial discontinuities.

Figure 6.19 illustrates the locations where the critical stress and strain values were sampled to represent the link web weld interface. Similar to Figure 6.18, this figure compares the longitudinal distribution of the equivalent plastic

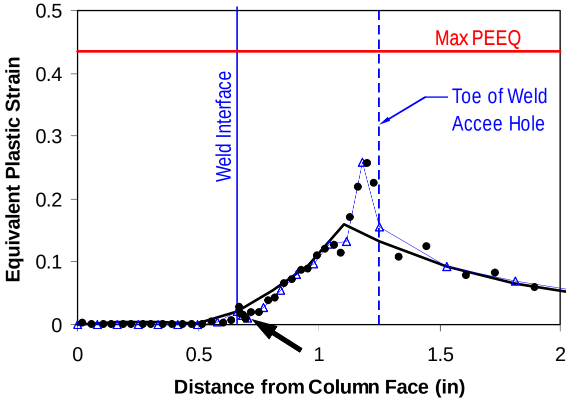

(a) Plastic Strain along Line-1 (γ = 0.058 rad)

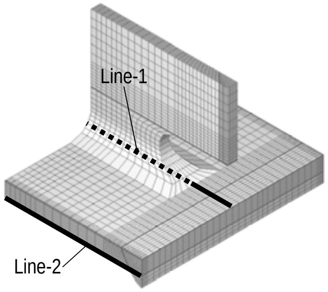

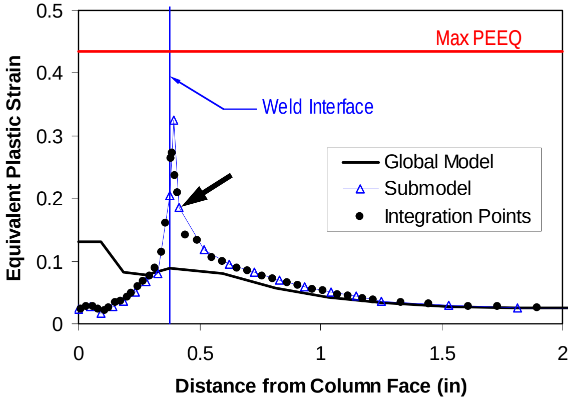

(c) Plastic Strain along Line-2 (γ = 0.058 rad)

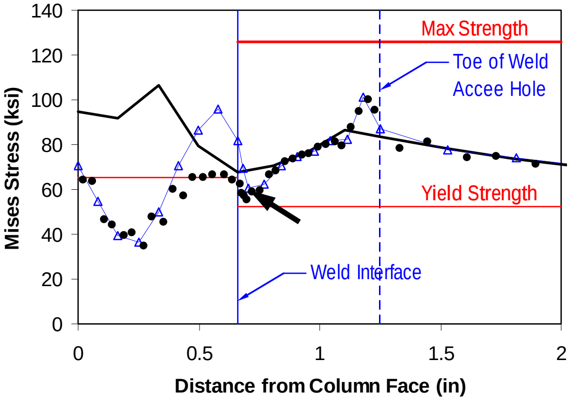

(b) Mises Stress along Line-1 (γ = 0.058 rad)

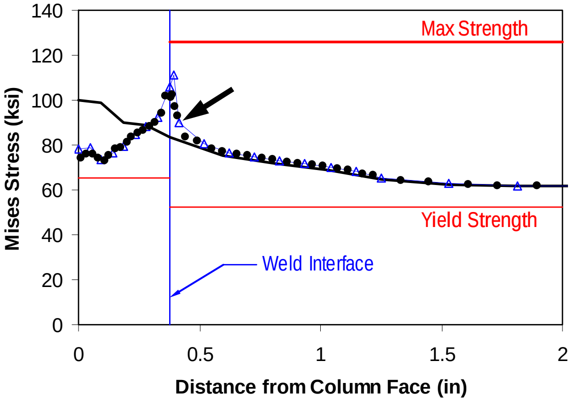

(d) Mises Stress along Line-2 (γ = 0.058 rad)

Figure 6.18 Sampling points near link flange groove weld

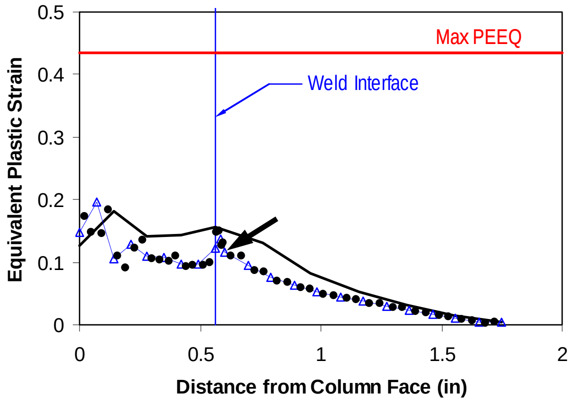

(a) Plastic Strain along Line-3 (γ = 0.058 rad)

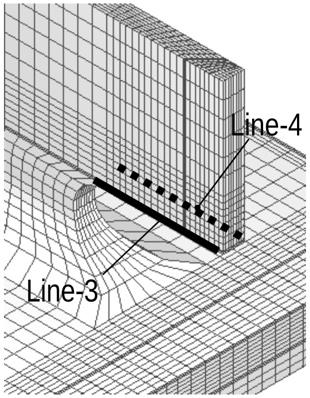

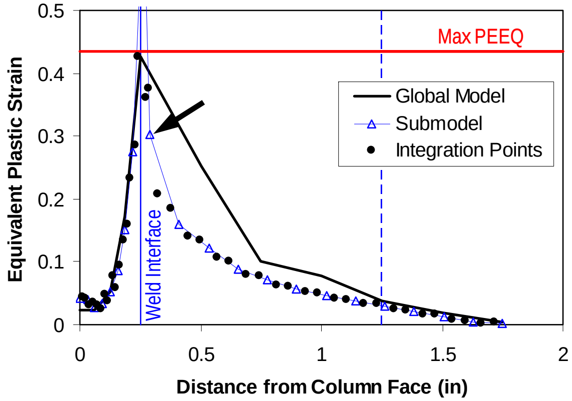

(c) Plastic Strain along Line-4 (γ = 0.058 rad)

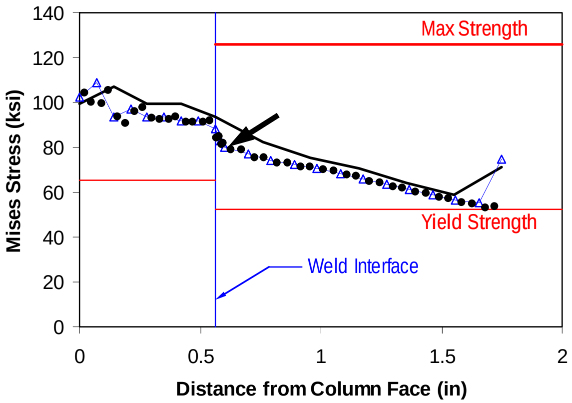

(b) Mises Stress along Line-3 (γ = 0.058 rad)

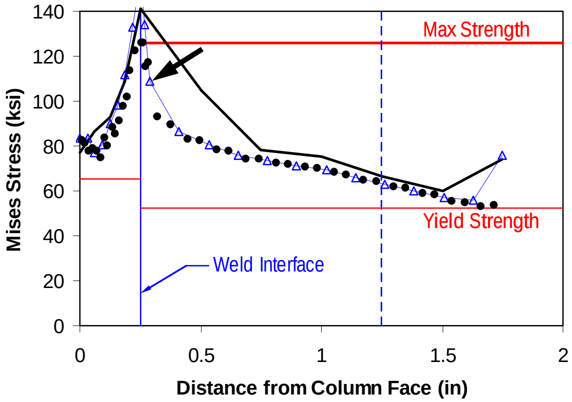

(d) Mises Stress along Line-4 (γ = 0.058 rad)

Figure 6.19 Sampling points near link web groove weld strain and Mises stress in the global model and submodel. The values were sampled along the two longitudinal lines, indicated as Lines-3 and 4, lying at the bottom edge of the link web, between the column face and the weld access hole. Line-3 is at the front of the link web, while Line-4 runs through the root of the link web groove weld. Although the difference between the submodel and the crudely meshed global model was substantial, the agreement between the nodal values and integration point values in the submodel suggests that the submodel solution was well converged. While the stress and strain values along Lines-3 and 4 were remarkably different inside the groove weld, the difference diminished within a short distance outside of the groove weld. It appears that the small thickness of the link web with non-uniform stiffness was restrained to undergo uniform strains. Along Line-4, where the stiffer weld metal occupied a smaller region than along Line-3, plastic strain concentrated near the weld interface. Consequently, the most critical location near the link web weld interface was at the root of the weld. Near the right end of the plots, corresponding to the tail end of the weld access hole, the global model and submodel do not provide accurate results, as previously demonstrated in Figure 6.16. The sampling points for the stress and strain values near the link web groove weld are indicated in Figure 6.19 by bold arrows. Similar to the sampling for the link flange weld interface, the nodal values at this location agreed very well with the integration point values, and the points were a sufficient distance from artificial discontinuities.

Figure 6.20 shows the stress-strain relationship measured at the sampling point shown in Figure 6.18c and d. For reference, the stress-strain relationship at the intersection of Line-2 and the weld interface is also shown. The two points were merely 0.04 inches apart from each other. Since the nodal values are obtained by averaging the values from surrounding elements, the intersection point located between the A992 steel and weld metal does not follow either of the two material models. However, the sampling point is distanced enough from the weld interface to avoid the effect of the material discontinuity.

All sampling points shown in Figure 6.18 and Figure 6.19 were located at a distance of 0.04-inches, two elements, and two nodal points into the link flange or link web from the weld interface. The above discussion demonstrated that the sampling points were located close enough to the geometrical and material discontinuities to capture the elevation in stress and strain values, while distanced enough from the artificial discontinuities.

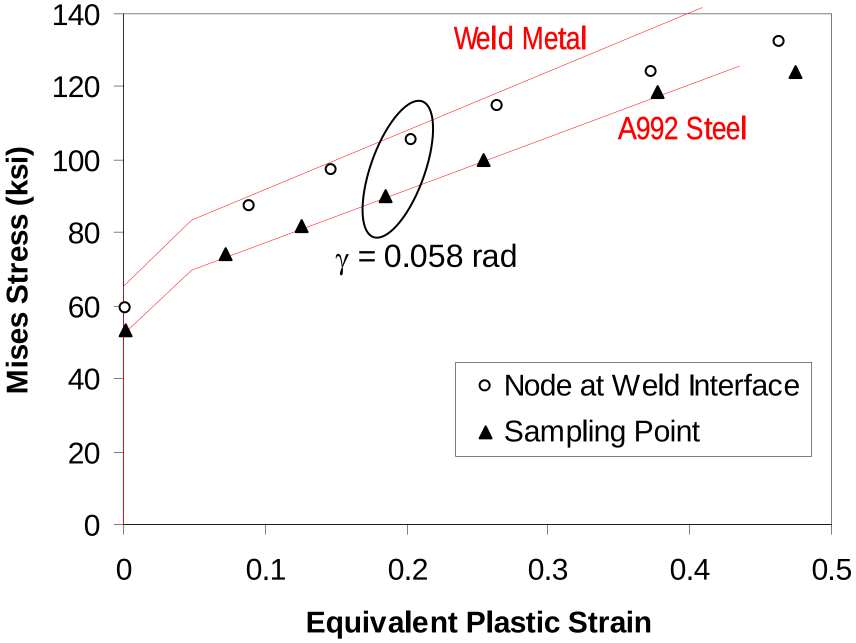

Figure 6.20 Stress-strain relationship measured at sampling point

6.5 SIMULATION AND OBSERVED FRACTURE BEHAVIOR

This section examines the correlation between the stress and strain environment predicted by the finite element simulations and the observed fracture behavior of the test specimens. The effect of link length and connection type on the simulated stress and strain distribution is studied. Test results (Refer to Section 4.6.5) suggest that failure of an EBF link-to-column connection is typically controlled by fracture initiating at one of the following three locations: (a) the link flange-groove weld interface; (b) the link web-groove weld interface; and (c) the shear tab-groove weld interface in FF-connections. Therefore, the computed stress and strain environment at the above three locations is compared against the fracture behavior observed in the tests.

6.5.1 Effect of Link Length on MW-Models

The effect of link length was studied using the MW-models. Figure 6.21 shows the distribution of equivalent plastic strain and bending stress at the link base metal-weld interface of the link flange groove weld. The bending stress plotted in this figure is the Cauchy stress component σ_{33}, where 3 is the coordinate axis fixed at the longitudinal direction of the original, undeformed link. The bending stress was chosen as a stress component relevant to the crack opening mode of fracture (Barsom and Rolfe 1999) perpendicular to axis-3. The distributions were sampled along the lines indicated in the figure as Lines-L and U. The two lines run across the width of the link flange, Line-L near the bottom end of the link flange-groove weld interface, and Line-U near the top end of the interface. The relative locations of the sampling lines with respect to the link flange-groove weld interface were selected based on the discussion in Section 6.4.5. The figure compares link-column models MWS, MWI, and MWM as well as a beam-column model, MWB. Results from the four models are represented at

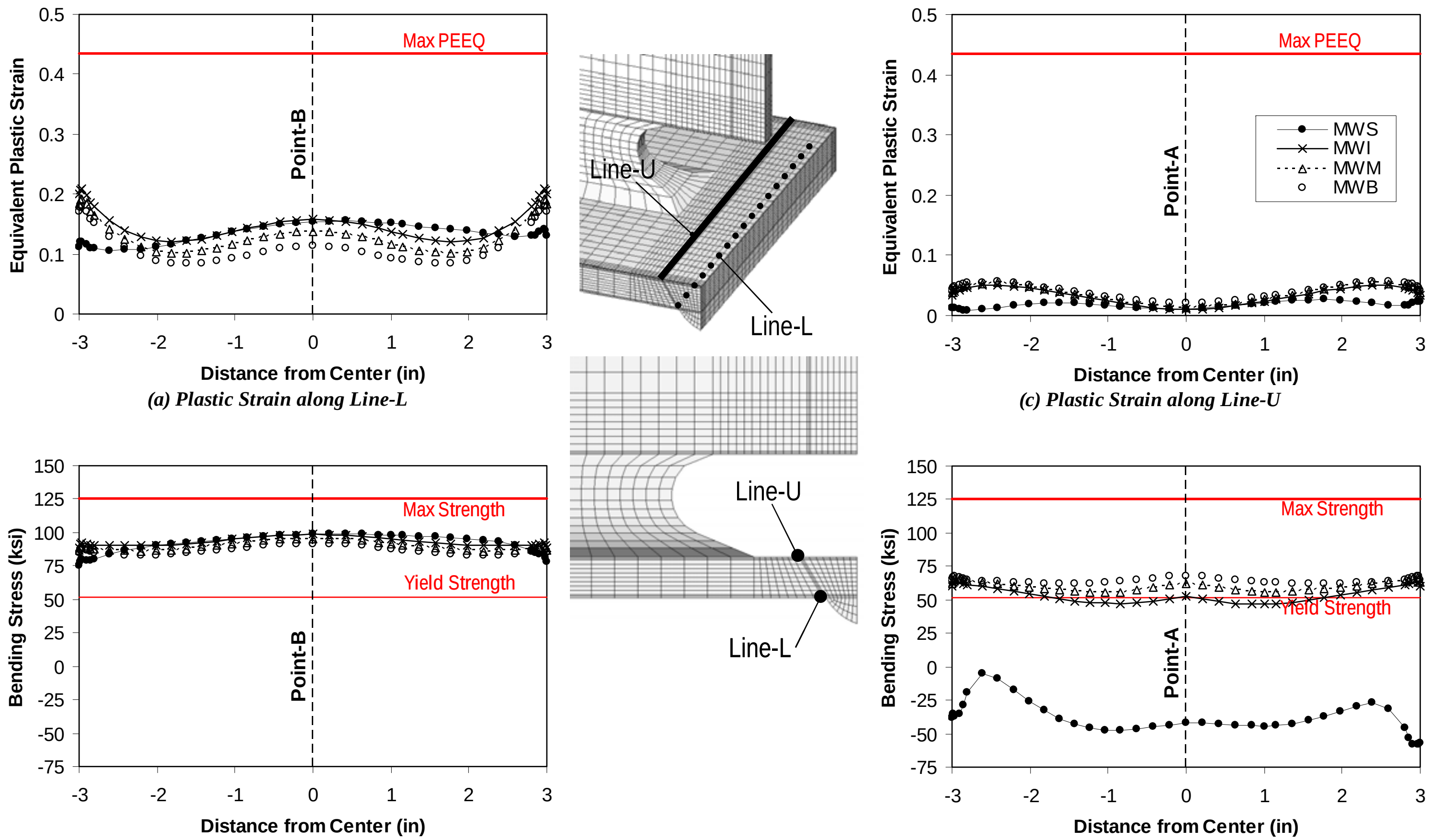

(a) *Plastic Strain along Line-L*

(c) *Plastic Strain along Line-U*

(b) *Bending Stress along Line-L*

(d) *Bending Stress along Line-U*

Figure 6.21 Effect of link length on the link flange-groove weld interface the same respective rotation levels previously used in Figure 6.11.

Figure 6.21 shows similar distributions of equivalent plastic strain and bending stress between Models MWI, MWM, and MWB. This similarity is remarkable, considering the significant differences in link or beam yielding mechanisms shown in Figure 6.11. However, the distributions in Model MWS are very different from that in the other three models. All four models show higher equivalent plastic strain and tensile stress values along Line-L than along Line-U. Model MWS show compressive stresses along Line-U and tensile stresses along Line-L. The other three models show roughly 20 ksi higher tensile stresses along Line-L than along Line-U. The different tensile stress values between Lines-U and L indicate that all four models developed secondary bending in the link flange, which adds tensile stresses to the outer half of the flange and adds compressive stresses to the inner half of the flange. Model MWS was influenced the most among the four models by secondary bending.

Models MWI, MWM, and MWB show elevated plastic strains at the side edges in Line-L, while Model MWS show higher plastic strain values near the middle than the edges in Line-L. This plastic strain distribution may be related to the observed occurrence of fracture at mid-width of the link flange in Specimen MWS and at the edge of the link flange in Specimen MWI.

Recall that the rotations of the models were scaled to match roughly 1.1 times the skeleton rotation capacity of the corresponding MW-test specimens, except for Model MWB. The skeleton rotation capacity was controlled by fracture of the link flange. According to the equivalent plastic strain and bending stress distribution shown in Figure 6.21, the local stress and strain environment at the link flange-groove weld interface was roughly similar in severity between Models MWS, MWI, and MWM. Therefore, the simulated stress and strain values appear to correlate with the observed fracture behavior of the test specimens. On the other hand, Model MWI was at only 1.1 times the link rotation required in the *AISC Seismic Provisions*, while the link rotation of the other three models ranged between 1.35 and 1.55 times their respective rotation requirement. Therefore, the force and deformation environment at the link-to-column connection produced by an I-link appears to be more severe than that produced by an S or M-link, or at a moment connection.

Figure 6.22 shows the distribution of equivalent plastic strain and bending stress at the link flange-groove weld interface, sampled along the thickness of the link flange. Points-A and B are located in the middle of Lines-U and L, respectively (also see Figure 6.21). Figure 6.22 suggests that the stress and strain values change monotonically along the thickness of the link flange, and therefore, are well represented by Lines-U and L used in Figure 6.21. As discussed above, the variation in bending stress along the thickness of the link flange indicates the influence of secondary bending in the link flange. The tensile stress distribution is similar between all four models in the bottom half of the link flange, while the sharp turn in the upper half of the link flange to compressive stresses is seen only in Model MWS.

Figure 6.23 illustrates the deformed link flange of Models MWS and MWM, along with the principal stresses in elements at mid-width of the link flange. The locations of Points-A and B (See Figure 6.21 and Figure 6.22) are shown in the figure. To the right of the “interface” line is the weld metal, to the left is the link flange base metal. The figure suggests that the maximum principal stress is roughly equivalent to the bending stress near the link flange-groove weld interface, except in the top half of the flange in Model MWS. While significant shear stresses are present in the weld metal, the link flange base metal is largely in tension, with the direction of the maximum principal stress following the distorted shape of the link flange. However, substantial compressive stresses are seen near

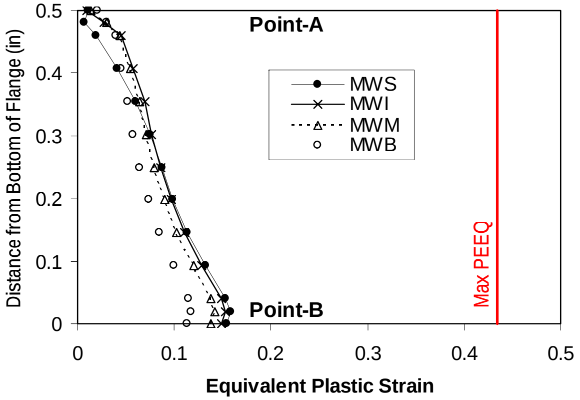

(a) Plastic Strain along Thickness of Flange

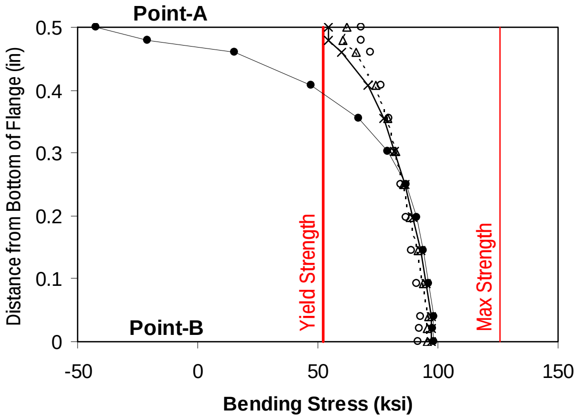

(b) Bending Stress along Thickness of Flange

Figure 6.22 Stress and strain distribution along thickness of link flange

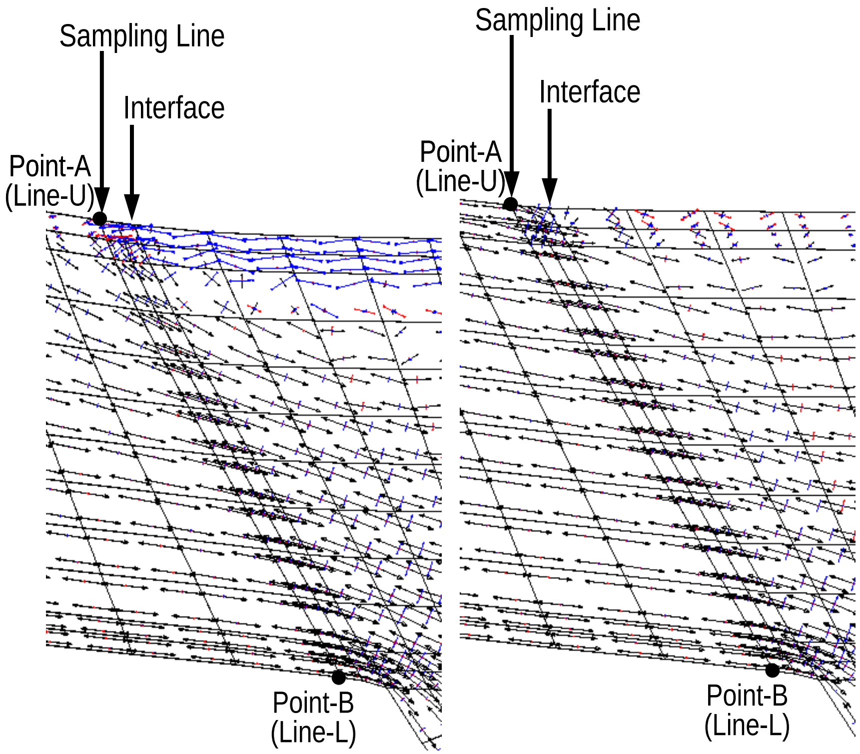

(a) Model MWS

(b) Model MWM

Figure 6.23 Principal stress distribution near link flange-groove weld interface the top side of the groove weld metal in Model WMS, which is reflected in the compressive stresses near Point-A shown in Figure 6.22b. In both Models MWS and MWM, the maximum principal stresses were better aligned with the distorted link flange at the bottom half of the flange. Further analysis results not presented here showed that, as the link rotation increases, the link flange near the column face approaches a state of uniform tension, with the tensile stress aligned with the distorted link flange.

Figure 6.24 shows the distribution of equivalent plastic strain and bending stress at the link web-groove weld interface. As indicated in the figure, the two sampling lines, R and F, run along the depth of the link, at the front and rear sides of the link web, respectively. The distributions are shown for the same four models at the same respective rotation levels as in Figure 6.21. As discussed in Section 6.4.5, the significant difference in stress and strain distribution between Lines-R and F was caused by the tapered geometry of the link web groove weld. All four models show the largest equivalent plastic strain and bending stress values at the bottom edge of Line-R.

Model MWS shows appreciable bending stress values only in the region within 0.7-inches from the bottom edge of the link web. The remaining region of the link web in Model MWS was controlled by shear yielding. Shear-flexure interaction is noted also in Model MWI, where the bending stress values decrease more rapidly with the distance from the bottom edge of the link web than in Models MWM and MWB. Regardless of the different distribution characteristics, the largest plastic strain and bending stress values are similar in all for models. The peak equivalent plastic strain value is 30% lower, and the peak bending stress value is 10% lower in Model MWB than in the other three models. Therefore, link web fracture may play a more prominent role in EBF link-to-column connections than in moment connections.

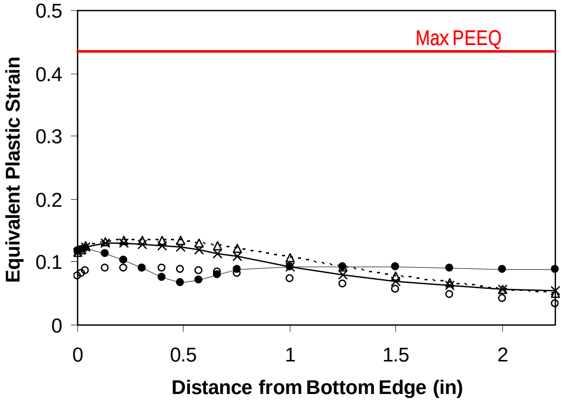

(a) Plastic Strain along Line-F

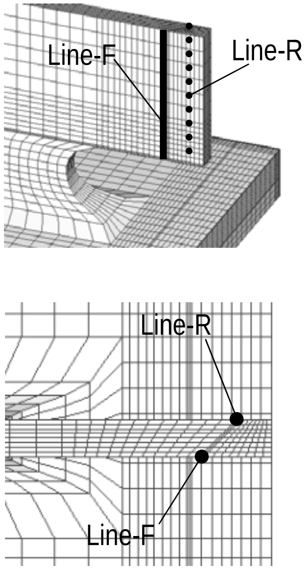

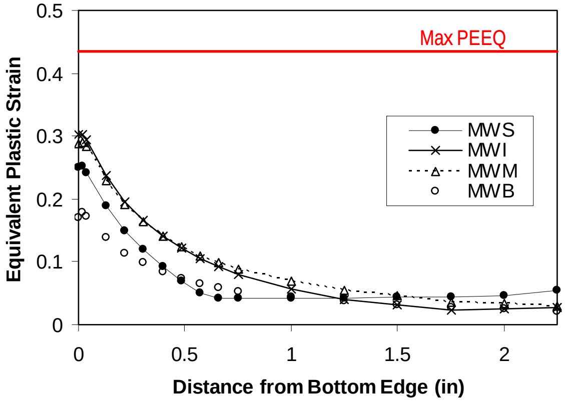

(c) Plastic Strain along Line-R

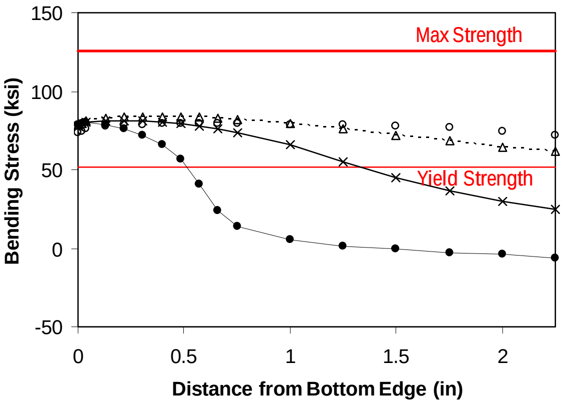

(b) Bending Stress along Line-F

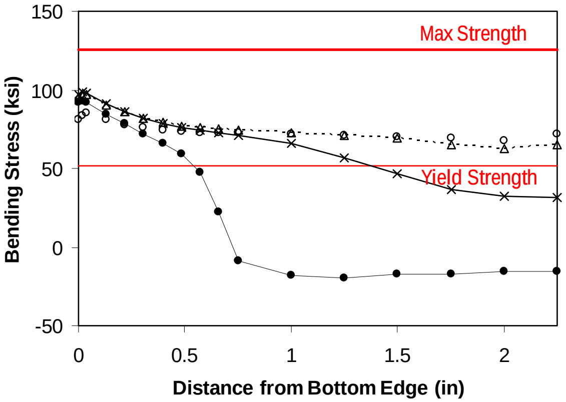

(d) Bending Stress along Line-R

Figure 6.24 Effect of link length on the link web-groove weld interface

6.5.2 Link Flange-Groove Weld Interface

Figure 6.25, Figure 6.26, and Figure 6.27 show the equivalent plastic strain and bending stress distribution along Lines-L and U in the S, I, and M-link models, respectively. As in Figure 6.21, Lines-L and U run across the width of then link flange, at the bottom and top edges of the link flange-groove weld interface. Figure 6.28 shows the same distributions for the beam-column models. Each figure compares the results from four connection types, PN, MW, FF, and NA. Note that these finite element simulations do not address the different fracture toughness of the weld metal, which was one of the key differences between PN- and MW-connections in the experimental program.

Figure 6.25 compares S-links with the four connection types, at a link rotation of γ = 0.117 rad. The figure shows that the FFS-model barely yielded along either Liner-L or U. The relatively similar bending stress values between Lines-L and B suggests that secondary bending was minor in the link flanges of Model FFS. On the other hand, Models PNS, MWS, and NAS showed significantly higher bending stress values along Line-L than along Line-U, indicating a substantial influence of secondary bending in these three models. Unlike the models with longer links, which are discussed later, the S-link models did not show significant elevation in equivalent plastic strain or bending stress near the edges of Line-L.

The substantial variation in bending stress values along Line-U in Models PNS and NAS was likely caused by restraint of the link web. The extended weld access holes in Models MWS and FFS relaxed the local restraint, and enabled a more uniform bending stress distribution along Line-U. Model PNS showed slightly elevated equivalent plastic strain values near the middle of Line-U. The toe of the weld access hole intersecting the link flange-groove weld interface

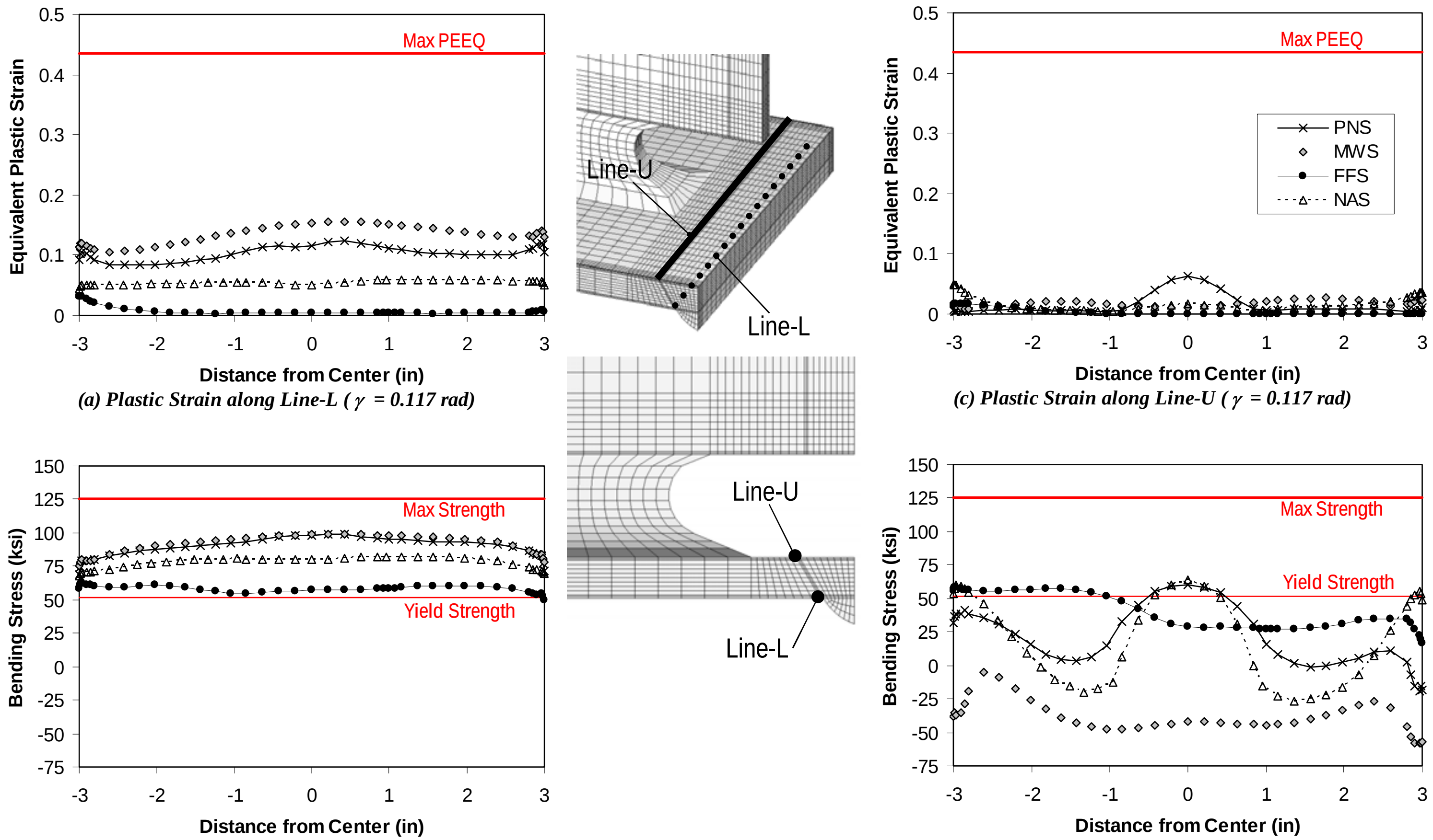

(a) Plastic Strain along Line-L (γ = 0.117 rad)

(c) Plastic Strain along Line-U (γ = 0.117 rad)

(b) Bending Stress along Line-L (γ = 0.117 rad)

(d) Bending Stress along Line-U (γ = 0.117 rad)

Figure 6.25 Link flange-groove weld interface in S-links

at the top face of the link flange caused stress and strain concentrations at this location. Since the largest equivalent plastic strain and bending stress values are higher in Model MWS than in Model PNS, the MW-connection may be no better suited for S-links than the PN-connections. The largest equivalent plastic strain values in Models FFS and NAS was less than half of the values in Model PNS or MWS.

Figure 6.26 compares Models PNI, MWI, FFI, and NAI, at a link rotation of γ = 0.058 rad. The difference in bending stress values between Lines-L and U was roughly 30 ksi in Models PNI, MWI, and NAI, and 15 ksi in Model FFI. Similar to Model FFS, Model FFI was successful in reducing the link shear transmitted to the link flange, and thereby reduced the secondary bending in the link flange. As discussed above, the PN-connection produces stress and strain concentration in the middle of Line-U, at the toe of the weld access hole. The MW-connection is clearly more beneficial than the PN-connection in removing the large concentration in the middle of Line-U. Elevated equivalent plastic strain and bending stress values are seen at the edges of Line-L in Model PNI, MWI, and FFI, and at the edges of Line-U in Model NAI. The largest equivalent plastic strain values in Models FFI and NAI were roughly one-third of the values in Model PNI and MWI.

Figure 6.27 compares Models PNM, MWM, FFM, and NAM, at a link rotation of γ = 0.039 rad. Figure 6.28 compares Models PNB, MWB, FFB, and NAB, at a beam rotation of θ = 0.060 rad. The distributions shown in Figure 6.27 and Figure 6.28 are very similar to those of I-link models shown in Figure 6.26. As stated earlier, this similarity is remarkable considering the significant differences in link or beam yielding mechanisms shown in Figure 6.11. It was found that although the column face moment varied by $0.15M_p$ and shear force by $0.7V_p$ between the three models, the resultant of the bending stresses and shear

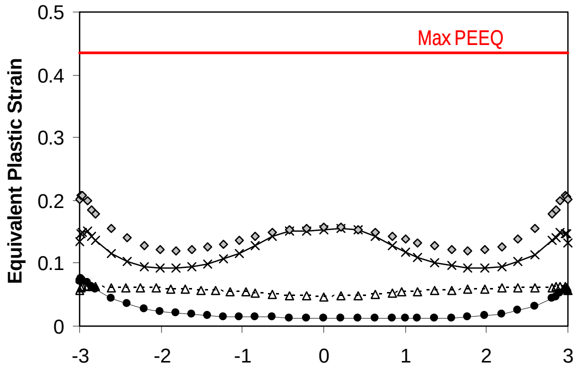

(a) Plastic Strain along Line-L (γ = 0.058 rad)

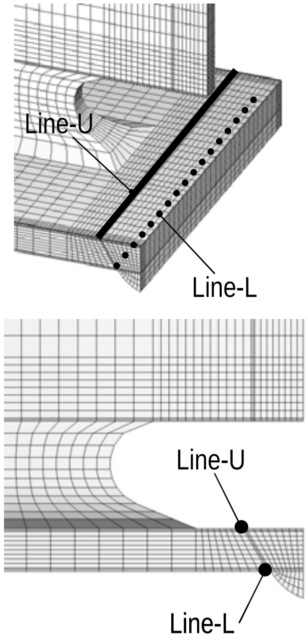

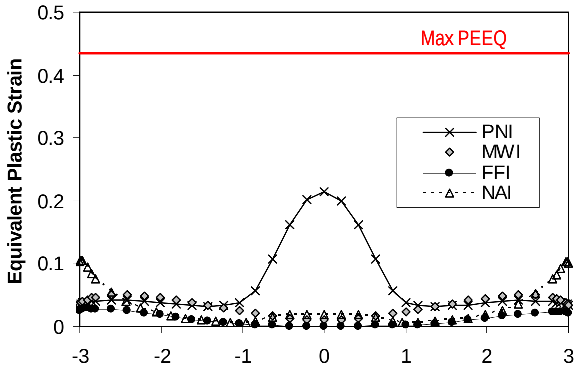

(c) Plastic Strain along Line-U (γ = 0.058 rad)

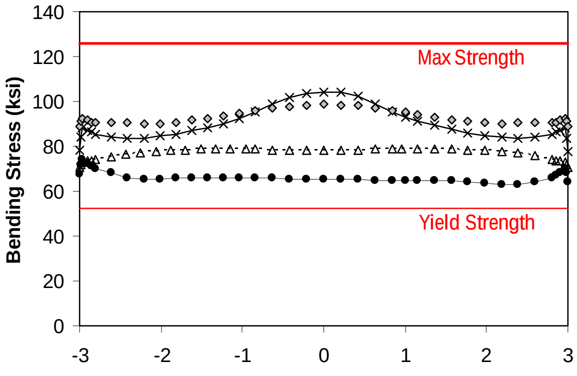

(b) Bending Stress along Line-L (γ = 0.058 rad)

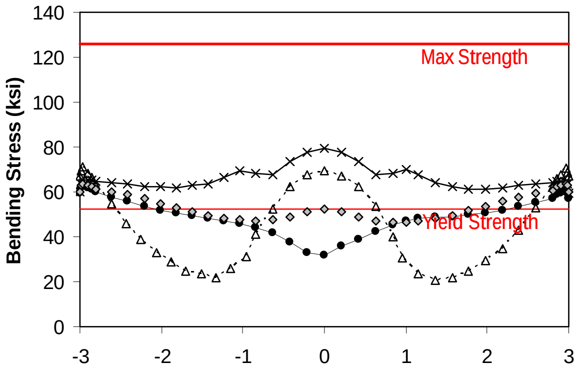

(d) Bending Stress along Line-U (γ = 0.058 rad)

Figure 6.26 Link flange-groove weld interface in I-links

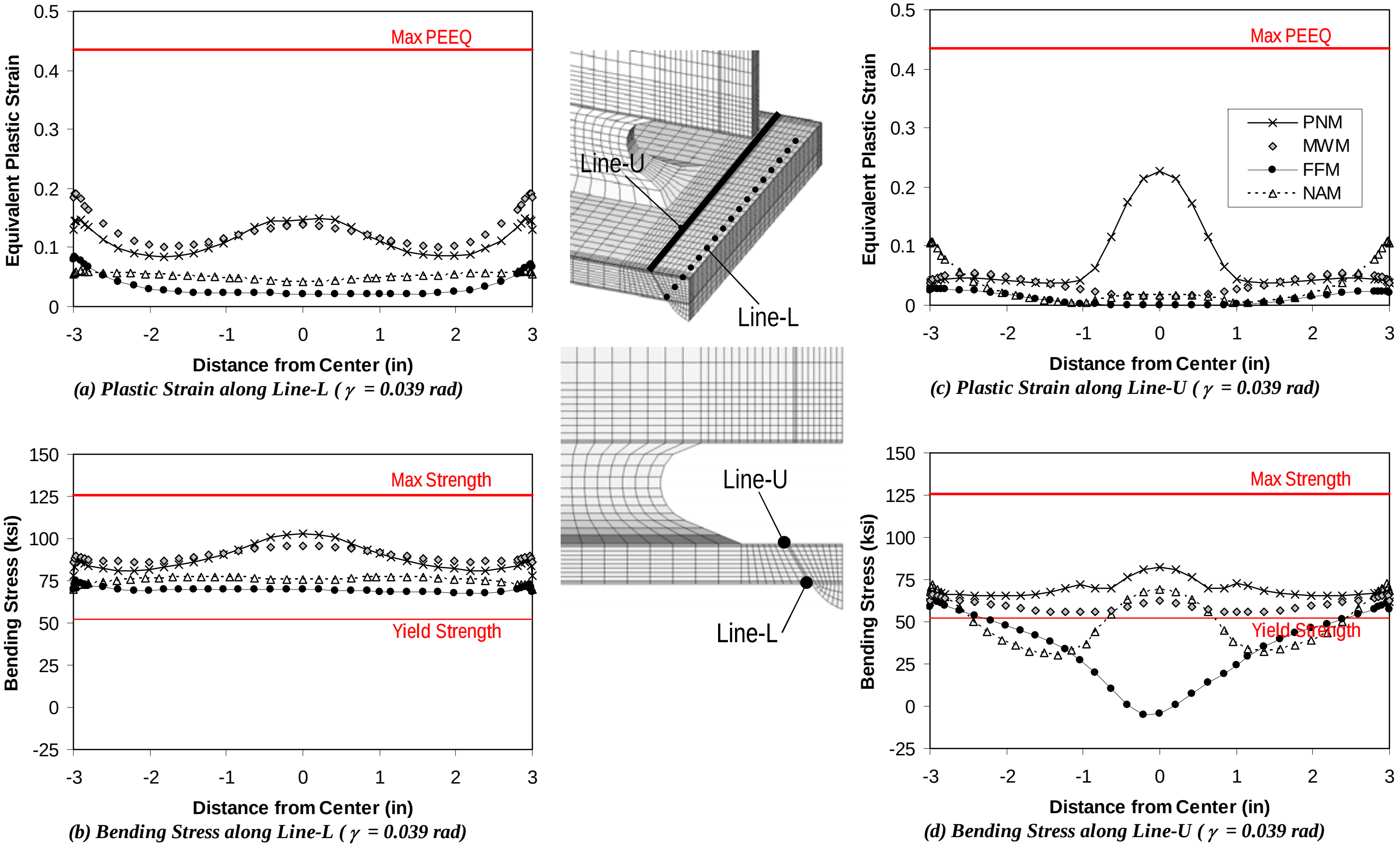

(a) Plastic Strain along Line-L (γ = 0.039 rad)

(b) Bending Stress along Line-L (γ = 0.039 rad)

(c) Plastic Strain along Line-U (γ = 0.039 rad)

(d) Bending Stress along Line-U (γ = 0.039 rad)

Figure 6.27 Link flange-groove weld interface in M-links

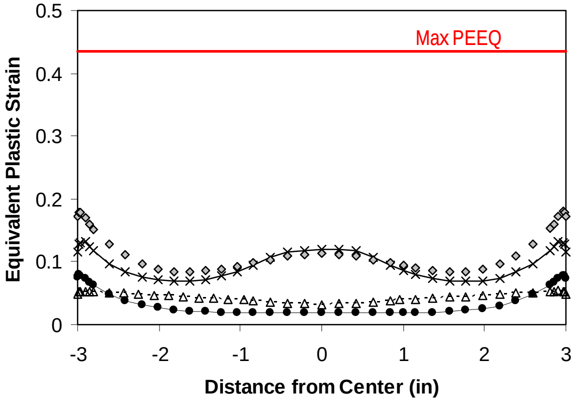

(a) Plastic Strain along Line-L (γ = 0.060 rad)

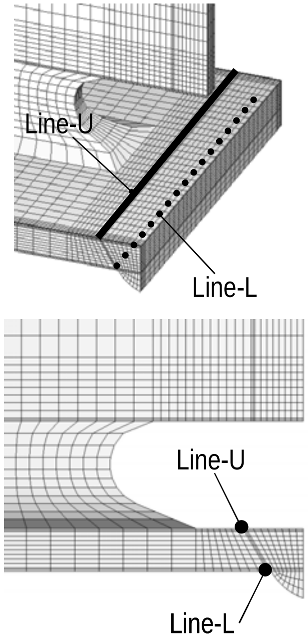

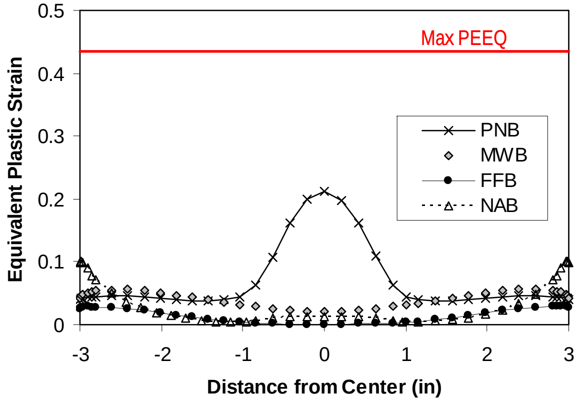

(c) Plastic Strain along Line-U (γ = 0.060 rad)

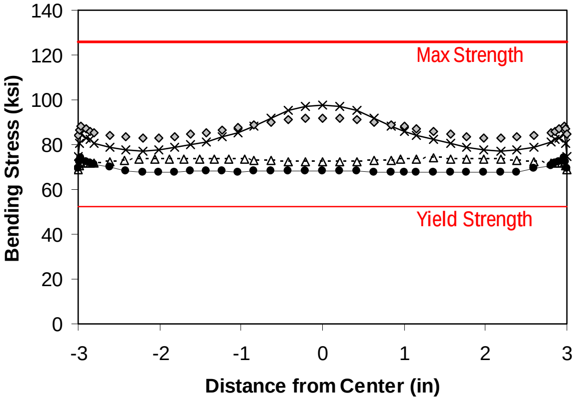

(b) Bending Stress along Line-L (γ = 0.060 rad)

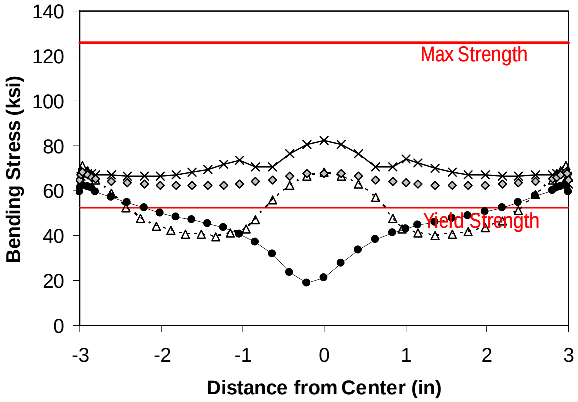

(d) Bending Stress along Line-U (γ = 0.060 rad)

Figure 6.28 Link flange-groove weld interface at moment connections

stresses in the link flange was similar.

6.5.3 Link Web and Shear Tab Groove Weld in FF-Models

The stress and strain environment at the link web-groove weld interface in the FF-models was significantly different from that in the MW-models discussed in Section 6.5.1. Due to the shear tab welded to the link web, the FF-models had a larger sectional-area of the link web at the link-to-column connection compared to the MW-models.

Figure 6.29 shows the distribution of equivalent plastic strain and bending stress at the link web-groove weld interface. Models FFS, FFI, FFM, and FFB were at the same respective rotation levels as the models with the same link length in Figure 6.24. As in Figure 6.24, the distributions are sampled along Lines-R and F, which run along the depth of the link. Comparison between Figure 6.29 and Figure 6.24 suggests that the FF-models developed much smaller plastic strains and bending stresses compared to the MW-models. The peak bending stress values at the bottom edge of Line-R were between 90 and 100 ksi in the MW-models, and between 50 and 70 ksi in the FF-models. The equivalent plastic strain and bending stress was distributed more uniformly between and along Lines-R and F in the FF-models. Models FFI, FFM, and FFB show very similar distributions. Model FFS developed bending stresses only near the edge of the link web, as did Model MWS.

Figure 6.30 shows the distribution of equivalent plastic strain and bending stress at the shear tab-groove weld interface. Models FFS and FFI are at the same respective rotation levels as in Figure 6.29. Models FFS-RLP and FFSL-RLP are at the same link rotations as Model FFS. The distributions are sampled along

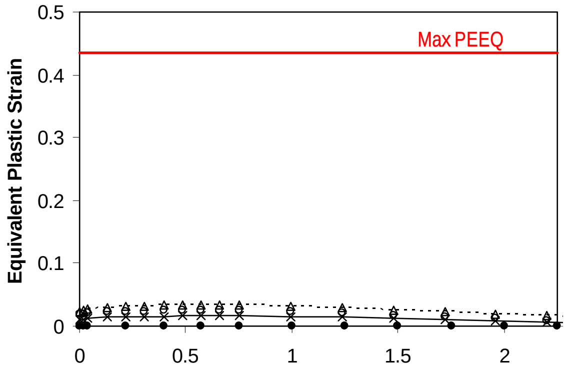

(a) Plastic Strain along Line-F

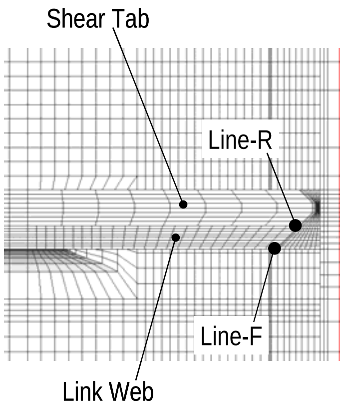

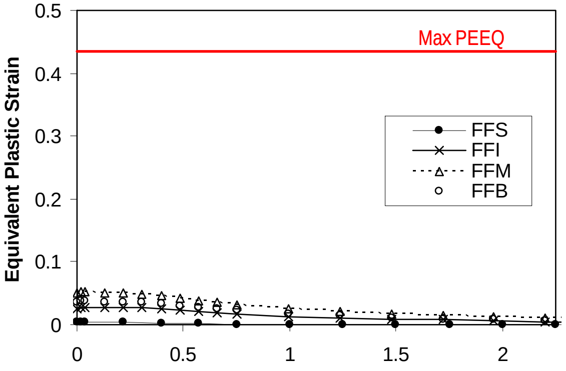

(c) Plastic Strain along Line-R

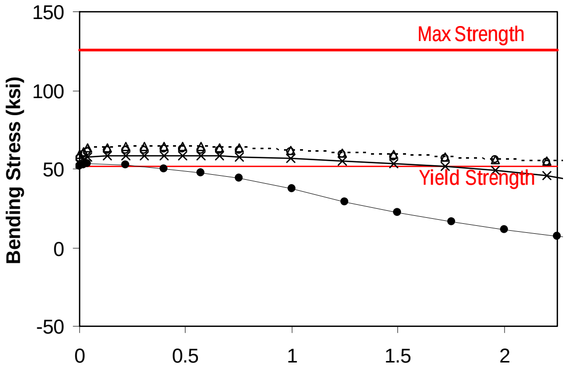

(b) Bending Stress along Line-F

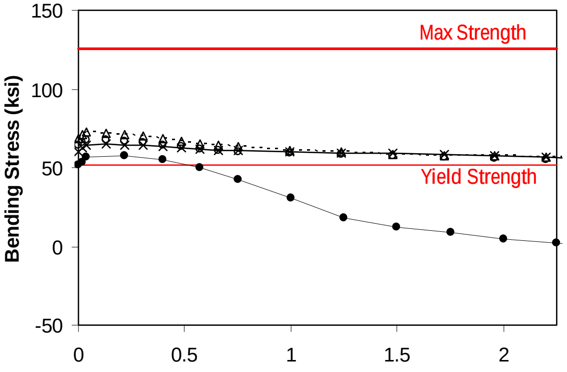

(d) Bending Stress along Line-R

Figure 6.29 Link web-groove weld interface in FF-models

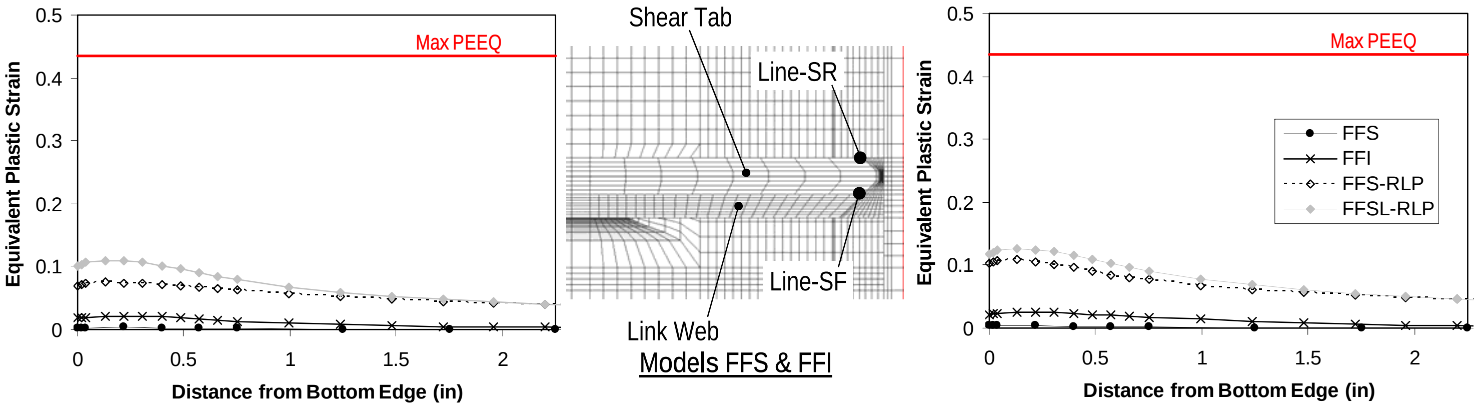

(a) Plastic Strain along Line-SF

(c) Plastic Strain along Line-SR

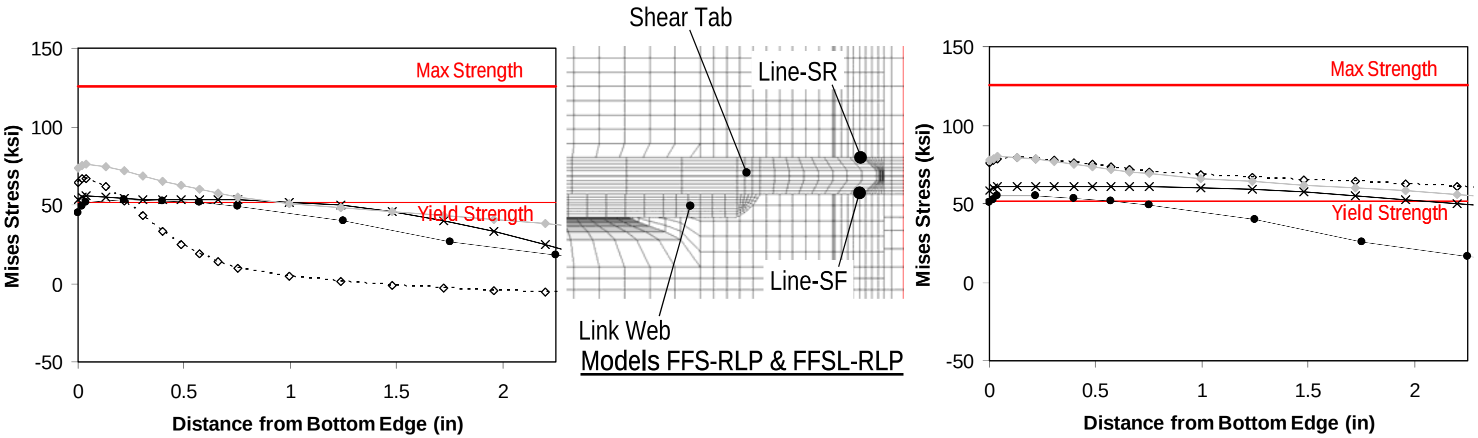

(b) Mises Stress along Line-SF

(d) Mises Stress along Line-SR

Figure 6.30 Shear tab-groove weld interface in FF-models

Lines-SF and SR, which run at the front and rear toes of the double-bevel groove weld. In Models FFS and FFI, Line-SF is tied to the Line-R used in Figure 6.29. Models FFS-RLP and FFSL-RLP relied solely on the shear tab to transmit link shear to the column flange. The peak bending stress is roughly 15 ksi higher in Models FFS-RLP and FFSL-RLP than in Models FFS and FFI. Yielding along Lines-SF and SR was minimal in Models FFS and FFI, but much more extensive in Models FFS-RLP and FFSL-RLP. The bending stress in Model FFS-RLP was distributed rather uniformly along Line-SF, but concentrated at the bottom edge of the shear tab along Line-SR. The discrepancy between the two lines was caused by the torsion discussed in Section 6.3.3. Models FFS-RLP and FFSL-RLP generated torsion by the eccentricity between the shear tab and link web, where large shear force is transmitted. Near the bottom edge of the shear tab, the torsion added tensile stresses along Line-SR and compressive stresses along Line-SF. The torsion had a smaller influence on Model FFSL-RLP than on Model FFS-RLP, due to the larger column face moment generating larger bending stresses. Further analysis results suggested that the relative significance of torsion increases with link rotation, as the larger spread of yielding in the link web reduces the torsional resistance of the link section.

6.5.4 Model NAS and Model NASL

Figure 6.31 shows the distribution of equivalent plastic strain and bending stress at the link flange-groove weld interface. Models NAS and NASL-RLP are compared at the same link rotation of γ = 0.117 rad. The figure shows similar distribution characteristics in both models. However, the largest equivalent plastic strain value was 100% higher in Model NASL-RLP than in Model NAS, suggesting that Model NAS can achieve significantly greater rotation.

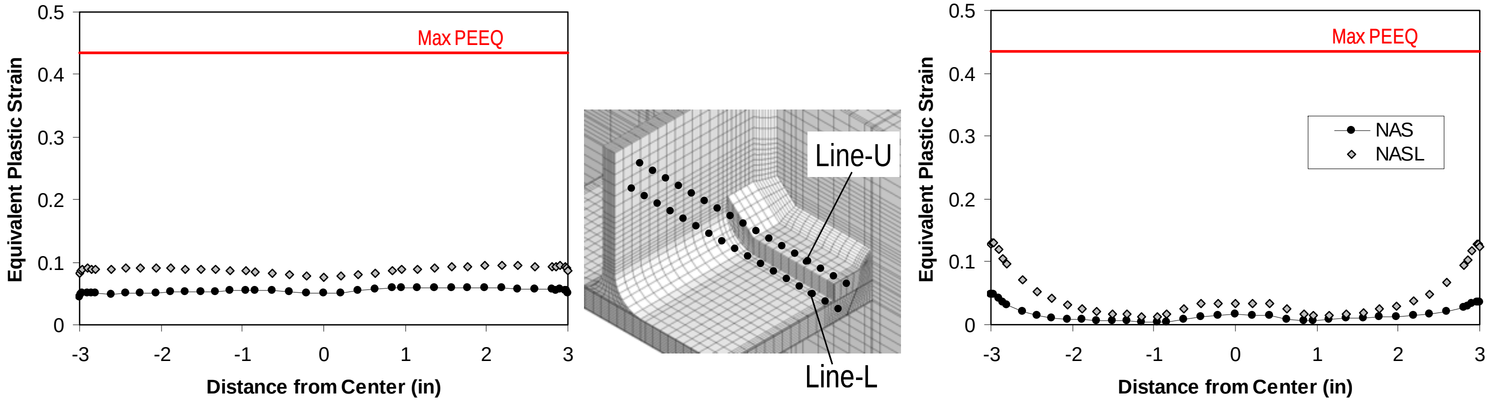

(a) *Plastic Strain along Line-L*

(c) *Plastic Strain along Line-U*

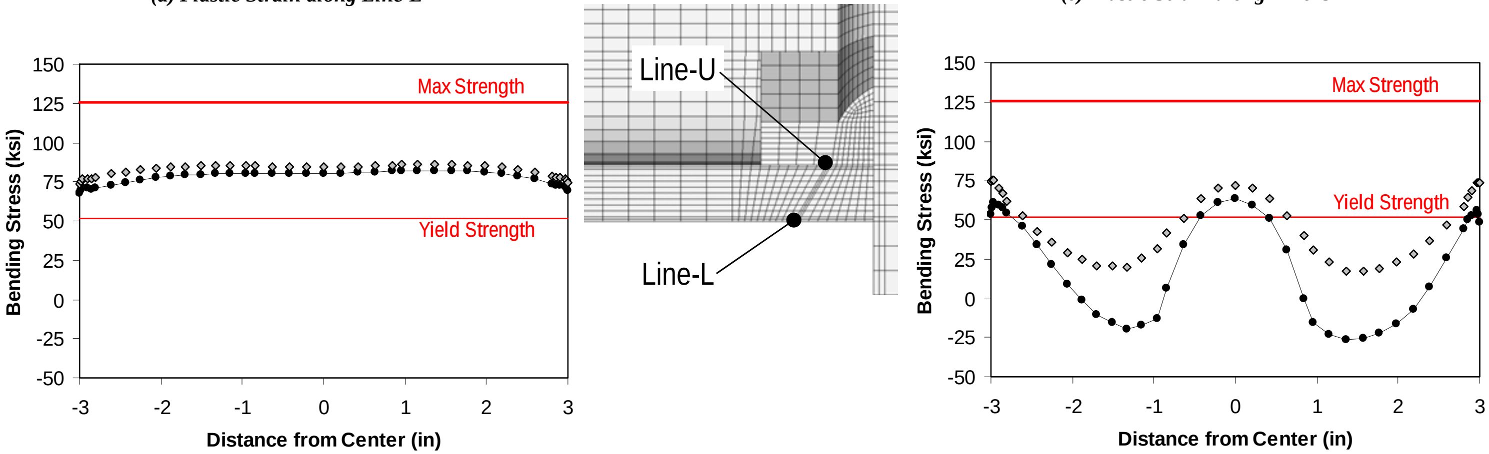

(b) *Mises Stress along Line-L*

(d) *Mises Stress along Line-U*

Figure 6.31 Comparison between Model NAS and Model NASL-RLP

6.5.5 Correlation with Observed Fracture Behavior

The finite element simulations demonstrated the significant effects of link length on the stress and strain environment at the link-to-column connection. Figure 6.25 suggests that S-links are strongly influenced by secondary bending in the link flange. Figure 6.31 suggests that the stress and strain environment at the link-to-column connection is more severe in SL-links than in S-links at the same rotation level. Figure 6.26 and Figure 6.27 suggest that secondary bending in the link flange was smaller in I-links and M-links than in the S-links. Particularly at the link flange-groove weld interface, the distributions of equivalent plastic strain and bending stress were very similar between I-links and M-links. The largest values of equivalent plastic strain and bending stress at the link flange-groove weld interface were equally high. These results agree with the trend obtained from the tests. For example, S-link specimens, NAS-RLP and FFS-RLP, achieved a 100 and 60% greater rotation capacity compared to SL-link specimens, NASL-RLP and FFSL-RLP. With the exception of Specimen FFI, the I-link and M-link specimens performed similarly in terms of the inelastic rotation capacity with respect to the plastic rotation required in the *AISC Seismic Provisions*. Both the tests and simulations suggests that fracture of the link flange near the groove welds is a major concern for EBF link-to-column connections regardless of the link length.

The effects of the connection configuration were also evident in the simulations. The PN-models had the toe of the weld access hole intersecting the link flange-groove weld interface. This configuration caused substantial stress and strain concentrations near the middle of Line-U in Models PNI, PNM, and PNB, but much less significant concentrations in Model PNS. The MW-models caused higher equivalent plastic strain and bending stress values along Line-L compared to the PN-models, while alleviating the concentrations near the middle of Line-U. Although the benefit of the MW-connection over the PN-connection was notable in I-link, M-link, and beam-column models, it was not realized in S-links. The design intent of the FF-connection to protect the link flange groove welds from high stresses worked successfully. The bending stresses along Lines-L and U were, on average, 30% smaller in the FF-models than in the PN or MW-models at the same rotation level. Due to the high restraints at the face of the column, the influence of secondary bending in the link flange was reduced in the NA-models compared to the PN and MW-models. The largest equivalent plastic strain and bending stress values along Lines-L and U were roughly similar between the NA and FF-models. The substantially less severe distribution of equivalent plastic strain and bending stress in the FF and NA-models compared to the PN and MW-models agreed well with the improved level of performance achieved by the FF and NA-specimens over the PN and MW-specimens.

Figure 6.30 shows high bending stress values in Models FFS-RLP and FFSL-RLP at the edge of the shear tab-groove weld interface, but minimal yielding in Model FFS. In fact, Specimens FFS-RLP and FFSL-RLP failed due to fracture of the shear tab, while Specimen FFS experienced no significant inelastic deformation in the shear tab.

Critical locations at the link flange-groove weld interface, with the largest equivalent plastic strain and bending stress values, can be identified from Figure 6.25, Figure 6.26, Figure 6.27, and Figure 6.31 for each link-column model. The critical locations were in the middle of Line-U in Specimens PNI and PNM, at the edges of Line-U in Specimens NAI, NAM, and NASL-RLP, and at the edges of Line-L in Specimens MWI, MWM, FFI, and FFM. The S-link specimens had uniformly distributed equivalent plastic strain and bending stress values along Line-L.

Although Specimens PNS, PNM, and MWM failed by fracture of the link flange, the fracture initiation location was not clearly observed during testing of these specimens. Examination of the fracture surfaces after testing also did not provide a clear indication of fracture initiation and propagation. Therefore, it was not possible to determine the fracture initiation point for these three specimens. For most other specimens, the observed fracture initiation location may be compared with the critical locations of high stresses and strain as discussed above. Note also that in the test specimens, it was not typically possible to determine whether the fracture initiated at the inner side of the flange (corresponding to Line-U) or outer side of the flange (corresponding to Line-L).

Specimen MWS was the only specimen where fracture was clearly seen to initiate at mid-width of the flange (at the outer face of the bottom flange). Although Model MWS predicted a uniformly critical stress and strain distribution along Line-L, the slight elevation in equivalent plastic strain and bending stress values near the middle of Line-L compared to the edge may have caused the observed fracture. For Specimens PNS, PNM, and MWM, it was not clear whether the fracture of the link flange initiated from mid-width or the edge of the flange. Specimen NAS and NAS-RLP appeared to develop fracture simultaneously along the toe of the link flange groove weld (at both the top and bottom flange, corresponding to Line-L). Fracture of the link flange was irrelevant to Specimens FFS, FFS-RLP, and FSSL-RLP. The remaining seven specimens failed by fracture of the link flange initiating at the edge of the flange. Therefore, reasonable agreement was seen between the critical locations in the finite element simulations and the observed fracture initiation in eight specimens, MWS, MWI, FFI, FFM, NAS, NAS-RLP, NAI, NAM. Four specimens, FFS, FFS-RLP, FFSL-RLP, and NAS did not fracture in the link flange. The fracture initiation point was not clear in three specimens, PNS, PNM, and MWM. The predicted critical location did not agree with the observed fracture initiation in one specimen, MWI. Therefore, the critical location identified from the simulation agreed with the observed fracture initiation point in eight of the nine relevant cases, but disagreed in one case.

Although the local stress and strain environment predicted by the simulations provides many useful insights, further investigation shows cases where predictions from the simulation are contradictory with test observations. For example, Figure 6.25 shows higher equivalent plastic strain and bending stress values in Model MWS than in Model PNS. However, Specimen MWS achieved a 25% larger rotation than Specimen PNS. This contradiction may be attributed to the difference in weld metal, which was not considered in the simulations. The link flange groove weld in Specimen MWS was made with an E70T-6 electrode, while the link flange groove weld in Specimen PNS was made with an E70T-4 electrode. It is also possible that the weld tabs, which were not modeled in the simulations, had detrimental effects on Specimen PNS.

Figure 6.21 and Figure 6.24 show larger equivalent plastic strain and bending stress values at the bottom edge of Line-R than at any point along Lines-U and L. A direct interpretation of this result may be that the MW-models are controlled by fracture of the link web rather than fracture of the link flanges. However, the three MW-specimens failed by fracture of the link flange. Although fractures were observed at the edges of the link web in Specimens MWS and MWI, they did not appear to significantly affect the performance of the specimen.

6.5.6 Limitations of the Finite Element Simulations

The location of fracture inferred from the simulation results did not necessarily agree with the observed fracture behavior for some specimens. The simulations presented herein are believed to be limited due to the following factors: (a) the difference in material properties between the E71T-8, E70T-6, and E70T-4 weld was not accounted for; (b) the possible presence of weld defects were not accounted for; (c) the monotonic loading behavior does not represent the full characteristics of the cyclic loading behavior; (d) the equivalent plastic strain and bending stress may not provide sufficient information to predict fracture behavior; (e) the material properties at the interface of base metal and weld metal may not be representative of that in the actual test specimens; and (f) the initiation, growth, and propagation of fracture was not explicitly modeled. Factors (d), (e), and (f) are discussed in further detail.

Fracture of ductile metal is caused by the nucleation of microscopic voids, followed by the growth and coalescence of the voids. McClintock (1968) and Rice and Tracey (1969) showed that the void growth process, which leads to ductile fracture initiation, is controlled by stress triaxiality and plastic strain. Stress triaxiality is defined as the mean stress (negative of the hydrostatic stress) divided by the Mises stress. Ductile fracture criteria to estimate critical plastic strain values as a function of stress triaxiality and material characteristics have been proposed, for example by Hancock and Mackenzie (1976), Kuwamura and Yamamoto (1997), and An *et al.* (2003). El-Tawil *et al.* (1999), Mao *et al.* (2001), Tabuchi *et al.* (2002), among others, related these ductile fracture criteria to the stress and strain values obtained from finite element simulations to evaluate the performance of moment connections. The limitation of these analyses is that they only consider the propensity of fracture initiation at critical local locations, and do not reflect strength degradation caused by crack growth and loss of cross-sectional area. Moreover, the fracture criteria are established for monotonic loading only, and do not apply to cyclic loading cases. While stress triaxiality is a better measure than the bending stress to predict fracture initiation, it may not represent the fracture growth process. It is not clear how any one or any combination of stress and strain measures can relate directly to failure of the member or connection by fracture.

As discussed in Section 6.4, the critical locations where fractures are likely to occur are typically near geometric and material discontinuities, where the local stress and strain values can vary substantially depending on the modeling. Since the finite element models in this research did not model realistically the material properties near the base metal-groove weld metal interface, the stress and strain values obtained from the finite element simulations may not represent the values in an actual specimen. In order to omit the influence of material properties, Tabuchi *et al.* (2002) compared the finite element simulation and test response of connections including no welds at critical locations where fracture was expected.

The finite element simulation in this study did not model the initiation, growth, and propagation of fracture. Even if fracture initiation were reliably predicted from the equivalent plastic strains and stress components, interpretation of the prediction must be treated with care. For example, the edge of the link web is provided with stiff restraints by the link flange, and the tensile stress decreases along the depth of the link web to which the fracture typically propagates. On the other hand, the link flange is subjected to high tensile stresses over the entire section. A fracture at the edge of the flange is provided with no restraint by surrounding elements, and thus, is more unstable than a crack at the edge of the link web. Therefore, while a fracture in the link web may redistribute tensile stresses within the link web and to the adjacent link flange, a fracture in the link flange may propagate much more rapidly, and drastically reduce the strength of the link-to-column connection or moment connection. While the simulations may provide a lower bound estimate of the link rotation without modeling fracture propagation, that lower bound estimate can be overly conservative in cases where the first fracture does not affect the strength of the specimen.

6.6 PANEL ZONE STRENGTH

An additional set of simulations were performed in order to investigate the effect of panel zone strength on the performance of link-to-column connections. Since panel zone strength was not considered explicitly in the experimental program, finite element simulations were conducted to provide information on possible effects associated with panel zone yielding.

6.6.1 Yielding Mechanism

The additional simulations used the MW-models but with the column web thickness reduced from 0.708-inches to 0.31-inches. In the following, the MW-models with the thickness of the column web reduced is denoted by the addition of a suffix "-WPZ" (Weak Panel Zone). The panel zone strength of the model, defined by Equation (5.4), was reduced from ϕM_v = 6420 kip-in in the MW-models to ϕM_v = 3558 kip-in in the MW-WPZ-models, using the yield strength of the material of F_y = 52 ksi. The ratio of panel zone strength to plastic moment capacity of the link was reduced from $\phi M_v/M_p$ = 1.57 in the MW-models to $\phi M_v/M_p$ = 0.87 in the MW-WPZ-models. While yielding was precluded from the panel zone in the MW-models as well as MW-test specimens, the vey weak panel zone of the MW-WPZ-models were designed to undergo significant yielding.

Figure 6.32 compares the link and panel zone deformation of the MW-models with the MW-WPZ-models. The figure shows global models at very large rotation levels, with the S-link models at γ = 0.157 rad, I- link models at γ = 0.078 rad, M-link models at γ = 0.074 rad, and beam-column models at θ = 0.080 rad. The figure also shows the distribution of equivalent plastic strain to illustrate the yielding mechanisms of each model.

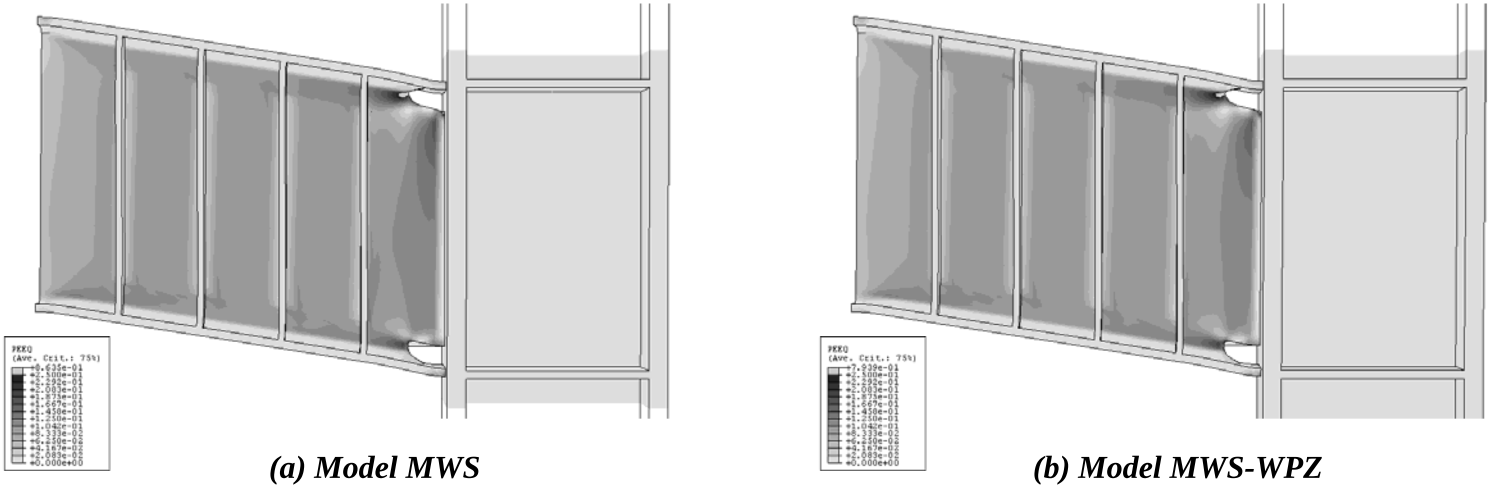

(a) Model MWS ***(b) Model MWS-WPZ***

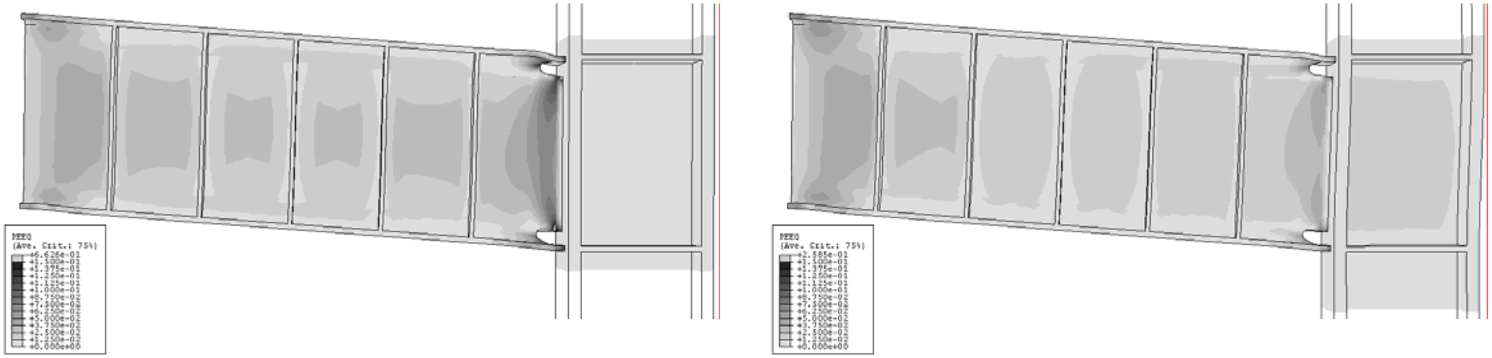

(c) Model MWI ***(d) Model MWI-WPZ***

Figure 6.32 Panel zone strength and link deformation

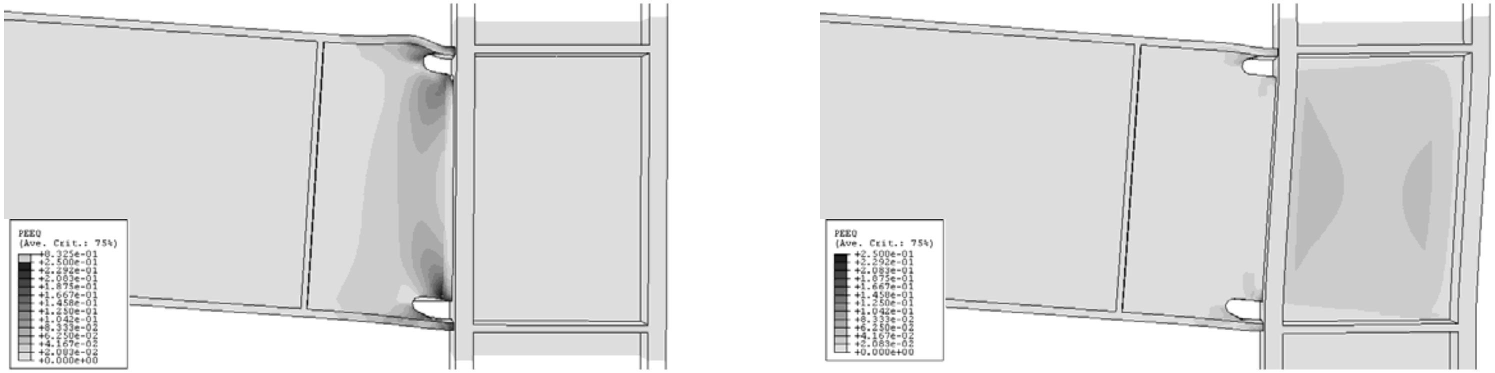

(e) Model MWM ***(f) Model MWM-WPZ***

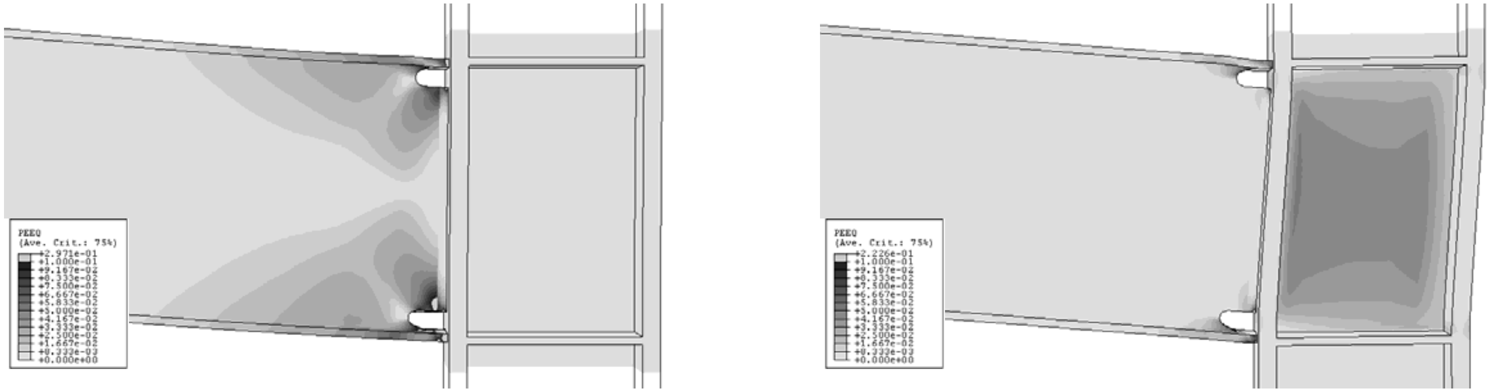

(g) Model MWB ***(h) Model MWB-WPZ***

Figure 6.32 Panel zone strength and link deformation (Continued)

The influence of a weak panel zone was more clearly seen in models with longer links, due to the greater moment at the column face with increasing link length. Figure 6.32b shows no yielding in the panel zone of Model MWS-WPZ. The column face moment developed in Model MWS-WPZ at this stage was M_C = 2,967 kip-in, which is 80% of the panel zone flexural strength ϕM_v discussed above. Comparison between Model MWS (See Figure 6.32a) and Model MWS-WPZ (Figure 6.32b) suggests that the panel zone strength had little effect on the behavior of the S-link.

The link-column models with longer links demonstrated significant influence of the panel zone strength. Models MWI-WPZ (See Figure 6.32d) and MWM-WPZ (Figure 6.32f) clearly indicate inelastic shear deformation in the panel zone. The column face moments developed in Models MWI-WPZ and MWM-WPZ at the stage shown in the figure were M_C = 4,069 and 4,462 kip-in, respectively, which exceed the panel zone flexural strength ϕM_v by 15 and 25 percent. While the corresponding MW-models (See Figure 6.32c and e) show extensive inelastic distortion of the link near the face of the column, the inelastic panel zone deformation in Models MWI-WPZ and MWM-WPZ appear to largely alleviate yielding in the link near the face of the column. This observation suggests that the weak panel zone can provide a substantial advantage for flexural yielding links by reducing the inelastic rotation demand on the link.

Comparison between Model MWI (See Figure 6.32c) and Model MWI-WPZ (Figure 6.32d) shows that the weaker panel zone significantly reduced the inelastic link deformation at the column end of the link, while it had little effect on the link at the beam end. In fact, the figure suggests that the yielding mechanism of Model MWI-WPZ combined Mechanisms (1) and (6) in Figure 5.1. Mechanism (1) is the link yield mechanism. Mechanism (6) produces plastic link rotation by plastic hinge rotation at the beam end of the link and plastic panel zone deformation without requiring plastic hinge rotation at the column end of the link. The mild inelastic flexural demand at the column end of the link suggests that the participation of Mechanism (6) was substantial in Model MWI-WPZ. Similarly, the participation of Mechanism (6) contributed to the reduced flexural demand at the column end of the link in Model MWM-WPZ.

As discussed in Section 2.4.1, Plastic beam rotation in MRFs can be supplied either by plastic hinge formation in the beam or by plastic panel zone deformation. These two mechanisms are parallel to Mechanisms (1) and (6) in Figure 5.1. Comparison between Model MWB (See Figure 6.32g) and Model MWB-WPZ (Figure 6.32h) suggests that inelastic panel zone deformation can reduce the inelastic rotation requirement of the beam. This observation is consistent with previous studies (*e.g.* Krawinkler 1978).

Figure 6.33 shows the relation between link/beam rotation and panel zone deformation in the MW-WPZ models. As discussed in Section 5.2.3, the plastic link rotation produced by Mechanism (6) is equal to the plastic panel zone deformation. Therefore, the ratio of panel zone deformation to link rotation indicates the contribution of Mechanism (6) to the overall link rotation. The plastic link rotation not produced by Mechanism (6) is attributed primarily to Mechanism (1). Figure 6.33 suggests that Mechanism (6) accounted for roughly 80% of the link rotation in Models MWM-WPZ and MWB-WPZ. Model MWS-WPZ developed small elastic panel zone deformation. In Model MWI-WPZ, Mechanism (6) was more influential during small rotations of up to $\gamma = 0.02$ rad than during larger rotations. A possible explanation for this behavior is discussed later. Mechanism (6) accounted for roughly 40% of the link rotation at $\gamma = 0.05$ rad or greater. Consequently, while Model MWS-WPZ was dominated by Mechanism (1), and Models MWM-WPZ and MWB-WPZ were dominated by Mechanism (6), Model MWI-WPZ was controlled by an interaction of

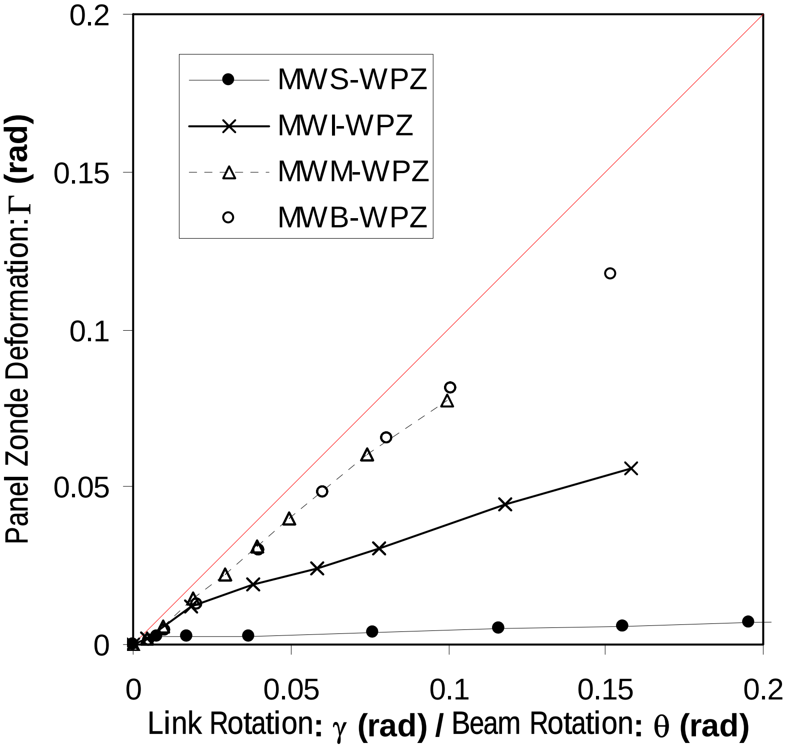

Figure 6.33 Contribution of panel zone deformation

Mechanisms (1) and (6).

Figure 6.34 shows the relationship between the column face moment and panel zone deformation. The panel zone developed a shear deformation very close to four times the theoretical elastic limit when the panel zone strength ϕM_v was developed, as assumed in the *AISC Seismic Provisions*. The figure also shows that the panel zone behaved very similarly in all four MW-WPZ-models, with its deformation being controlled by the column face moment.

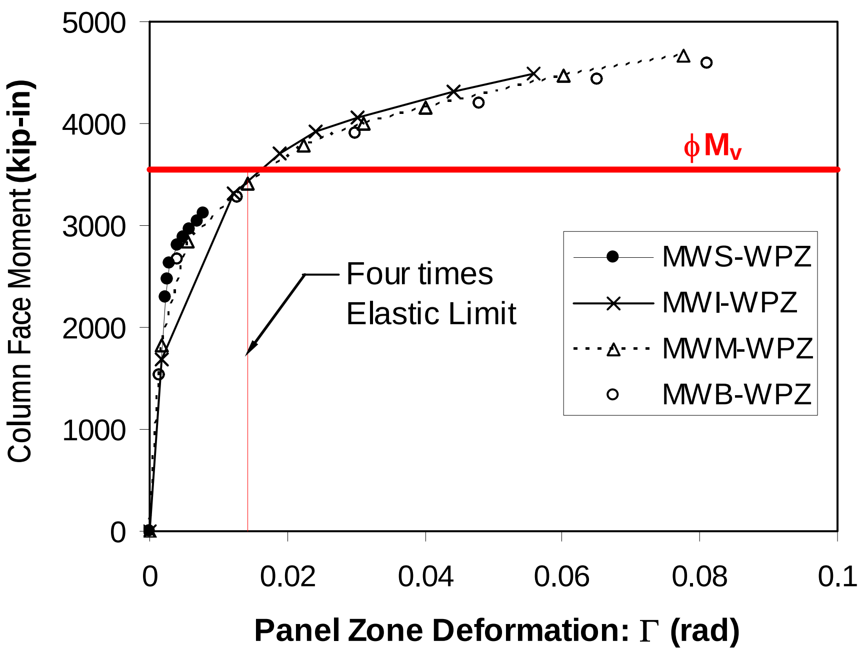

Figure 6.34 Column face moment vs. panel zone deformation

6.6.2 Response of Link-Column Subassemblage

Figure 6.35 shows the response of the MW and MW-WPZ-models. The figure shows the relation of link shear force versus link/beam rotation and column face moment versus link/beam rotation.

Model MWS-WPZ developed smaller column face moment (See Figure 6.35b) but similar shear force (See Figure 6.35a) compared to Model MWS. The column face moment of at most 85% of the panel zone strength ϕM_v suggests that the panel zone in Model MWS-WPZ did not yield. The smaller column face moment in Model MWS-WPZ than in Model MWS is attributed to the reduced web thickness of the column producing smaller rotational restraint at the column end of the link. As discussed in Section 2.7.3, the ratio of the link end moments is affected significantly by the rotational restraints at the ends of the link.

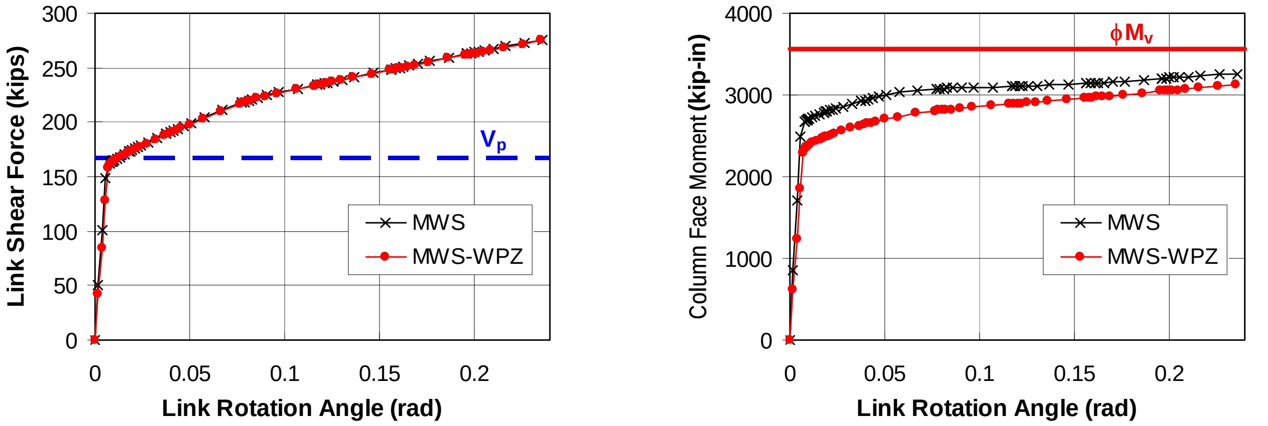

(a) Link Shear vs. Rotation Angle

(b) Column Face Moment vs. Rotation Angle

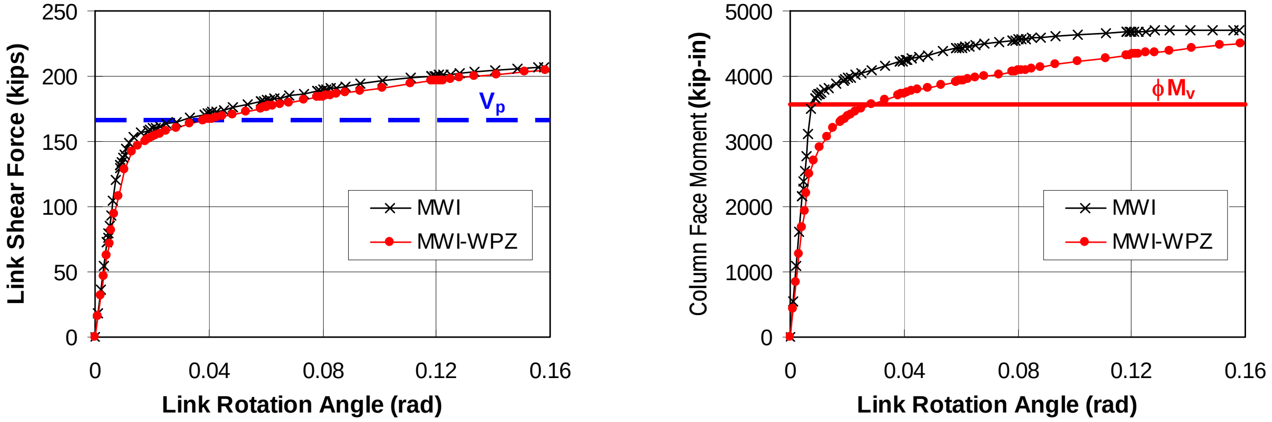

(c) Link Shear vs. Rotation Angle

(d) Column Face Moment vs. Rotation Angle

Figure 6.35 Effect of weak panel zone on response of link-column assemblage

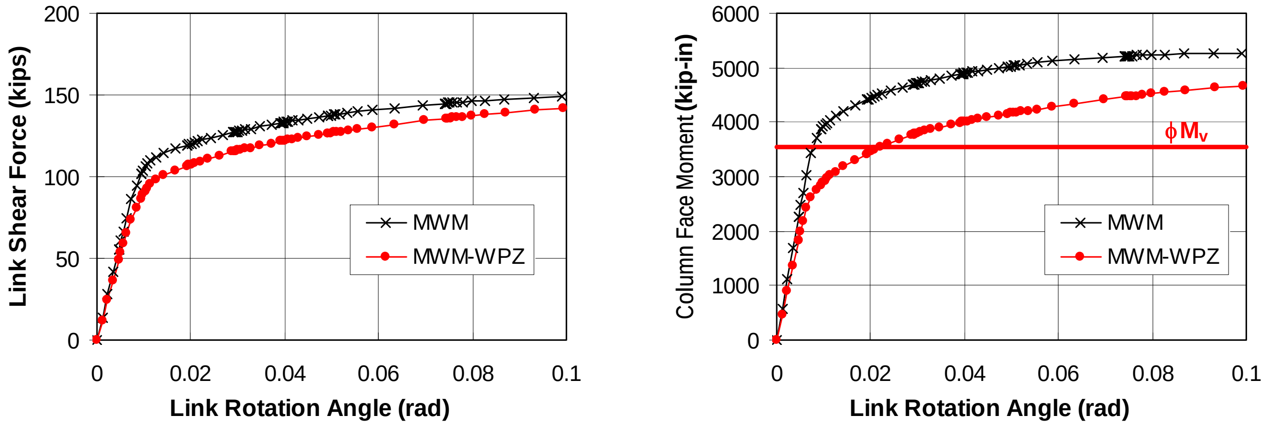

(e) Link Shear vs. Rotation Angle

(f) Column Face Moment vs. Rotation Angle

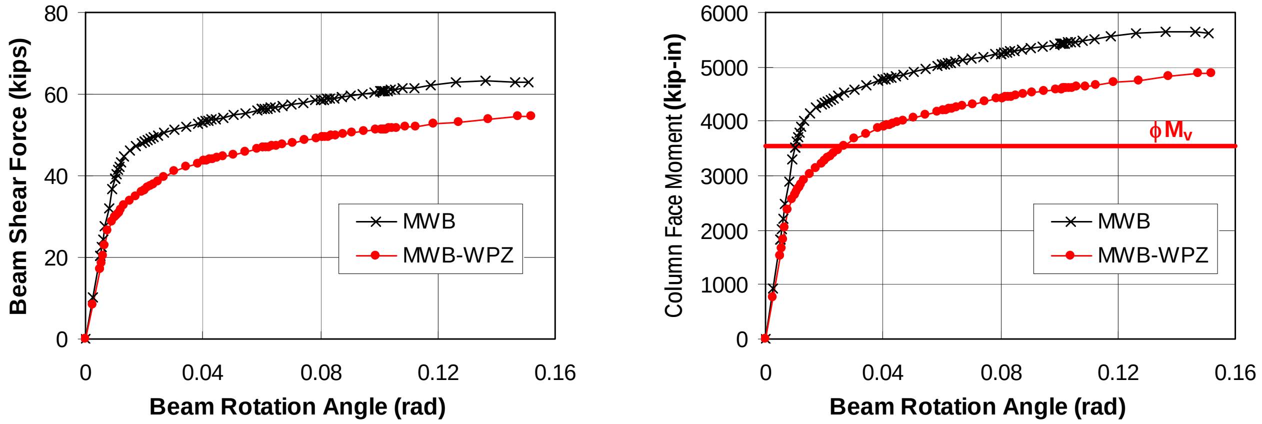

(g) Beam Shear vs. Rotation Angle

(h) Column Face Moment vs. Rotation Angle

Figure 6.35 Effect of weak panel zone on response of link-column assemblage (Continued)

The difference in end moment ratio had little effect on the shear strength of the S-link.

Model MWI-WPZ developed a column face moment equal to the panel zone strength ϕM_v at a link rotation of $\gamma = 0.028$ rad (See Figure 6.35d), and a link shear equal to the link strength V_p at $\gamma = 0.039$ rad (See Figure 6.35c). It appears that yielding in the panel zone deformation preceded shear yielding of the link, and therefore, at small rotations of up to $\gamma = 0.015$ rad, inelastic rotation was supplied primarily by panel zone deformation. This observation corresponds to the data shown in Figure 6.34a, which suggests that Mechanism (6) involving panel zone deformation is more influential during link rotations of up to roughly $\gamma = 0.02$, while at larger rotations, Mechanism (6) is less influential. Figure 6.35c suggests that at rotations of $\gamma = 0.03$ or greater, shear yielding of the link contributed significantly to inelastic link rotation. Note that shear yielding of the link can supply link rotation independent of panel zone yielding. While the weaker panel zone reduced the column face moment by 15% (See Figure 6.35d), the shear strength of the I-link was relatively unaffected by the panel zone strength (See Figure 6.35c).

Models MWM-WPZ and MWB-WPZ were both influenced significantly by inelastic panel zone deformation. Figure 6.35f and Figure 6.35h suggest that panel zone strength has similar influence on the two models, with the reduction in panel zone strength causing a 20% reduction in the column face moment. However, while the 20% reduction in column face moment resulted in a proportionally reduced beam shear in the beam-column model (See Figure 6.35f), the link shear in the M-link model was reduced by only 10% (See Figure 6.35e). While the beam-column model can supply plastic beam rotation solely by plastic panel zone deformation, the link-column models require plastic hinge formation at the beam end of the link in addition to plastic panel zone deformation to generate plastic link rotation. Consequently, the link shear force is less affected by panel zone strength than the beam shear force.

Yielding of Model MWI-WPZ was controlled by shear-flexure interaction, while yielding of Model MWM-WPZ was controlled predominantly by flexure. The large role of shear in Model MWI-WPZ resulted in a relatively limited role of panel zone deformation shown in Figure 6.33. The dominance of flexure in Model MWM-WPZ allowed the panel zone deformation to have a large control in its yielding behavior.

6.6.3 Local Stress and Strain Environment

Figure 6.36 shows the distribution of equivalent plastic strain and bending stress along the link flange-groove weld interface in the MW-WPZ-models. The effect of panel zone strength can be studied by comparing Figure 6.36 with Figure 6.21.

Figure 6.36 shows that the effect of panel zone strength was limited in the S-link model, likely because neither the stronger panel zone in Model MWS nor the weaker panel zone in Model MWS-WPZ yielded. Nonetheless, the slight reduction in column face moment in Model MWS-WPZ compared to Model MWS resulted in reduced values of bending stress and plastic strain. The effect of the weak panel zone was substantial in the I-link, M-link, and beam-column models. The bending stress values along Line-L were reduced by roughly 15% in the MW-WPZ-models compared to the MW-models. The bending stress distribution along Line-U was altered significantly. While the peak values at the edges of Line-U were reduced by 20 ksi to barely yielding level, the values near the middle of Line-U was reduced to nearly zero. Therefore, in the I-link, M-link, and beam-column models, the stress and strain environment at the link flange-groove weld interface was significantly relaxed by the reduced panel zone strength.

Figure 6.37 shows the distributions of equivalent plastic strain and bending stress along the link web-groove weld interface in the MW-WPZ-models. The effect of panel zone strength can be studied by comparing Figure 6.37 with Figure 6.24.

Figure 6.37 shows limited effect of the panel zone strength in the S-link models. The 5 to 10% smaller peak bending stress values in Model MWS-WPZ than in Model MWS was likely caused by the smaller column face moment. The bending stress and plastic strain values in the M-link and beam-column models were substantially reduced by the weaker panel zone. While Models MWM and MWB show peak bending stress values of 100 ksi at the bottom edge of Line-R, the bending stress values at the same location in Models MWM-WPZ and MWB-WPZ were 65 ksi. The influence of the panel zone strength in the I-link model was less significant than in the M-link and beam-column models. The peak bending stress value along Line-R was 100 ksi in Model MWI and 75 ksi in Model MWI-WPZ.

Therefore, Figure 6.36 and Figure 6.37 suggest that the effect of panel zone strength on the stress and strain environment near the link flange-groove weld interface and link web-groove weld interface is related to the significance of flexure in the inelastic behavior of the link or beam. This observation agrees with the discussions in previous sections, 6.6.1 and 6.6.2.

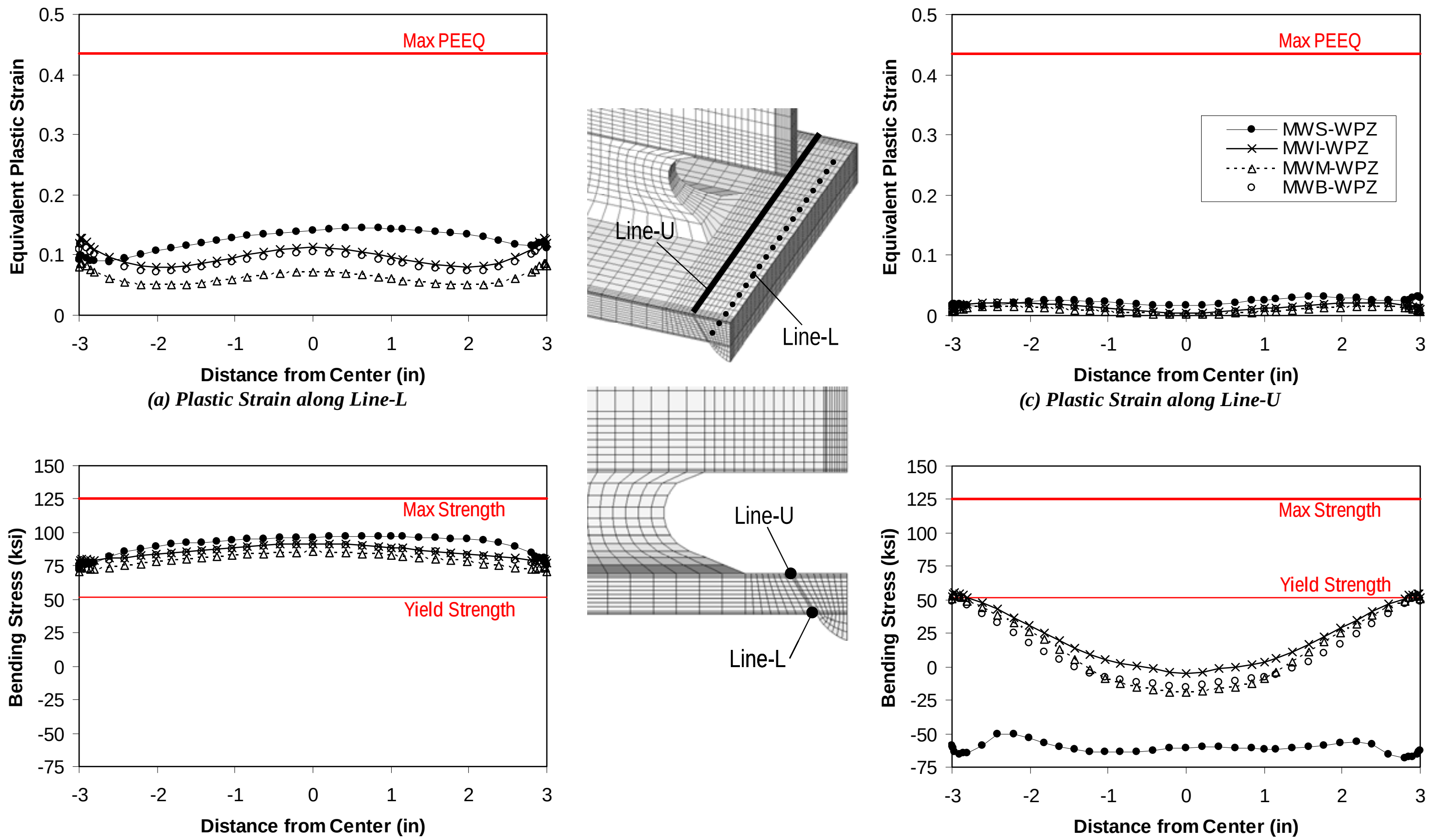

(a) Plastic Strain along Line-L

(c) Plastic Strain along Line-U

(b) Bending Stress along Line-L

(d) Bending Stress along Line-U

Figure 6.36 Effect of weak panel zone on link flange weld interface

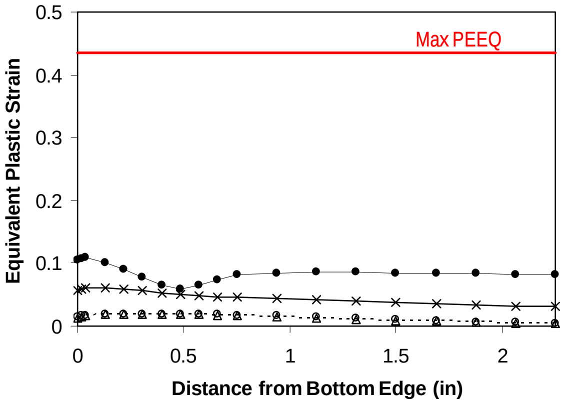

(a) Plastic Strain along Line-F

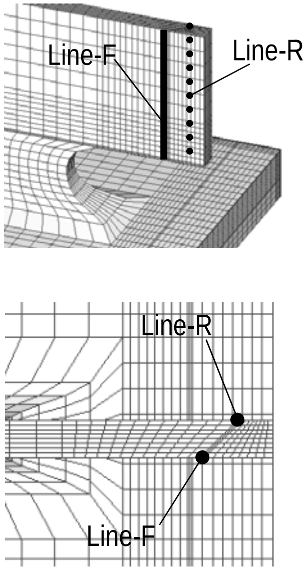

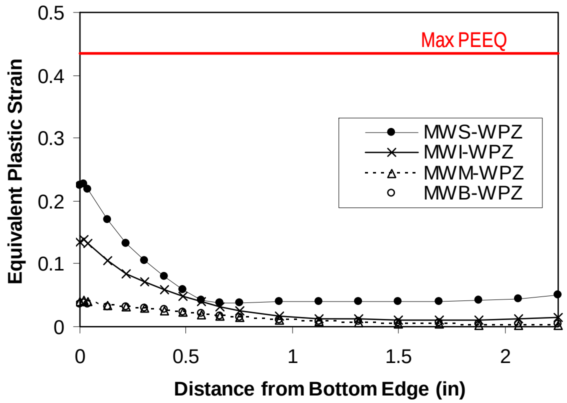

(c) Plastic Strain along Line-R

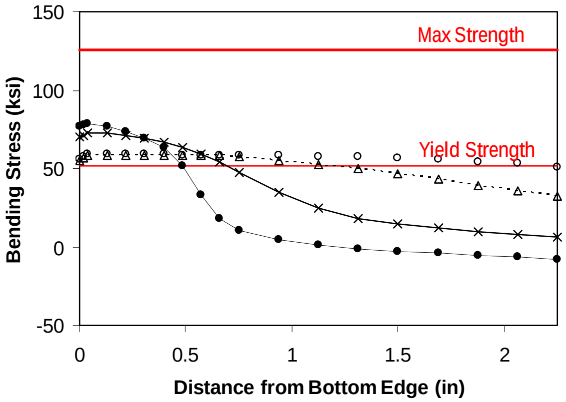

(b) Bending Stress along Line-F

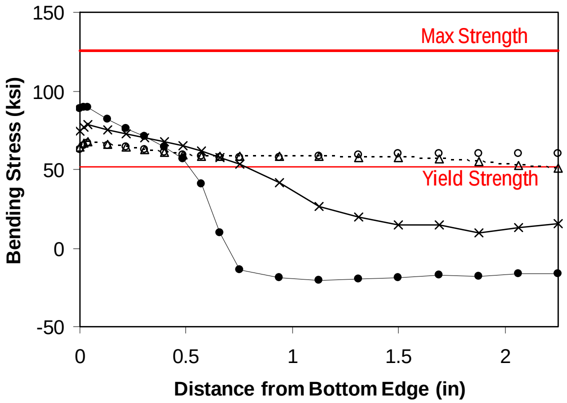

(d) Bending Stress along Line-R

Figure 6.37 Effect of weak panel zone in link web weld interface

6.6.4 Discussion

The finite element simulations discussed in this section support the previous discussion on energy dissipation mechanisms (Refer to Section 5.2.3) and design criteria for panel zone strength (Refer to Section 5.7). The simulations demonstrated that plastic panel zone deformation in a link-to-column joint cannot supply plastic link rotation without the link simultaneously forming a plastic hinge at the beam/brace end. Inelastic panel zone deformation can significantly reduce the inelastic flexural rotation demand at the column end of the link. However, the effect of panel zone deformation may be realized only in moment links, which subject the panel zone to large forces, and supply inelastic link rotation by rotation concentrated at the link ends. Panel zone deformation can have limited participation in shear links, whose yielding mechanism is independent of panel zone deformation. In addition, the simulations suggest that panel zone yielding can significantly relax the stress and strain environment along the link flange-groove weld interface and link web-groove weld interface in intermediate and moment links. Large inelastic shear deformation in shear links causes severe stresses and strain at the column face regardless of the panel zone strength.

The results discussed above only highlight the beneficial effects of a weak panel zone, but provide no indication of the detrimental effects of excessive panel zone deformation observed in previous studies (Refer to Section 2.4.4.3). Figure 6.32 shows that, despite large panel zone deformation, the column flange was thick enough to prevent significant local deformation in the link/beam flanges and in the column flange. Had the column flange been thinner than in this model, large local deformations could have subjected the link flanges to concentrated stress and strains near the groove welds.

6.7 SUMMARY

Finite element simulations of the link-column test specimens were conducted to supplement the findings from the experimental study. Correlation between the fracture behavior observed in the tests and the stress and strain environment predicted by the simulations was studied. Additional analyses were conducted to evaluate the effect of panel zone strength on the performance of EBF link-to-column connections. The key observations from this analytical study are summarized in the following:

- The simulated global behavior of the link-column models and beam-column models agreed well with the experimental behavior. The simulated monotonic loading response agreed well with the skeleton curve constructed from the cyclic loading tests. Therefore, the environment imposed on the local region where detailed stress and strain values were sampled was expected to agree reasonably well with the actual environment in the test specimens, in the range of link rotations where large deformation effects can be neglected.

- The finite element simulations indicated that the stress and strain environment near the critical link flange, link web, and shear tab groove welds depend significantly on the link length and connection configuration. Severe bending stress and plastic strain values were predicted near the link flange groove welds regardless of the link length. This result agrees with the frequent occurrence of fracture near the link flange groove weld observed in test specimens of all link lengths.

- The finite element simulations predicted significantly greater strains at the outer faces of the flanges than at the inner faces of the flanges. The variation in bending stress across the thickness of the flange was more significant in S-link models than in I-link, M-link, and beam-column models. This variation was likely caused by the large portion of shear force transmitted through the link/beam flanges, which generated secondary bending in the link/beam flanges near the column face.

- Despite the variance in column face moment by $0.15M_p$ and shear force by $0.7V_p$ between the I-link, M-link, and beam-column models, the stress and strain environment near the link/beam flange groove weld was affected little between these three models. However, these models were at rotation levels corresponding to 1.1, 1.4, and 1.55 times the link/beam rotation required in the *AISC Seismic Provisions* for I-links, M-links, and moment connections, respectively. Therefore, the environment at the link/beam flange groove weld appears to be more severe in an I-link than in an M-link or beams in MRFs.

- The local stress and strain distributions predicted by the simulations correlated well with the different performance levels achieved by the individual test specimens. The substantially smaller equivalent plastic strain and bending stress values obtained in the FF and NA-models compared to the PN and MW-models agreed with the improved level of performance achieved by the FF and NA-specimens over the PN and MW-specimens. The locations where the simulation predicted elevated stress and strain values, for example, near the link flange groove welds at the edges of the flange or at mid-width of the flange, roughly coincided with the locations where fractures initiated in the test specimens. Therefore, the finite element simulation is an effective tool to gain better insights into connection behavior.

- The performance of the specimens and location of fracture inferred from the finite element simulations did not necessarily agree with the observed fracture behavior. Since the simulations do not model the growth and propagation of fracture, it cannot reliably evaluate the strength degradation process caused by fracture propagation.

- Finite element simulations demonstrated that panel zone yielding in a link-to-column joint cannot supply plastic link rotation without the link simultaneously forming a plastic hinge at the beam/brace end. The design strength of the column panel zone provided in the commentary to the *2002 AISC Seismic Provisions* was developed at four times the elastic limit deformation, as intended in the provisions.

- The simulations indicate that inelastic panel zone deformation can reduce the inelastic rotation demand of a moment link at the face of the column, and thereby relax the stress and strain environment near the critical link flange groove welds and link web groove welds. However, the benefit of panel zone yielding may be limited for shear links, which have much greater rotation demands than moment links, and typically do not produce plastic hinge rotation at the beam/brace end.

CHAPTER 7

Summary and Conclusions

7.1 SUMMARY

This research program investigated the cyclic loading performance of link-to-column connections in seismic-resistant steel EBFs. The program consisted of a literature review and synthesis (Chapter 2), an experimental study involving large-scale cyclic loading tests (Chapters 3, 4, and 5), and an analytical study including detailed finite element simulations (Chapter 6).

7.1.1 Literature Review and Synthesis

The literature study included a comprehensive review of seismic-resistant steel EBFs and MRFs. Particular emphasis was placed on recent research on EBF links and the development of improved moment connections following the Northridge and Kobe Earthquakes. These past studies were synthesized to identify and evaluate important design elements that can affect the seismic performance of link-to-column connections in steel EBFs. Based on this background study, three key parameters were selected for investigation in this program, notably the connection type, link length, and loading protocol. Other important design elements considered in this program included the unequal link end moments, welding process and welding details, and panel zone strength.

7.1.2 Experimental Study

A total of sixteen large-scale cyclic loading tests were conducted. The test specimens consisted of a W18x40 link and a W12x120 column, both of A992 steel. These tests were believed to be the first series of experiments specifically aimed at studying the seismic performance of large-scale EBF link-to-column connections constructed using realistic detailing and welding according to the US practices. Each test subjected a link-column specimen to a force and deformation environment very similar to that realized in actual EBFs. Four connection types, four link lengths, and two loading protocols were examined. The connection types ranged from a connection detailed and constructed according to the pre-Northridge practices, a connection adopting modifications in welding, a connection based on the free flange moment connection, and a no weld access hole connection concept developed in Japanese research. The last two connection types were selected as promising details based on the literature study. The links ranged from shear yielding links to flexural yielding links. The two loading protocols included the protocol specified in the *2002 AISC Seismic Provisions* for testing EBF link-to-column connections and a new protocol developed and proposed by Richards and Uang (2003) during the course of this research program.

7.1.3 Finite Element Simulation

Monotonic loading, 3-D nonlinear finite element simulations were conducted to supplement the findings from the experimental study. Beam-column models were analyzed in addition to link-column models to provide further insights into connection behavior. The stress and strain distributions at the link flange groove welds and link web groove welds were compared with the observed fracture behavior of the tested specimens in order to evaluate the correlation between the simulations and experiments. Additional simulations were performed in order to investigate the effect of panel zone strength on the performance of EBF link-to-column connections.

7.2 RESULTS AND DESIGN IMPLICATIONS

The key results and design implications from this research program are summarized in the following:

1. Specimens featuring the pre-Northridge practices in design, detailing, and welding of EBF link-to-column connections performed poorly for the full range of link lengths, achieving no more than half of the inelastic rotation required in the *2002 AISC Seismic Provisions*. These specimens typically failed due to fracture of the link flange initiating near the groove weld. The poor performance of the pre-Northridge type connections raises questions concerning the safety of existing EBFs constructed prior to the 1994 Northridge Earthquake.

2. Specimens using weld filler metal with specified notch toughness and other modifications and improvements in welding details, but using an otherwise conventional connection configuration, showed marginal improvement over the pre-Northridge type connections. Similarly to the pre-Northridge type connection, the connection with modifications in welding was also controlled by fracture of the link flange initiating near the groove weld.

3. The free flange connections were configured with a shear tab welded to the link web and an extended weld access hole. The intent of this design was to relax the force and deformation environment at the link flange groove welds. The free flange connection specimens achieved significantly greater link rotations compared to the pre-Northridge type specimens. Nonetheless, the free flange connections failed to meet their link rotation requirements,

except in one specimen with a link of length $e = 2.2M_p/V_p$. However, this specimen exceeded its link rotation requirement by only a small margin.

4. The test results and finite element simulations suggest that the design intent of the free flange connections to protect the link flange groove welds from high stresses and strains work successfully. However, the free flange connections were very sensitive to fracture initiating at the top and bottom edges of the link web and shear tab. It appeared that propagation of fracture in the link web weld and shear tab weld accelerated the development of the link flange fractures in the free flange connection specimens with links of length $e = 2.2$ and $3.3M_p/V_p$. Unlike for moment connections (Choi 2000), cutting the link web short of reaching the column, and only using the shear tab for the web connection, was found to be disadvantageous. Considerably better performance was demonstrated by specimens with the link web welded directly to the column flange.

5. The no weld access hole connection featured the elimination of the weld access holes and a fabrication procedure that enabled continuous placement of the link bottom flange groove weld. The performance of the no weld access hole connection depended strongly on the link length. While one specimen with a link of length $e = 1.1M_p/V_p$ achieved an inelastic link rotation 49% greater than the required level, all specimens with longer links ($e = 1.7$, 2.2, and $3.3M_p/V_p$) fell short of the inelastic link rotation by 17 to 37%. Fracture of the link flange initiating near the groove weld was the dominant failure mode of the no weld access hole connection specimens of all link lengths.

6. A no weld access hole connection specimen with a link of length e = $1.1M_p/V_p$ failed due to fracture of the link web initiating at the termination of the fillet welds connecting the stiffeners to the link web. Other specimens with links of length e = $1.1M_p/V_p$ as well as previous tests by Arce (2002), Galvez (2004), and Ryu (2004) suggest that the failure of short shear links is dominated by fracture of the web at the stiffener welds.

7. The performance of the link-to-column connection depended strongly on the link length, with the inelastic link rotation decreasing significantly with increase in link length. The effect of the link length was reflected in the substantial difference in link shear force and column face moment. The maximum link shear force ranged between 0.73 and $1.40V_p$ depending on the link length, while the maximum column face moment ranged between 0.83 and $1.28M_p$.

8. Strain gauge data indicate that significant plastic strain developed in shear link specimens near the link flanges groove welds, as the column face moment exceeded a reduced flexural capacity removing the contribution of the link web. The strain gauge data also indicate that the link web of this specimen developed only very limited bending strains, and hence contributed little to the flexural strength of the link. Therefore, moment-shear interaction can cause a substantial decrease in flexural strength of shear links. This yielding behavior of shear links was also observed in the finite element simulations.

9. Compared to the flange connections welded using an E70T-4 electrode (used in the pre-Northridge type connections), weld defects were much less

perceptible in the fracture surfaces of flange connections welded using an E70T-6 electrode (used in the other three connection types). Examination of the surfaces suggests that, in a large number of specimens, fracture initiated at the edge of the link flange at the interface of the link flange base metal and groove weld metal. Therefore, it is likely that the material properties at the weld interface, including the heat affected zone, had a significant influence on the flange fractures. The fracture surfaces in the connections also suggested that the free flange connections and no weld access hole connections are effective in reducing the incidence of weld defects in the link bottom flange at the root of the weld access hole.

10. Two practically identical no weld access hole connection specimens with links of length $e = 1.1M_p/V_p$ were tested under different loading protocols. Comparison of these two tests shows that the loading protocol can have a very significant effect on the inelastic link rotation capacity of the link-column specimen. Similarly, Ryu (2004) and Galvez (2004) observed that the loading sequence can significantly alter the inelastic rotation capacity of the link. Therefore, it is important to select a loading protocol that realistically represents the demands caused by earthquake ground motions, as does the new loading protocol developed by Richards and Uang (2003; 2004). However, except for four specimens that used Richards and Uang’s protocol, the current program used the protocol provided in the *2002 AISC Seismic Provisions*, which may not necessarily be representative of seismic demands.

11. The simulated global behavior of the link-column models agreed well with experimental behavior. Very good agreement was found between the

simulated monotonic loading curves and skeleton curves constructed from cyclic loading tests.

12. As expected from the experimental results, the finite element simulations indicate that the stress and strain environment near the critical link flange, link web, and shear tab groove welds depend significantly on the link length and configuration of the link-to-column connection. Nonetheless, severe bending stresses and plastic strains can develop near the link flange groove welds regardless of the link length. Therefore, fracture of the link flange near the groove welds is a major concern for links of all practical lengths.

13. The finite element simulations as well as strain gauge data indicate that significantly greater strains develop at the outer faces of the flanges than at the inner faces of the flanges. The variation in bending stress across the thickness of the flange was more significant in shear links than in intermediate links or moment links. This variation may be caused by the large portion of shear force transmitted through the link flanges, which generates secondary bending in the flanges near the column face.

14. The local stress and strain distributions predicted by the simulations correlated well with the different performance levels achieved by the individual test specimens. Specimens whose simulation predicted lower peak equivalent plastic strain and bending stress values achieved a larger link rotation capacity in the experiment. The locations where the simulation predicted elevated stress and strain values, for example, near the link flange groove welds at the edges of the flange or at mid-width of the flange, roughly coincided with the locations where fractures initiated in the

experiment. Therefore, finite element simulation is an effective tool to gain better insights into connection behavior.

15. The link overstrength factors evaluated from the sixteen tests averaged at 1.25, ranging from 1.05 to 1.47. For S-links, the overstrength factor averaged at 1.36, ranging from 1.27 to 1.47. The overstrength factor for I-links averaged at 1.18, ranging from 1.11 to 1.26. The overstrength factor for M-links averaged at 1.26, ranging from 1.19 to 1.37. Considering that the majority of specimens failed prematurely, and could have developed somewhat greater forces if they have developed their required link rotation, these overstrength factors are in reasonable agreement with those measured from previous tests. Therefore, the factor of 1.5 assumed in the *2002 AISC Seismic Provisions* is reasonable.

16. Limited test data as well as finite element simulations suggest that panel zone yielding in a link-to-column joint cannot supply plastic link rotation without the link simultaneously forming a plastic hinge at the beam/brace end. The design strength of the column panel zone provided in the commentary to the *2002 AISC Seismic Provisions* appears to be appropriate. The finite element simulations indicate that inelastic panel zone deformation can reduce the inelastic rotation demand of a moment link at the face of the column, and thereby relax the stress and strain environment near the critical link flange groove welds and link web groove welds. However, the benefit of panel zone yielding may be limited for shear links, which have much greater rotation demands than moment links, and typically do not produce plastic hinge rotation at the beam/brace end.

In conclusion, the majority of link-column test specimens failed prematurely by fracture of the link flange near the groove weld. These fractures resulted in an abrupt and drastic degradation in the strength of the specimens. It appeared that the excellent buckling control provided by the link stiffeners left fracture at the link-to-column connection as the dominating failure mode of the specimens rather than link local web or flange buckling. The observed flaking of whitewash, strain gauge measurements, and finite element simulations suggest that even a short shear link of length $e = 1.1M_p/V_p$ develops severe bending stresses near the link flange groove welds. Therefore, premature fracture of the link flanges is a major concern not only for connections of a long link ($e > 1.6M_p/V_p$) to a column, as noted previously, but also for connections with a short shear link, such as a link of length $e = 1.1M_p/V_p$.

Connection details which have shown good performance for beam-to-column moment connections in MRFs, such as the unreinforced welded flange-welded web connection, free flange connection, and no weld access hole connection, do not necessarily provide good performance for EBF link-to-column connections. The force and deformation demands at link-to-column connections are significantly more severe than at moment connections. Therefore, until further research is available, EBF arrangements with links attached to columns should be avoided.

7.3 RECOMMENDATIONS FOR FUTURE RESEARCH

1. Further research is required to develop design and detailing procedures for link-to-column connections that can reliably sustain the large inelastic rotations and forces developed by a ductile link.

2. Connections in which the link is directly welded to a heavy end plate through the use of all-around fillet welds appear promising (Refer to Appendix A), and merit further study.

3. The performance of EBF link-to-column connections with link sections other than the W18x40 should be examined. The link cross-sectional dimensions can significantly alter the moment gradient developed in links of the same length category. The W18x40 link section used in this research was expected to develop more severe plastic strain demands at the link-to-column connection than the majority of rolled wide-flange shapes due to its large depth-to-width ratio (or equivalently, flange to web area ratio). Testing of link-to-column connections with link sections of much smaller depth-width ratio than the W18x40 could verify the effect of link cross-sectional dimensions on the performance of EBF link-to-column connections.

4. The effect of other factors not explicitly addressed in this research program, such as composite concrete slabs, frame arrangement (elastic end moment ratio), yielding in the beam outside of the link, and dynamic loading, should be further clarified.

5. The finite element simulation conducted in this study could be combined with ductile fracture criteria (*e.g.* Hancock and Mackenzie 1976; Kuwamura and Yamamoto 1997; An *et al.* 2003) to evaluate the propensity of fracture at critical locations, and possibly evaluate or predict the rotation capacity of the EBF link-to-column connection. El-Tawil *et al.* (2000), Mao *et al.* (2001), and Tabuchi *et al.* (2002) have applied this approach to study the rotation capacity of moment connections.

6. Advancement in metallurgical studies to improve the material properties near the heat affected zone in link flange groove welds may be crucial in improving the performance of welded steel connections. Experimental observation from this research suggests that fracture initiating near the interface of the link flange base metal and the groove weld metal is a critical failure mode for link-to-column connections. Similarly, past research suggests that fracture of beam flanges in moment connections typically initiate at the interface of the beam flange base metal and groove weld metal.

7. Material properties near the heat affected zone of welds must be better characterized. Realistic modeling of these properties is essential for the finite element simulations to reliably estimate the fracture behavior of welded link-to-column connections in EBFs or beam-to-column moment connections in MRFs.

APPENDIX A

End Plate Welds

A.1 GENERAL

When subjected to large inelastic deformations, the link-column specimens experienced bending moment at the beam side end of the link at least as large as at the column side end of the link. Failure at the beam side would have altered the force distribution in the link, and hence limited the validity of the data collected from further loading. In order to minimize the occurrence of such unwanted damage, a heavy end plate type connection using a 2-inch thick steel plate was used at the beam side end of the link (See Figure 3.7). This steel plate was, in turn, connected to the loading frame by means of high-strength bolts. Large size fillet welds were used to connect the link to the end plate. These fillet welds were made with a shielded metal arc welding (SMAC) process using an E7018 electrode (Lincoln Electric product Jetweld LH-70) with 5/32-inch diameter.

This appendix details the problems encountered in pervious link tests in end plate welds using this test setup, and discusses the welding process used for fabricating the specimens. The end plate connection detail used at the beam side end of the link for this test program was not intended to represent a connection that would be used in an actual EBF. These end plate connections were used simply to facilitate the test program. Nonetheless, these end plate connections showed excellent performance, and therefore may provide some insights into alternative approaches for link-to-column connections.

A.2 FAILURES OBSERVED BY ARCE (2002)

Arce (2000) tested isolated links using the same test setup used in this test program. However, In Arce's tests, end plate connections were used at both ends of the link. Three of the sixteen specimens tested by Arce failed by fracture in the flanges near or at a fillet weld connecting the link flange to the steel end plate. The failures of these specimens were considered artifacts of the test, since the tests did not represent the link end connections used in actual EBFs. Failures in the end plate welds were not within the scope of the study, and all attempts were made to eliminate damage at these welds.

Of the three specimens, designated as 1A, 1B, and 6A, 1A and 1B had W10x19 links with length $e = 1.8\ M_p/V_p$, while 6A had a W10x33 link with length $e = 2.3\ M_p/V_p$. Both links fall in the link length category of intermediate links ($1.6\ M_p/V_p \leq e \leq 2.6\ M_p/V_p$). Since the tests conducted by Arce (2002) shared many features with this program, the experience from those tests was reflected in the test plans for this current program.

A.2.1 Specimens 1A, 1B and 1C

Specimen 1A employed an SS-FCAW process using an E70T-6 electrode (Lincoln Electric product NR305) with 2/32-inch diameter for the end plate welds. Short of achieving the required inelastic rotation amplitude of $\gamma_p = 0.07$ rad, at $\gamma_p = 0.04$ rad, a weld interface fracture propagated rapidly in a link flange, as shown in Figure A1, resulting in significant drop in link strength. In an attempt to avoid similar failures in other specimens, the welding process used for the link-to-end plate welds was changed to the SMAW process.

Specimen 1B was identical to Specimen 1A except for the replacement of the SS-FCAW process by an SMAW process using an E7018 electrode (Lincoln Electric product Jetweld LH-70) with 5/32-inch diameter for the end plate welds.

Figure A1 Fracture in Specimen 1A

Short of reaching the required inelastic rotation, during loading amplitude of γ_p = 0.06 rad, the link strength dropped significantly due to a fracture in a flange, as shown in Figure A2. The fracture initiated at the edge of the flange, and propagated in the flange away from the end plate. After observing the fracture in Specimen 1B, it was suspected that the flange edges were quite susceptible to fracture initiation due to possible weld flaws (since the weld beads were initiated and/or terminated at this location) and due to local stress concentration. It was also observed that the wrapping of welds around the flange edges, as seen in Figure A1 and Figure A2, inevitably introduced small undercuts. The notch effects of these undercuts might have further added to the susceptibility of fracture initiation at the flange edges.

A third identical specimen, designated as Specimen 1C, was therefore fabricated with another change in welding details. Specimen 1C used the same welding process as in Specimen 1B for the end plate welds, but with weld tabs

Figure A2 Fracture in Specimen 1B

placed at the flange edges, as shown in Figure A3. Weld tabs with thickness equal to the link flange thickness were placed to extend the fillet welds beyond the width of the flanges. The weld bead initiation and termination were moved away from the flange edges, onto the weld tabs. The fillet welds thus placed introduced no wrapping weld and no undercut at the flange edges. It was also expected that the extra weld placed on the weld tabs outside of the flange width may help in reducing potential stress concentrations at the termination of the welds on the flange edges. After the welds were placed, the weld tabs and fillet welds were ground to provide the flange edges with smoothly transitioning fillets. Specimen 1C performed better than Specimens 1A and 1B, and achieved an inelastic rotation of 0.08 rad, which exceeds the required 0.07 rad. Specimen 1C degraded in strength due to flange and web buckling. No damage was detected at

Figure A3 Fillet weld made for Specimen 1C

the end plate welds at the end of the test. Therefore, it was concluded that the welding procedure developed for Specimen 1C was adequate for making the end plate welds.

A.2.2 Specimens 6A and 6B

Specimen 6A used the same welding procedure as in Specimen 1B for the end plate welds, but no wrapping weld was placed at the flange edges, as shown in Figure A4. It was suspected that a similar improvement in connection performance seen in Specimen 1C in comparison to Specimen 1B could be achieved by not using the weld tabs, while avoiding weld wrapping at the flange edges. After undergoing severe flange and web buckling near its ends, the link started to lose its strength during the inelastic rotation cycles of 0.057 rad. At that stage, a throat crack had propagated along the entire width of a flange to end plate fillet weld and then propagated further into the web, as shown in Figure A4.

Although Specimen 6A achieved inelastic rotation greater than the required 0.038 rad, it was decided that the test did not demonstrate the full rotation capacity of the link. Consequently, a repeat test was conducted. The repeat specimen, designated as Specimen 6B, was identical to Specimen 6A except that weld tabs were added at the flange edges as part of the welding procedure, and the weld size was increased to prevent throat cracking. Unlike Specimen 1C, the weld tabs were not ground after welding, and were left in place. Specimen 6B surpassed Specimen 6A in inelastic rotation. At completion of the first inelastic rotation cycle of 0.057 rad, after completing one and a half more loading cycles than did Specimen 6A, the link strength degraded significantly. Figure A5 shows the severe flange and web buckling observed after the test. No damage was detected in the end plate welds at the end of the test.

A.2.3 Discussion

The fracture in the flanges near or at the end plate welds, as observed in Specimen 1A, 1B, and 6A is attributed to multiple factors, including: quality of weld; notch effect caused by weld undercut and/or laminar tearing in the flange edges; and high stresses. A welding procedure using a SMAW process with a notch-tough electrode, a very large weld size, and weld tabs at the flange edges was developed to mitigate the occurrence of fracture.

Other than Specimen 1A, end plate welds in all the remaining fifteen specimens were made with the SMAW process using an E7018 electrode. The impact of the upgrade in welding metal is evident from the superior performance of Specimen 1B over Specimen 1A. However, Specimen 1B also failed prematurely due to fracture initiating at the flange edge near the weld interface. The primary cause of this fracture was believed to be the notch effect of the weld undercut at this location. By placing weld tabs at the flange edges, and extending

Figure A4 Fracture in Specimen 6A

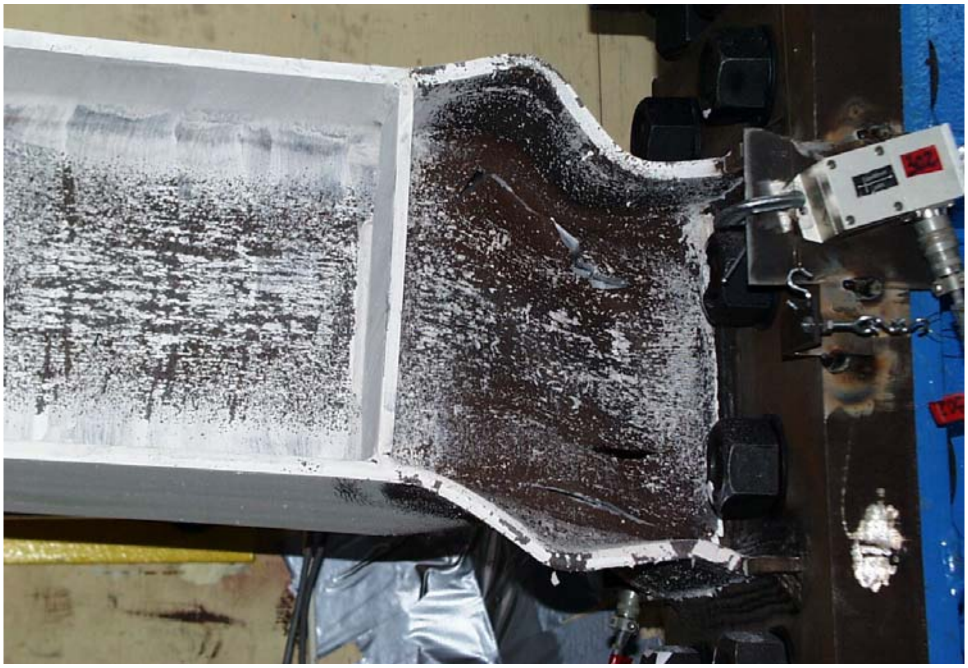

Figure A5 Specimen 6B after test

the fillet welds beyond the flange width, Specimen 1C successfully achieved the link rotation required by the *AISC Seismic Provisions*. This specimen ultimately failed by severe flange and web buckling.

Of the sixteen specimens tested, six specimens employed the welding procedure identical to that developed for Specimen 1C. A slight revision was made for Specimens 10 and 11. These two specimens had the link flanges connected to the end plate with a partial joint penetration groove weld at one side of the flange, and with a fillet weld at the other side of the flange. The end plate welds in these combined eight specimens, with link length ranging from 1.3 M_p/V_p to 3.8 M_p/V_p, achieved or nearly achieved the link rotation required by the AISC *Seismic Provisions*. Among the eight specimens, only two specimens, Specimens 2 and 3 exhibited fracture near or at the end plate welds. However, Specimens 2 and 3 exceeded their required inelastic rotation by 87% and 95%, respectively, and experienced severe flange and web buckling prior to the onset of fracture. Overall, the performance of end plate welds in the eight specimens was satisfactory. With the exception of specimen 1C, the weld tabs were left in place after placing the welds. The alternative finishes at the flange edges after welding did not appear to affect the performance of the end plate welds.

Three specimens did not use weld tabs, but the fillet welds were terminated short of reaching the flange edges. It was suspected that by omitting the weld wrapping at the flange edges, and hence preventing undercut at the flange edges, the fracture observed in Specimen 1B could be avoided. Of the three specimens, only Specimen 6A exhibited damage near or at the end plate welds. The poor performance of Specimen 6A can be attributed partly to the insufficient size for the end plate fillet welds. The remaining two specimens, Specimens 4A and 4B had link length of $e = 1.1\ M_p/V_p$, and ultimately failed by fracture in the web away from the link ends. However, these two specimens developed bending moment of no more than 0.80 M_p, as opposed to 1.27 M_p developed in Specimen 6A. The superior performance observed in Specimens 4A and 4B is likely attributed to the relaxed stress environment.

A.3 END PLATE WELDS IN OTHER TESTS

End plate connections were used in many tests on EBF links conducted to date. For example, Hjelmstad and Popov (1983), Malley and Popov (1983), and Kasai and Popov (1986) tested link specimens with both ends of the links fillet welded to steel end plates, similar to the specimens tested by Arce (2002). Kasai and Popov report facture of the end plate welds in three specimens (Specimens 4, 5, and 6). More recently, Ghobarah *et al.* (1994) observed that fracture of the end plate welds control failure of the link specimens with end plate connections.

Although no clear conclusion can be drawn, it is suspected that the difference in steel properties was at least partly responsible for the failure in end plate welds observed by Arce (2002) and Ghobarah *et al.* (1994). These tests used A992 steel for the link specimens instead of the A36 steel used in many of the previous tests. The higher strength of A992 steel results in lower weld to base metal strength ratio, which can be unfavorable for welded connections. Since all specimens tested in this research were fabricated using A992 steel, it was believed that the same caution as in Arce (2002) was necessary for making the end plate welds.

A.4 WELDING PROCEDURE USED FOR END PLATE WELDS

All the specimens fabricated for this research had the beam side end of the link fillet welded to 2-inch steel end plates. The welding procedure for these fillet welds was chosen based on the observations detailed in this appendix. The sizes of the end plate fillet welds were 3/4-inch at the link flanges and 1/2-inch at the link web. The fillet welds were made with an SMAW process using an E7018 electrode (Lincoln Electric product Jetweld LH-70) with 1/8-inch or 5/32-inch diameter. Weld tabs were placed at the flange ends. Figure A6 shows an example of the end plate weld at the link flange.

The weld size was determined based on the following requirement:

$$\gamma P_y \leq \phi P_n \tag{A.1}$$

In the above relation,

P_y = maximum tensile force, kips.

P_n = nominal strength of the welds as shown in Figure A7, kips.

γ = load factor.

ϕ = resistance factor.

The left hand side of equation (A.1) can be decomposed as follows.

$$\gamma P_y = R_y \Omega_y \left(F_y L t \right) \tag{A.2}$$

In the above equation,

R_y = ratio of the expected yield strength to the minimum specified yield strength. For A992 steel, R_y = 1.1 according to the *AISC Seismic Provisions*.

Ω_y = overstrength of link flange or web (See Figure A7).

F_y = minimum specified yield strength of link flange or web (See Figure A7), ksi. For A992 steel, F_y = 50 ksi.

L = length of weld, in.

t = thickness of link flange or web (See Figure A7), in.

Based on the overstrength in link end moments observed by Arce (2002), Ω_y = 1.35 was selected.

Figure A6 Typical end plate weld (Specimen PNI)

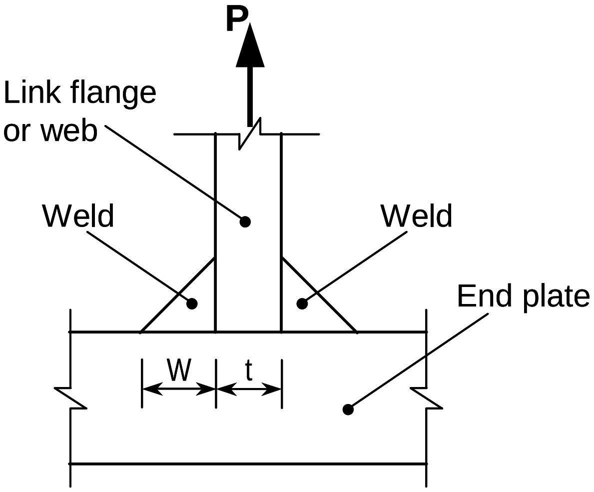

Figure A7 Schematic view of end plate fillet weld

The right hand side of equation (A.1) can be decomposed as follows.

$$\phi P_y = \phi \frac{2W}{\sqrt{2}} L \frac{F_{Exx}}{\sqrt{3}} \tag{A.3}$$

In the above equation,

W = leg size of each of the two fillet welds (See Figure A7), in.
L = length of weld, in.
F_{Exx} = minimum specified tensile strength of weld metal, ksi. For all welds used in this research, F_{Exx} = 70 ksi.

Equations (A.1) to (A.3) can be rearranged as follows.

$$W = \frac{1}{\phi}\sqrt{\frac{3}{2}}\frac{R_y \Omega_y F_y}{F_{Exx}} t \approx \frac{1.3}{\phi} t \tag{A.4}$$

Based on equation (A.4), it was decided that the weld size be designed as follows.

$$W = 1.5\,t \tag{A.5}$$

The chosen factor of 1.5 corresponds to a resistance factor of ϕ = 0.87. Note that the weld size specified by equation (A.5) is significantly larger than the size used in typical fillet welds. The fillet weld size in the link web was also determined based on tensile force demands rather than by the shear force demands, since the former was considered more critical.

Besides the link-column specimens tested in this research, six of the specimens tested by Arce (2002) had end plate welds made according to the design procedure described herein, as well as ten specimens tested by Ryu (2004) and ten specimens tested by Galvez (2004). No damage in the end plate welds was observed in any of the combined forty-two specimens.

APPENDIX B

Tension Coupon Test Summary

B.1 GENERAL

This appendix summarizes the details of tension coupon tests conducted on the steels used to fabricate the link-column specimens.

B.2 CERTIFIED MILL TEST REPORT

According to the mill test reports included in Appendix C, the W18x40 steel met the *ASTM A36* and *ASTM A572* Grade 50 requirements; the W12x120 steel met the *ASTM A992* and *ASTM A572* Grade 50 requirements. The former was manufactured by Chaparral Steel, the latter was manufactured by Nucor-Yamato Steel Company.

The yield stress F_y, tensile strength F_u, and percent elongation values reported in Table 3.4 were evaluated by taking the average of the corresponding two values reported in the certified mill test reports.

B.3 MEASURED TENSION PROPERTIES

Tension tests were conducted per *ASTM E8*, and largely following the requirements of Appendix D of *SAC/BD-97/02* (1997). Six coupons were taken from the W18x40 section, and four coupons were taken from the W12x120 section, as discussed in Section 3.3.3. The coupons had a gauge length of 2 inches, width of 1/2 inch, and thickness ranging between 1/4 inch and 3/8 inch. The coupon test results for the W18x40 and W12x120 sections are summarized in Table B1 and Table B2, respectively. The tables also summarize the mechanical properties of the flange, web, and k-area (k-area properties measured for the

Table B1 W18x40 Tension Coupon test results

Coupon	Young's Mudulus (ksi)	Strain Hardening Modulus (ksi)	Upper Yield Point (ksi)	Static Yield Stress (ksi)	Dynamic Yield Stress (ksi)	Dynamic Tensile Strength (ksi)	Yield Stress-to-Tensile Stresngth Ratio	Strain at Onset of Strain Hardening	Strain at Onset of Necking	Elongation
LF1	29049	521	55.2	51.9	54.9	72.6	0.76	2.1%	18.0%	34.4%
LF2	29632	414	52.5	49.8	52.2	71.8	0.73	1.5%	17.4%	32.8%
LF3	28873	486	56.9	53.1	56.2	74.4	0.76	1.9%	17.4%	33.6%
LF4	29185	500	53.2	49.3	52.2	70.8	0.74	1.9%	18.1%	33.6%
LK	29802	357	N.A.	N.A.	78.8	89.6	0.88	N.A.	5.9%	15.0%
LW	29836	500	62.5	57.0	60.8	76.4	0.80	2.5%	12.7%	31.4%
Flange	29185	480	54.4	51.0	53.9	72.4	0.74	1.8%	17.7%	33.6%
Web	29836	500	62.5	57.0	60.8	76.4	0.80	2.5%	12.7%	31.4%
k-area	29802	357	N.A.	N.A.	78.8	89.6	0.88	N.A.	5.9%	15.0%

Table B2 W12x120 Tension Coupon test results

Coupon	Young's Mudulus (ksi)	Strain Hardening Modulus (ksi)	Upper Yield Point (ksi)	Static Yield Stress (ksi)	Dynamic Yield Stress (ksi)	Dynamic Tensile Strength (ksi)	Yield Stress-to-Tensile Stresngth Ratio	Strain at Onset of Strain Hardening	Strain at Onset of Necking	Elongation
CF1	29336	364	48.5	45.5	48.1	64.4	0.75	1.4%	15.1%	29.5%
CF2	27445	457	52.8	48.2	50.3	67.6	0.74	1.4%	14.4%	28.5%
CW1	30167	486	56.6	52.2	54.7	70.7	0.77	1.5%	14.4%	33.2%
CW2	30167	350	57.3	50.2	53.9	70.1	0.77	1.6%	15.5%	32.6%
Flange	28391	411	50.6	46.9	49.2	66.0	0.75	1.4%	14.8%	29.0%
Web	30167	418	56.9	51.2	54.3	70.4	0.77	1.6%	14.9%	32.9%

W18x40 section only).

The tension coupon tests were conducted on an MTS 810 material test system. This system permits full control of crosshead speed. A loading rate of 0.02 inches per minute (cross-head speed) was used for the measurement of the upper yield point, the dynamic yield stress, the strain at onset of hardening, and the strain hardening modulus. This speed corresponded to a loading rate of 78 ksi per minute in the elastic range, and to an average strain rate of 0.27% per minute. After determination of strain at onset of hardening, the loading rate was increased to 0.125 inches per minute (cross-head speed) for the measurement of the dynamic tensile strength. This loading rate was maintained until the failure of the coupon.

Static yield stress values were taken by stopping the crossheads and waiting for 3 minutes. The static yield stresses reported in Table B1 and Table B2 were evaluated by taking the averaged value of three readings for each coupon. Since the yield plateau was not present for coupon LK (See Figure 3.17), the static yield stress was not evaluated for this coupon. The dynamic yield stress was evaluated using the 0.2% offset method per *ASTM A370*. The yield stress F_y and tensile strength F_u values reported in Table 3.4 correspond to the static yield stress and dynamic tensile strength values.

APPENDIX C

Certified Mill Test Reports

This appendix contains the certified mill test reports for the W18x40 steel and W12x120 steel used for the link-column specimens.

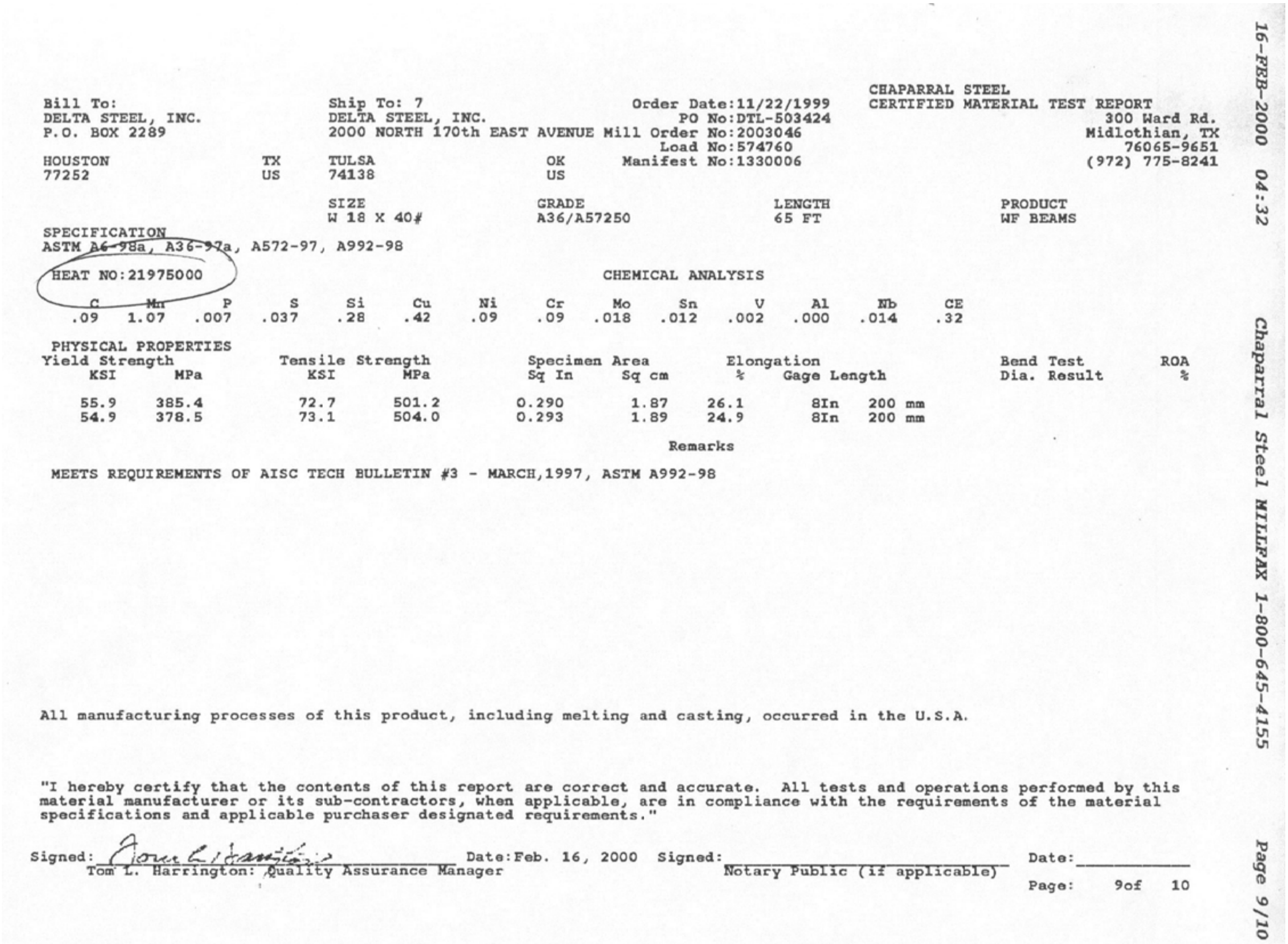

16-FEB-2000 04:32 Chaparral Steel MILLFAX 1-800-645-4155 Page 9/10

CHAPARRAL STEEL
CERTIFIED MATERIAL TEST REPORT
300 Ward Rd.
Midlothian, TX
76065-9651
(972) 775-8241

Bill To:		Ship To: 7		
DELTA STEEL, INC.		DELTA STEEL, INC.		Order Date:11/22/1999
P.O. BOX 2289		2000 NORTH 170th EAST AVENUE		PO No:DTL-503424
				Mill Order No:2003046
				Load No:574760
HOUSTON	TX	TULSA	OK	Manifest No:1330006
77252	US	74138	US	

SIZE	GRADE	LENGTH	PRODUCT
W 18 X 40#	A36/A57250	65 FT	WF BEAMS

SPECIFICATION
ASTM A6-98a, A36-97a, A572-97, A992-98

HEAT NO:21975000

CHEMICAL ANALYSIS

C	Mn	P	S	Si	Cu	Ni	Cr	Mo	Sn	V	Al	Nb	CE
.09	1.07	.007	.037	.28	.42	.09	.09	.018	.012	.002	.000	.014	.32

PHYSICAL PROPERTIES

Yield Strength		Tensile Strength		Specimen Area		Elongation			Bend Test		ROA
KSI	MPa	KSI	MPa	Sq In	Sq cm	%	Gage Length		Dia.	Result	%
55.9	385.4	72.7	501.2	0.290	1.87	26.1	8In	200 mm			
54.9	378.5	73.1	504.0	0.293	1.89	24.9	8In	200 mm			

Remarks

MEETS REQUIREMENTS OF AISC TECH BULLETIN #3 - MARCH,1997, ASTM A992-98

All manufacturing processes of this product, including melting and casting, occurred in the U.S.A.

"I hereby certify that the contents of this report are correct and accurate. All tests and operations performed by this material manufacturer or its sub-contractors, when applicable, are in compliance with the requirements of the material specifications and applicable purchaser designated requirements."

Signed: Tom L. Harrington Date:Feb. 16, 2000 Signed:________ Date:________
Tom L. Harrington: Quality Assurance Manager Notary Public (if applicable)

Page: 9of 10

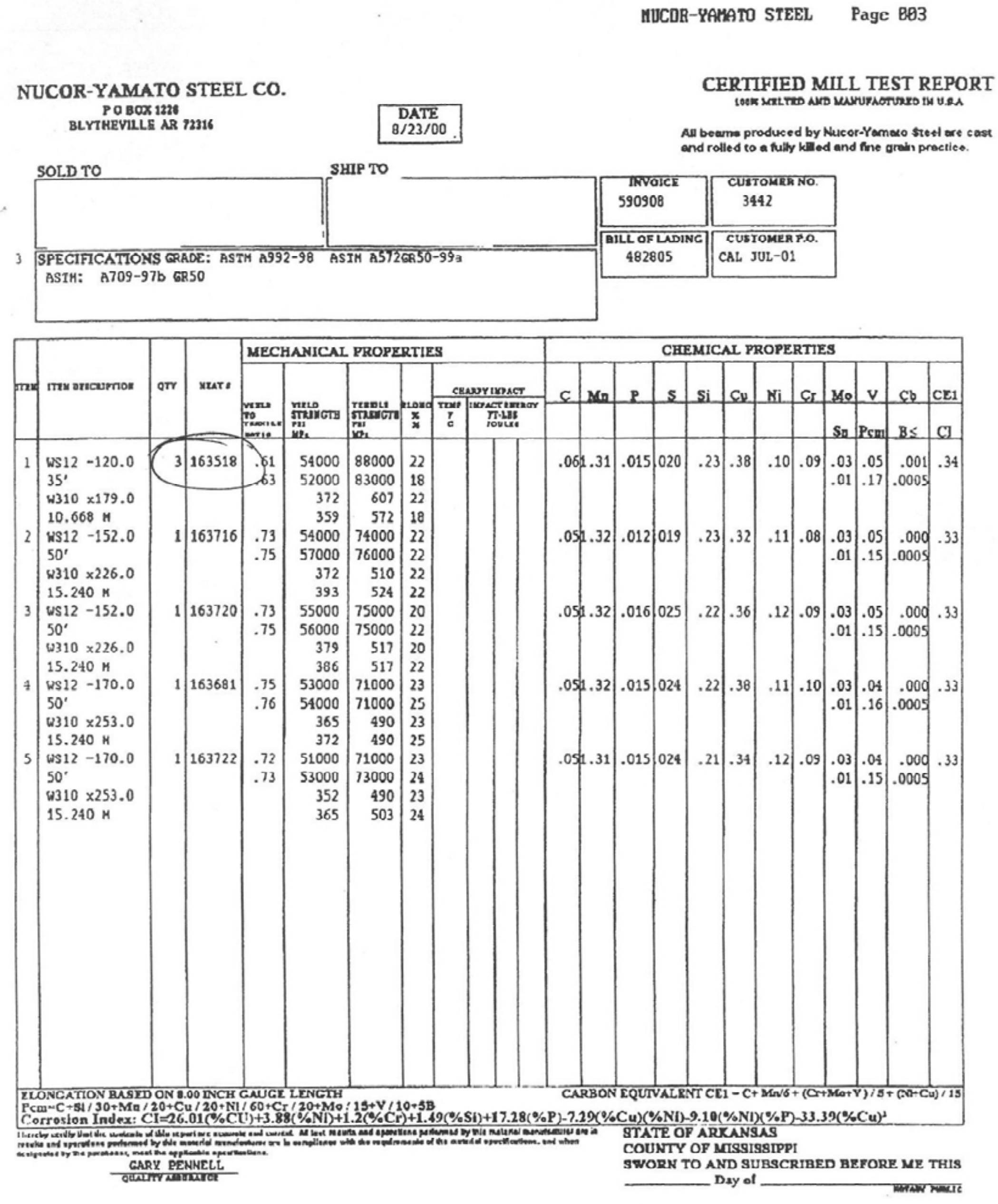

NUCOR-YAMATO STEEL Page 003

NUCOR-YAMATO STEEL CO.
P O BOX 1228
BLYTHEVILLE AR 72316

DATE
8/23/00

CERTIFIED MILL TEST REPORT
100% MELTED AND MANUFACTURED IN U.S.A.

All beams produced by Nucor-Yamato Steel are cast and rolled to a fully killed and fine grain practice.

SOLD TO

SHIP TO

INVOICE	590908
CUSTOMER NO.	3442
BILL OF LADING	482805
CUSTOMER P.O.	CAL JUL-01

3 SPECIFICATIONS GRADE: ASTM A992-98 ASTM A572GR50-99a
ASTM: A709-97b GR50

				MECHANICAL PROPERTIES						CHEMICAL PROPERTIES											
								CHARPY IMPACT													
ITEM	ITEM DESCRIPTION	QTY	HEAT #	YIELD TO TENSILE RATIO	YIELD STRENGTH PSI MPa	TENSILE STRENGTH PSI MPa	ELONG % %	TEMP F C	IMPACT ENERGY FT-LBS JOULES	C	Mn	P	S	Si	Cu	Ni	Cr	Mo Sn	V Pcm	Cb B≤	CE1 CI
1	WS12 -120.0	3	163518	.61	54000	88000	22			.06	1.31	.015	020	.23	.38	.10	.09	.03	.05	.001	.34
	35'			.63	52000	83000	18											.01	.17	.0005	
	W310 x179.0				372	607	22														
	10.668 M				359	572	18														
2	WS12 -152.0	1	163716	.73	54000	74000	22			.05	1.32	.012	019	.23	.32	.11	.08	.03	.05	.000	.33
	50'			.75	57000	76000	22											.01	.15	.0005	
	W310 x226.0				372	510	22														
	15.240 M				393	524	22														
3	WS12 -152.0	1	163720	.73	55000	75000	20			.05	1.32	.016	025	.22	.36	.12	.09	.03	.05	.000	.33
	50'			.75	56000	75000	22											.01	.15	.0005	
	W310 x226.0				379	517	20														
	15.240 M				386	517	22														
4	WS12 -170.0	1	163681	.75	53000	71000	23			.05	1.32	.015	024	.22	.38	.11	.10	.03	.04	.000	.33
	50'			.76	54000	71000	25											.01	.16	.0005	
	W310 x253.0				365	490	23														
	15.240 M				372	490	25														
5	WS12 -170.0	1	163722	.72	51000	71000	23			.05	1.31	.015	024	.21	.34	.12	.09	.03	.04	.000	.33
	50'			.73	53000	73000	24											.01	.15	.0005	
	W310 x253.0				352	490	23														
	15.240 M				365	503	24														

ELONGATION BASED ON 8.00 INCH GAUGE LENGTH

CARBON EQUIVALENT CE1 = C+ Mn/6 + (Cr+Mo+V) / 5 + (Ni+Cu) / 15

Pcm=C+Si / 30+Mn / 20+Cu / 20+Ni / 60+Cr / 20+Mo / 15+V / 10+5B

Corrosion Index: CI=26.01(%CU)+3.88(%Ni)+1.2(%Cr)+1.49(%Si)+17.28(%P)-7.29(%Cu)(%Ni)-9.10(%Ni)(%P)-33.39(%Cu)²

I hereby certify that the contents of this report are accurate and correct. All test results and operations performed by this material manufacturer are in results and operations performed by this material manufacturer are in compliance with the requirements of the material specifications, and when designated by the purchaser, meet the applicable specifications.

GARY PENNELL
QUALITY ASSURANCE

STATE OF ARKANSAS
COUNTY OF MISSISSIPPI
SWORN TO AND SUBSCRIBED BEFORE ME THIS
__________ Day of __________
NOTARY PUBLIC

APPENDIX D

Charpy V-Notch Test Reports

This appendix contains Charpy V-Notch test reports for the two weld filler metals used to construct the link flange groove welds for the specimens in this research project. An-Tech Laboratories, Inc. of Houston, Texas performed all Charpy V-Notch tests.

Identification #NS3M is the sample weld constructed using an E70T-4 electrode (Lincoln Electric product NS-3M) with 0.120-inch diameter. Identification #305 was constructed using an E70T-6 electrode (Lincoln Electric product NR-305), with 3/32-inch diameter

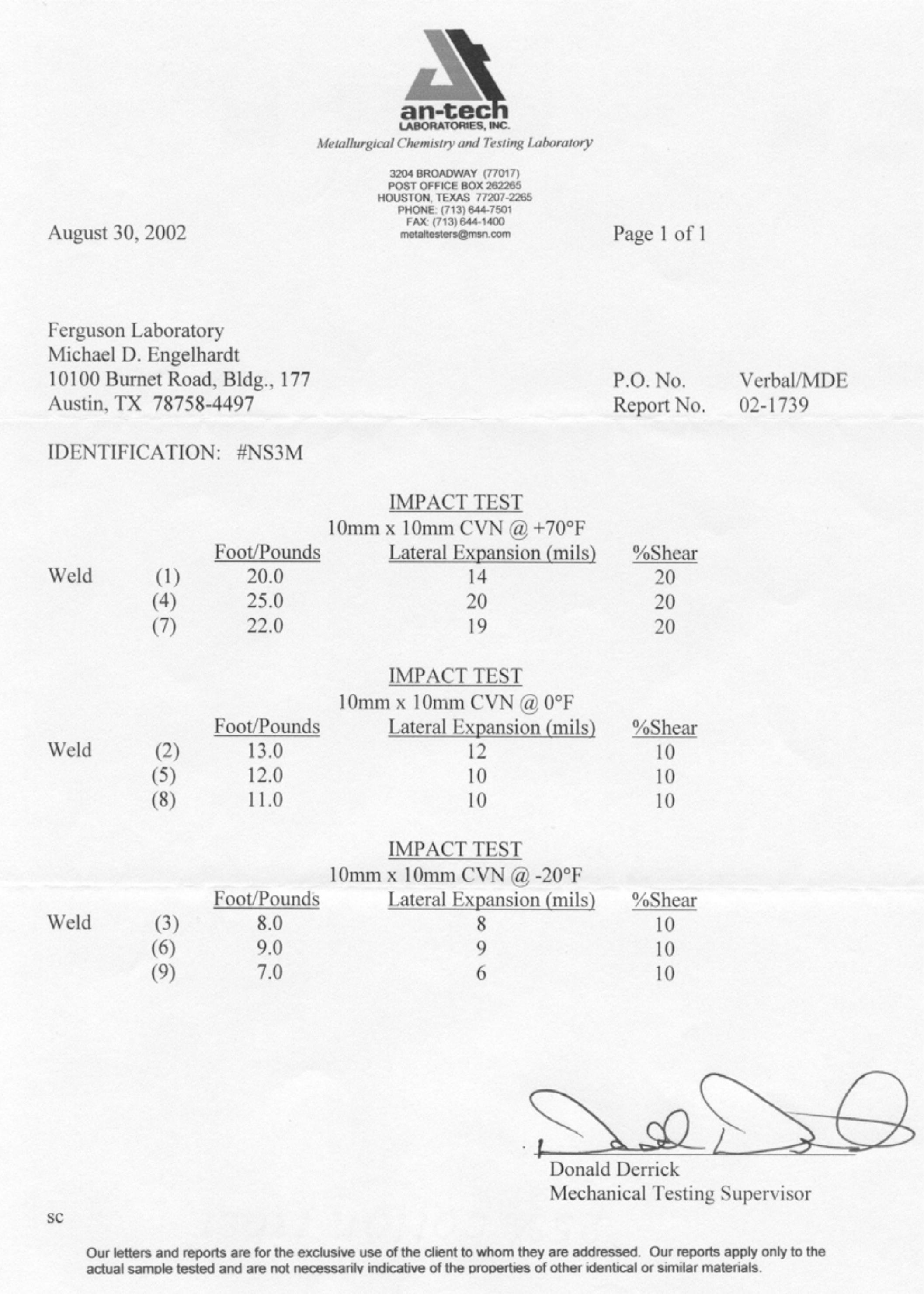

an-tech
LABORATORIES, INC.
Metallurgical Chemistry and Testing Laboratory

3204 BROADWAY (77017)
POST OFFICE BOX 262265
HOUSTON, TEXAS 77207-2265
PHONE: (713) 644-7501
FAX: (713) 644-1400
metaltesters@msn.com

August 30, 2002

Page 1 of 1

Ferguson Laboratory
Michael D. Engelhardt
10100 Burnet Road, Bldg., 177
Austin, TX 78758-4497

P.O. No. Verbal/MDE
Report No. 02-1739

IDENTIFICATION: #NS3M

IMPACT TEST
10mm x 10mm CVN @ +70°F

		Foot/Pounds	Lateral Expansion (mils)	%Shear
Weld	(1)	20.0	14	20
	(4)	25.0	20	20
	(7)	22.0	19	20

IMPACT TEST
10mm x 10mm CVN @ 0°F

		Foot/Pounds	Lateral Expansion (mils)	%Shear
Weld	(2)	13.0	12	10
	(5)	12.0	10	10
	(8)	11.0	10	10

IMPACT TEST
10mm x 10mm CVN @ -20°F

		Foot/Pounds	Lateral Expansion (mils)	%Shear
Weld	(3)	8.0	8	10
	(6)	9.0	9	10
	(9)	7.0	6	10

Donald Derrick
Mechanical Testing Supervisor

sc

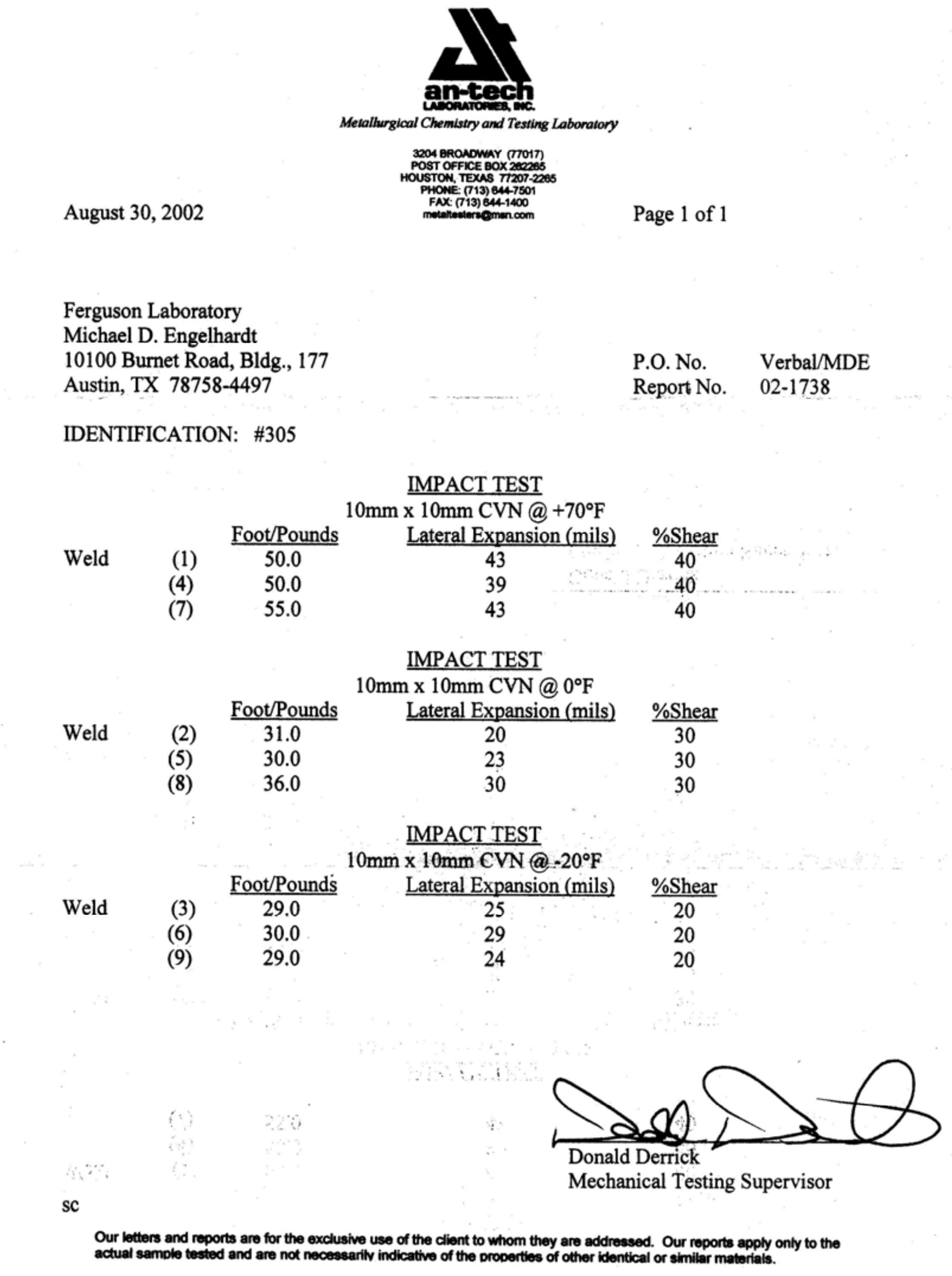

an-tech
LABORATORIES, INC.
Metallurgical Chemistry and Testing Laboratory

3204 BROADWAY (77017)
POST OFFICE BOX 262265
HOUSTON, TEXAS 77207-2265
PHONE: (713) 644-7501
FAX: (713) 644-1400
metaltesters@msn.com

August 30, 2002

Page 1 of 1

Ferguson Laboratory
Michael D. Engelhardt
10100 Burnet Road, Bldg., 177
Austin, TX 78758-4497

P.O. No. Verbal/MDE
Report No. 02-1738

IDENTIFICATION: #305

IMPACT TEST
10mm x 10mm CVN @ +70°F

		Foot/Pounds	Lateral Expansion (mils)	%Shear
Weld	(1)	50.0	43	40
	(4)	50.0	39	40
	(7)	55.0	43	40

IMPACT TEST
10mm x 10mm CVN @ 0°F

		Foot/Pounds	Lateral Expansion (mils)	%Shear
Weld	(2)	31.0	20	30
	(5)	30.0	23	30
	(8)	36.0	30	30

IMPACT TEST
10mm x 10mm CVN @ -20°F

		Foot/Pounds	Lateral Expansion (mils)	%Shear
Weld	(3)	29.0	25	20
	(6)	30.0	29	20
	(9)	29.0	24	20

Donald Derrick
Mechanical Testing Supervisor

sc

APPENDIX E

Welding Procedures

E.1 GENERAL

This appendix details the welding procedures used to construct the link-to-column connections of the sixteen specimens tested in this program. In this program, the individual links and columns were fabricated separately at the FSEL at the University of Texas at Austin. Subsequently, a commercial structural steel welder completed the welds at the link-to-column connections.

The welding procedures described herein are separated into the following three categories:

(a) The welds between the continuity plate and column;
(b) The welds between the shear tab and column flange; and
(c) The welds at the link-to-column connections.

Procedure (a) was the same for all specimens, except that for the PN- and MW-specimens, an FCAW procedure with an E70T-7 electrode was used, while for the FF- and NA-specimens, a procedure with an E70T-6 electrode was used. Procedures (b) and (c) were unique for each connection type. The improved welding details for the flange groove welds, specified by *FEMA-350* (2000) and *FEMA-353* (2000), were adopted for all but the PN-specimens.

Section E.2 discusses the specified welding procedures for each of the three categories listed above. The welding records are provided in Section E.3

E.2 SPECIFIED PROCEDURES

The specified welding procedures used for the link flange groove welds and beam web welds are discussed in this section. Table E1 categorizes the different welding procedures used for the fabrication in terms of the three categories discussed in Section E.1 and of the specimen type that adopted the procedure. The table refers to welding procedures reproduced in Figure E1 to Figure E9. Many of these procedures are nearly identical to those documented by Engelhardt *et al.* (2000a; 2000b).

Table E1 Summary of Welding Procedures

Category	Procedure	Specimen
Between the continuity plate and column	Figure E1	PN, MW
	Figure E2	FF, NA
Between the shear tab and column flange	Figure E3	PN
	Figure E4	MW
	Figure E5	FF
Link-to-column connections	Figure E6	PN
	Figure E7	MW
	Figure E8	FF
	Figure E9	NA

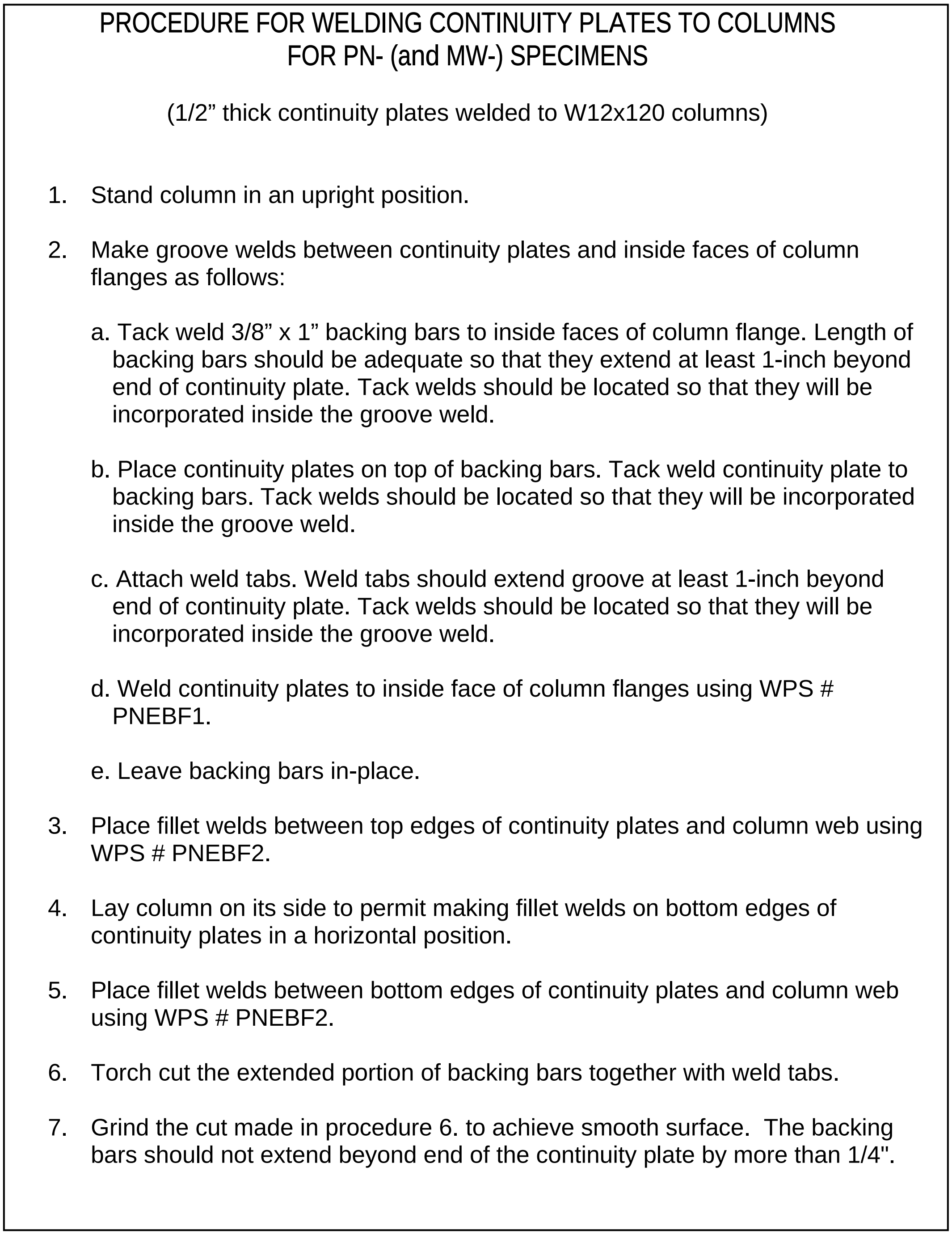

PROCEDURE FOR WELDING CONTINUITY PLATES TO COLUMNS
FOR PN- (and MW-) SPECIMENS

(1/2” thick continuity plates welded to W12x120 columns)

1. Stand column in an upright position.
2. Make groove welds between continuity plates and inside faces of column flanges as follows:
   a. Tack weld 3/8” x 1” backing bars to inside faces of column flange. Length of backing bars should be adequate so that they extend at least 1-inch beyond end of continuity plate. Tack welds should be located so that they will be incorporated inside the groove weld.
   b. Place continuity plates on top of backing bars. Tack weld continuity plate to backing bars. Tack welds should be located so that they will be incorporated inside the groove weld.
   c. Attach weld tabs. Weld tabs should extend groove at least 1-inch beyond end of continuity plate. Tack welds should be located so that they will be incorporated inside the groove weld.
   d. Weld continuity plates to inside face of column flanges using WPS # PNEBF1.
   e. Leave backing bars in-place.
3. Place fillet welds between top edges of continuity plates and column web using WPS # PNEBF2.
4. Lay column on its side to permit making fillet welds on bottom edges of continuity plates in a horizontal position.
5. Place fillet welds between bottom edges of continuity plates and column web using WPS # PNEBF2.
6. Torch cut the extended portion of backing bars together with weld tabs.
7. Grind the cut made in procedure 6. to achieve smooth surface. The backing bars should not extend beyond end of the continuity plate by more than 1/4".

Figure E1 Specified welding procedures for continuity plates in PN- (and MW-) Specimens

PRE-QUALIFIED WELDING PROCEDURE SPECIFICATION

COMPLETE JOINT PENETRATION SINGLE BEVEL GROOVE WELD FLAT POSITION WELD BETWEEN CONTINUITY PLATE AND COLUMN FLANGE

WPS # PNEBF1

Material Specification: ASTM A36, A572-Gr. 50, A992
Welding Process: Flux Cored Arc Welding – Self Shielded
Position of Welding: 1G
Filler Metal: AWS Specification: 5.20
AWS Classification: E70T-7
Brand Designation: Lincoln NR-311
Diameter: 3/32”
Current: DC – Electrode Negative

Joint Detail:

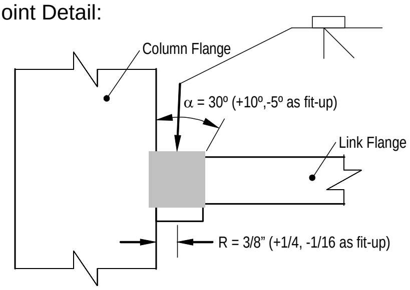

Minimum Preheat and Interpass Temperature:

Thickness	Temperature (deg F)
Up to 3/4″	50
Over 3/4″to 1-1/2″	50
Over 1-1/2″ to 2-1/2″	150
Over 2-1/2″	225

Maximum Interpass Temperature: 550° F

Joint Designation: TC-U4a-GF

Welding Procedure

Pass No.	Electrode Diameter	Wire Feed Speed (in / min)	Volts	Approx. Current (amps)	Travel Speed (in / min)
All as Req’d	3/32″	135 - 150	24 - 25	300 - 325	10 - 18
Electrical Stickout = 1-1/2”					

Weld Pass Sequence and Size

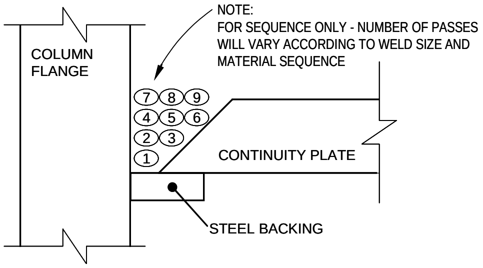

MAX. SINGLE PASS LAYER SIZE:
WIDTH: 5/8“ MAX
THICKNESS: 1/4" MAX

Weld Pass Technique

- Stringer passes only. No weaving or wash passes.
- Weld stringer passes using sequence shown above. Start the first stringer pass in each layer against the face of the column.
- Slag each pass thoroughly.
- Each stringer pass to melt at least 1/3 of the preceding pass for good fusion between passes and to prevent valley between passes which are hard to clean.

Figure E1 Specified welding procedures for continuity plates in PN- (and MW-) Specimens (Continued)

PRE-QUALIFIED WELDING PROCEDURE SPECIFICATION

FILLET WELD
FLAT POSITION WELD BETWEEN CONTINUITY PLATE AND COLUMN FLANGE

WPS # PNEBF2

Material Specification: ASTM A36, A572-Gr. 50, A992
Welding Process: Flux Cored Arc Welding – Self Shielded
Position of Welding: 1G
Filler Metal: AWS Specification: 5.20
AWS Classification: E70T-7
Brand Designation: Lincoln NR-311
Diameter: 3/32"
Current: DC – Electrode Negative

Minimum Preheat and Interpass Temperature:

Thickness	Temperature (deg F)
Up to 3/4″	50
Over 3/4″to 1-1/2″	50
Over 1-1/2″ to 2-1/2″	150
Over 2-1/2″	225

Maximum Interpass Temperature: 550° F

Joint Detail:

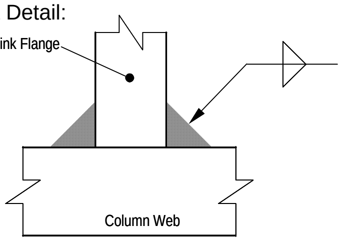

Welding Procedure

Pass No.	Electrode Diameter	Wire Feed Speed (in / min)	Volts	Approx. Current (amps)	Travel Speed (in / min)
All as Req'd	3/32″	135 - 150	24 - 25	300 - 325	10 - 18
Electrical Stickout = 1-1/2"					

Figure E1 Specified welding procedures for continuity plates in PN- (and MW-) Specimens (Continued)

PROCEDURE FOR WELDING CONTINUITY PLATES TO COLUMNS FOR FF- and NA-SPECIMENS

(1/2” thick continuity plates welded to W12x120 columns)

1. Stand column in an upright position.

2. Make groove welds between continuity plates and inside faces of column flanges as follows:

    a. Tack weld 3/8” x 1” backing bars to inside faces of column flange. Length of backing bars should be adequate so that they extend at least 1-inch beyond end of continuity plate. Tack welds should be located so that they will be incorporated inside the groove weld.

    b. Place continuity plates on top of backing bars. Tack weld continuity plate to backing bars. Tack welds should be located so that they will be incorporated inside the groove weld.

    c. Attach weld tabs. Weld tabs should extend groove at least 1-inch beyond end of continuity plate. Tack welds should be located so that they will be incorporated inside the groove weld.

    d. Weld continuity plates to inside face of column flanges using WPS # MWEBF1.

    e. Leave backing bars in-place.

3. Place fillet welds between top edges of continuity plates and column web using WPS # MWEBF2.

4. Reposition column upside-down to permit making fillet welds on bottom edges of continuity plates in a horizontal position.

5. Place fillet welds between bottom edges of continuity plates and column web using WPS # MWEBF2.

6. Arc gauge the extended portion of backing bars together with weld tabs.

7. Grind the cut made in procedure 6. to achieve smooth surface. The backing bars should not extend beyond end of the continuity plate by more than 1/4".

Figure E2 Specified welding procedures for continuity plates in FF- and NA-Specimens

PRE-QUALIFIED WELDING PROCEDURE SPECIFICATION

COMPLETE JOINT PENETRATION SINGLE BEVEL GROOVE WELD
FLAT POSITION WELD BETWEEN CONTINUITY PLATE AND COLUMN FLANGE

WPS # MWEBF1

Material Specification: ASTM A36, A572-Gr. 50, A992
Welding Process: Flux Cored Arc Welding – Self Shielded
Position of Welding: 1G
Filler Metal: AWS Specification: 5.20
AWS Classification: E70T-6
Brand Designation: Lincoln NR-305
Diameter: 3/32”
Current: DC – Electrode Positive

Minimum Preheat and Interpass Temperature:

Thickness	Temperature (deg F)
Up to 3/4″	50
Over 3/4″to 1-1/2″	50
Over 1-1/2″ to 2-1/2″	150
Over 2-1/2″	225

Maximum Interpass Temperature: 550° F

Joint Designation: TC-U4a-GF

Joint Detail:

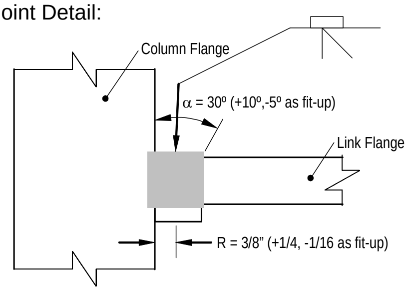

Welding Procedure

Pass No.	Electrode Diameter	Wire Feed Speed (in / min)	Volts	Approx. Current (amps)	Travel Speed (in / min)
All as Req’d	3/32″	240 - 300	25 - 29	390 - 475	9 - 15
Electrical Stickout = 1-1/2” to 2-1/2”					

Weld Pass Sequence and Size

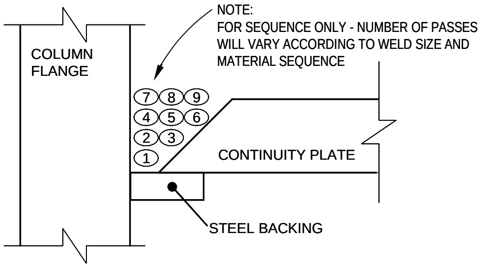

MAX. SINGLE PASS LAYER SIZE:
WIDTH: 5/8" MAX
THICKNESS: 1/4" MAX

Weld Pass Technique

- Stringer passes only. No weaving or wash passes.
- Weld stringer passes using sequence shown above. Start the first stringer pass in each layer against the face of the column.
- Slag each pass thoroughly.
- Each stringer pass to melt at least 1/3 of the preceding pass for good fusion between passes and to prevent valley between passes which are hard to clean.

Figure E2 Specified welding procedures for continuity plates in FF- and NA-Specimens (Continued)

PRE-QUALIFIED WELDING PROCEDURE SPECIFICATION

FILLET WELD
FLAT POSITION WELD BETWEEN CONTINUITY PLATE AND COLUMN FLANGE

WPS # MWEBF2

Material Specification: ASTM A36, A572-Gr. 50, A992
Welding Process: Flux Cored Arc Welding – Self Shielded
Position of Welding: 2F
Filler Metal: AWS Specification: 5.20
AWS Classification: E70T-6
Brand Designation: Lincoln NR-305
Diameter: 3/32”
Current: DC – Electrode Positive

Joint Detail:

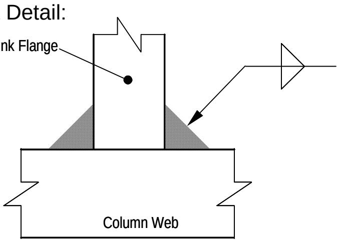

Minimum Preheat and Interpass Temperature:

Thickness	Temperature (deg F)
Up to 3/4″	50
Over 3/4″to 1-1/2″	50
Over 1-1/2″ to 2-1/2″	150
Over 2-1/2″	225

Maximum Interpass Temperature: 550° F

Welding Procedure

Pass No.	Electrode Diameter	Wire Feed Speed (in / min)	Volts	Approx. Current (amps)	Travel Speed (in / min)
All as Req’d	3/32″	240 - 300	25 - 29	390 - 475	9 - 15
Electrical Stickout = 1-1/2” – 2-1/2”					

Figure E2 Specified welding procedures for continuity plates in FF- and NA-Specimens (Continued)

PROCEDURE FOR WELDING SHEAR TABS TO COLUMNS FOR PN-SPECIMENS

(3/8” thick shear tabs welded to flange of W12x120 columns)

1. Lay column on its side with flange surface facing upwards, to permit making fillet welds of shear tab in a horizontal position.
2. Place fillet welds between the two sides of shear tab and column flange using WPS # PNEBF3.

Figure E3 Shear tab welds for PN-connection

NOTE: WPS # PNEBF3 is identical to WPS # PNEBF2 shown in Figure E1, by replacing the link flange with shear tab, and column web with column flange.

PROCEDURE FOR WELDING SHEAR TABS TO COLUMNS FOR MW-SPECIMENS

(3/8” thick shear tabs welded to flange of W12x120 columns)

1. Lay column on its side with flange surface facing upwards, to permit making fillet welds of shear tab in a horizontal position.

2. Place fillet welds between the two sides of shear tab and column flange using WPS # MWEBF3.

PRE-QUALIFIED WELDING PROCEDURE SPECIFICATION

FILLET WELD
FLAT POSITION WELD BETWEEN LINK WEB AND SHEAR TAB

WPS # MWEBF3

Material Specification: ASTM A36, A572-Gr. 50, A992
Welding Process: Flux Cored Arc Welding – Self Shielded
Position of Welding: 2G
Filler Metal: AWS Specification: 5.20
AWS Classification: E71T-8
Brand Designation: Lincoln NR-232
Diameter: 0.072”
Current: DC - Electrode Negative

Joint Detail:

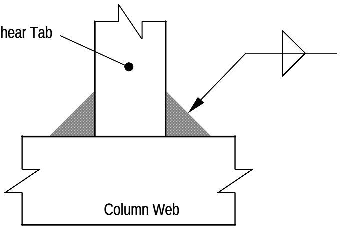

Minimum Preheat and Interpass Temperature:

Thickness	Temperature (deg F)
Up to 3/4″	50
Over 3/4″to 1-1/2″	50
Over 1-1/2″ to 2-1/2″	150
Over 2-1/2″	225

Maximum Interpass Temperature: 550° F

Welding Procedure

Pass No.	Electrode Diameter	Wire Feed Speed (in / min)	Volts	Approx. Current (amps)	Travel Speed (in / min)
All as Req’d	0.072”	155 - 170	19 - 23	240 - 255	8 - 12
Distance from contact tube to work = 0.5 to 1”					

Figure E4 Shear tab welds for MW-connection

PROCEDURE FOR WELDING SHEAR TABS TO COLUMNS FOR FREE FLANGE EBF SPECIMENS

(3/8" thick shear tabs welded to flange of W12x120 columns)

1. Lay column on its side with flange surface facing upwards, to permit making fillet welds of shear tab in a horizontal position.

2. Place groove welds between the two bevels of shear tab and column flange using WPS # FFEBF1. Procedure should be in accordance with the following:

   a. Tack weld shear tab in upright position on top of column flange. Tack welds should be located so that they will be incorporated inside the groove weld.

   b. Weld one bead on one side of the shear tab.

   c. Back gauge root of the first bead thoroughly from the other side.

   d. Weld one bead on the other side of the shear tab.

   e. Continue placing beads on alternate sides of the shear tab in accordance to (d) above until weld is completed.

Figure E5 Shear tab welds for FF-connection

PRE-QUALIFIED WELDING PROCEDURE SPECIFICATION

COMPLETE JOINT PENETRATION DOUBLE BEVEL GROOVE WELD
FLAT POSITION WELD BETWEEN SHEAR TAB AND COLUMN FLANGE

WPS # FFEBF1

Material Specification: ASTM A36, A572-Gr. 50, A992
Welding Process: Flux Cored Arc Welding – Self Shielded
Position of Welding: 2F
Filler Metal: AWS Specification: 5.20
AWS Classification: E70T-6
Brand Designation: Lincoln NR-305
Diameter: 3/32”
Current: DC – Electrode Positive

Joint Detail:

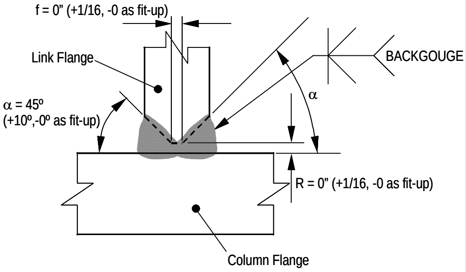

Minimum Preheat and Interpass Temperature:

Thickness	Temperature (deg F)
Up to 3/4″	50
Over 3/4″to 1-1/2″	50
Over 1-1/2″ to 2-1/2″	150
Over 2-1/2″	225

Maximum Interpass Temperature: 550° F

Joint Designation:

Welding Procedure

Pass No.	Electrode Diameter	Wire Feed Speed (in / min)	Volts	Approx. Current (amps)	Travel Speed (in / min)
All as Req’d	3/32″	240 - 300	25 - 29	390 - 475	9 - 15
Electrical Stickout = 1-1/2” – 2-1/2”					

Figure E5 Shear tab welds for FF-connection (Continued)

PROCEDURE FOR WELDING LINK-TO-COLUMN CONNECTION FOR PN-SPECIMENS

(W18x40 link members welded to W12x120 columns)

1. Install erection bolts in shear tab to connect link to shear tab. Fully tension bolts using turn of nut method.

2. Tack weld 3/8” x 1” backing bars to inside faces of link flange and to outside face of column flange. Length of backing bars should be adequate so that they extend at least 1-inch beyond end of link flange. The backing bar should be continuous over the entire length of the groove weld including the area of the weld tab and link web. Tack welds should be located so that they will be incorporated inside the groove weld.

3. Attach weld tabs. Weld tabs should extend groove at least 1-inch beyond end of continuity plate. Tack welds should be located so that they will be incorporated inside the groove weld.

4. Make groove weld between link top flange and outside face of column flange using WPS # PNEBF4. Each weld bead should start on a weld tab and end on the opposite weld tab.

5. Make groove weld between link bottom flange and outside face of column flange using WPS # PNEBF4. Welding at the bottom flange should be in accordance with the following:

   a. Weld one bead on one side of the bottom flange, starting at the weld access hole. After arc is initiated, travel should progress toward the edge of the flange. The bead should be terminated on the weld tab. The start of the bead in the weld access hole should be visually inspected to ensure fusion, soundness, freedom from slag inclusions, and excess porosity. The resulting bead profile should be suitable for obtaining good fusion by the subsequent pass to be initiated on the opposite side of the beam web. If the profile is not conductive to good fusion, the start of the weld bead should be gauged, chipped, or otherwise prepared to ensure food fusion.

   b. Weld one bead on the other side of the bottom flange. Follow same instructions as in (a).

Figure E6 Link-to-column connection welds in PN-connection

PROCEDURE FOR WELDING LINK-TO-COLUMN CONNECTION FOR PN-SPECIMENS

(W18x40 link members welded to W12x120 columns)

c. Continue placing beads on alternate sides of the link web in accordance to (a) and (b) above until weld in completed.

d. Leave backing bars and weld tabs in place.

6. Make groove weld between link web and outside face of column flange using WPS # PNEBF5.

Figure E6 Link-to-column connection welds in PN-connection (Continued)

PRE-QUALIFIED WELDING PROCEDURE SPECIFICATION

COMPLETE JOINT PENETRATION SINGLE BEVEL GROOVE WELD FLAT POSITION WELD BETWEEN LINK FLANGE AND COLUMN FLANGE

WPS # PNEBF4

Material Specification: ASTM A36, A572-Gr. 50, A992
Welding Process: Flux Cored Arc Welding – Self Shielded
Position of Welding: 1G
Filler Metal: AWS Specification: 5.20
AWS Classification: E70T-4
Brand Designation: Lincoln NS-3M
Diameter: 0.120”
Current: DC + Electrode Positive

Joint Detail:

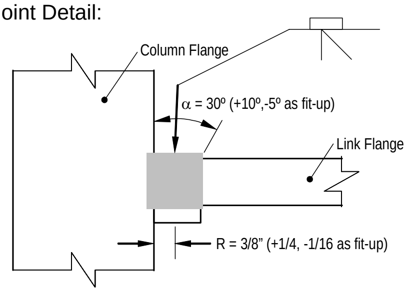

Minimum Preheat and Interpass Temperature:

Thickness	Temperature (deg F)
Up to 3/4″	50
Over 3/4″to 1-1/2″	50
Over 1-1/2″ to 2-1/2″	150
Over 2-1/2″	225

Maximum Interpass Temperature: 550° F

Joint Designation: TC-U4a-GF

Welding Procedure

Pass No.	Electrode Diameter	Wire Feed Speed (in / min)	Volts	Approx. Current (amps)	Travel Speed (in / min)
All as Req’d	0.120”	160 - 190	29 - 32	495 - 600	11 - 18
Electrical Stickout = 2-3/4”					

Weld Pass Sequence and Size

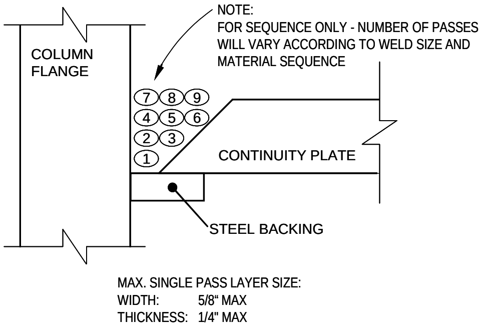

Weld Pass Technique

- Stringer passes only. No weaving or wash passes.
- Weld stringer passes using sequence shown above. Start the first stringer pass in each layer against the face of the column.
- Slag each pass thoroughly.
- Each stringer pass to melt at least 1/3 of the preceding pass for good fusion between passes and to prevent valley between passes which are hard to clean.

Figure E6 Link-to-column connection welds in PN-connection (Continued)

PRE-QUALIFIED WELDING PROCEDURE SPECIFICATION

COMPLETE JOINT PENETRATION SINGLE BEVEL GROOVE WELD
VERTICAL POSITION WELD BETWEEN LINK WEB AND COLUMN FLANGE

WPS # PNEBF5

Material Specification: ASTM A36, A572-Gr. 50, A992
Welding Process: Flux Cored Arc Welding – Self Shielded
Position of Welding: 3G
Filler Metal: AWS Specification: 5.20
AWS Classification: E71T-8
Brand Designation: Lincoln NR-232
Diameter: 0.072”
Current: DC - Electrode Negative

Minimum Preheat and Interpass Temperature:

Thickness	Temperature (deg F)
Up to 3/4″	50
Over 3/4″to 1-1/2″	50
Over 1-1/2″ to 2-1/2″	150
Over 2-1/2″	225

Maximum Interpass Temperature: 550° F

Joint Detail:

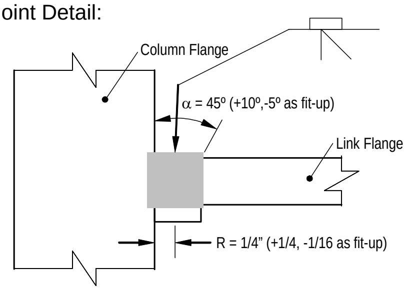

Welding Procedure

Pass No.	Electrode Diameter	Wire Feed Speed (in / min)	Volts	Approx. Current (amps)	Travel Speed (in / min)
All as Req’d	0.072”	155 - 170	19 - 23	240 - 255	8 - 12
Distance from contact tube to work = 0.5 to 1”					

Figure E6 Link-to-column connection welds in PN-connection (Continued)

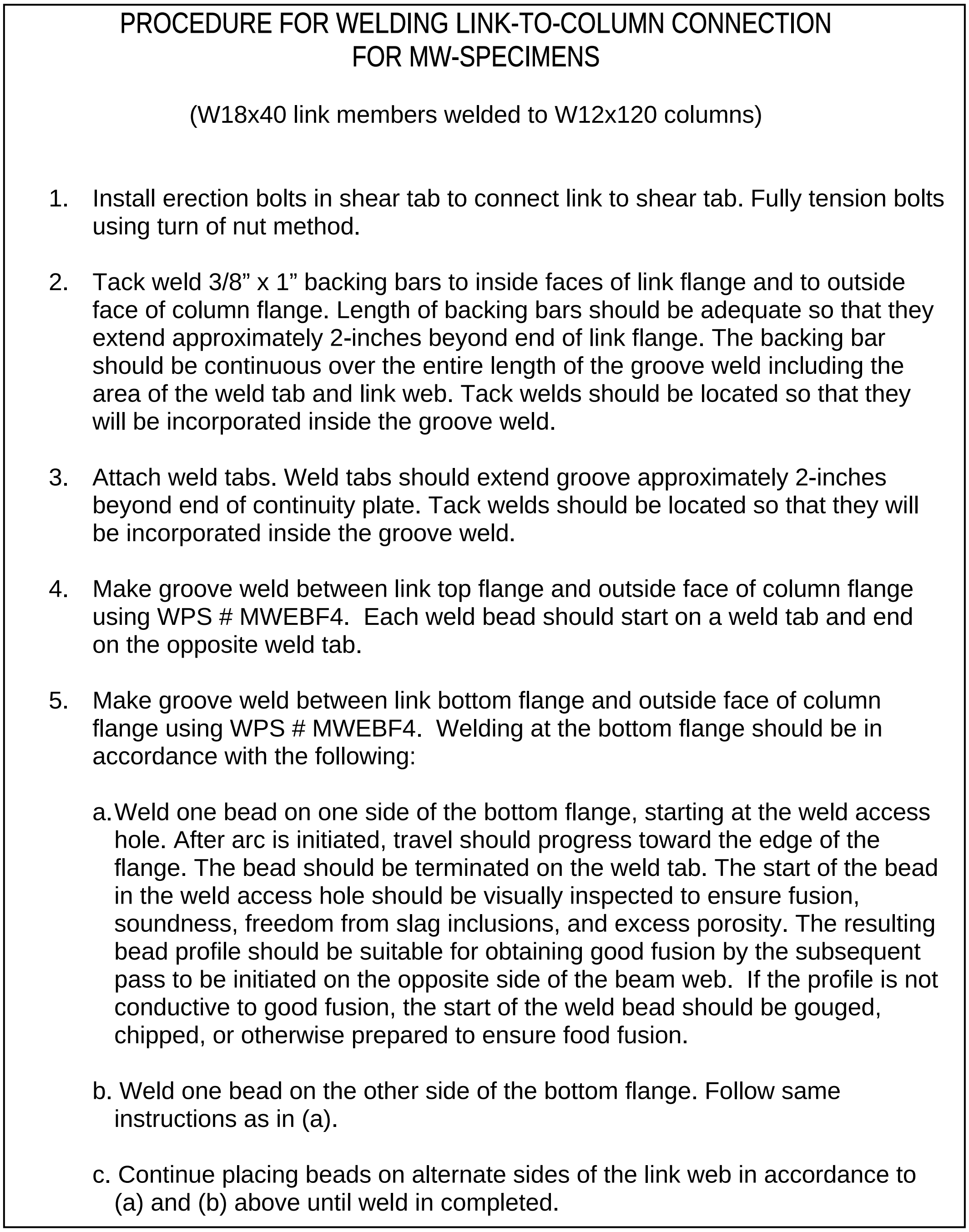

PROCEDURE FOR WELDING LINK-TO-COLUMN CONNECTION FOR MW-SPECIMENS

(W18x40 link members welded to W12x120 columns)

1. Install erection bolts in shear tab to connect link to shear tab. Fully tension bolts using turn of nut method.

2. Tack weld 3/8” x 1” backing bars to inside faces of link flange and to outside face of column flange. Length of backing bars should be adequate so that they extend approximately 2-inches beyond end of link flange. The backing bar should be continuous over the entire length of the groove weld including the area of the weld tab and link web. Tack welds should be located so that they will be incorporated inside the groove weld.

3. Attach weld tabs. Weld tabs should extend groove approximately 2-inches beyond end of continuity plate. Tack welds should be located so that they will be incorporated inside the groove weld.

4. Make groove weld between link top flange and outside face of column flange using WPS # MWEBF4. Each weld bead should start on a weld tab and end on the opposite weld tab.

5. Make groove weld between link bottom flange and outside face of column flange using WPS # MWEBF4. Welding at the bottom flange should be in accordance with the following:

   a. Weld one bead on one side of the bottom flange, starting at the weld access hole. After arc is initiated, travel should progress toward the edge of the flange. The bead should be terminated on the weld tab. The start of the bead in the weld access hole should be visually inspected to ensure fusion, soundness, freedom from slag inclusions, and excess porosity. The resulting bead profile should be suitable for obtaining good fusion by the subsequent pass to be initiated on the opposite side of the beam web. If the profile is not conductive to good fusion, the start of the weld bead should be gouged, chipped, or otherwise prepared to ensure food fusion.

   b. Weld one bead on the other side of the bottom flange. Follow same instructions as in (a).

   c. Continue placing beads on alternate sides of the link web in accordance to (a) and (b) above until weld in completed.

Figure E7 Link-to-column connection welds in MW-connection

PROCEDURE FOR WELDING LINK-TO-COLUMN CONNECTION FOR MW-SPECIMENS

(W18x40 link members welded to W12x120 columns)

6. Remove the backing bar at the beam bottom flange groove weld and backgouge root of CJP groove weld sound to metal. Care should be taken so as not to damage the base metal when removing the backing bar and during backgouging. Any pits, gouges, discontinuities and slag pockets discovered at the root of the groove weld should be grounded out. Reweld root of CJP groove weld from underneath the weld and place a 5/16” fillet weld using WPS # MWEBF5.

7. Place a 5/16” fillet weld between the backing bar and the column flange at the top beam flange groove weld using WPS # MWEBF6.

8. Remove weld tabs from both the top and bottom beam flange groove welds. Grind smooth and inspect ground surfaces for discontinuities. Inclusions 1/16” or less in depth shall be removed by grinding. Deeper indications should be removed and replaced by welding.

9. Make groove weld between link web and outside face of column flange using WPS # PNEBF5.

Figure E7 Link-to-column connection welds in MW-connection (Continued)

NOTE: WPS # PNEBF5 is shown in Figure E6, and is not repeated here.

PRE-QUALIFIED WELDING PROCEDURE SPECIFICATION

COMPLETE JOINT PENETRATION SINGLE BEVEL GROOVE WELD
FLAT POSITION WELD BETWEEN LINK FLANGE AND COLUMN FLANGE

WPS # MWEBF4

Material Specification: ASTM A36, A572-Gr. 50, A992
Welding Process: Flux Cored Arc Welding – Self Shielded
Position of Welding: 1G
Filler Metal: AWS Specification: 5.20
AWS Classification: E70T-6
Brand Designation: Lincoln NR-305
Diameter: 3/32”
Current: DC – Electrode Positive

Joint Detail:

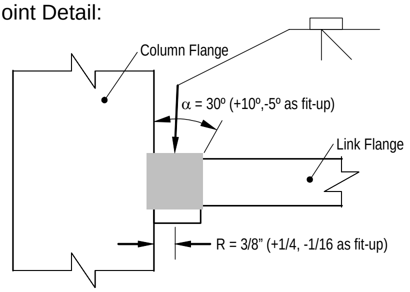

Minimum Preheat and Interpass Temperature:

Thickness	Temperature (deg F)
Up to 3/4″	50
Over 3/4″to 1-1/2″	50
Over 1-1/2″ to 2-1/2″	150
Over 2-1/2″	225

Maximum Interpass Temperature: 550° F

Joint Designation: TC-U4a-GF

Welding Procedure

Pass No.	Electrode Diameter	Wire Feed Speed (in / min)	Volts	Approx. Current (amps)	Travel Speed (in / min)
All as Req’d	3/32”	240 - 300	25 - 29	390 - 475	9 - 15
Distance from contact tube to work = 1-1/2 to 2-1/2”					

Weld Pass Sequence and Size

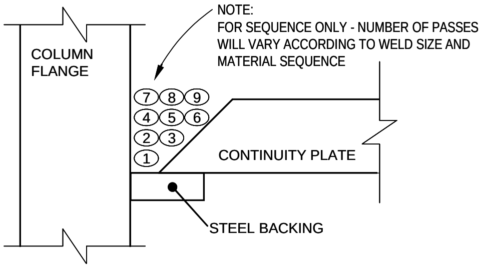

NOTE:
FOR SEQUENCE ONLY - NUMBER OF PASSES WILL VARY ACCORDING TO WELD SIZE AND MATERIAL SEQUENCE

MAX. SINGLE PASS LAYER SIZE:
WIDTH: 5/8“ MAX
THICKNESS: 1/4" MAX

Weld Pass Technique

- Stringer passes only. No weaving or wash passes.
- Weld stringer passes using sequence shown above. Start the first stringer pass in each layer against the face of the column.
- Slag each pass thoroughly.
- Each stringer pass to melt at least 1/3 of the preceding pass for good fusion between passes and to prevent valley between passes which are hard to clean.

Figure E7 Link-to-column connection welds in MW-connection (Continued)

PRE-QUALIFIED WELDING PROCEDURE SPECIFICATION

OVERHEAD REINFORCING FILLET WELD FOR BACKGOUGED CJP GROOVE WELD

WPS # MWEBF5

Material Specification: ASTM A36, A572-Gr. 50, A992
Welding Process: Flux Cored Arc Welding – Self Shielded
Position of Welding: 4F
Filler Metal: AWS Specification: 5.20
AWS Classification: E71T-8
Brand Designation: Lincoln NR-232
Diameter: 0.072”
Current: DC – Electrode Negative

Minimum Preheat and Interpass Temperature:

Thickness	Temperature (deg F)
Up to 3/4″	50
Over 3/4″to 1-1/2″	50
Over 1-1/2″ to 2-1/2″	150
Over 2-1/2″	225

Maximum Interpass Temperature: 550° F

Joint Detail:

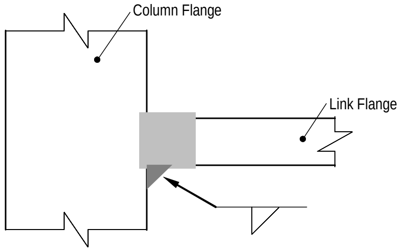

Welding Procedure

Pass No.	Electrode Diameter	Wire Feed Speed (in / min)	Volts	Approx. Current (amps)	Travel Speed (in / min)
All as Req’d	0.072”	155 - 170	19 - 23	240 - 275	8 - 12
Distance from contact tube to work = 0.5 to 1”					

Figure E7 Link-to-column connection welds in MW-connection (Continued)

PRE-QUALIFIED WELDING PROCEDURE SPECIFICATION

OVERHEAD FILLET WELD FOR WELDING BACKING BAR TO COLUMN FLANGE

WPS # MWEBF6

Material Specification: ASTM A36, A572-Gr. 50, A992
Welding Process: Flux Cored Arc Welding – Self Shielded
Position of Welding: 4F

Filler Metal:	AWS Specification:	5.20
	AWS Classification:	E71T-8
	Brand Designation:	Lincoln NR-232
	Diameter:	0.072”
Current:	DC – Electrode Negative	

Joint Detail:

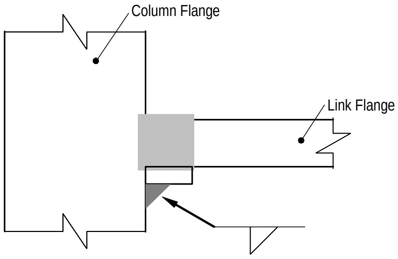

Minimum Preheat and Interpass Temperature:

Thickness	Temperature (deg F)
Up to 3/4″	50
Over 3/4″to 1-1/2″	50
Over 1-1/2″ to 2-1/2″	150
Over 2-1/2″	225

Maximum Interpass Temperature: 550° F

Welding Procedure

Pass No.	Electrode Diameter	Wire Feed Speed (in / min)	Volts	Approx. Current (amps)	Travel Speed (in / min)
All as Req’d	0.072”	155 - 170	19 - 23	240 - 255	8 - 12
Distance from contact tube to work = 0.5 to 1”					

Figure E7 Link-to-column connection welds in MW-connection (Continued)

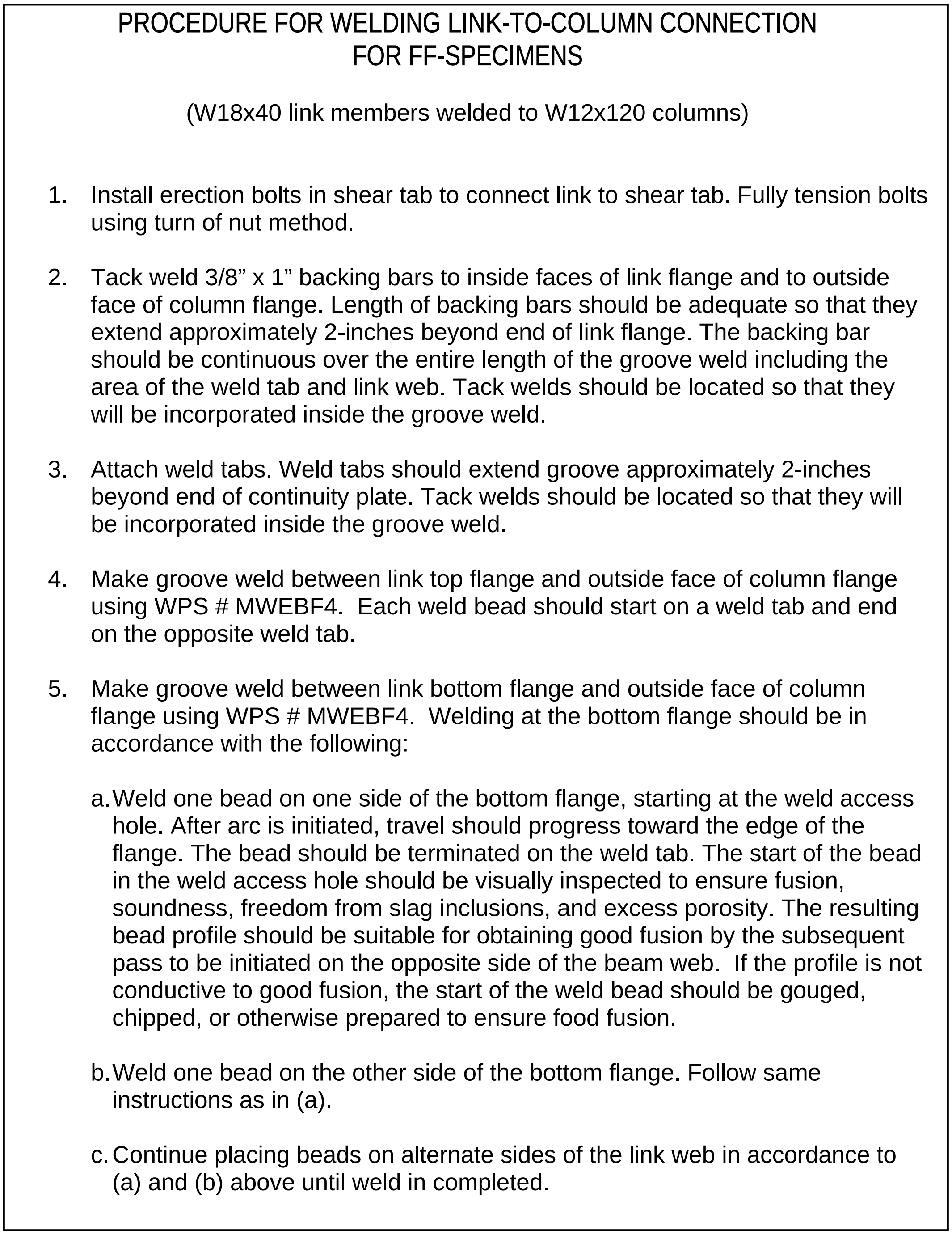

PROCEDURE FOR WELDING LINK-TO-COLUMN CONNECTION FOR FF-SPECIMENS

(W18x40 link members welded to W12x120 columns)

1. Install erection bolts in shear tab to connect link to shear tab. Fully tension bolts using turn of nut method.

2. Tack weld 3/8" x 1" backing bars to inside faces of link flange and to outside face of column flange. Length of backing bars should be adequate so that they extend approximately 2-inches beyond end of link flange. The backing bar should be continuous over the entire length of the groove weld including the area of the weld tab and link web. Tack welds should be located so that they will be incorporated inside the groove weld.

3. Attach weld tabs. Weld tabs should extend groove approximately 2-inches beyond end of continuity plate. Tack welds should be located so that they will be incorporated inside the groove weld.

4. Make groove weld between link top flange and outside face of column flange using WPS # MWEBF4. Each weld bead should start on a weld tab and end on the opposite weld tab.

5. Make groove weld between link bottom flange and outside face of column flange using WPS # MWEBF4. Welding at the bottom flange should be in accordance with the following:

   a. Weld one bead on one side of the bottom flange, starting at the weld access hole. After arc is initiated, travel should progress toward the edge of the flange. The bead should be terminated on the weld tab. The start of the bead in the weld access hole should be visually inspected to ensure fusion, soundness, freedom from slag inclusions, and excess porosity. The resulting bead profile should be suitable for obtaining good fusion by the subsequent pass to be initiated on the opposite side of the beam web. If the profile is not conductive to good fusion, the start of the weld bead should be gouged, chipped, or otherwise prepared to ensure food fusion.

   b. Weld one bead on the other side of the bottom flange. Follow same instructions as in (a).

   c. Continue placing beads on alternate sides of the link web in accordance to (a) and (b) above until weld in completed.

Figure E8 Link-to-column connection welds in FF-connection

PROCEDURE FOR WELDING LINK-TO-COLUMN CONNECTION FOR FF-SPECIMENS

(W18x40 link members welded to W12x120 columns)

6. Remove the backing bar at the beam bottom flange groove weld and backgouge root of CJP groove weld sound to metal. Care should be taken so as not to damage the base metal when removing the backing bar and during backgouging. Any pits, gouges, discontinuities and slag pockets discovered at the root of the groove weld should be grounded out. Reweld root of CJP groove weld from underneath the weld and place a 5/16” fillet weld using WPS # MWEBF5.

7. Place a 5/16” fillet weld between the backing bar and the column flange at the top beam flange groove weld using WPS # MWEBF6.

8. Remove weld tabs from both the top and bottom beam flange groove welds. Grind smooth and inspect ground surfaces for discontinuities. Inclusions 1/16” or less in depth shall be removed by grinding. Deeper indications should be removed and replaced by welding.

9. Make groove weld between link web and outside face of column flange using WPS PNEBF5.

10. Place a fillet weld between link web and edge of shear tab using WPS # FFEBF2.

Figure E8 Link-to-column connection welds in FF-connection (Continued)

CAUTION: For Specimens FFS-RLP and FFSL-RLP, step 9 was altered as follows: “Make groove weld between link web and shear tab using WPS PNEBF5.”

NOTE: WPS # PNEBF5 is shown in Figure E6. WPS # MWEBF3, WPS # MWEBF4, and WPS # MWEBF5 are shown in Figure E7. WPS # FFEBF2 is similar to WPS # PNEBF5, shown in Figure E6. The above mentioned pre-qualified welding procedures are not repeated here.

PROCEDURE FOR WELDING LINK-TO-COLUMN CONNECTION FOR NA-SPECIMENS

(W18x40 link members welded to W12x120 columns)

1. Lay column in horizontal position. Then, place link in upright position on top of column.

2. Tack weld link web to column flange. Tack welds should be located so that they will be incorporated inside the groove weld.

3. Place 1/4" fillet welds between the two faces of link web and outside face of column flange using WPS # NAEBF1. The fillet weld should not exceed 9 inches in length, and should be centered at the mid-depth of the link.

4. Reposition link-to-column subassemblage so that the column is in upright position, and top flange of the link faces up.

5. Tack weld 3/8” x 1” backing bars to inside faces of link flange and to outside face of column flange. Length of backing bars should be adequate so that they extend approximately 2-inches beyond end of link flange. The backing bar should be continuous over the entire length of the groove weld including the area of the weld tab and link web. The backing bar should be adequate in geometry to cover the bevel extended from the link flange into the link web. Tack welds should be located so that they will be incorporated inside the groove weld.

5. Attach weld tabs. Weld tabs should extend groove approximately 2-inches beyond end of continuity plate. Tack welds should be located so that they will be incorporated inside the groove weld.

7. Fill in the bevel extended in the link web with weld metal.

8. Make groove weld between link top flange and outside face of column flange using WPS # MWEBF4. Each weld bead should start on a weld tab and end on the opposite weld tab.

9. Place a 5/16” fillet weld between the backing bar and the column flange at the top beam flange groove weld using WPS # MWEBF6.

Figure E9 Link-to-column connection welds in NA-connection

PROCEDURE FOR WELDING LINK-TO-COLUMN CONNECTION FOR NA-SPECIMENS

(W18x40 link members welded to W12x120 columns)

10. Reposition link-to-column subassemblage so that the column is in upright position, and bottom flange of the link faces up.
11. Repeat procedures 5 to 9 for the groove weld between the link bottom flange and column flange.
12. Complete fillet weld between the two faces of link web and outside face of column flange using WPS # NAEBF 1.
13. Remove weld tabs from both the top and bottom beam flange groove welds. Grind smooth and inspect ground surfaces for discontinuities. Inclusions 1/16" or less in depth shall be removed by grinding. Deeper indications should be removed and replaced by welding.

Figure E9 Link-to-column connection welds in NA-connection (Continued)

NOTE: WPS # NAEBF1 is identical to WPS # MWEBF3 (See Figure E4) by replacing the shear tab with the link web. WPS # PNEBF5 is shown in Figure E7. The above mentioned pre-qualified welding procedures are not repeated here.

E.3 WELDING RECORDS

E.3.1 Notes on actual procedures

The same welder completed the link-to-column connection for all sixteen specimens. The same welding equipment was used for all welds. The welder and equipment were as follows:

Welder:	Dwayne Schuessler S&S Welding Company Spicewood, Texas
Equipment:	Lincoln IdealArc DC-600 power supply Lincoln LN-9 Wire Feeder with K116 gun

The actual welding parameters recorded during welding of the flat position beam flange CJP groove welds and the vertical position beam web CJP groove welds are summarized in Tables E2 and E3, respectively. Also listed in the tables are the corresponding parameters in the specified procedure (See Section E.2 for details). The wire feed speed and voltage was read from a digital readout in the LN-9 Wire Feeder. The current was read from a meter on the IdealArc DC-600 power supply. The travel speed was estimated by measuring the time required to complete a pass, and then dividing the time by the approximate length of the pass. The electrical stickout was estimated by the welder.

The specified welding procedures were mostly followed in the actual construction of the test specimens. However, the welding parameters used by the welder were somewhat different than in the specified procedure due to the preferences of the welder. Most notably, the wire feed speed for the E70T-6 electrode was set slower than suggested in the specified procedure.

Table E2 Welding records for link flange CJP groove welds

Specimen	Electrode	Diameter (in)	Wire Feed Speed (in/min)	Volts	Approx. Current (Amps)	Travel Speed (in/min)	Electrical Stickout (in)
PNS	E70T-4	0.120	175	30	570	15 – 20	2-3/4
PNI							
PNM							
MWS	E70T-6	3/32	190	24	400 – 450	8 – 15	2
MWI							
MWM							
FFS							
FFI			186	23	420	8 – 15	
FFM			160	22.5	400	7 – 9	
NAS			186	23	420	8 – 15	
NAI			160	22.5	400	7 - 9	
NAM							
FFS-RLP							
FFSL-RLP							
NAS-RLP							
NASL-RLP							
Mockup							
Specified Procedure	E70T-4	0.120	160 – 190	29 – 32	495 – 600	11 – 18	2-3/4
	E70T-6	3/32	240 – 300	25 – 29	390 – 475	9 – 15	1-1/2 to 2-1/2

Table E3 Welding records for link web CJP groove welds

Specimen	Electrode	Diameter (in)	Wire Feed Speed (in/min)	Volts	Approx. Current (Amps)	Travel Speed (in/min)	Electrical Stickout (in)
PNS	E71T-8	0.072	136	21	190 - 240	6 - 10	1/2 to 1
PNI							
PNM							
MWS			130	21	200 – 240	5 – 7	
MWI							
MWM							
FFS			98	21	200	3 – 6	
FFI			110	21	200	3 - 6	
FFM							
FFS-RLP			95	21	150 – 180	N.A.	
FFSL-RLP							
Mockup			140	21	N.A.	7	
Specified Procedure	E71T-8	0.072	155 – 170	19 – 23	240 – 275	8 – 12	1/2 to 1

Figure E10 shows the weld profile for each link flange CJP groove weld. The numbers in the figure indicates the sequence of weld beads placed. On average, three to four passes were required to complete the CJP groove weld. Some of the weld paths were full of porosities, and therefore, were removed extensively by grinding. For example, the first four weld beads in the top flange of Specimen PNS were repeatedly removed before the following beads were placed. Other such examples include the top and bottom flanges of Specimens MWS and MWI, and the top flange of Specimen FFS-RLP.

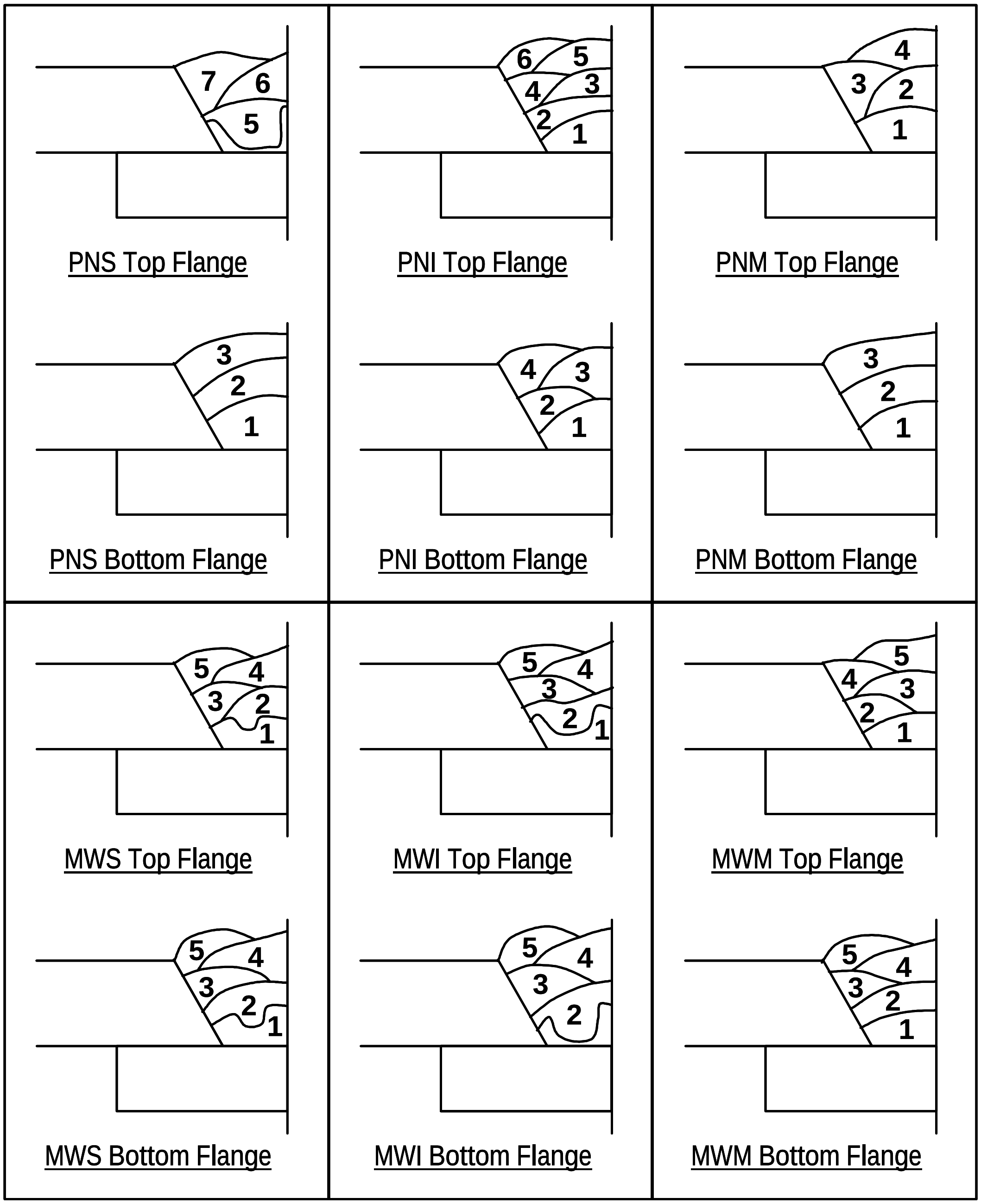

PNS Top Flange

PNI Top Flange

PNM Top Flange

PNS Bottom Flange

PNI Bottom Flange

PNM Bottom Flange

MWS Top Flange

MWI Top Flange

MWM Top Flange

MWS Bottom Flange

MWI Bottom Flange

MWM Bottom Flange

Figure E10 Weld Profile

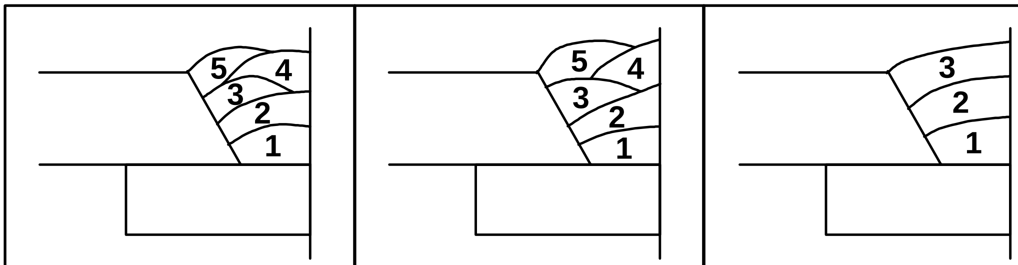

FFS Top Flange

FFI Top Flange

FFM Top Flange

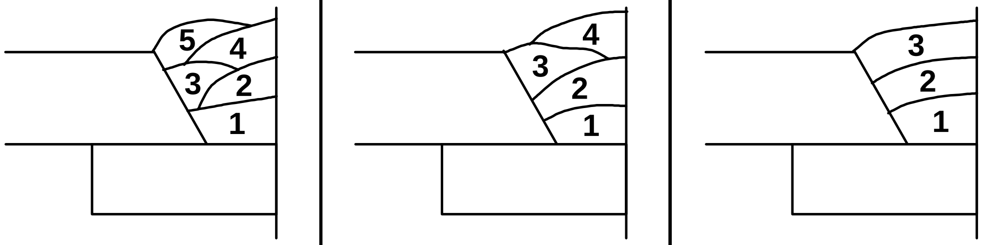

FFS Bottom Flange

FFI Bottom Flange

FFM Bottom Flange

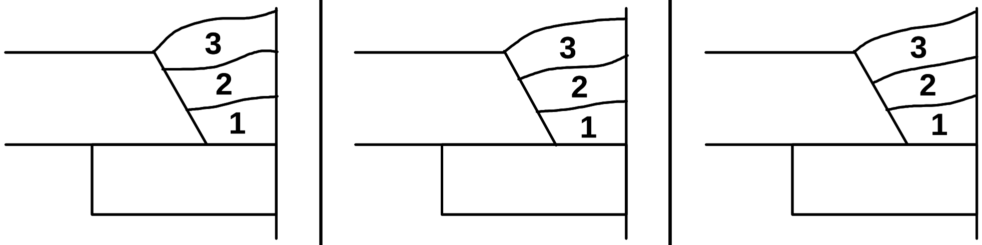

NAS Top Flange

NAI Top Flange

NAM Top Flange

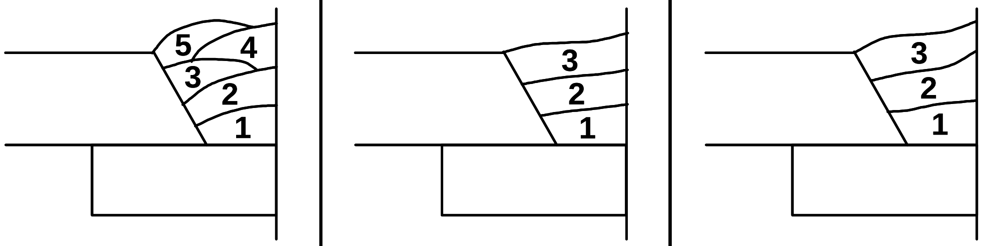

NAS Bottom Flange

NAI Bottom Flange

NAM Bottom Flange

Figure E10 Weld Profile (Continued)

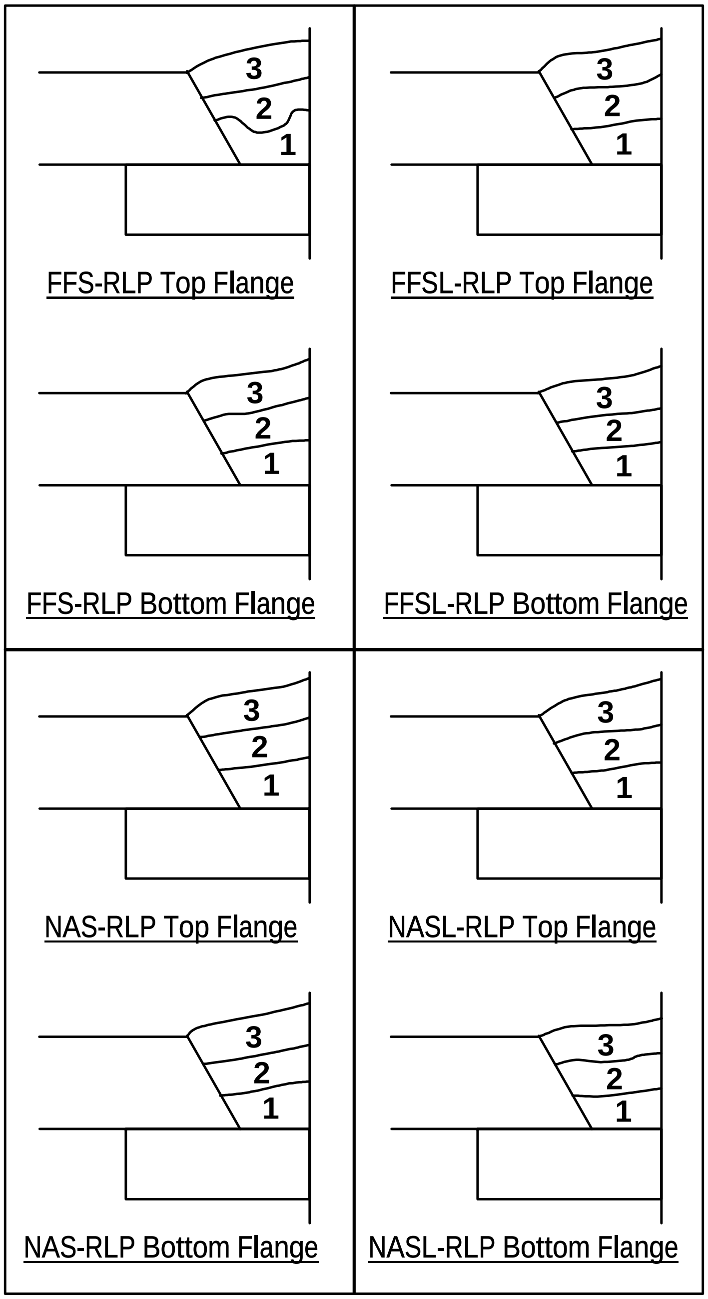

FFS-RLP Top Flange

FFSL-RLP Top Flange

FFS-RLP Bottom Flange

FFSL-RLP Bottom Flange

NAS-RLP Top Flange

NASL-RLP Top Flange

NAS-RLP Bottom Flange

NASL-RLP Bottom Flange

Figure E10 Weld Profile (Continued)

E.3.2 Tack weld location

The welding procedure (*e.g.*, Figures E.6 and E.7) specifies placing tack welds so that they will be incorporated inside the CJP groove weld. The tack welds were made with the same welding process and electrode used for the primary weld, and cleaned thoroughly. Figure E11 shows typical placements of tack welds. This figure shows the link top flange groove of Specimen NASL-RLP prior to placement of the groove weld. For this specimen, two backing bars were placed for the two sides of the link flange. A total of four tack welds were made. One tack weld was used to connect each backing bar to the link flange groove. One tack weld was used to connect each weld tab to a backing bar. Although the proximity of the tack welds to the edges of the flange may have affected fracture initiation, they are not in violation of *AWS D1.1*, which does not provide detailed specifications for the location of tack welds.

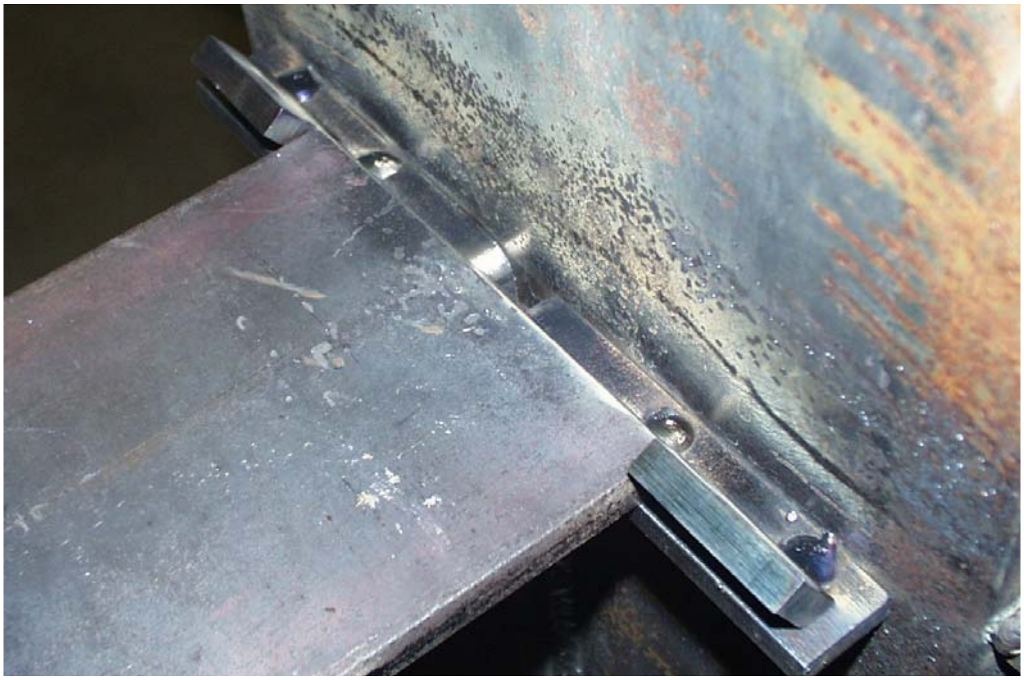

Figure E11 Tack welds for link top flange of Specimen NAS-RLP

E.3.3 Weld repair

The link top flange welds of Specimens MWS and FFS-RLP were rejected due to discontinuities in the weld. Detailed ultrasonic test reports are reproduced in Appendix F. The discontinuities were verified visually after being exposed by gouging or grinding. After the discontinuities were removed by grinding, and the welds were repaired, both welds passed inspection and ultrasonic testing. No other weld was rejected.

Figure E12 shows the discontinuity in the link top flange of Specimen FFS-RLP exposed after arc gouging. The discontinuity was located near the root of the weld at the edge of the flange. The discontinuity was removed and the surface cleaned before the weld was repaired. Two weld paths were required to reconstruct the removed weld.

Figure E12 Discontinuity in link top flange of Specimen FFS-RLP

APPENDIX F

Ultrasonic Testing Inspection Reports

This appendix contains ultrasonic test reports for all sixteen test specimens fabricated for this research project. WITS International, Inc. of Georgetown, Texas performed all ultrasonic testing.

As discussed in Section 3.2.2, the sixteen specimens were fabricated in six stages: (1) PN-specimens; (2) MW- specimens; (3) Specimen FFS; (4) Specimens FFI and NAS; (5) Specimens FFM, NAI, and NAM; and (6) Specimens FFS-RLP, FFSL-RLP, NAS-RLP, and NASL-RLP. Correspondingly, the ultrasonic test reports consist of six separate documents.

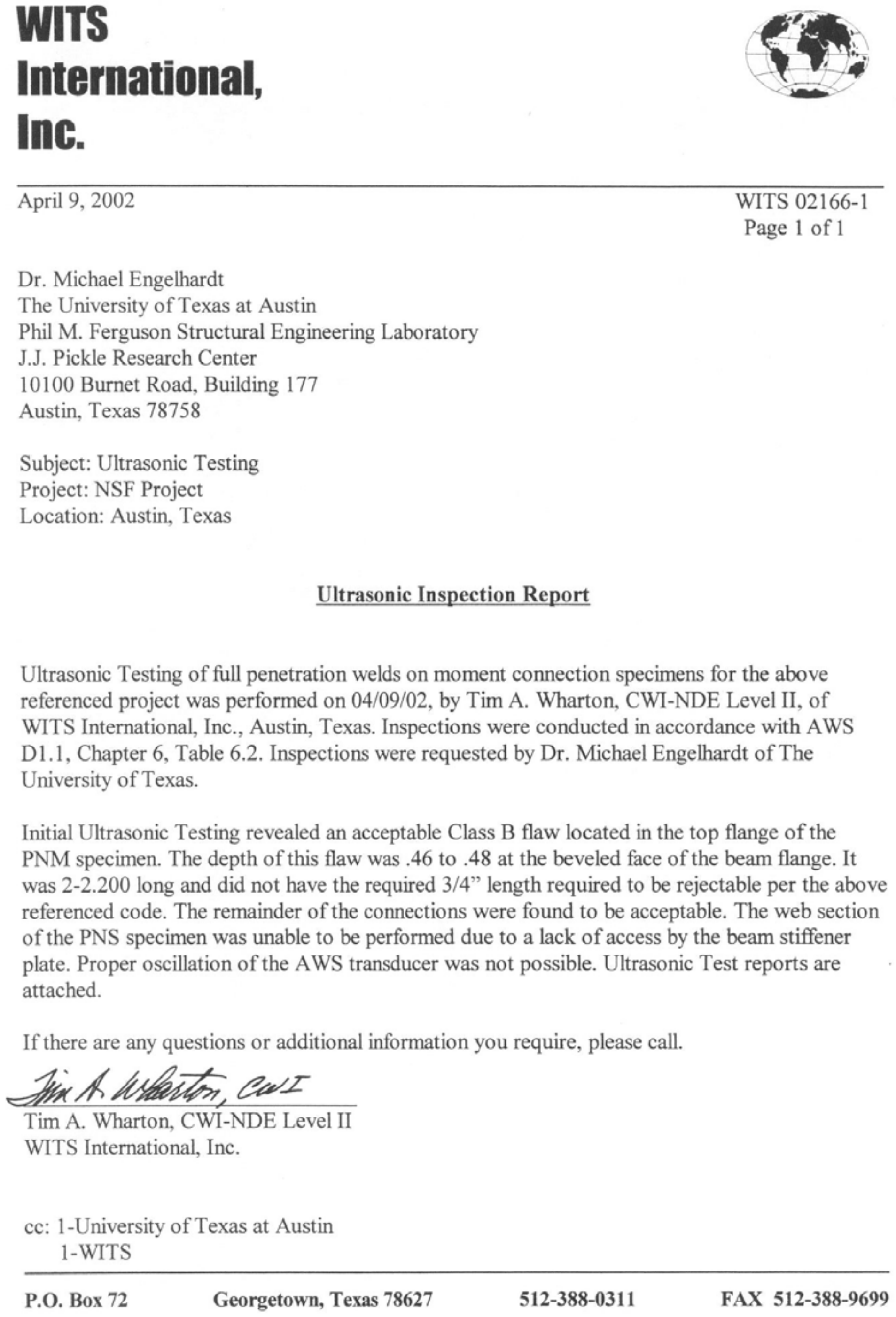

WITS
International,
Inc.

April 9, 2002

WITS 02166-1
Page 1 of 1

Dr. Michael Engelhardt
The University of Texas at Austin
Phil M. Ferguson Structural Engineering Laboratory
J.J. Pickle Research Center
10100 Burnet Road, Building 177
Austin, Texas 78758

Subject: Ultrasonic Testing
Project: NSF Project
Location: Austin, Texas

Ultrasonic Inspection Report

Ultrasonic Testing of full penetration welds on moment connection specimens for the above referenced project was performed on 04/09/02, by Tim A. Wharton, CWI-NDE Level II, of WITS International, Inc., Austin, Texas. Inspections were conducted in accordance with AWS D1.1, Chapter 6, Table 6.2. Inspections were requested by Dr. Michael Engelhardt of The University of Texas.

Initial Ultrasonic Testing revealed an acceptable Class B flaw located in the top flange of the PNM specimen. The depth of this flaw was .46 to .48 at the beveled face of the beam flange. It was 2-2.200 long and did not have the required 3/4" length required to be rejectable per the above referenced code. The remainder of the connections were found to be acceptable. The web section of the PNS specimen was unable to be performed due to a lack of access by the beam stiffener plate. Proper oscillation of the AWS transducer was not possible. Ultrasonic Test reports are attached.

If there are any questions or additional information you require, please call.

Tim A. Wharton, CWI

Tim A. Wharton, CWI-NDE Level II
WITS International, Inc.

cc: 1-University of Texas at Austin
1-WITS

P.O. Box 72 **Georgetown, Texas 78627** **512-388-0311** **FAX 512-388-9699**

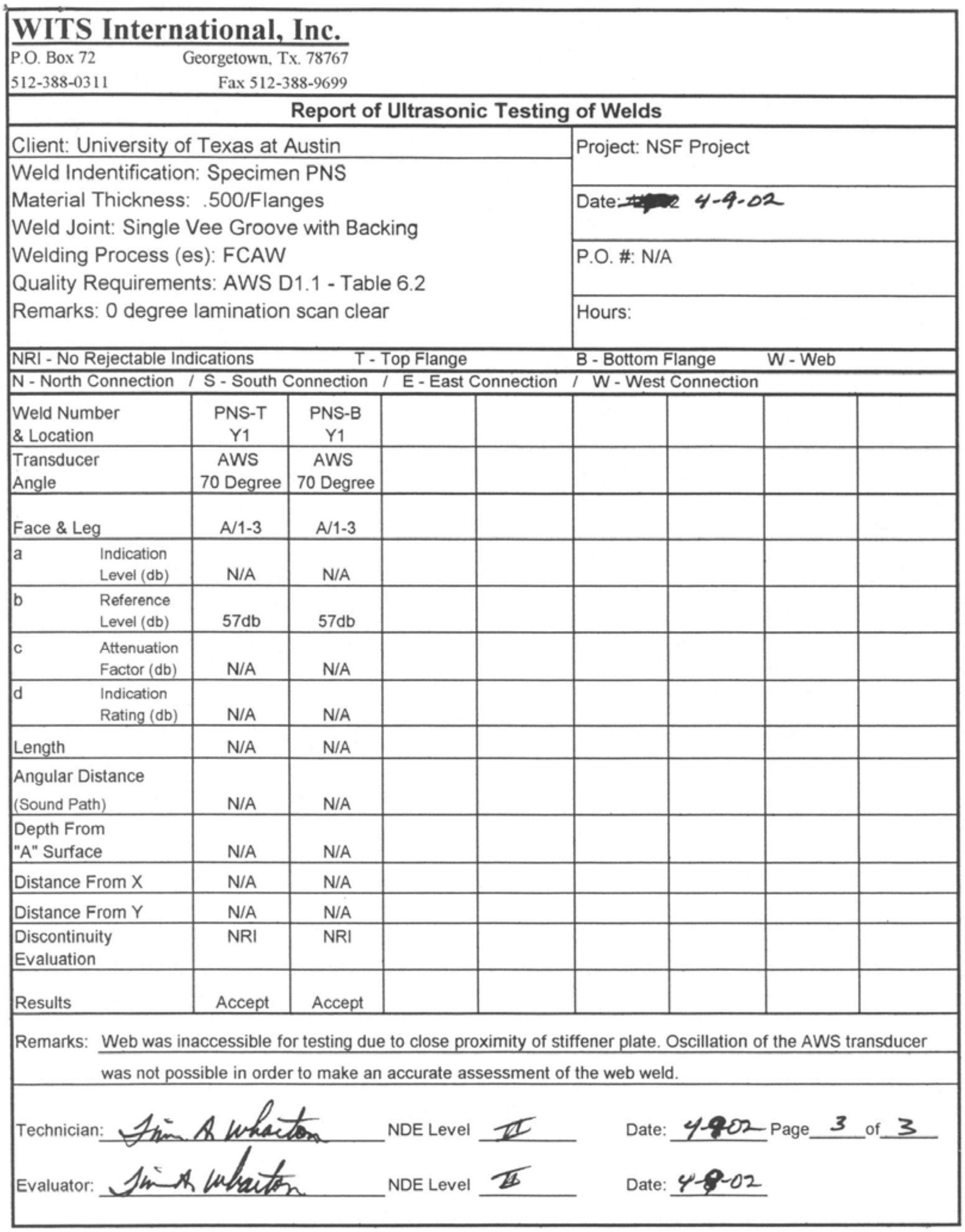

WITS International, Inc.
P.O. Box 72 Georgetown, Tx. 78767
512-388-0311 Fax 512-388-9699

Report of Ultrasonic Testing of Welds

Client: University of Texas at Austin
Weld Indentification: Specimen PNS
Material Thickness: .500/Flanges
Weld Joint: Single Vee Groove with Backing
Welding Process (es): FCAW
Quality Requirements: AWS D1.1 - Table 6.2
Remarks: 0 degree lamination scan clear

Project: NSF Project
Date: [illegible] 4-9-02
P.O. #: N/A
Hours:

NRI - No Rejectable Indications T - Top Flange B - Bottom Flange W - Web
N - North Connection / S - South Connection / E - East Connection / W - West Connection

Weld Number & Location	PNS-T Y1	PNS-B Y1								
Transducer Angle	AWS 70 Degree	AWS 70 Degree								
Face & Leg	A/1-3	A/1-3								
a Indication Level (db)	N/A	N/A								
b Reference Level (db)	57db	57db								
c Attenuation Factor (db)	N/A	N/A								
d Indication Rating (db)	N/A	N/A								
Length	N/A	N/A								
Angular Distance (Sound Path)	N/A	N/A								
Depth From "A" Surface	N/A	N/A								
Distance From X	N/A	N/A								
Distance From Y	N/A	N/A								
Discontinuity Evaluation	NRI	NRI								
Results	Accept	Accept								

Remarks: Web was inaccessible for testing due to close proximity of stiffener plate. Oscillation of the AWS transducer was not possible in order to make an accurate assessment of the web weld.

Technician: Jim A Wharton NDE Level II Date: 4-8-02 Page 3 of 3

Evaluator: Jim A Wharton NDE Level II Date: 4-8-02

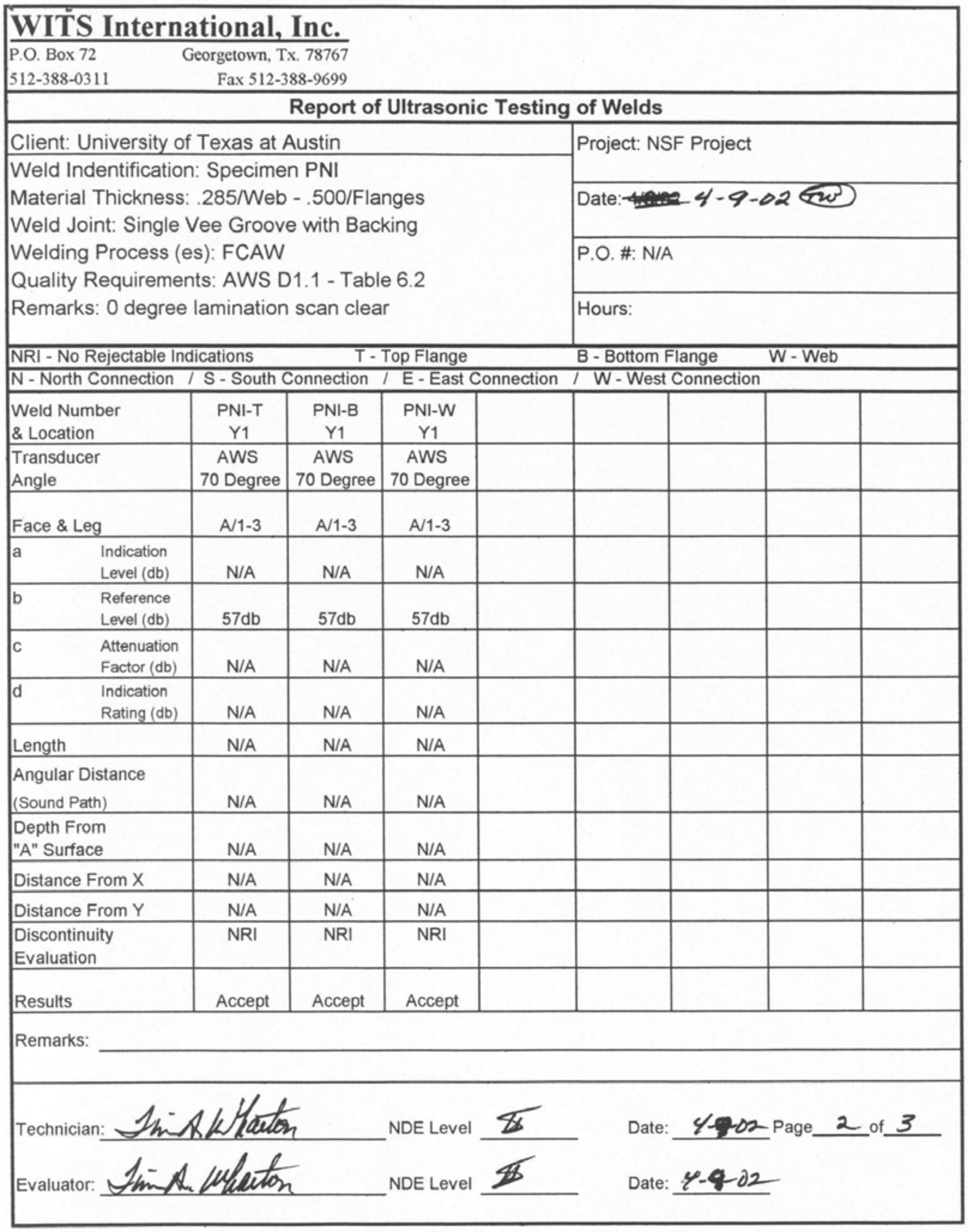

WITS International, Inc.
P.O. Box 72 Georgetown, Tx. 78767
512-388-0311 Fax 512-388-9699

Report of Ultrasonic Testing of Welds

Client: University of Texas at Austin
Weld Indentification: Specimen PNI
Material Thickness: .285/Web - .500/Flanges
Weld Joint: Single Vee Groove with Backing
Welding Process (es): FCAW
Quality Requirements: AWS D1.1 - Table 6.2
Remarks: 0 degree lamination scan clear

Project: NSF Project
Date: ~~[illegible]~~ 4-9-02 TW
P.O. #: N/A
Hours:

NRI - No Rejectable Indications T - Top Flange B - Bottom Flange W - Web
N - North Connection / S - South Connection / E - East Connection / W - West Connection

Weld Number & Location	PNI-T Y1	PNI-B Y1	PNI-W Y1						
Transducer Angle	AWS 70 Degree	AWS 70 Degree	AWS 70 Degree						
Face & Leg	A/1-3	A/1-3	A/1-3						
a Indication Level (db)	N/A	N/A	N/A						
b Reference Level (db)	57db	57db	57db						
c Attenuation Factor (db)	N/A	N/A	N/A						
d Indication Rating (db)	N/A	N/A	N/A						
Length	N/A	N/A	N/A						
Angular Distance (Sound Path)	N/A	N/A	N/A						
Depth From "A" Surface	N/A	N/A	N/A						
Distance From X	N/A	N/A	N/A						
Distance From Y	N/A	N/A	N/A						
Discontinuity Evaluation	NRI	NRI	NRI						
Results	Accept	Accept	Accept						

Remarks:

Technician: Tim A Wharton NDE Level II Date: 4-9-02 Page 2 of 3
Evaluator: Tim A. Wharton NDE Level II Date: 4-9-02

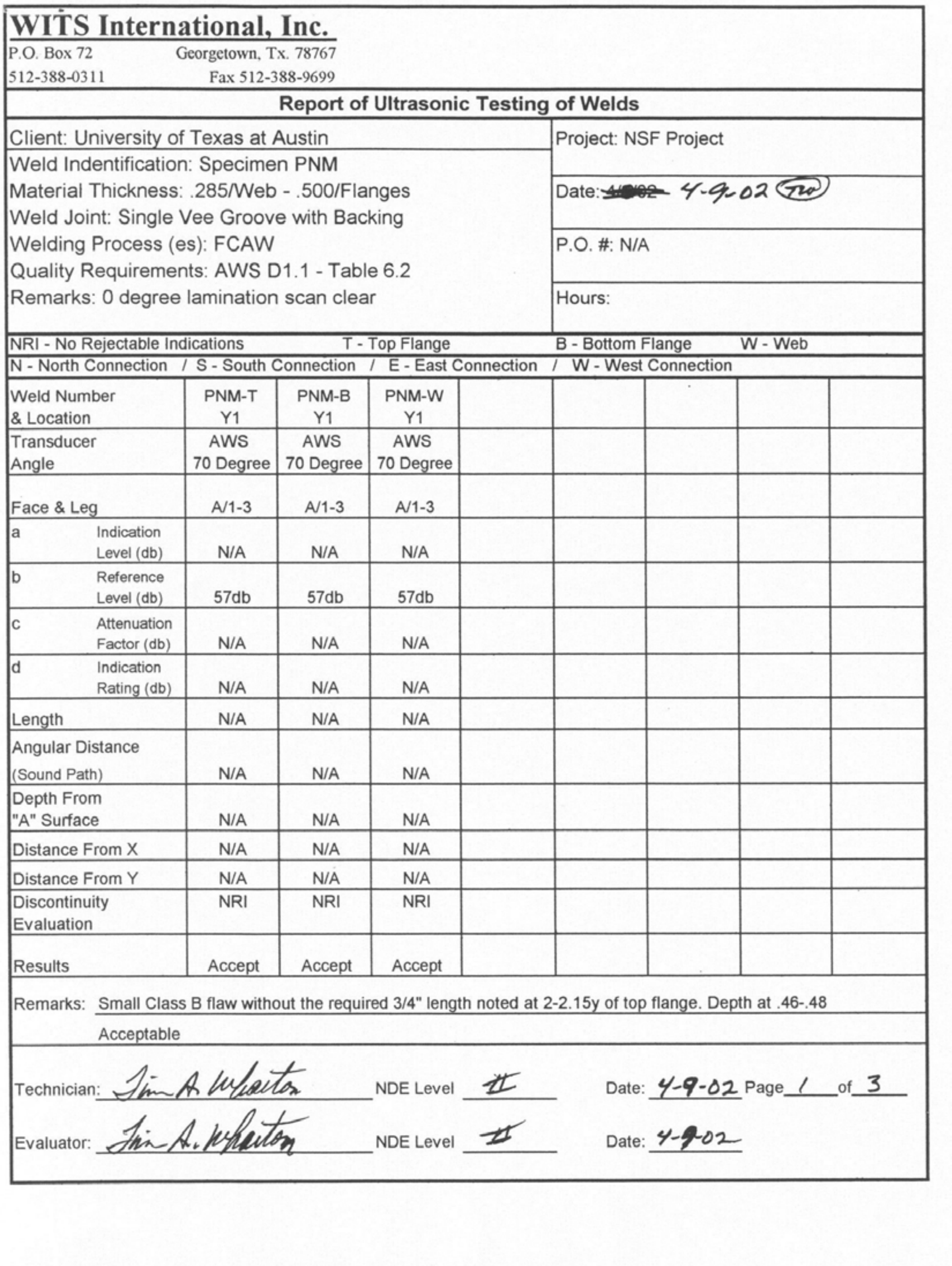

WITS International, Inc.

P.O. Box 72 Georgetown, Tx. 78767

512-388-0311 Fax 512-388-9699

Report of Ultrasonic Testing of Welds

Client: University of Texas at Austin

Project: NSF Project

Weld Indentification: Specimen PNM

Material Thickness: .285/Web - .500/Flanges

Date: ~~4/[illegible]/02~~ 4-9-02 TAW

Weld Joint: Single Vee Groove with Backing

Welding Process (es): FCAW

P.O. #: N/A

Quality Requirements: AWS D1.1 - Table 6.2

Remarks: 0 degree lamination scan clear

Hours:

NRI - No Rejectable Indications T - Top Flange B - Bottom Flange W - Web

N - North Connection / S - South Connection / E - East Connection / W - West Connection

Weld Number & Location	PNM-T Y1	PNM-B Y1	PNM-W Y1					
Transducer Angle	AWS 70 Degree	AWS 70 Degree	AWS 70 Degree					
Face & Leg	A/1-3	A/1-3	A/1-3					
a Indication Level (db)	N/A	N/A	N/A					
b Reference Level (db)	57db	57db	57db					
c Attenuation Factor (db)	N/A	N/A	N/A					
d Indication Rating (db)	N/A	N/A	N/A					
Length	N/A	N/A	N/A					
Angular Distance (Sound Path)	N/A	N/A	N/A					
Depth From "A" Surface	N/A	N/A	N/A					
Distance From X	N/A	N/A	N/A					
Distance From Y	N/A	N/A	N/A					
Discontinuity Evaluation	NRI	NRI	NRI					
Results	Accept	Accept	Accept					

Remarks: Small Class B flaw without the required 3/4" length noted at 2-2.15y of top flange. Depth at .46-.48 Acceptable

Technician: Tim A. Wharton NDE Level II Date: 4-9-02 Page 1 of 3

Evaluator: Tim A. Wharton NDE Level II Date: 4-9-02

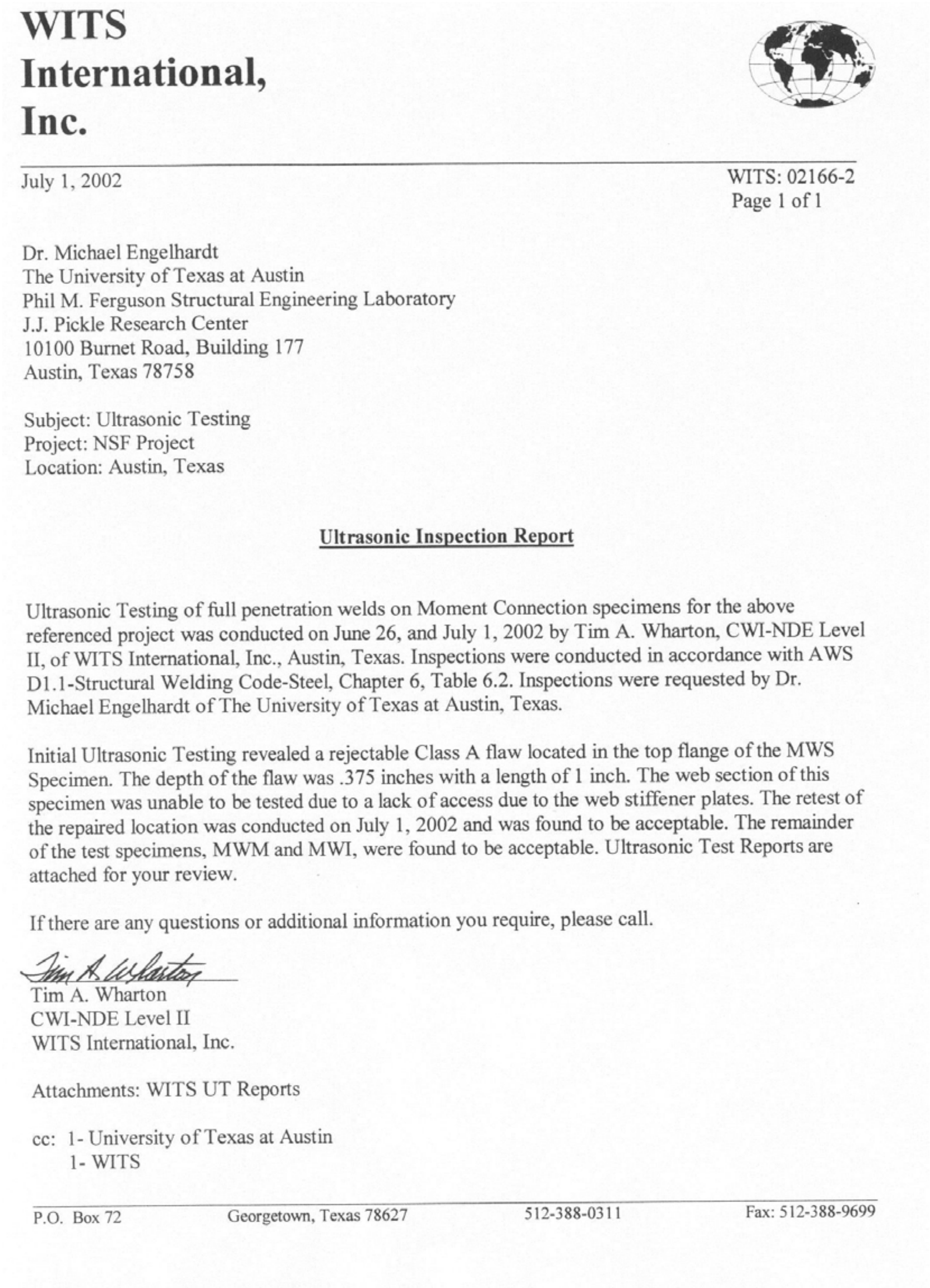

WITS
International,
Inc.

July 1, 2002

WITS: 02166-2
Page 1 of 1

Dr. Michael Engelhardt
The University of Texas at Austin
Phil M. Ferguson Structural Engineering Laboratory
J.J. Pickle Research Center
10100 Burnet Road, Building 177
Austin, Texas 78758

Subject: Ultrasonic Testing
Project: NSF Project
Location: Austin, Texas

Ultrasonic Inspection Report

Ultrasonic Testing of full penetration welds on Moment Connection specimens for the above referenced project was conducted on June 26, and July 1, 2002 by Tim A. Wharton, CWI-NDE Level II, of WITS International, Inc., Austin, Texas. Inspections were conducted in accordance with AWS D1.1-Structural Welding Code-Steel, Chapter 6, Table 6.2. Inspections were requested by Dr. Michael Engelhardt of The University of Texas at Austin, Texas.

Initial Ultrasonic Testing revealed a rejectable Class A flaw located in the top flange of the MWS Specimen. The depth of the flaw was .375 inches with a length of 1 inch. The web section of this specimen was unable to be tested due to a lack of access due to the web stiffener plates. The retest of the repaired location was conducted on July 1, 2002 and was found to be acceptable. The remainder of the test specimens, MWM and MWI, were found to be acceptable. Ultrasonic Test Reports are attached for your review.

If there are any questions or additional information you require, please call.

Tim A. Wharton

Tim A. Wharton
CWI-NDE Level II
WITS International, Inc.

Attachments: WITS UT Reports

cc: 1- University of Texas at Austin
1- WITS

P.O. Box 72 Georgetown, Texas 78627 512-388-0311 Fax: 512-388-9699

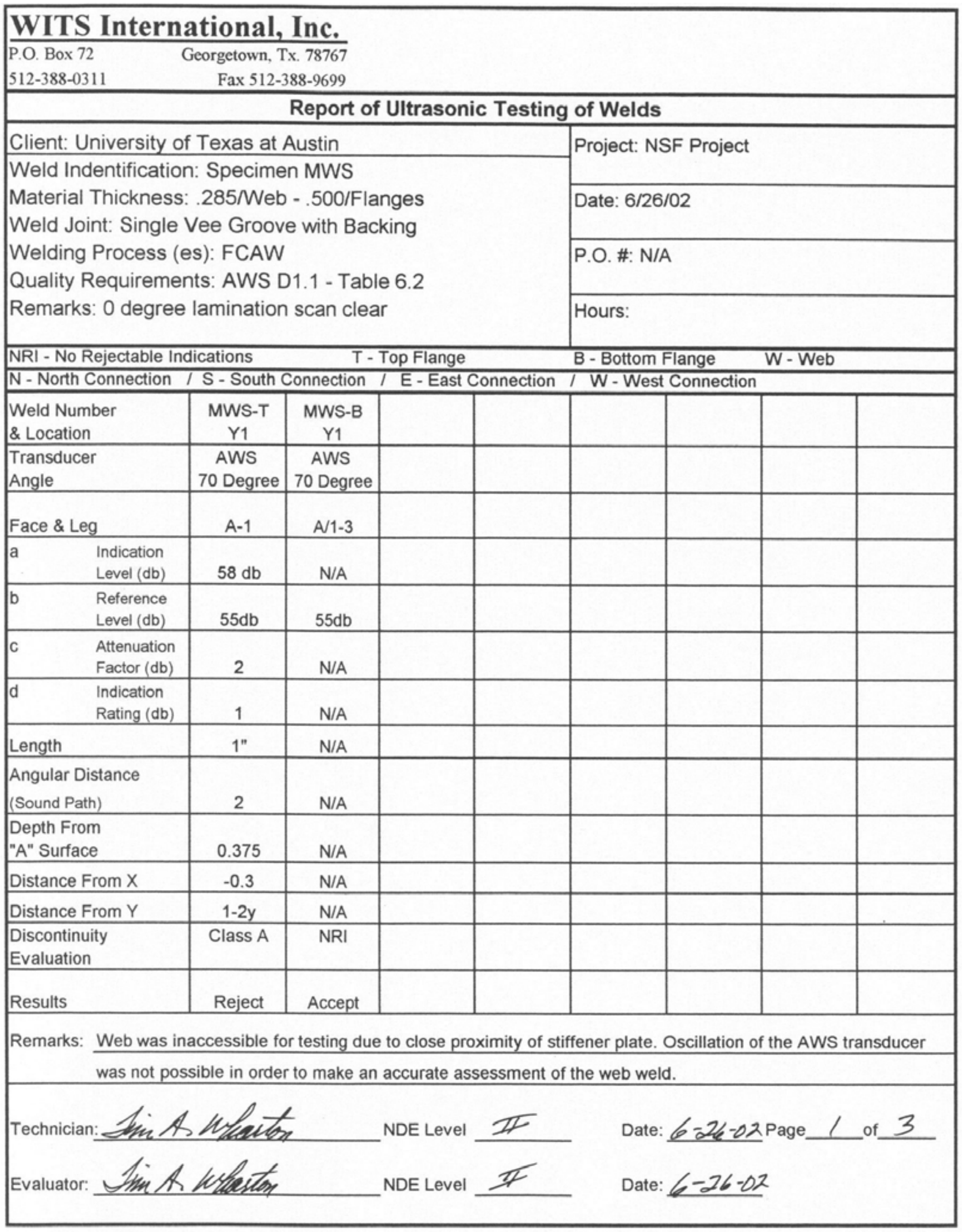

WITS International, Inc.

P.O. Box 72 Georgetown, Tx. 78767
512-388-0311 Fax 512-388-9699

Report of Ultrasonic Testing of Welds

Client: University of Texas at Austin

Weld Indentification: Specimen MWS

Material Thickness: .285/Web - .500/Flanges

Weld Joint: Single Vee Groove with Backing

Welding Process (es): FCAW

Quality Requirements: AWS D1.1 - Table 6.2

Remarks: 0 degree lamination scan clear

Project: NSF Project

Date: 6/26/02

P.O. #: N/A

Hours:

NRI - No Rejectable Indications T - Top Flange B - Bottom Flange W - Web

N - North Connection / S - South Connection / E - East Connection / W - West Connection

Weld Number & Location	MWS-T Y1	MWS-B Y1						
Transducer Angle	AWS 70 Degree	AWS 70 Degree						
Face & Leg	A-1	A/1-3						
a Indication Level (db)	58 db	N/A						
b Reference Level (db)	55db	55db						
c Attenuation Factor (db)	2	N/A						
d Indication Rating (db)	1	N/A						
Length	1"	N/A						
Angular Distance (Sound Path)	2	N/A						
Depth From "A" Surface	0.375	N/A						
Distance From X	-0.3	N/A						
Distance From Y	1-2y	N/A						
Discontinuity Evaluation	Class A	NRI						
Results	Reject	Accept						

Remarks: Web was inaccessible for testing due to close proximity of stiffener plate. Oscillation of the AWS transducer was not possible in order to make an accurate assessment of the web weld.

Technician: Tim A. Wharton NDE Level II Date: 6-26-02 Page 1 of 3

Evaluator: Tim A. Wharton NDE Level II Date: 6-26-02

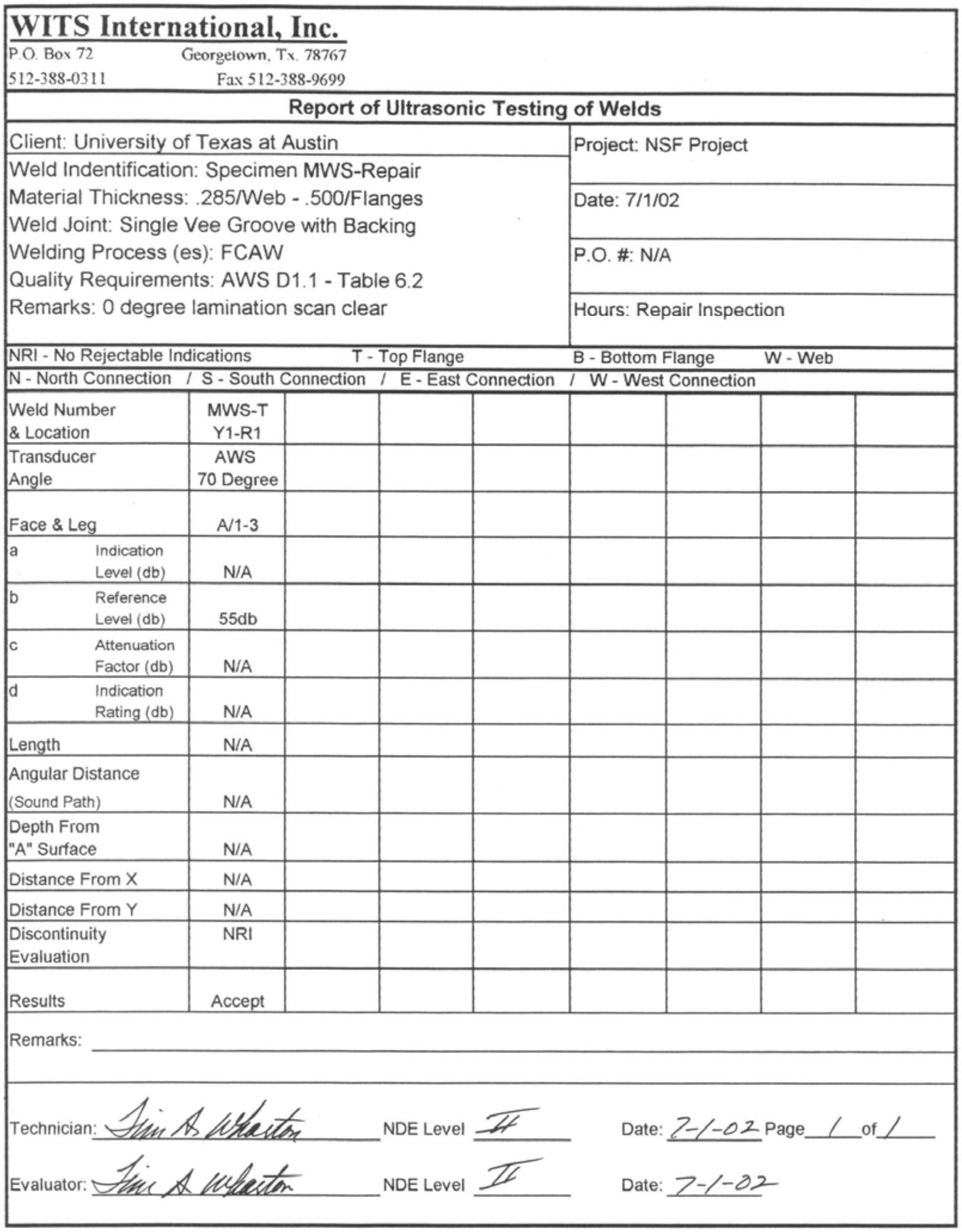

WITS International, Inc.
P.O. Box 72 Georgetown, Tx. 78767
512-388-0311 Fax 512-388-9699

Report of Ultrasonic Testing of Welds

Client: University of Texas at Austin
Weld Indentification: Specimen MWS-Repair
Material Thickness: .285/Web - .500/Flanges
Weld Joint: Single Vee Groove with Backing
Welding Process (es): FCAW
Quality Requirements: AWS D1.1 - Table 6.2
Remarks: 0 degree lamination scan clear

Project: NSF Project
Date: 7/1/02
P.O. #: N/A
Hours: Repair Inspection

NRI - No Rejectable Indications T - Top Flange B - Bottom Flange W - Web
N - North Connection / S - South Connection / E - East Connection / W - West Connection

Weld Number & Location	MWS-T Y1-R1							
Transducer Angle	AWS 70 Degree							
Face & Leg	A/1-3							
a Indication Level (db)	N/A							
b Reference Level (db)	55db							
c Attenuation Factor (db)	N/A							
d Indication Rating (db)	N/A							
Length	N/A							
Angular Distance (Sound Path)	N/A							
Depth From "A" Surface	N/A							
Distance From X	N/A							
Distance From Y	N/A							
Discontinuity Evaluation	NRI							
Results	Accept							

Remarks:

Technician: Tim A. Wharton NDE Level II Date: 7-1-02 Page 1 of 1

Evaluator: Tim A. Wharton NDE Level II Date: 7-1-02

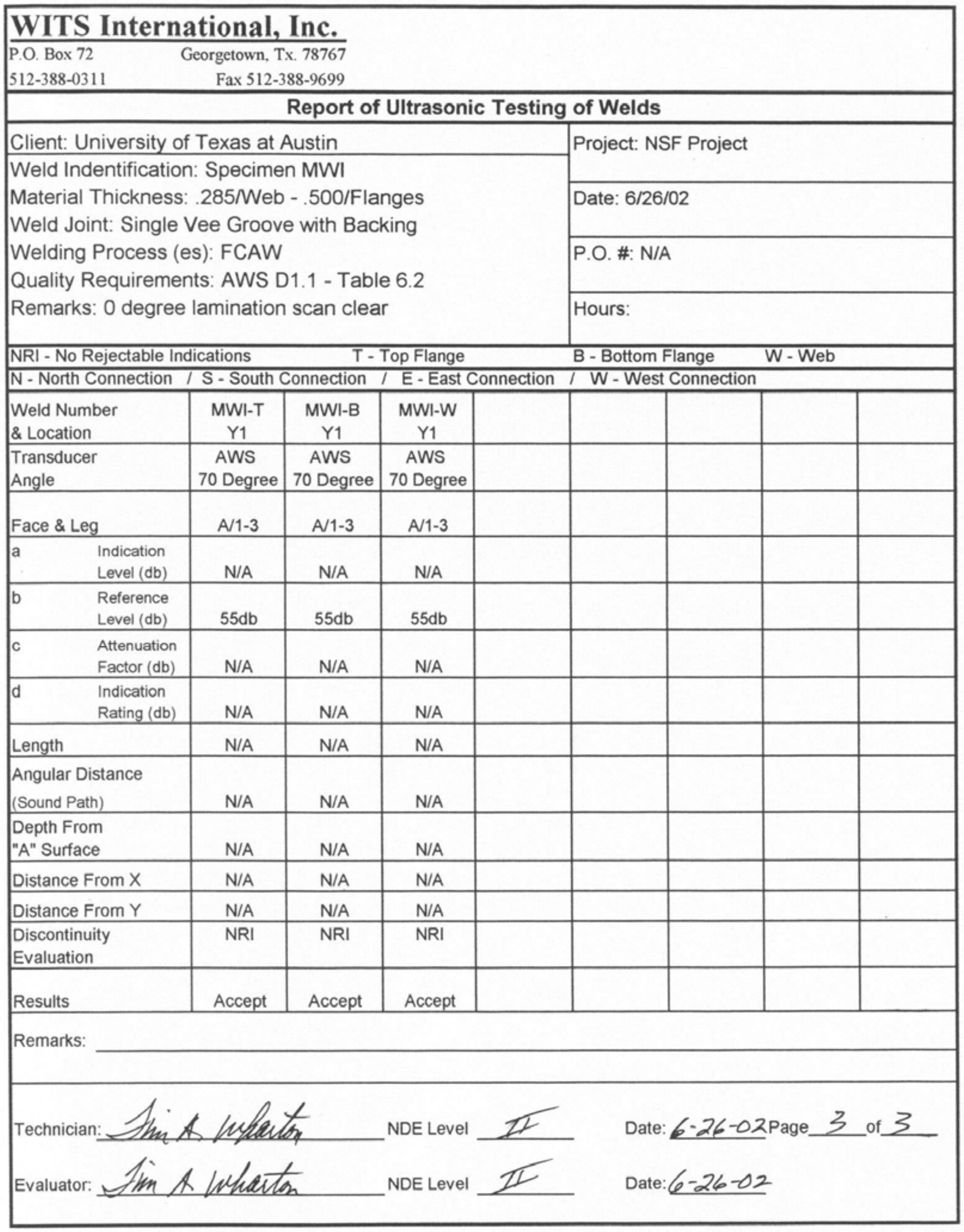

WITS International, Inc.

P.O. Box 72 Georgetown, Tx. 78767
512-388-0311 Fax 512-388-9699

Report of Ultrasonic Testing of Welds

Client: University of Texas at Austin
Weld Indentification: Specimen MWI
Material Thickness: .285/Web - .500/Flanges
Weld Joint: Single Vee Groove with Backing
Welding Process (es): FCAW
Quality Requirements: AWS D1.1 - Table 6.2
Remarks: 0 degree lamination scan clear

Project: NSF Project
Date: 6/26/02
P.O. #: N/A
Hours:

NRI - No Rejectable Indications T - Top Flange B - Bottom Flange W - Web
N - North Connection / S - South Connection / E - East Connection / W - West Connection

Weld Number & Location	MWI-T Y1	MWI-B Y1	MWI-W Y1					
Transducer Angle	AWS 70 Degree	AWS 70 Degree	AWS 70 Degree					
Face & Leg	A/1-3	A/1-3	A/1-3					
a Indication Level (db)	N/A	N/A	N/A					
b Reference Level (db)	55db	55db	55db					
c Attenuation Factor (db)	N/A	N/A	N/A					
d Indication Rating (db)	N/A	N/A	N/A					
Length	N/A	N/A	N/A					
Angular Distance (Sound Path)	N/A	N/A	N/A					
Depth From "A" Surface	N/A	N/A	N/A					
Distance From X	N/A	N/A	N/A					
Distance From Y	N/A	N/A	N/A					
Discontinuity Evaluation	NRI	NRI	NRI					
Results	Accept	Accept	Accept					

Remarks:

Technician: Tim A. Wharton NDE Level II Date: 6-26-02 Page 3 of 3

Evaluator: Tim A. Wharton NDE Level II Date: 6-26-02

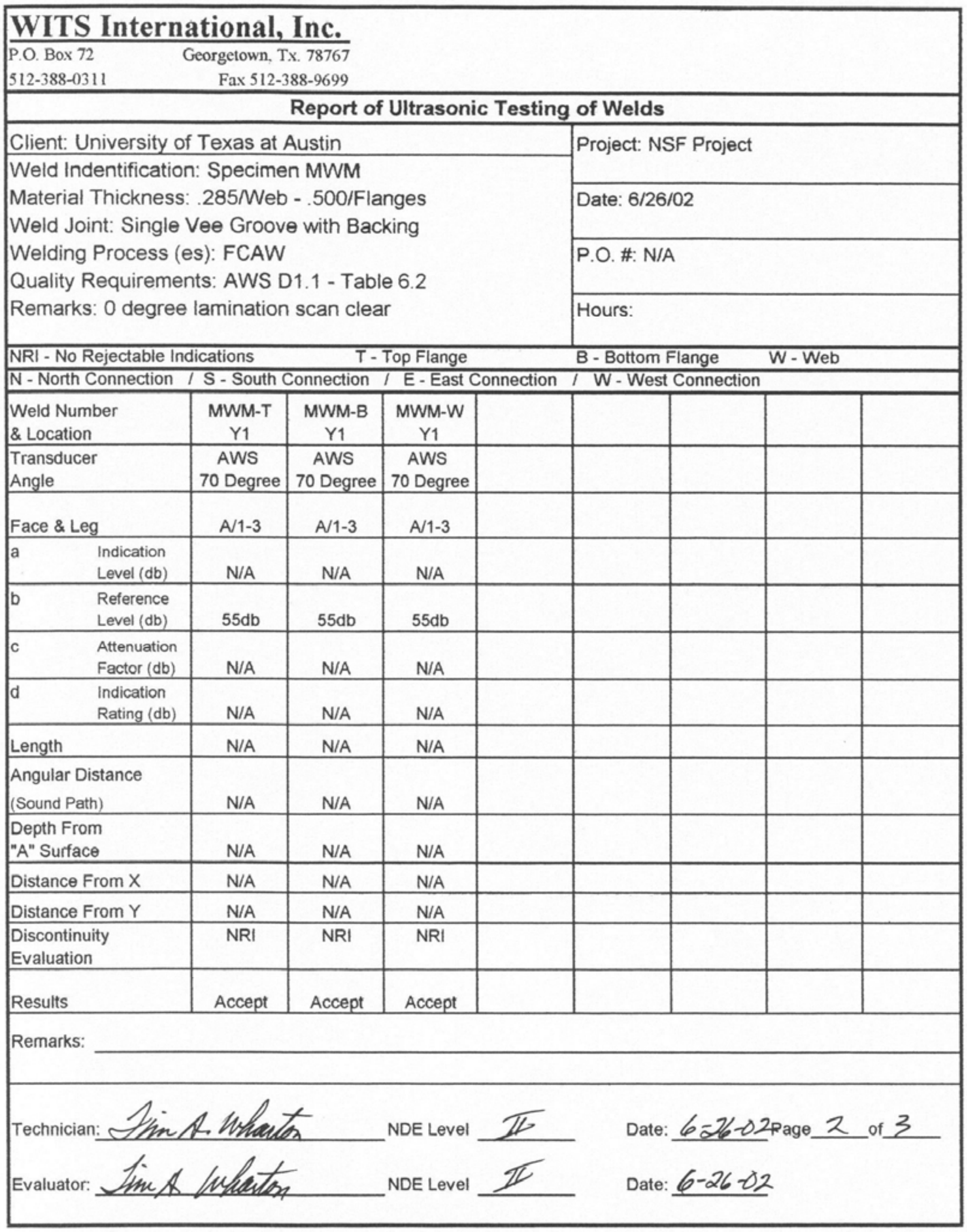

WITS International, Inc.

P.O. Box 72 Georgetown, Tx. 78767
512-388-0311 Fax 512-388-9699

Report of Ultrasonic Testing of Welds

Client: University of Texas at Austin
Weld Indentification: Specimen MWM
Material Thickness: .285/Web - .500/Flanges
Weld Joint: Single Vee Groove with Backing
Welding Process (es): FCAW
Quality Requirements: AWS D1.1 - Table 6.2
Remarks: 0 degree lamination scan clear

Project: NSF Project
Date: 6/26/02
P.O. #: N/A
Hours:

NRI - No Rejectable Indications T - Top Flange B - Bottom Flange W - Web
N - North Connection / S - South Connection / E - East Connection / W - West Connection

Weld Number & Location	MWM-T Y1	MWM-B Y1	MWM-W Y1						
Transducer Angle	AWS 70 Degree	AWS 70 Degree	AWS 70 Degree						
Face & Leg	A/1-3	A/1-3	A/1-3						
a Indication Level (db)	N/A	N/A	N/A						
b Reference Level (db)	55db	55db	55db						
c Attenuation Factor (db)	N/A	N/A	N/A						
d Indication Rating (db)	N/A	N/A	N/A						
Length	N/A	N/A	N/A						
Angular Distance (Sound Path)	N/A	N/A	N/A						
Depth From "A" Surface	N/A	N/A	N/A						
Distance From X	N/A	N/A	N/A						
Distance From Y	N/A	N/A	N/A						
Discontinuity Evaluation	NRI	NRI	NRI						
Results	Accept	Accept	Accept						

Remarks:

Technician: Tim A. Wharton NDE Level II Date: 6-26-02 Page 2 of 3

Evaluator: Tim A Wharton NDE Level II Date: 6-26-02

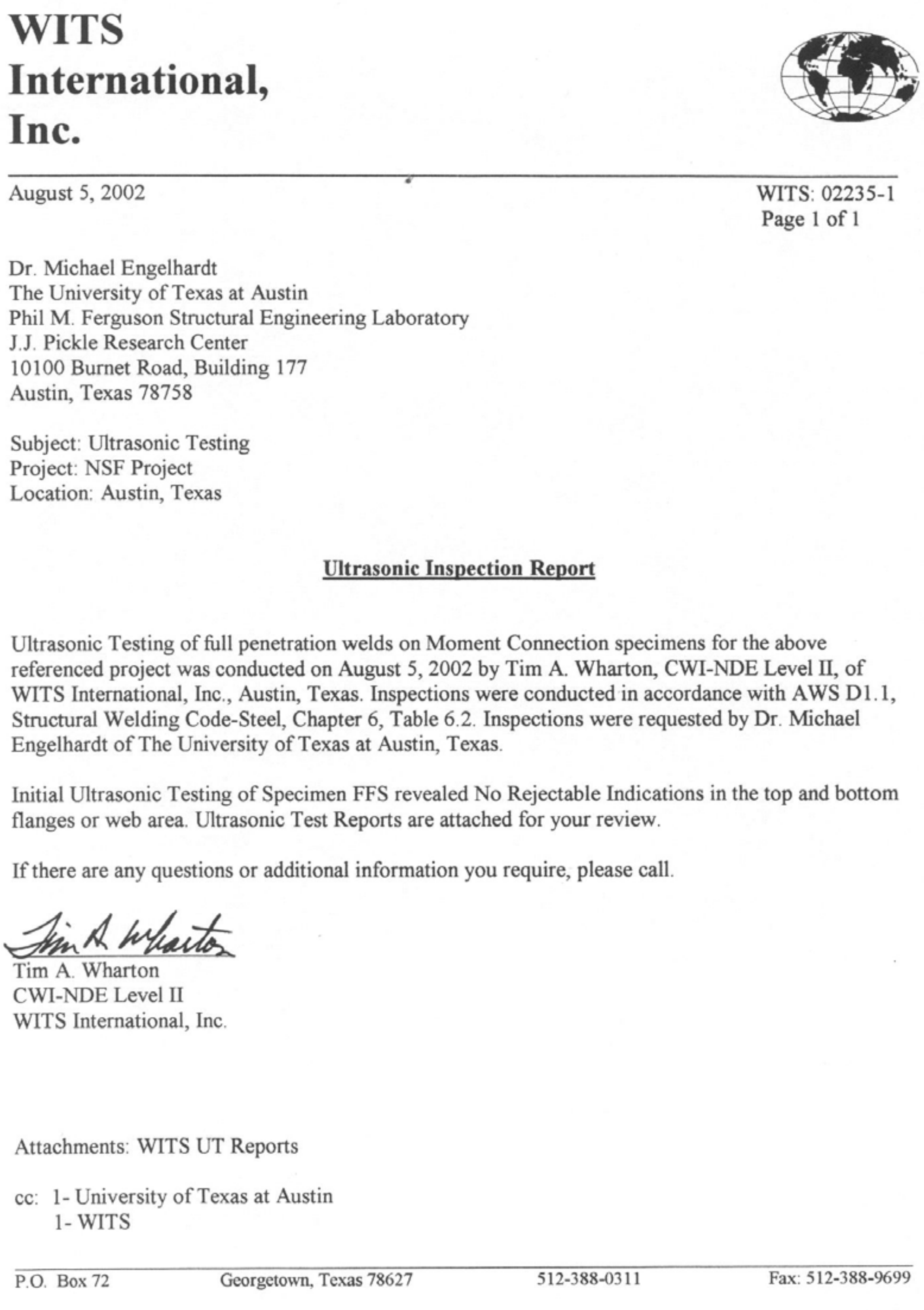

WITS
International,
Inc.

August 5, 2002

WITS: 02235-1
Page 1 of 1

Dr. Michael Engelhardt
The University of Texas at Austin
Phil M. Ferguson Structural Engineering Laboratory
J.J. Pickle Research Center
10100 Burnet Road, Building 177
Austin, Texas 78758

Subject: Ultrasonic Testing
Project: NSF Project
Location: Austin, Texas

Ultrasonic Inspection Report

Ultrasonic Testing of full penetration welds on Moment Connection specimens for the above referenced project was conducted on August 5, 2002 by Tim A. Wharton, CWI-NDE Level II, of WITS International, Inc., Austin, Texas. Inspections were conducted in accordance with AWS D1.1, Structural Welding Code-Steel, Chapter 6, Table 6.2. Inspections were requested by Dr. Michael Engelhardt of The University of Texas at Austin, Texas.

Initial Ultrasonic Testing of Specimen FFS revealed No Rejectable Indications in the top and bottom flanges or web area. Ultrasonic Test Reports are attached for your review.

If there are any questions or additional information you require, please call.

Tim A. Wharton

Tim A. Wharton
CWI-NDE Level II
WITS International, Inc.

Attachments: WITS UT Reports

cc: 1- University of Texas at Austin
1- WITS

P.O. Box 72 Georgetown, Texas 78627 512-388-0311 Fax: 512-388-9699

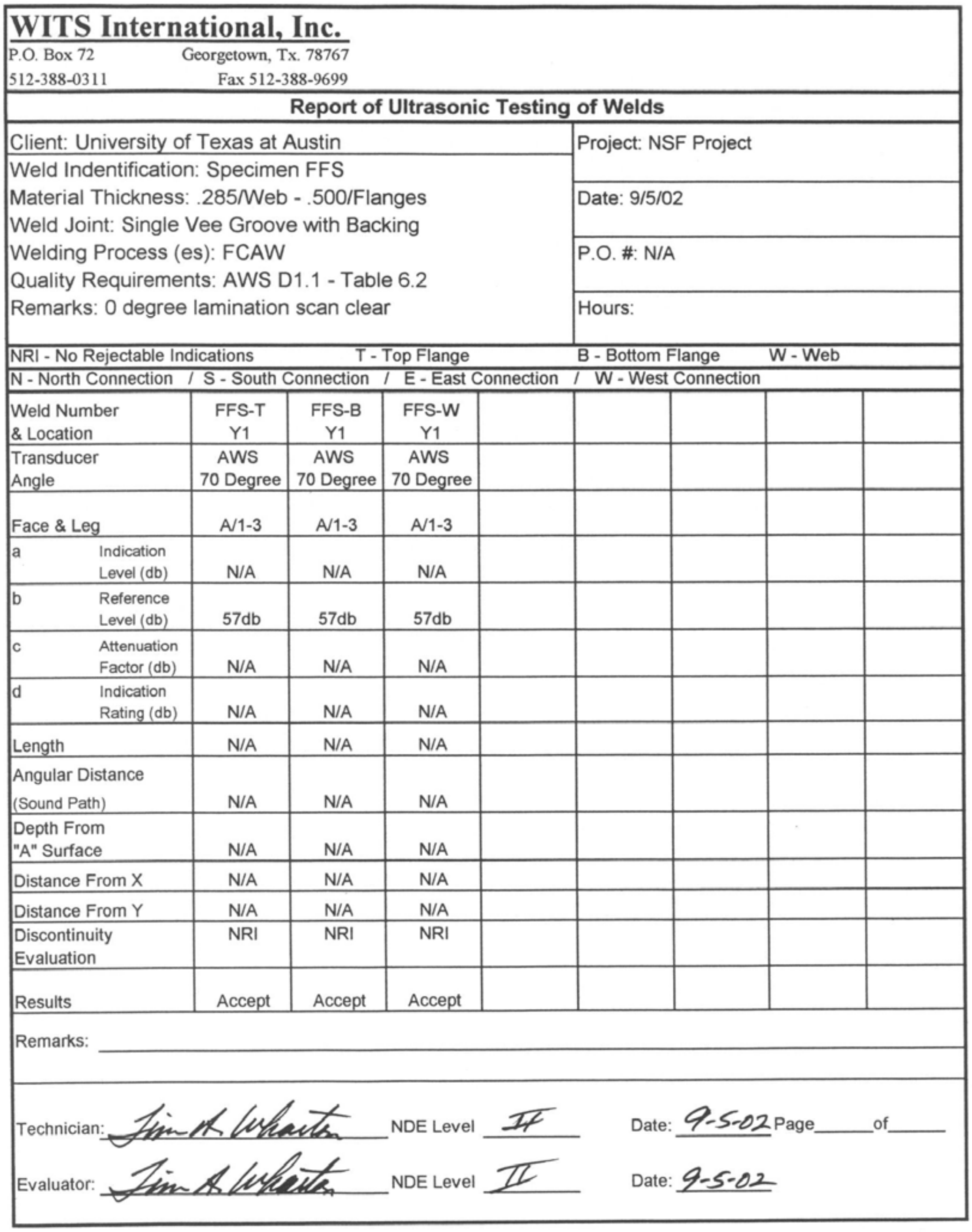

WITS International, Inc.

P.O. Box 72 Georgetown, Tx. 78767
512-388-0311 Fax 512-388-9699

Report of Ultrasonic Testing of Welds

Client: University of Texas at Austin
Weld Indentification: Specimen FFS
Material Thickness: .285/Web - .500/Flanges
Weld Joint: Single Vee Groove with Backing
Welding Process (es): FCAW
Quality Requirements: AWS D1.1 - Table 6.2
Remarks: 0 degree lamination scan clear

Project: NSF Project

Date: 9/5/02

P.O. #: N/A

Hours:

NRI - No Rejectable Indications T - Top Flange B - Bottom Flange W - Web
N - North Connection / S - South Connection / E - East Connection / W - West Connection

Weld Number & Location	FFS-T Y1	FFS-B Y1	FFS-W Y1					
Transducer Angle	AWS 70 Degree	AWS 70 Degree	AWS 70 Degree					
Face & Leg	A/1-3	A/1-3	A/1-3					
a Indication Level (db)	N/A	N/A	N/A					
b Reference Level (db)	57db	57db	57db					
c Attenuation Factor (db)	N/A	N/A	N/A					
d Indication Rating (db)	N/A	N/A	N/A					
Length	N/A	N/A	N/A					
Angular Distance (Sound Path)	N/A	N/A	N/A					
Depth From "A" Surface	N/A	N/A	N/A					
Distance From X	N/A	N/A	N/A					
Distance From Y	N/A	N/A	N/A					
Discontinuity Evaluation	NRI	NRI	NRI					
Results	Accept	Accept	Accept					

Remarks: ______________________

Technician: Tim A. Wharton NDE Level II Date: 9-5-02 Page_____of_____

Evaluator: Tim A. Wharton NDE Level II Date: 9-5-02

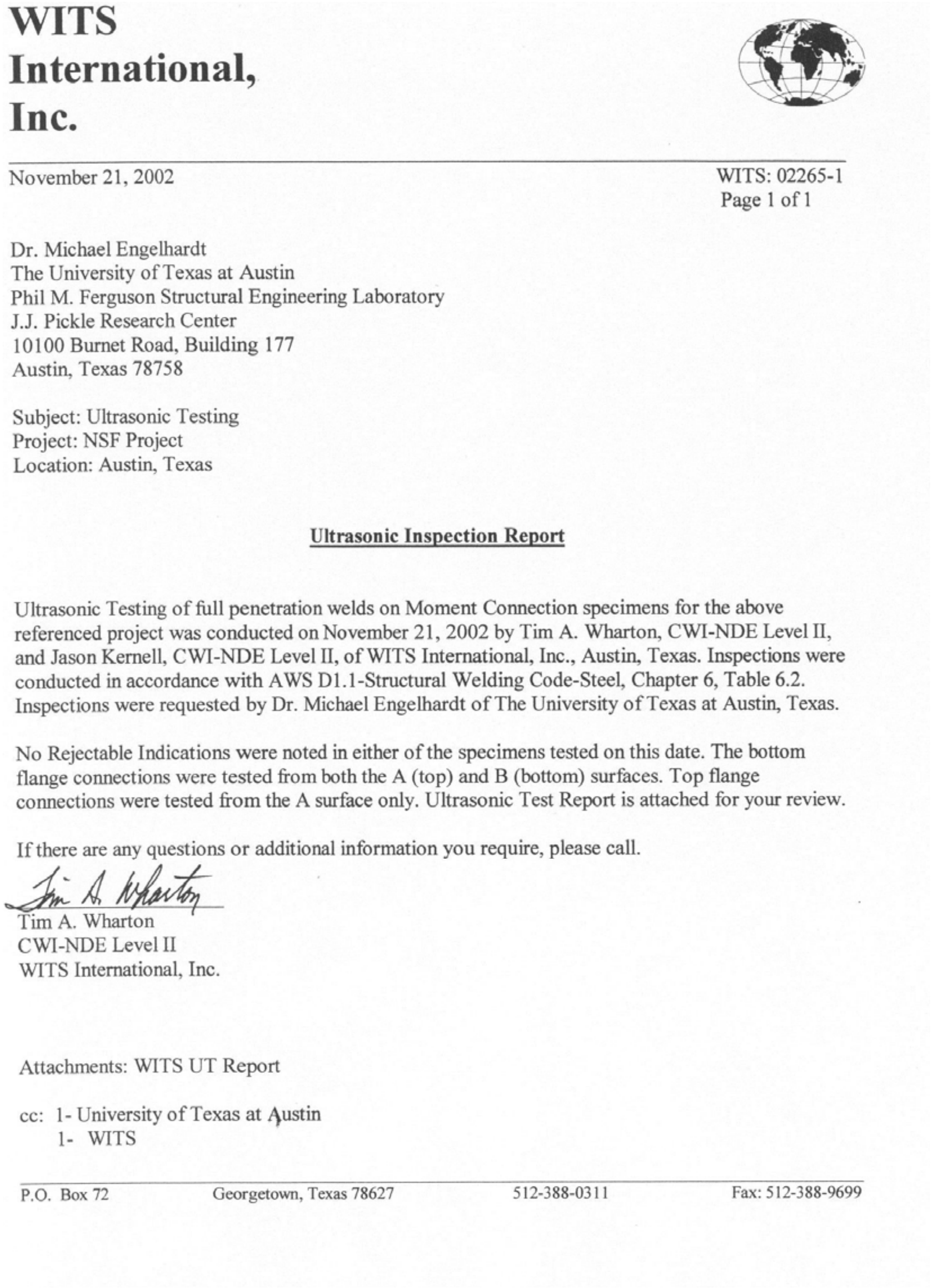

WITS
International,
Inc.

November 21, 2002

WITS: 02265-1
Page 1 of 1

Dr. Michael Engelhardt
The University of Texas at Austin
Phil M. Ferguson Structural Engineering Laboratory
J.J. Pickle Research Center
10100 Burnet Road, Building 177
Austin, Texas 78758

Subject: Ultrasonic Testing
Project: NSF Project
Location: Austin, Texas

Ultrasonic Inspection Report

Ultrasonic Testing of full penetration welds on Moment Connection specimens for the above referenced project was conducted on November 21, 2002 by Tim A. Wharton, CWI-NDE Level II, and Jason Kernell, CWI-NDE Level II, of WITS International, Inc., Austin, Texas. Inspections were conducted in accordance with AWS D1.1-Structural Welding Code-Steel, Chapter 6, Table 6.2. Inspections were requested by Dr. Michael Engelhardt of The University of Texas at Austin, Texas.

No Rejectable Indications were noted in either of the specimens tested on this date. The bottom flange connections were tested from both the A (top) and B (bottom) surfaces. Top flange connections were tested from the A surface only. Ultrasonic Test Report is attached for your review.

If there are any questions or additional information you require, please call.

Tim A. Wharton

Tim A. Wharton
CWI-NDE Level II
WITS International, Inc.

Attachments: WITS UT Report

cc: 1- University of Texas at Austin
1- WITS

P.O. Box 72 Georgetown, Texas 78627 512-388-0311 Fax: 512-388-9699

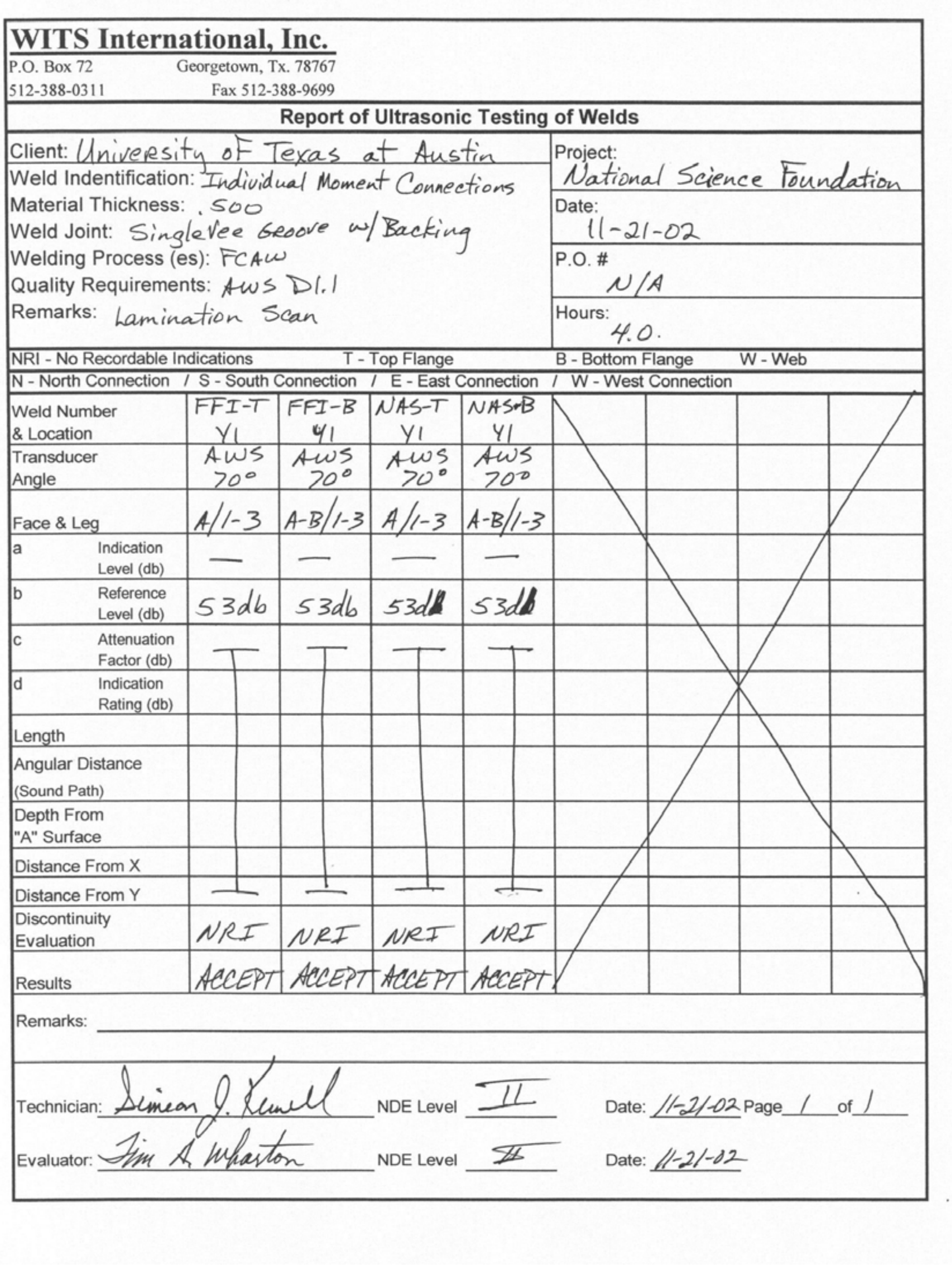

WITS International, Inc.
P.O. Box 72 Georgetown, Tx. 78767
512-388-0311 Fax 512-388-9699

Report of Ultrasonic Testing of Welds

Client: University oF Texas at Austin
Weld Indentification: Individual Moment Connections
Material Thickness: .500
Weld Joint: SingleVee Groove w/ Backing
Welding Process (es): FCAW
Quality Requirements: AWS D1.1
Remarks: Lamination Scan

Project: National Science Foundation
Date: 11-21-02
P.O. #: N/A
Hours: 4.0.

NRI - No Recordable Indications T - Top Flange B - Bottom Flange W - Web
N - North Connection / S - South Connection / E - East Connection / W - West Connection

Weld Number & Location	FFI-T Y1	FFI-B Y1	NAS-T Y1	NAS-B Y1				
Transducer Angle	AWS 70°	AWS 70°	AWS 70°	AWS 70°				
Face & Leg	A/1-3	A-B/1-3	A/1-3	A-B/1-3				
a Indication Level (db)	—	—	—	—				
b Reference Level (db)	53db	53db	53db	53db				
c Attenuation Factor (db)								
d Indication Rating (db)								
Length								
Angular Distance (Sound Path)								
Depth From "A" Surface								
Distance From X								
Distance From Y								
Discontinuity Evaluation	NRI	NRI	NRI	NRI				
Results	ACCEPT	ACCEPT	ACCEPT	ACCEPT				

Remarks:

Technician: Simeon J. Kemell NDE Level II Date: 11-21-02 Page 1 of 1
Evaluator: Tim A. Wharton NDE Level II Date: 11-21-02

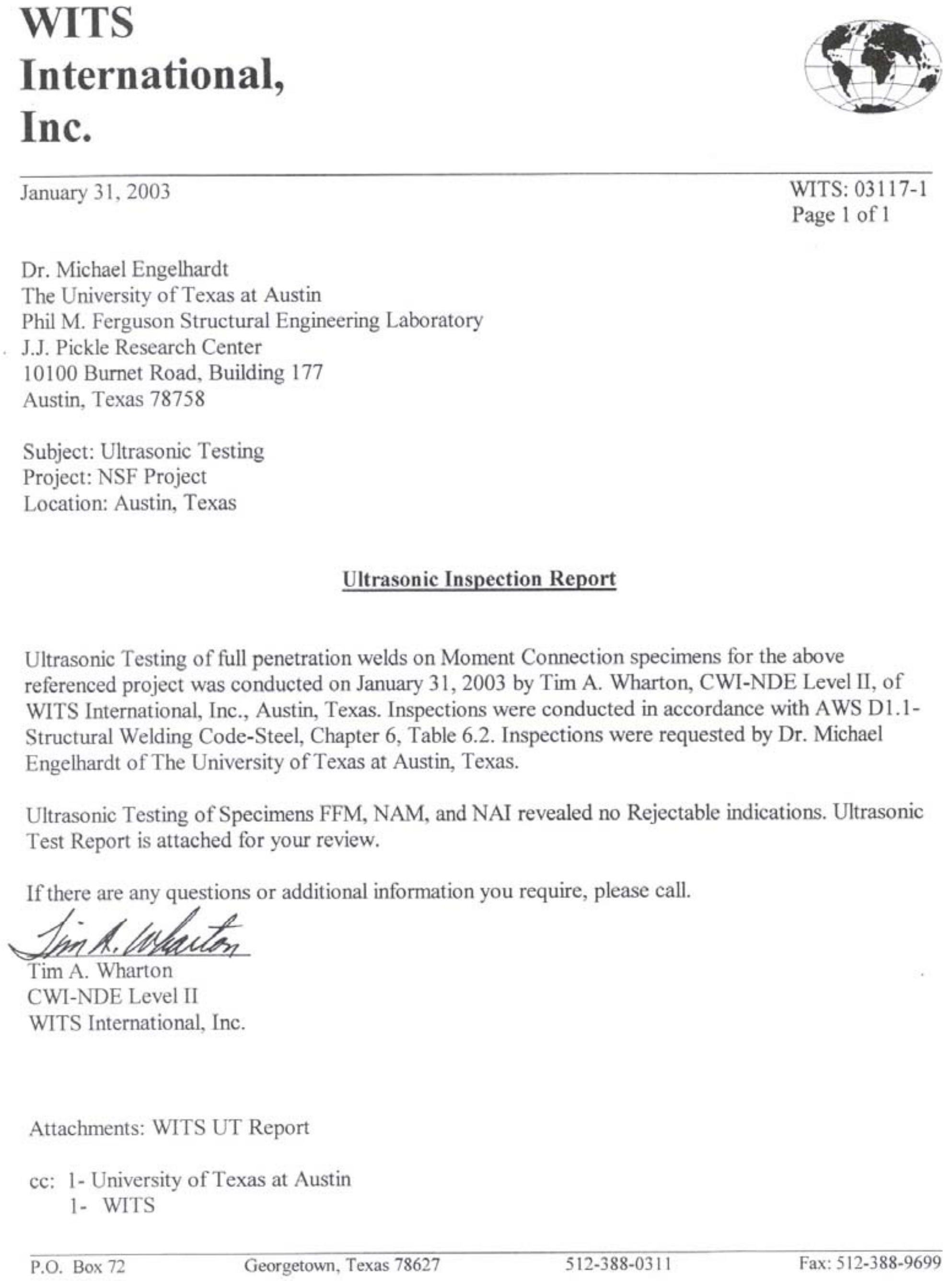

WITS
International,
Inc.

January 31, 2003

WITS: 03117-1
Page 1 of 1

Dr. Michael Engelhardt
The University of Texas at Austin
Phil M. Ferguson Structural Engineering Laboratory
J.J. Pickle Research Center
10100 Burnet Road, Building 177
Austin, Texas 78758

Subject: Ultrasonic Testing
Project: NSF Project
Location: Austin, Texas

Ultrasonic Inspection Report

Ultrasonic Testing of full penetration welds on Moment Connection specimens for the above referenced project was conducted on January 31, 2003 by Tim A. Wharton, CWI-NDE Level II, of WITS International, Inc., Austin, Texas. Inspections were conducted in accordance with AWS D1.1-Structural Welding Code-Steel, Chapter 6, Table 6.2. Inspections were requested by Dr. Michael Engelhardt of The University of Texas at Austin, Texas.

Ultrasonic Testing of Specimens FFM, NAM, and NAI revealed no Rejectable indications. Ultrasonic Test Report is attached for your review.

If there are any questions or additional information you require, please call.

Tim A. Wharton

Tim A. Wharton
CWI-NDE Level II
WITS International, Inc.

Attachments: WITS UT Report

cc: 1- University of Texas at Austin
1- WITS

P.O. Box 72 Georgetown, Texas 78627 512-388-0311 Fax: 512-388-9699

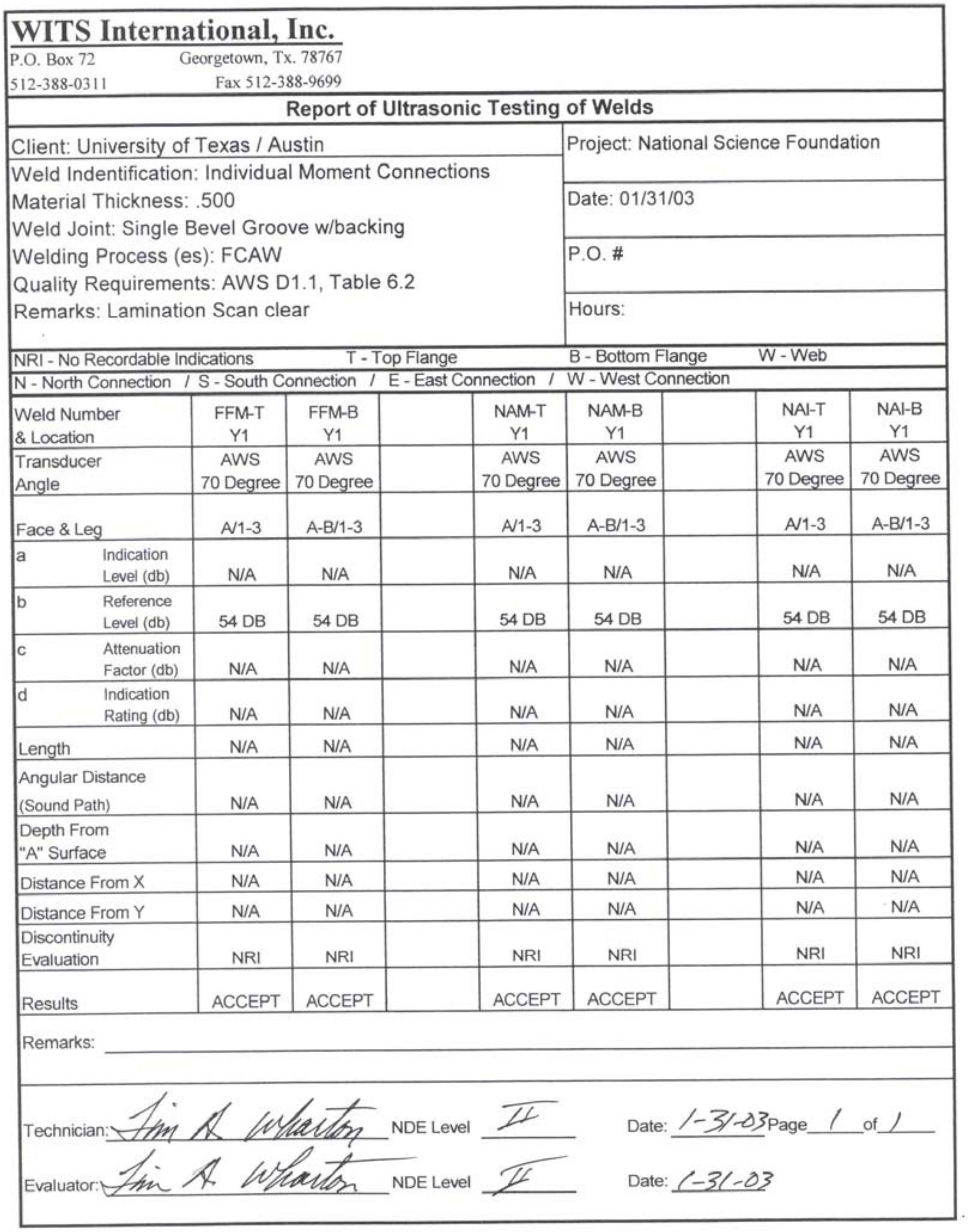

WITS International, Inc.
P.O. Box 72 Georgetown, Tx. 78767
512-388-0311 Fax 512-388-9699

Report of Ultrasonic Testing of Welds

Client: University of Texas / Austin	Project: National Science Foundation
Weld Indentification: Individual Moment Connections	
Material Thickness: .500	Date: 01/31/03
Weld Joint: Single Bevel Groove w/backing	
Welding Process (es): FCAW	P.O. #
Quality Requirements: AWS D1.1, Table 6.2	
Remarks: Lamination Scan clear	Hours:

NRI - No Recordable Indications T - Top Flange B - Bottom Flange W - Web
N - North Connection / S - South Connection / E - East Connection / W - West Connection

Weld Number & Location	FFM-T Y1	FFM-B Y1		NAM-T Y1	NAM-B Y1		NAI-T Y1	NAI-B Y1
Transducer Angle	AWS 70 Degree	AWS 70 Degree		AWS 70 Degree	AWS 70 Degree		AWS 70 Degree	AWS 70 Degree
Face & Leg	A/1-3	A-B/1-3		A/1-3	A-B/1-3		A/1-3	A-B/1-3
a Indication Level (db)	N/A	N/A		N/A	N/A		N/A	N/A
b Reference Level (db)	54 DB	54 DB		54 DB	54 DB		54 DB	54 DB
c Attenuation Factor (db)	N/A	N/A		N/A	N/A		N/A	N/A
d Indication Rating (db)	N/A	N/A		N/A	N/A		N/A	N/A
Length	N/A	N/A		N/A	N/A		N/A	N/A
Angular Distance (Sound Path)	N/A	N/A		N/A	N/A		N/A	N/A
Depth From "A" Surface	N/A	N/A		N/A	N/A		N/A	N/A
Distance From X	N/A	N/A		N/A	N/A		N/A	N/A
Distance From Y	N/A	N/A		N/A	N/A		N/A	N/A
Discontinuity Evaluation	NRI	NRI		NRI	NRI		NRI	NRI
Results	ACCEPT	ACCEPT		ACCEPT	ACCEPT		ACCEPT	ACCEPT

Remarks:

Technician: Jim A Wharton NDE Level II Date: 1-31-03 Page 1 of 1

Evaluator: Jim A. Wharton NDE Level II Date: 1-31-03

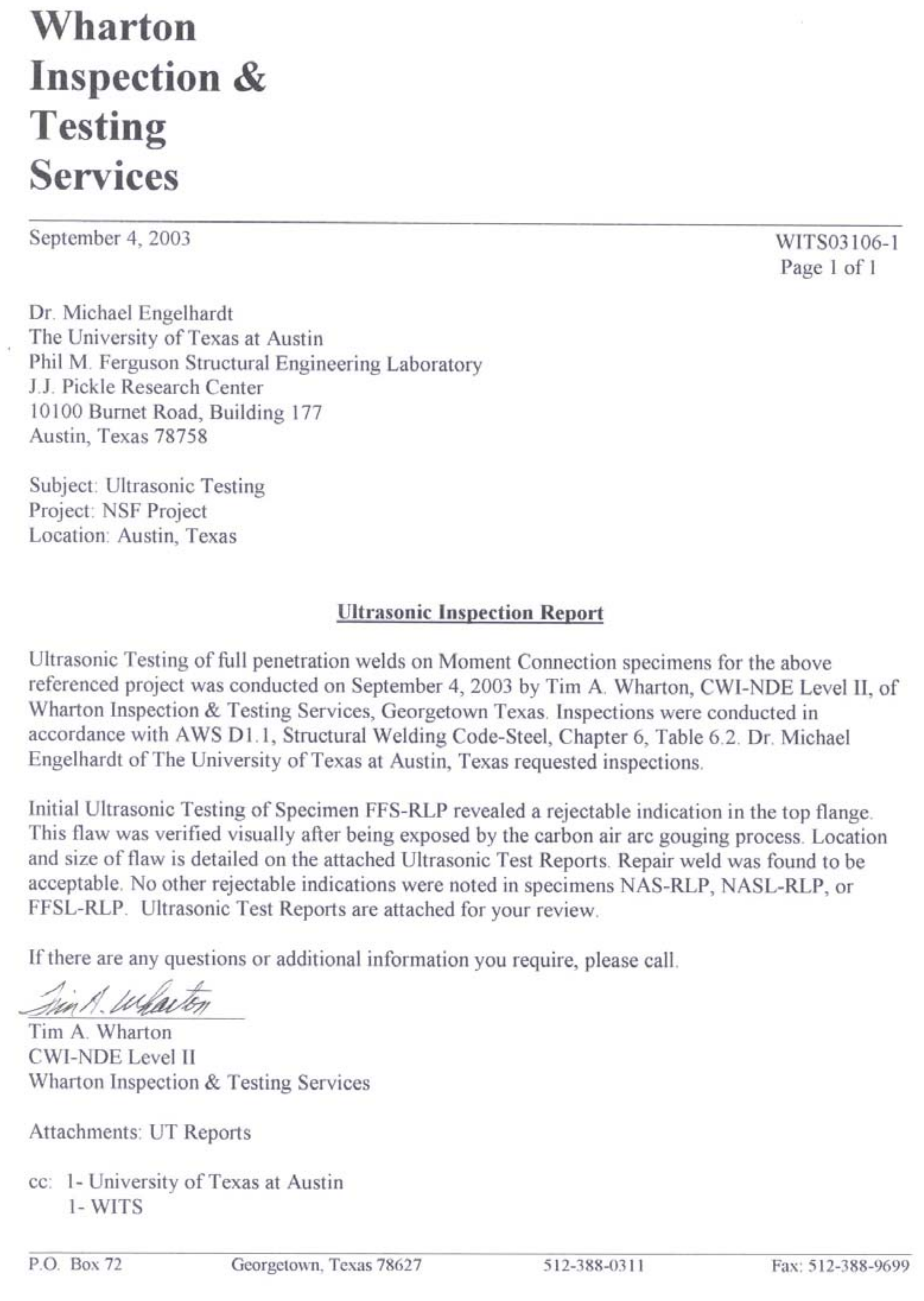

Wharton
Inspection &
Testing
Services

September 4, 2003

WITS03106-1
Page 1 of 1

Dr. Michael Engelhardt
The University of Texas at Austin
Phil M. Ferguson Structural Engineering Laboratory
J.J. Pickle Research Center
10100 Burnet Road, Building 177
Austin, Texas 78758

Subject: Ultrasonic Testing
Project: NSF Project
Location: Austin, Texas

Ultrasonic Inspection Report

Ultrasonic Testing of full penetration welds on Moment Connection specimens for the above referenced project was conducted on September 4, 2003 by Tim A. Wharton, CWI-NDE Level II, of Wharton Inspection & Testing Services, Georgetown Texas. Inspections were conducted in accordance with AWS D1.1, Structural Welding Code-Steel, Chapter 6, Table 6.2. Dr. Michael Engelhardt of The University of Texas at Austin, Texas requested inspections.

Initial Ultrasonic Testing of Specimen FFS-RLP revealed a rejectable indication in the top flange. This flaw was verified visually after being exposed by the carbon air arc gouging process. Location and size of flaw is detailed on the attached Ultrasonic Test Reports. Repair weld was found to be acceptable. No other rejectable indications were noted in specimens NAS-RLP, NASL-RLP, or FFSL-RLP. Ultrasonic Test Reports are attached for your review.

If there are any questions or additional information you require, please call.

Tim A. Wharton

Tim A. Wharton
CWI-NDE Level II
Wharton Inspection & Testing Services

Attachments: UT Reports

cc: 1- University of Texas at Austin
1- WITS

P.O. Box 72 Georgetown, Texas 78627 512-388-0311 Fax: 512-388-9699

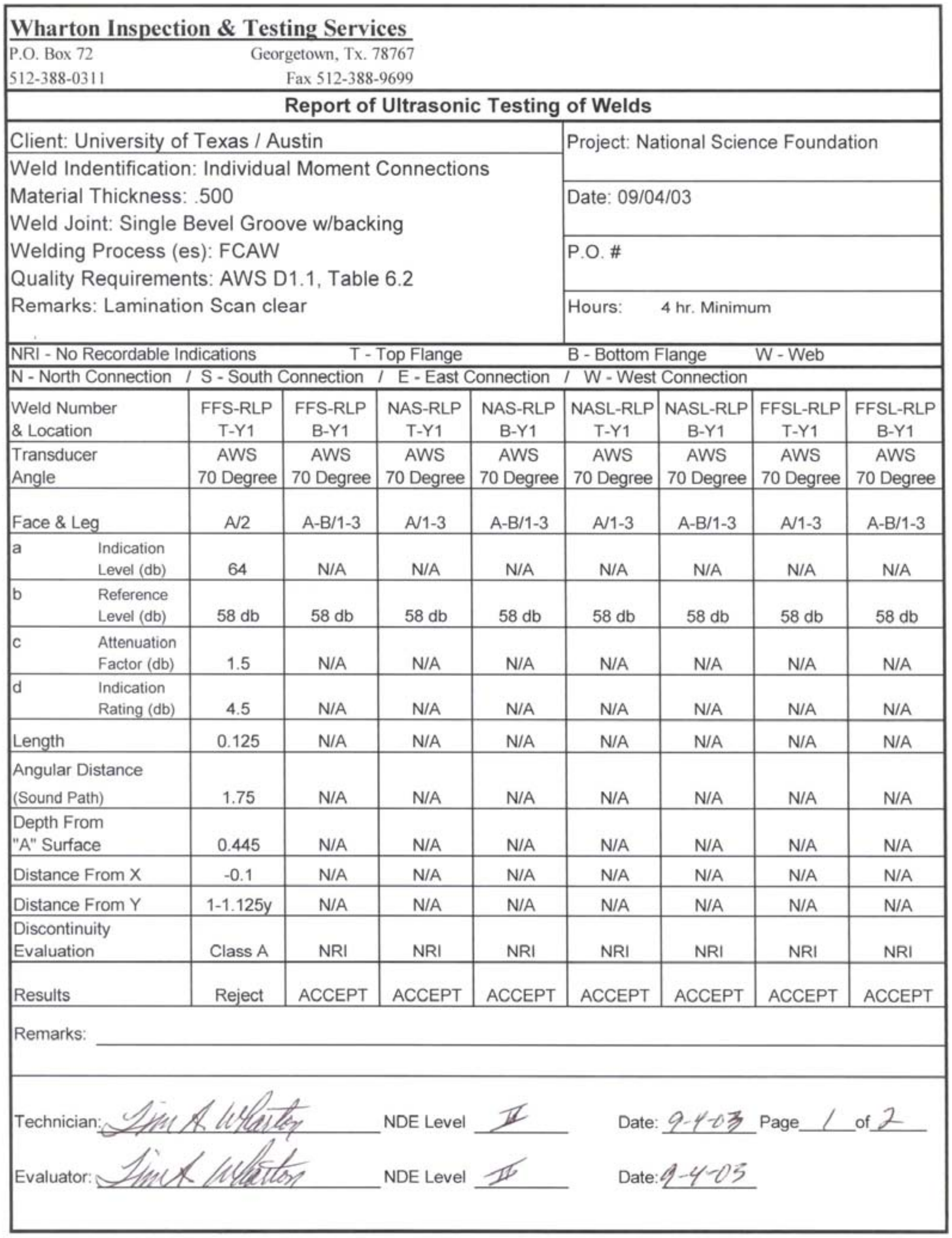

Wharton Inspection & Testing Services

P.O. Box 72 Georgetown, Tx. 78767
512-388-0311 Fax 512-388-9699

Report of Ultrasonic Testing of Welds

Client: University of Texas / Austin
Weld Indentification: Individual Moment Connections
Material Thickness: .500
Weld Joint: Single Bevel Groove w/backing
Welding Process (es): FCAW
Quality Requirements: AWS D1.1, Table 6.2
Remarks: Lamination Scan clear

Project: National Science Foundation
Date: 09/04/03
P.O. #
Hours: 4 hr. Minimum

NRI - No Recordable Indications T - Top Flange B - Bottom Flange W - Web
N - North Connection / S - South Connection / E - East Connection / W - West Connection

Weld Number & Location	FFS-RLP T-Y1	FFS-RLP B-Y1	NAS-RLP T-Y1	NAS-RLP B-Y1	NASL-RLP T-Y1	NASL-RLP B-Y1	FFSL-RLP T-Y1	FFSL-RLP B-Y1
Transducer Angle	AWS 70 Degree	AWS 70 Degree	AWS 70 Degree	AWS 70 Degree	AWS 70 Degree	AWS 70 Degree	AWS 70 Degree	AWS 70 Degree
Face & Leg	A/2	A-B/1-3	A/1-3	A-B/1-3	A/1-3	A-B/1-3	A/1-3	A-B/1-3
a Indication Level (db)	64	N/A	N/A	N/A	N/A	N/A	N/A	N/A
b Reference Level (db)	58 db	58 db	58 db	58 db	58 db	58 db	58 db	58 db
c Attenuation Factor (db)	1.5	N/A	N/A	N/A	N/A	N/A	N/A	N/A
d Indication Rating (db)	4.5	N/A	N/A	N/A	N/A	N/A	N/A	N/A
Length	0.125	N/A	N/A	N/A	N/A	N/A	N/A	N/A
Angular Distance (Sound Path)	1.75	N/A	N/A	N/A	N/A	N/A	N/A	N/A
Depth From "A" Surface	0.445	N/A	N/A	N/A	N/A	N/A	N/A	N/A
Distance From X	-0.1	N/A	N/A	N/A	N/A	N/A	N/A	N/A
Distance From Y	1-1.125y	N/A	N/A	N/A	N/A	N/A	N/A	N/A
Discontinuity Evaluation	Class A	NRI	NRI	NRI	NRI	NRI	NRI	NRI
Results	Reject	ACCEPT	ACCEPT	ACCEPT	ACCEPT	ACCEPT	ACCEPT	ACCEPT

Remarks:

Technician: Tim A. Wharton NDE Level II Date: 9-4-03 Page 1 of 2

Evaluator: Tim A. Wharton NDE Level II Date: 9-4-03

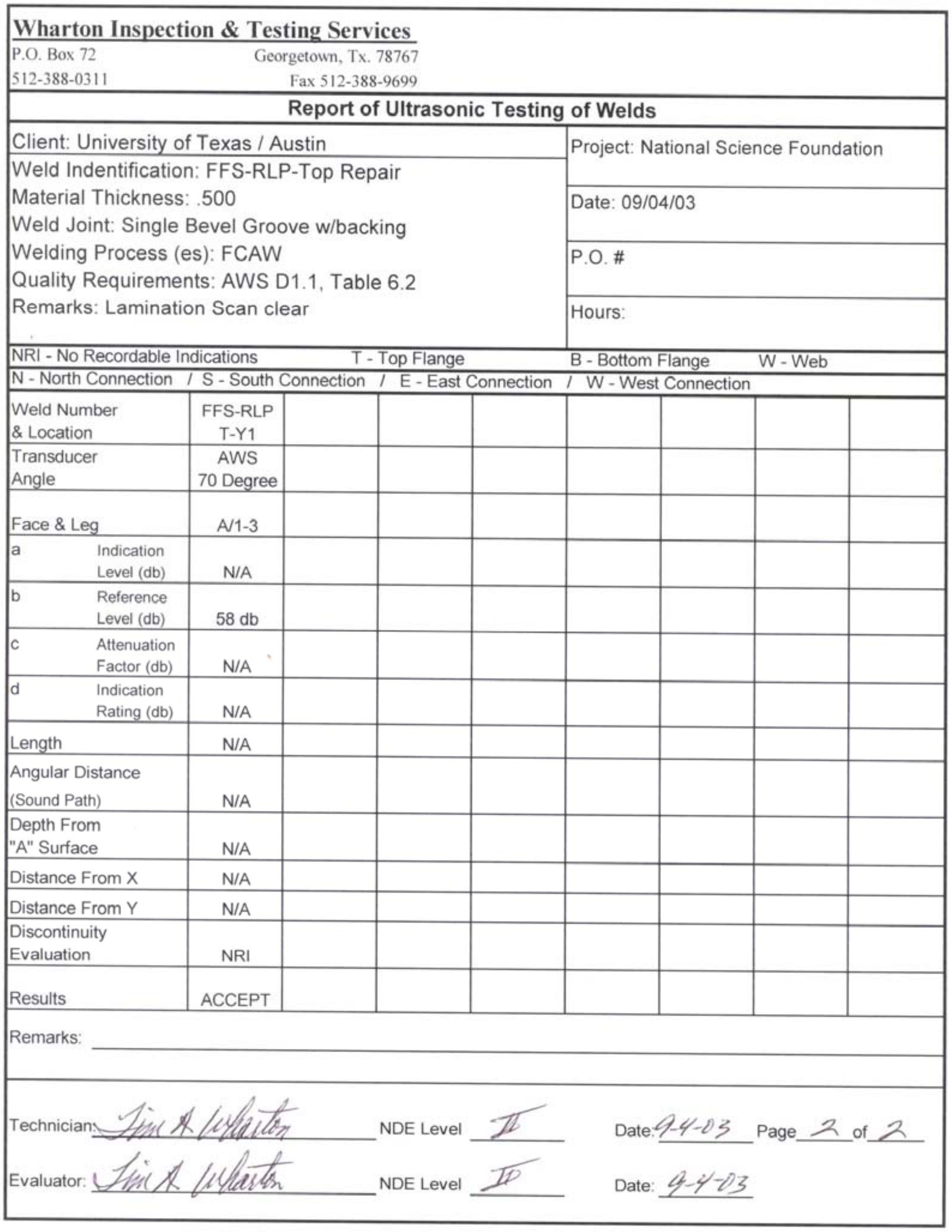

Wharton Inspection & Testing Services
P.O. Box 72 Georgetown, Tx. 78767
512-388-0311 Fax 512-388-9699

Report of Ultrasonic Testing of Welds

Client: University of Texas / Austin
Weld Indentification: FFS-RLP-Top Repair
Material Thickness: .500
Weld Joint: Single Bevel Groove w/backing
Welding Process (es): FCAW
Quality Requirements: AWS D1.1, Table 6.2
Remarks: Lamination Scan clear

Project: National Science Foundation
Date: 09/04/03
P.O. #
Hours:

NRI - No Recordable Indications T - Top Flange B - Bottom Flange W - Web
N - North Connection / S - South Connection / E - East Connection / W - West Connection

Weld Number & Location	FFS-RLP T-Y1							
Transducer Angle	AWS 70 Degree							
Face & Leg	A/1-3							
a Indication Level (db)	N/A							
b Reference Level (db)	58 db							
c Attenuation Factor (db)	N/A							
d Indication Rating (db)	N/A							
Length	N/A							
Angular Distance (Sound Path)	N/A							
Depth From "A" Surface	N/A							
Distance From X	N/A							
Distance From Y	N/A							
Discontinuity Evaluation	NRI							
Results	ACCEPT							

Remarks:

Technician: Tim A. Wharton NDE Level II Date: 9-4-03 Page 2 of 2
Evaluator: Tim A. Wharton NDE Level II Date: 9-4-03

APPENDIX G

Strain Gauge Data

This appendix compiles all data obtained from the strain gauges. Post-yield strain gauges were placed in the MW-Specimens, as discussed in Section 3.2.4. Tokyo Sokki products YFLA-2-3LT (uniaxial gauge; gauge length 2 mm) and YEFRA-2-3LT (rosette gauge; gauge length 2 mm) were used. The locations of the strain gauges are summarized in Figure 3.11. The data collected from these strain gauges provide additional useful insights into the behavior of the specimens.

Caution is required in interpreting the strain gauge data, since TML warns against use of post-yield strain gauges for cyclic loading. The gauges and the adhesive are not designed for use in cyclic testing. *TML strain gauge performance characteristics* (Tokyo Sokki Kenkyujo Co., Ltd.) reports that under strain cycles of ±1%, the measured strain would gradually drift in the positive direction. This trend could be present in the strain hysteresis reported herein.

Table G1 summarizes the figures included in this appendix. The longitudinal strain hysteresis is illustrated by the relation between the strain in percent and link shear force. The shear strain hysteresis is illustrated by two types of figures. One figure shows the relation between the shear strain in radians and link shear force. Another figure shows the relation between the shear strain and link rotation (denoted as global-γ), both in radians.

Table G1 Summary of Strain Gauge Hysteresis Data

Specimen	Location	Strain Type	Figure
MWS	Top Flange Outer Face	Longitudinal	Figure G1
	Top Flange Inner Face	Longitudinal	Figure G2
	Bottom Flange Inner Face	Longitudinal	Figure G3
	Bottom Flange Outer Face	Longitudinal	Figure G4
	Near Column Face	Longitudinal	Figure G5
	Web Panels	Shear	Figure G6
MWI	Top Flange Outer Face	Longitudinal	Figure G7
	Top Flange Inner Face	Longitudinal	Figure G8
	Bottom Flange Inner Face	Longitudinal	Figure G9
	Bottom Flange Outer Face	Longitudinal	Figure G10
	Near Column Face	Longitudinal	Figure G11
	Web Panels	Shear	Figure G12
MWM	Top Flange Outer Face	Longitudinal	Figure G13
	Top Flange Inner Face	Longitudinal	Figure G14
	Bottom Flange Inner Face	Longitudinal	Figure G15
	Bottom Flange Outer Face	Longitudinal	Figure G16
	Near Column Face	Longitudinal	Figure G17
	Web Panels	Shear	Figure G18

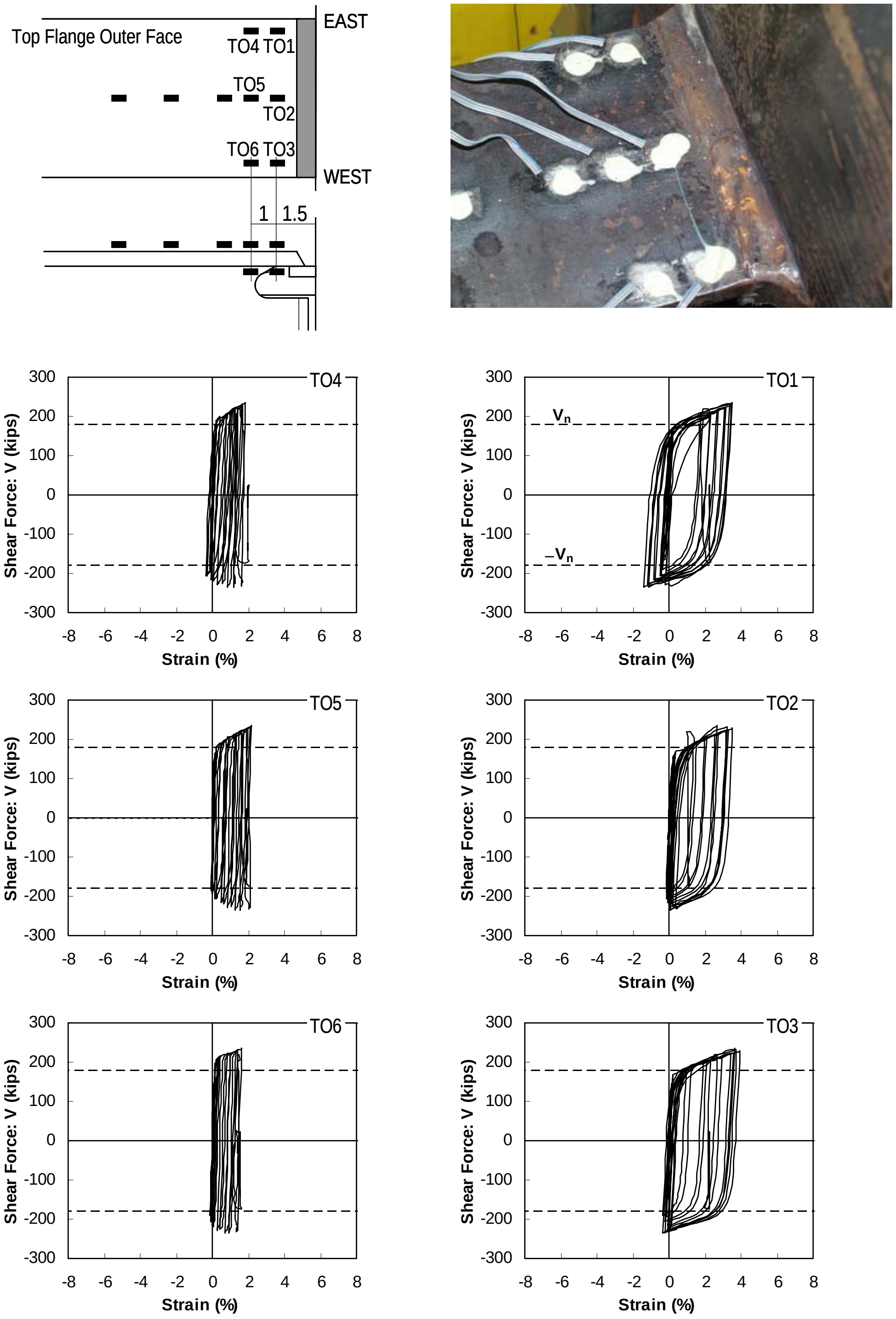

Figure G1 Specimen MWS: Top flange outer face

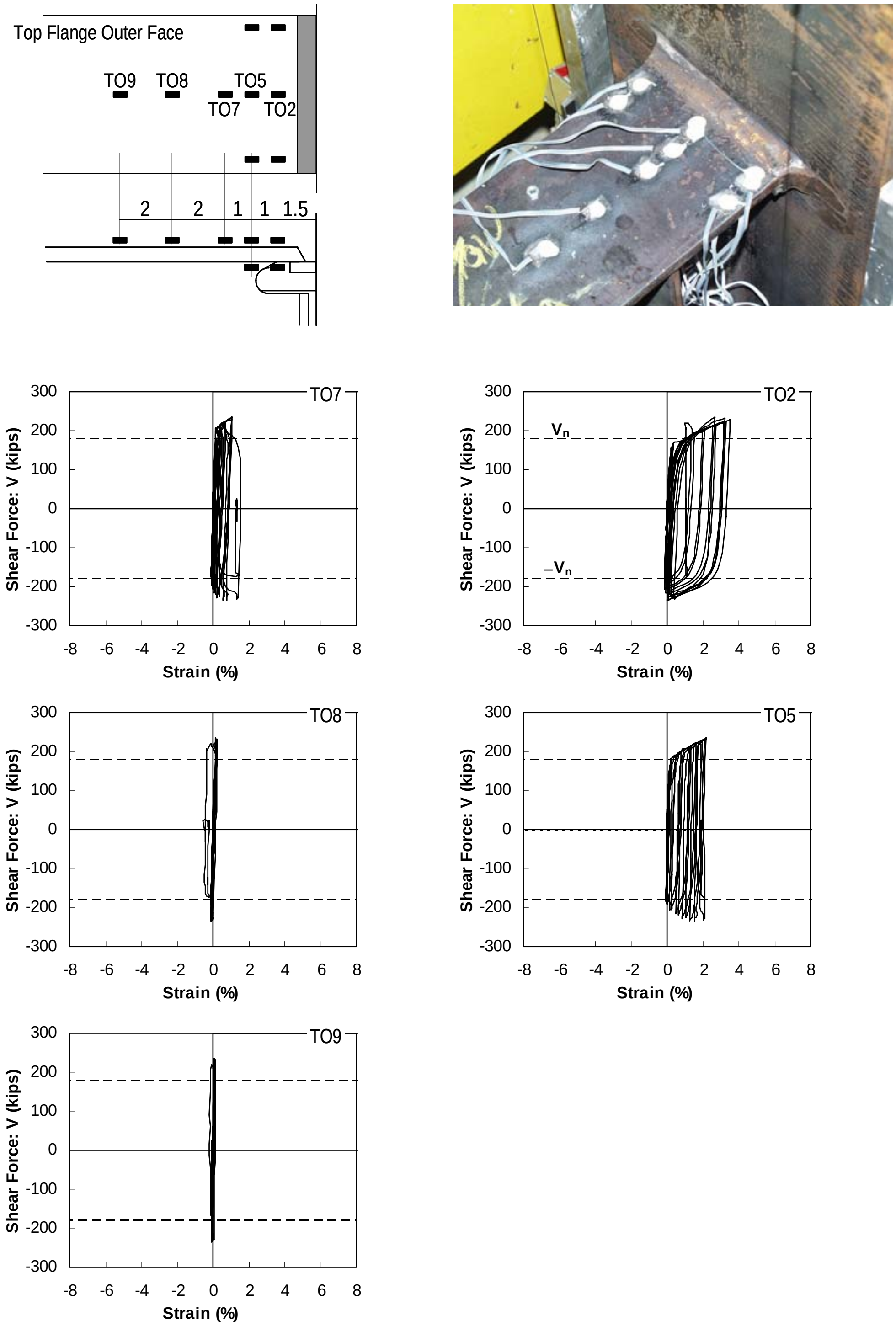

Figure G1 Specimen MWS: Top flange outer face (Continued)

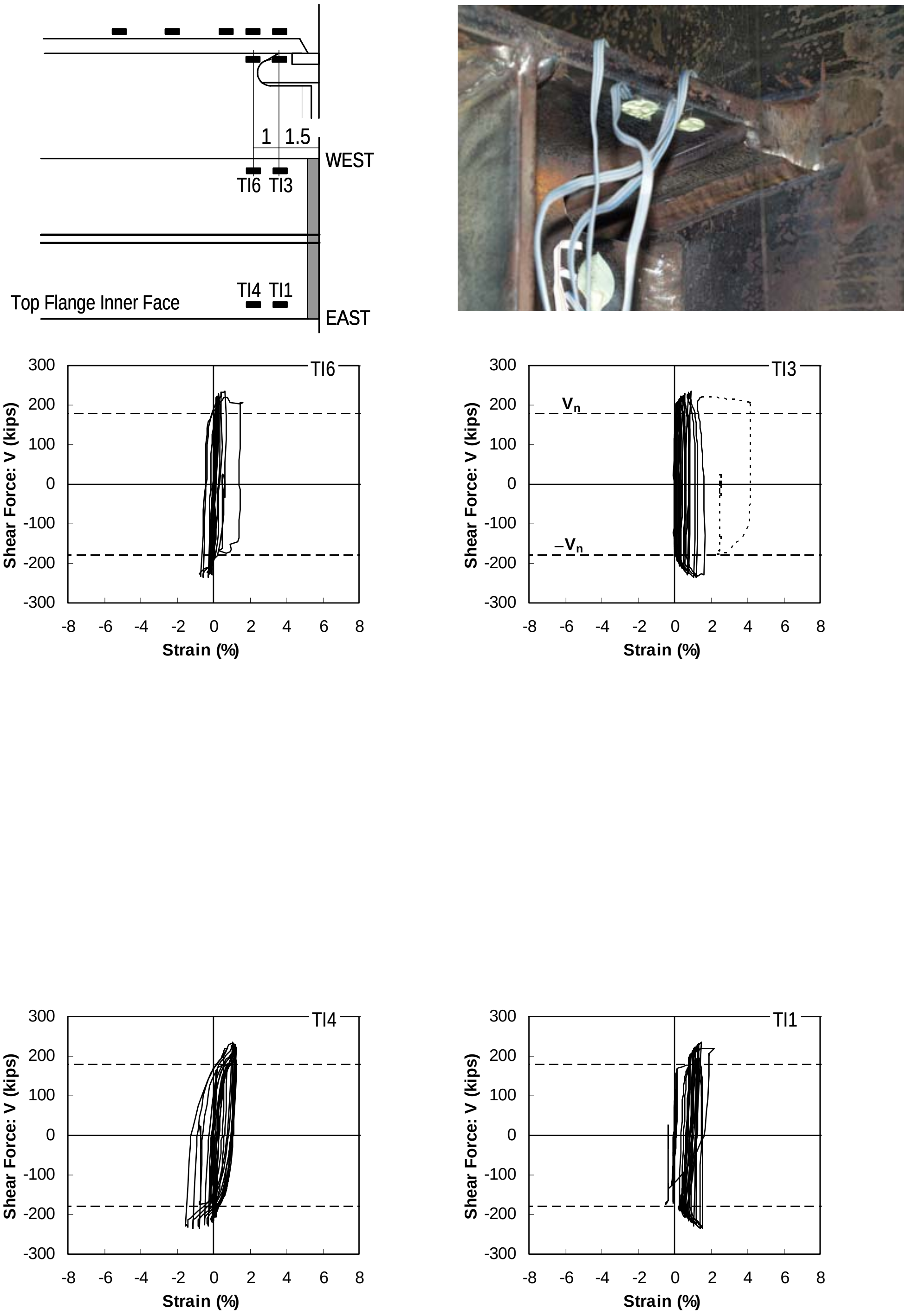

Figure G2 Specimen MWS: Top flange inner face

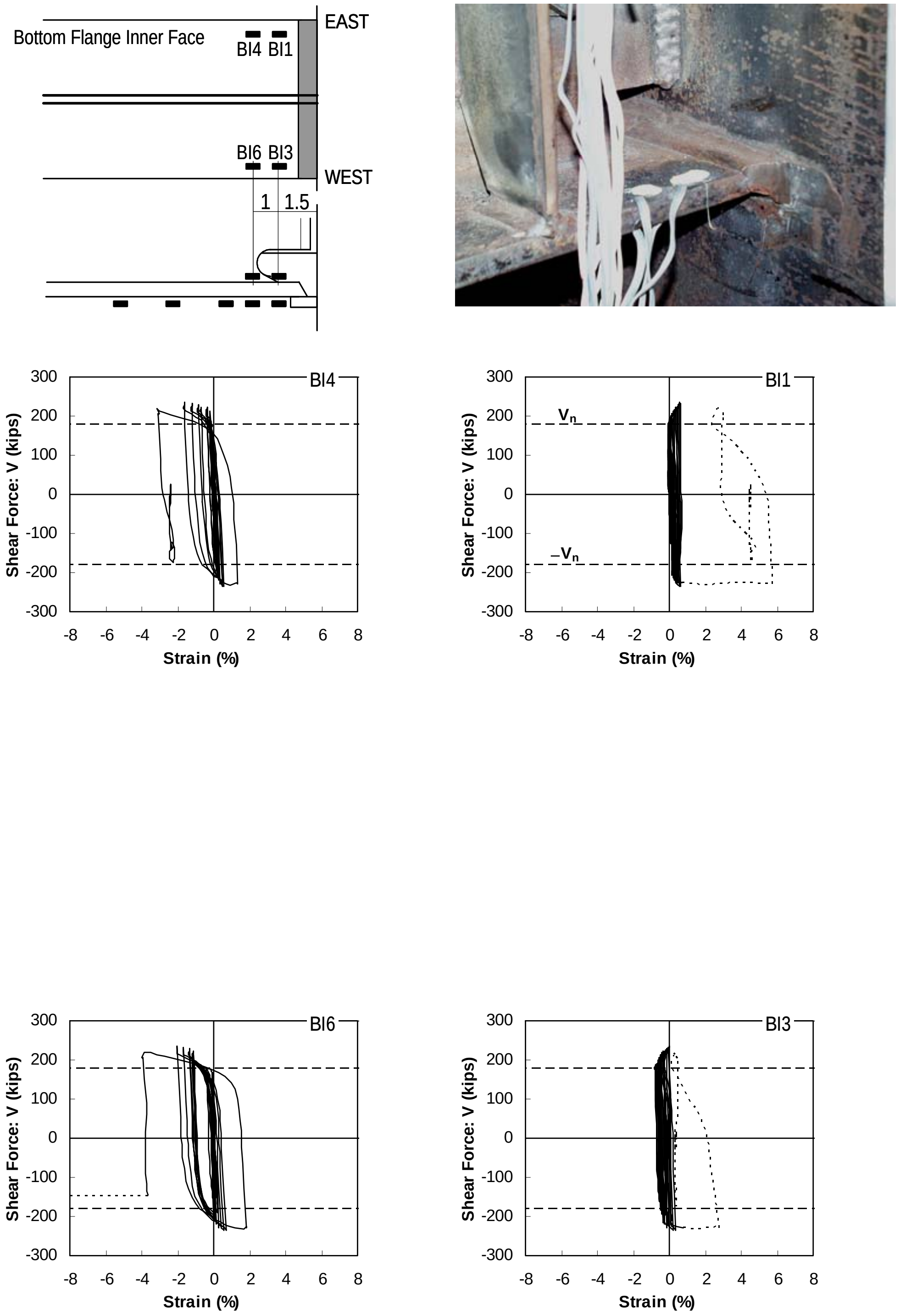

Figure G3 Specimen MWS: Bottom flange inner face

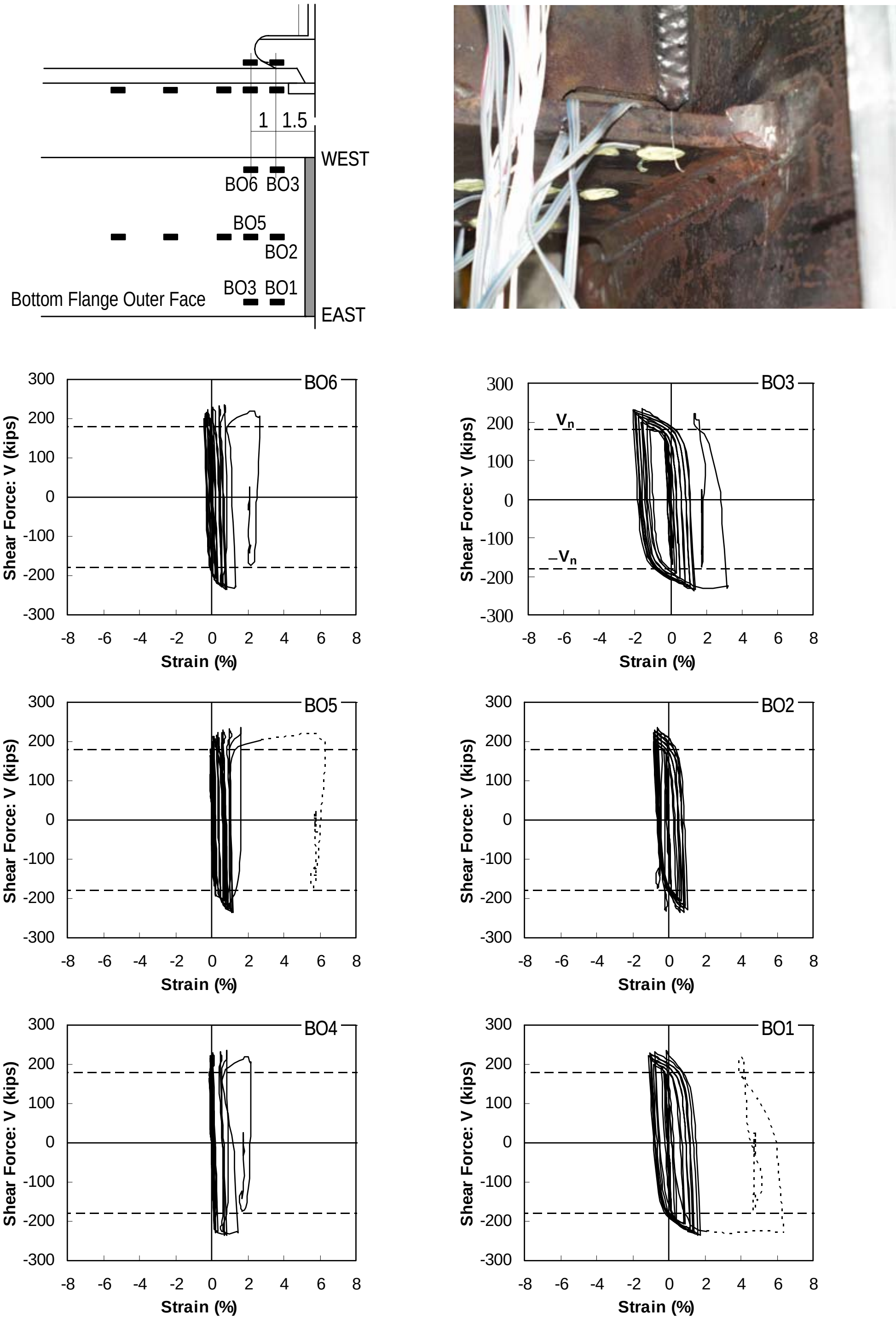

Figure G4 Specimen MWS: Bottom flange outer face

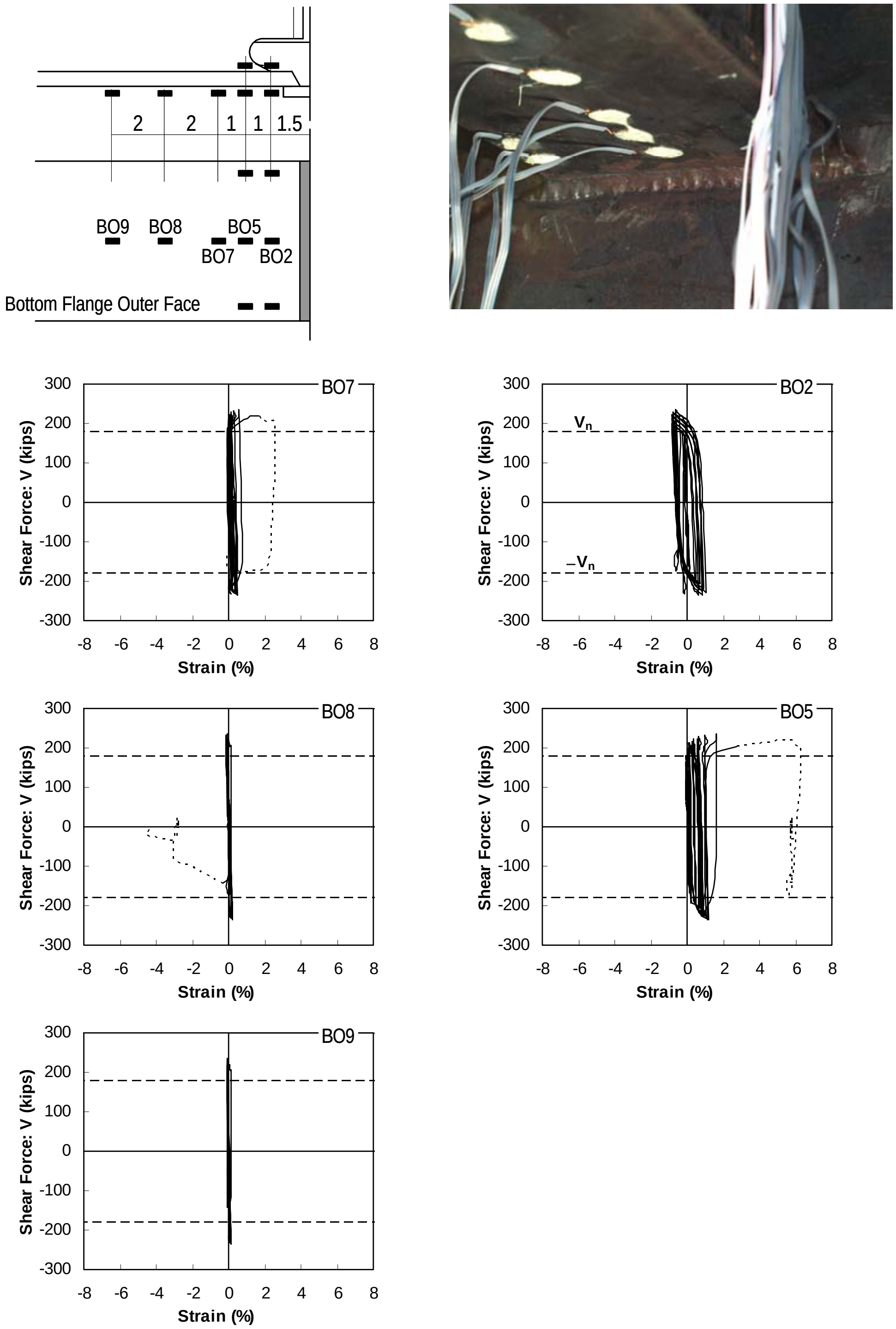

Figure G4 Specimen MWS: Bottom flange outer face (Continued)

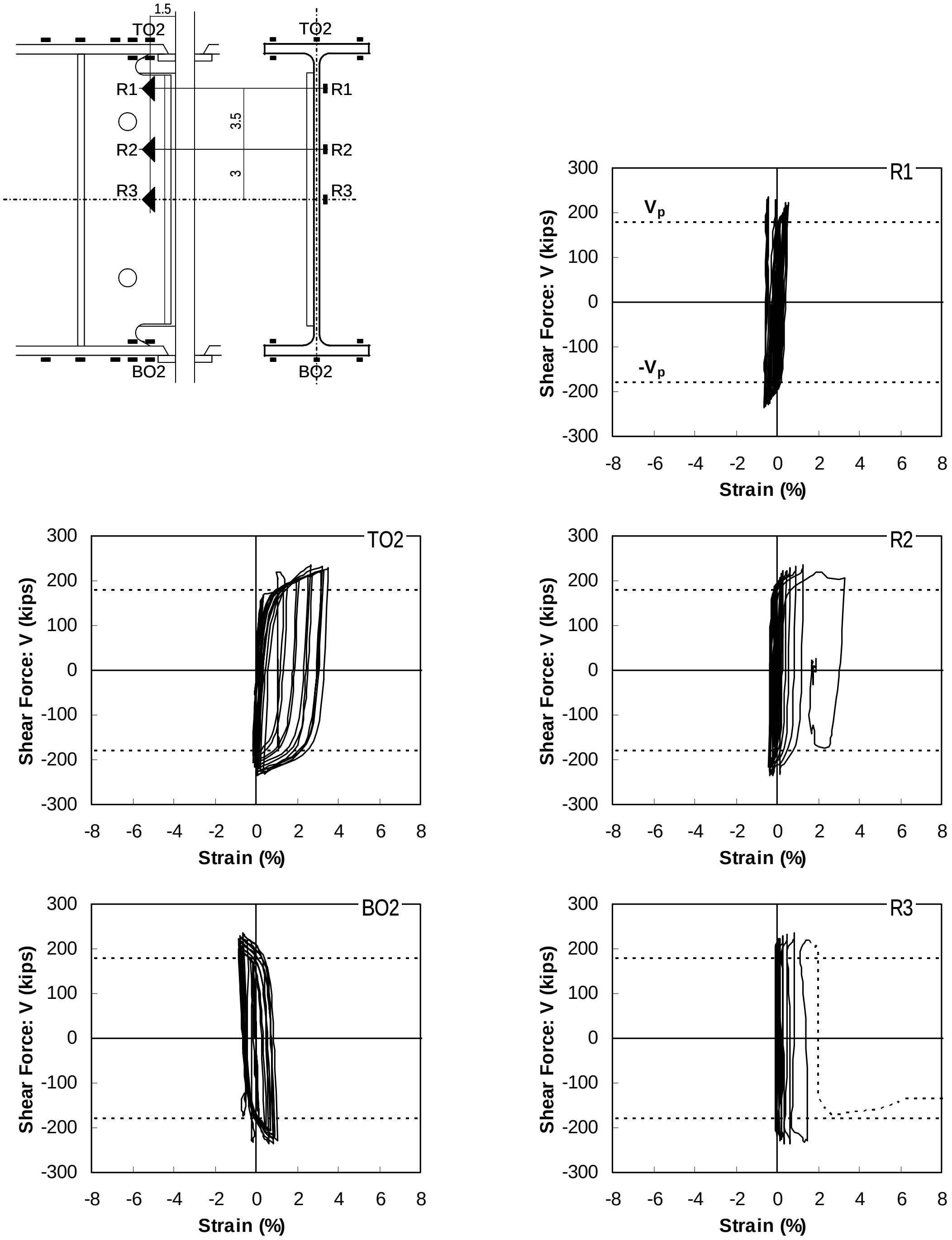

Figure G5 Specimen MWS: Bending stress near column face

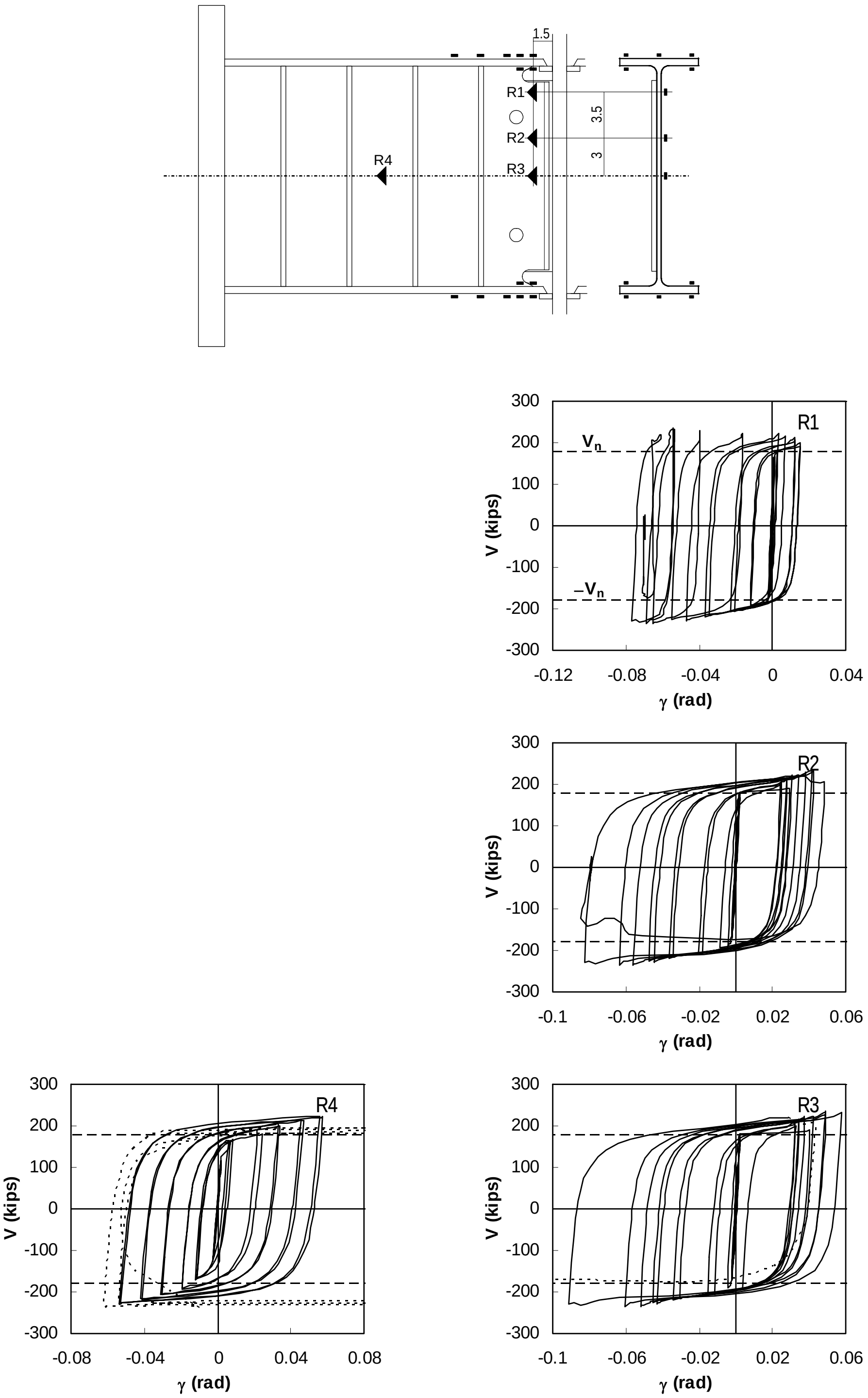

Figure G6 Specimen MWS: Web panel shear stress

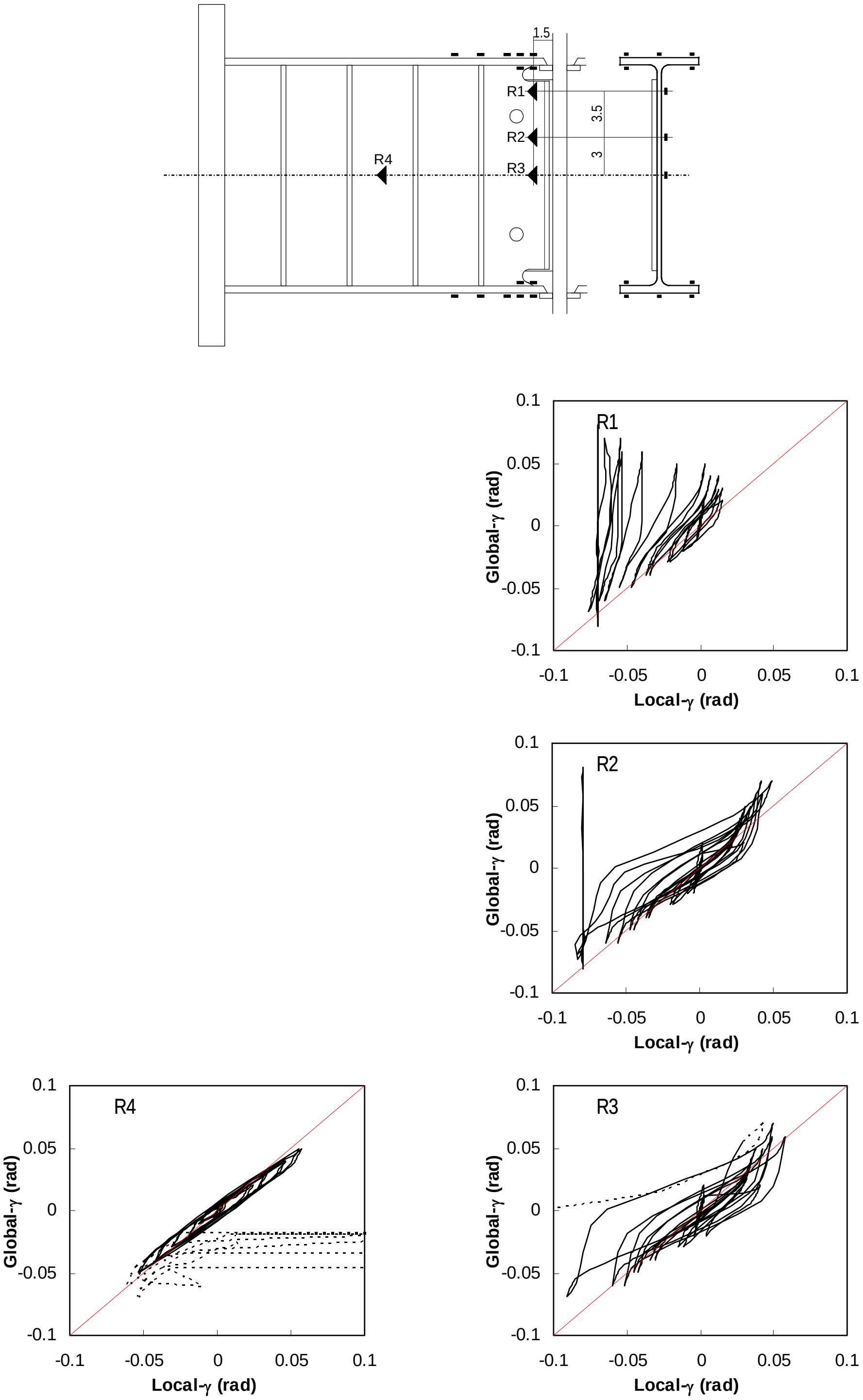

Figure G6 Specimen MWS: Web panel shear stress (Continued)

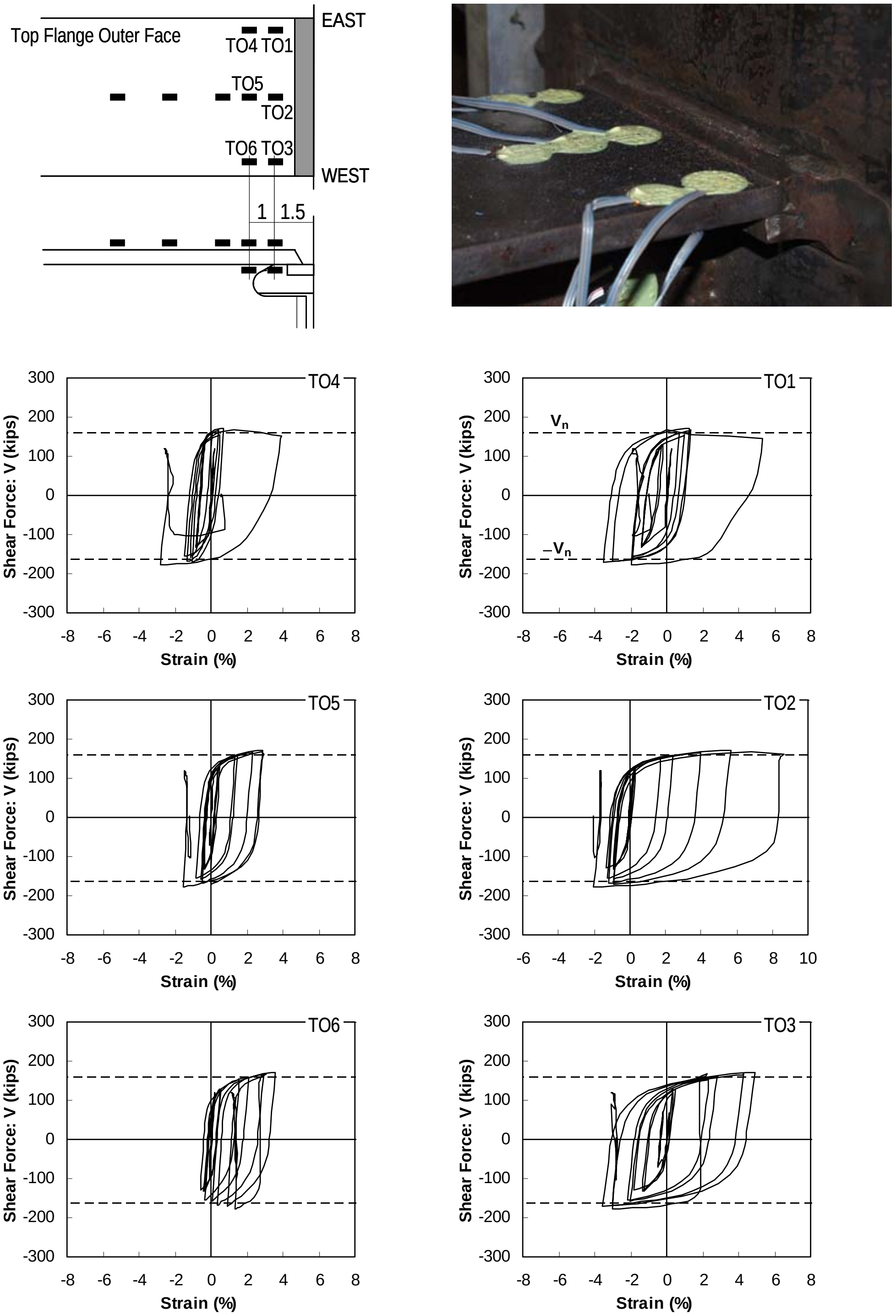

Figure G7 Specimen MWI: Top flange outer face

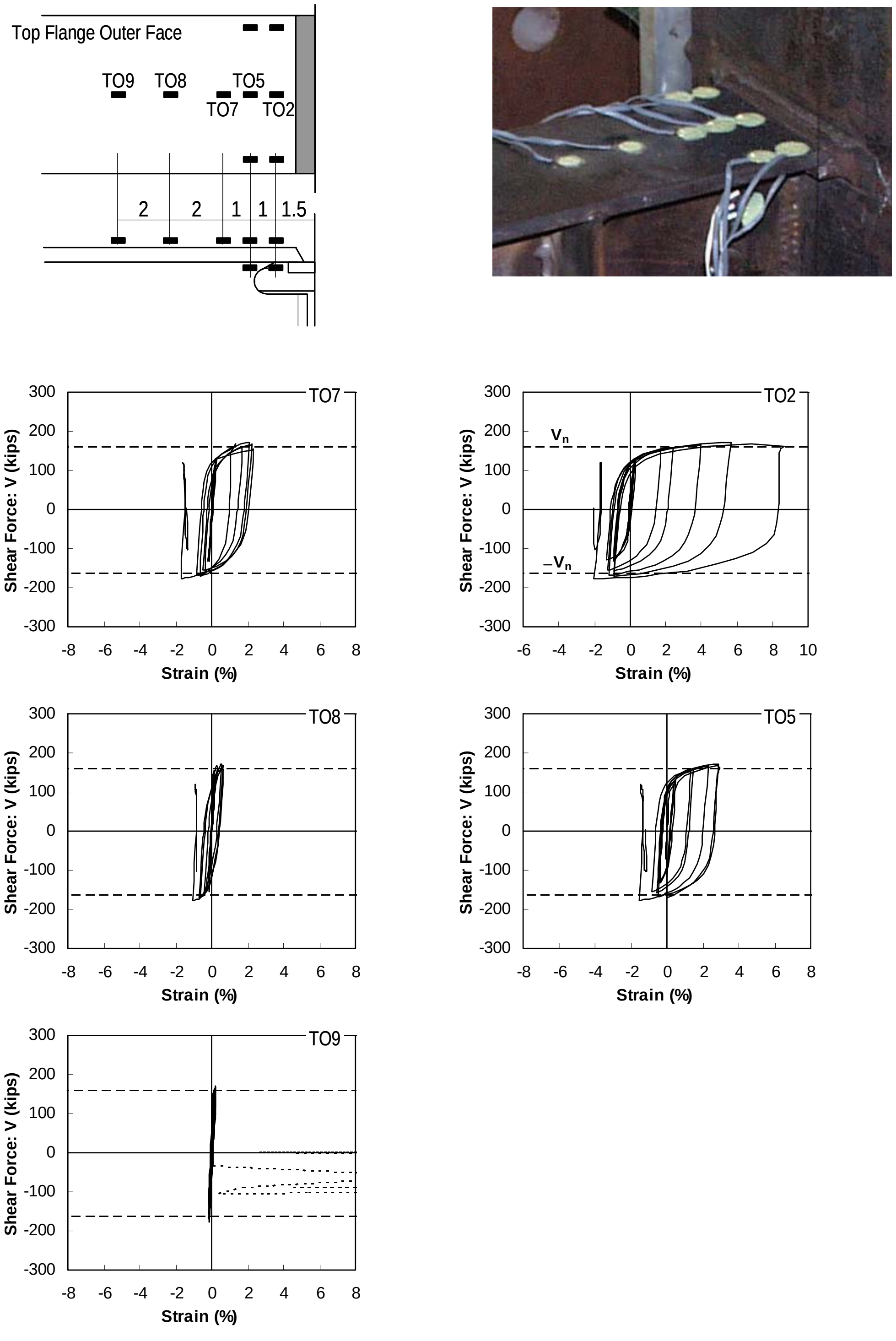

Figure G7 Specimen MWI: Top flange outer face (Continued)

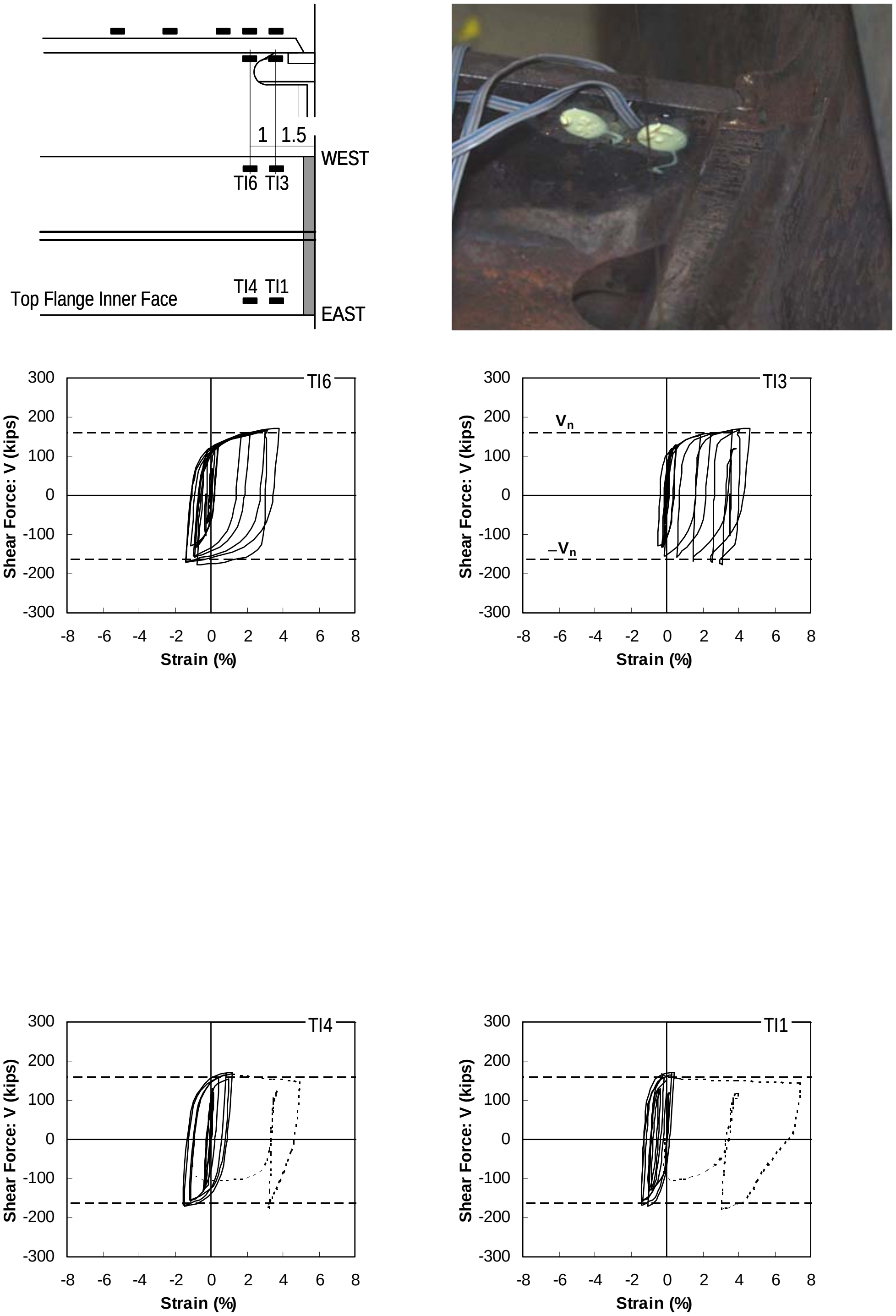

Figure G8 Specimen MWI: Top flange inner face

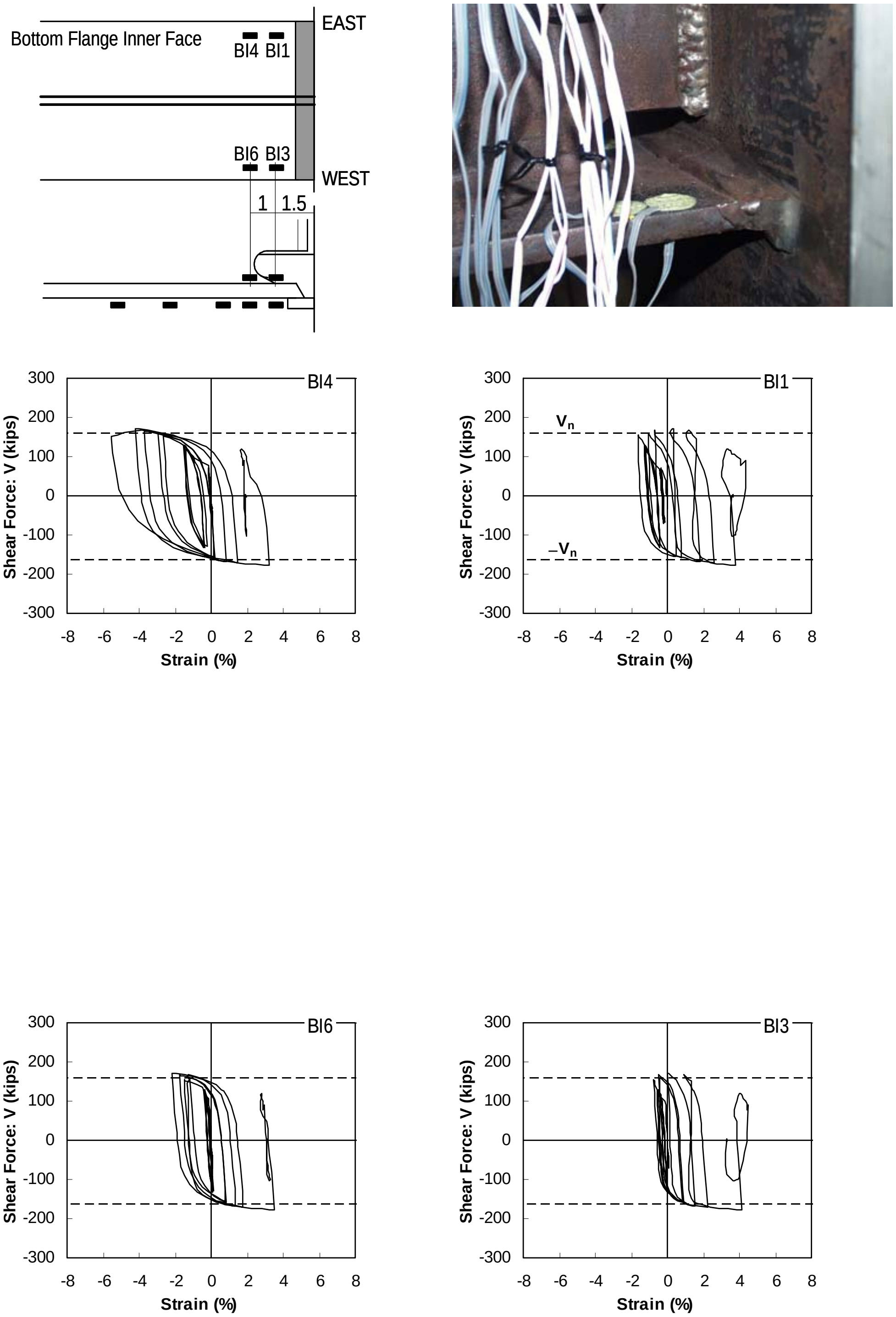

Figure G9 Specimen MWI: Bottom flange inner face

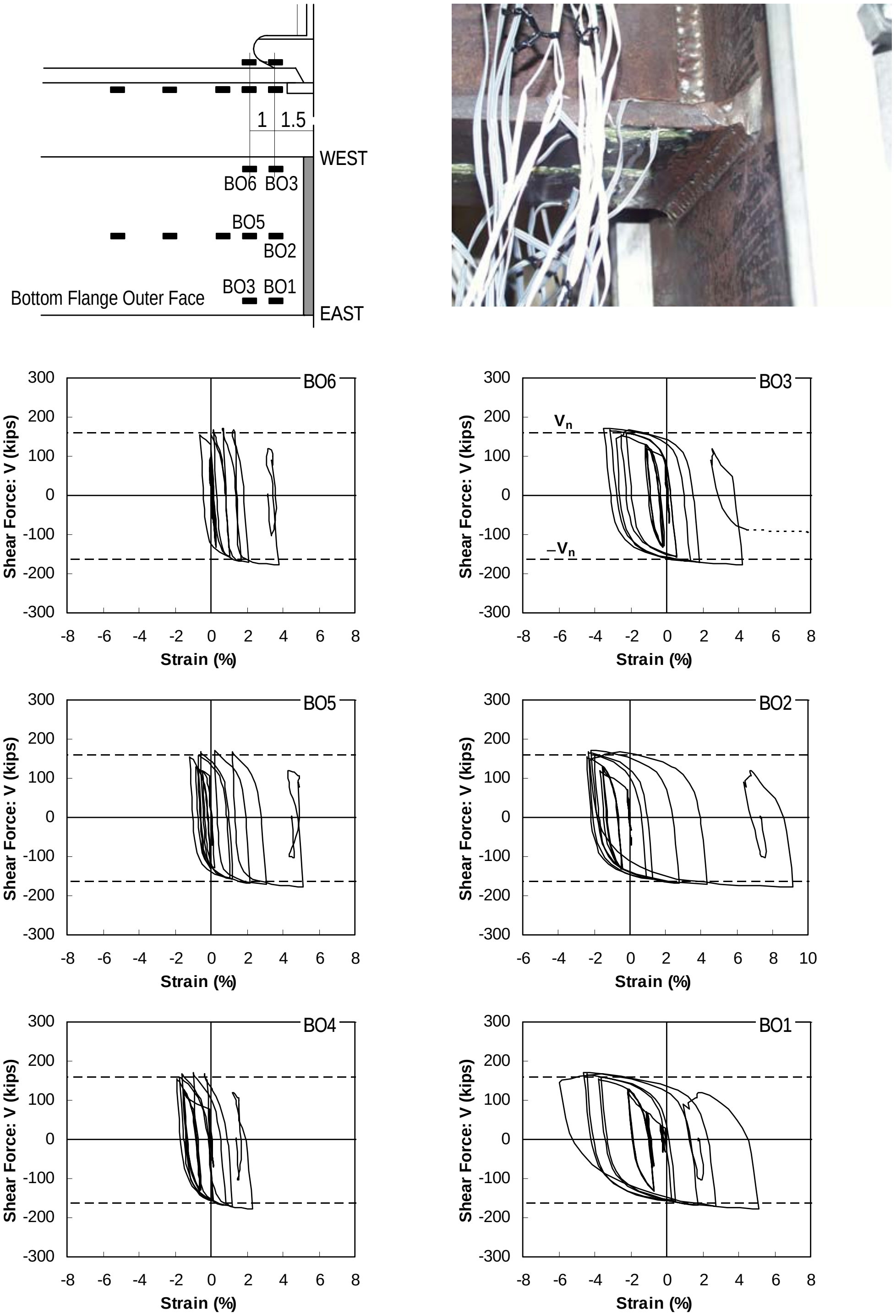

Figure G10 Specimen MWI: Bottom flange outer face

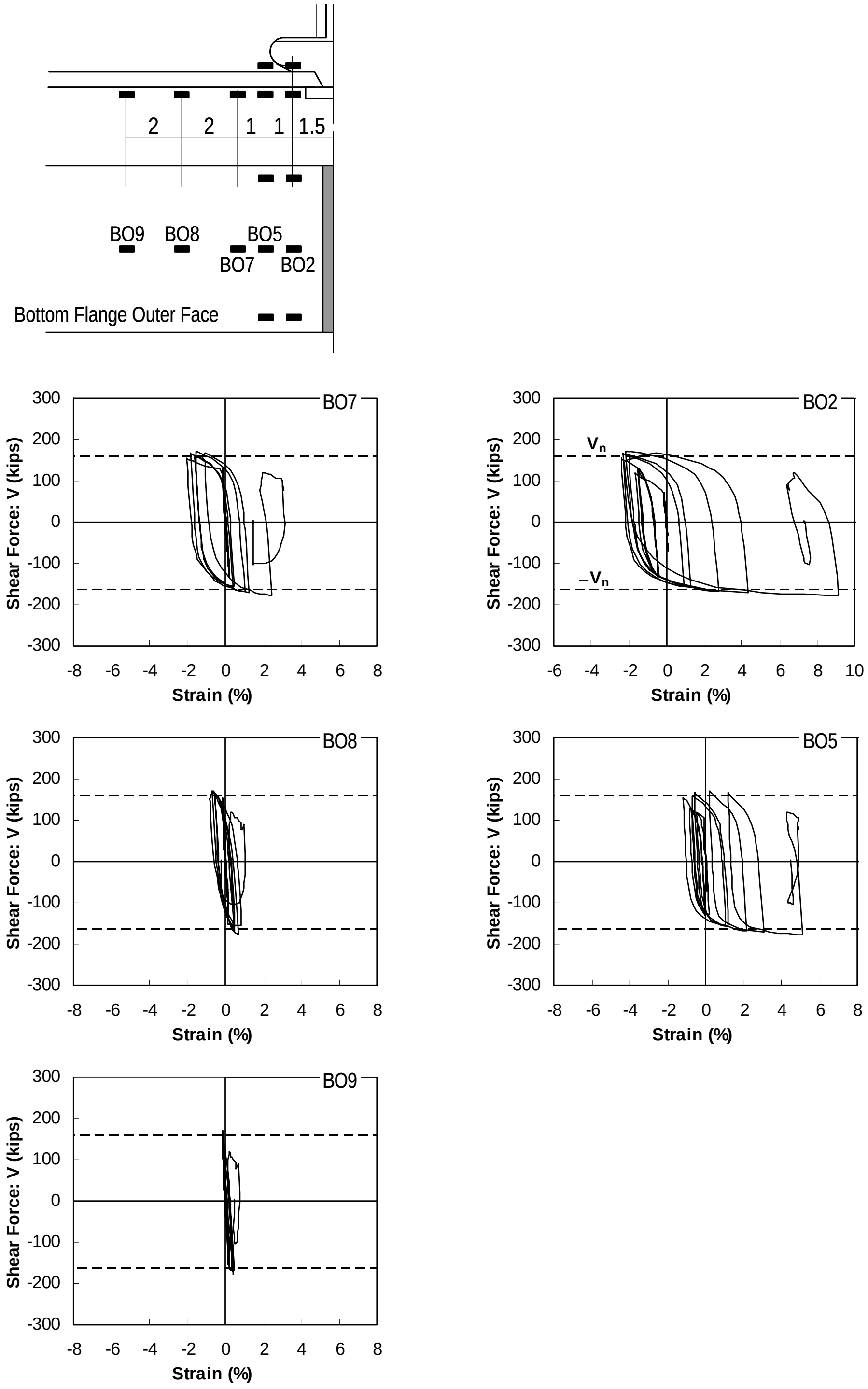

Figure G10 Specimen MWI: Bottom flange outer face (Continued)

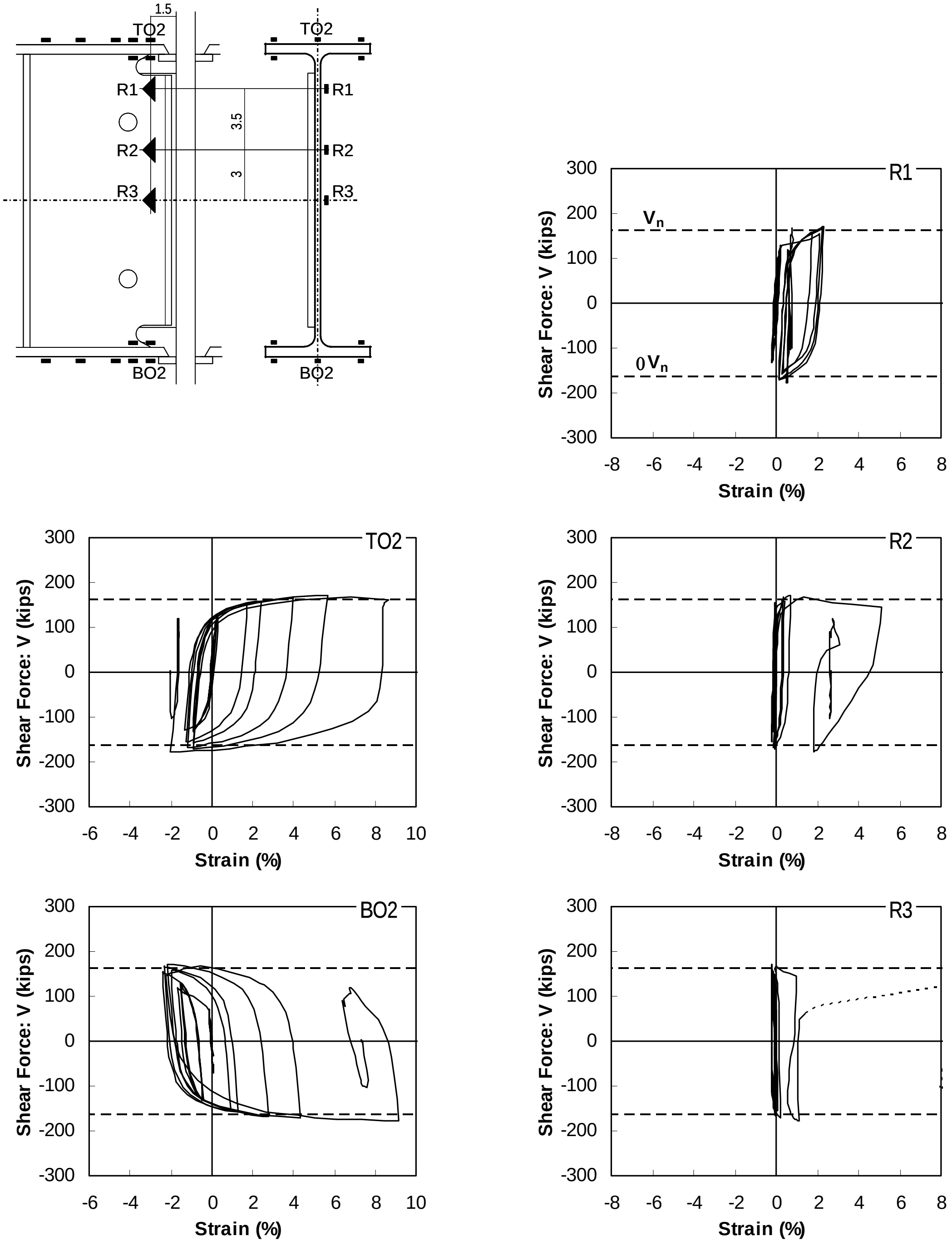

Figure G11 Specimen MWI: Bending stress near column face

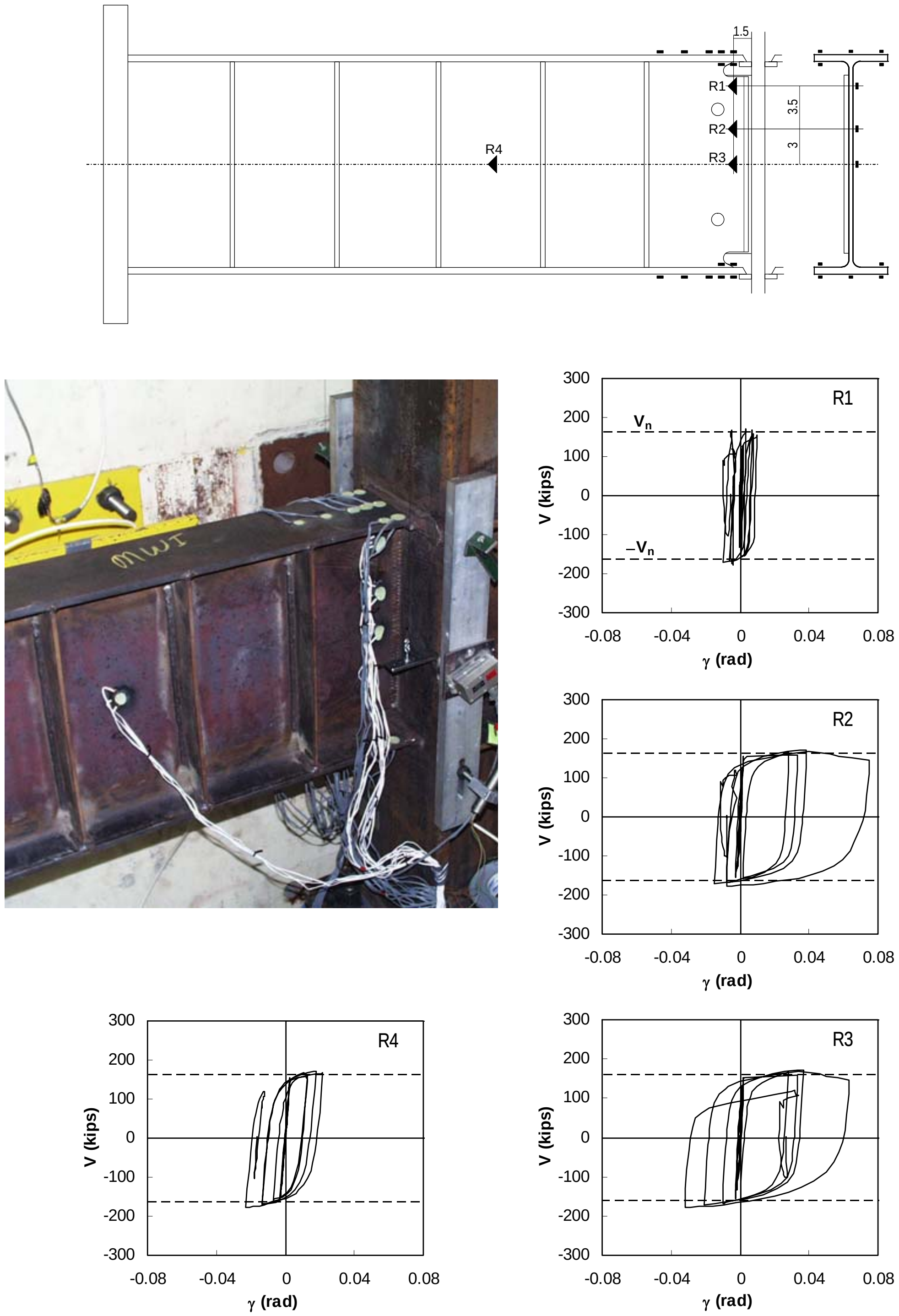

Figure G12 Specimen MWI: Web panel shear stress

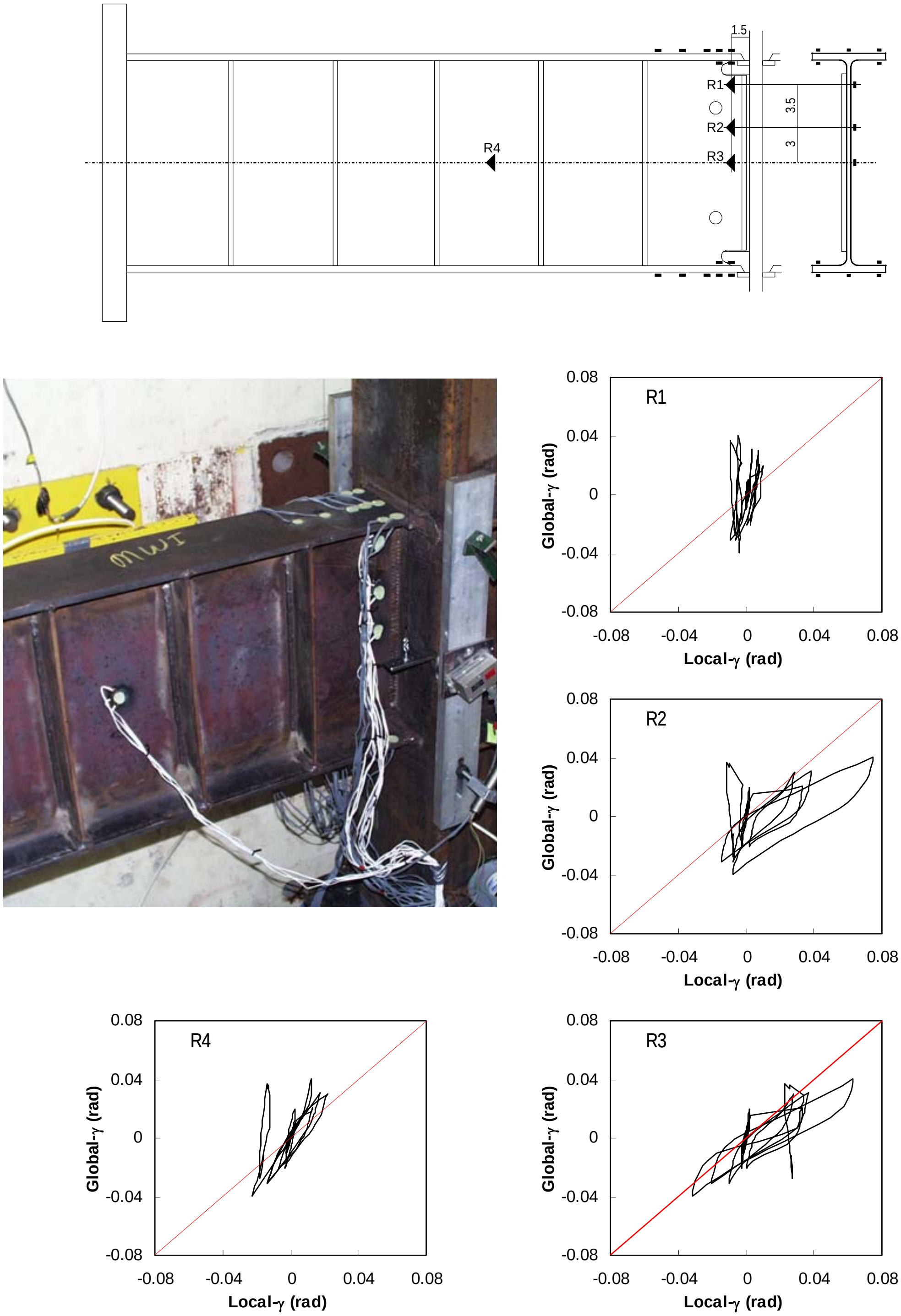

Figure G12 Specimen MWI: Web panel shear stress (Continued)

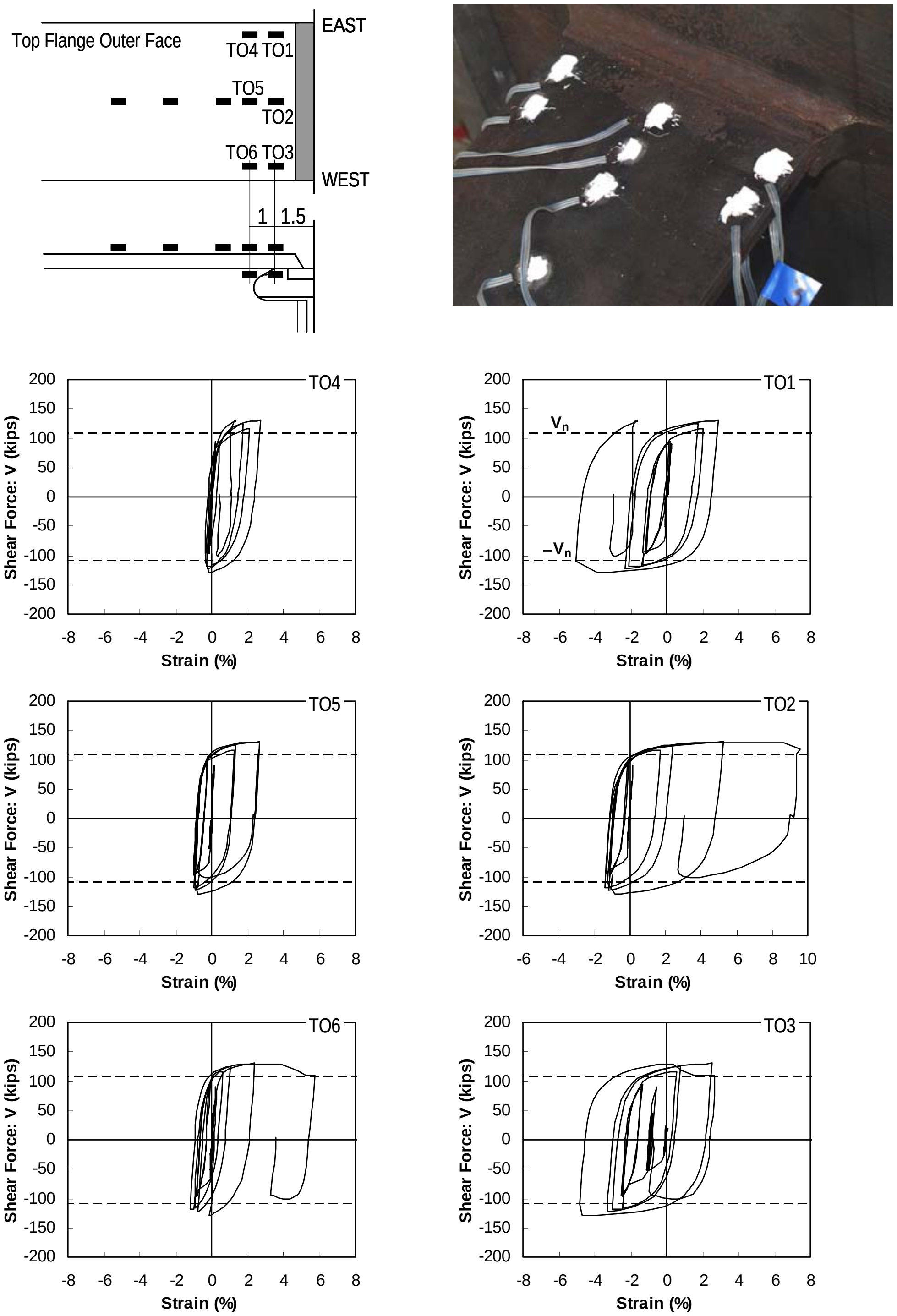

Figure G13 Specimen MWM: Top flange outer face

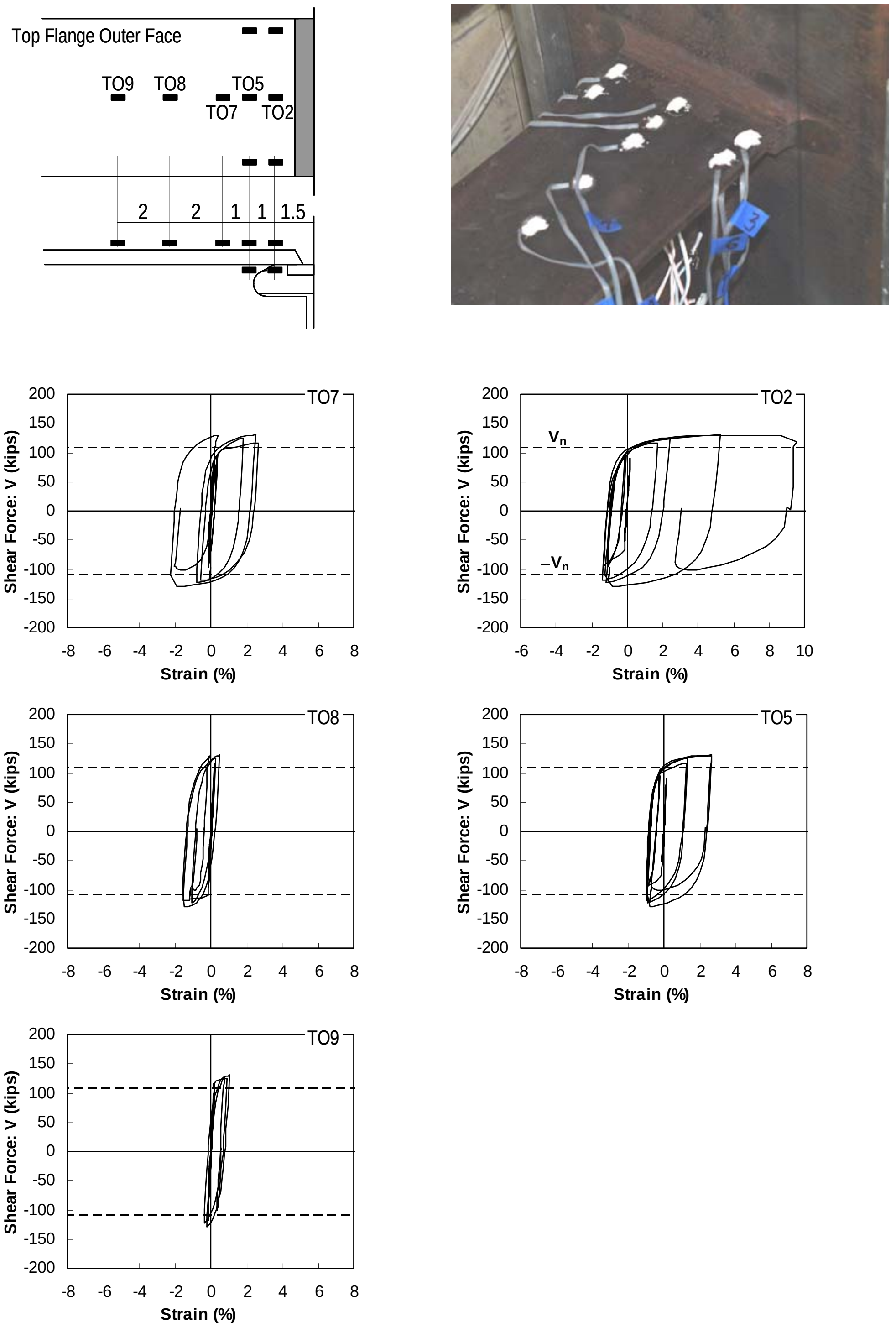

Figure G13 Specimen MWM: Top flange outer face (Continued)

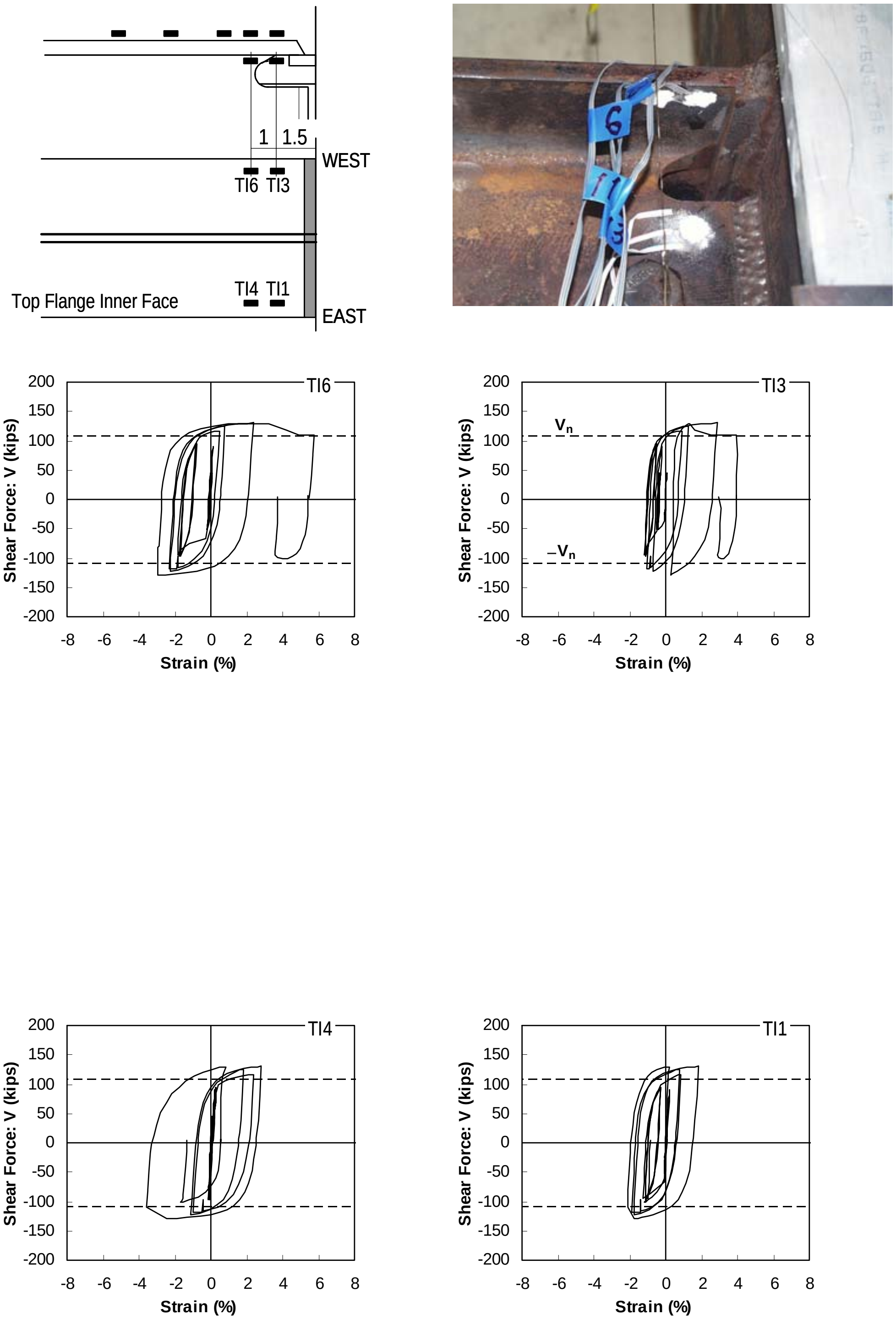

Figure G14 Specimen MWM: Top flange inner face

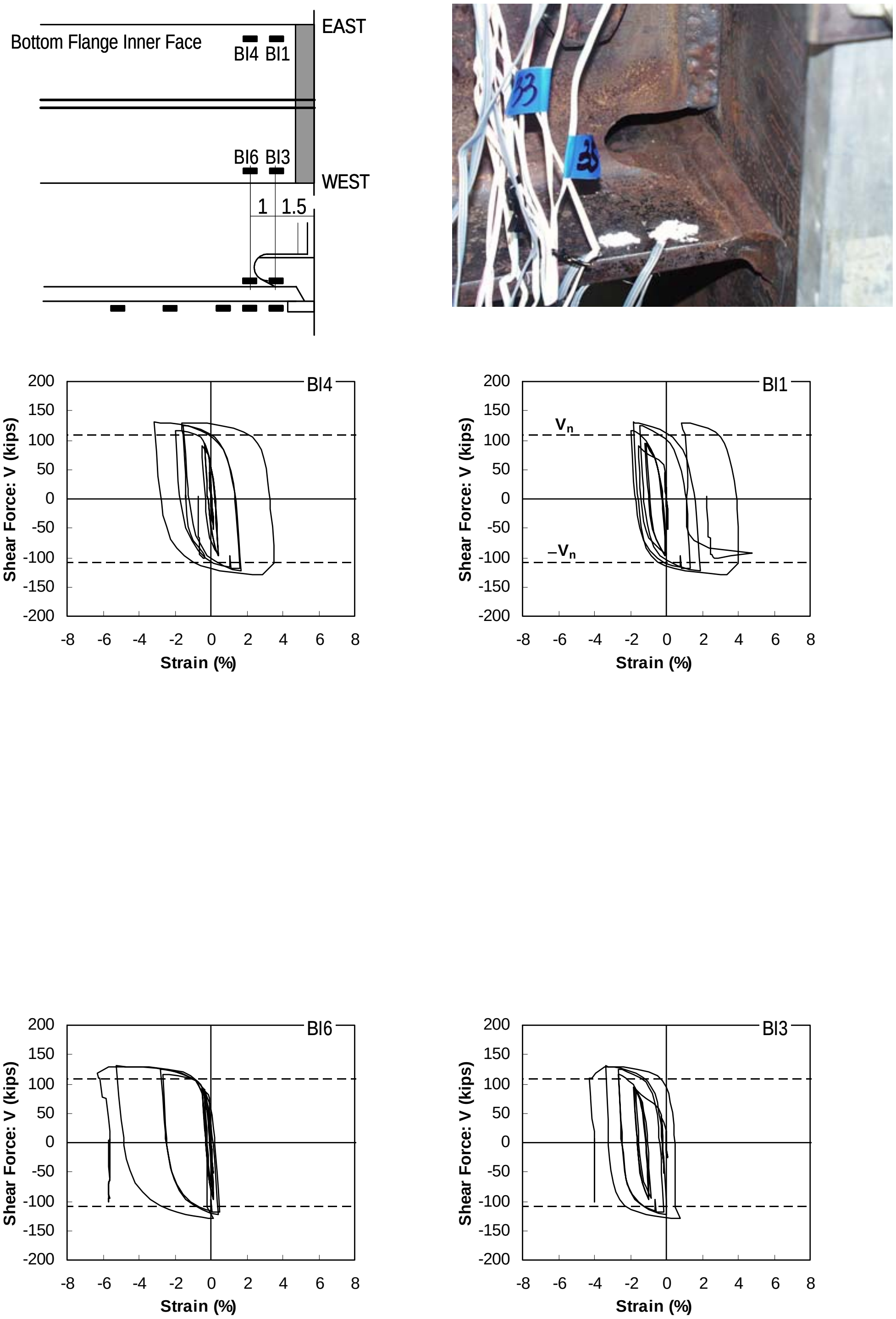

Figure G15 Specimen MWM: Bottom flange inner face

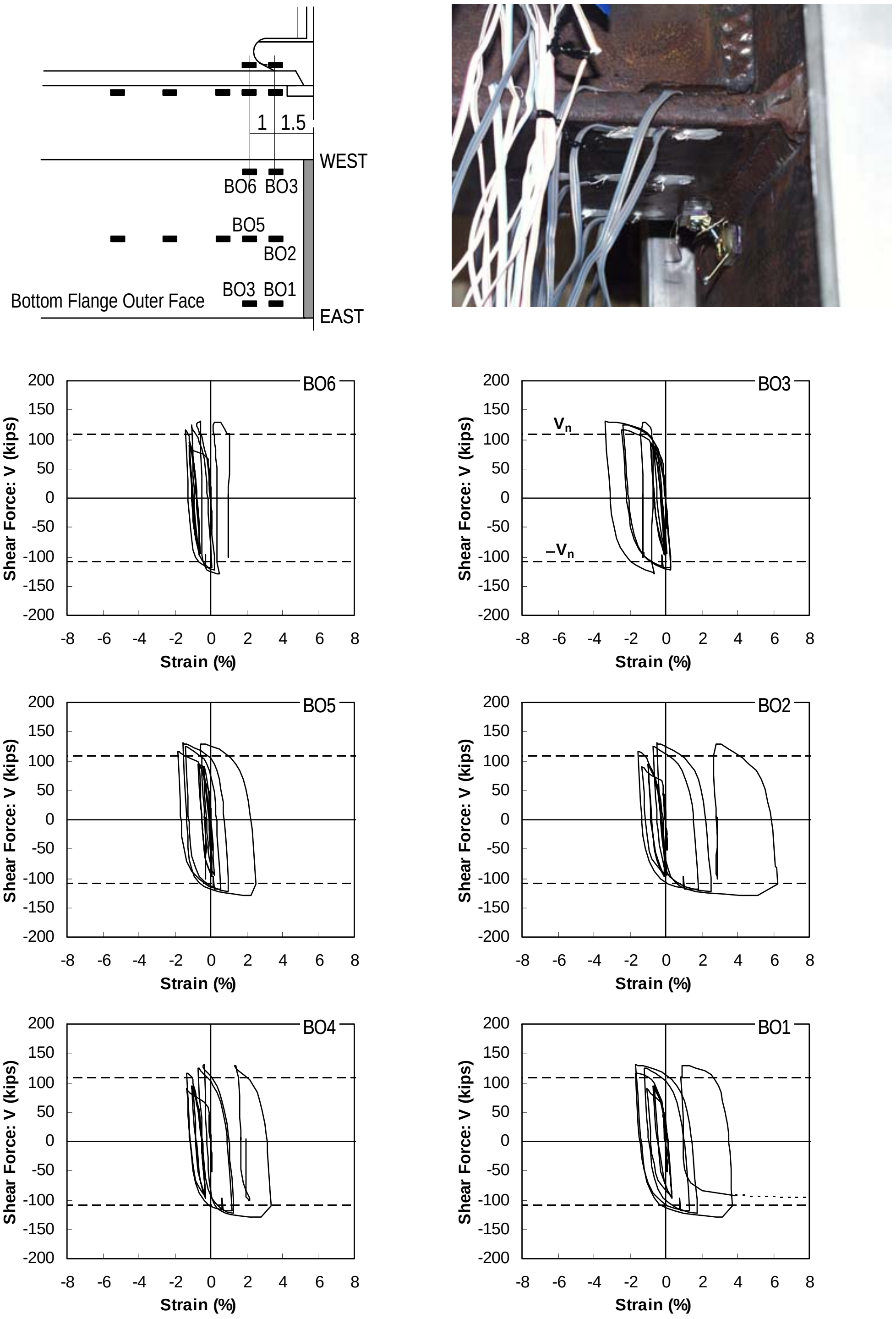

Figure G16 Specimen MWM: Bottom flange outer face

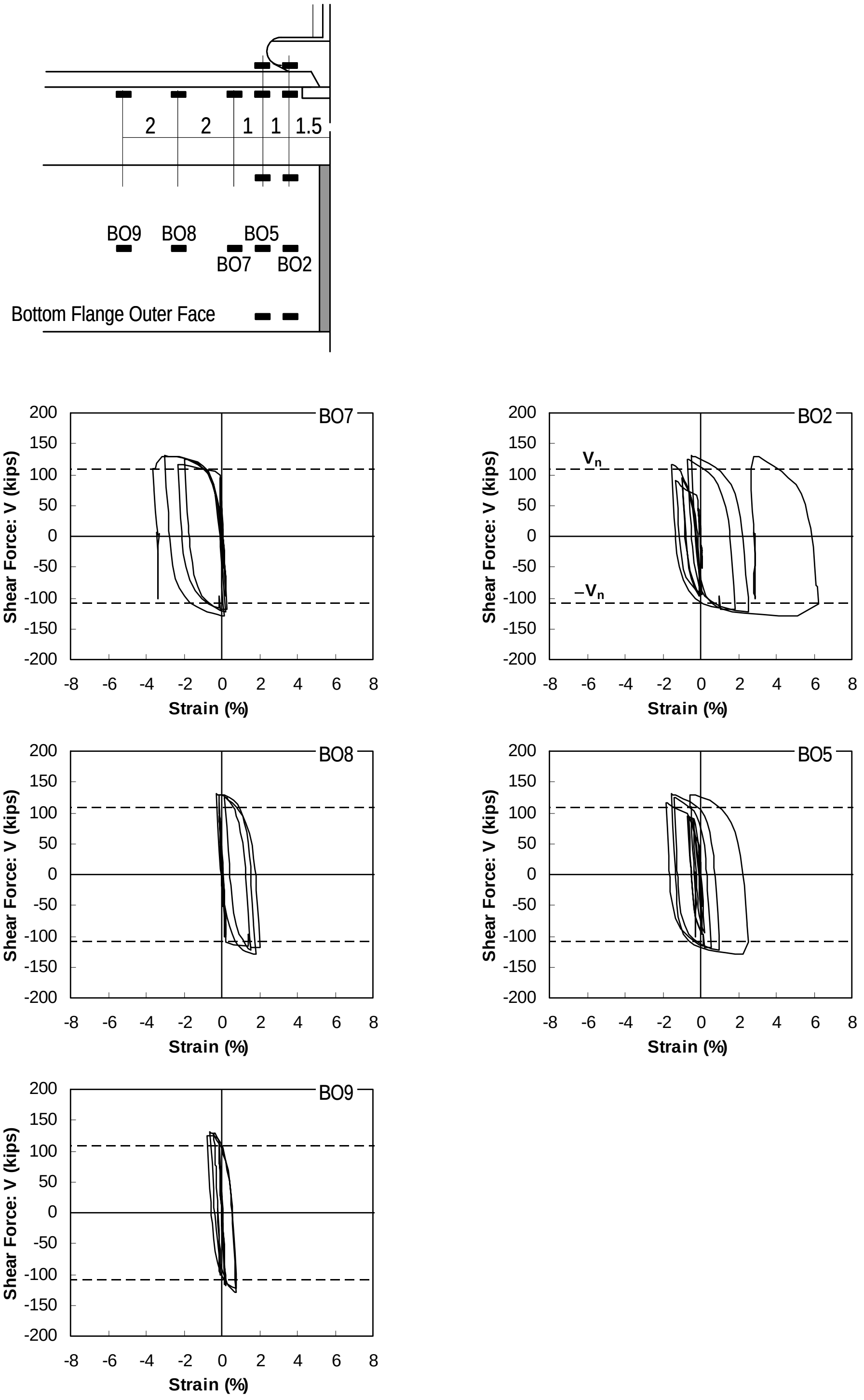

Figure G16 Specimen MWM: Bottom flange outer face (Continued)

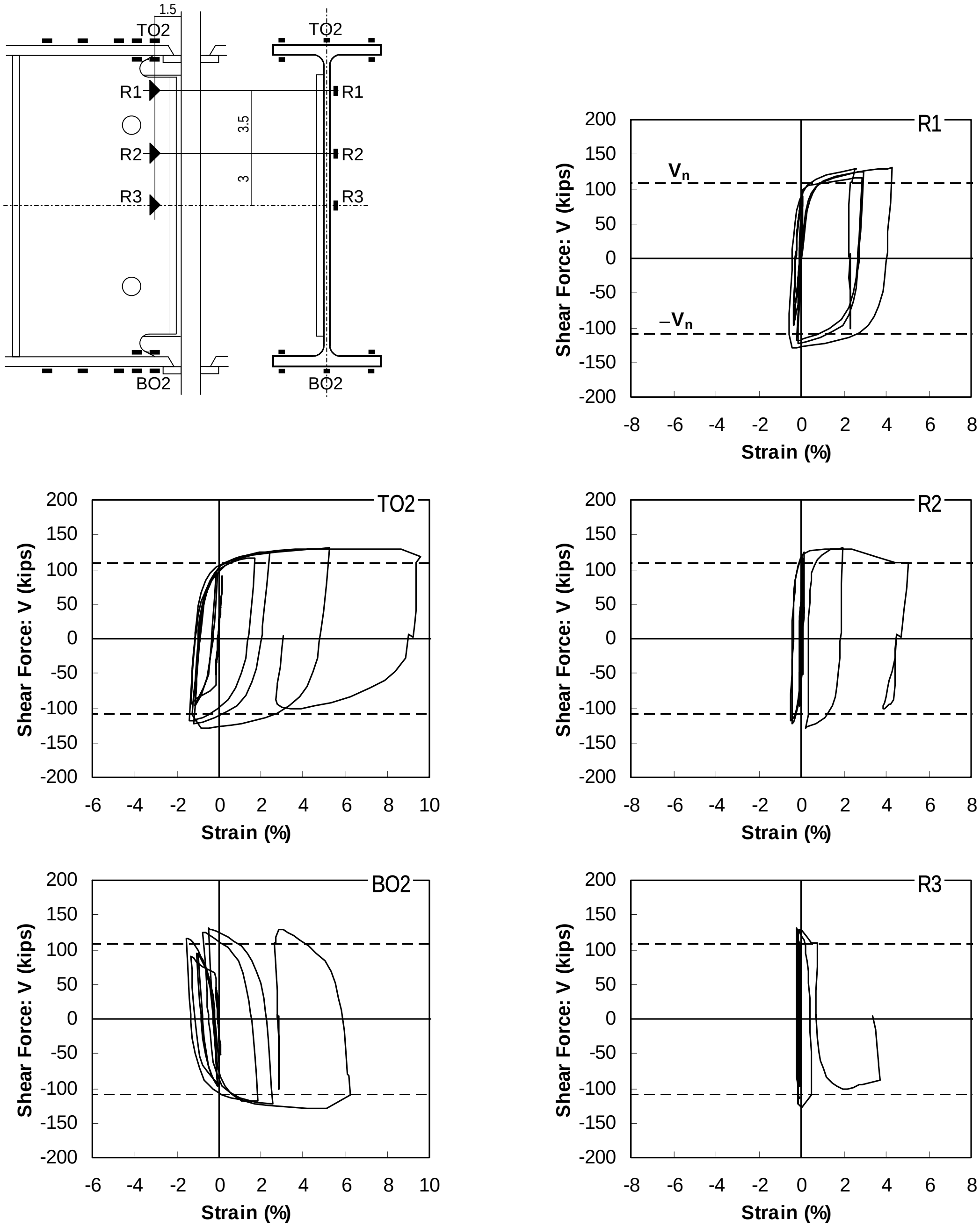

Figure G17 Specimen MWM: Bending stress near column face

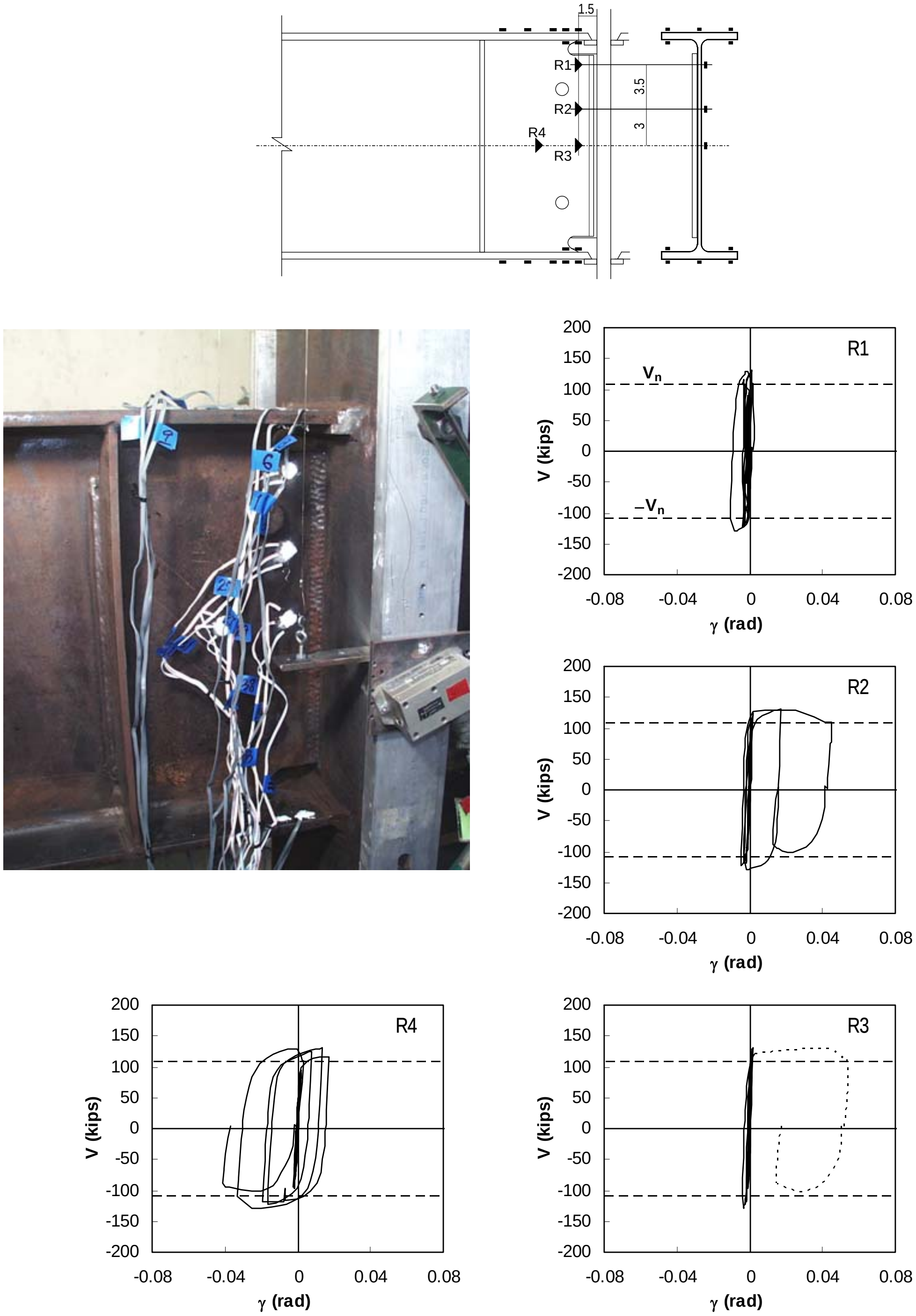

Figure G18 Specimen MWM: Web panel shear stress

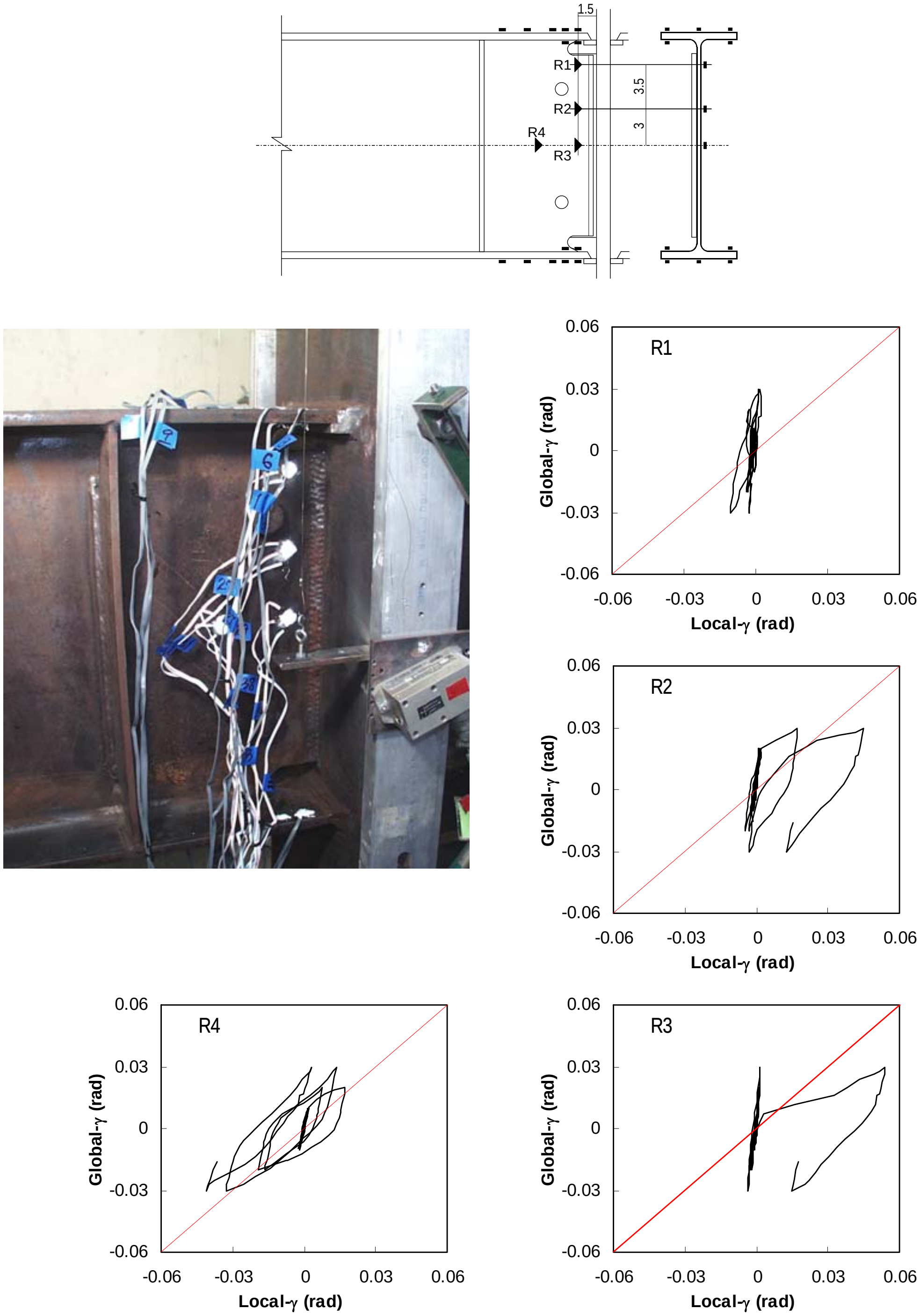

Figure G18 Specimen MWM: Web panel shear stress (Continued)

References

ABAQUS/Standard User's Manual. (2003). Hibbitt, Karlsson, & Sorensen, Inc., Pawtucket , RI.

Kato, B. and Akiyama, H. (1969). "Inelastic bar subjected to thrust and cyclic bending." *Journal of the Structural Division*, American Society of Civil Engineers, 95(ST1), 33-56.

Akiyama, H. (1985). Earthquake-resistant limit-state design for buildings. University of Tokyo Press, Tokyo, Japan.

An, G.-B., Ohata, M., and Toyoda, M. (2003). "Effect of strength miss-match and dynamic loading on ductile fracture initiation." *Engineering Fracture Mechanics*, 70, 1359-1377.

Arce, G. (2002). "Impact of higher strength steels on local buckling and overstrength of links in eccentrically braced frames." *Master's Thesis*, The University of Texas at Austin, Austin, TX.

Asai, H. and Suita, K. (2004). "Comparison of weld provisions and seismic capacity of welded connections in Japan and the United States." *Journal of Steel Construction Engineering*, Japan Society of Steel Construction, (Accepted for publication, in Japanese).

Bartlett, F.M., Dexter, R.J., Greaser, M.D. Jelinek, J.J., Schimidt, B.J. and Galambos, T.V. (2001). "Updating standard shape material properties database foe design and reliability (k-area 4)." *Technical report for American Institute for Steel Construction*, University of Western Ontario, London, Canada.

Barsom, J.M. and Rolfe, S.T. (1999). *Fracture and fatigue control in structures — Applications of fracture mechanics. Third Edition*, Butterworth-Heinemann, Woburn, MA.

Bertero, V.V., Popov, E.P., and Krawinkler, H. (1972). "Beam-to-column subassemblages under repeated loading." *Journal of the Structural Division*, American Society of Civil Engineers, 98(ST5), 1137-1159.

Bertero, V.V., Anderson, J.C., and Krawinkler, H. (1994). "Performance of steel building structures during the Northridge Earthquake." *Report No. UCB/EERC-94/09*, Earthquake Engineering Research Center, University of California, Berkeley, CA.

Bruneau, M., Uang, C.-M., and Whittaker, A. (1998). *Ductile design of steel structures*. McGraw Hill, New York, NY.

Chen, S.-J., Tsao, Yeh, C.H., and Chu, J.M. (1996). "Ductile steel beam-to-column connections for seismic resistance." *Journal of Structural Engineering*, American Society of Civil Engineers, 122(11), 1292-1299.

Chen, S.-J. and Chao, Y.C. (1997). "Dynamic behavior of steel frames with beam flanges shaved around connection." *Journal of Constructional Steel Research*, 42(1), 49-70.

Chen, S.-J., Tsao, Y.C., and Chao, Y.C. (2001a). "Enhancement of ductility of existing seismic steel moment connections." *Journal of Structural Engineering*, American Society of Civil Engineers, 127(5), 538-545.

Chen, S.-J. and Chao, Y.C. (2001b). "Effect of composite action on seismic performance of steel moment connections with reduced beam sections." *Journal of Constructional Steel Research*, 57, 417-434.

Chi, B., and Uang, C.-M. (2002). "Cyclic performance and design recommendations of reduced beam section moment connections with deep columns." *Journal of Structural Engineering*, American Society of Civil Engineers, 128(4), 464-473.

Chi, W.-M., Deierlein, G.G., and Ingraffea, A. (2000). "Fracture toughness demands in welded beam-column moment connections." *Journal of Structural Engineering*, American Society of Civil Engineers, 126(1), 88-97.

Choi, J.-H., Stojadinovic, B. and Goel, S.C. (2000). "Parametric tests on the free flange moment connections." *Report No. SAC/BD-00/02*, SAC Joint Venture, Sacramento, CA.

Choi, J.-H., Stojadinovic, B. and Goel, S.C. (2003). "Design of free flange moment connection." *Engineering Journal*, AISC, 40(1), 1-44.

Christopoulos, C., Filiatrault, A., Uang, C.-M., and Folz, B. (2002). "Posttensioned energy dissipating connections for moment-resisting frames." *Journal of Structural Engineering*, American Society of Civil Engineers, 128(9), 1111-1120.

Civjan, S.A., Engelhardt, M.D., and Gross, J. (2000). "Retrofit of pre-Northridge moment-resisting connections." *Journal of Structural Engineering*, American Society of Civil Engineers, 126(4), 445-452.

Civjan, S.A., Engelhardt, M.D., and Gross, J. (2001). "Slab effects in SMRF retrofit connection tests." *Journal of Structural Engineering*, American Society of Civil Engineers, 127(3), 230-237.

Clark, P., Frank, K., Krawinkler, H., and Shaw, R. (1997). "Protocol for fabrication, inspection, testing, and documentation of beam-column connection tests and other experimental specimens." *Report No. SAC/BD-97/02*, SAC Joint Venture, Sacramento, CA.

Counsel on New Frame Systems (CNFS). (2003). "Manual for the design and fabrication of square tube column-to-wide flange beam connection using vertical stiffeners and omitting through diaphragms." *Technical Report*.

Dexter, R.J., Graeser, M.D., Saari, W.K., Pascoe, C., Gardner, C.A., and Galambos, T.V. (2000). "Structural shape material property survey." *Final Report to the Structural Shape Producers Council*, University of Minnesota, Minneapolis, MN.

Dexter, R.J. and Melendrez, M.I. (2000). "Through thickness properties of column flanges in welded moment connections." *Journal of Structural Engineering*, American Society of Civil Engineers, 126(1), 24-31.

Dexter, R.J., Hajjar, J.F., and Lee, D. (2004). "Effect of Column Stiffener Detailing and Weld Fracture Toughness on the Performance of Welded Moment Connections." *European Convention for Constructional Steelwork, Connections in Steel Construction V: Innovations in Steel Connections*, Amsterdam, the Netherlands.

El-Tawil, E., Mikesell, T., S., Vidarsson, and Kunnath, S.K. (1998). "Strength and ductility of FR welded-bolted connections." *Report No. SAC/BC-98/01*, SAC Joint Venture, Sacramento, CA.

El-Tawil, S. (2000). "Panel zone yielding in steel moment connections." *Engineering Journal*, AISC, 37(3), 120-131.

El-Tawil, S., Vidarsson, E., Mikesell, T., and Kunnath, S.K. (1999). "Inelastic behavior and design of steel panel zones." *Journal of Structural Engineering*, American Society of Civil Engineers, 125(2), 183-193.

Engelhardt, M.D. and Popov, E.P. (1989a). "Behavior of long links in eccentrically braced frames." *Report No. UCB/EERC-89/01*, Earthquake Engineering Research Center, University of California, Berkeley, CA.

Engelhardt, M.D. and Popov, E.P. (1989b). "On design of eccentrically braced frames." *Earthquake Spectra*, 5(3).

Engelhardt, M.D. and Popov, E.P. (1992). "Experimental performance of long links in eccentrically braced frames." *Journal of Structural Engineering*, American Society of Civil Engineers, 118(11), 3067-3088.

Engelhardt, M.D., Tsai, K.C., and Popov, E.P. (1992). "Stability of beams in eccentrically braced frames." *Proceedings of the US-Japan Joint Seminar on Stability and Ductility of Steel Structures under Cyclic Loading*, Osaka. Fukumoto, Y. and Lee, G.C., CRC Press, Boca Raton, FL, 99-112

Engelhardt, M.D. and Husain, A.S. (1993). "Cyclic-loading performance of welded flange-bolted web connections." *Journal of Structural Engineering*, 119(12), 3537-3550.

Engelhardt, M.D. and Sabol, T.A. (1994). "Testing of welded steel moment connections in response to the Northridge earthquake." *Progress report to the AISC advisory Subcommittee on Special Moment Resisting Frame Research*.

Engelhardt, M.D. and Sabol, T.A. (1997). "Seismic-resistant steel moment connections: developments since the 1994 Northridge earthquake." *Progress in Structural Engineering and Materials*, 1(1), 68-77.

Engelhardt, M.D., Winneberger, T. Zekany, A.J., and Potyraj, T.J. (1998a). "Experimental investigation of dogbone moment connections." *Engineering Journal*, AISC, 35(4), 128-139.

Engelhardt, M.D. and Sabol, T.A. (1998). "Reinforcing of steel moment connections with cover plates: benefits and limitations." *Engineering Structures*, 20(4-6), 510-520.

Engelhardt, M.D. (1999) "The 1999 T. R. Higgins Lecture: Design of Reduced Beam Section Moment Connections," *Proceedings: 1999 North American Steel Construction Conference*, American Institute of Steel Construction, Toronto, Canada, pp. 1-1 to 1-29.

FEMA-267. Interim guidelines: Evaluation, repair, modification and design of welded steel moment frame structures. (1995). Prepared by the SAC joint venture for the Federal Emergency Management Agency (FEMA), Washington, DC.

FEMA-350. Recommended seismic design criteria for new steel moment-frame buildings. (2000). Prepared by the SAC joint venture for the Federal Emergency Management Agency (FEMA), Washington, DC.

FEMA-351. Recommended seismic evaluation and upgrade criteria for existing welded steel moment-frame buildings. (2000). Prepared by the SAC joint venture for the Federal Emergency Management (FEMA), Washington, DC.

FEMA-355A. State of the art report on base metals and fracture. (2000). Prepared by the SAC joint venture for the Federal Emergency Management Agency (FEMA), Washington, DC.

FEMA-355D. State of the art report on connection performance. (2000). Prepared by the SAC joint venture for the Federal Emergency Management Agency (FEMA), Washington, DC.

FEMA-355E. State of the art report on past performance of steel moment-frame buildings in earthquakes. (2000). Prepared by the SAC joint venture for the Federal Emergency Management Agency (FEMA), Washington, DC.

Foutch, D.A. (1989). "Seismic behavior of eccentrically braced steel building." *Journal of Structural Engineering*, American Society of Civil Engineers, 115(8), 1857-1876.

Full-scale test on plastic rotation capacity of steel wide-flange beams connected with square tube columns. (1997). Kinki Branch, Architectural Institute of Japan, Osaka, Japan (in Japanese with attached abridged English version).

Galvez, P. (2004). "Investigation of factors affecting web fractures in shear links." *Master's Thesis*, The University of Texas at Austin, Austin, TX.

Ghobarah. A., and Ramadan, T. (1994). "Bolted link-column joints in eccentrically braced frames." *Engineering Structures*, 16(1), 33-41.

Gilton, C.S., Chi, B., and Uang, C.-M. (2000). "Cyclic testing of a free flange moment connection." *Report No. SAC/BD-00/19*, SAC Joint Venture, Sacramento, CA.

Gilton, C.S. and Uang, C.-M. (2002). "Cyclic response and design recommendations of weak-axis reduced beam section moment connections." *Journal of Structural Engineering*, American Society of Civil Engineers, 128(4), 452-463.

Goel, S.C., Stojadinovic, B., and Lee, K.-H. (1997). "Truss analogy for steel moment connections." *Engineering Journal*, AISC, 33(2), 43-53.

Gross, J.L., Engelhardt, M.D., Uang, C.M., Kasai, K., and Iwankiv, N.R. (1999). "Modification of existing welded steel moment frame connections for seismic resistance." *Steel Design Guideline Series No. 12*, American Institute of Steel Construction, Chicago, IL.

Gupta, A., and Krawinkler, H. (1999). "Prediction of seismic demands for SMRFs with ductile connection and elements." *Report No. SAC/BD-99/06*, SAC Joint Venture, Sacramento, CA.

Hajjar, J.F., Leon, R.T., Gustafson, M.A., and Shield, C.K. (1998). "Seismic response of composite moment-resisting connections. II: Behavior." *Journal of Structural Engineering*, American Society of Civil Engineers, 124(8), 877-885.

Hancock, J.W. and Mackenzie, A.C. (1976). "On the mechanisms of ductile failure in high-strength steel subjected to multi-axial stress-states." *Journal of the Mechanics and Physics of Solids*, 24, 147-169.

Hjelmstad, K.D. and Popov, E.P. (1983a). “Seismic behavior of active beam links in eccentrically braced frames.” *Report No. UCB/EERC-83/24*, Earthquake Engineering Research Center, University of California, Berkeley, CA.

Hjelmstad, K.D. and Popov, E.P. (1983b). “Cyclic behavior and design of link beams.” *Journal of the Structural Division*, American Society of Civil Engineers, 109(10), 2387-2403.

Hjelmstad, K.D. and Popov, E.P. (1984). “Characteristics of eccentrically braced frames.” *Journal of Structural Engineering*, American Society of Civil Engineers, 110(2), 340-353.

Ichinohe, Y. and Kuwamura, H. (2000). “Effects of deflection amplitude on brittle fracture of steel members. — Research of steel fracture Part 3.” *Journal of Structural and Construction Engineering*, Architectural Institute of Japan, 534, 145-151. (in Japanese).

Itani, A.M., Douglas, B.M., and El-Fass, S. (1998). “Cyclic behavior of shear links in retrofitted Richmond-San Rafael Bridge towers.” *Proceedings of the First World Congress on Structural Engineering* — San Francisco, Paper No. T155-3, Elsevier Science Ltd.

Itani, A.M., Elfass, S., and Douglas, B.M. (2003). “Behavior of built-up shear links under large cyclic displacement.” *Engineering Journal*, AISC, 40(4), 221-234.

Iwankiv, N. (1997). “AISC advisory statement on mechanical properties near the fillet of wide flange shapes and interim recommendations. January 10, 1997” *Modern Steel Construction*, AISC, Chicago, IL.

Iwankiv, N. and Zoruba, S. (2002). “Steel moment frames: resolution of recent seismic detailing and material shape issues.” *Journal of Constructional Steel Research*, 58, 495-510.

Johnson, M.Q., Mohr, W., and Barsom, J. (2000). “Evaluation of mechanical properties in full-scale connections and recommended minimum weld toughness for moment resisting frames.” *Report No. SAC/BD-00/14*, SAC Joint Venture, Sacramento, CA.

Jones, S.L., Fry, G.T., and Engelhardt, M.D. (2002). “Experimental evaluation of cyclically loaded reduced beam section moment connections.” *Journal of Structural Engineering*, American Society of Civil Engineers, 128(4), 441-451.

Kasai, K. and Popov, E.P. (1986a). “A study of seismically resistant eccentrically braced frames.” *Report No. UCB/EERC-86/01*, Earthquake Engineering Research Center, University of California, Berkeley, CA.

Kasai, K. and Popov, E.P. (1986b). “General Behavior of WF steel shear link beams.” *Journal of Structural Engineering*, 112(2), 362-382.

Kasai, K. and Popov, E.P. (1986c). “Cyclic web buckling control for shear link beams.” *Journal of Structural Engineering*, American Society of Civil Engineers, 112(3), 505-523.

Kaufmann E.J. and Fisher, J.W. (1995). “Fracture analysis of failed moment frame weld joints produced innfull scale laboratory tests and buildings damaged in the Northridge earthquake.” *Technical Report: Experimental investigation of material, weldments, and nondestructtive examination techniques. Report No. SAC 95-08*. SAC Joint Venture, Sacramento, CA.

Kauffman, E.J. (1997). “Dynamic tension tests of simulated moment resisting frame weld joints.” *Steel Tips*, Structural Steel Engineering Council, Moraga, CA.

Kaufmann, E.J., Fisher, J.W., Di Julio, R.M., and Gross, J.L. (1997). “Failure analysis of welded steel moment frames damaged in the Northridge earthquake.” *NISTIR 5944*, National Institute of Standards and Technology, Gaithersburg, MD.

Kim, T., Whittaker, A.S., Gilani, A. S., Bertero, V.V., and Takhirov, S.M. (2002a). “Cover-plate and flange-plate steel moment-resisting connections.” *Journal of Structural Engineering*, American Society of Civil Engineers, 128(4), 474-482.

Kim, T., Whittaker, A.S., Gilani, A. S., Bertero, V.V., and Takhirov, S.M. (2002b). “Experimental evaluation of plate-reinforced steel moment-resisting connections.” *Journal of Structural Engineering*, American Society of Civil Engineers, 128(4), 483-491.

Krawinkler, H., Beretero, V.V., and Popov, E.P. (1971). “Inelastic behavior of steel beam-to-column subassemblages.” *Report No. UCB/EERC-71/07*, Earthquake Engineering Research Center, University of California, Berkeley, CA.

Krawinkler, H. (1978). “Shear in beam-column joints in seismic design of steel frames.” *Engineering Journal*, AISC, 15(3), 82-91.

Krawinkler, H., Gupta, A., Medina, R., and Luco, N. (2000). “Loading histories for seismic performance of testing of SMRF components and assemblies.” *Report No. SAC/BD-00/10*, SAC Joint Venture, Sacramento, CA.

Kuwamura, H. and Yamamoto, K. (1997). “Ductile crack as a trigger of brittle fracture in steel.” *Journal of Structural Engineering*, American Society of Civil Engineers, 123(6), 729-735.

Kuwamura, H. and Takagi, N. (2004). “Similitude law of prefracture hysteresis of steel members.” *Journal of Structural Engineering*, American Society of Civil Engineers, 130(5), 752-761.

Lee, C.-H. and Uang, C.-M. (2001). “Analytical modeling and seismic design of steel moment connections with welded straight haunch.” *Journal of Structural Engineering*, American Society of Civil Engineers, 127(9), 1028-1035.

Lee, C.-H., Jung, J.-H., and Uang, C.-M. (2003). “Cyclic seismic testing of steel moment connections reinforced with welded straight haunch.” *Engineering Structures*, 25, 1743-1753.

Lee, K.-H. (1998). “Boundary effects in welded steel moment connections.” Technical *Report UMCEE 97-20*, Department of Civil and Environmental Engineering, The University of Michigan, Ann Arbor, MI.

Lee, S., Suita, K., and Inoue, K. (2002). “Plastic deformation capacity of perforated reduced beam section moment connection.” *Journal of Steel Construction Engineering*, Japan Society of Steel Construction, 9(36), 47-54.

Leon, R.T., Hajjar, J.F., and Gustafson, M.A. (1998). “Seismic response of composite moment-resisting connections. I: Performance.” *Journal of Structural Engineering*, American Society of Civil Engineers, 124(8), 868-876.

Libby, J.R. (1981). “Eccentrically braced frames construction — A case history.” *Engineering Journal*, AISC, 18(4), 149-153.

Malley, J.O., and Popov, E.P. (1983). “Design considerations for shear links in eccentrically braced frames.” *Report No. UCB/EERC-83/24*, Earthquake Engineering Research Center, University of California, Berkeley, CA.

Malley, J.O. and Popov, E.P. (1984). “Shear links in eccentrically braced frames.” *Journal of the Structural Division*, American Society of Civil Engineers, 110(ST9), 2275-2295.

Manual of Steel Construction. Load and Resistance Factor Design Specification for Structural Steel Buildings. Third Edition. (1999). American Institute of Steel Construction, Inc. (AISC), Chicago, IL.

Mao, C., Ricles, J., Lu, L.-W., and Fisher, J. (2001). “Effect of local details on ductility of welded moment connections.” *Journal of Structural Engineering*, American Society of Civil Engineers, 127(9), 1036-1044.

Matsumoto, Y., Asai, H., and Okazaki, T. (2004). “Comparison of design concept and structural performance of beam-to-column connections in Japan and the United

States." *Journal of Steel Construction Engineering*, Japan Society of Steel Construction, (Accepted for publication, in Japanese).

McDaniel, C.C., Uang, C.-M., and Seible, F. (2003). "Cyclic testing of built-up steel shear links for the new Bay Bridge." *Journal of Structural Engineering*, American Society of Civil Engineers, 129(6), 801-809.

Mele, E. (2002). "Moment resisting welded connections: an extensive review of design practice and experimental research in USA, Japan and Europe." *Journal of Earthquake Engineering*, 6(1), 2002, 111-145, Imperial College Press.

Merovich, A.T., Nicoletti, J.P., and Hartle, E. (1982). "Eccentric bracing in tall buildings." *Journal of the Structural Division*, American Society of Civil Engineers, 108(ST9), 2066-2080.

Miller, D.K. (1998). "Lessons learned from the Northridge earthquake." *Engineering Structures*, 20(4-6), 249-260.

Miller, K.R. (1999). "Study of the material properties associated with the web-flange transition region of rolled shapes." *Master's Thesis*, The University of Texas at Austin, Austin, TX.

Nakagomi, T., Yabe, Y., and Sakamoto, S. (1992). "Effect of scallops at beam-end on mechanical behaviors of H-shaped steel beams connected to H-shaped columns." *Journal of Structural and Construction Engineering*, Architectural Institute of Japan, 432, 51-59. (in Japanese).

Nakagomi, T. and Fujita, T. (1994). "Mechanical behavior of rolled H-shaped steel beam connected to square-shaped steel pipe column with through diaphragms — Effect of scallops and unevenness on fracture." *Journal of Structural and Construction Engineering*, Architectural Institute of Japan, 455, 187-196. (in Japanese).

Nakashima, M., Fujiwara, T., Suzuki, Y., Bruneau, M., Iwai, S., and Kitahara, A. (1994). "Damage to engineered buildings from the 1995 Hyogoken-Nambu Earthquake." *Journal of Natural Disaster Science*, 16(2), 71-78.

Nakashima, M., Suita, K., Morisako, K., and Maruoka, Y. (1998). "Tests of welded beam-column subassemblages. I: Global behavior." *Journal of Structural Engineering*, American Society of Civil Engineers, 124(11), 1236-1244.

Nakashima, M., Roeder, C.W., and Maruoka, Y. (2000). "Steel moment frames for earthquakes in United States and Japan." *Journal of Structural Engineering*, American Society of Civil Engineers, 126(8), 861-868.

Nakashima, M., Kanao, I., and Liu, D. (2002). “Lateral instability and lateral bracing of steel beams subjected to cyclic loading.” *Journal of Structural Engineering*, American Society of Civil Engineers, 128(10), 1308-1316.

Plumier, A. (1997). “The Dogbone: Back to the future.” *Engineering Journal*, AISC, 34(2), 61-67.

Popov, E.P. and Pinkney, R.B. (1969). “Cyclic yield reversal in steel building connections.” *Journal of the Structural Division*, American Society of Civil Engineers, 95(ST3), 327-353.

Popov, E.P. and Stephen, R.M. (1970). “Cyclic loading of full-size steel connections.” *Report No. UCB/EERC-70/03*, Earthquake Engineering Research Center, University of California, Berkeley, CA.

Popov, E.P. and Bertero, V.V. (1973). “Cyclic loading of steel beams and connections.” *Journal of the Structural Division*, American Society of Civil Engineers, 99(ST6), 1189-1204.

Popov, E.P. (1987). “Panel zone flexibility in seismic moment joints.” *Journal of Constructional Steel Research*, 8, 91-118.

Popov, E.P., Kasai, K. and Engelhardt, M.D. (1987). “Advances in Design of Eccentrically Braced Frames.” *Earthquake Spectra*, 3(1).

Popov, E.P. and Engelhardt M.D. (1988). “Seismic eccentrically braced frames.” *Journal of Constructional Steel Research*, 10, 321-354.

Popov, E.P., Engelhardt, M.D., and Ricles, J.M. (1989a). “Eccentrically braced frames: U.S. practice.” *Engineering Journal*, AISC, 26(2), 66-80.

Popov, E.P. Tsai, K.-C., and Engelhardt, M.D. (1989b). “On seismic steel joints and connections.” *Engineering Structures*, 11(3), 148-162.

Popov, E.P., Ricles, J.M., and Kasai, K. (1992). “Methodology for optimum EBF link design.” *Proceedings of the Tenth World Conference on Earthquake Engineering, Madrid*, 19-24 July 1992, A A Balkema, Rotterdam, 7, 3983-3988.

Popov, E.P., Balan, T.A., and Yang, T.-S. (1998). “Post-Northridge earthquake seismic steel moment connections.” *Earthquake Spectra*, 14(4), 659-677.

Popov, E.P., Yang, T.-S., and Chang, S.-P. (1998). “Design of steel MRF connections before and after 1994 Northridge earthquake.” *Engineering Structures*, 20(12), 1030-1038.

Reconnaissance report on damage to steel building structures observed from the 1995 Hyogoken-Nanbu (Hanshin/Awaji) Earthquake. (1997). Kinki Branch, Architectural Institute of Japan, Osaka, Japan (in Japanese with attached abridged English version).

Rice, J.R. and Tracey, D.M. (1969). "On the ductile enlargement of voids in triaxial stress fields." *Journal of the Mechanics and Physics of Solids*, 17, 201-217.

Richards P. and Uang, C.M. (2002). "Evaluation of rotation capacity and overstrength of links in eccentrically braced frames." *Report No. SSRP-2002/108*, Department of Structural Engineering, University of California, San Diego, CA.

Richards P. and Uang, C.M. (2003). "Development of testing protocol for short links in eccentrically braced frames." *Report No. SSRP-2003/08*, Department of Structural Engineering, University of California, San Diego, CA.

Richards P. and Uang, C.M. (2004a). "Effect of flange width-thickness ration on EBF link cyclic rotation capacity." *Journal of Structural Engineering*, American Society of Civil Engineers. (Submitted for publication).

Richards P. and Uang, C.M. (2004b). "Testing protocol for short links in eccentrically braced frames." *Journal of Structural Engineering*, American Society of Civil Engineers. (Submitted for publication).

Richards P. and Uang, C.M. (2004c). "Recommended EBF link loading protocol for the AISC Seismic Provisions." *Technical Note*.

Ricles, J.M. and Popov, E.P. (1987a). "Dynamic analysis of seismically resistant eccentrically braced frames." *Report No. UCB/EERC-87/07*, Earthquake Engineering Research Center, University of California, Berkeley, CA.

Ricles, J.M. and Popov, E.P. (1987b). "Experiments on eccentrically braced frames with composite floors." *Report No. UCB/EERC-87/06*, Earthquake Engineering Research Center, University of California, Berkeley, CA.

Ricles, J.M. and Popov, E.P. (1989). "Composite action in eccentrically braced steel frames." *Journal of Structural Engineering*, American Society of Civil Engineers, 115(8), 2064-2066.

Ricles, J.M. and Popov, E.P. (1994). "Inelastic link element for EBF seismic analysis." *Journal of Structural Engineering*, American Society of Civil Engineers, 120(2), 441-463.

Ricles, J.M., Sause, R., Garlock, M.M., and Zhao, C. (2001). "Posttentioned seismic-resistant connections for steel frames." *Journal of Structural Engineering*, American Society of Civil Engineers, 127(2), 113-121.

Ricles, J.M., Mao, C, Lu, L.-W., and Fisher, J.W. (2002). "Inelastic cyclic testing of welded unreinforced moment connections." *Journal of Structural Engineering*, American Society of Civil Engineers, 128(4), 429-440.

Roeder, C.W. and Popov, E.P. (1977). "Inelastic behavior of eccentrically braced steel drames under cyclic loading." *Report No. UCB/EERC-77/18*, Earthquake Engineering Research Center, University of California, Berkeley, CA.

Roeder, C.W. and Popov, E.P. (1978a). "Eccentrically braced frames for earthquakes." *Journal of the Structural Division*, American Society of Civil Engineers, 104(ST3), 391-412.

Roeder, C.W. and Popov, E.P. (1978b). "Cyclic shear yielding of wide-flange beams." *Journal of Engineering Mechanics*, American Society of Civil Engineers, 104(4), 763-780.

Roeder, C.W., Foutch, D.A., and Goel, S.C. (1987). "Seismic testing of full-scale steel building—Part II." *Journal of Structural Engineering*, American Society of Civil Engineers, 113(11), 2130-2145.

Roeder, C.W. and Foutch, D.A. (1996). "Experimental results for seismic resistant steel moment frame connections." *Journal of Structural Engineering*, American Society of Civil Engineers, 122(6), 581-588.

Ryu, H.-C. Okazaki, T., and Engelhardt, M.D. (2004). "Cyclic loading tests on shear links for EBFs: Link performance under revised loading protocol." *Unpublished report*.

Seismic Provisions for Structural Steel Buildings. (1992). American Institute of Steel Construction, Inc. (AISC), Chicago, IL.

Seismic Provisions for Structural Steel Buildings. (1997). American Institute of Steel Construction, Inc. (AISC), Chicago, IL.

Seismic Provisions for Structural Steel Buildings. (1997) Supplement No. 2. (2000). American Institute of Steel Construction, Inc. (AISC), Chicago, IL.

Seismic Provisions for Structural Steel Buildings. (2002). ANSI/AISC Standard 341-02, American Institute of Steel Construction, Inc. (AISC), Chicago, IL.

Shuey, B.D., Engelhardt, M.D. and Sabol, T.A., (1996) "Testing Repair Concepts for Damaged Steel Moment Connections." Experimental Investigations of Beam-Column Subassemblages; *Report No. SAC 96-01*, SAC Joint Venture, Sacramento, CA.

Stojadinovic, B., Goel, S.C., Lee, K.-H. Margarian, A.G. and Choi, J.-H. (2000). "Parametric tests on unreinforced steel moment connections." *Journal of Structural Engineering*, American Society of Civil Engineers, 126(1), 40-49.

Structural Stability Research Council (SSRC) (1998). "Technical memorandum No. 8: Standard methods and definitions for tests for static yield stress." *Guide to Stability Design Criteria for Metal Structures*, Fifth Edition, Edited by Galambos, T.V. John Wiley & Sons, Inc.

Structural Steelwork Specification for Building Construction: JASS 6. (2000). Japanese Architectural Standard Specification, Architectural Institute of Japan, Tokyo (in Japanese).

Suita, K., Nakashima, M., and Maruoka, Y. (1998). "Tests of welded beam-column subassemblages. II: Detailed behavior." *Journal of Structural Engineering*, American Society of Civil Engineers, 124(11), 1245-1252.

Suita, K., Tamura, T., Morita, S., Nakashima, M., and Engelhardt, M.D. (1999). "Plastic rotation capacity of steel beam-to-column connections using a reduced beam section and no weld access hole design — Full scale tests for improved steel beam-to-column subassemblages — Part 1 —." *Journal of Structural and Construction Engineering*, Architectural Institute of Japan, 526, 177-184. (in Japanese).

Suita, K., Inoue, K., Takeuchi, I., and Uno, N. (2001). "Mechanical behavior of bolted beam-to-column connections with hysteretic damper." *The Third Japan-Korea-Taiwan Joint Seminar on Earthquake Engineering for Building Structures*, Taipei, Taiwan.

Suita, K., Inoue, K., Takeuchi, I., and Uno, N. (2003). "Mechanical behavior of bolted beam-to-column connections with buckling-restrained knee brace dampers." *Journal of Structural and Construction Engineering*, Architectural Institute of Japan, 571, 153-160. (in Japanese).

Tabuchi, M., Tanaka, T., and Iguchi, T. (2002). "Effects of end-tab shapes on plastic deformation capacity of wide-flange beams connected with SHS column." *Journal of Steel Construction Engineering*, Japan Society of Steel Construction, 9(35), 1-16. (in Japanese).

Tanaka, N., Sawamoto, Y., Saeki, T., and Fukada, Y. (1998). "Elasto-plastic behavior of horizontal haunched beam-to-box column connection." *Journal of Steel Construction Engineering*, Japan Society of Steel Construction, 5, 20, 101-111. (in Japanese).

Tateyama, E., Inoue, K., Sugimoto, S., Matsumura, H. (1998). "Study on ultimate bending strength and deformation capacity of H-shaped beam connected to RHS column with through diaphragms." *Journal of Structural and Construction Engineering*, Architectural Institute of Japan, 389, 109-121. (in Japanese).

Tide, R.H.R. (2000). "Evaluation of steel properties and cracking in "k"-area of W shapes." *Engineering Structures*, 22, 128-134.

Tsai, K.-C. and Popov E.P. (1988). "Steel beam-column joints in seismic moment resisting frames." *Report No. UCB/EERC-88/19*, Earthquake Engineering Research Center, University of California, Berkeley, CA.

Tsai, K.C., Engelhardt, M.D., and Nakashima, M. (2000). "Cyclic performance of link-to-box column connections in steel eccentrically braced frames." *The First International Conference on Structural Stability and Dynamics*, Taipei, Taiwan.

Uang, C.-M. Bondad, D., and Lee, C.-H. (1998). "Cyclic performance of haunch repaired steel moment connections: experimental testing and analytical modeling." *Engineering Structures*, 20(4-6), 552-561.

Uang, C.-M. Yu, Q.-S. Noel., S. and Gross, J. (2000). "Cyclic testing of steel moment connections rehabilitated with RBS or welded haunch." *Journal of Structural Engineering*, American Society of Civil Engineers, 126(1), 57-68.

Uang, C.-M. and Fan, C.-C. (2001). "Cyclic stability criteria for steel moment connections with reduced beam section." *Journal of Structural Engineering*, American Society of Civil Engineers, 127(9), 1021-1027.

Venti, M. and Engelhardt, M.D. (2000). "Test of a free flange connection with a composite floor slab." *Report No. SAC/BD-00/18*, SAC Joint Venture, Sacramento, CA.

Whittaker, A.S., Uang C.M. and Bertero, V.V. (1987). "Earthquake simulation test and associated studies of 0.3-scale model of six-story eccentrically braced steel structure." *Report No. UCB/EERC-87/02*, Earthquake Engineering Research Center, University of California, Berkeley, CA.

Whittaker, A.S., Uang C.M. and Bertero, V.V. (1989). "Experimental behavior of dual steel system." *Journal of Structural Engineering*, American Society of Civil Engineers, 115(1), 183-200.

Youssef, N.F.G. and Gross, J.L. (1995). "A survey of steel moment-resisting frames buildings affected by the 1994 Northridge earthquake." *NISTIR 5944*, National Institute of Standards and Technology, Gaithersburg, MD.

Yu, Q.-S., Uang, C.-M., and Gross, J,. (2000). "Seismic rehabilitation design of steel moment connection with welded haunch." *Journal of Structural Engineering*, American Society of Civil Engineers, 126(1), 69-78.

Zhang, X., Ricles, J.M., Fisher, J.W., and Lu, L.W. (2004). “Analytical and experimental studies on seismic behavior of deep column-to-beam welded reduced beam section steel moment connections.” *The Thirteenth World Conference on Earthquake Engineering*, Paper No. 1599, Vancouver, B.C., Canada.

Vita

Taichiro Okazaki was born on September 28, 1971, in Kyoto, Japan, the son of Takeshi Okazaki and Kazuko Okazaki. He graduated from Rakusei High School, Kyoto, Japan in March 1990, and entered the School of Architecture of the Faculty of Engineering, Kyoto University, Japan. He graduated from Kyoto University with the degree of Bachelor of Engineering in March 1994, and entered the Department of Architecture and Architectural Systems of the Graduate School of Engineering, Kyoto University. He received the degree of Master of Engineering from Kyoto University in March 1996. In September 1997, he entered the Ph.D. program in the Department of Civil Engineering and Operations Research at Princeton University. He received the degree of Master of Arts from Princeton University in May 2000. In August 2000, Mr. Okazaki joined the Ph.D. program in the Department of Civil Engineering at the University of Texas at Austin.

Permanent address: 9-10 Iwakubo, Shinomiya, Yamashina,
Kyoto, Kyoto, 607 Japan

This dissertation was typed by Taichiro Okazaki.